

Limestone as a Sorbent for CO₂ Capture and its Application in Enhanced Biomass Gasification

by

James Butler

B.Sc., Queen's University, 2005

M.A.Sc., Dalhousie University, 2007

A THESIS SUBMITTED IN PARTIAL FULFILLMENT OF
THE REQUIREMENTS FOR THE DEGREE OF

DOCTOR OF PHILOSOPHY

in

THE FACULTY OF GRADUATE AND POSTDOCTORAL STUDIES
(Chemical and Biological Engineering)

THE UNIVERSITY OF BRITISH COLUMBIA

(Vancouver)

OCTOBER 2013

© James Butler, 2013

Abstract

Global greenhouse gas emissions continue to increase despite the knowledge that the rise in atmospheric concentrations will have devastating effects on climate and human lives. Carbon dioxide capture and storage can be a stop-gap measure to mitigate CO₂ emissions from existing fossil fuel facilities during their gradual replacement by low-carbon alternatives such as biomass. Calcium oxide-based CO₂ capture is a relatively mature technology, ready for implementation. Limestone CaO precursor is relatively low-cost and readily available. A thorough understanding of the CaO-CO₂ reaction and its reversibility over multiple cycles is required to aid in design, improve efficiency and reduce costs of industrial capture processes. A novel method of CaO cycling involving pressure swing is demonstrated which was found to give improved calcium utilization up to 16.1%, after 250 carbonation/calcination cycles. The kinetics of pressure swing cycling are examined, and a mechanism to describe the loss in calcium utilization resulting from cycling, is presented linking the morphological changes of sorbent particles to the decay in calcium utilization. Coupling CaO-based CO₂ capture and storage with energy production from biomass has the potential for energy production with negative CO₂ emissions.

Biomass is a carbon neutral source of energy and through gasification can be converted in a variety of energy carriers. Biomass was steam-gasified in a semi-batch fashion in a fluidized bed of CaO, which absorbed CO₂ as it was produced, resulting in a 55% increase in hydrogen production and decreases in CO, CH₄, CO₂ and higher hydrocarbons of 63%, 16%, 47% and 4% respectively. Limestone enhanced gasification (L.E.G.) of biomass also increased carbon and hydrogen utilization efficiencies. Cycling of CaO between gasification/carbonation and calcination was conducted in a single reactor by switching the mass flows from biomass and steam to air, up to eight cycles. Syngas composition and gasification efficiency were only marginally affected by cycling, reducing H₂ concentration by less than 5%. The degree to which the sorbent was re-calcined had a greater impact on system operation. A simple equilibrium model is provided to predict syngas composition.

Preface

At the time of writing this thesis, one article has been published and another accepted and awaiting publication. In addition the author has given research talks at three international conferences and several local and national scientific forums. The author carried out all stages of the research described in the published and submitted papers, prepared responses to the reviewer and handled correspondence with the journal editors. The co-authors supervised the work and made minor revisions. The two articles are:

Butler JW, Lim CJ, Grace JR. "CO₂ capture capacity of CaO in long series of pressure swing sorption cycles." Chemical Engineering Research and Design 2011;89:1794–804.

Butler JW, Lim CJ, Grace JR. "Kinetics of CO₂ absorption by CaO through pressure swing cycling." Fuel, Article In Press, 2013.

Chapter 2 of this thesis corresponds to the first paper entitled "CO₂ capture capacity of CaO in long series of pressure swing sorption cycles." Chapter 3 of this thesis corresponds to the second paper entitled "Kinetics of CO₂ absorption by CaO through pressure swing cycling."

Table of Contents

Abstract	ii
Preface	iii
Table of Contents	iv
List of Tables	viii
List of Figures	ix
Nomenclature	xiv
Acknowledgements	xix
Dedication	xx
1 Introduction	1
1.1 CaO Based CO ₂ Capture	2
1.1.1 The Capture Process	5
1.2 Carbonation	7
1.2.1 Reaction-Controlled Carbonation	10
1.2.1.1 Fast Stage Carbonation Kinetics	11
1.2.1.2 Effect of Operating Parameters	12
1.2.2 Diffusion-Controlled Carbonation	13
1.2.3 Ionic Diffusion	15
1.3 Calcination	18
1.3.1 Factors Affecting Calcination	20
1.4 Hydration	21
1.5 CaO - CaCO ₃ Cycling	21
1.5.1 Factors Affecting Utilization Decay	24
1.5.2 Application of CaO Cycling	26
1.6 Sintering of CaO	27
1.6.1 Grain Growth	28

1.6.2	Pore Coarsening.....	29
1.6.3	Factors Affecting Sintering.....	31
1.7	Improving Capture Capacity.....	33
1.7.1	Hydration Reactivation.....	33
1.7.2	Thermal Pretreatment	34
1.7.3	Dolomite	36
1.7.4	Synthetic Sorbents	37
1.8	CaO and Biomass Gasification.....	39
1.8.1	Biomass Gasification.....	39
1.8.2	Sorbent-Enhanced Biomass Gasification.....	43
1.8.3	Modeling.....	46
1.9	Thesis Objectives.....	50
2	CO ₂ Capture Capacity of CaO in Long Series of Pressure Swing Sorption Cycles.....	51
2.1	Introduction.....	51
2.2	Materials and Methods	52
2.3	Results and Discussion	55
2.3.1	Pressure Swing Cycling.....	55
2.3.2	Influence of Sample Size	59
2.3.3	Influence of De-Pressurization Rate.....	61
2.3.4	Pressure Swing Comparison.....	63
2.4	Conclusions.....	64
3	Kinetics of CO ₂ Absorption by CaO through Pressure Swing Cycling	65
3.1	Introduction.....	65
3.2	Materials and Methods	66
3.3	Kinetic Model	67
3.4	Results and Discussion	70

3.4.1	Pressure Swing Cycling	70
3.4.2	Reaction-Controlled Regime	73
3.4.3	Mechanism of Dispersed Contraction	77
3.4.4	Diffusion-Controlled Regime	79
3.5	Conclusions.....	81
4	Limestone-Enhanced Gasification of Biomass: Cyclic Gasification and Regeneration in a Bubbling Fluidized Bed	82
4.1	Introduction.....	82
4.2	Experimental.....	84
4.3	Results and Discussion	90
4.3.1	Effect of Bed Material	90
4.3.2	Effect of Temperature.....	97
4.3.3	Tar and Char	98
4.3.4	Sorbent Gasification Cycling.....	100
4.3.5	Equilibrium Model.....	105
4.4	Conclusions.....	108
5	Conclusions and Recommendations.....	110
5.1	Pressure Swing of CaO for CO ₂ capture.....	110
5.1.1	Research Significance.....	112
5.1.2	Future Research	112
5.2	Lime-Enhanced Gasification of Biomass	112
5.2.1	Research Significance.....	114
5.2.2	Future Research	114
	References	115
Appendix 1:	Dual-Environment Thermogravimetric Reactor.....	129
Appendix 2:	PTGA Start-Up Sequence	140
Appendix 3:	PTGA Data Analysis MatLab™ Code	141

Appendix 4:	Pressure Swing Cycling – Supplemental Material	145
Appendix 5:	SEM Micrographs of PTGA Runs	156
Appendix 6:	Cycling Snapshot Data	168
Appendix 7:	SEM Micrographs of 10 bar Snapshot	170
Appendix 8:	SEM Micrographs of 20 bar Snapshots.....	172
Appendix 9:	Utilization and Weight Change Curves During Individual Cycles	175
Appendix 10:	Grain Model Kinetic Plots for Determination of Reaction Rates.....	182
Appendix 11:	Pressure Swing Kinetics - Supplemental Figures.....	189
Appendix 12:	Activation Energy of Pressure Swing Kinetics	193
Appendix 13:	AMPEL BFB.....	198
Appendix 14:	BFB Gasifier Design and Operation.....	199
Appendix 15:	BFB Gasifier Operational Issues.....	215
Appendix 16:	BFB Gasifier Parametric Design.....	220
Appendix 17:	BFB Gasifier Equipment Calibrations	225
Appendix 18:	Enhanced Gasification Supplementary Material	230
Appendix 19:	Typical Equilibrium Model Output.....	242
Appendix 20:	Condenser System Design Upgrade	248
Appendix 21:	Heat Generation in the Sample Bed	258

List of Tables

Table 1.1: Elemental properties of different CaO-based compounds.....	8
Table 1.2: Activation energies of fast stage carbonation reported by different authors	12
Table 1.3: Activation energies of slow stage carbonation reported by different authors [23,25,31].....	15
Table 1.4: Experimentally determined activation energies for calcination	20
Table 1.5: Thermal and physical properties of calcium oxide based compounds	27
Table 1.6: Melt formation in the CaO–CaCO ₃ , CaO–Ca(OH) ₂ and CaCO ₃ –Ca(OH) ₂ binary systems; reproduced from Florin and Harris (2008) [10]	32
Table 1.7: Proximate analyses of coal and biomass; adapted from Demirbaş (2005) [101]	40
Table 1.8: Primary gasification reactions	41
Table 1.9: Gas composition during breakthrough of biomass gasification at 600°C and 1 atm [118].....	46
Table 2.1: Chemical composition of fresh Strasburg limestone.....	53
Table 2.2: Conditions for pressure swing cycling experiments. Temperature was 1000°C for all carbonation and calcination intervals. Calcination at 1 bar was 8 minutes in all cases.	53
Table 2.3: Experimental operating conditions of previous work included in Figure 2.11, calcination was at atmospheric pressure in all cases.....	63
Table 3.1: Duration of different stages of carbonation.....	70
Table 4.1: Primary gasification reactions	83
Table 4.2: Pine sawdust analysis	86
Table 4.3: Bed material analysis	87
Table 4.4: Bed inventory and pressures of different gasification runs; bed pressure drop is the differential between the transducers at 5 and 40 cm above the distributor.	91
Table 4.5: Results from all runs; thermocouples distance above the distributor is indicated in brackets; pressures given are from 50 mm above distributor; the last digit of CCL runs refers to the cycle number.	95

List of Figures

Figure 1.1: Options for CO ₂ separation from point sources	3
Figure 1.2: Equilibrium partial pressure of CO ₂ for calcium carbonate (CaCO ₃).....	6
Figure 1.3: A typical carbonation / calcination cycle.....	7
Figure 1.4: Progression of carbonation: (a) sintered calcine; (b) initial carbonation; (c) carbonation with progression along grain boundaries; (d) critical product layer reached on free surfaces; (e) critical product layer reached along all grain boundaries with only bulk diffusion processes remaining.....	9
Figure 1.5: CaO-CO ₂ reaction mechanism proposed by Bhatia and Perlmutter (1983) [25]	17
Figure 1.6: Intermediate carbonate surface compounds; adapted from [45]	18
Figure 1.7: Example of a single pressure swing carbonation / calcination cycle	22
Figure 1.8: Mass and energy streams in a lime-based fluidized bed CO ₂ capture system	22
Figure 1.9: Typical utilization decay curves [33,38,61].....	23
Figure 1.10: Representation of initial stages of cycling induced sintering.....	29
Figure 1.11: Schematic illustration of sintering mechanism reducing micro-pores while increasing meso-pores	30
Figure 1.12: Effect of thermal pre-treatment on utilization decay [33,38,61,89,90].....	35
Figure 1.13: Steps in gasification of solid fuels	40
Figure 1.14: Sorbent enhanced biomass gasification dual reactor system configuration.....	44
Figure 1.15: Equilibrium concentrations of syngas during sorbent-enhanced biomass gasification. The shaded area represents the area of active CO ₂ capture at atmospheric pressure; adapted from Florin and Harris (2007) [55].	48
Figure 2.1: Schematic of pressurized thermogravimetric reactor.....	52
Figure 2.2: Pressure and conversion for pressure swing absorption for run 3.	54
Figure 2.3: Effect of carbonation pressure of cyclic performance of limestone during pressure swing absorption/desorption. For operating conditions see Table 2.2.....	55
Figure 2.4: SEM micrographs of sorbent particles, (a) initial calcined limestone, (b) carbonate from run 1 [after 1138 cycles], (c) carbonate from run 2 [after 275 cycles], (d) carbonate from run 3	

[after 228 cycles]. For operating conditions see Table 2.2.....	57
Figure 2.5: Carbonation breakthrough profiles for the first cycle during pressure swing absorption showing the effect of carbonation pressure. For operating conditions see Table 2.....	58
Figure 2.6: Carbonation breakthrough profiles for cycles 1, 2, 10, 50 and 200 of limestone during pressure swing sorption showing effect of carbonation pressure. For operating conditions see Table 2.....	59
Figure 2.7: Cyclic performance of limestone during pressure swing absorption/desorption of CO ₂ showing effect of sample size, 21 bar carbonation pressure, 26.5 min and 35.2 carbonation and cycle duration respectively.	60
Figure 2.8: SEM micrographs of carbonated particles after 254 cycles, run 7: (a) particle from exterior of sample, (b) particle from interior of sample. For operating conditions see Table 2.2.	61
Figure 2.9: Cyclic performance of limestone during pressure swing absorption/desorption of CO ₂ showing effect of depressurization rate. For operating conditions see Table 2.2.	62
Figure 2.10: SEM micrographs of carbonated samples after cycling with different de-pressurization rates: (a) run 11, after 378 cycles; (b) run 9, after 500 cycles. For operating conditions see Table 2.2.....	62
Figure 2.11: Comparison of pressure swing CO ₂ absorption on limestone with previous studies utilizing temperature or partial pressure swing. For operating conditions see Table 2.3 [38,61,123,128].	63
Figure 3.1: Pressure and calcium utilization during the first three cycles of pressure swing carbonation; 1000°C and 20 bar carbonation pressure.....	67
Figure 3.2: Calcine of Strasburg limestone after one cycle at 1000°C and 10 bar carbonation pressure..	68
Figure 3.3: 100 th cycle kinetics modeled using Szekely's grain model for cycling at 10 bar carbonation pressure, solid lines used to find rate of reaction: a) reaction controlled regime, equation 3.2; b) diffusion controlled regime, equation 3.4.	69
Figure 3.4: CO ₂ partial pressure at onset of carbonation and calcination; solid line represents the equilibrium pressure as obtained from equation 1.4, and the dotted lines are ± 10 kPa.	71
Figure 3.5: Cycle 1 utilization (a) and pressure (b) profiles during 1000°C cycling.	72
Figure 3.6: Evolution of calcium utilization over long series of carbonation/calcination cycles. 10 bar cycling can be seen in Appendix 8.....	73
Figure 3.7: Kinetics of reaction-controlled carbonation over 100 cycles at: a) 5 bar _g , b) 10 bar _g , c) 20	

bar _g ; error bars represent standard errors in rates derived from the grain model.	74
Figure 3.8: SEM micrographs of calcined sorbent cycled at: a) 5 bar and 850°C for 267 cycles; b) 5 bar and 1000°C for 1130 cycles. Note that scales differ.	75
Figure 3.9: Surface area of calcined sorbent cycled at 20 bar _g , 1000°C; error bars represent multiple surface area measurements of the same sample.	75
Figure 3.10: SEM micrographs of calcines cycled at 20 bar _g and 1000°C: a) 1 st cycle, b) 5 th cycle, c) 10 th cycle, d) 50 th cycle.....	76
Figure 3.11: SEM micrographs of calcines cycled at 10 bar _g and 1000°C: a) initial calcine, b) 5 th cycle, c) 25 th cycle, d) 250 th cycle.....	77
Figure 3.12: Surface “dispersed contraction” mechanism of sorbent re-activation and surface area increase due to grain boundary reduction: a) initial calcine, with distinct grains connected by point contacts; b) sintered carbonate with rounded grains connected by grain boundaries; c) sintered calcine with molar volume contraction occurring at grain boundaries; d) highly sintered carbonate with few grain boundaries remaining; e) highly sintered calcine with volume contraction distributed on grain surfaces	78
Figure 3.13: Kinetics of reaction-controlled carbonation over 100 cycles at: a) 1000°C, b) 1025°C; error bars represent standard errors in rates derived from the grain model.	79
Figure 3.14: Kinetics of diffusion-controlled carbonation over 100 cycles at: a) 5 bar _g , b) 20 bar _g cycling; error bars represent standard errors in rates derived from the grain model.....	80
Figure 3.15: Kinetics of diffusion-controlled carbonation over 100 cycles at: a) 975°C, b) 1025°C; error bars represent standard errors in rates derived from the grain model.	80
Figure 4.1: Schematic of a lime-based enhanced biomass gasification process using a single reactor, semi-batch process.	84
Figure 4.2: Bubbling fluidized gasifier setup: (1) fuel hopper, (2) steam generator, (3) preheater, (4) fluidized bed, (5) internal cyclone, (6) condenser, (7) condensate collection, (8) particle filter, (9) mass flow meter, (10) Agilent 4900 micro-GC, (11) afterburner, (12) 5 micron particle filter, (13) tar sampling impinger bottles, (14) APEX XC-60 gas sampler.....	85
Figure 4.3: Particle size distributions of biomass and fluidized bed materials	86
Figure 4.4: Carbon balance in lime enhanced biomass gasification.....	89
Figure 4.5: Gasification results for a sand bed (SB-08-12); a) water and nitrogen-free syngas composition and local temperatures, b) higher heating value and utilization efficiencies. Heights of the	

temperature probes above distributor are given in the legend.....	92
Figure 4.6: Gasification results for limestone bed (LB-04-12); a) water and nitrogen-free syngas composition and local temperatures, b) higher heating value and utilization efficiencies..	93
Figure 4.7: Gasification results for CaO bed (CB-06-12); a) water and nitrogen-free syngas composition and local temperatures, b) higher heating value and utilization efficiencies.....	94
Figure 4.8: Syngas production with different bed materials.	96
Figure 4.9: Concentration of heavier components in the produced gases for (a) sand bed (SB-08-12) and (b) CaO bed (CB-06-12), nitrogen and moisture-free.....	97
Figure 4.10: Effect of temperature on biomass gasification; points are experimental data, lines represent linear best fits; (a) data from two sand bed runs, (b) CaO bed.....	98
Figure 4.11: Tar yield for different bed materials.	98
Figure 4.12: Large bed char from limestone bed gasification (LB-04-12).....	99
Figure 4.13: Particle size distribution and char content of bed after gasification: (a) sand bed (SB-08-12), (b) CaO bed (CB-06-12), dashed lines are fitted Boltzman functions of the cumulative distribution data.....	100
Figure 4.14: Concentrations, temperature and pressures during gasification cycling in a CaO bed (CCL-07-12): (a) cycle 1 gasification; (b) calcination, with shaded area representing difference between CO ₂ equilibrium pressure and CO ₂ partial pressure, ($P_{CO_2} - P_{CO_2,eq}$).....	101
Figure 4.15: Concentrations and temperature during gasification cycling in a CaO bed (CCL-10-12): (a) cycle 1 gasification; (b) cycle 8 gasification.	102
Figure 4.16: Effect of sorbent cycling on biomass gasification (CCL-10-12): (a) change in syngas composition and calcium utilization, (b) carbon and hydrogen utilization efficiency and syngas production rate (volume of syngas divided by mass of biomass).....	103
Figure 4.17: Photograph of bed samples: (i) initial calcined bed; (1a to 7a) bed after corresponding gasification cycle; (1b to 7b) bed after re-calcination cycles 1 to 7; (8) final bed.	103
Figure 4.18: Change in sorbent specific surface area during gasification / calcination cycling obtained by single point N ₂ absorption BET.....	104
Figure 4.19: Cumulative particle size distributions after different degrees of cycling: "original limestone" sorbent pre-cursor, 1 cycle (CaO-06-12), 2 cycles (CCL-07-12) and 8 cycles (CCL-10-12).	105

Figure 4.20: ASPEN flowsheet of enhanced biomass gasification model	105
Figure 4.21: Results from equilibrium model of biomass gasification. Dark symbols indicate gasification with a CaO sorbent; light symbols indicate gasification without any sorbent.	106
Figure 4.22: Comparison of equilibrium model predictions and experimental results for: (a) sand bed gasification (SB-04-12), and (b) CaO bed gasification (CB-06-12).	107
Figure 4.23: Comparison of equilibrium model predictions and experimental data for effect of temperature on syngas composition: (a) sand bed, and (b) CaO bed.	108

Nomenclature

a	stoichiometric coefficient [-]
A_g	grain surface area [m ²]
A_p	particle surface area [m ²]
b	stoichiometric coefficient [-]
$c(x)$	concentration at position x into the sorbent particle [kg/m ³]
C_{CO_2}	concentration of CO ₂ in gas [mol/m ³]
$C_{CO_2}^{eq}$	equilibrium concentration of CO ₂ in CaCO ₃ [mol/m ³]
C_s	concentration of diffusing species on the pore surface [mol/m ³]
d_{gb}	average grain size [m]
D	diffusion coefficient [m ² /s]
D_{eff}	effective diffusivity in product layer [m ² /s]
e_o	loss in pore volume per unit mass during reaction [m ³ /kg]
E_{cap}	CO ₂ capture efficiency [-]
f_{CaO}	mass fraction of CaO in sorbent [-]
F_{CaO}	CaO circulation rate between carbonator and calciner [kmol/s]
F_{CO_2}	CO ₂ flow to carbonator [kmol/s]
F_g	grain shape factor [-]
F_o	make-up sorbent flow [kmol/s]
F_p	particle shape factor [-]
F_R	sorbent circulation rate [kmol/s]
g	gravity [m/s ²]
$g(x)$	grain model conversion for reaction-controlled carbonation [-]
ΔG_{rxn}^o	standard Gibbs free energy change for reaction [kJ/kmol]
GCV	gross calorific value of fuel [kJ/kg]

h	bed height [m]
ΔH_{298}^o	standard heat of reaction at 298K [kJ/kmol]
HHV_{fg}	higher heating value of flue gas [kJ/m ³]
HHV_{tar}	higher heating value of tar [kJ/kg]
J	mass flux [kg/m ² *s]
k	initial sorbent calcium utilization [-]
k_c	calcination rate constant [mol/(s/m ²)]
k_s	rate constant for surface reaction [m ⁴ /(mol*s)]
k_x	reaction rate constant [m ³ /(mol*s)]
K_e	equilibrium constant for calcination [mol/m ³]
K_E	equilibrium constant for ccarbonation [mol/m ³]
L	grain length [m]
L_A	grain boundary thickness per surface area [m/m ²]
L_o	initial total length of pores per unit volume [m/m ³]
m	mass of sorbent [g]
\dot{m}_{bio}	fuel flow rate [g/min]
m_{CaO}	mass of calcine [kg]
M_{CaO}	molecular weight of CaO [g/mol]
M_{CaCO_3}	molecular weight of CaCO ₃ [g/mol]
n_{CaO}	moles of CaO [mol]
n_{CaCO_3}	moles of CaCO ₃ [mol]
Δn_{CaCO_3}	moles of CO ₂ absorbed by CaO during gasification [mol]
$n_{C,fuel}$	carbon entering with fuel [mol]
$n_{C,gas}$	moles of carbon in syngas [mol]
n_c^{out}	unconverted carbon [mol]

$n_{H,gas}$	moles of hydrogen in syngas [mol]
$n_{H,biomass}$	moles of hydrogen in biomass feed, moisture and elemental hydrogen [mol]
$n_{H,steam}$	moles of hydrogen in steam feed [mol]
N	number of cycles [-]
$N_{1/2}$	cycle age of half the particles in dual bed capture system [-]
$p(x)$	grain model conversion for diffusion-controlled carbonation [-]
P	pressure [kPa]
P_{CO_2}	partial pressure of CO ₂ [kPa]
$P_{CO_2}^{eq}$	equilibrium partial pressure of CO ₂ within CaCO ₃ [kPa]
ΔP_{bed}	bed pressure drop [kPa]
r	reaction rate [mol/(s·m ²)]
r_c	radius of CaCO ₃ particle [m]
$r_{C/S}$	carbon-to-sulphur molar ratio in fuel [-]
r_o	radius of CaO particle [m]
R	ideal gas constant [kJ/kg·K]
ΔR_{CaCO_3}	thickness of product layer [m]
R_o	radius of limestone particle [m]
S	specific surface area [m ² /g]
S_a	specific surface area of highly cycled sorbent [m ² /m ³]
S_o	initial specific surface area per unit volume [m ² /m ³]
S_p	specific pore surface area [m ³ /g]
t	time [s]
t_{carb}	total carbonation time [min]
U_{mf}	minimum fluidizing velocity [m/s]
U_t	particle terminal velocity [m/s]
T	temperature [K]

V	volumetric flow [L/min]
V_g	grain volume [m ³]
V_p	particle volume [m ³]
V_ε	specific pore volume [cm ³ /g]
y_t	tar yield [kg _{tar} /kg _{fuel}]
x	distance into particle [m]
X	calcium utilization [-]
X_{avg}	average calcium utilization of sorbent in dual-bed capture system [-]
X_c	carbon conversion [-]
X_N	carbonation conversion in N th cycle [-]
X_r	asymptotic residual utilization after infinite number of cycles [-]
X_{CO}	syngas composition of CO [m ³ /m ³]
z	molar volume ratio [-]
Z	molar volume parameter [-]

Greek symbols

α_{CaCO_3}	molar volume of calcium carbonate [mol/m ³]
α_{CaO}	molar volume of calcium oxide [mol/m ³]
ε	fluidized bed voidage [-]
ε_l	loss in pore volume per unit mass during reaction [m ³ /kg]
ε_o	porosity available for carbonation [-]
ε_p	initial particle porosity [-]
ε_t	theoretical maximum porosity for complete carbonation [-]
η_{cg}	cold gas efficiency [-]
η_C	carbon utilization efficiency [-]
η_H	hydrogen utilization efficiency [-]

v_{fg}	specific dry gas volume [$\text{m}^3/\text{kg}_{\text{fuel}}$]
ρ_{CaO}	density of calcium oxide [kg/m^3]
ρ_{CaCO_3}	density of calcium carbonate [kg/m^3]
ρ_p	particle density [kg/m^3]
ρ_s	molar concentration of solid reactant [mol/m^3]
ρ_T	crystal density [kg/m^3]
ψ	grain length per unit surface area parameter [-]

Acknowledgements

I would like to thank everyone who had a part in helping me through my Ph.D. To my supervisors Prof. John Grace and Prof. Jim Lim for their support in all my research efforts and their invaluable guidance and assistance; as well, for being models of successful academics that I aspire to be. To my supervisory committee who offered their guidance, in particular Prof. Naoko Ellis, who was a great mentor and friend and helped me make the most of my experience at UBC. To Professors Ellis and Watkinson for the use of their fluidized bed reactor that made my experimental studies into enhanced gasification possible.

To my research assistants over the years, Omid, Christopher, and Andreas, without whom I could not have accomplished as much as I did experimentally. To the members of the Fluidization Research Group, whom I was able to bounce ideas off and look to for assistance. To the workshop crew – Doug, Graham, David, Serge and Richard – from whom I learned a great deal and who helped with constructing and repairing my experimental apparatus. To the office staff, who keep the department running and allowed me to focus on research, in particular Joanne whose door was always open. To all my friends and colleagues in the department who offered advice, encouragement and diversions along the way. To Kristin who is always there for me with love and encouragement.

I'd like to recognize NSERC for providing me with personal financial support as well as funding for my research. As well, I thank the University of British Columbia and the Department of Chemical and Biological Engineering for their financial support.

For Tyler



1 Introduction

On May 10th 2013 the daily average level of atmospheric carbon dioxide, as recorded by The National Oceanic and Atmospheric Administration (NOAA) at their Mauna Loa research station, surpassed 400 ppm. This CO₂ level has not existed in the atmosphere for tens of millions of years. "If humanity wishes to preserve a planet similar to that on which civilization developed and to which life on Earth is adapted, paleoclimate evidence and ongoing climate change suggest that CO₂ will need to be reduced ... to at most 350 ppm" [1]. Many climate scientists believe that the current levels of CO₂ will lead to irreversible changes in the earth's climate. It is imperative that actions be taken immediately to stabilize and eventually reduce the current CO₂ emissions of 6 Gt of carbon per year, in order to mitigate further effects to the climate [2].

Stabilizing CO₂ emissions will require the concurrent initiation of a number of different reduction strategies [3]. Pacala and Socolow (2004) outlined a variety of reduction strategies, including an increase in vehicle emission standards, increased electrical end use efficiency, switching from coal power to nuclear or renewables, and carbon capture and storage (CCS) from fossil fuel power plants and fossil fuel upgraders. Any of these strategies alone will not achieve the emission reductions required; instead, all must be implemented together. To meet CO₂ reductions with CCS alone would require 600 Gt of carbon storage [2]. CCS offers a near term option for CO₂ emission reductions using available technology. Going forward, alternative low-carbon energy sources such as hydro-electric, solar, wind and biomass will need to replace the existing carbon-intensive energy generation fleet.

Many of the processes for capturing and sequestering CO₂ have already been implemented on an industrial scale. CO₂ separation is commonplace in natural gas processing and ammonia production facilities. The vast majority of these facilities use a liquid Monoethanolamine (MEA) capture process. The task now is to refine and improve CO₂ capture processes to reduce their energy and economic penalties.

For long term storage, underground sequestration is the easiest route to store large amounts of CO₂ [2]. Underground storage of CO₂ is already underway in the Southwestern United States, where 59 million tons/yr of CO₂ is used for enhanced oil recovery (EOR) and pipelines for transporting CO₂ stretch from Colorado to Texas [4]. Currently 47 million tons/yr of this CO₂ is sourced from underground deposits, with no net emissions reductions; however, a market for CO₂ has been created with a price of \$8 - 22 / tonne [5]. The least expensive method of sequestration is to inject CO₂ into suitable deep alkaline mineral strata, forming carbonates or bicarbonates, eliminating the need to monitor wellheads for long term leakage; however these formations are not widespread [2]. In EOR processes, CO₂ is injected into active oil wells to increase their production (Weyburn, Canada and Shute Creek, USA). CO₂ could also be

injected into depleted oil and gas reservoirs (In Salah, Algeria) or deep saline aquifers (Sleipner and Snohvit, Norway).

Just as there is no singular solution to CO₂ emission reductions, there is no single energy technology that will satisfy all future energy demands. The future low-carbon energy supply will be a mixture of sources including biomass. Biomass is defined as any fuel source of recent biological origin, such as sawdust, wood construction waste, energy crops (switch grass, alder, etc.), household waste, animal waste, or biosolids from waste treatment plants. For the purpose of this thesis, biomass discussion is limited to wood products. Energy production from this un-processed biomass is an attractive option for regions rich in forestry resources, such as British Columbia, Canada.

Biomass can be considered a carbon neutral energy source as the carbon released during its conversion is equivalent to the carbon taken up during its growth, disregarding emissions from harvesting and transportation. If coupled with CO₂ capture and storage, energy production from biomass is a net negative CO₂ process, offering a means of reducing atmospheric CO₂ concentration.

The conversion of biomass into a more convenient energy carrier can be conducted by either biological or thermo-chemical means. Thermo-chemical conversion has the advantage of much faster kinetics and typically a smaller plant footprint. For thermo-chemical conversion, the biomass fuel is either combusted in excess oxygen to produce heat and/or electricity or gasified / pyrolyzed in a depleted oxygen environment, typically with the addition of steam, producing gaseous and liquid fuels. Conversion of biomass by means of gasification offers potential for the production of a wide range of energy carriers, including electricity, heat, hydrogen, and other gaseous and liquid fuels.

The purpose of the research contained in this thesis was to examine the use of a limestone-based CaO sorbent for high temperature CO₂ capture. A novel pressure swing technique of sorbent cycling was demonstrated and studied. As well, the feasibility of utilizing CaO in an integrated biomass gasification / CO₂ capture cycle has been demonstrated. The remainder of this chapter is devoted to a thorough review of the progress of recent research on CaO-based CO₂ capture and sorbent-enhanced gasification to give the reader a detailed understanding of the relevant research areas.

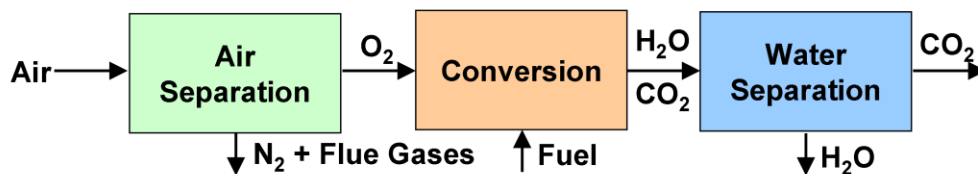
1.1 CaO Based CO₂ Capture

CO₂ capture from large point sources (upgraders, power plants, etc.) requires energy and decreases the efficiency of the process. Thus, a well-designed and highly integrated system is necessary. Geological sequestration requires that the CO₂ be highly compressed and injected underground, imposing a further energy penalty. To minimize this it is important that a nearly pure stream of CO₂ be generated from the capture system to avoid the unnecessary compression, pumping and sequestration of non-greenhouse gases. For example, the Weyburn EOR project in Saskatchewan, Canada obtains CO₂ from a coal

gasification facility in North Dakota, USA, under contract to supply a minimum CO₂ purity of 95 vol% [6].

There are two options for producing this pure stream of CO₂ from energy generation facilities, see Figure 1.1. The first is to conduct the thermal conversion of the fuel (combustion / gasification) in an atmosphere free of the diluents in air, particularly nitrogen, obtained from a pre-conversion separation process. This is accomplished through the use of oxygen separation, such as in the case of oxy-fuel combustion or the use of a metal oxide oxygen carrier in a chemical looping combustion (CLC) process. Cryogenic production of O₂ imposes a large energy penalty on the process of up to 25 kJ_{elec}/mol O₂ produced [7]. CLC has been successfully demonstrated for combustion of gaseous fuels [8], but faces a number of challenges for solid fuel conversion [9].

Oxy-fuel firing



CO₂ Stripping

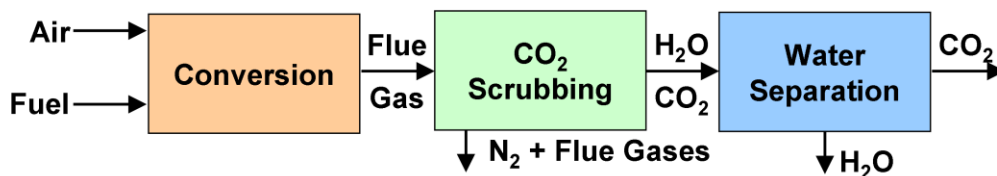


Figure 1.1: Options for CO₂ separation from point sources

The second option is to capture and purify the CO₂ gas post-conversion in a CO₂ stripping process. A number of different options exist for post-combustion capture, including [10]:

- Organic solvents (e.g. MEA, chilled ammonia)
- Metal oxides (e.g. CaO)
- Membrane separation
- Synthetic adsorbent materials (molecular sieves, activated carbon, zeolites...)
- Cryogenic condensation

The chemical absorption options (organic solvents and metal oxides), cycle the sorbent between absorption and desorption conditions. These represent the lowest cost of all the options, \$30 - 60 per ton_{CO2} avoided, vs. \$50 - \$78 for membrane separation and give the highest selectivity, > 90% [11]. Consequently they are the main options being considered and implemented for CO₂ capture from point

sources [11,12]. Their drawback is the energy intensity and the difficulty of finding further cost reductions through research [11]. These absorbents operate on a cyclical basis where CO₂ is absorbed from a low-concentration stream in one reactor and released in a second reactor to produce a nearly pure stream of CO₂.

MEA CCS systems are the most widely used in existing capture systems due to their high capture rates, good long term stability and relatively low cost. Other technologies must match or surpass MEA sorbent make-up costs of about \$2/ton CO₂ captured [13]. Abanades et al. (2004) reported that existing CO₂ capture systems have total costs of \$40/ton CO₂ captured [14]. The MEA CCS process has the disadvantage of requiring very tight controls on sulphur (<10 ppm) to avoid de-activation and subsequent make-up costs, in addition to the high toxicity of the sorbent. As well, MEA is typically diluted to 20 vol% in water and the thermal load of cyclic heating and cooling the diluent water greatly reduces the capture process efficiency [15].

For sorbents to be viable they must have high selectivity, adequate absorption kinetics, adequate mechanical strength and stable absorption level over repeated cycles [16]. Lime-based sorbents have all of these qualities, except for stable absorption over many cycles. This is the primary challenge of natural lime-based sorbents and will be discussed later in section 1.5. Lime-based sorbents have a number of advantages over other sorbent options:

- Inexpensive
- Capture at elevated temperature
- Absorbs CO₂ at low concentrations
- Less sensitive to poisoning from sulphur

Lime-based sorbents are the cheapest option on a material cost basis, approximately 50% cheaper than MEA [14]. One of their drawbacks is the decay in the calcium utilization (moles of CO₂ captured / moles of CaO available, equation 1.5) over many CO₂ capture and release cycles. This is partially offset by the low cost of naturally occurring limestone as it can be readily replaced. No large (>50 MW_e) lime-based capture facilities yet exist, but there are several industrial scale demonstration facilities operating or under construction in Europe [17].

There are a number of lime-based solid sorbents, both natural and synthesized, being considered for CO₂ capture. Although synthetic sorbent particles have shown improved CO₂ capture capacity, in order to be cost-competitive they need to last at a minimum 10,000 cycles without substantive decay [14]. Due to their lower cost and wide availability, natural sorbents are currently a more viable option for CO₂ capture than synthetic sorbents. There are two naturally occurring lime-based sorbents: limestone (~ 95% CaCO₃ by wt) and dolomite (~50% CaCO₃ by wt). Dolomite (MgCO₃·CaCO₃) has shown higher capture

capacity in terms of moles of CO₂ captured per moles of CaO present, but the lower mass fraction of CaO available gives limestone the advantage in terms of CO₂ captured per unit mass of sorbent [18]. In addition, dolomite is more prone to attrition than limestone.

Lime-based sorbents have the added advantage that they can capture CO₂ at the elevated temperatures of combustion and gasification conversion processes (450-850°C), compared to MEA (~60°C). This allows the solid sorbent to be used in-situ in the reaction chamber of a packed or fluidized bed conversion system, eliminating the need for a separate absorbing reactor or sub-cooling the flue gas. The CaO sorbent can be re-generated at temperatures of between 750 and 900°C, dependent on CO₂ concentration.

Another benefit of lime-based capture systems is the ability of lime to co-capture sulfur dioxide. MEA rapidly deactivates in the presence of SO₂, with levels in the flue gas limited to 10 ppm to avoid excessive replacement requirements [14]. CaO is used currently in many industrial applications as a single use sorbent for sulphur capture according to the following reaction:



If CaO cycling for CCS is desired, SO₂ will impede limestone carbonation due the formation of a calcium sulphate (CaSO₄) shell around the sorbent particle, blocking pores and limiting further carbonation [19]. Sun et al. (2007a) found that it took high SO₂ concentrations (>1100 ppm) to affect the calcium utilization over a number of cycles [19]. Ultimately, highly sulphated sorbent will need to be replaced.

1.1.1 The Capture Process

CO₂ capture on calcium oxide occurs by the carbonation reaction:



The reverse reaction is known as calcination. The exothermic nature of the carbonation reaction has the benefit of providing heat to endothermic conversion processes such as steam gasification. The downside of this, however, is the large heat demand on the calciner for sorbent regeneration. Supplying the heat for calcination, without diluting the produced CO₂ stream, is one of the main obstacles to implementation of lime-based CO₂ capture on an industrial scale.

Carbon dioxide capture by CaO is dependent on the difference between the CO₂ partial pressure in the reactor (P_{CO_2}) and the equilibrium pressure of CO₂ in the calcium carbonate lattice ($P_{CO_2}^{eq}$). The equilibrium partial pressure of CO₂ in CaCO₃ can be defined as a function of the Gibbs free energy of the carbonation reaction (ΔG°_{rxn}). Hu and Scaroni (1996) have presented the following empirical equation for the equilibrium partial pressure of CO₂ (in Pa) as a function of temperature, T (in K) [10,20–22]:

$$K_a = P_{CO_2}^{eq} = \exp\left(\frac{-\Delta G_{rxn}^o(T)}{RT}\right) \quad (1.3)$$

$$P_{CO_2}^{eq} = 1.87 \times 10^9 \exp\left(\frac{-19697}{T}\right) \quad (1.4)$$

Figure 1.2 plots $P_{CO_2}^{eq}$ versus temperature based on equation 1.4. The region above the equilibrium line represents conditions where carbonation occurs, whereas calcination occurs below the equilibrium line. If the carbonation temperature increases, P_{CO_2} must be increased [23], in reality the transition between carbonation and calcination is not as sharp as portrayed in Figure 1.2, with the rate of carbonation increasing as $P_{CO_2} - P_{CO_2}^{eq}$ increases from 0 to 10 kPa [24].

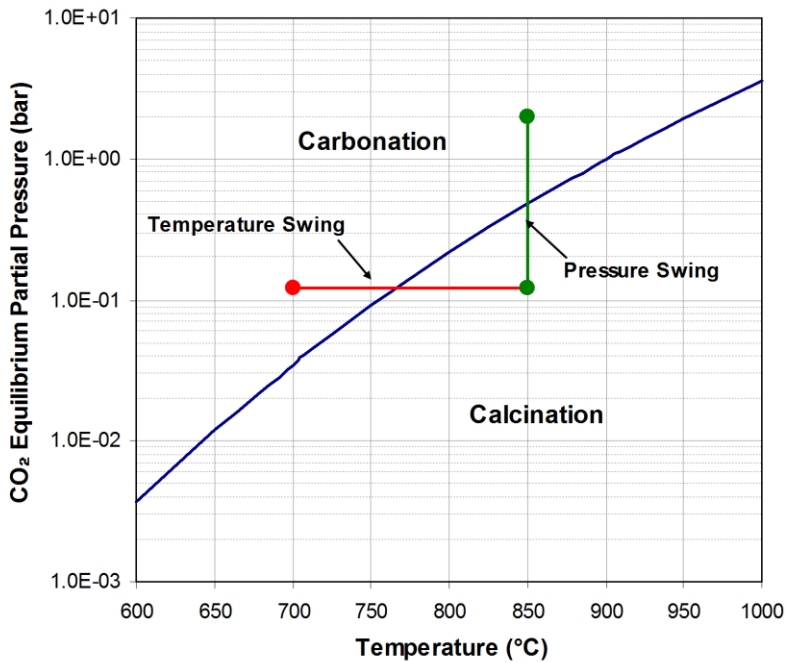


Figure 1.2: Equilibrium partial pressure of CO₂ for calcium carbonate (CaCO₃)

Cyclic absorption and desorption of CO₂ is accomplished by cycling the sorbent between carbonation and calcination conditions. Temperature swing cycling, represented by the horizontal line in Figure 1.2, has received the most attention in experimental studies to date. In industrial applications cycling using temperature swing alone would be difficult due to the large thermal load required to heat the solids, including inert material, to the calcination temperature, as well as provide the heat required for the endothermic calcination reaction. A less energy-intensive and more industrially viable option might be to swing the CO₂ partial pressure while keeping the temperature nearly constant, represented by the vertical line in Figure 1.2. This can be accomplished through the use of a diluent gas, or by cycling the reactor

pressure. It is necessary to use steam as the diluent gas in the calciner to avoid adding impurities to the CO_2 destined for sequestration; however, the use of large amounts of steam creates a high energy penalty on the industrial process. Alternatively the reactor pressure could be increased and decreased to accomplish sorbent cycling, lowering the CO_2 partial pressure without the need for steam sweep gas.

1.2 Carbonation

Research into the CaO-CO_2 reaction dates back to 1867 when DuMotay and Marechal first patented the use of lime to aid the gasification of carbon by steam [25]. Carbonation occurs in two distinct stages: an initial, fast-reaction-controlled regime followed by a slow, near-zero-order carbonation stage governed by solid state diffusion of CO_2 through the CaCO_3 product layer, see Figure 1.3 [20,26–29]. The surface reaction and solid state diffusion in the product layer are rate-limiting factors, assuming that the CaCO_3 product layer is non-porous [28].

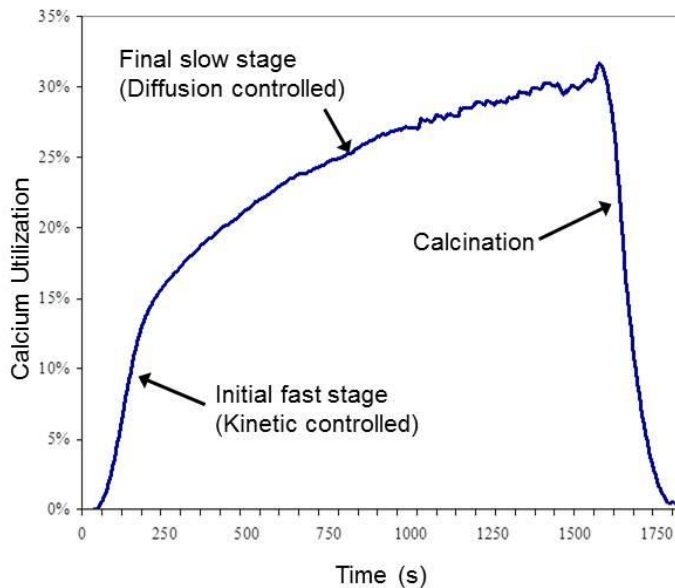


Figure 1.3: A typical carbonation / calcination cycle

The abrupt transition between the two stages is typical of gas-solid reactions [30]. In carbonation it is the result of the formation of a critical product layer of carbonate product on the surface of the sorbent [26,28]. Pore blockage effects are not important in marking the transition between the fast and slow regimes [31]. After the fast carbonation stage (1-3 min at 650°C) a product layer of CaCO_3 forms on the free surfaces, making large amounts of the CaO in the particle interior inaccessible [31].

The critical layer thickness is defined as the thickness of the CaCO_3 product layer at the onset of slow stage carbonation, after the end of the reaction fast period [31]. It has been found that the critical product layer thickness is between 20 and 220 nm [31,32]. These estimates assume an even distribution of CaCO_3 product layer on the entire particle and cylindrical pore geometry. Due to the abrupt decrease in

rate at the critical product layer thickness, the overall surface area of the sorbent and the pore size distribution are very important for the CaO-CO₂ reaction [28].

The interior of CaCO₃ after the carbonation stage does show signs of carbonation, suggesting that gas penetrated before the external layer was fully closed, or gas entered through very small pores [33]. Carbonation does not stop because of sealing of the outer layer, but due to lack for porosity, CO₂ penetration occurs only through product layer diffusion. Figure 1.4 shows the process of carbonation up to the stage where the critical product layer thickness is reached.

The moles of CO₂ captured over the moles of CaO available is termed calcium utilization, given by the equation [24]:

$$X = \frac{n_{CaCO_3}}{(n_{CaO})_o} = \frac{m(t) - m(0)}{m(0) * f_{CaO}} \times \frac{M_{CaO}}{M_{CO_2}} \quad (1.5)$$

where f_{CaO} is the mass fraction of CaO in the sorbent, m is the mass of the sorbent at time 0 or t , and M is the molecular weight of the different species, see Table 1.1.

Table 1.1: Elemental properties of different CaO-based compounds

Element	Molar Mass (g/mol)	Specific Volume (cm ³ /gmol)
CaO	56.08	16.9
CaCO ₃	100.09	36.9
Ca(OH) ₂	74.09	33.5
CaSO ₄	136.14	49.2

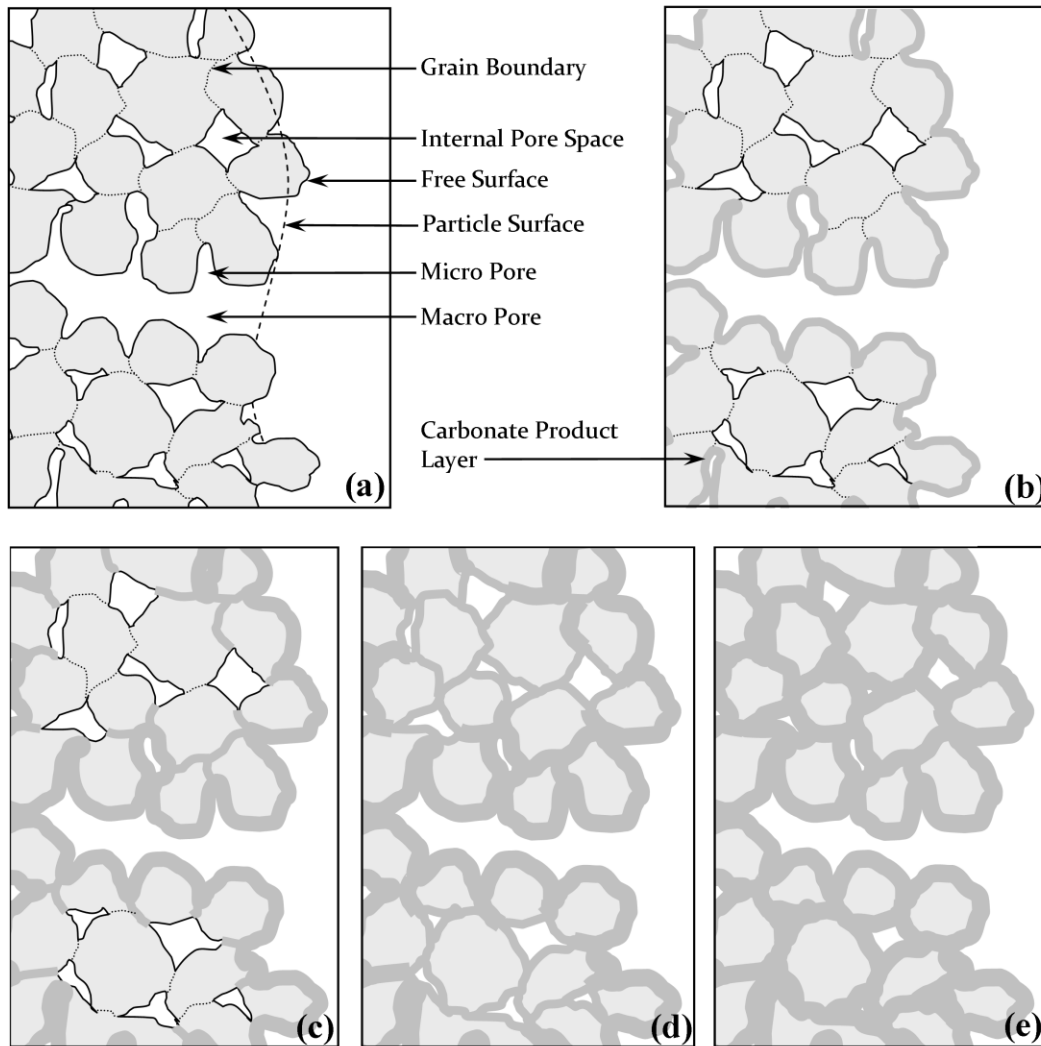


Figure 1.4: Progression of carbonation: (a) sintered calcine; (b) initial carbonation; (c) carbonation with progression along grain boundaries; (d) critical product layer reached on free surfaces; (e) critical product layer reached along all grain boundaries with only bulk diffusion processes remaining.

The main drawback of CaO as a CO₂ sorbent is its low calcium utilization after approximately 20 cycles. Prompt carbonation to 3.5% occurs very rapidly, in about one minute, but full re-carbonation of calcined CaCO₃ requires an extremely long time [32]. Sun et al. (2008) carbonated a highly cycled sample for a full 24 hr resulting in a calcium utilization of only 49% [34]. Bhatia and Perlmutter (1983) found that the reaction virtually stopped 30 min after completing the fast stage reaction for all carbonation temperatures (400 - 725°C) and particle sizes (81 - 137 μm) tested [26]. The fast stage of carbonation was found to reach completion in roughly 7 min for a 15 kPa driving force [35].

The main reason for the low conversion is the formation of the product layer [31]. After its formation, slow solid state diffusion processes govern the progress of the reaction. The final calcium utilization after this critical product layer has been reached is between 70 - 80%, for calcined limestone [26,27].

Carbonation is much slower than calcination and is affected by the sorbent properties [33]. In large pores the reaction becomes limited by the growth of the product layer and the onset of slow product layer diffusion [33]. In small pores it is limited by plugging of these pores due to the formation of the larger molar volume CaCO_3 . Table 1.1 shows the properties of the relevant calcium based compounds.

As the carbonation progresses, the CaCO_3 product layer grows on the particle surface. Abanades and Alvarez (2003) characterized the growth of the product layer based on the increase in the particle diameter with conversion:

$$\Delta R_{\text{CaCO}_3} = R_o \left[\left(X \left(\frac{M_{\text{CaCO}_3} \rho_{\text{CaO}}}{\rho_{\text{CaCO}_3} M_{\text{CaO}}} - 1 \right) + 1 \right)^{\frac{1}{3}} - (1 - X)^{\frac{1}{3}} \right] \quad (1.6)$$

where X is the carbonation conversion, R_o is the radius of limestone particle, M is the molar mass and ρ is density.

Bhatia and Perlmutter (1983) reported that the size of the CaO particle has no effect on the calcium utilization in the particle size range of 81 to 137 μm [26]. This indicates that the incomplete conversion of CaO is not due to surface pore closure blocking the interior of the particle, but is the result micro-pore closure throughout the particle. After the closure of small pores, carbonation continues in the larger pores by diffusion through the product layer. The conversion is proportional to the particle porosity and surface area [26]:

$$X = \rho_T e_l / (Z - 1) \quad (1.7)$$

$$\text{with } Z = 1 + \rho_{\text{CaO}} (\alpha_{\text{CaCO}_3} - \alpha_{\text{CaO}}) M_{\text{CaO}} \quad (1.8)$$

where α is the molar volume, ρ_{CaO} is the density of lime, M_{CaO} is the molecular weight of CaO, ρ_T is the crystal density of CaO (3.32 g/cm^3), and e_l is the loss in pore volume per unit mass during reaction.

The kinetics are independent of sample size if the CaO particles are only in a few layers [26]. Bhatia and Perlmutter (1983) found that sample size below 1.3 mg, close to a mono layer of CaO particles, had no effect on the carbonation kinetics.

1.2.1 Reaction-Controlled Carbonation

The initial conversion rate is linear and rapid up to about 55-60% conversion, at which point the product layer reaches a critical thickness, slowing the reaction dramatically [26]. Prior to cycling, CaO sorbent particles are highly porous, with a high specific surface area. The initial fast reaction regime is dependent on this micro-porous structure, specifically on pores smaller than 100 nm [33,36]. Sun et al. (2007b) found that the extent of carbonation in the fast stage is directly related to porosity by [36]:

$$X = \frac{\varepsilon_o}{(1/z - 1)(1 - \varepsilon_o)} \quad (1.9)$$

where z is the molar volume ratio of CaO/CaCO₃ (0.46) and ε_o is the porosity available for carbonation, related to the measured specific pore surface area, S_p (m³/g), by:

$$\varepsilon_o = \frac{S_p}{S_p + 1/\rho_{CaO}} \quad (1.10)$$

In the reaction-controlled regime, conversion for a reversible, first order system can be described by the first order relationship with CO₂ concentration [26]:

$$\frac{1}{\psi} \left(\sqrt{1 - \psi \ln(1 - X)} - 1 \right) = \frac{k_s S_o (C_{CO_2} - C_{CO_2}^{eq})}{2(1 - \varepsilon_l)} \quad (1.11)$$

$$\text{where the structural parameter } \psi = \frac{4\pi L_o (1 - \varepsilon_l)}{S_o^2} \quad (1.12)$$

where k_s is the rate constant for the surface reaction, S_o is the initial surface area per unit volume, C is the concentration of CO₂, L_o is the initial total length of pores per unit volume, and ε_l is the loss in pore volume per unit mass during reaction.

1.2.1.1 Fast Stage Carbonation Kinetics

There remains some debate in the literature over whether the intrinsic order of the fast stage carbonation reaction is first order or zero order with respect to the CO₂ concentration / partial pressure driving force, $(P_{CO_2} - P_{CO_2}^{eq})$. Nitsch (1962) studied the carbonation reaction between 800 and 850°C and found that the reaction was first order with CO₂ concentration. The relation for the conversion X , as a function of the CO₂ concentration driving force and the degree of conversion was given as [37]:

$$\frac{dX}{dt} = k_x (1 - X)^{2/3} (C_{CO_2} - C_{CO_2}^{eq}) \quad (1.13)$$

The inclusion of the conversion term on the right hand side of equation 1.13 indicates a reduction in the conversion rate as the CaCO₃ product layer builds up on the surface.

Sun et al. (2008a) found that the order of the reaction with respect to the pressure driving force was initially one, but dropped to near zero at higher CO₂ partial pressures. Increasing the CO₂ partial pressure from 0.1 to 800 kPa had no significant effect on carbonation kinetics, indicating a zero order reaction [24]. Their conclusion was that for CO₂ partial pressure driving forces greater than approximately 10 kPa, the CaO-CO₂ transition complex saturates the CaO surface sites, and the reaction step becomes rate

limiting. The reaction rate is then likely controlled by product-layer diffusion, not surface reaction. Rate constants of 1.13 and 1.17 $\text{g}_{\text{CO}_2} / (\text{g}_{\text{CaO}} \cdot \text{s})$ were found for limestone and dolomite respectively. Mess et al. (1999) confirmed this less-than-linear dependence of the initial rate on CO_2 partial pressure [32].

The reaction is said to be independent of P_{CO_2} because the product layer quickly thickens, and much slower product layer diffusion becomes dominant [28]. At later stages the bulk CO_2 concentration in the product layer becomes very similar for different CO_2 partial pressures, causing the CO_2 driving forces at the reaction front to become very low [28].

There is also some contradiction in the literature about the activation energy for fast stage carbonation. Early work by Nitsch (1962) found the rate constant (k_x) to have zero activation energy, and this was later supported in the temperature range of 400 - 725°C by Bhatia and Perlmutter (1983); however, more recent studies [24,38] have found a small, but non-zero activation energy [26,37]. Activation energies found by various authors are shown in Table 1.2.

Table 1.2: Activation energies of fast stage carbonation reported by different authors [24,26,37,39].

Reference	Sorbent	Particle Size (μm)	Temperature Range ($^{\circ}\text{C}$)	Environment	Activation Energy (kJ/mol)
Nitsch (1962)	--	--	--	--	0
Bhatia and Perlmutter (1983)	Limestone	74 - 149	550 - 725	10-20% CO_2 balance N_2	0
Sun et al. (2008)	Limestone	38 - 45	550 - 850	100% CO_2	29
Sun et al. (2008)	Dolomite	38 - 45	550 - 850	100% CO_2	24
Symonds et al. (2009)	Limestone	250 - 425	580 - 700	8% CO_2 , H_2O , balance N_2	30
Symonds et al. (2009)	Limestone	250 - 425	580 - 700	8% CO_2 , 21% H_2 , 42% CO , 17% H_2O , 12% N_2	60

Dolomite had slightly lower activation energy due to MgO impurities. These cause dislocations in the crystal structure allowing for lower strain energy in the crystal lattice and increased diffusion rate of CO_2 , as discussed in section 1.2.3. MgO impurities may also act as points of nucleation for carbonation [24].

1.2.1.2 Effect of Operating Parameters

Reducing the temperature decreases the rate of reaction in the fast regime to the point where it becomes indistinguishable from the slow reaction rate [26]. A slow reaction rate is also seen in carbonates calcined in a CO_2 atmosphere. This slower reaction rate is attributed to the decreased surface area and increased pore size resulting from sintering, increased by CO_2 , see section 1.6.3 [26]. The maximum carbon conversion after the fast stage is insensitive to P_{CO_2} [40]. Higher P_{CO_2} initially performs worse, likely due to increased sintering.

Symonds et al. (2009) found that the presence of CO and H_2 increased the initial reaction rate by about 71% at 620°C. This was attributed to the catalytic effect of CaO surface sites on the water-gas shift reaction increasing localized CO_2 concentration. This catalytic effect was also deemed to be the cause of

an increase in activation energy of the fast carbonation reaction from 29.7 to 60.3kJ/mol, due to the formation of intermediate complexes of CaO with CO and H₂ that must first be broken down before carbonation can proceed.

Steam does not affect the reaction rate during the initial kinetically controlled reaction stage; however, it does enhance diffusion through the product layer, causing bulk diffusion to become the rate limiting step later and increasing the rate of carbonation of the slow stage of the reaction [27,41,42]. This is particularly important for conditions where product layer diffusion is rate limiting sooner, i.e., at low carbonation temperatures or for highly sintered sorbents. Water vapour enhances the exchange of CO₂ with CaO even at room temperature, where 3% utilization over 5 hours, is possible in a water rich atmosphere [29]. These two effects are caused by enhanced solid state diffusion, possibly through an intermediate CaO hydration step reversibly forming Ca(OH)₂, followed by Ca(OH)₂ carbonation [41].

The addition of steam improves carbonation, without the irreversible formation of Ca(OH)₂ [41]. The addition of steam at 0.1 MPa partial pressure increased total conversion from 12.9% to 43.4% after 25 min of carbonation at 550°C and an H₂O partial pressure below the equilibrium partial pressure of Ca(OH)₂ of 0.198 MPa [41]. This enhancing effect of steam is only present, however, at low temperatures (< 800°C), and the effect decreases with increasing temperature due to the effects of steam on sintering [27], as discussed in section 1.6.

There is a limit to the effect of steam, as increasing steam concentration from 10 to 20% does not significantly affect the rate of conversion [27]. As well, in La Blanca and Cadomin limestones, steam had little effect [27]. These limestone varieties have intrinsically high levels of solid state diffusion due to impurities with the result that further enhancement would be minimal [27].

1.2.2 Diffusion-Controlled Carbonation

The crystalline structure of the carbonate product layer is very important to the reaction rate in the diffusion-controlled regime. Lattice imperfections such as grain boundaries, vacancies, interstitials and dislocations increase the diffusivity of ions through the product layer. After carbonation is complete, particles become more rounded, supporting the idea of a uniform product layer made up of grains of a re-crystallized structure whose boundaries meet at 120° [32]. Grains grow by coalescence dependent on temperature.

Nitsch (1962) and Dedman and Owen (1962) found that the second stage of carbonation to be independent of gas composition below 600°C and independent of CO₂ partial pressure above 1.34 kPa [37,43]. Bhatia and Perlmutter (1983) also found the slow stage reaction to be independent of CO₂ partial pressure when P_{CO_2} was well in excess of $P_{CO_2}^{eq}$ [26]. However, when the difference in these pressures is

low the second stage rate becomes dependent on P_{CO_2} . Mess et al. (1999) discovered that after a large amount of time, the carbonation rate changes from zero order to first order with respect to CO_2 pressure at high temperature [32]. The reaction rate was approximately 1st order in CO_2 concentration driving force for high temperatures (950 - 1000°C) and long carbonation times (620 min). This suggests a change in dominant mechanism for the transport of ions through the product layer as the rate decreases with increasing product layer thickness. They suggest a dual-mechanism carbonation during the second slow stage [32]:

1. Grain boundary diffusion, independent of CO_2 partial pressures, and
2. Bulk diffusion of CO_2 , first order dependence on CO_2 concentration gradient.

Mess et al. (1999) developed a model to describe this dual mechanism involving the product of these two forms of diffusion [32]:

$$\rho \frac{dR}{dt} = 4\pi L_A d_{gb} + 4\pi (C_{CO_2} - C_{CO_2}^{eq}) D_{eff} \frac{1}{(1/r_o - 1/r_c)} \quad (1.14)$$

where L_A is the grain boundary thickness per surface area (m/m^2), d_{gb} is the average grain size, D_{eff} is the effective diffusivity, r_o is the radius of the oxide particle and r_c is the radius of $CaCO_3$ particle. Grain boundary concentration (L_A) can be found through SEM micrographs of the particles by counting the grain boundary intersections per unit length (P_L) and multiplying by $\pi/2$. The first term on the right hand side of the expression represents grain boundary diffusion, whereas the second term represents bulk diffusion through the crystal lattice. The carbonation rate decreased more rapidly than expected for diffusion through a uniform product layer alone, suggesting a more complex mechanism than pure bulk diffusion. The bulk diffusion term becomes more important with increasing carbonation time, and changes the order of the reaction from near zero to first with CO_2 concentration.

Solid state diffusion is a high activation energy process, greatly influenced by temperature [27]. Activation energies for solid diffusion-controlled carbonation are much higher than for the reaction controlled regime, shown in Table 1.3.

Table 1.3: Activation energies of slow stage carbonation reported by different authors [24,26,32].

Reference	Sorbent	Particle Size (μm)	Temperature Range (°C)	Environment	Activation Energy (kJ/mol)
Bhatia and Perlmutter (1983)	Limestone	74 - 149	< 515	10-20% CO ₂ , balance N ₂	89
Bhatia and Perlmutter (1983)	Limestone	74 - 149	> 515	10-20% CO ₂ , balance N ₂	179
Mess et al. (1999)	CaO	15 - 20	550 - 1050	100% CO ₂	238
Mess et al. (1999)	Single Crystal CaO	15 - 20	550 - 1050	100% CO ₂	368
Sun et al. (2008)	Limestone	38 - 45	570 - 850	80% CO ₂ , balance N ₂	215
Sun et al. (2008)	Dolomite	38 - 45	570 - 850	100% CO ₂	187

In the diffusion-controlled regime, calcium utilization can be modeled based on the different diffusivities within the product layer [26]:

$$\frac{1}{\psi} \left(\sqrt{1 - \psi \ln(1 - X)} - 1 \right) = \frac{S_o}{(1 - \varepsilon_l)} \sqrt{\frac{bM_{CaO} D_{eff} C_s t}{2aZ\rho_{CaO}}} \quad (1.15)$$

where ψ is defined in equation 1.12, a and b are stoichiometric coefficients, D_{eff} is the effective diffusivity in the product layer, S_o is the initial surface area per unit volume, C_s is the concentration of diffusing species on the pore surface, t is time, Z is the ratio of the solid phase volume after reaction to that before the reaction as defined by equation 1.8, and ε_l is the loss in pore volume per unit mass during the reaction.

Diffusivities were obtained by plotting the left-hand side of equation 1.15 vs. \sqrt{t} [26]. The calculated low diffusivities and high activation energies are inconsistent with gas molecule diffusion through the crystal lattice. An observed change in activation energy near the Tamman temperature at 515°C is consistent with solid state diffusion, hinting that diffusion of ions through the lattice is the underlying diffusion pathway [26].

1.2.3 Ionic Diffusion

Matter diffuses in a manner that decreases concentration gradients [44]. The flux of matter is proportional to the concentration gradient across that plane, and one-dimensional steady state diffusion is defined by Fick's first law:

$$J_1 \left\langle \frac{mass}{L^2 t} \right\rangle = -D_1 \left\langle \frac{L^2}{t} \right\rangle \left(\frac{\partial c_1}{\partial x} \right)_t \left\langle \frac{mass/L^3}{L} \right\rangle \quad (1.16)$$

where D is the diffusion coefficient, J is the flux of component 1 and c is the concentration at axial position x . The diffusion coefficient is independent of the flux or concentration gradient and, one-dimensional transient diffusion is defined by Fick's second law:

$$\frac{\partial c}{\partial t} = \frac{\partial}{\partial x} \left(D \frac{\partial c_1}{\partial x} \right) \quad (1.17)$$

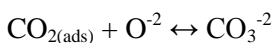
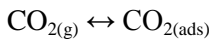
Diffusion occurs by the periodic jumping of atoms from one lattice site to another as a result of natural oscillations, which periodically become energetic enough to allow the atom to change sites. The incredible speed of the lattice vibration is such that atoms can jump between lattice planes up to 100 billion times per second or about one jump every 10,000-100,000 oscillations [44]. There are two mechanisms of atomic diffusion through a crystal lattice:

1. Interstitial diffusion
2. Vacancy diffusion

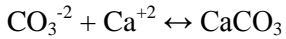
The interstitial mechanism of diffusion involves the diffusion of an atom from one interstitial site to another. The nearby matrix atoms must oscillate apart to give sufficient space for the smaller interstitial atom to go through, this mechanism of diffusion is relatively fast due to the high number of vacant sites [44]. In the case of CaO, this is believed to be the predominant mechanism of diffusion of CO_3^{-2} ions through the CaCO_3 product layer.

The vacancy mechanism is the movement of a matrix atom into an adjoining vacancy (a lattice site missing an atom). The neighboring atoms must oscillate apart enough to allow the atom to enter the vacancy [44]. This process is slow and directly related to the number of vacancies present. In the case of the CaCO_3 - CaO system this would be the primary mechanism for volume sintering of the sorbent through movement of CaCO_3 or CaO molecules. In ionic solids, defects must occur in opposing pairs so that the solid does not have a charge separation, i.e. if a cation vacancy is present, there must be an associated anion vacancy nearby in the lattice.

Diffusion through metal oxides occurs through the movement of charged ions through the crystal lattice [45]. In the CaO- CaCO_3 system, the most likely candidates for ionic diffusion through the lattice are Ca^{+2} and CO_3^{-2} ions as they predominate in the CaCO_3 system [26]. Ca^{+2} diffusivity is 6 times greater than electron conduction through CaO [26]. Similarly charged ions must move counter-currently to maintain charge neutrality within the crystal lattice; therefore, counter-diffusion of CO_3^{-2} and O^{-2} species would be the most probable mechanism for diffusion through the product layer. CO_2 could be chemisorbed on CaCO_3 through reaction with O^{-2} ions to form CO_3^{-2} [46]. CO_3^{-2} decomposes to CO_2 and O^{-2} and CO_2 moves to similar neighboring site where it again forms CO_3^{-2} . The reaction mechanism is displayed in Figure 1.5 and outlined below.



The plausible reaction mechanism at the product layer interface is:



The overall reaction is then:

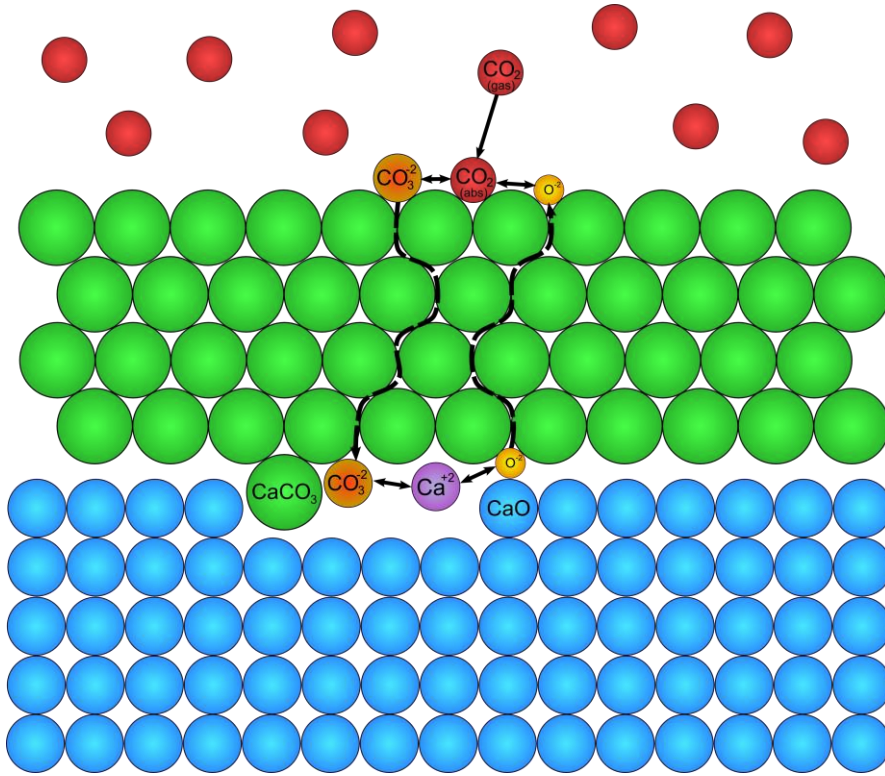


Figure 1.5: CaO-CO₂ reaction mechanism proposed by Bhatia and Perlmutter (1983) [26]

Above the Tamman temperature of 515°C, the activation energy of carbonation matches the heat of decomposition [26]. Above this temperature it is suspected that the diffusion mechanism changes slightly from counter-current diffusion of anions, to the site-to-site diffusion of CO₂. CO₃²⁻ at one site decomposes to CO₂ and O₂²⁻, the CO₂ then moves to a neighbouring vacant site and again forms CO₃²⁻ [26]. In this way CO₂ and vacancies diffuse counter-currently.

For $P_{\text{CO}_2} \gg P_{\text{CO}_2}^{\text{eq}}$ the rate-limiting step is likely to be the formation of CO₃²⁻ [26]. Either mechanism is compatible with the initial fast stage of the reaction if the initial product layer has extremely high diffusivity. This could arise from anomalies in the surface layer of CaCO₃, such as grain boundaries, nano-pores and other lattice imperfections which promote diffusion. The transition from the initial rapid stage to the slower diffusion-controlled stage is then caused by the formation of a more compact product layer [26].

Initially surface carbonates such as unidentate carbonate, bidentate carbonate, bicarbonate and carbonate ions are produced in the carbonation reaction during the CO₂ absorption step [47]. Unidentate carbonates predominated in reaction of CO₂ with surface metal oxide at room temperature. Unidentate carbonate mostly desorbs at high temperatures, with a small portion being transformed into other states. With the introduction of H₂O, more bicarbonate is formed through interaction of CO₂ with surface hydroxyl ions. These intermediate compounds, see Figure 1.6, may also form at the product layer reaction interface.

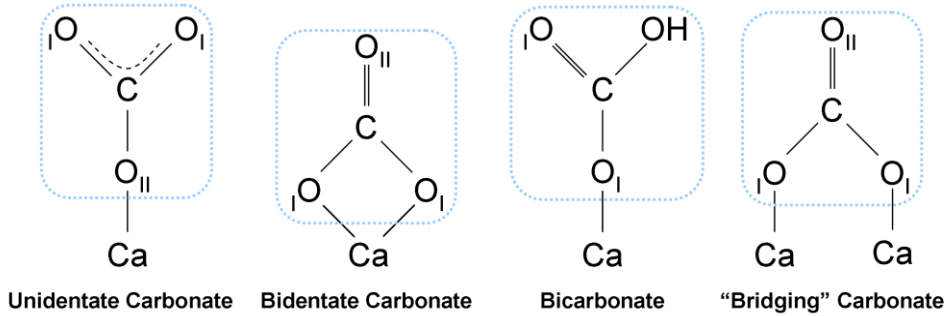


Figure 1.6: Intermediate carbonate surface compounds; adapted from [47]

The mean jump frequency of an atom in regions of dislocations, free surfaces and grain boundaries is much higher than in the lattice [44]. There are far more vacancies at grain boundaries than in the lattice. The activation energy for grain boundary diffusion is appreciably less than for lattice diffusion, so that diffusion is greatly enhanced by the presence of grain boundaries.

Grain boundaries are aligned dislocations which increase diffusion in the plane of the grain boundary, while lattice dislocations increase diffusion in all directions [44]. The chemical potential on a particle surface is greatest at the grain boundary. The flux of atoms during sintering is away from the grain boundary, widening and deepening the groove at the grain boundary with successive CO₂ capture cycles [44].

1.3 Calcination

The calcination reaction receives less attention than carbonation as it is a much faster reaction, suited to a wide range of conditions, and goes to completion quickly (<5 min). Calcination occurs quickly if the driving force exceeds 30 kPa [35]; however, due to the high temperatures required for the endothermic calcination reaction (850 - 1000°C), sintering during calcination is critical to the effectiveness of the CaO sorbent over multiple cycles, as discussed in section 1.6.

The overall rate of calcination appears to be mass transfer limited and depends on how quickly CO₂ can be removed from the surface of the particle to the sweep gas [48]. Observations support a bulk diffusion controlled regime governed by internal pore diffusion. As a result, higher porosity leads to an increase in

calcination rate [48]. Consistent with this, the addition of inert ceramic zirconia to the calciner prevented contact of CaO particles increasing the resulting surface area and the calcination rate [48].

Calcination begins at the surface of the CaCO₃ and progresses inward, forming a reaction interface where the crystal structure is changing from rhombohedral CaCO₃ crystalline to cubic CaO crystalline [49]. The reaction interface progresses inward at a rate governed by the crystallographic conversion [49]. The calcination reaction mechanism consists of [50]:

1. breakdown of rhombohedral CaCO₃ lattice,
2. desorption of CO₂,
3. nucleation and growth of cubic CaO.

Calcination is believed to progress in a shrinking-core manner; therefore, a shrinking core model can be used to model its kinetics [36]:

$$r = k_c (1 - C(t, x) / K_e) \quad (1.19)$$

where K_e is the equilibrium constant fitted [20] by:

$$K_e = 10^{(8308/T+7.079)} / (R_o T), \quad (1.20)$$

k_c is the calcination rate constant given [51] by:

$$k_c = 3.013 * 10^7 \exp(-200 / (R_o T)), \quad (1.21)$$

$C(t, x)$ is the CO₂ concentration at time t and distance x into the particle. This gives an overall expression for the shrinking core model [36]:

$$\frac{dX}{dt} = \frac{1 - \frac{C(x)}{k_e}}{\rho_{CaCO_3} (n) R_o \left(\frac{1}{3k_m k_e} \right) + (1 - X)^{-2/3} / k_c + R_o / (3D_e K_e) ((1 - X)^{-1/3} - 1)} \quad (1.22)$$

Due to the highly endothermic nature of the reaction, activation energies are quite high for the calcination reaction, as given in Table 1.4 below.

Table 1.4: Experimentally determined activation energies for calcination [48,51–56].

Reference	Sorbent	Particle Size (μm)	Temperature Range ($^{\circ}\text{C}$)	Environment	Activation Energy (kJ/mol)
Borgwardt (1985)	Fredona limestone, Georgia marble	1-10	740-1000	N_2	201
Ingraham and Marier (1963)	Calcite, reagent grade PCC pellet		790-850	Air	170
Rao et al. (1989)	CaCO_3 pellet	6400 - 6600	680-875	N_2	185
Rajeswara Rao (1993)	CaCO_3 pellet	440 - 860	670-740	N_2	192
Samtani et al. (2002)	Limestone	75-90	$dT/dt=10^{\circ}\text{C}/\text{min}$	N_2	193
	Dolomite	75-90	$dT/dt=10^{\circ}\text{C}/\text{min}$	N_2	176
	Natural Magnesite	75-90	$dT/dt=10^{\circ}\text{C}/\text{min}$	N_2	226
Koga and Criado (1998)	Reagent grade CaCO_3			Vacuum	224
Sakadjian et al. (2007)	Precipitated CaCO_3		700-750	Vacuum, N_2	186
	Limestone	45-75	700-750	Vacuum, N_2	164

1.3.1 Factors Affecting Calcination

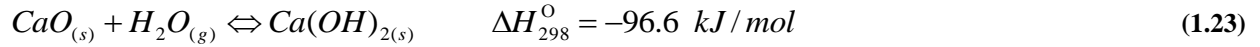
The decomposition time of CaCO_3 decreases with increasing temperature and decreasing CO_2 concentration in the sweep gas. Full calcination of a naturally occurring sorbent is possible in 2 minutes at 950°C using a CO_2 -free sweep gas [50]. Naturally, a high partial pressure of CO_2 requires a higher temperature to decompose CaCO_3 [57].

The first calcination of the sorbent is special in establishing the textural characteristics of the sorbent for future cycles [33]. Calcines prepared in CO_2 were more crystalline than those prepared in N_2 [26,58]. An increase in mean pore size and a narrowing of the pore size distribution occurs with increasing CO_2 concentration in the calcination sweep gas [26]. As well, diffusivity is reduced by half when limestone is calcined in a partial CO_2 atmosphere [26]. More crystalline particles have a slower rate of diffusion due to fewer vacancies, dislocations and grain boundaries. Lime cooled between calcination and carbonation showed slower nucleation prior to the fast stage of the reaction, due to re-crystallization of CaO during cooling [26].

Sakadjian et al. (2007) showed that CaO calcined under vacuum (0.66-0.17 atm) resulted in an increased calcination rate and resulted in a structure with enhanced reactivity towards hydration [48]. They found that calcination rate increases with decreasing absolute pressure and with increasing sweep gas flow rate, due to the increased driving force ($P_{\text{CO}_2} - P_{\text{CO}_2}^{\text{eq}}$). Calcination rate also increased with an increase in sweep gas thermal conductivity, through increased heat transfer to the sorbent particle, driving the endothermic calcination reaction [48].

1.4 Hydration

The hydration reaction is similar to the carbonation reaction, with the difference that calcium utilization for hydration is typically 100%. It is important to examine studies on hydration as they can give insights into the mechanism of carbonation. Like carbonation, hydration is an exothermic reaction:



The equilibrium partial pressure of H₂O with Ca(OH)₂ is significantly higher than for CO₂; therefore, the sorbent will be preferentially utilized for CO₂ capture at elevated temperatures [59]. The decomposition of Ca(OH)₂ becomes significant at temperatures of 410°C and above.

Like carbonation, hydration is a reversible reaction, and CaO sorbent can be cycled between hydration and calcination. CaO is completely converted to Ca(OH)₂ even after 20 hydration / calcination cycles with no decay in utilization [60]. However, the rate of hydration decreases with increasing number of cycles, rapidly at first, then reaching a near-asymptotic value. The decreasing reaction rate can be attributed to surface area reduction and crystal growth, leading to a reduction in lattice defects where ionic diffusion is accelerated [60]. Lin, et al. (2009) found that product layer diffusion did not affect the hydration rate and that the fast initial regime dominated the conversion kinetics [60]. They also found through XRD studies that CaO crystallization was lowest for the initial calcined lime and grew over a number of cycles, rapidly to 5 cycles and then more slowly. This was accompanied by an exponential decrease in surface area, indicating that sintering was occurring, even at the low temperatures used (550 - 650°C). One difference was that no significant morphology changes were observed through SEM, specifically no eutectic melting was observed. In addition, the compression strength decreased by 41% over 20 cycles.

1.5 CaO - CaCO₃ Cycling

An efficient CaO-based CO₂ capture system requires that the sorbent be carbonated and calcined multiple times to reduce sorbent costs. As previously discussed, sorbent cycling is accomplished by shifting the difference between the CO₂ partial pressure and the CO₂ equilibrium partial pressure ($P_{\text{CO}_2} - P_{\text{CO}_2}^{\text{eq}}$) from negative (calcination) to positive (carbonation), see Figure 1.7 for a typical carbonate curve with pressure swing cycling. The most likely CCS process design would include two separate reactors, one for carbonation and the other for calcination, with solids circulating between the two, see Figure 1.8.

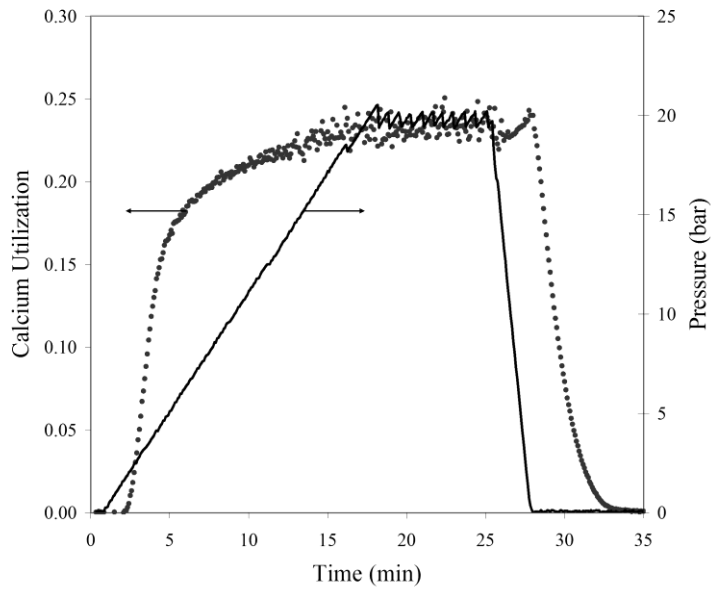


Figure 1.7: Example of a single pressure swing carbonation / calcination cycle

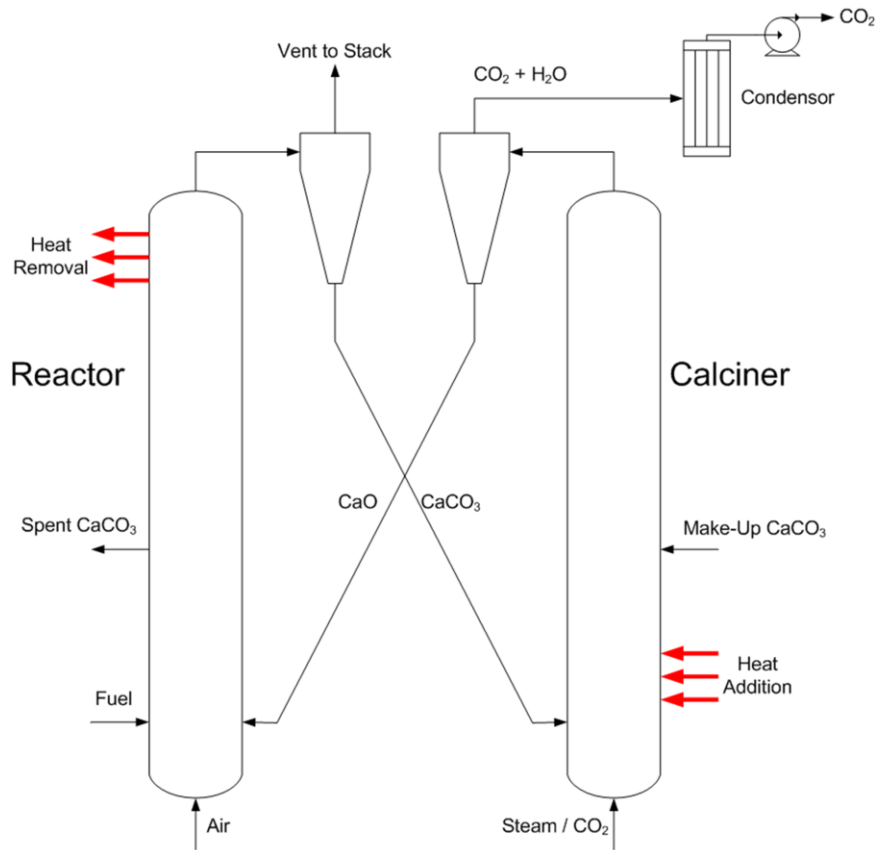


Figure 1.8: Mass and energy streams in a lime-based fluidized bed CO₂ capture system

As a result of sorbent particle sintering, the calcium utilization decreases over multiple carbonation / calcination cycles. Limestone-derived sorbents show a rapid decrease in utilization in the first 20 cycles and have residual utilization values of 7.5 - 15% after many cycles, see Figure 1.9 [34,40,61–64]. After

250 cycles there is no discernible difference in the carbonation mass profile [34]. Wang and Anthony (2005) provided a semi-empirical equation based on sintering theory and catalyst deactivation for the residual utilization after N cycles:

$$\int_1^{X_N} \frac{-dX}{(X - X_r)^2} = \int_0^N kdN$$

$$X_N = \frac{1}{1/(1 - X_r) + kN} + X_r \quad (1.24)$$

where X_r is the asymptotic residual utilization after an infinite number of cycles and k is the initial sorbent utilization, having least square fitted values of 0.075 and 0.52, respectively [65].

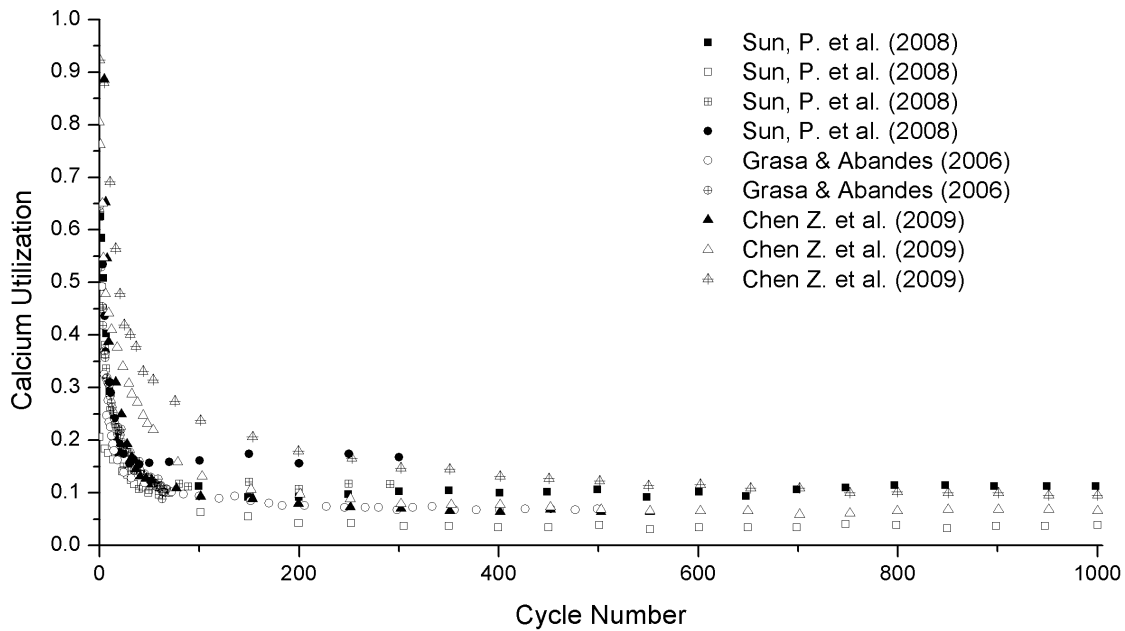


Figure 1.9: Typical utilization decay curves [34,40,63]

The majority of studies involving $\text{CaCO}_3\text{-CO}_2$ cycling have been conducted to 20 or fewer cycles. In an industrial lime-based CO_2 capture plant the sorbent could be cycled many hundreds of times before being replaced by fresh sorbent. To examine the industrial viability of the capture process the behaviour of the sorbent beyond 100 cycles is needed. Only a few studies to date have done this. Grasa and Abanades (2006) conducted experiments with CaO in a long series (~500) of calcination/carbonation cycles [40]. They found that calcium utilization decreased rapidly in the first 20 cycles reaching an asymptotic value of 7.5 - 8% residual calcium utilization.

Sun et al. (2008) examined capture capacity up to 1000 cycles and showed that after 150 cycles the carbonation approached an asymptotic value between 4 and 17% [34]. A bimodal pore size, pore evolution model was developed to predict the decay in sorbent reactivity as a function of cycle number.

Particle sintering and the subsequent shift in the bimodal pore distribution through loss of micro-pores and increase in meso-pores were shown to be consistent with the progressive loss of activity.

1.5.1 Factors Affecting Utilization Decay

In the area of CaO-based CO₂ capture, there exist numerous contradictory results for the effect of different parameters on the decay in utilization. A number of authors [33,38,40,65] have suggested that the residual utilization depends almost entirely on the number of cycles, and to a lesser extent operating conditions. With calcination temperatures below 950°C, Grasa and Abanades (2006) found residual activity insensitive to cycle conditions (sorbent type, particle size and CO₂ partial pressure); however, the initial rate of decay in activity is strongly influenced by cycle conditions. For example rate of decay increased when calcination time was increased [40].

For naturally-occurring calcium oxide-based sorbents, the carbonation temperature has no substantial effect on the level of calcium utilization over repeated calcination/carbonation cycles. It has been shown that the decay in utilization is primarily related to the calcination conditions [14,38–40,66]. Manovic & Anthony (2008b) disputed these finding and found that increasing carbonation temperature led to increased activity loss (55% utilization for 650°C, 28% for 850°C carbonation temperature) due to enhanced ion migration and sintering [64].

The presence of steam during carbonation has been shown to improve the long-term residual utilization [38]. Steam had a “no memory” effect on conversion efficiency, and quickly returned to normal with the removal of H₂O during carbonation [18]. Steam present during carbonation (1:1 steam:CO₂ by vol.) increased the duration of the fast stage 30 – 100%.

High temperatures (> 950°C) and pressure in the calciner enhance sintering and lead to a faster decline in calcium utilization, consistent with the idea that sintering of CaO is the cause of decreasing utilization [10,23,40]. The calcination conditions strongly influence the pore structure of the CaO. In addition, the sweep gas used in the calciner affects sorbent sintering and decay in utilization. Calcining in the presence of CO₂ causes increased sintering and decay [67]. Calcining in a H₂O atmosphere has a similar effect, increasing the ion mobility within the sorbent crystal lattice and enhancing sintering. High calcination temperatures (> 950°C) and extended calcination times accelerated the decay in sorbent reactivity.

A longer calcination time was found to increase particle sintering and decrease the volume of small pores (< 220 nm) [36]. Pore coarsening occurred when the sorbent was calcined for a long period of time (80 min) following 6 calcination / carbonation cycles, suggesting intermediate solid-state sintering [36]. Grasa and Abanades (2006) reported that, provided the sorbent is completely calcined ($t > 3$ min, at 950°C), increasing the calcination time from 3 to 60 min, only decreased the calcium utilization slightly [40]. Manovic and Anthony (2008b) found that increased calcination time increased the cyclical

conversion at lower temperatures ($< 850^{\circ}\text{C}$) except for extreme times (240 min) [64]. At high temperatures, the diffusion rate was much higher, and sintering was enhanced. The residual utilization for a sorbent cycled at calcination conditions of 240 min and 850°C , was higher than for a sorbent that underwent the first 10 cycles with 240 min calcination time and was subsequently decreased to 20 min [64]. This suggests that the sorbent can remember its thermal history. This is discussed in greater detail in section 1.7.2 dealing with thermal pretreatment.

The asymptotic calcium utilization increased with increasing carbonation time [34]. An increase in carbonation time from 9 to 15 min increased multi-cycle utilization from 10% to 14% [34]. It has also been found that limestone can be reactivated by long term carbonation [32,34,61]. A period of extended carbonation following cycling was found to re-activate CaO [34]. During extended carbonation, large pores gradually fill. The subsequent rapid calcination opens micro-pores and returns the pore size distribution to be similar to that of the initial calcine. SEM photos showed more small pores following long carbonation, suggesting that extended carbonation can cause the sorbent to "forget" its cycling history [34]. Conversion following re-activation increased from 10% to 49% [34]. Switching from long to short cycles after 60 or 120 cycles caused conversion to quickly approach short cycle asymptotic values. The duration of the cycle does not alone effect sorbent reversibility, but is very important to sintering and pore evolution because of CO_2 outward diffusion. It has also been shown that longer carbonation times increased the rate of sorbent decay due to sintering [64].

Both long and short cycle times showed a similar volume of small pores (< 220 nm) after multiple cycles, indicated by similar initial carbonation rates [36]. With short cycling time, the utilization reduced to a low asymptotic value of only 3.5%, even when the carbonation time was sufficiently long to finish the fast stage [34].

Sorbents derived from different limestone varieties show similar cyclic behaviour with extended cycles [23,62]. The exception being that sorbents prepared from a $\text{Ca}(\text{OH})_2$ precursor show an increased residual utilization [61]. This differs from sulphation of CaO, where different limestone varieties perform differently in the absorption of SO_2 [68,69].

Particle size was found to have no effect on the initial rate of decay and only affects the reaction rate during the initial fast carbonation stage (1 - 3 min), but the majority of carbonation cycles studied are longer (> 5 min) [10,40]. Manovic and Anthony (2008) found a different result, and after a few cycles the utilization of small particles was less and the decrease in utilization was faster for small particles [64]. Particle size affected the shift between the fast and slow regimes, but this disappeared at higher number of cycles as larger pores formed. The different results could be a factor of different impurity levels, as the smaller particles were less pure [64]. Impurities enhance sintering by providing crystal defects for ion migration and would enhance the reaction rate by the same means. Sorbent activity can be

increased by grinding already cycled samples, exposing un-reacted CaO in the particle interior so that it is made available for calcination [64].

Larger sample sizes show higher conversions [64]; however, the carbonation rate is slower in large samples due to greater diffusional resistances, see section 1.2. To fast a carbonation rate may lead to un-reacted CaO due to bottlenecks.

1.5.2 Application of CaO Cycling

The economics of lime-based carbon capture are strongly affected by deactivation over multiple cycles [14]. As calcium utilization decreases, more solids must be circulated between the calciner and carbonator to maintain the same level of CO₂ capture. This increases the heat load and solid handling complexity. When cycling low-utilization sorbents with a temperature swing, a large amount of heat addition to the calciner and removal from the carbonator would be required to raise and lower the temperature of the inert portion of the sorbent. In addition to the heat of reaction, this would put a large heating demand on the calciner.

To compensate for the low level of residual sorbent utilization, fresh sorbent can be added to the system to increase the average level of sorbent calcium utilization. The average capture capacity of CaO in the system can be described [17] by:

$$X_{ave} = \sum_{N=1}^{N=\infty} r_N X_N - \frac{F_{CO_2}}{F_o r_{C/S}} \quad (1.25)$$

$$\text{where } r_N = \frac{F_o / F_{CaO}}{(1 + F_o / F_{CaO})^N}, \quad (1.26)$$

F_o is the make-up sorbent flow (kmol/s), F_{CaO} is the CaO circulation rate between carbonator and calciner (kmol/s), F_{CO_2} is the CO₂ flow to the carbonator, X_N is the carbonation conversion in the Nth cycle and $r_{C/S}$ is the carbon-to-sulphur molar ratio in the fuel.

New sorbent materials should be cycled $N_{1/2}$ times to test for long term reactivity [14], where:

$$N_{1/2} = \frac{\ln 2}{\ln \left(\frac{F_o}{F_R} \right)} \quad (1.27)$$

F_R is the sorbent circulation rate.

Rodriguez et al. (2008) found that the minimum heat input into the system, 30.2% of the total plant heat, occurred at a sorbent makeup ratio (F_o / F_{CO_2}) of 0.13 and a sorbent to CO₂ ratio (F_{CaO} / F_{CO_2}) of 3. This would give an average utilization of 23%. As the sorbent make-up flow is decreased, so too does the

average utilization, causing an increase in the heat requirement. In the presence of sulphur and ash from the fuel (ash = 0.29 wt%, sulphur = 0.06 wt%) the minimum heat input increases, 39.3%, along with the required sorbent make-up ratio, 0.43. The existence of a high (>20%) residual utilization after numerous cycles without sorbent make-up could support an efficient CO₂ separation system [33].

1.6 Sintering of CaO

The reduction in calcium utilization during CaO cycling can be directly attributed to particle sintering [33]. Sintering is the process of densification of a porous solid due to fusing of interior surfaces, when held at a temperature below its melting point. The temperature of relevance for sintering in metal oxides is the Tammann temperature, see Table 1.5. It is the temperature necessary for bulk lattice re-crystallization, at which point the rate of bulk sintering becomes significant. It can be approximated as 0.52 times the melting temperature [70].

Table 1.5: Thermal and physical properties of calcium oxide based compounds

Element	Tammann Temperature (°C)	Decomposition Temperature (°C)	Melting Temperature (°C)
CaO	1000 - 1250 ¹	--	2927
CaCO ₃	527	750-850 ¹	1339
Ca(OH) ₂	302	385	580
CaSO ₄	860 ²	1150-1300 ¹	1448 ²

¹[71], ²[72]

Sintering of CaO causes a rapid change in the sorbent particle morphology [33], a decrease in surface area and porosity, and an increase in average grain size [73]. SEM pictures after sintering show more rounded particles with lower surface energy [74].

Most solids sinter through grain boundary, lattice or volume diffusion [30]. In the case of CaO, sintering results primarily from lattice diffusion, as well as some volume diffusion [33,73]. Beruto et al. (1984) found that initial, rapid coarsening occurred through CO₂ catalyzed surface diffusion, followed by slower coarsening occurring through grain boundary or volume / bulk diffusion. The change in surface area was not consistent with a surface diffusion limited process alone. They postulated that the sintering rate limiting step was chemi-sorption / desorption.

The mechanism of CaO sintering is similar to the mechanism of carbonation through the product layer with ions diffusing through the solid lattice. Vacancies generated by temperature and ion-sensitive lattice defects migrate through the lattice, directing void volume from small to larger pores [33]. The evolution of CO₂ from CaCO₃ during calcination leaves lattice vacancies which enhance sintering [74]. CO₃²⁻ or Ca²⁺ diffusion is one possible mechanism of coarsening [46]. The chemi-sorption activation energy is 61 ± 10 kJ/mol_{CO₂}. The enthalpy of desorption is found to exceed the equilibrium enthalpy by this amount.

An understanding of sintering and methods to minimize it is important for maintaining the reactivity of CaO through multiple cycles. Initial sintering of CaO is very rapid due to a high initial surface area and surface free energy, and the rate is proportional to the initial surface area of the particle [75]. As sintering progresses, the rate of decay in calcium utilization decreases due to a reduction in available surface area where rapid surface sintering would otherwise occur [33].

1.6.1 Grain Growth

Grain growth of CaCO₃ occurs at carbonation temperatures above 600°C, near its Tammann temperature, on the free surfaces of the particle [32]. Temperatures above 750°C cause continuous grain growth until grain boundaries are scarce. At high temperatures (> 850°C) after several hundred minutes there are virtually no grain boundaries left [32].

Sintering-induced grain growth occurs much more slowly than pore coarsening with the grain structure still recognizable after 40 carbonation / calcination cycles [33]. A multi-crystalline CaO particle will eventually become a single crystal particle after a high number of cycles at high temperature, but this would take many thousands of cycles or extreme sintering conditions [76]. Grain size increases with increasing calcination temperature, with increased calcination duration and increased CO₂ and H₂O concentrations in the sweep gas [50]. The catalytic effects are similar to the results of increased ion mobility, as discussed in section 1.2.3.

Grain size is directly related to pore volume and surface area, Grain length (L) can be estimated by the following empirical equations [50]:

$$L = 744.67 + 464.64 \log\left(\frac{1}{S}\right) \quad (1.28)$$

$$L = -608.5 + 1342.42 \log\left(\frac{1}{V_\epsilon}\right) \quad (1.29)$$

where S is the specific surface area (m²/g) and V_ϵ is specific pore volume (cm³/g).

Crystalline size increases as a result of CO₂ absorption / desorption cycling-enhanced sintering [35]. CaO forms an open packed array of spherical grains during sintering with an initial diameter of roughly 174 Å [73]. These grains interact through neck formation and growth at points of contact, see Figure 1.10.

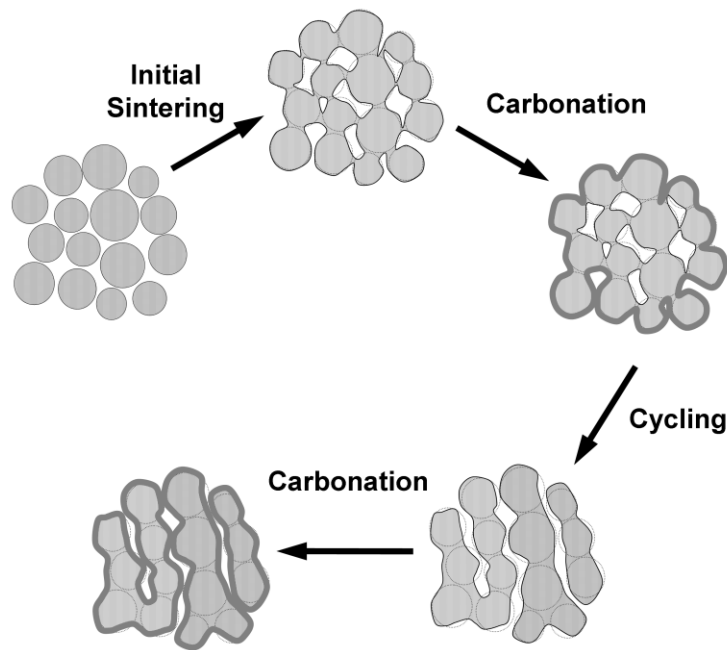


Figure 1.10: Representation of initial stages of cycling induced sintering

1.6.2 Pore Coarsening

A decrease in utilization efficiency is always accompanied by a significant decrease in pore volume and surface area [35]. The rate of the surface area reduction is proportional to the surface area squared [77,78]. Eventually the surface area levels off at an asymptotic value [50]. Pores coarsen through two paths [46]:

1. *Surface path* which produces the initial rapid decrease in surface area with little reduction in meso-porosity. It may be a non-diffusion path that governs the rate of the initial rapid path.
2. *Diffusion* path characterized by pore coarsening and the growth of meso-pores with relatively little decrease in total porosity. This is consistent with a diffusion limited process [79].

The surface area reduction during the initial stages of sintering is consistent with the neck growth kinetic model of German and Munir (1976) [79]. The initial phase of sintering shows formation of cylindrical micro-pores (0 - 100 nm in diameter) within grain clusters and a network of meso-pores (100 - 250 nm) between clusters [73]. The intermediate stage of sintering is characterized by a reduction of porosity when clusters coalesce, eliminating micro-pores and shifting the pore size distribution towards macro-pores, as indicated in Figure 1.10.

A clear division in the pore size exists in the particle size distribution of calcined limestone, making it bimodal, with pores typically smaller than 1000 nm [36]. Nano pores (<20 nm) likely arise from CO₂ off-gassing during calcination. During cycling large pores are formed as a result of sintering, combining small pores into larger ones. This process is driven by vacancy gradients within the sorbent crystal lattice

and surface energy gradients [50]. Beruto et al. (1984) found that after 16.3 hours of CaCO_3 sintering at 686°C , meso-pore volume decreased by 79%, but total volume only decreased by 10% [46].

With increased number of cycles, micro pores decrease and the bimodal distribution shifts towards macro pores, see Figure 1.11 [36]. The threshold between micro and meso-pores is defined by the product layer thickness (~ 50 nm) as micro-pores (< 100 nm, twice the product layer thickness) have the potential of being plugged, but meso (100 - 250 nm) and macro-pores (> 250 nm) do not [33]. Initially calcined limestone had a large number of micro-pores, and lacked macro-pores, but after 1000 cycles, no micro-pores remained, with the average pore size close to 1000 nm [36]. Short cycling duration resulted in even larger pores (1000 - 3000 nm); as longer carbonation produced nano-pores (< 20 nm) during the rapid off-gassing of CO_2 during calcination.

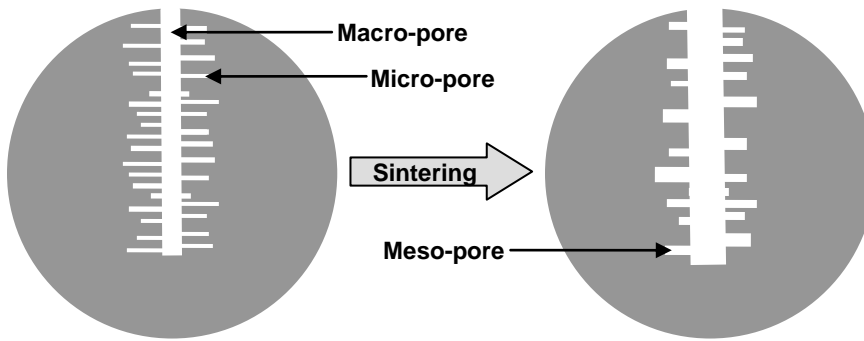


Figure 1.11: Schematic illustration of sintering mechanism reducing micro-pores while increasing meso-pores

The interior of CaO can be thought of as being arranged in small parallel rods (~ 100 nm wide) [33,80]. Thermal cycling of CaO reduces micro and meso-porosity by the packing of the CaO rods closer together, generating macro-pores.

The specific surface area of the sorbent decreases primarily with increasing number of cycles [36]. The specific surface area has been found to be a function of the micro and meso-pores (< 250 nm) in the sorbent and can thus be defined by [36]:

$$dS = AdV_1 \quad (1.30)$$

where $V_1 = \frac{(S - S_a)}{A} + V_a$

$$A = (S_o - S_a)(1 - \varepsilon_t)\rho_{\text{CaO}} / \varepsilon_t \quad (1.31)$$

where S is the specific surface area, a represents the asymptotic values, o represents initial values and ε_t is the theoretical maximum porosity for complete calcination, given as 0.54 [36]. This model neglects

any particle shrinkage that may occur due to sintering which only becomes dominant during the later stage of intermediate and final sintering.

1.6.3 Factors Affecting Sintering

Overall sorbent particle sintering results from three different types of sintering during CaO cycling: CaCO₃ sintering during carbonation, CaO sintering during calcination and cycle induced sintering. All three cause increased grain size and reduced particle surface area [26,31,33,50]. During this shift the mobility of the ions within the lattice is greatly increased and sintering results. Elevated levels of sintering result from increased mobility in the solid phase [74]. In carbonation and calcination, the crystal lattice undergoes a shift from a rhombohedral to a cubic structure.

Sintering of ultrapure CaO is up to 10 times slower than for natural limestone, as impurity-induced lattice defects, including vacancies, grain boundaries and interstitials, enhance solid-state diffusion [73]. This increases the mobility of molecules that move as a result of vacancy diffusion (section 1.2.3). As a result, sintering differs for each limestone and should be assessed on a case by case basis. Limestone varieties with high levels of impurities may not be suitable for CO₂ capture cycling due to elevated levels of sintering [73]. Hanson and Tullin (1996) found lime mud surface area decreased by 86%, compared to 50% for commercial grade limestone when sintered at 850°C [74]. This results from the increased impurities in the lime mud.

Sun et al. (2007) found that carbonation conditions had little impact on the micro-porous structure of the sorbent. During calcination all structural changes caused by carbonation were eliminated, so that carbonation effectively had no memory. Only extended carbonation (>24 h) was capable of filling intra-particle pores of highly-cycled sorbents. Despite this finding, sintering on the scale of the crystal lattice is likely to occur during carbonation. The Tammann temperature for CaCO₃ is low, 533°C, suggesting that sintering during carbonation does occur [61]. Due to the strong influence of temperature on the sintering rate, above this temperature sintering occurs quite rapidly. During carbonation sintering occurs as a result of mass transfer through the carbonate phase [64]. This explains the activation energy change observed at 515°C, where due to a loss of lattice defects, pure solid state diffusion dominates [26]. Hanson and Tullin (1996) noted that sintering of CaCO₃ increased between 500 - 850°C but was not significant below 700°C.

Sorbents are significantly deactivated by high-temperature calcination due to increased ion mobility within the CaO lattice, leading to crystal growth [81]. Lower calcination temperatures result in less sintering, leaving larger surface area and pore volume [48]. A higher sweep gas flow rate in the calciner better preserves the pore structure of the particle, because of more rapid calcinations, less residence time

of the sorbent in the hot calciner and higher heat transfer to the decomposing sorbent [48]. A shorter calcination time reduces sintering and maintains small pore volumes [36].

CO₂ is known to catalyze sintering of CaO [46,64,73,82,83]. Surface area and pore volume decrease with increasing CO₂ concentration in the sweep gas and the pore diameter of CaO calcined in an O₂/CO₂ atmosphere is between 4 – 30 nm [50]. 1.6 µm limestone particles lost 60% of their surface area when sintered at a CO₂ partial pressure of 0.1 MPa at 850°C for 9 min [84]. The CO₂ released during calcination could also contribute to the increased sintering.

Vacuum decomposition of CaCO₃ at 650°C helped to prevent particle sintering and showed high surface areas of 92 m²/g [85]. Pressures of CO₂ up to 0.1 torr influence the surface area of the CaO by influencing the pore dimensions at the CaCO₃ - CaO reaction interface. Sintering of CaO is negligible at 650°C in CO₂ partial pressures of ≤0.1 torr; however, even a slightly elevated pressure of 9 torr in CO₂ showed significant sintering.

In a CO₂ capture and sequestration process, steam would be used as a sweep gas in the calciner to facilitate easy separation and subsequent high concentration CO₂ sequestration. It is known that the presence of CO₂ and steam during the calcination of CaO leads to increased sintering and reduced capture capacity over a number of cycles [10]. Tertiary eutectic melts containing CaO, CaCO₃ and Ca(OH)₂ can form at temperatures well below the melting temperature of each individual component [10,81]. Melt formation in the Ca(OH)₂ system can form at temperatures as low as 655°C (at 8.8 atm), see Table 1.6, leading to increased particle sintering and faster utilization decay. There is a limitation of H₂O partial pressure on the formation of melts, where a further increase in the partial pressure of H₂O does not cause an increase in particle sintering.

Table 1.6: Melt formation in the CaO–CaCO₃, CaO–Ca(OH)₂ and CaCO₃–Ca(OH)₂ binary systems; reproduced from Florin and Harris (2008) [10].

Binary system	Composition (mol %)	Temperature (°C)	Pressure (atm)	Reference
CaO – CaCO ₃	88.3% CaCO ₃ ^a	1242	39.5 (CO ₂ partial pressure)	Baker (1962)
CaO – Ca(OH) ₂	69.2% Ca(OH) ₂	807	54 (H ₂ O partial pressure)	Curran et al. (1967)
CaCO ₃ – Ca(OH) ₂	47% CaCO ₃	655.5	8.8 (H ₂ O partial pressure)	Curran et al. (1967)
CaCO ₃ – Ca(OH) ₂	73.4% Ca(OH) ₂	700	50 (H ₂ O partial pressure)	Lin et al. (2006)

^aAt temperatures exceeding the eutectic point, binary melts were observed in equilibrium with solid CaCO₃ and CaO. Baker (1962) reports the composition, presented in the table, for the molten fraction only at the eutectic point.

1.7 Improving Capture Capacity

The decay in calcium utilization over a large number of cycles is a major drawback of using limestone as a CO₂ sorbent. Much research is focused on increasing the residual utilization of CaCO₃, either through modification of the capture process or the sorbent particle. A few of the methods to improve residual utilization are discussed below to give more insight into the research ongoing to improve capture capacity, something the present work seeks to do as well. The thermal pretreatment discussed is particularly important as the trends seen in the utilization over multiple cycles closely match those found in the present work.

1.7.1 Hydration Reactivation

One of the more promising methods of improving capture capacity is the use of low-temperature (~300°C) hydration of spent CaO. The molar mass of Ca(OH)₂ is close to that of CaO, while its specific volume is close to that of limestone, giving it a much lower molar density, see Table 1.1. The drop in density during hydration produces a popcorn effect, expanding the sorbent particle; subsequent re-heating and de-hydration of the hydrate causes particle shrinkage and micro-pore formation. Steam hydration can occur at temperatures up to 400°C [86]. Increased conversion was reported when CaO was hydrated prior to cycling (up to 10 cycles) [87]. Hydration pre-treatment resulted in increased pore volume and sorbent surface area. Hydration pre-treatment of lime achieved 60 - 70% calcium utilization after 4 cycles, compared to 45% without pretreatment [87].

It has been proposed to add a third hydration step in the CaO-CO₂ looping cycling to increase the capacity of the sorbent [81,88]. This has the potential to increase the carbon capture by up to 600% [86]. Zeman (2008) conducted ten cycle experiments with calcination (960°C, 1 bar CO₂), hydration (300°C, 1 bar CO₂ and excess steam) and carbonation (780°C, 1 bar CO₂) stages [86]. Asymptotic calcium utilization was 60% after ten cycles, compared to 8% without the hydration step.

CaO conversion with a steam hydration intermediate step was found to follow a similar trend to that without hydration, but with a much larger residual utilization [86]:

$$X_N = \left(\frac{1}{1 - X_r} + kN \right)^{-1} + X_r \quad (1.32)$$

where $k = 0.505$ and $X_r = 0.48$.

A system with a hydration step would require much less solid inventory, up to 37% less, for a given overall capture. The sorbent replacement cost would be reduced to \$1/tonne CO₂ captured, not accounting for losses due to attrition, compared to \$1.88/ton CO₂ using MEA [86]. The thermal load of the CO₂ capture system is also reduced due to the smaller solid inventory required. One major drawback

of this would be the additional heat required, approximately 5.7 kJ_h/mol CO₂, to re-heat the sorbent following the low-temperature hydration [86]. The other major drawback is a drastic reduction in particle durability. The increase in volume and porosity weakens the particle structure, making it much more prone to attrition in a fluidized bed.

Manovic et al. (2008) found that spent sorbents from a 75kW_{th} dual fluidized bed oxy-fuel fired with biomass and coal could be reactivated through hydration. Even short hydration times (~15 min at 1 atm and 100°C) improved the spent sorbent morphology, showing increased surface area, improved pore volume distribution and particle swelling. These three particle properties all led to improved calcium utilization.

Laursen et al. (2001) investigated the hydration of sulfated calcium sorbents in an effort to increase their effectiveness for sulfur capture. Both pure limestone and spent sorbents were calcined, sulfated, hydrated in steam (250 - 450°C) and then re-sulfated. Spent sorbent was more difficult to re-activate than pure sorbents. Only very low temperature hydration (250°C) increased spent sorbent utilization. Hydration of pure sorbents prior to sulphation did increase the calcium utilization.

1.7.2 Thermal Pretreatment

As mentioned above long calcination times were found to increase the residual sorbent utilization. Switching from a long calcination to a short calcination did not reduce the residual utilization [64]. This suggests that the sorbent remembers its thermal calcination history. The loss of activity is less in the cycle immediately following a long (600 min) calcination [64]. After a third long calcination, there is no more loss in activity. Sintering the limestone as a pretreatment before cycling also increases the asymptotic calcium utilization in a similar manner [34,89].

When thermally pretreated samples are cycled for CO₂ capture, they initially show lower utilization in the first carbonation cycle compared to un-treated sorbents [34,40,63,90]. In the first 10 - 20 cycles the utilization of pre-treated sorbents increases, showing the opposite trend to that observed for un-treated sorbents, see Figure 1.12. Following this increase, the utilization decreases, reaching an asymptotic value greater than for un-treated sorbents [63].

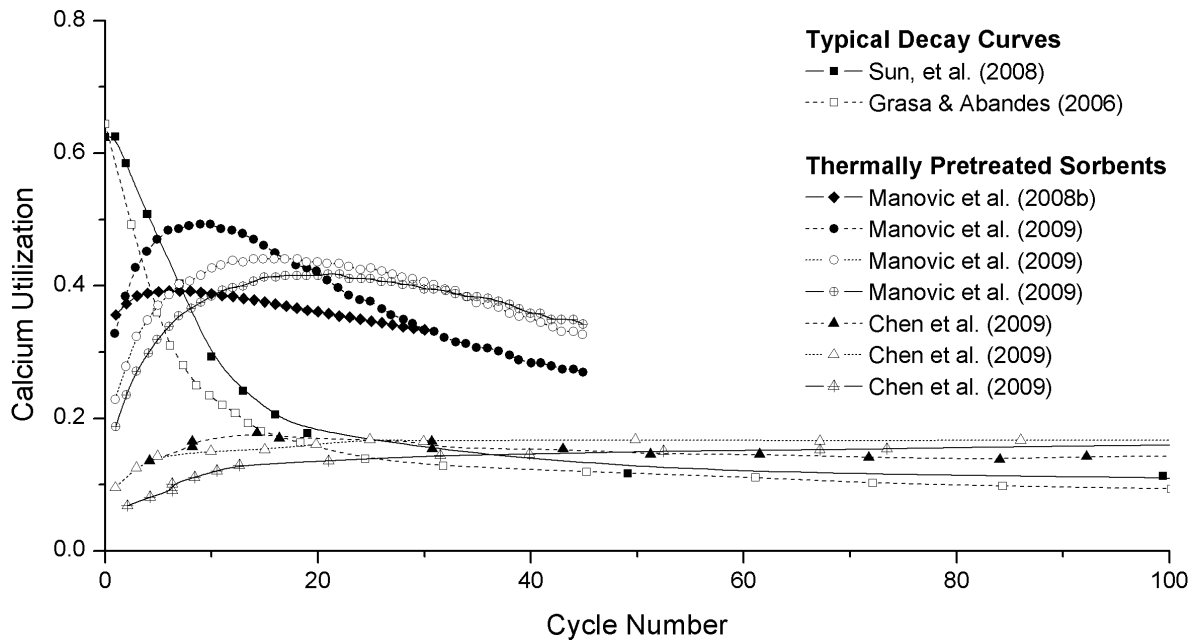


Figure 1.12: Effect of thermal pre-treatment on utilization decay [34,40,63,89,90]

Sorbent preheating may stabilize the minimum carbonation level through the formation of a stable CaO crystal skeleton within the sorbent particle that better maintains the porous structure [64]. Skeletal densities after CO₂ looping were higher than for the initial calcine [91]. Formation and decomposition of CaCO₃ have a strong sorbent sintering effect and leads to a loss of utilization. This effect could be tempered by the stable CaO skeleton, as CaO is more thermally stable and not as affected by sintering. Pretreatment at 800°C for 24 h produced a sorbent with higher residual activity (28%) than for untreated sorbents (15%), see Figure 1.12 [64].

Manovic et al. (2008) found that different limestone pre-cursors responded differently to thermal pretreatment [89]. La Blanca limestone (400 - 600 μm) showed no improvement with pretreatment and experienced reduced utilization. This might be due to its low impurity content; the main impurity is Na₂O at 1.07%. Interestingly, when powdered, it showed modest 'self-reactivation' at higher temperatures (1200°C), likely due to increased impurities from sieving out the larger more pure particles [64]. La Blanca has previously been shown to be more sensitive to temperature than other limestone varieties, see 1.5.1 [40].

Doping La Blanca limestone with Al₂O₃ reduced capacity in the first few cycles [89]. When doped with 5-10 wt% it showed the increase associated with self-reactivation. Doping with 2.5 wt% did not lead to an increase; however, it still maintained better performance in the long term than un-doped [89]. The lack of Al was deemed the probable cause of the absence of the 'self-reactivation' effect in La Blanca, showing the importance of impurities in sorbent sintering [89]. Areas with more Al₂O₃ showed smaller

grains and less sintering after repeated cycles, implying that the underlying CaO skeleton was held more intact. This suggests that Al acts as a binder, stabilizing the CaO structure.

Kelly Rock limestone (300 - 425 μm), which contains higher levels of impurities, specifically Al, was also tested and showed significant "self-reactivation", as shown by the three curves from Manovic et al. (2008) in Figure 1.12 [89]. Interestingly, doping Kelly Rock with Na_2CO_3 increased utilization during initial cycles, but decreased the residual utilization. It is thought that Na^+ impurities increase mobility of Ca^{2+} in the lattice which accelerated sintering. The formation of other compounds ($\text{Na}_2\text{Ca}(\text{CO}_3)_2$, $\text{Na}_2\text{Ca}_2(\text{CO}_3)_3$, etc) with lower melting points would also increase sintering. SEM images show decreased surface area in Na-doped samples. In the case of Kelly Rock, the un-doped samples performed best with 60% utilization after 30 cycles.

A higher CO_2 concentration increased conversion within 30 cycles, but increased the rate of decay after 'self-reactivation' [89], likely due to increased sintering, and surface area loss during cycling. Increased carbonation duration favours the 'self-reactivation' mechanism [89].

1.7.3 Dolomite

A number of studies have examined dolomite ($\text{CaCO}_3 \cdot \text{MgCO}_3$) as a CO_2 sorbent. Due to its close relation to limestone, dolomite can give some insights into the function of limestone-based sorbents. Dolomite shows a much higher CaO utilization, but a similar CO_2 capture ratio on a mass basis to limestone [35,40]. In one study, utilization of 90 – 95% was obtained for the first few cycles, decreasing by only 1-2% after 5 cycles [92]. Superior conversion efficiency makes up for the lower fraction of CaO (~50 wt%) after only a few cycles. The CaO- CO_2 surface reactions are affected by the local environment and the temperature-time-environment history of the solid.

The presence of MgO facilitates solid-state CO_2 diffusion and decreases sintering by stabilizing the sorbent morphology. CaO crystals in dolomite are much smaller than in lime [18]. The magnesium in dolomite is inactive and its ultrafine dispersion serves to support the micro-porous structure of the sorbent [18]. The CaO utilization is governed by the micro-porosity of the product layer.

As in limestone-based sorbents, more deactivation occurs at higher temperatures due to increased sintering. Sintering increases the CaO crystal size and decreases lattice imperfections. Calcination of dolomite in N_2 at 800°C produces the most reactive CaO, due to reduced sintering in an inert environment [18]. Conversely, immersing the sorbent in CO_2 above 925°C results in severe loss of utilization, as CO_2 catalyses ion diffusion in the CaO lattice, enhancing sintering.

The use of 50% steam in carbonation of dolomite at 20.7 bar_g accelerated the carbonation rate by 15 - 50 times [18]. Steam acts as a catalyst for carbonation, much in the same way as for limestone-based sorbents; it also catalyses both the CaCO_3 decomposition and intermediate reactions during calcination.

This catalytic effect has been found to have no memory and once steam usage is stopped subsequent cycles show no increased rate of carbonation [18].

The reaction rate is governed by size and lattice strain of solid crystals and macro-pore structure of the material. The rate is slower at elevated pressure for equivalent partial pressures of CO₂ [18]. The temperature and cycle number do not affect the initial reaction rates, but do affect the asymptotic utilization level [18].

One of the problems with dolomites is their poor mechanical strength; however, cycle-induced sintering reduces pore volume and strengthens the particle, with attrition rates dropping below 0.5 wt% per cycle [35].

1.7.4 Synthetic Sorbents

A considerable amount of research is focused on the creation of synthetic CaO-based sorbents, in an effort to eliminate the shortcomings of 'natural' limestone. The low residual utilization of natural sorbents, 7.5% or 60 mg(CO₂) / g(sorbent) and their susceptibility to attrition are the main properties of interest [17].

Nano-sized CaO particles distributed on an inert support, similar to industrial catalysts, have been investigated by a number of researchers [76,93,94]. Theoretically, if CaO particles are smaller than the critical product layer thickness, then conversions of 100% should be possible [95]. Feng et al. (2006) investigated CaO on a γ -Al₂O₃ support, fabricated using wet impregnation of CaCl₂ on γ -Alumina. They found that conversion of 90% was maintained through 9 cycles, compared to 20% for limestone. The synthetic sorbent showed no change in size or shape. The high conversion was attributed to the very fine CaO particles on the alumina support; however, this sorbent faced issues with degradation in mechanical strength over many cycles. Aihara et al. (2001) investigated CaO supported on CaTiO₃, primarily for use as a high-temperature heat pump. Conversion of 60% was maintained after 10 cycles. Other precipitated CaO sorbents have shown conversions of 46% after 100 cycles [94]. Precipitation creates a meso-porous structure (2 - 50 nm) that prevents pore blocking and enhances access to the entire CaO surface area.

The drawback of CaO-supported sorbents is their low CO₂ capture capacity, on a mass basis, due to low sorbent loading, which in the above case [94] translated to 4.3% capture by weight, or about 30.4 mg(CO₂) / g(sorbent). This deficiency could be avoided if nano-sized CaO particles could be used without a support. Barker (1973) reported 93% conversion after 30 cycles using nano-sized CaO particles. In an industrial system, elutriation would be a major issue for nano-sized particles [96].

Li et al. (2005) tried a mixed CaO and Ca₁₂Al₁₄O₃₃ sorbent and obtained a utilization of 65% after 50 cycles, with increased calcination temperature leading to a decreased utilization, similar to natural sorbent behaviour.

Attrition is a major problem facing CaO sorbents in industrial facilities. Calcination of a sorbent particle greatly reduces the molar density of the particle, making it more susceptible to attrition. Attrition in a flow reactor leads to particle elutriation and the need for make-up sorbent. Akiti et al. (2002) created a “core-in-shell” sorbent particle of CaO and alumina pellet for sulphur capture. Pellets of CaO and alumina or calcium sulfate hemi-hydrate were coated with CaO and alumina powder, and heat treated (at 1100°C) to convert the shell into a robust porous media.

Another method to reduce attrition is through manufacture of lime-based pellets with more favourable attrition characteristics than raw limestone. Wu et al. (2012) fabricated pellets from powdered limestone and calcium-aluminate cement (71 wt% Al_2O_3 and 28 wt% CaO). These pellets gave a slightly increased utilization over 100 cycles as they had a much larger initial surface area for absorption. Attrition of the pellets over 2 h was also reduced relative to raw limestone [99].

Other researchers [100] have examined CaO-based sorbent material mixed with catalyst. The purpose of these sorbents is not to enhance CO_2 capture, but to combine CO_2 with a catalyst needed in a particular chemical process such as steam-methane reforming. They obtained a very low capture capacity of 2 $\text{g}(\text{CO}_2) / \text{g}(\text{sorbent})$ after 1 cycle with their combined particle [100].

1.8 CaO and Biomass Gasification

One of the more promising applications of CaO-based CO₂ capture is for in-situ capture in gasification or reforming processes. Gasification can be used to produce alternative fuels including electricity for battery-powered vehicles, H₂ for fuel cells, dimethyl ether (DME) for diesel engines and methanol for spark ignition engines. Biomass gasification coupled with CO₂ capture could produce transportation fuels with net negative CO₂ emissions.

As mentioned previously, CaO captures CO₂ at elevated temperatures between 550 – 700°C (at atmospheric pressure), well suited to the range of temperatures used in gasification and reforming processes. If biomass is used as the feedstock in a gasification process with CO₂ capture, net removal of CO₂ from the atmosphere can be achieved. The low carbon content of biomass fuels means they can be gasified at lower temperatures than coal, in a range more suitable for CaO-based sorbents [57].

In addition to capturing CO₂, in-situ use of a CaO-based sorbent in a biomass gasifier or reformer increases product gas yield, by shifting the equilibrium of the gasification reactions further towards the desired products (H₂, CO and/or CH₄) [10,23]. When using limestone sorbent precursor, this process is entitled Limestone-Enhanced Gasification (L.E.G.) of Biomass.

Biomass fuel costs make up about 40% of the H₂ cost from biomass gasification [10]. Much of the remaining costs are associated with hot gas clean-up and hydrogen separation. If a higher concentration of hydrogen could be generated, these costs could be reduced.

1.8.1 Biomass Gasification

Gasification is a method of converting a solid fuel into a more easily consumed form. Gasification thermally breaks down the complex hydrocarbons in the fuel into simpler compounds, primarily non-condensable gases. These gases can be used to generate heat and electricity, produce hydrogen for use in fuel cells, or converted into liquid fuels through the Fischer-Tropsch process:



Gasification is a thermo-chemical process involving several steps in the production of gaseous fuels. The three main reaction steps are pyrolysis of the raw fuel when volatiles are released, char gasification and tar cracking, see Figure 1.13. Pyrolysis occurs very rapidly as the solid fuel particles are heated, resulting in the release of the more volatile components of the fuel. These gaseous volatiles, composed of high molecular weight hydrocarbon compounds, react with the gasification agent (O₂, H₂O or CO₂), and are cracked into lower molecular weight compounds (H₂, CO, CO₂, CH₄). Due to kinetic limitations, not all these compounds are fully cracked and can remain as condensable tars. The solid char (CH_x, x < 1)

remaining from pyrolysis also reacts with the gasifying agent to produce gaseous products (H_2 , CO , CO_2 , CH_4).

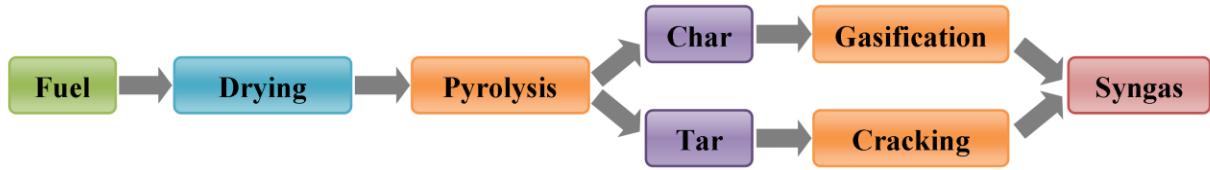


Figure 1.13: Steps in gasification of solid fuels

Tar cracking is of great importance in gasification of biomass as the high mass fraction of volatiles in biomass cause large amounts of tar to be produced, compared to coal, see Table 1.7. Tar is defined as hydrocarbons which condense at ambient temperatures. These tars can become problematic in downstream equipment and lead to fouling and blockages. Tars can be minimized through thermal cracking at high temperatures ($> 900^{\circ}C$) or catalytic cracking using Ni, dolomite, or alkali metals catalysts [10].

Table 1.7: Proximate analyses of coal and biomass; adapted from Demirbaş (2005) [101]

	Volatiles (dwt%)	Fixed Carbon (dwt%)	Ash (dwt%)
Coal	41.7	53.2	5.1
Spruce Wood	70.8	28.3	0.9
Wheat Straw	62.8	17.6	15.5

Tar contains numerous condensable compounds with a typical composition of: 78% [C], 6% [H], 0.7% [N], 12% [O], 0.5% [S] [102]. The two compounds that make up the majority of tar from biomass are indene and naphthalene, 29.5 wt% and 49.6 wt%, respectively [103]. These condensable tars can cause blockage and damage in equipment downstream of the gasifier.

Tar cracking reactions are highly endothermic, and tar yield can be decreased by increasing temperature. Tar yield in a circulating fluidized bed gasifier, showed exponential decay with increasing temperature, with an increase from 715 to $815^{\circ}C$ reducing tar from 15.2 to 0.4 g/Nm^3 [102]. It was also reduced by up to 62% using a catalyst and a minimum of 0.15 g/Nm^3 was achieved with a catalyst at $800^{\circ}C$ [102]. Narvaáz et al. (1996) obtained a 74% reduction in gravimetric tar yield from 19 to 5 g/m^3 when the temperature was increased from 700 to $850^{\circ}C$ [104].

There are numerous reactions involved in the pyrolysis, char cracking and char gasification steps. The most relevant reactions are listed in Table 1.8.

Table 1.8: Primary gasification reactions

Reaction		Heat of Reaction (kJ/mol)
Pyrolysis		
1	$4C_nH_m \Rightarrow mCH_4 + (4n - m)C$	Exothermic
Gas Phase Reactions		
2	$CO + H_2O \Leftrightarrow CO_2 + H_2$	(Water-gas shift) -35
3	$CH_4 + H_2O \Leftrightarrow CO + 3H_2$	(Methane reforming) 225
Char Gasification		
4	$C + H_2O \Leftrightarrow CO + H_2$	(Water-gas 1) 136
5	$C + 2H_2O \Leftrightarrow CO_2 + 2H_2$	(Water-gas 2) 100
6	$C + CO_2 \Leftrightarrow 2CO$	(Boudouard) 171
7	$C + 2H_2 \Leftrightarrow CH_4$	(Methanation) -89
Char Combustion		
8	$C + O_2 \Rightarrow CO_2$	-394
9	$C + 0.5O_2 \Rightarrow CO$	-112

The design of biomass gasifiers generally fits into one of four categories: fixed bed, moving bed, fluidized bed and entrained flow gasifiers. In fixed bed gasifiers, solid fuel is fed into the reactor using a screw feeder and the reactive gases are passed through the resulting pile or bed of solids. A moving bed is similar, except that the solids are transported through the gasifier by a moving horizontal grate or by gravity in the case of a vertical moving bed. These gasifiers have a very simple design and operation and are widely used in small installations, but have low carbon conversion efficiency and produce a large amount of tar [105]. They are also unsuitable for large installations due to non-uniform temperature distributions [106].

Entrained flow gasifiers gasify small fuel particles transported by a flow of gas. These units are frequently used in large scale coal gasification facilities. They suffer from low carbon conversion due to entrained char fines and slagging issues with the liquid ash due to their high operation temperature. In a fluidized bed gasifier the fuel particles are gasified in a bed of solid particles suspended by an upward flow of reaction gases. Fluidized bed reactors are best suited to biomass gasification with in-situ CO₂ capture as sorbent particles can be used as the bed material [10]. Fluidized beds facilitate good heat and mass transfer; have good temperature uniformity and high sorbent / catalyst utilization. A fluidized bed gasifier produces the least amount of tar and generates more lighter gases due to the high heating rate of fuel particles injected into the bed [107].

The final composition of the product gas can be manipulated by changing the reaction parameters: temperature, pressure, steam/biomass ratio [10]. There are numerous experimental studies into fluidized bed biomass gasification; the following is a sample of those studies describing the effects of different parameters on the process.

Li et al (2004) conducted experimental studies into biomass gasification using a circulating fluidized bed (CFB) [102]. Concentrations of combustibles decreased with increasing air ratio, down by a factor of 0.6, due to the increasing dilution with N₂. The optimal air equivalence ratio (ER) was approximately 0.23 [102]. A typical air-blown gasifier will produce 1.4 to 2.6 m³ of syngas / kg of biomass, with lower heating values (LHV) of 6.74 to 9.14 kJ/m³ [108]. The addition of secondary air has a similar, but less substantial, effect on the HHV, decreasing it by less than 5% (4.20-4.02 MJ/Nm³) [102]. The addition of secondary air has the beneficial effect of decreasing tar yield due to the formation of high-temperature cracking zones above the fluidized bed [109]. Li et al. (2004) found that the oxygen-to-carbon ratio (O/C) should be in the range of 1.3-1.6 to maximize gasification efficiency [102]. They defined the cold gas efficiency by:

$$\eta_{cg} = \frac{(HHV_{fg} \times v_{fg} + HHV_{tar} y_{tar})}{(GCV_{fuel})} \quad (1.34)$$

where higher heating value (HHV) of the flue gas and the tar are expressed in kJ/m³ and kJ/kg respectively, v_{fg} is the specific dry gas volume (m³/kg_{fuel}), y_t is the tar yield (kg_{tar}/kg_{fuel}) and GCV is the gross heating value of the fuel (kJ/kg).

The maximum yield from biomass gasification is found to occur in the absence of oxygen when steam is used as the primary reaction gas [110,111]. The use of steam during biomass gasification is significant. It improves gas quality by enabling CH₄ reforming and C and CO-shift reactions, reactions 2-5 in Table 1.8 [102,108]. Yields of up to 0.13 kg of H₂ / kg of biomass are possible in steam gasification [10]. There are diminishing returns, however, with the rate of increase in H₂ yield decreasing with increasing steam-to-biomass ratio [10]. An increase in the steam-to-biomass mass ratio beyond 2.7 offers little improvement to the resulting gas [108].

Increased steam decreases the char and tar yields, in addition to improved syngas quality. Excess steam increases the heat duty of the system and if the latent heat of the steam is not recuperated, the energy penalty of increasing steam can become prohibitive. Recovering the latent heat from steam can be difficult.

Increasing temperature has a positive effect on gasification, with the HHV increasing by 10% between 700 and 800°C, due to improved carbon conversion efficiency [102]. In a separate study, an increase in temperature from 700 to 900°C increased the carbon conversion efficiency from 78 to 93% [108]. Hydrogen production increases at the expense of CH₄ with increasing temperature as the methane reforming reaction is highly endothermic, reaction 3 in Table 1.8 [112]. High temperatures also aid the thermal cracking of tars. An optimum temperature exists to balance the exothermic water-gas-shift and endothermic reforming and tar cracking reactions [10]. An increase in H₂ yield with an increase in temperature can be attributed [10] to:

- i) increased gas production during pyrolysis,
- ii) steam cracking of heavy hydrocarbons and tar,
- iii) enhanced char gasification reactions

Smaller fuel particles, sawdust, showed better conversion than wood chips due to faster heating and reaction rates [10]. It has also been found that an increase in suspension density in the fluidized bed increased the HHV due to improved contacting and heating of solid reactants [102]. Particle segregation in the bed can increase char yields, due to poor contacting [10].

Entrainment of char fines from a fluidized bed can be a major factor affecting the carbon conversion efficiency of the system. Fly ash re-injection increases HHV due to the high carbon content in the fly ash; however, this reaches a beneficial limit at a given reactor temperature and residence time [102].

The sum of the primary gasification reactions, 1 - 7 in Table 1.8, is highly endothermic, so that a large amount of heat must be supplied to drive the reactions. In air / oxy-fuel gasification this heat is supplied by combustion of char, equations 8 and 9 in Table 1.8. Due to the dilution by nitrogen, air blown gasifiers produce a low heating value syngas (HHV of 4 - 7 MJ/Nm³) [102]. Oxy-fuel gasification produces a much higher calorific value syngas (HHV of 10 - 18 MJ/Nm³), but the oxygen separation unit imposes a large energy penalty on the system [102].

The heat needed for gasification could also be supplied by an external source. One of the more efficient ways to supply this heat is to circulate hot particles to transfer heat from a secondary combustion reactor into the gasifier. Combustion of fuel in the secondary reactor heats the solids which are then transferred to the gasification reactor, eliminating the dilution of the syngas by air. To supply all the required heat, a high flow rate of solids between the reactors must be maintained. The exothermic heat of reaction of CaO carbonation, equation 1.2, could supply much of the heat needed for gasification [23]. If a concentrated CO₂ stream is desired for sequestration, O₂ combustion must take place in the calciner; however, the O₂ demand of the calciner would be 54% of conventional oxy-fuel firing [23].

1.8.2 Sorbent-Enhanced Biomass Gasification

The concept of enhanced gasification dates back to the 19th century when Du Motay and Maréchal (1868) produced hydrogen through steam reforming of various hydrocarbons in the presence of CaO [113]. The idea was more thoroughly explored later by Curran et al (1967). With its potential benefits over standard gasification, sorbent-enhanced gasification is gaining interest, and there have been a number of studies looking at the design and performance of such gasifiers. CaO is chosen for CO₂ removal because it can remove CO₂ at low concentrations and capture CO₂ at temperatures and pressures suitable for biomass gasification [57].

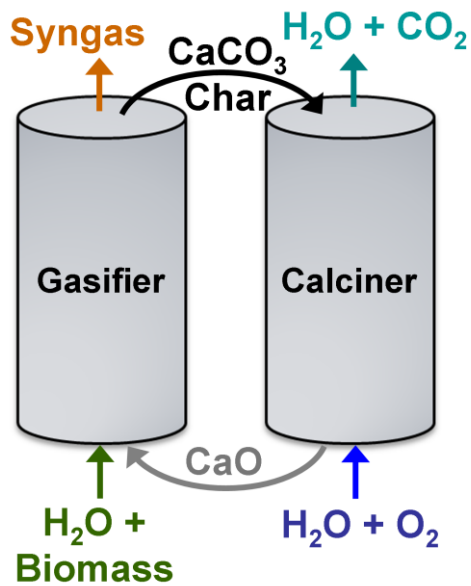


Figure 1.14: Sorbent enhanced biomass gasification dual reactor system configuration

In-situ use of CaO in the gasifier can increase H₂ yield, while lowering the required gasification temperature and reducing CO₂ emissions [114]. As well, the energy required for the endothermic gasification reactions can be provided by the sensible heat of the sorbent if using a dual-reactor system as shown in Figure 1.14 and exothermic CaO carbonation [23,103]. The circulation rate of the hot solids can be adjusted to satisfy the gasifier heat requirements. Biomass gasification experiments have shown the added benefit of increased H₂ production versus coal gasification, with CaO [10].

Optimization of reaction conditions for both CO₂ capture and fuel conversion requires a compromise of temperature and pressure [10]. To avoid compromising the CO₂ capture reaction by operating at elevated temperature, the reaction could be conducted at higher pressure. High temperature favours the endothermic gasification reaction, but not the exothermic CO₂-CaO reaction or H₂O-gas shift reaction. Most current research investigating enhanced coal gasification use elevated pressures of 5 - 20 bar [10].

With an increase in pressure, sorbent-enhanced coal gasification showed increased H₂ production and decreased CO + CO₂ concentrations. H₂ yield from biomass initially increases with pressure up to 12.8 atm, then decreases at higher pressure [10]. The technical issue of maintaining a pressure seal between the gasification and calcination chambers remains. This could be accomplished in part through the use of hydrostatic pressure from a fluidized bed of sorbent particles.

Tar production is an issue in sorbent-enhanced gasification as tar and its decomposition product coke, can deactivate CaO through pore plugging [10]. Elevated temperature and increased steam-to-biomass ratio can reduce tar formation. In addition, CaO can catalyze tar decomposition; however, there are operating limits for CaO for both tar elimination and CO₂ capture.

The majority of experimental studies have examined limestone enhanced gasification (L.E.G.) for the conversion of coal. There have been a few studies on the gasification of biomass, to be discussed separately below, as the experimental setup and conditions vary widely and make it difficult to discuss the results collectively.

Curran et al. (1967) conducted a "CO₂ acceptor gasification process" with a bed of char, fluidized using steam [35]. Lime sorbent was fed on top of the bed, sinking to the bottom and removed by a screw. For full conversion of the CaO the residence time of sorbent in the bed was greater than 7 min. Steam partial pressure must be kept below 13 atm to avoid excessive melt formation as the CaO - Ca(OH)₂ eutectic point was found to occur at 807°C and 54 atm steam partial pressure, Table 1.6. Char combustion in a separate calciner had an adverse effect on the calcium utilization when cycling the sorbent for 10 cycles, due an increase in the localized temperature of the sorbent from combustion of the char, causing sintering.

The HyPr-RING process under development at the Institute for Energy Utilization in Japan incorporates gasification, reforming, and CO₂ capture in a single high pressure (3 - 12 MPa) reactor [115]. The process uses a dual-fluidized bed system, with a number of heat exchangers for efficient heat integration. The gasifying agent is steam at temperatures of 600 - 700°C, requiring a highly reactive fuel, such as bituminous coal or biomass. Due to the elevated pressures, CaO re-generation requires a high temperature (1000°C). Hydrogen production of greater than 80 vol% (dry basis) in the syngas was achieved at conversion efficiencies of > 90%. High (10%) moisture content of the fuel was preferred to provide moisture for the reforming reactions.

Pfeifer et al. (2007) performed experimental studies on a 100kW_{th} dual fluidized bed, steam, biomass gasifier [103]. The use of a limestone-based sorbent as the bed material in the dual-bed system increased the hydrogen content in the syngas from 40 to 75 vol% (dry basis). The system was self-stabilizing, as a decrease in gasification temperature increased the char carryover into the combustion, increasing the temperature in the combustor and the temperature of the solids circulating back to the gasifier. From mass and energy balances, they found that only about 20% of the circulating CaO material was actively involved in CO₂ absorption / desorption reactions. The remaining solids had residence times too short to be effective. Stable operation at 700°C for 6 h was achieved with stable hydrogen and carbon dioxide concentrations of 65 vol% and 13 vol%, respectively. The elevated CO₂ concentration indicates that the system did not achieve 100% CO₂ capture at this temperature as the CO₂ partial pressure was similar to the equilibrium partial pressure. Finally, Pfeifer et al. (2007) found an inverse correlation between the tar yield and solid circulation rate. As the circulation increased, there was more un-reacted CaO available for tar cracking reactions. The tar yield at 600 - 700°C, ~2 g/m³, was similar to that for biomass gasification using a fluidized bed of olivine at a temperature of 850°C.

Florin and Harris (2008a) conducted L.E.G. experiments in a thermo-gravimetric, mass spectrometer (TG-MS) system [116]. They showed that the use of CaO in methyl cellulose pyrolysis (100% Ar atmosphere) caused the formation of H₂, whereas in the absence of CaO, no H₂ was formed. CaO hydration to Ca(OH)₂ was found to be a dominant reaction, with the exothermic hydration and, to a lesser extent, carbonation reactions driving secondary decomposition reactions and particle swelling, facilitating the escape of evolved species from the reaction vessel. Addition of water vapour caused a substantial reduction in char formation and a 14.4% increase in hydrogen yield in the presence of CaO.

Hanaoka et al. (2005) gasified biomass on the gram scale in the presence of CaO (with CaO / C ratios of 1 - 4) and obtained a product gas devoid of CO₂ [117]. A pressure of 0.6 MPa was found to give the highest conversion. An increase in pressure above this decreased the yield and conversion because tar cracking is favoured by a low pressure. The maximum H₂ yield occurred at a CaO / C ratio of 2. The higher-than-stoichiometric ratio required was attributed to an increased contact frequency of CaO and biomass in the sample dish. The yield and conversion decreased to 66% when the biomass and CaO were separated. It was found that CaO acted as a CO₂ sorbent, as well as a catalyst for gasification.

Mahishi & Goswami (2007) gasified pine bark batch-wise and fed the produced gas through a separate reactor containing reagent grade CaO [118]. The experiment was conducted with a 5 g sample of biomass gasified in steam for 75 min. The breakthrough period is defined as the period of maximum CO₂ absorption, before the sorbent has become saturated with CO₂. Even with the CO₂ capture decoupled from the gasification, during the initial breakthrough period of CO₂ capture, the syngas was of much high quality and more rich in H₂, see Table 1.9. The breakthrough period lasted for 15 min before the H₂ concentration began to drop off.

Table 1.9: Gas composition during breakthrough of biomass gasification at 600°C and 1 atm [118]

	Gas Composition (vol%)				Gas Yield (ml/g)	Carbon Conversion (%)
	H ₂	CH ₄	CO	CO ₂		
No CaO	60.2	3.1	9.0	27.7	875	30.3
With CaO	83.0	1.5	6.3	9.2	1418	55.6

Over the entire batch run with a CaO-to-biomass molar ratio of 1:1, the hydrogen yield increased by 48.6%, the total gas yield increased by 62.2% and the carbon conversion efficiency increased by 83.5% at 600°C and 1 atm. This was attributed to the reforming of higher hydrocarbons and tar catalyzed by the CaO, increasing carbon conversion with sorbent present.

1.8.3 Modeling

To date, studies into integrated biomass gasification and CO₂ capture have been mostly computer-based models of the reaction process. The majority of models have been thermodynamic, based on Gibbs free energy minimization, with a few models based on reaction kinetics [17,119]. Although models without experimental validation do not always depict the experimental situation accurately, they offer a starting

point for experimental design. Experimental studies are required to validate the models and demonstrate the feasibility of sorbent-enhanced biomass gasification.

Florin and Harris (2007) noted that thermodynamic equilibrium should be considered the upper limit for representing fuel conversion, as equilibrium models contain oversimplifications; the most important of which is the representation of biomass by its ultimate analysis (H, C, O, N and ash composition) and not the collection of complex organic compounds it is made of [57]. This and other oversimplifications lead to the following common problems [57]:

1. Over-prediction of carbon conversion;
2. Under-prediction of CH₄ concentration, as CH₄ formation is associated with non-equilibrium pathways including incomplete reforming and cracking;
3. Tar formation is poorly modeled;
4. Over-prediction of H₂ concentrations, as low carbon conversion reduces H₂O shift reactions and unconverted coke containing hydrogen (CH_x, 0 < x < 1) and tar are often neglected.

Florin and Harris (2007) completed an equilibrium model in ASPEN Plus to identify a suitable operating window for sorbent-enhanced biomass gasification [57]. The highest H₂ yield during gasification without CaO was 59%, occurring at atmospheric pressure and 825°C. With active CO₂ capture, this maximum could be increased to ~83%. With CaO present, the CH₄ concentration was drastically reduced and the CO₂ concentration was close to zero in the active temperature range of CO₂ capture at atmospheric pressure, as shown in Figure 1.15.

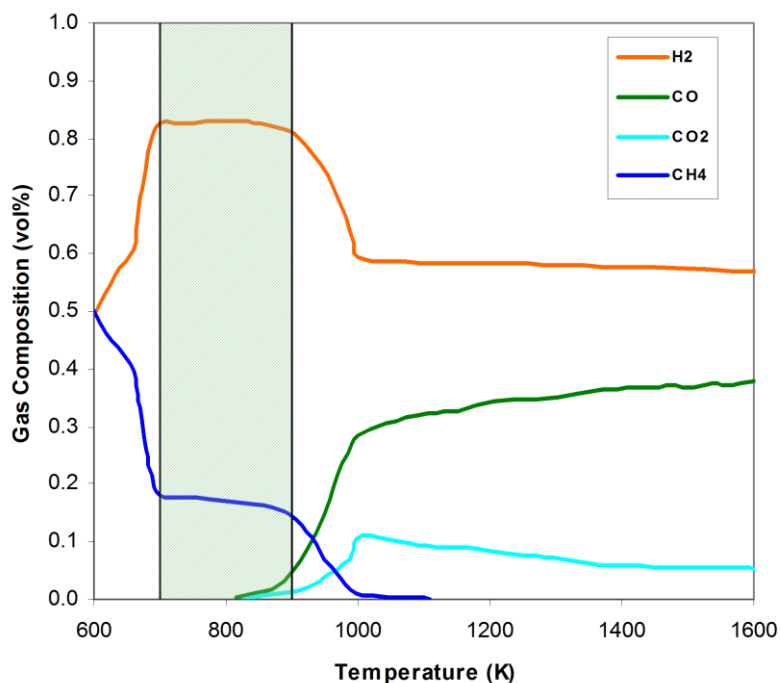


Figure 1.15: Equilibrium concentrations of syngas during sorbent-enhanced biomass gasification. The shaded area represents the area of active CO₂ capture at atmospheric pressure; adapted from Florin and Harris (2007) [57].

Temperatures greater than 625°C greatly reduced CO₂ capture, and the H₂ concentration decreased dramatically as a result. At lower temperatures exothermic methanation, reaction 7 in Table 1.8, led to high CH₄ concentrations.

H₂ yield was only sensitive to the steam-to-biomass ratio at low temperatures, 325 - 625°C [57]. Maximum H₂ yield occurred at a steam-to-biomass ratio of 2; however, increasing the steam concentration in the product gas reduced the overall H₂ concentration, and a ratio of 1.5 was considered the best choice for optimization of H₂ yield and concentration. High pressure favored CaCO₃ formation at higher temperatures, but also promoted formation of Ca(OH)₂, leaving less CaO available for CO₂ capture. Moreover, hydrogen was locked into Ca(OH)₂, lowering the H₂ yield. An increase in the Ca:C ratio caused increased formation of Ca(OH)₂, which absorbs hydrogen, reducing the H₂ yield. Modeling predicted that the best conditions for biomass gasification with CaO-based CO₂ capture are 1 atm pressure, temperatures between 525 - 625°C, a steam-to-biomass ratio of 1.5 and a calcium-to-carbon ratio of 0.9 [57].

Mahishi et al. (2008) developed a Gibbs free energy based model in ASPEN Plus to determine optimum parameters for sorbent-enhanced biomass gasification [114]. They modeled three different gasification scenarios: Gasification over a Cu/Ni catalyst, gasification in the presence of CaO, and the use of CaO in a water gas shift reactor post gasification. The first case with gasification in the presence of a catalyst

gave the highest H₂ yield at 725°C and 1 atm. Increasing the steam-to-biomass ratio up to 3, increased the product gas yield. Beyond this, additional steam had no effect.

In the second case with CaO present in the reactor, H₂ yield increased by 19% and CO₂ decreased by 50% relative to the base case, gasification over the Cu/Ni catalyst, without CO₂ capture. Gasification efficiency increased from 62.9% without CaO to 72.1% with CaO, calculated based on the LHV of the product gas. At temperatures above 750°C and at 1 atm pressure, no CO₂ capture occurred, and the yield was similar to the base case. The maximum yield occurred at 650°C. Pressures above 1 atm had the effect of increasing CH₄ production at the expense of H₂. CaO-to-biomass ratios above 3 offered little improvement. With carbonation occurring in-situ, the gasifier heat duty was reduced by 42%. The third case of CaO in the downstream water-gas-shift reactor offered little improvement over the first case, with H₂ production reduced by 13% versus the CaO case. CH₄ concentrations for all cases were very low compared to experimental results, highlighting one of the deficiencies of biomass gasification models.

Bretado et al. (2008) utilized a chemical equilibrium model based on Gibbs free energy minimization, with HSC Chemistry 5.1 software to determine the best CO₂ sorbents for an enhanced water-gas shift reaction [121]. Three sorbents were examined: CaO·MgO, Li₄SiO₄ and Na₂ZrO₃ and results showed H₂ yields of 98%, 81% and 95% respectively on a molar basis. Na₂ZrO₃ was selected as the preferred sorbent due to its high H₂ yield and previously found high thermal and mechanical stability during repeated carbonation / regeneration cycles. With Na₂ZrO₃ sorbent the highest H₂ concentration occurred using molar feed ratios of CO:Na₂ZrO₃:H₂O of 1:1:2 at 500°C.

Weimer et al. (2008) developed a comprehensive, Gibbs free energy minimization model based on ASPEN simulation of L.E.G., demonstrating the influence of process conditions and sulfur concentration on CaO carbon capture [23]. They found that unconverted char from the gasifier could supply sufficient heat to drive the calcination of CaCO₃ in a separate combustion / calcination reactor. To maintain high CO₂ capture efficiency (>80%) with increasing temperature, pressure must also increase (e.g. 0.9 MPa at 750°C); however, there is a maximum capture efficiency with increasing pressure, and methane forming reactions are favoured by higher pressure. An increase in the steam-to-carbon ratio substantially increased carbon capture due to reduced methane formation [23]. Again the issue of increased steam decreasing the energetic efficiency arises due to the heat required. The CO₂ capture efficiency was calculated based [23] on:

$$E_{cap} = \frac{n_{CaCO_3}}{X_c n_{C, fuel}} \quad (1.35)$$

where n_{CaCO_3} denotes the moles of CO₂ captured by lime, $n_{C, fuel}$ is the carbon entering with the fuel, X_c is the carbon conversion given by $(n_{C, fuel} - n_c^{out})/n_{C, fuel}$, and n_c^{out} is the unconverted carbon.

Solid purge from the L.E.G. process is required to remove sulfated CaO and ash, with a purge fraction of 0.061 (solids purged / regenerator solid output). Sulphur causes the formation of CaS in the gasifier, which is oxidized to CaSO₄ in the calciner. The sulfate formed can block sorbent pores and increase the sorbent deactivation rate [23]. The presence of CaSO₄ in the gasifier increases carbon capture and decreases H₂ and CH₄ due to the following reduction [23]:



If the L.E.G. process is used in conjunction with cement production, electrical efficiencies of up to 42% can be achieved using an integrated gasification combined cycle (IGCC). For cement production the limitations on impurity concentrations in the produced CaO are: ash < 30 wt%, CaSO₄ < 10 wt% [23].

Weimer et al. (2008) found optimal gasifier operating conditions of 750°C and 2.0 MPa, producing a syngas LHV of 5728 kJ/kg_{fuel}, with effective carbon capture of 80% [23]. In the calciner, conditions of 920°C and 0.1 MPa were suggested, with heat supplied entirely through char combustion.

Soliman et al. (2009) used a computer model in ASPEN Plus, of a natural gas combined cycle with integrated CaO-based CO₂ capture. They concluded that a combination of temperature swing, pressure swing, and steam as a sweep-gas in the calciner would be necessary to minimize the energy requirements for CO₂ capture. The minimum temperature swing was found to be ~180°C for a calciner atmosphere of 1 bar and a H₂O:CO₂ molar ratio of 5. They also found that calcium utilization of 14% or greater must be maintained to avoid large efficiency losses due to cyclic heating and cooling of deactivated sorbent.

1.9 Thesis Objectives

The preceding introduction gave an overview of the current knowledge in the areas of CaO-based CO₂ capture and limestone-enhanced gasification of biomass. As well, it gives a glimpse of the research atmosphere in which this thesis work was conducted. Due to the interest in CCS and alternative energy, a great deal of research is in progress in this area. In the following chapters, the author presents research demonstrating a novel method of pressure swing cycling of CaO for CO₂ capture, with an in-depth examination of the kinetics of this method to gain a better understanding of the morphological mechanisms at work in sorbent particles that reduce and limit calcium utilization. Experiments into the use of steam during CaO cycling are outlined in Appendix 1. These experiments were not taken to completion for reasons outlined in Appendix 1 and for this reason were excluded from in-depth analysis. In addition, an experimental investigation of CaO cycling in a fluidized bed coupled with biomass gasification is presented. There are few previous experimental studies investigating H₂ production from biomass coupled with CO₂ capture, and the thesis attempts to shed light on this process.

2 CO₂ Capture Capacity of CaO in Long Series of Pressure Swing Sorption Cycles

2.1 Introduction

Solid, lime-based sorbents are inexpensive and able to capture carbon dioxide in-situ at high temperatures and at the low CO₂ concentrations found in solid fuel boilers [122]. Lime sorbent is cycled between calcination and carbonation reactors, with absorption/desorption governed by equation 1.2. Absorption and desorption of CO₂ in the CaO/CaCO₃ particle depends on the partial pressure of CO₂ in the reaction gas (P_{CO_2}) and the equilibrium partial pressure of CO₂ in CaCO₃ ($P_{CO_2}^{eq}$), see equation 1.4. Cycling of the sorbent between carbonation and calcination conditions can be accomplished by swinging the temperature, CO₂ partial pressure and/or reactor pressure. To date, research has focused on cycling through the use of temperature and/or CO₂ partial pressure swing [34,40,61–65,87,92,122,123]. Pressure swing would significantly reduce the heating requirements of the calciner. In gasifiers/reformers, pressure swing absorption could be accomplished utilizing hydrostatic pressure, without the need for additional energy to pressurize the carbonation reactor or elaborate pressurization/depressurization switching.

Limitations in solid inventory in the capture system would require relatively short residence times of the sorbent in the carbonation reactor. As a result, most CO₂ capture would take place in the fast stage of the reaction. The calcium utilization is subsequently highly dependent on the overall surface area of the porous particle. The loss in calcium utilization is widely attributed to a reduction in surface area of the particles over time due to pore coarsening as a result of sintering during sorbent cycling [24,33,36,63]. This decay is enhanced by CaO sintering during high-temperature (> 950°C) calcination [40,61,64]. Sintering of CaO has been attributed to lattice diffusion, driven by surface energy gradients [73]. CO₂ has been reported to increase CaO sintering through reversible chemisorption of CO₂ in the CaO lattice [46,67]. Manovic et al. (2009b) showed that cycling limestone sorbent in a CO₂ atmosphere does result in increased particle sintering and reduced capture capacity [123].

Naturally occurring lime-based sorbents show a rapid initial decrease in calcium utilization within the first 20 carbonation/calcination cycles [18,34,62–64,86,123–125]. After a large number of cycles (e.g. 250), calcium utilization reaches an asymptotic value, with the majority of untreated limestone-based sorbents typically having residual capacities of 7-15% at atmospheric pressure and for practical carbonation times less than 10 minutes where fast stage carbonation has reached completion [34,40,61,122].

Designs of industrial scale CO₂ capture facilities typically account for the low calcium utilization by incorporating a make-up flow of fresh sorbent and a corresponding purge of spent sorbent to increase the average utilization of the sorbent population within the system [57,62]. For proper design and operation of such industrial scale CO₂ capture processes, accurate determination of the residual calcium utilization is required. The focus of the current research is to examine the calcium utilization over many pressure swing cycles.

2.2 Materials and Methods

Pressure swing absorption/desorption reactions were studied in a pressurized Thermogravimetric Analyzer (TGA), the TherMax 500, shown schematically in Figure 2.1. The TGA utilizes a Chan D-101 balance with 1 μg sensitivity. The reaction chamber consists of a quartz tube enclosed in a stainless steel pressure vessel. The reactor pressure is regulated by a computer-controlled regulator. Nitrogen and carbon dioxide flows are set at the start of each experiment using mass flow controllers. Two solenoid valves, actuated by the computer, control the gas flows. The sorbent particles are contained in a platinum basket with a cross-sectional area of 1 cm². Weight, temperature and pressure data are recorded on a personal computer using TherMax DAQ software. Calcium utilization is based on the mass change measured at the end of the carbonation stage immediately prior to calcination, assuming that mass change is solely due to the forward or reverse reaction (equation 1.2).

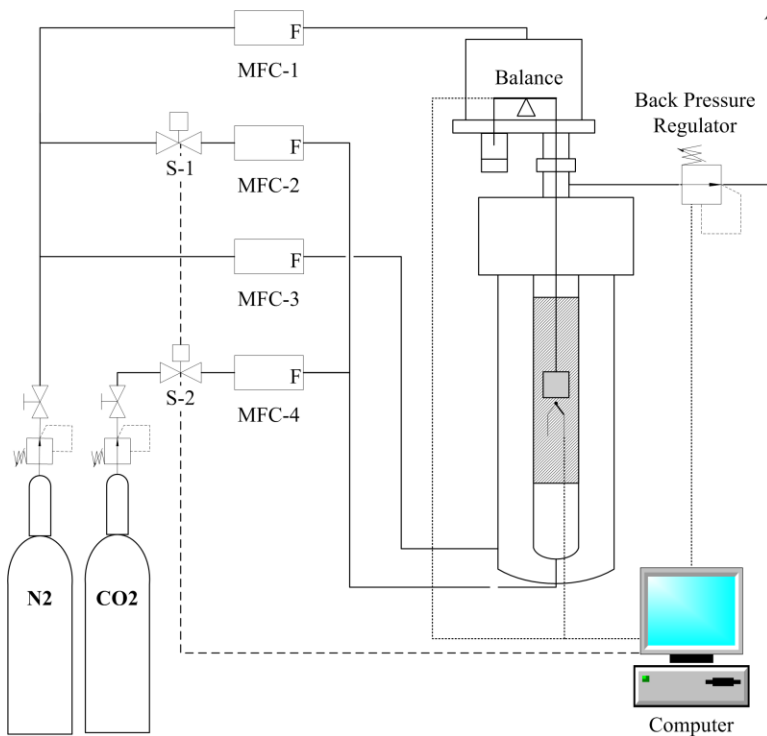


Figure 2.1: Schematic of pressurized thermogravimetric reactor

Tests were conducted using a single natural sorbent, Strasburg limestone, with particle diameters in the range of 150-250 μm and chemical composition provided in Table 2.1. Studies have shown that most natural sorbents show similar residual activity over a large number of cycles when exposed to similar cycling conditions [33,66]. However, recent studies examining the effect of ‘self-reactivation’ on sorbent performance have shown that different limestone varieties respond to thermal pre-treatment differently [89,91]. Within the first 30 cycles the effect of pre-treatment was found to be dependent on the type and quantity of impurities within the sorbent [89].

Table 2.1: Chemical composition of fresh Strasburg limestone

	CaO	MgO	Al ₂ O ₃	Fe ₂ O ₃	K ₂ O	Na ₂ O	SiO ₂	LOI*
Wt %	53.7	1.25	0.19	0.94	0.08	0.02	0.94	42.9

*LOI = loss on ignition

Carbonation / calcination cycling was conducted at a constant reactor temperature of 1000°C. The temperature differential in the bed due to the exothermic and endothermic was calculated, see Appendix 21, and was minimal. The conditions for each run are listed in Table 2.2. Many additional runs were conducted to verify repeatability and test for the effect of different system parameters, a list of all runs can be seen in Appendix 4. A limited sample of runs is presented here in order to highlight the noteworthy findings.

Carbonation was at high pressure in a flow of CO₂ (99.5% purity) for all runs. Calcination occurred at atmospheric pressure in CO₂ (99.5% purity) for runs 1-11, whereas calcination for run 12 was conducted in a flow of N₂ (99.995% purity) at 6-bar pressure. The PTGA start-up procedure can be found in Appendix 2. Sample size was varied after it was initially found to affect the calcium utilization of the cycled limestone, as discussed in section 2.3.2.

Table 2.2: Conditions for pressure swing cycling experiments. Temperature was 1000°C for all carbonation and calcination intervals. Calcination at 1 bar was 8 minutes in all cases.

Run	Sample Mass (mg)	Cycle Duration (min)	Carbonation		Calcination		Depressurization Rate (bar/min)	Number of Cycles
			P (bar)	t (min)	P (bar)	Gas		
1	347	35.2	6	23.0	1	CO ₂	2	1138
2	424	35.2	11	24.8	1	CO ₂	4	275
3	567	35.2	21	26.5	1	CO ₂	8	228
4	108	35.2	21	26.5	1	CO ₂	8	241
5	838	35.2	21	26.5	1	CO ₂	8	268
6	52	35.2	21	26.5	1	CO ₂	8	272
7	357	35.2	21	26.5	1	CO ₂	8	282
8	105	19.5	6	10.0	1	CO ₂	10	158
9	133	19.5	6	10.0	1	CO ₂	10	514
10	131	19.5	6	10.0	1	CO ₂	13.5	345
11	138	19.5	6	10.0	1	CO ₂	2.5	378
12	142	17	6	7	6	N ₂	N/A	237

Start-up of runs 1-11 involved: 1) pressurization of the reactor to carbonation pressure; 2) heating of the reactor to operating temperature (1000°C) at a rate of 25°C/min; 3) reducing pressure to 1 bar pressure

over 150 s; and 4) holding at 1 bar for 40 min to ensure complete calcination. For run 12, the pressure was held constant with the gas flow switched from CO₂ to N₂ for the calcination stage.

For accurate determination of the instantaneous calcium utilization of a population of sorbent particles in a CO₂ capture system, it is necessary to determine the residual calcium utilization of the sorbent [62]. Initial results indicated that residual calcium utilization was reached after approximately 250 cycles. Most of the experimental runs in this study exceeded this target number of cycles. The utilization for each cycle was calculated using equation 1.5, based on the sample mass immediately prior to depressurization. TGA data points for weight, temperature and pressure were acquired every 10 s, leading to the accumulation of a large amount of data. This data was processed to obtain cycle utilizations using MatLab[®], the code is presented in Appendix 3.

Long cycle durations (35.2 min) were used for runs 1-7 to accommodate the long pressurization time required to reach 21 bar. In these runs the pressure rise was accomplished in 1000 s resulting in pressurization rates of 0.02 bar/s, 0.01 bar/s and 0.005 bar/s for carbonation pressures of 21, 11, and 6 bar respectively. Pressurization was followed by 480 s of high-pressure carbonation for runs 1-11. As a result, carbonation occurred during the pressure rise with carbonation times in Table 2.2 representing the period during which $P_{CO_2} > P_{CO_2}^{eq}$. Carbonation was followed by depressurization and calcination, with a total duration of 630 s, sufficient to ensure complete calcination for all runs. A typical cycle for a high-pressure carbonation cycle is portrayed in Figure 2.2.

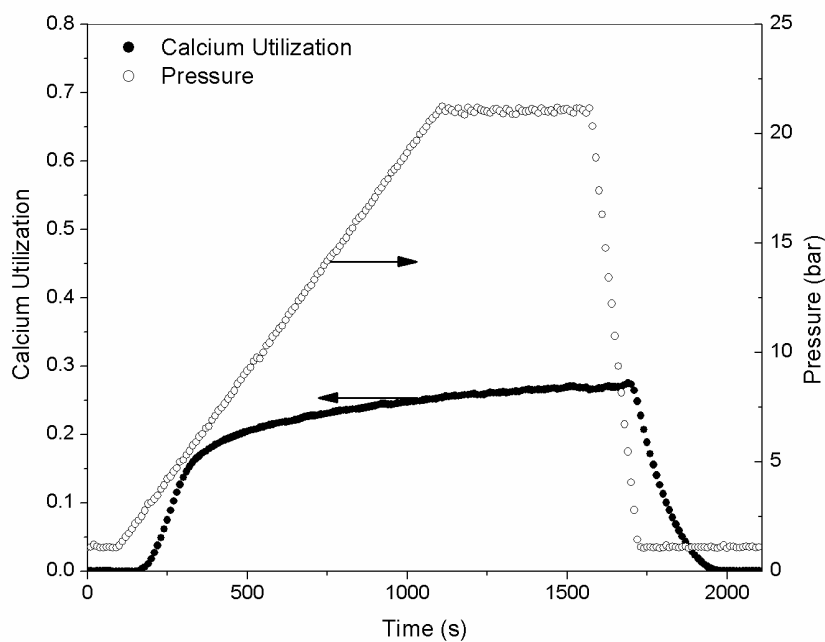


Figure 2.2: Pressure and conversion for pressure swing absorption for run 3.

Upon completion of each run, samples were collected and stored in a desiccator. The samples were later analyzed by SEM imaging using a HITACHI S-3000 SEM.

2.3 Results and Discussion

2.3.1 Pressure Swing Cycling

Initial investigations were designed to determine the effect of pressure swing cycling of lime-based CO₂ sorbents on the calcium utilization over many cycles. Runs 1, 2 and 3 were conducted using a similar pressure profile to that in Figure 2.2, but with varying carbonation pressure. The results showed an initial rapid decline in calcium utilization, as in previous studies [24,36,40,61–64,122,124]. After this decrease, the samples exposed to carbonation pressures of 11 and 21 bar showed a small increase in calcium utilization, as shown in Figure 2.3. After 200 cycles, only the test at 6 bar carbonation (run 1) appeared to have reached a non-zero asymptote, expected from other studies [34,40,63,64]. Runs 1 and 2 continued to show a decay in calcium utilization until completion of the run. The effect of pressure was significant, with calcium utilization values during cycle 50 of 0.149, 0.274 and 0.337 for carbonation pressures of 6, 11 and 21 bar, respectively.

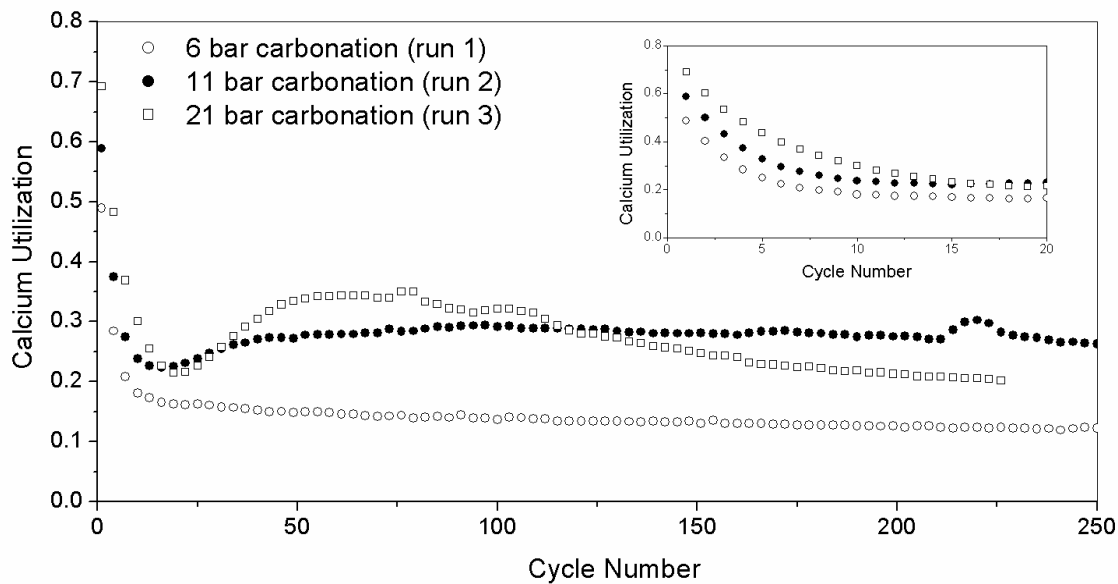


Figure 2.3: Effect of carbonation pressure of cyclic performance of limestone during pressure swing absorption/desorption. For operating conditions see Table 2.2.

This increase in calcium utilization is similar to that seen by others [63,90,91] following high-temperature thermal pre-treatment of limestone samples. In these three studies pre-treatment led to increased multi-cycle calcium utilization compared to sorbent without pre-treatment. This gain was attributed to ion diffusion within the sorbent particle, causing the CaO to re-crystallize into a more stable network of pores, a process labeled ‘self-reactivation’ [91]. These authors later reported that pre-treatment in CO₂ increased the calcium utilization over many cycles compared to pre-treatment in N₂ [90]. This finding is believed to result from enhanced sintering due to increased surface diffusion and

grain boundary mobility within the CaO particle as a result of reversible CO₂ chemisorption in the CaO lattice [67].

As calcination conditions were identical for runs 1-11, the differences in calcium utilization must result from differences in carbonation pressure. Carbonation was favourable to sintering of the CaCO₃ by lattice diffusion due to the high temperature (1000°C), well above the Tammann temperature of 561°C for CaCO₃ [70].

The pressures (> 6 bar) examined in this study likely also enhanced sintering. Elevated pressure has been shown to increase the mobility of atoms in solid systems when closed pores exist within the interior of particles [126]. Sintering during the first few calcination/carbonation cycles could lead to the formation of such closed pores. Elevated pressure during carbonation acting on these closed pores would result in an increased rate of sintering.

Cycling results in pore coarsening, i.e., a shift in the pore size distribution from small to large pores within the product layer [36,123]. During the first 20 cycles, this causes a rapid reduction in the number of micro pores, leading to a rapid decay in calcium utilization [36]. Further coarsening would allow access to the inner stable network of pores, eventually leading to an increase in calcium utilization [91]. Run 3 (21 bar carbonation) showed a higher rate of increase in calcium utilization, reaching a higher peak utilization earlier than for run 2 (11 bar carbonation). This is likely due to an increased rate of sintering causing more rapid pore coarsening. Run 3 also showed a higher rate of decay following its peak, compared to that of run 2. This indicates that the extensive sintering at 21 bar, eventually became detrimental to calcium utilization as surface area decreased.

The macro-pore structure resulting from repeated carbonation/calcination cycles can be seen in the SEM micrographs in Figure 2.4. In Figure 2.4b, an SEM micrograph of the carbonate from run 1 after 1138 cycles, it can be seen that over many cycles, pores become coarse, with diameters of 0.18 to 3.6 μm, compared to the calcined limestone in Figure 2.4b. SEM micrographs from run 3 (21 bar carbonation) and run 2 (11 bar carbonation), Figure 2.4c and 2.4d, show that the external network of pores was very similar for the two runs, with run 2 showing a slightly higher density of pores. SEM micrographs of particles from all initial pressure swing runs can be found in Appendix 5.

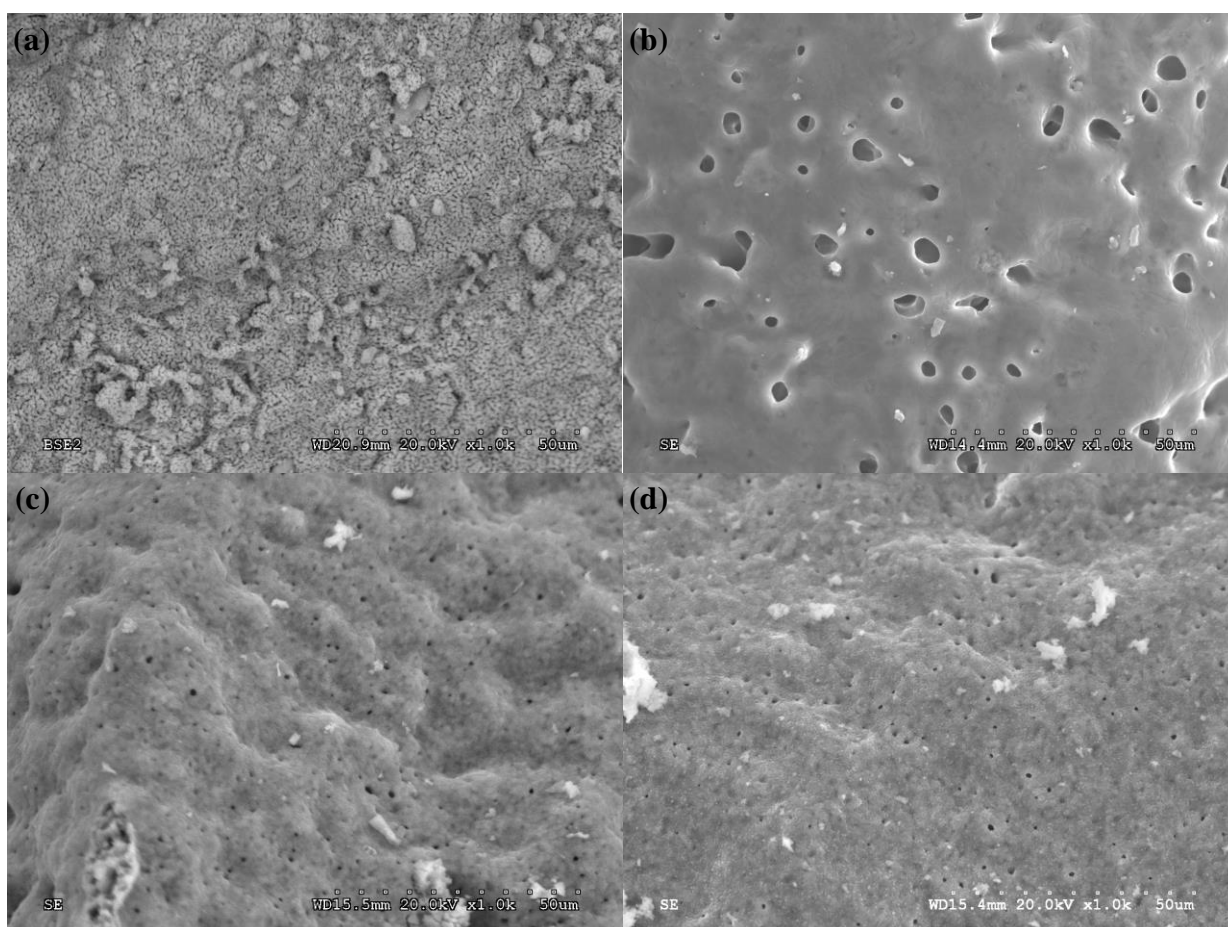


Figure 2.4: SEM micrographs of sorbent particles, (a) initial calcined limestone, (b) carbonate from run 1 [6 bar cycling, 1138 cycles], (c) carbonate from run 2 [11 bar cycling, 275 cycles], (d) carbonate from run 3 [21 bar cycling, 228 cycles]. For operating conditions see Table 2.2.

The carbonation breakthrough curves in Figure 2.5 at different pressure swings show large differences between rates of CO₂ uptake. The rate and extent of the fast stage reaction increase with carbonation pressure. This occurs before the maximum carbonation pressure is reached, suggesting a residual effect of the initial high-pressure phase. One possible explanation is that the initial high-pressure, high-temperature stage stabilizes the porous network in a manner similar to that proposed by Manovic and Anthony (2008b). Increased pressure during the high-pressure stage leads to increased ion mobility within the sorbent leading to a more stabilized network of pores [91]. A portion of the particle interior remains un-carbonated through successive cycles, allowing the continued development of a stable porous network over many cycles.

All three runs showed similar carbonation rates during the slow-stage reaction, indicating that diffusion through the product layer is independent of CO₂ pressure within the reactor, a result consistent with previous studies [24,26,32].

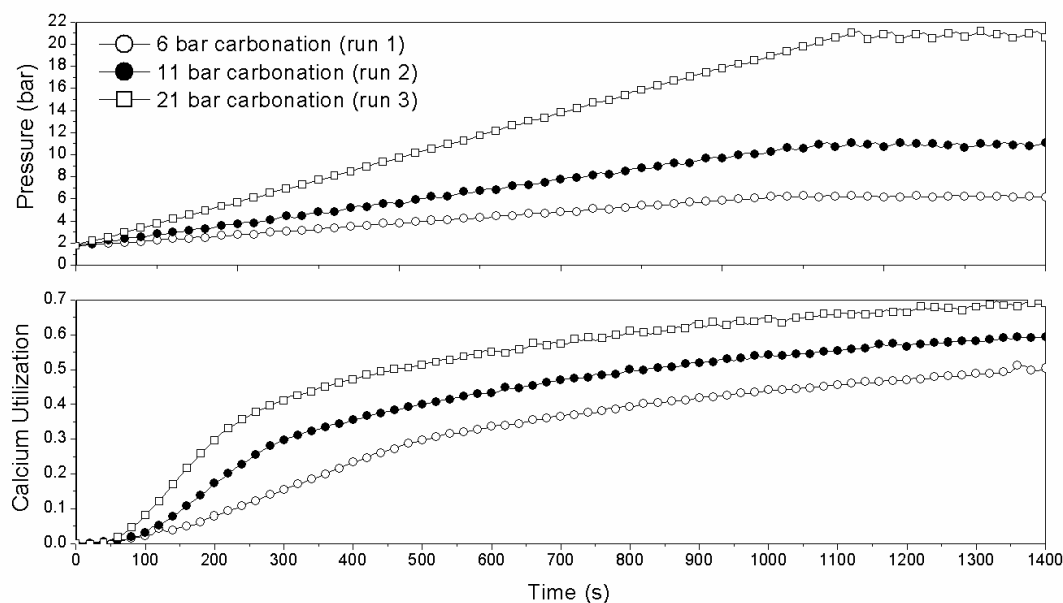


Figure 2.5: Carbonation breakthrough profiles for the first cycle during pressure swing absorption showing the effect of carbonation pressure. For operating conditions see Table 2.

During the first 100 cycles, the fast-stage reaction proceeded further at higher carbonation pressure as is clear from Figure 2.6. The extent of the fast stage reaction is dependent on the micro-porous sorbent structure [24,33]. The increased extent of the fast-stage reaction in run 3 indicates a more micro-porous structure, providing evidence of a more stable porous network.

After 60 cycles, run 3 began to show a decline in calcium utilization, as portrayed in Figure 2.3. Around cycle 125, this decay reduced the calcium utilization for run 3 to a level below that of run 2. This likely resulted from continued particle sintering, breaking down the stable porous network, causing a reduction in the pore volume and surface area available for the fast stage carbonation reaction. The evolution of the carbonation breakthrough curves can be seen in Figure 2.6. The rate of the fast stage and slow stage carbonation reactions do not change substantially with increased cycling for runs 2 and 3, i.e., for 11 and 21 bar carbonation, respectively. After the first few cycles of run 1 (6 bar carbonation) the fast stage of carbonation is indistinguishable from the slow, diffusion controlled stage, suggesting a dramatic shift in pore size distribution. Figure 2.6.C indicates that the extent of the fast stage reaction for run 3 (21 bar) decreased considerably between the 1st and 200th cycles, suggesting a breakdown of the micro-porous structure of the particles, leading to diminished calcium utilization.

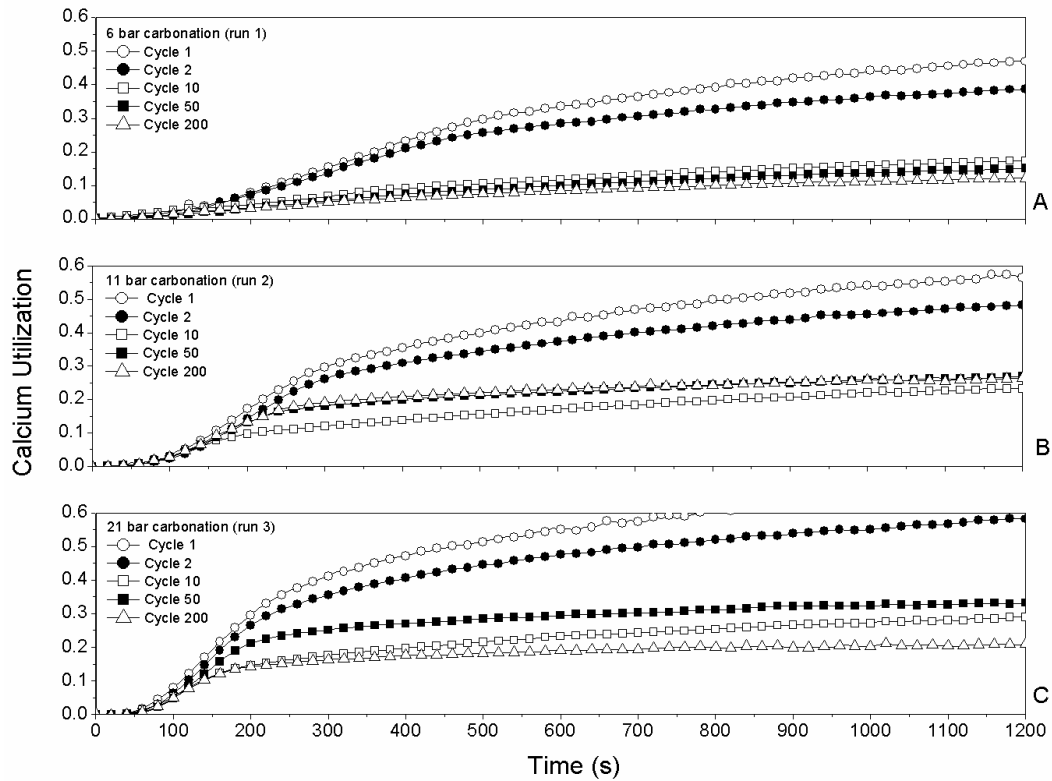


Figure 2.6: Carbonation breakthrough profiles for cycles 1, 2, 10, 50 and 200 of limestone during pressure swing sorption showing effect of carbonation pressure. For operating conditions see Table 2.

2.3.2 Influence of Sample Size

A series of experimental tests (runs 4-8) was conducted at 21 bar carbonation pressure to determine the extent to which limestone sample size affected the utilization, with the sample mass varied from 50 to 850 mg. The results are presented in Figure 2.7.

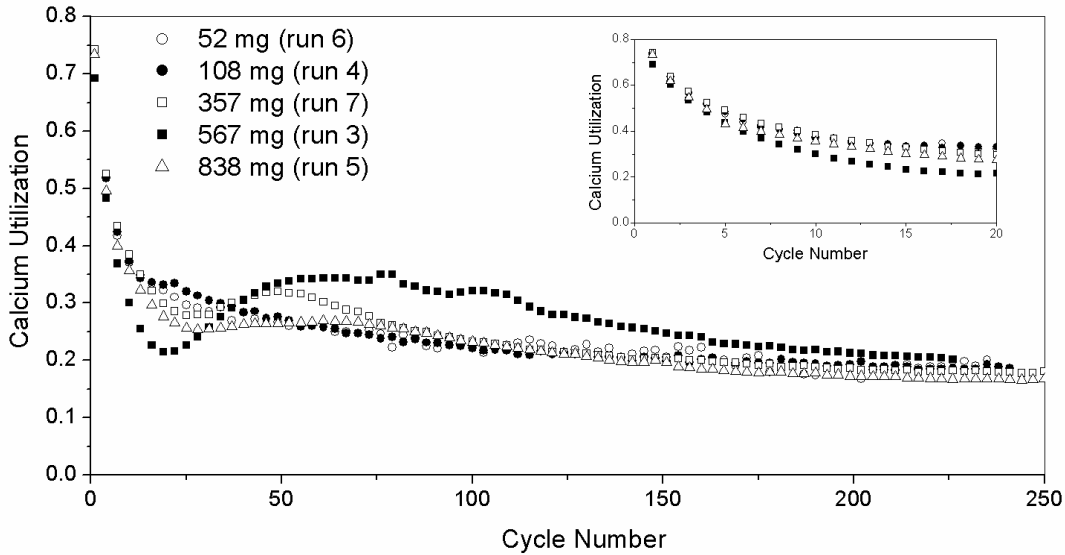


Figure 2.7: Cyclic performance of limestone during pressure swing absorption/desorption of CO₂ showing effect of sample size, 21 bar carbonation pressure, 26.5 min and 35.2 carbonation and cycle duration respectively.

Each of these runs was conducted in a 100% CO₂ atmosphere for carbonation, as well as for calcination, so that mass transfer resistances were absent. The dependence on sample size can be attributed to heat transfer differences within the sample. The low gas velocity within the PTGA, 0.42 cm/s at 21 bar and 1000°C, ensures that the samples behaved as packed beds in all cases. Gas flow through the sample suspended in the basket would be limited. Conductive heat transfer within packed beds is also very low [127], leading to temperature gradients within the samples during the exothermic/endergonic carbonation/calcination reactions. Larger samples would experience larger temperature gradients from the sample interior to the exterior.

During the exothermic carbonation reaction, the temperature of particles in the interior of the sample would exceed those on the exterior. This higher temperature would increase ion mobility within the sample, amplifying the ‘self-reactivation’ effect on the inner particles and led to an increase in peak calcium utilization, as shown in Figure 2.7.

The largest of the samples (run 5) showed only a slight peak in calcium utilization vs. cycle number. The inner particles in this sample likely underwent extensive sintering, so that much of the beneficial effect was lost. This was also observed by Manovic et al. (2009a), who noted an optimum sintering pre-treatment temperature [90]. After many cycles (~200) the ‘self-reactivation’ was reduced due to further sintering. Samples that experienced similar cycling conditions showed similar residual calcium utilization after many cycles.

The existence of temperature gradients within the samples was verified by examining interior and exterior particles from the same sample. As observed in Figure 2.8, particles in the interior of larger samples experienced considerable surface fracturing. The elevated temperature within the interior of the

sample led to an increased rate of calcination, causing particles to fracture as the surface product layer rapidly shrunk, due to the lower specific volume of CaO ($16.9 \text{ cm}^3/\text{g}\cdot\text{mol}$) compared to that of CaCO_3 ($36.9 \text{ cm}^3/\text{g}\cdot\text{mol}$). Increased particle fracturing did not, however, result in an increase in calcium utilization, as might be expected, as it would be offset by extensive particle sintering.

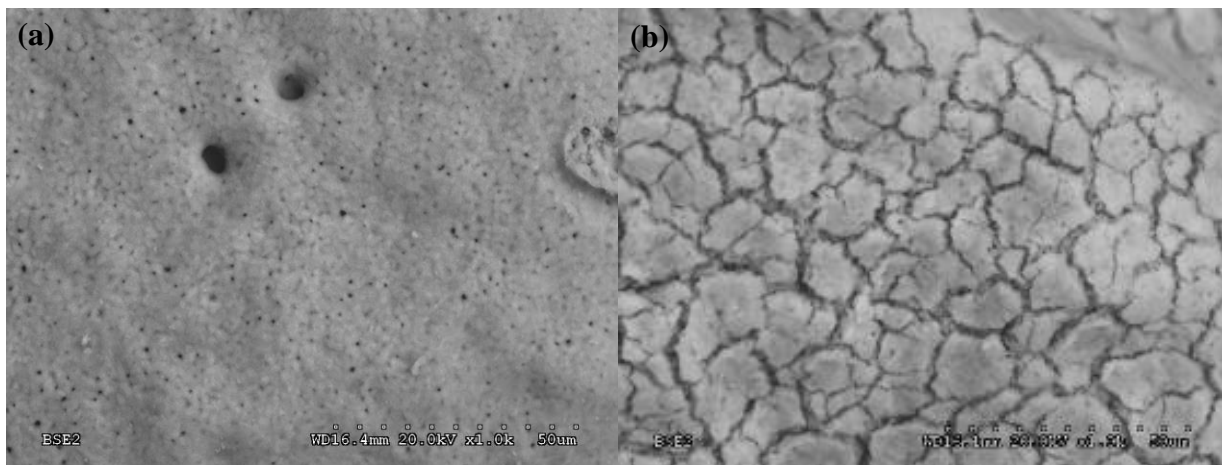


Figure 2.8: SEM micrographs of carbonated particles after 254 cycles, run 7: (a) particle from exterior of sample, (b) particle from interior of sample. For operating conditions see Table 2.2.

2.3.3 Influence of De-Pressurization Rate

To determine the effect of de-pressurization rate, a series of pressure swing runs (runs 9-11) was conducted at 6 bar carbonation pressure. Total cycle duration was kept the same for each run, but the ramp time from 6 bar to 1 bar was varied from 22 to 150 s, leading to differing rates of de-pressurization, 13.5 to 2 bar/min respectively. The results in Figure 2.9 show a slight improvement in calcium utilization from 0.119 to 0.161 with increased de-pressurization rate from 2.5 to 10 bar/s. This is attributed to the fracturing of the sorbent particle during rapid de-pressurization as visualized in Figure 2.10. This fracturing increased the porosity of the particles, promoting increased carbonation during fast-stage reaction. There was little improvement from 10 to 13.5 bar/s. Run 1, gave the lowest utilization and fastest decay in the first 20 cycles, but had a cycle twice as long, enhancing sintering.

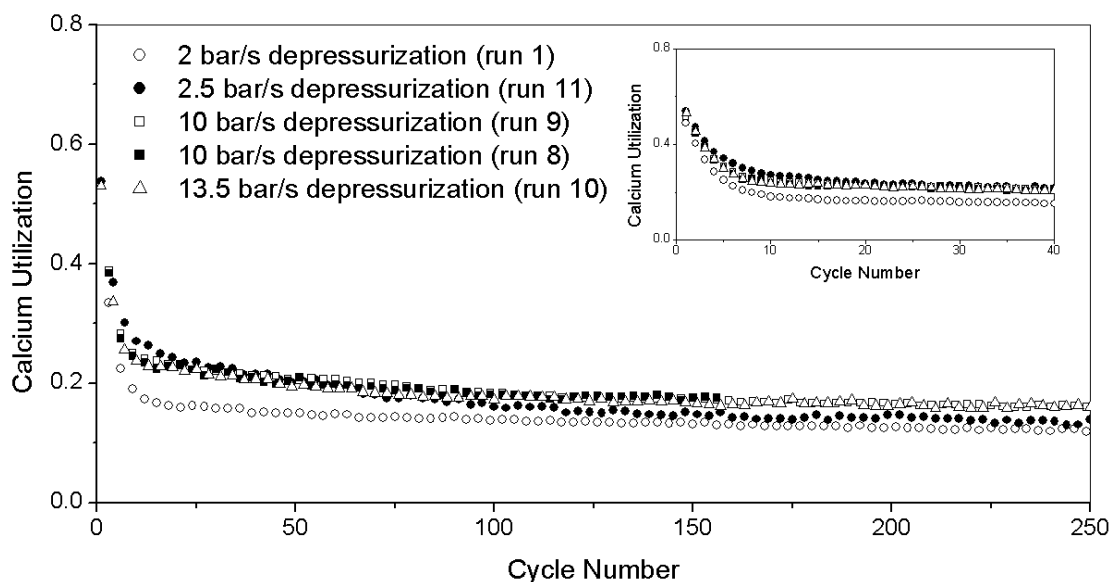


Figure 2.9: Cyclic performance of limestone during pressure swing absorption/desorption of CO₂ showing effect of depressurization rate. For operating conditions see Table 2.2.

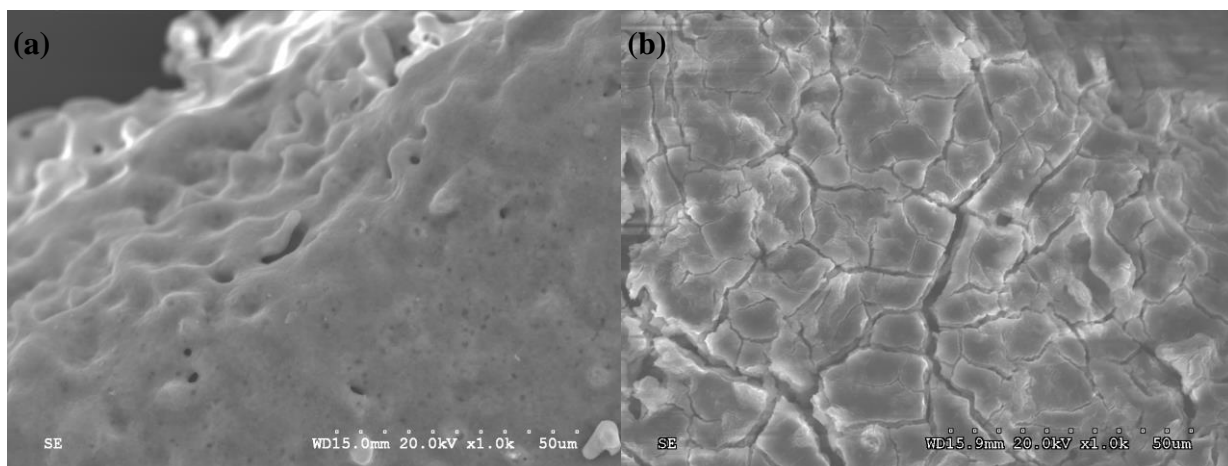


Figure 2.10: SEM micrographs of carbonated samples after cycling with different de-pressurization rates: (a) run 11, after 378 cycles; (b) run 9, after 500 cycles. For operating conditions see Table 2.2.

Although tests at higher carbonation pressures gave faster de-pressurization rates, the increase in calcium utilization observed due to de-pressurization alone (0.119 to 0.161) does not fully account for the extent of the increase in utilization observed with increased carbonation pressure, shown in Figure 2.3. This gives further support to pore stabilization as a mechanism for increased calcium utilization.

Although rapid depressurization resulted in an increase in calcium utilization, the highly fractured state of the particle likely resulted in a significant decrease in particle strength. This would be detrimental to fluidized bed CO₂ capture, as sorbent particle attrition and resulting elutriation are of major concern.

2.3.4 Pressure Swing Comparison

Pressure swing cycling compares favourably with other methods of lime-based CO₂ capture cycling. A separate experiment (run 12) was conducted at constant pressure (6 bar) for both carbonation and calcination in order to assess the benefit of pressure swing cycling. Absorption/desorption of CO₂ was accomplished by alternating the gas flow over the sample from CO₂ to N₂. Carbonation for this run lasted 7 min, long enough to complete the fast stage of the reaction. Results from this test are compared to those for pressure swing with similar operating conditions and cycle duration (run 9) in Figure 2.11.

A number of results from other studies for highly cycled limestone are also compared to those from the current investigation in Figure 2.11. Experimental conditions for these tests are summarized in Table 2.3.

Table 2.3: Experimental operating conditions of previous work included in Figure 2.11, calcination was at atmospheric pressure in all cases [28,40,63,90].

Author	Limestone	Carbonation			Calcination			
		P (bar)	t (min)	T (°C)	Gas	t (min)	T (°C)	Gas
Sun et al. (2008)	Strasburg	1	9	850	100% CO ₂	8	850	100% N ₂
Grasa and Abanades (2006)	La Blanca	1	5	650	10% CO ₂	5	850	10% CO ₂
Chen et al. (2009)	Strasburg	1	9	750	100% CO ₂	8	750	100% N ₂
Manovic et al. (2009)	Kelly Rock	1	10	800	50% CO ₂	10	800	100% N ₂
Current work - Run 9	Strasburg	6	10	1000	100% CO ₂	9	1000	100% CO ₂
Current work - Run 12	Strasburg	6	7	1000	100% CO ₂	10	1000	100% N ₂

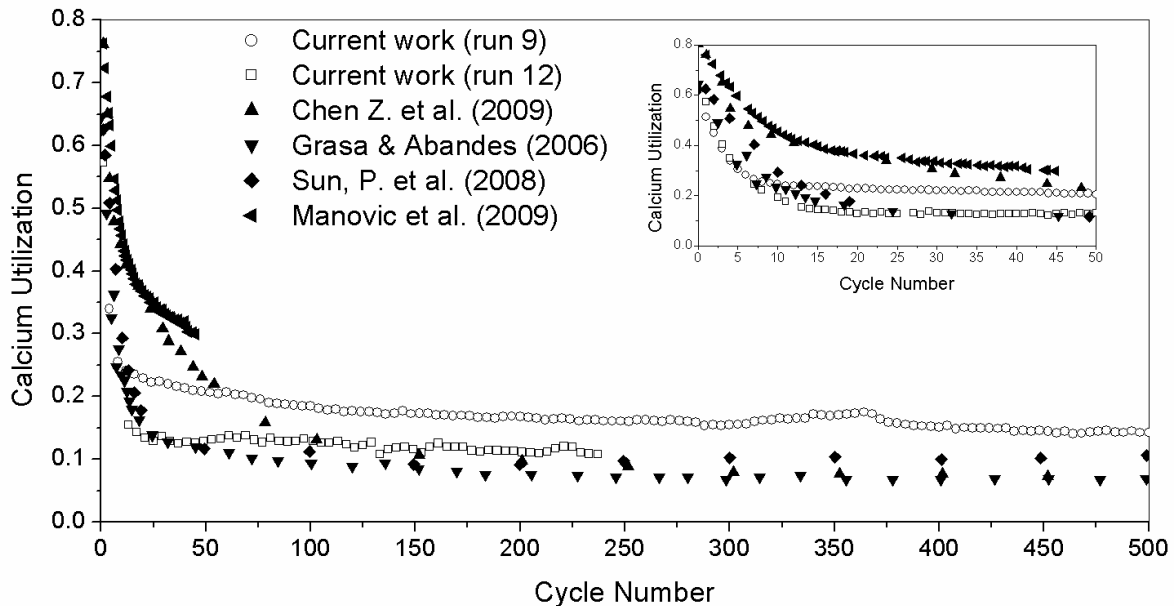


Figure 2.11: Comparison of 6 bar pressure swing CO₂ absorption on limestone with previous studies utilizing temperature or partial pressure swing (run 9: CO₂/CO₂, run 12: CO₂/N₂), for operating conditions see Table 2.3 [40,63,123,128].

It can be seen that despite the extreme cycling conditions (1000°C, 100% CO₂), pressure swing cycling eventually displayed calcium utilization equal to or greater than those for temperature or partial pressure cycling.

2.4 Conclusions

Pressure swing calcination/carbonation over a large number of cycles was studied, with each run at 1000°C in a flow of pure CO₂. Carbonation took place at high pressure (6, 11 or 21 bar), followed by calcination at atmospheric pressure. Results showed that pressure swing cycling offers increased calcium utilization over many (> 200) cycles, compared to temperature or partial pressure cycling. After 250 cycles calcium utilization reached near-asymptotic values of 12.5 – 27.7%. The highest residual calcium utilization was obtained through cycling between 1 and 11 bar. Increased sintering during carbonation at 21 bar resulted in a decrease in residual utilization, compared to cycling with a carbonation pressure of 11 bar. These findings suggest that there is an optimum carbonation pressure for carbon capture by cyclic pressure swing calcination / carbonation.

Sample size was found to play a significant role in calcium utilization during the first 200 cycles. Larger samples displayed an increase in calcium utilization after ~30 cycles due to poor heat transfer within the sample, causing increasing sintering in the sample interior during the exothermic carbonation reaction. This elevated temperature initially led to the formation of a stable porous network through solid diffusion within the particle, as observed by Manovic et al. (2009) [90]. Continued cycling gradually decreased this effect.

The rate of de-pressurization for calcination also influenced the residual calcium utilization. A five-fold increase in the rate of de-pressurization resulted in an increase in the residual calcium utilization from 11.9 to 16.1% as a result of fracturing sorbent particle surfaces, producing more surface area for carbonation.

The findings of this study suggest that pressure swing cycling can be effective for the capture of CO₂, with improved residual calcium utilization relative to temperature and partial pressure cycling.

3 Kinetics of CO₂ Absorption by CaO through Pressure Swing Cycling

3.1 Introduction

In recent years, much attention has been paid to CO₂ capture systems utilizing calcium oxide (CaO) based sorbents. A number of pilot scale capture systems are in operation or under construction, and a large number of scientific articles have been published examining CaO sorbent properties and performance. For a detailed review of CaO-based CO₂ capture, see Blamey et al. [122]. In Chapter 2, the benefits of pressure swing cycling were discussed. One major technical obstacle to the implementation of solid, lime-based capture processes is the loss in calcium utilization (CO₂ capture capacity). This loss primarily results from cycle and temperature-induced sintering, leading to a reduction in particle available surface area after repeated carbonation-calcination cycles [34,40,62,63,124,129].

Elevated temperatures during calcination (> 900°C) cause a reduction in the volume of small pores and a shift to larger pores [40,61,64]. Sintering of CaO has been attributed to lattice diffusion, driven by surface energy gradients and is enhanced by CO₂ through its reversible chemisorption in the CaO lattice [46,67]. Initial CaO sintering reduces surface area through a shift in the pore size distribution from small micro pores (1-10 nm) to meso pores (10-100nm) [33,36]. The formation and decomposition of CaCO₃ is also a major cause of reduced particle surface area [46,64]. Breakdown of the rhombohedral CaCO₃ and re-nucleation of cubic CaO allows the CaO to pack together much more closely, reducing micro porosity [46]. Sintering of CaCO₃ is also significant at elevated temperatures. Hanson and Tullin (1996) found that sintering at 850°C and a CO₂ partial pressure of 1 atm for 60 min led to a 50% decrease in CaCO₃ surface area [74]. For conditions of interest in this study, sintering of both CaO and CaCO₃ are expected to play roles in the decay of calcium utilization.

Natural lime-based sorbents show a rapid initial decrease in calcium utilization within the first 20 carbonation/calcination cycles [18,34,62–64,86,124,125]. After many cycles (>100), calcium utilization reaches an asymptotic value, with the majority of untreated limestone-based sorbents typically having residual capacities of 7-15% at atmospheric pressure for practical carbonation times (<10 minutes) where fast-stage carbonation has reached completion [34,40,61,122].

In Chapter 2, cycling of CaO by pressure swing cycles was found to improve calcium utilization over many cycles, compared to temperature or partial pressure swing. Higher carbonation pressures (>10 bar) led to an increase in residual calcium utilization. As well, it was found that at higher pressures the calcium utilization increased after approximately 25 cycles. This effect was similar to that seen by other investigators examining the effect of thermal pre-treatment on the decay in calcium utilization and was

attributed to ion diffusion within the CaO, causing it to re-crystallize into a more stable CaO skeleton that maintained their pore structure [63,89,90]. These authors also reported that pretreatment in CO₂ had a greater "self-reactivation" effect than an N₂ atmosphere. This is due to increased surface diffusion and grain boundary mobility within CaCO₃ particles in a CO₂ atmosphere (Borgwardt, 1989).

Elevated temperatures (1000°C) and CO₂ partial pressures (>6 bar) in Chapter 2, caused a high degree of sintering. Increased pressure gave rise to a higher rate of increase and peak calcium utilization. The aim of the current study is to explore and characterize this mechanism through an examination of the carbonation kinetics.

3.2 Materials and Methods

The materials methods used in this section are very similar to those in Chapter 2. Carbonation / calcination cycling was conducted isothermally by decreasing or increasing the pressure in a Pressurized Thermogravimetric Analyzer (PTGA), TherMax 500, shown schematically in Figure 2.1. The reaction chamber consists of a quartz tube enclosed in a stainless steel pressure vessel. The sorbent particles are held in a platinum mesh basket with a cross-sectional area of 1 cm². The reactor pressure is controlled by a computer-controlled regulator. Reaction gas flows are controlled by electronic mass flow controllers. Weight, temperature and pressure data are recorded on a personal computer with the aid of TherMax DAQ software.

Sample masses were between 150 and 170 mg in order to minimize heat transfer limitations within the particle bed, as seen in Chapter 2, and at the same time reduce the impact of fluctuations in the weight signal, caused by the operation of the electronic pressure regulator. Experiments were conducted on Strasburg limestone, screened to particle diameters of 150-250 μm, and having the chemical composition provided in Table 2.1. A single type of limestone was used, as previous studies [23,62] have shown that most natural sorbents show similar residual activity over a large number of cycles when exposed to similar cycling conditions.

All carbonation and calcination cycles were conducted isothermally at 975, 1000 and 1025°C, in a flow of un-diluted CO₂. Carbonation was performed at 5, 10 and 20 bar_g, whereas calcination was at atmospheric pressure. The flow varied from 0.2 to 1 SLPM in order to achieve the same time for pressurization (1000 s), and hence overall cycle and high pressure carbonation durations, for different carbonation pressures, see Figure 3.1. The pressurization time was limited by the gas flow rate into the reactor. Pressurization was followed by 480 s of high-pressure carbonation, followed by 150 s depressurization and 480 s calcination stages. A typical cycle for a high-pressure carbonation cycle is portrayed in Figure 3.1. Initial calcination was performed in the PTGA by heating the reactor at the

carbonation pressure to 1000°C, reducing the pressure to 1 bar in 150 s and holding at 1 bar for 40 min to ensure complete calcination.

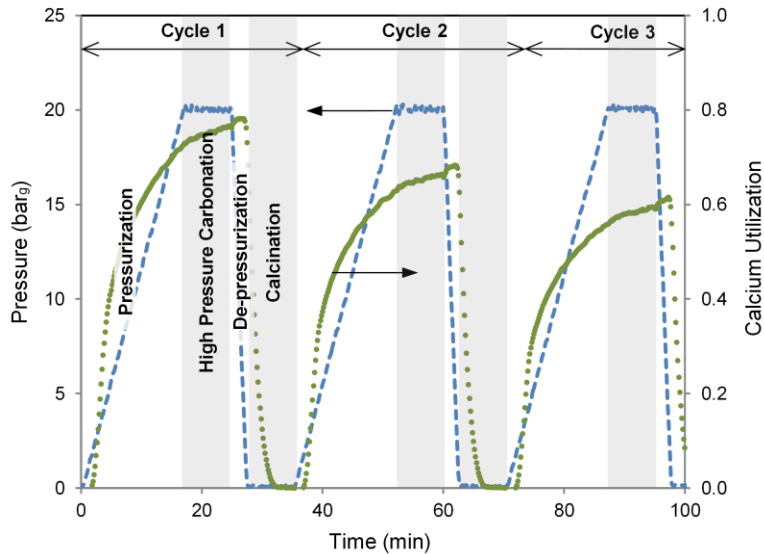


Figure 3.1: Pressure and calcium utilization during the first three cycles of pressure swing carbonation; 1000°C and 20 bar carbonation pressure.

Calcium utilization, equation 1.5, is based on the mass change measured at the end of the carbonation stage, immediately prior to reactor depressurization, assuming that mass change is solely due to the forward or reverse reaction. Calcined samples were collected and stored in a desiccator. These samples were later analyzed by SEM imaging using a HITACHI S-3000 SEM. Surface area was found using single-point N₂ sorption with a Micrometrics 2300 apparatus.

3.3 Kinetic Model

The kinetics of the carbonation reaction have been shown to be zero order with respect to CO₂ partial pressure when $P - P_{CO_2} > 10 \text{ kPa}$, due to saturation of the surface reaction sites by the CaO-CO₂ transition complex [24]. Therefore for the range of pressure in our experiments, the kinetics of gas-solid absorption are rate limiting. The sorbent particles were modeled as a collection of identical, spherical CaO grains based on qualitative analysis of SEM images of calcined limestone obtained by the author (e.g. Figure 3.2.)

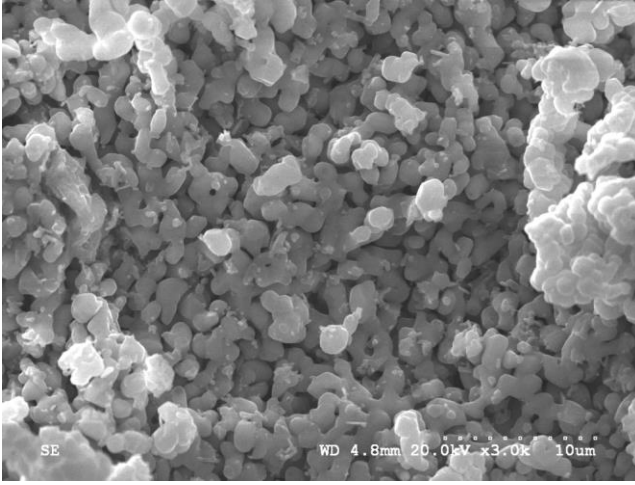


Figure 3.2: Calcine of Strasburg limestone after one cycle at 1000°C and 10 bar carbonation pressure.

The reaction of CO₂ with CaO proceeds in two distinct stages [26]. The rate in the initial stage is controlled by the kinetics of the CaO-CO₂ reaction. When the CaCO₃ product layer reaches a critical thickness of ~50 nm, the reaction changes from the fast-kinetic-control to a much slower regime controlled by gas-solid diffusion of CO₂ through the product layer [31]. The grain model of Szekely [30] for spherical grains can be used to model the reaction kinetics of both stages.

Reaction-controlled:

$$\frac{dX}{dt(1-X)} = 3r(1-X)^{-1/3} \quad (3.1)$$

In integral form,

$$g(X) = 1 - (1-X)^{1/3} = r \times t \quad (3.2)$$

$$\text{where, } g(X) = \left(\frac{k_x C_s}{\rho_s} \right) \left(\frac{A_g}{F_g V_g} \right)$$

where, k_x is the reaction rate constant, C_s is the concentration of diffusing species on the pore surface, ρ_s is the molar concentration of solid reactant, A_g is the grain surface area, F_g is the grain shape factor and V_g is the grain volume.

Diffusion-controlled:

$$\frac{dX}{dt(1-X)} = \frac{r}{2((1-X)^{2/3} - (1-X))} \quad (3.3)$$

In integral form,

$$p(X) = 1 - 3(1-X)^{2/3} + 2(1-X) = r \times t \quad (3.4)$$

$$\text{where, } p(X) = \left(2F_p D_{eff} (C_{CO_2} - C_{CO_2}^{eq}) (1 - \varepsilon_p) \rho_s \right) \left(\frac{A_p}{F_p V_p} \right)^2 \left(\frac{K_E}{1 + K_E} \right) t$$

where, D_{eff} effective diffusivity in the product layer, C_{CO_2} is the concentration of CO_2 , ε_p internal particle porosity, A_p is the particle surface area, F_p is the particle shape factor, V_p is the particle volume and K_E is the equilibrium constant for carbonation.

The carbonation rate for the reaction-controlled regime was found by plotting the grain model conversion function, $g(X)$ in equation 3.2, against normalized time and taking the slope during the initial fast phase of the reaction, see Figure 3.3. The rate for the diffusion-controlled regime is obtained from the slope of the grain model conversion function for product layer diffusion, $p(X)$ in equation 3.4, against normalized time during the second slow phase of the reaction. Both rates were found for carbonation of the 1st, 5th, 10th, 25th, 50th and 100th cycles.

Kinetic results were normalized using $t^* = t - t_o$, where t_o is the time at which carbonation starts. Figure 3.3 shows the results from the 100th carbonation cycle for 10 bar_g carbonation pressure and all temperatures. For all kinetic curves, see Appendix 10. The carbonation duration varies slightly as a result of the different temperatures, affecting the onset of carbonation.

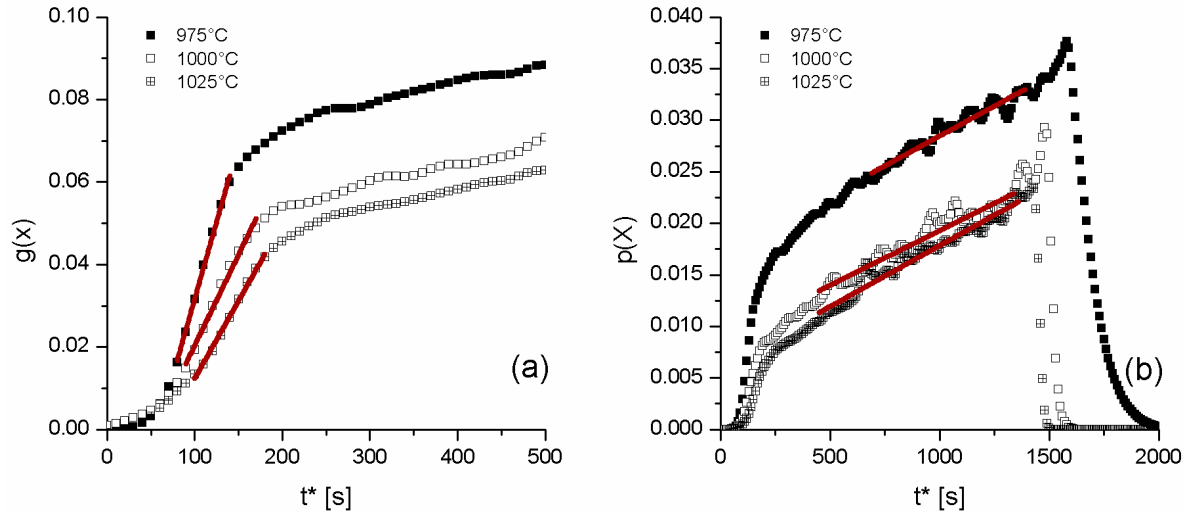


Figure 3.3: 100th cycle kinetics modeled using Szekely's grain model for cycling at 10 bar carbonation pressure, solid lines used to find rate of reaction: a) reaction controlled regime, equation 3.2; b) diffusion controlled regime, equation 3.4.

3.4 Results and Discussion

3.4.1 Pressure Swing Cycling

The decay in calcium utilization followed similar trends as reported in Chapter 2. Again, increased pressure greatly increased the calcium utilization over both the short and long term, see Figure 3.6. The residual utilization, defined as the utilization after 250 cycles or the final utilization recorded, increased more than twofold from 0.128 ± 0.005 to 0.271 ± 0.035 from 5 and 20 bar_g, after 100 cycles. This represents an improvement in calcium utilization over temperature swing cycling.

The calcium utilization was measured at the end of the high-pressure carbonation. The duration of the pressurization stage was the same for each ultimate carbonation pressure, 1000 s. This resulted in slightly different carbonation times obtained from experimental data, as seen in Table 3.1. Carbonation begins prior to reaching the equilibrium partial pressure [130], as defined in equation 1.4. Figure 3.4 shows the partial pressure of CO₂ at the onset of carbonation and calcination. The overall carbonation times deviated by no more than a few minutes; the exception being carbonation at 5 bar_g pressure and 1000 and 1025°C, where the transition between the kinetic and diffusion regimes is less sharp and more difficult to pinpoint, see Figure 3.5. The change in carbonation time with pressure and cycle number can be seen in Appendix 11.

Table 3.1: Duration of different stages of carbonation

Temperature (°C)	Pressure (bar _g)	Carbonation Time (mins)		
		Kinetic Regime	Diffusion Regime	Total
975	5	3.3 ± 0.3	21.9 ± 0.4	25.1 ± 0.3
	10	2.6 ± 0.6	23.4 ± 0.5	26.0 ± 0.3
	20	2.2 ± 0.5	24.2 ± 0.5	26.4 ± 0.1
1000	5	$6.9 \pm 1.2^*$	$16.6 \pm 0.9^*$	23.6 ± 0.8
	10	3.6 ± 0.8	21.2 ± 0.8	24.8 ± 0.4
	20	3.0 ± 1.1	22.7 ± 1.2	25.6 ± 0.2
1025	5	$6.3 \pm 0.8^*$	$13.8 \pm 0.8^*$	20.1 ± 0.5
	10	3.6 ± 0.6	20.0 ± 0.8	23.6 ± 0.4
	20	3.4 ± 0.6	22.0 ± 0.6	25.4 ± 0.1

*The transition between fast and slow stage carbonation is indistinct

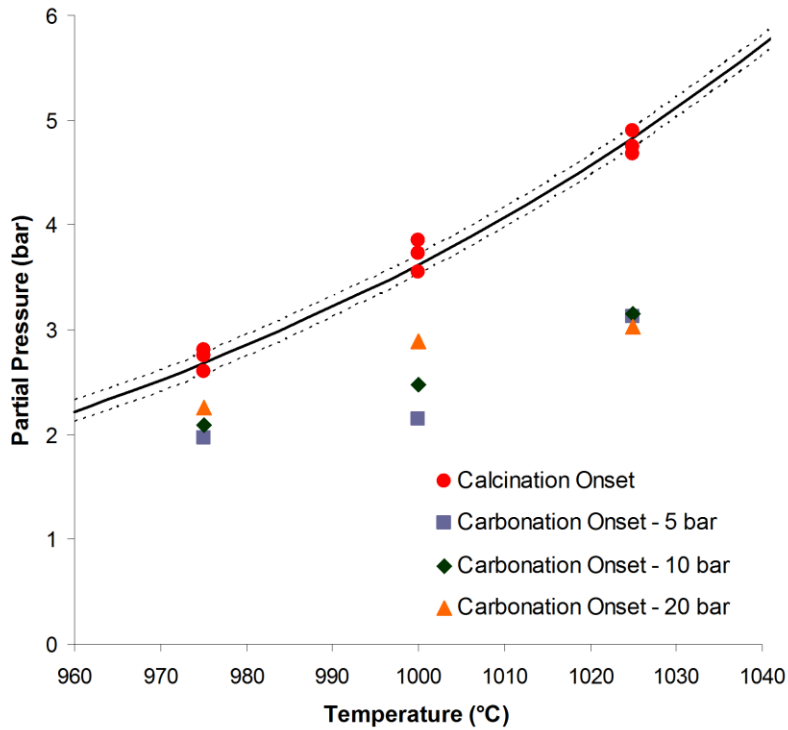


Figure 3.4: CO₂ partial pressure at onset of carbonation and calcination; solid line represents the equilibrium pressure as obtained from equation 1.4, and the dotted lines are ± 10 kPa.

An increase in carbonation time leads to an increase in residual calcium utilization [34,95,131]. This is attributed to carbonation of internal CaO during the diffusion regime which, upon subsequent calcination, re-activates the CaO by opening of micro-pores in the surface layer [34,131]. According to Arias et al. (2011), the relatively long duration of the diffusion regime, Table 3.1, could lead to a two fold increase in calcium utilization as compared to a cycle with no carbonation occurring in the diffusion regime. Between the different experimental runs the difference in duration of the diffusion controlled regime would have little effect, on the order of approximately 5% increase in residual utilization [131]. It was found that during the first cycle, the initial pressurization during start-up affected the rate of the kinetic-controlled regime, Figure 3.5, suggesting other mechanisms at work on sorbent. All individual calcium utilization curves can be seen in Appendix 9.

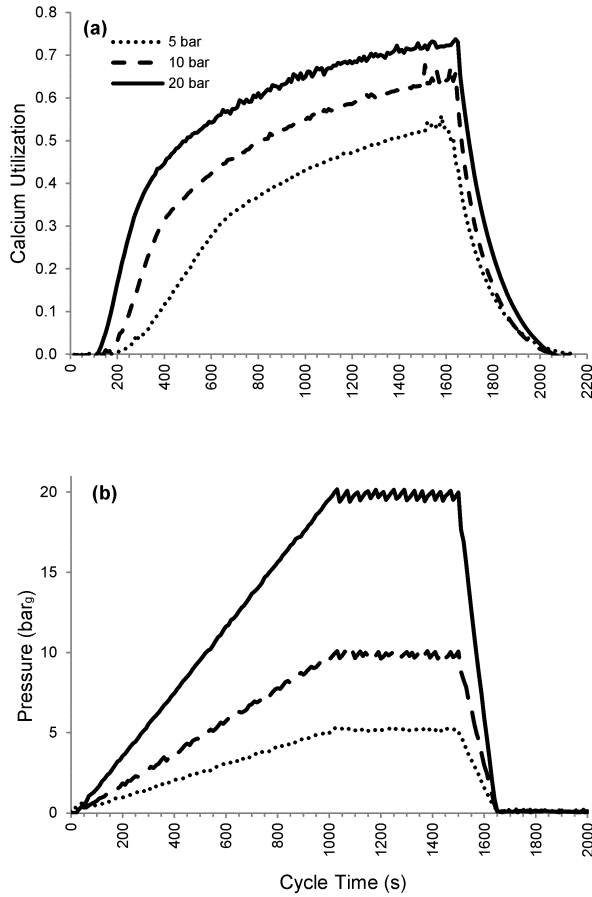


Figure 3.5: Cycle 1 utilization (a) and pressure (b) profiles during 1000°C cycling.

An increase in calcination / carbonation temperature caused an increase in calcium utilization within the first few cycles, at lower carbonation pressures. Sintering is enhanced at higher temperatures, and this leads to a more rapid shift in pore size distribution from micro to meso-pores within the first few cycles. The initial pore coarsening opens up the un-reacted interior CaO to carbonation. This effect declined rapidly in the following cycles due to continued sintering.

At higher carbonation pressures, an increase in temperature reduces the residual calcium utilization after 100 cycles, as a result of enhanced sintering causing a more rapid decrease in surface area. It is likely that, if allowed to go to a very high number of cycles at a given carbonation pressure, the residual utilization will be the same for different temperatures. Additional cycling results can be seen in Appendices 4 and 11.

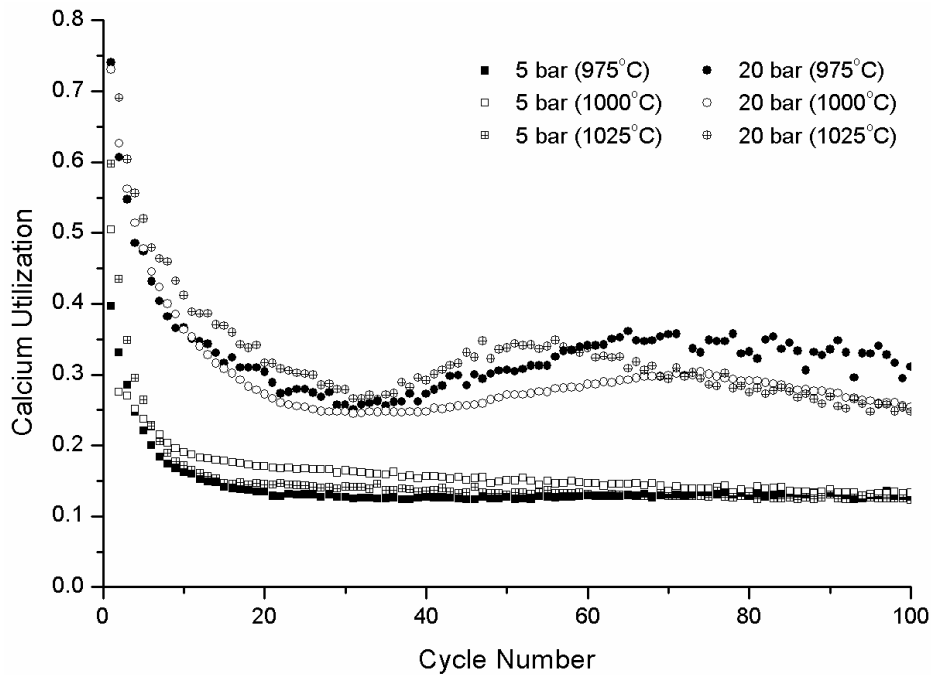


Figure 3.6: Evolution of calcium utilization over long series of carbonation/calcination cycles. 10 bar cycling can be seen in Appendix 11.

3.4.2 Reaction-Controlled Regime

To obtain a better understanding of the effect of pressure cycling on the sorbent, the reaction rates (dX/dt) at 1, 5, 10, 25, 50 and 100 cycles were plotted against cycle number. Results show a similar trend in the reaction-controlled rate to that seen in the decay in utilization over 100 cycles, see Figure 3.7. The rate of the reaction controlled regime decreases rapidly in the first 20 cycles. This decrease results from a loss in micro porosity of the particle due to rapid pore coarsening. It has been found that the kinetic rate in the initial phase is proportional to the particle micro porous surface area [33].

The main mechanism for sintering of calcium oxide is lattice diffusion and, to a lesser extent, volume diffusion [73]. The driving force underlying sintering is free energy minimization of the crystal lattice. In the lattice, this occurs through reductions in grain boundaries and lattice imperfections, resulting in an increase in grain size and densification of the sorbent particle [32]. On the particle surface, free energy minimization causes pore coarsening and elimination, thereby reducing the particle surface area and rate in the reaction-controlled regime.

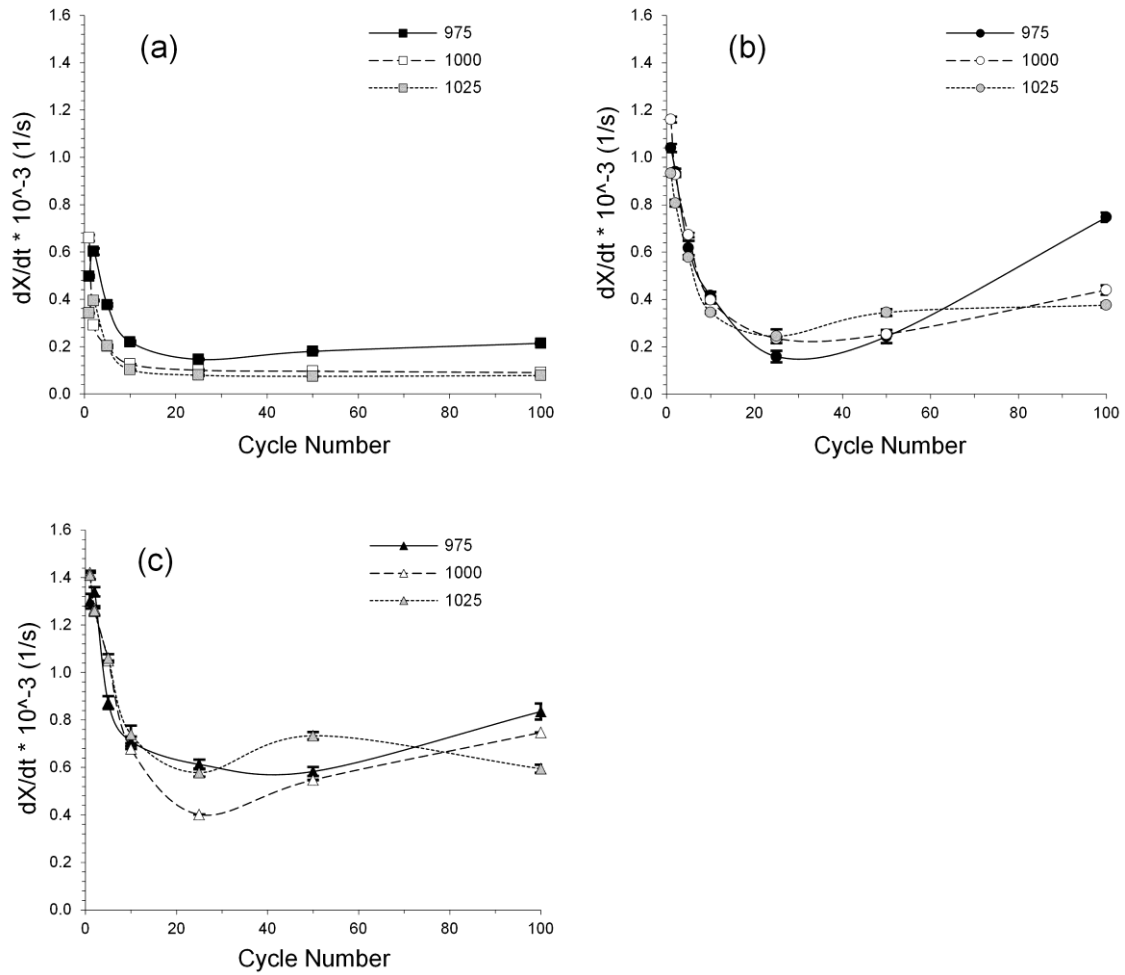


Figure 3.7: Kinetics of reaction-controlled carbonation over 100 cycles at: a) 5 bar_g, b) 10 bar_g, c) 20 bar_g; error bars represent standard errors in rates derived from the grain model.

Following the initial decrease, the rate for carbonation at 5 bar remained nearly constant, indicating that sintering has progressed to a point where the particle surface area has stabilized, see Figure 3.7a. At this point, there is insufficient driving force to sinter the particle further. It can be seen in Figure 3.8 that, although sintering has eliminated smaller pores and smoothed the particle surface, it has not eliminated all lattice defects, as grain boundaries are still visible.

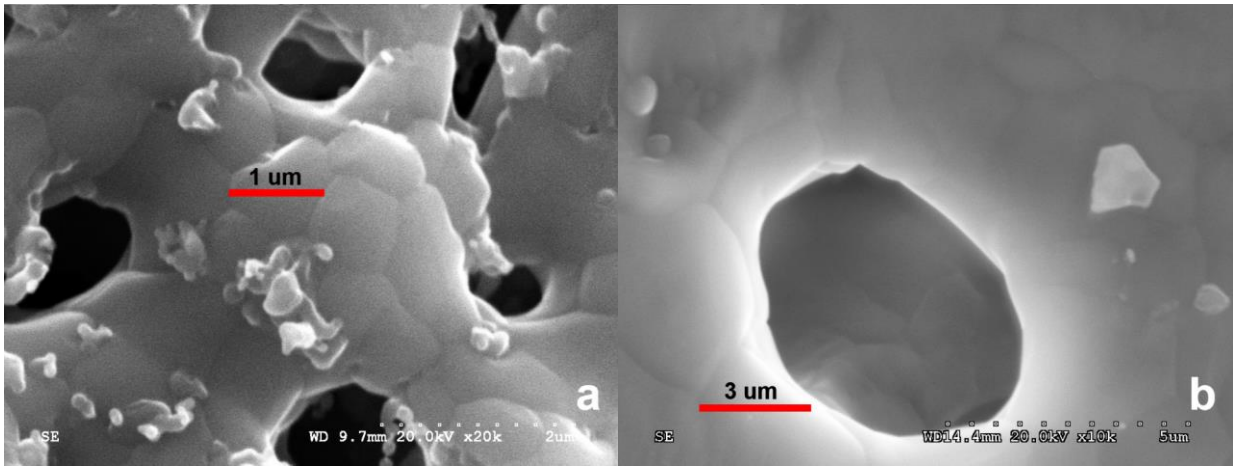


Figure 3.8: SEM micrographs of calcined sorbent cycled at: a) 5 bar and 850°C for 267 cycles; b) 5 bar and 1000°C for 1130 cycles. Note that scales differ.

At 10 and 20 bar carbonation pressures, following the initial decrease, the initial carbonation rate increased, see Figure 3.7. This suggests an increase in particle surface area between 20 and 100 cycles. Results from single point BET analysis in Figure 3.9 show this increase in surface area, confirming the relationship between the fast reaction rate and particle surface area. For the utilization curves of the different samples shown in Figure 3.9, see Appendix 6.

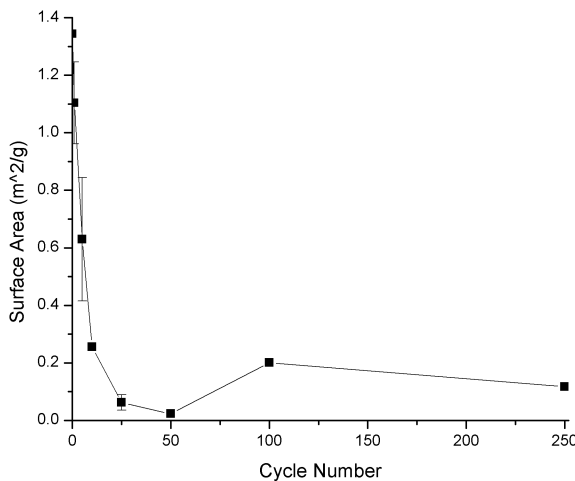


Figure 3.9: Surface area of calcined sorbent cycled at 20 bar_g, 1000°C; error bars represent multiple surface area measurements of the same sample.

The decrease in surface area in the first 20 cycles is also seen in data from 10 bar cycling in Appendix 4. The difficulties of measuring the surface area of such small samples with low surface areas resulted in inconsistent data from 10 bar cycling as there were fewer samples analyzed compared to 20 bar cycling, and repetition of BET measurements did not occur.

An indication of the cause of this increase in surface area can be seen in the SEM micrographs of the calcines at different levels of cycling shown in and Figures 3.10 and 3.11. In these micrographs, one can see rapid pore coarsening and grain growth within the first 25 cycles. Further cycling led to an increase

in fine features on the surface of the particle, with highly cycled samples exhibiting a textured surface, see Figure 3.10d. This can be explained by the following mechanism with the knowledge that sintering leads to the formation of very large grains within the particle. For all SEM micrographs of sorbent with varying degrees of sintering, see Appendices 5 and 6.

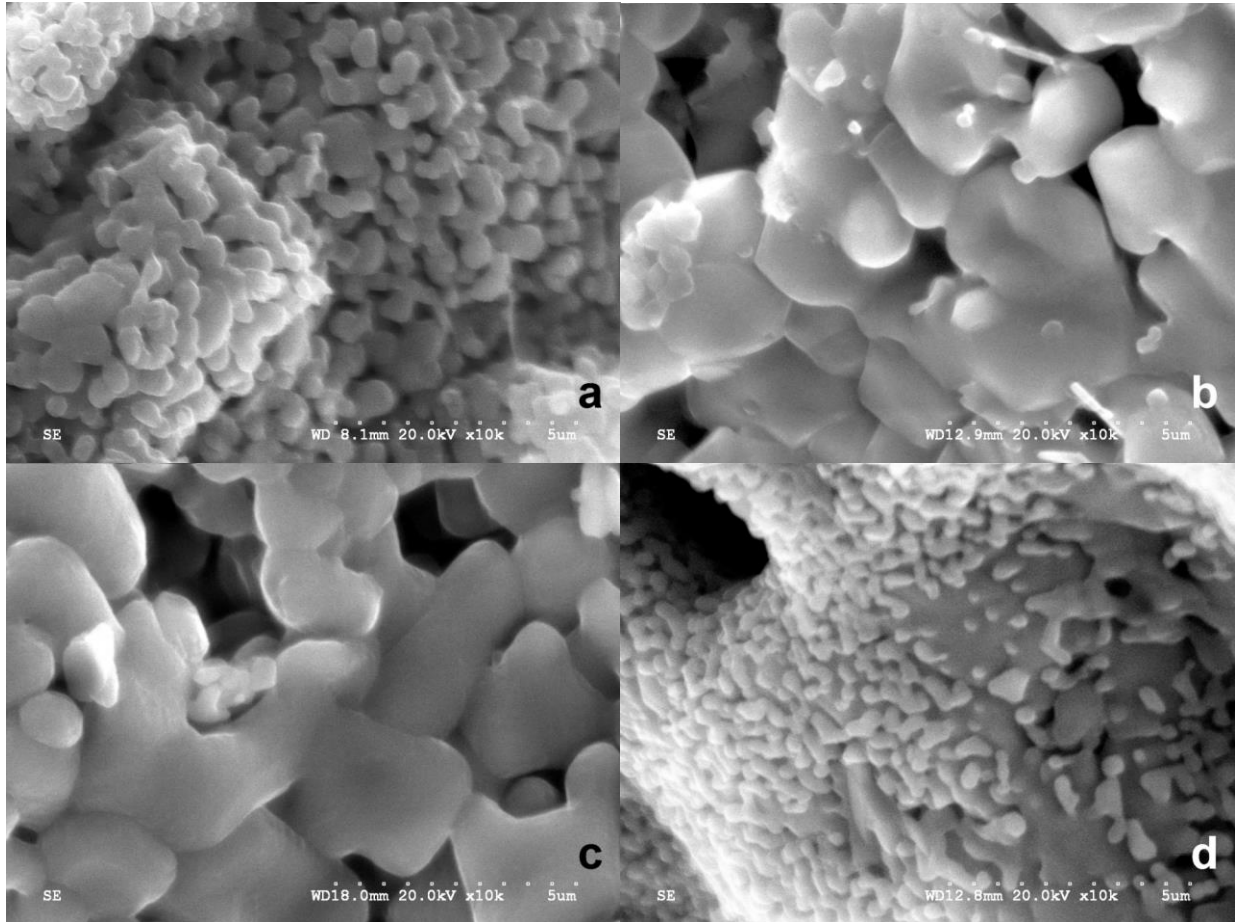


Figure 3.10: SEM micrographs of calcines cycled at 20 bar_g and 1000°C: a) 1st cycle, b) 5th cycle, c) 10th cycle, d) 50th cycle.

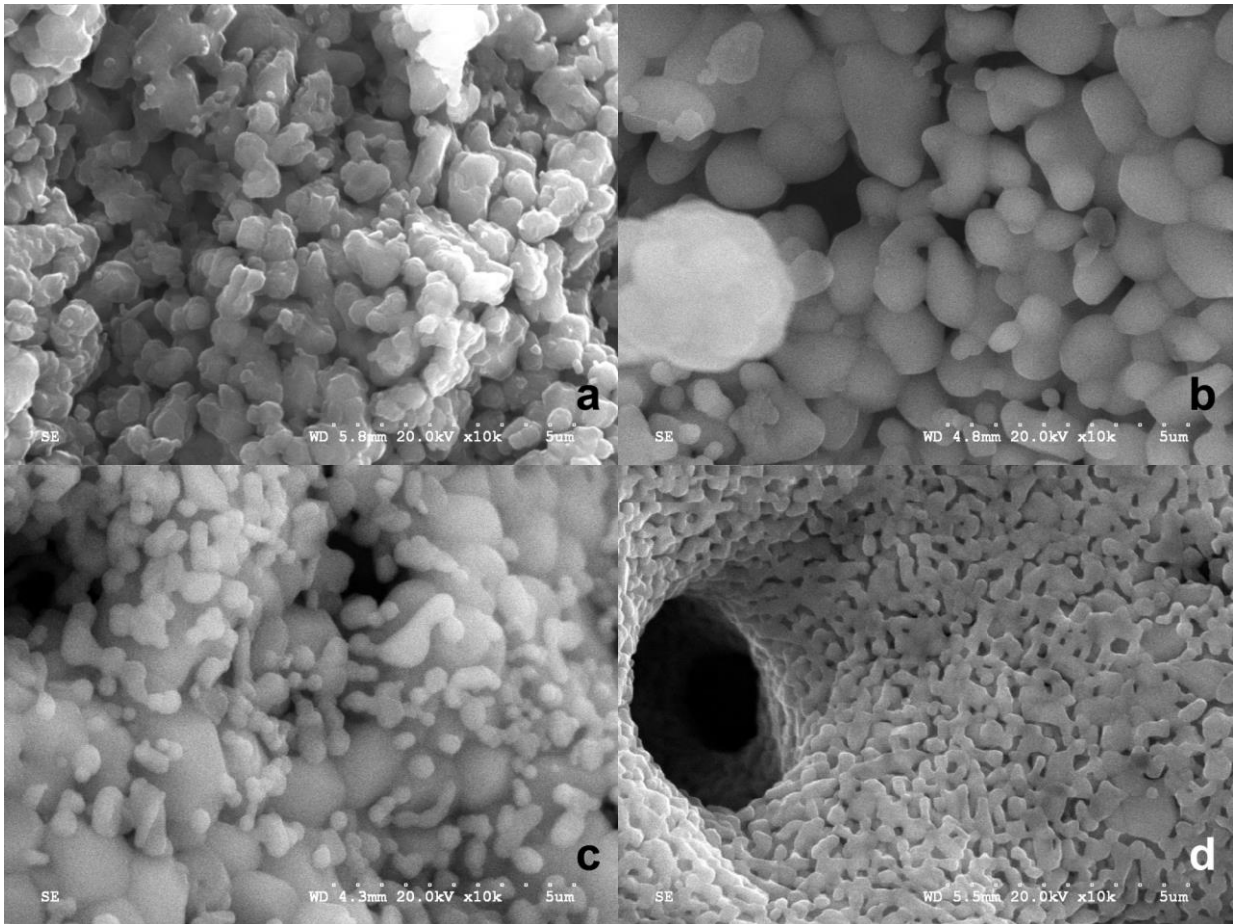


Figure 3.11: SEM micrographs of calcines cycled at 10 bar_g and 1000°C: a) initial calcine, b) 5th cycle, c) 25th cycle, d) 250th cycle.

3.4.3 Mechanism of Dispersed Contraction

Carbonation and calcination are gas/solid reactions which occur at nucleation sites on the solid surface [30]. These sites typically arise at points of crystal lattice irregularities, such as grain boundaries. In the case of calcination, there is a decrease in molar volume due to release of CO₂. This decrease in molar volume is accommodated at the nucleation sites by a contraction of the particle surface around the grain boundaries and shrinking of the grain size. In the absence of small grains and their numerous boundaries, the nucleation sites are randomly dispersed over the surface of the particle, and molar contraction occurs non-uniformly around these dispersed sites. This leads to the textured surface seen in the SEM micrographs (Figure 3.10 and Figure 3.11) and an increase in surface area (Figure 3.9). Elevated temperatures and pressures used in this study create conditions favourable to particle sintering, causing grains to enlarge. This results in an increase in particle surface area, and subsequent increase in the fast reaction rate and residual calcium utilization. The proposed “dispersed contraction” mechanism is depicted in Figure 3.12.

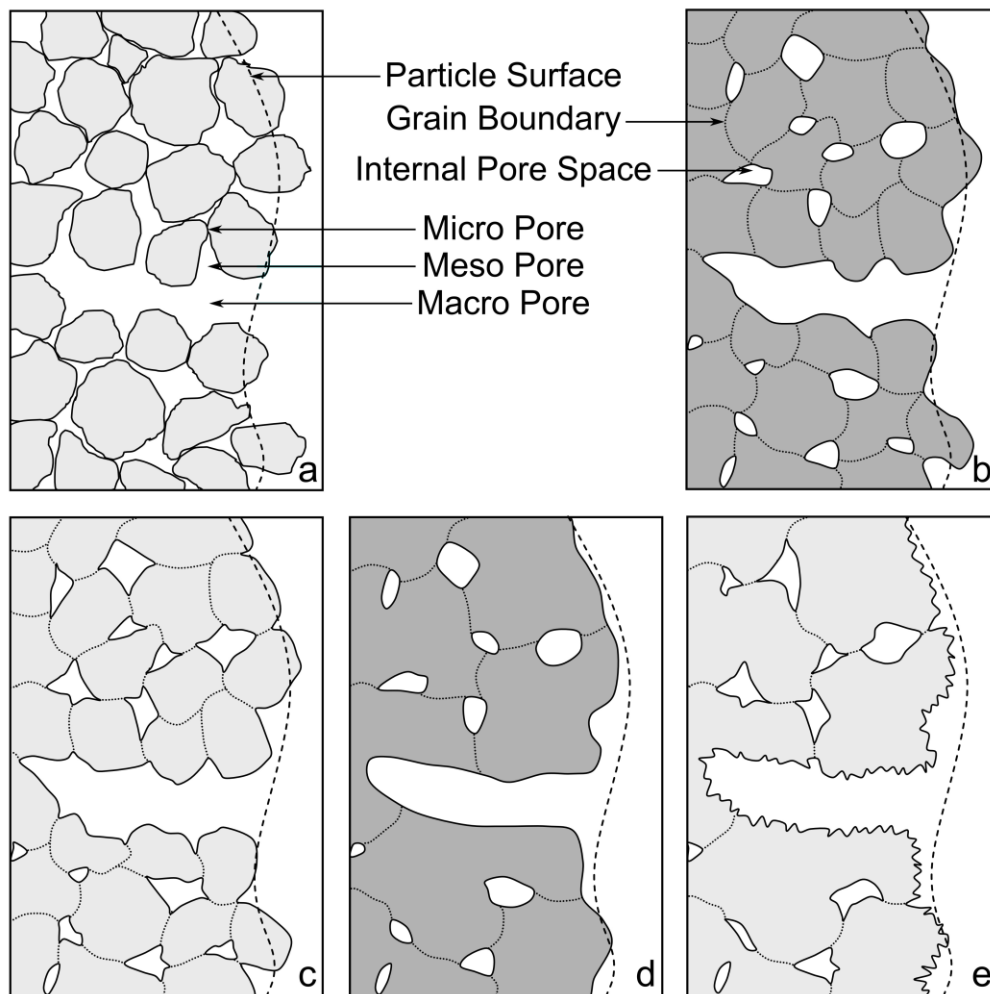


Figure 3.12: Surface “dispersed contraction” mechanism of sorbent re-activation and surface area increase due to grain boundary reduction: a) initial calcine, with distinct grains connected by point contacts; b) sintered carbonate with rounded grains connected by grain boundaries; c) sintered calcine with molar volume contraction occurring at grain boundaries; d) highly sintered carbonate with few grain boundaries remaining; e) highly sintered calcine with volume contraction distributed on grain surfaces .

This dispersed contraction mechanism likely works in conjunction with stabilization of the sorbent skeletal structure, as proposed by others, to increase the residual calcium utilization [63,91]. Manovic et al. [91] examined the effect of “self-reactivation” on sorbent performance and showed that different limestone varieties respond differently to thermal pre-treatment. Within the first 30 cycles, the effect of pre-treatment was found to depend on the type and quantity of impurities within the sorbent. Limestone varieties with higher levels of impurities, in particular Al_2O_3 , showed a higher degree of “self-reactivation.” Impurities within the CaO enhance particle sintering, and high levels result in enhanced sintering [73], leading to the dispersed contraction effect described above. As well, higher pressure increases the mobility of atoms within the sorbent particles, leading to the formation of a stable network of pores and a higher degree of “self-reactivation” [126].

At the highest temperature and pressure tested (20 bar_g and 1025°C), the reaction rate decreases between 50 and 100 cycles, as see in Figure 3.13. The intense sintering at these conditions causes pore coarsening to the point of offsetting a portion of the surface area gains from the dispersed contraction mechanism.

The higher reaction-controlled rate in the first 25 cycles indicates dependence on carbonation pressure, with increasing pressure resulting in an increase in rate. Beyond 25 cycles, the dispersed contraction mechanism dominates the reaction rate, causing a high rate at higher pressure, due to elevated levels of sintering.

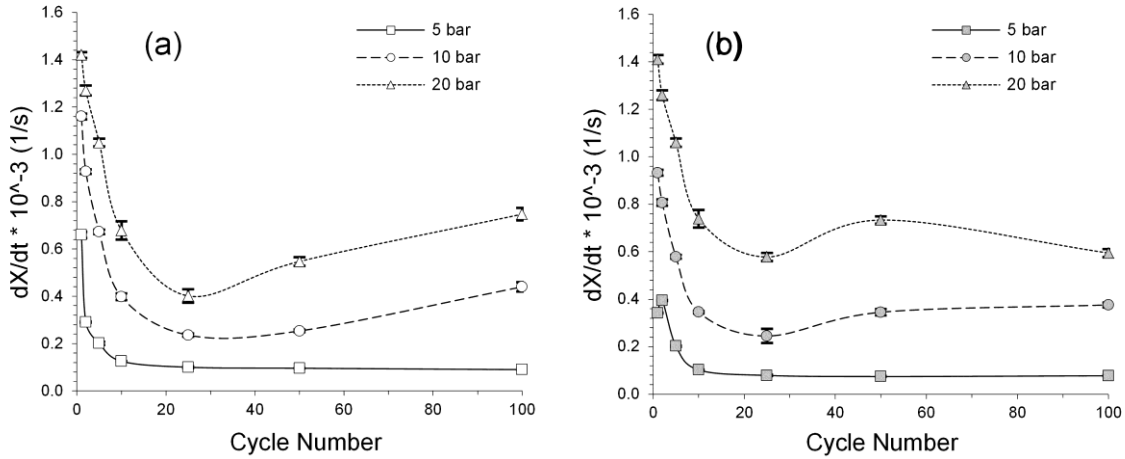


Figure 3.13: Kinetics of reaction-controlled carbonation over 100 cycles at: a) 1000°C, b) 1025°C; error bars represent standard errors in rates derived from the grain model.

3.4.4 Diffusion-Controlled Regime

The kinetics of the diffusion-controlled carbonation was studied to further elucidate the mechanism underlying the rise in calcium utilization. This carbonation regime is rate-limited by the bulk diffusion of reactants through the solid product layer; characterized by a sharp boundary between the unreacted and product layers.

Beruto et al. (1984) suggested that diffusion occurs by migration of CO_3^{2-} or Ca^{2+} through the product layer [46], enhanced by lattice defects such as vacancies, dislocations and grain boundaries, which facilitate ion diffusion. Results show a sharp decline in the rate of product layer diffusion within the first 10 cycles, as the initial stage of sintering causes a sharp decline in lattice defects and growth in grain size, resulting in the loss of grain boundaries along which ion diffusion can occur more easily, see Figure 3.14 and Figure 3.15.

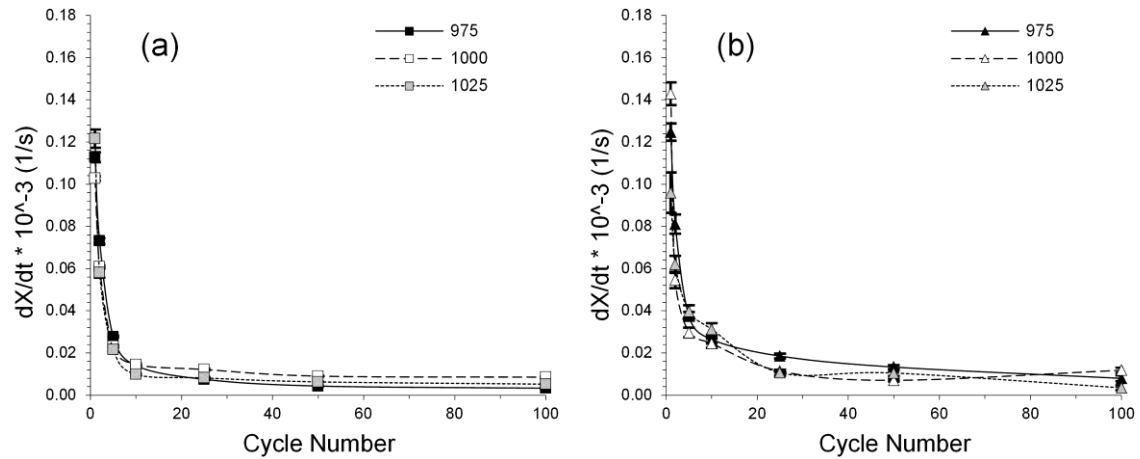


Figure 3.14: Kinetics of diffusion-controlled carbonation over 100 cycles at: a) 5 bar_g, b) 20 bar_g cycling; error bars represent standard errors in rates derived from the grain model.

Unlike the trend of increasing rate after 20 cycles seen for the reaction-controlled carbonation rate, there is little or no increase in the diffusion rate with cycling. All conditions led to a similarly low asymptotic diffusion rate. This asymptotic value represents pure bulk diffusion.

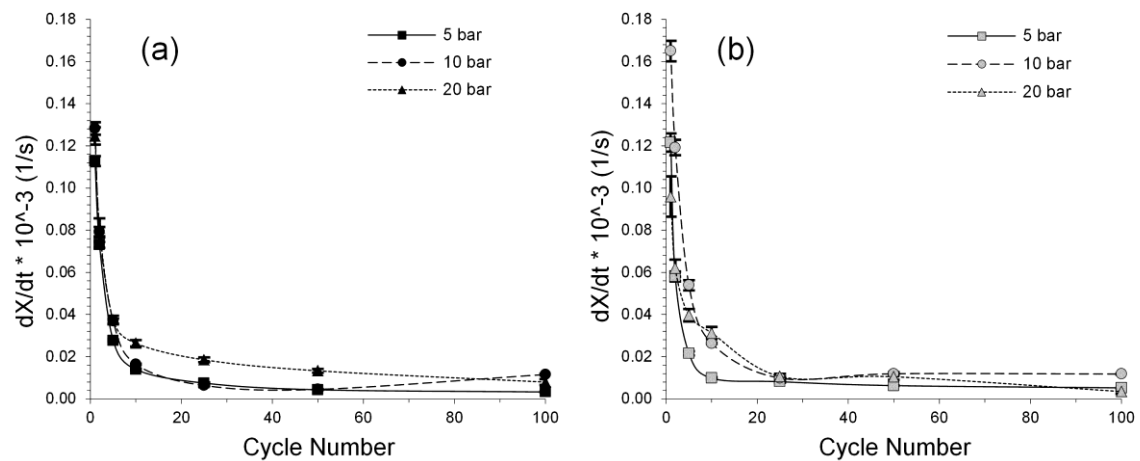


Figure 3.15: Kinetics of diffusion-controlled carbonation over 100 cycles at: a) 975°C, b) 1025°C; error bars represent standard errors in rates derived from the grain model.

There is no clear correlation between the diffusion-controlled rate and temperature. There is a somewhat higher diffusion rate at 20 bar_g carbonation pressure and 975°C. This likely resulted from a slightly shorter duration of calcination at the elevated pressure and the lower temperature during the fixed pressurization and de-pressurization times. Shorter calcination duration has been shown to decrease the sintering of CaO particles. This effect quickly diminished within the first 20 cycles at high temperature.

An analysis of the activation energy and reaction order was performed on data for each individual cycle to determine whether they are affected by cycling, see Appendix 12. The results were not conclusive, and

it is likely that the method of determination of activation energy and reaction order magnified the error in the kinetic rate determinations. For this reason, an interpretation of these results is not presented.

3.5 Conclusions

The kinetics of high pressure carbonation of 150-250 μm Strassburg limestone particles during 100 or more carbonation-calcination cycles were studied, with pressures varied from 5 - 20 bar_g and temperatures from 975 - 1025°C. The kinetics of the reaction-controlled and diffusion-controlled regimes pointed to a possible mechanism behind the effect of cycling on the sorbent morphology over 100 cycles.

High temperature pressure swing cycling caused a rapid reduction in calcium utilization in the first 20 cycles. Following this initial decrease, cycles conducted at carbonation pressures of 10 and 20 bar_g showed a rise in calcium utilization. Increased carbonation pressure resulted in increased residual utilization over 100 cycles, from 0.128 ± 0.005 to 0.271 ± 0.035 for pressure raised from 5 and 20 bar_g . The rate of the reaction-controlled regime showed a similar trend to the calcium utilization over 100 cycles, with an initial rapid decrease followed by an increase between 25 and 50 cycles.

Cycling resulted in rapid particle sintering, leading to a reduction in particle surface area through pore coarsening and growth in grains within the particle, reducing the number of grain boundaries. Solid-gas reactions are initiated at nucleation sites where lattice free energy is highest, such as vacancies, dislocations and grain boundaries. The mechanism of dispersed contraction was proposed to explain the increase in calcium utilization during cycling at $>10 \text{ bar}_g$ carbonation pressure. During calcination, a reduction in the molar volume causes particle shrinkage around these nucleation sites, typically along grain boundaries. Where grain boundaries are fewer, surface contraction at dispersed nucleation sites causes a texturing of the grain surface, an increase in particle surface area, resulting in an increased initial reaction rate and a gain in residual calcium utilization. The bulk diffusion rate decreased rapidly in the first 10 cycles and reached an asymptotic value, similar for all conditions tested. This asymptotic value represents pure bulk diffusion.

The reaction-controlled rate was found to be a function of the carbonation pressure, with increased pressure increasing the rate of the reaction-controlled carbonation. The bulk diffusion rate was independent of reaction pressure.

4 Limestone-Enhanced Gasification of Biomass: Cyclic Gasification and Regeneration in a Bubbling Fluidized Bed

4.1 Introduction

CO₂ capture during gasification can increase the yield and heating value of the product gas by shifting the reversible gasification reactions further towards the valuable product gases (H₂, CO, and CH₄). Equilibrium studies indicate up to 83 vol% H₂ production is possible with virtually no CO or CO₂ in the product stream [57].

In addition to improving syngas quality, the exothermic carbonation reaction, equation 1.2, could supply most of the heat required for the endothermic steam gasification reactions. CaO is a suitable sorbent for CO₂ capture during gasification as it exhibits the following beneficial characteristics:

- high reactivity in the lower gasification temperature range of 500-700°C (1 atm);
- relatively low decomposition temperature (750°C at atmospheric pressure);
- low vulnerability to chemical poisoning;
- low cost and wide availability;
- low toxicity when ultimately disposed.

Lime-enhanced gasification (L.E.G.) of biomass can be accomplished by gasifying biomass feedstock within a fluidized bed of CaO. Fluidized beds have a number of advantages over other solid fuel gasification reactor types (moving bed, entrained bed, etc.), including greater temperature homogeneity, better bed-to-surface heat and mass transfer due to enhanced particle motion, and faster fuel particle heating. As a result, fluidized beds are widely used in solid fuel conversion applications [132].

Heat to drive the endothermic gasification reactions, equations 4.1 - 4.6 in Table 4.1, is typically supplied through combustion of a portion of the fuel, equations 4.7 and 4.8. The heat supplied by the carbonation reaction can reduce or eliminate the amount of combustion heat required by the gasifier/carbonator, though an equivalent input of heat would then be required in a calciner to produce the needed CaO.

Table 4.1: Primary gasification reactions

Water-gas shift	$CO + H_2O \leftrightarrow CO_2 + H_2 + 35.6 \text{ kJ/mol}$	(4.1)
Methane reforming	$CH_4 + H_2O \leftrightarrow CO + 3H_2 - 225 \text{ kJ/mol}$	(4.2)
Water-gasification	$C + H_2O \leftrightarrow CO + H_2 - 136 \text{ kJ/mol}$	(4.3)
Water-gasification	$C + 2H_2O \leftrightarrow CO_2 + 2H_2 - 100 \text{ kJ/mol}$	(4.4)
Boudouard	$C + CO_2 \leftrightarrow 2CO - 171 \text{ kJ/mol}$	(4.5)
Methanation	$C + 2H_2 \leftrightarrow CH_4 + 89 \text{ kJ/mol}$	(4.6)
Oxidation	$C + O_2 \rightarrow CO_2 + 394 \text{ kJ/mol}$	(4.7)
Oxidation	$C + 0.5O_2 \rightarrow CO + 112 \text{ kJ/mol}$	(4.8)
Pyrolysis	$4C_nH_m \rightarrow mCH_4 + (4n - m)C$	(4.9)

Gasification of solid fuels proceeds in three stages: fuel drying, pyrolysis and char gasification, see Figure 1.13. Pyrolysis drives volatile compounds out of the solid particle, leaving behind char, CH_x where $x < 1$. The volatiles are converted to gaseous hydrocarbons and condensable tars, which must be cracked to avoid fouling of downstream equipment. One of the major challenges of biomass gasification is the production of large amounts of these condensable tars. The basic-metallic nature of CaO has the added benefit of catalytically cracking the tars [133]. Indeed limestone was one of the first additives used to improve gasification in fluidized beds [134]. The presence of CaO in high temperature (900°C) fuel gas removed the majority of tar compounds in gasification experiments [135]. Water adsorbed on the alkaline earth oxide dissociates to highly reactive H^+ and OH^- ions which react with adsorbed tar species producing lower molecular weight gas species and char, equation 4.9 in Table 4.1 [136].

CO_2 absorption on CaO occurs when the partial pressure of CO_2 in the reactor (P_{CO_2}) is less than the equilibrium partial pressure of CO_2 on $CaCO_3$ ($P_{CO_2,eq}$). The calcium utilization of the sorbent is directly related to the surface area available for reaction. To be practical for continuous, steady-state carbon capture and storage, the $CaCO_3$ formed in the gasifier/carbonator must be re-calcined to CaO in a separate reactor (calciner) for re-use.

A number of parameters influence gasification and product gas composition. Steam gasification of char is a highly endothermic process, benefitting from elevated temperatures, $> 800^\circ\text{C}$. As well, tars formed during the pyrolysis stage are thermally cracked at elevated temperatures [137]. A high steam-to-biomass mass ratio of 2.5, benefits gasification through reduced tar yield and increased H_2 concentration [138]. Conversely, an increased steam-to-biomass ratio reduces the product gas higher heating value due to reduced CO production and requires additional energy. There is a trade-off between improved syngas quality and the energy penalty of producing excess steam [116].

Fine char produced by pyrolysis accumulates on the bed material and is gasified in the rate-limiting char gasification step. Following gasification, this accumulated char can be combusted to supply the heat for the endothermic calcination reaction required for sorbent regeneration.

This chapter presents results from experiments into the effect of using a calcium oxide (CaO) sorbent as the bed material in a bubbling fluidized bed biomass gasifier, as well as the effects of cycling the sorbent between gasification and calcination.

4.2 Experimental

A typical L.E.G. system design utilizes dual-fluidized bed reactors with gasification taking place in one reactor, calcination in the other, and solids circulated between the two in a loop, as shown in Figure 1.14. To simulate this with a single reactor in this study, L.E.G. was conducted in a semi-batch fashion, as depicted in Figure 4.1, using a single reactor for both carbonation and calcination. The use of a single bubbling fluidized bed reactor instead of a dual-fluidized bed system is likely to reduce particle attrition and elutriation due to the lower gas velocities.

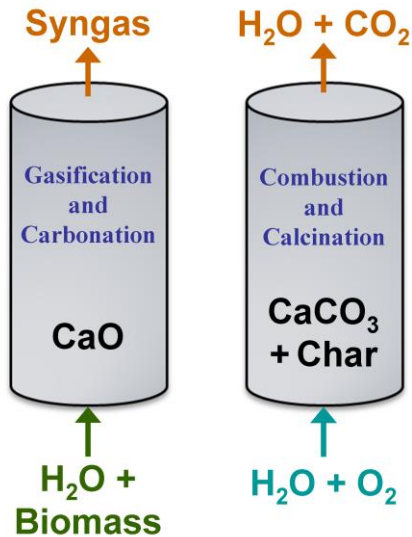


Figure 4.1: Schematic of a lime-based enhanced biomass gasification process using a single reactor, semi-batch process.

Biomass fuel and steam were fed into a bed of calcined limestone where CO₂ was absorbed until the maximum calcium utilization of the CaO sorbent was reached. Following gasification, the biomass and steam flows were stopped, and the fluidizing gases were switched to nitrogen and air for in-situ calcination, see Figure 4.1. Calcination progressed slowly as the O₂ supplied to the bed was limited to prevent the temperatures at the bottom of the bed from exceeding 900°C. The bed temperature gradually increased until the fuel:O₂ ratio became favourable for pure combustion. For continued cycling, the stages were repeated. The results presented in this chapter show the breakthrough of CO₂ and other product gases during the gasification stage.

Lime-enhanced gasification experiments were performed in a 76 mm ID, 707 mm tall, atmospheric pressure, bubbling fluidized reactor, see Figure 4.2. The reactor had an internal cyclone of 50 mm ID,

with the dip leg returning the solids to the lower bed through the use of a trickle valve, see Appendix 12 for details. The distributor was a perforated plate of 3.2 mm holes, 6.4 mm apart, 95 in total. The plate was covered with a single layer of stainless steel mesh, 400 mesh, to prevent solids from slipping into the pre-heater. This column was modified from the set-up constructed by Masakazu Sakaguchi, and further details can be found in his thesis and published work [139,140]. The bed was adapted for solids fuel feeding, and the parametric design / calculations are found in Appendix 14. Originally limestone-enhanced gasification experiments were to be conducted in a larger (100 mm ID) bubbling fluidized bed, but serious flaws with the reactor made it un-suitable for high-temperature operation, see Appendix 13.

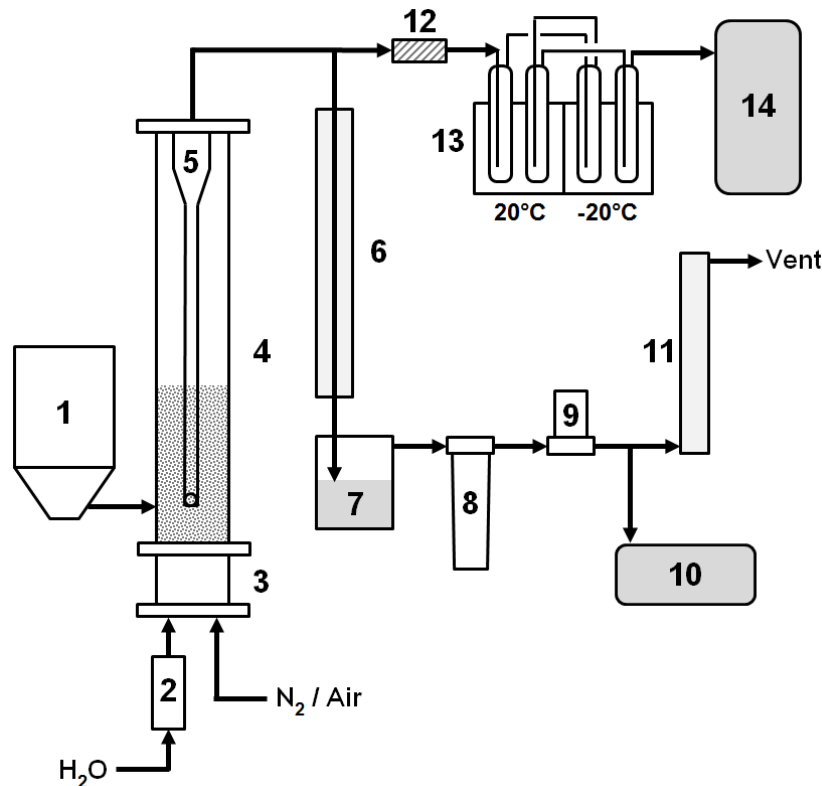


Figure 4.2: Bubbling fluidized gasifier setup: (1) fuel hopper, (2) steam generator, (3) preheater, (4) fluidized bed, (5) internal cyclone, (6) condenser, (7) condensate collection, (8) particle filter, (9) mass flow meter, (10) Agilent 4900 micro-GC, (11) afterburner, (12) 5 micron particle filter, (13) tar sampling impinger bottles, (14) APEX XC-60 gas sampler.

The static bed height at the beginning of each run was 350 to 400 mm, calculated based on the mass of solids added. The biomass fuel used was ground pine wood pellets. The size distributions of biomass fuel and fluidized bed particles are shown in Figure 4.3. The biomass ultimate and proximate analyses are provided in Table 4.2.

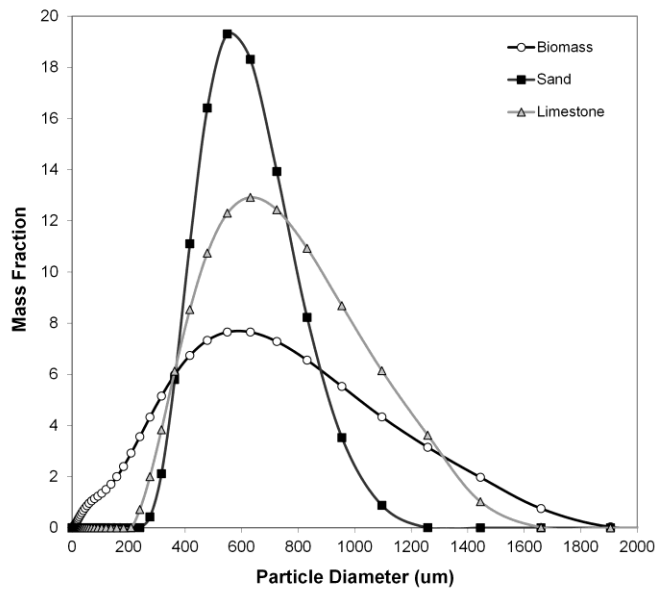


Figure 4.3: Particle size distributions of biomass and fluidized bed materials

Biomass was fed into the side of the column at a height of 100 mm above the distributor using a water-cooled screw feeder, at a rate of 0.45 kg/h. The screw was 12.7 mm in diameter, 600 mm in length and drew the biomass fuel from a Schenck Accu-Rate Tuf-Flex 300 feed hopper. A low flow of nitrogen (~0.11 L/min) was passed through the hopper, into the bed, to ensure that bed gases and steam did not backflow into the hopper.

Table 4.2: Pine sawdust analysis

High Heating Value (kJ/kg)	17,647
d_p , volume weighted (μm)	469
Proximate Analysis (wt% dry)	
Volatile	86.85
Fixed Carbon	12.71
Ash	0.44
Ultimate Analysis (wt% as received)	
Moisture	7.40
Carbon	46.60
Hydrogen	5.71
Nitrogen	0.03
Sulphur	0.07
Oxygen	39.78

The bed material was loaded before the start of each run, with no addition or removal of bed material during the run. Three different bed materials were used: silica sand, un-treated limestone and calcined limestone particles, see Table 4.3 for chemical composition of sand and limestone and Table 4.4 for particle hydrodynamic properties. The velocity values in Table 4.4 were calculated based the relations shown in Appendix 16.

Limestone was calcined at 850°C in an external oven, in a crucible (140 x 140 mm), with a packed bed depth of 70-80 mm, for 24 h and subsequently cooled under a flow of dry nitrogen, ~200 mL/min. The

calcined sorbent was then immediately added to the reactor through the biomass feed port. A small amount of hydration, 1.2 wt%, was found to have occurred during the loading of the reactor. Gasification runs without cycling were conducted using silica sand and limestone, as a basis for comparison to sorbent enhanced gasification. Gasifier standard operating procedures can be found in Appendix 14.

Table 4.3: Bed material analysis

(wt%)	CaO	MgO	Al ₂ O ₃	Fe ₂ O ₃	K ₂ O	Na ₂ O	SiO ₂	LOI*
Limestone	53.7	1.25	0.19	0.94	0.08	0.02	0.94	42.9
Sand	0.04	0.02	0.64	0.15	0.27	0.08	98.14	--

*LOI - loss on ignition

Table 4.4: Particle properties

(wt%)	d _p (μm)	ρ _p (kg/m ³)	U _{mf} (m/s)	U _t (m/s)
Limestone	623	2711	0.17	1.08
Sand	559	2402	0.12	0.88
Biomass	469	670	--	0.60

U_{mf} = minimum fluidizing velocity (calculated); U_t = particle terminal velocity (calculated).

The feedstock was gasified using steam, generated by pumping de-ionized water through a steam generator where it was heated to 250°C, then into the pre-heater, which was held at or near the bed temperature. Nitrogen was used as a fluidizing gas, in addition to steam, to ensure consistent fluidization on the small scale, with a steam-to-nitrogen mass ratio of 2, see Table 4.5 for operating conditions. All gas flows were controlled using rotometers. See Appendix 17 for all flow and pressure calibrations. Nitrogen and steam were mixed in the pre-heater before entering the bed. The product gas was cooled through a shell-in-tube condenser and filtered through a 10 micron fabric filter. The product gas flow was measured by an electronic mass flow meter. The flue gas was then mixed with air and re-heated in the after-burner to 600°C to combust the remaining syngas. The composition of the product gas was measured using a four-column Agilent 4900 gas chromatograph (GC), and results are reported on a nitrogen-free basis.

Table 4.5: Operating conditions

Gasification Conditions	
Biomass feed rate (kg/hr)	0.45
Steam to biomass ratio	2.5
Calcination conditions	
Air flow (LPM @ ambient)	8.8
Fluidizing gas	
Design gas velocity (m/s)	0.34
Nitrogen flow (LPM @ ambient)	6.60
Hopper N ₂ purge (LPM)	0.11

The column and its contents were electrically heated by four radiative clam-shell heaters, two heating the pre-heater and lower bed and the other two heating the upper half of the fluidized bed. The two heating sections were independently controlled by programmable logic controllers. A ceramic fibre baffle was installed around the reactor outside wall, between the heating sections, to retain heat in the lower bed.

The bed temperature was held as close as possible to 700°C during the gasification stages. The heat required for calcination was supplied by feeding air into the bed in order to combust the residual char. Thirteen K-type thermocouples were used throughout the reactor system. Thermocouples in the reactor measured temperature in the radial center. The axial location of each temperature measurement, above the distributor, is specified in the results.

The bed pressure was near atmospheric, in the range of 10 - 30 kPa_g and was measured at three positions: the pre-heater, the lower bed (50 mm above the distributor), and the freeboard (400 mm above the distributor). Reported pressures are those of the lower bed, unless otherwise specified. Pressure was limited to below 40 kPa, due to the low pressure feed hopper, see Appendix 15 for a detailed explanation of this and other operational issues of the BFB gasifier.

The bed material for each run was classified by sieving, and each particle size fraction was then analyzed in a Shimadzu-50 TGA to determine the fractions of char and carbonate in the sample. Samples were also collected from the bed during each stage of cycling and analyzed using the TGA. Bed material from the calcination stages of cycling experiments was further characterized using a Micrometrics ASAP 2020 physi-sorption BET unit to determine the specific surface area of the calcined bed particles.

Tar production was measured by a modified CEN/TS 15439 gravimetric sampling and analysis procedure [141]. This involved four, 250 mL impinger bottles filled with 50 mL iso-propanol. Two were at 20°C and two at -20°C, with gas flow as depicted in Figure 4.2. The collected solvent / tar mixture was then passed through a 0.02 µm filter to remove fines. All glassware was rinsed with methylene chloride to collect all tars. The collected solvent / tar mixture was treated in a rotary evaporator at 55°C and 17 kPa_{abs} until all the solvent was extracted, as determined once the drip rate in the evaporator had fallen to one every 4 s. 20 mL of ethanol was then added to the vacuum flask for water removal. The evaporation was continued until a drip rate of one every 4 s was reached. Air flow into the vacuum flask was then initiated, with the vacuum was held below 68 kPa_{abs}. This procedure removed the remaining water droplets. Air flow continued for 20 minutes. The vacuum flask was then removed, allowed to cool in a desiccator and weighed to determine the produced tar. See Appendix 14 for complete tar sampling procedures.

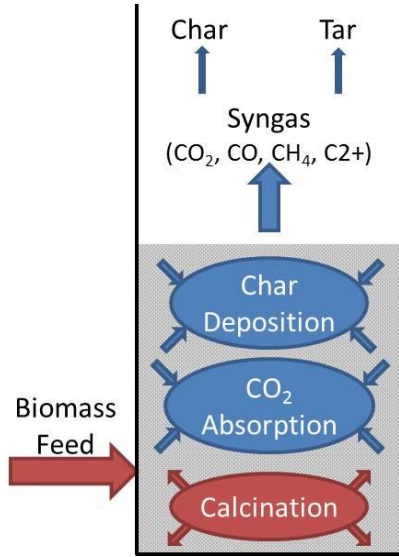


Figure 4.4: Carbon balance in lime enhanced biomass gasification

Carbon utilization was calculated based on a carbon balance of the fluidized bed, see Figure 4.4. The condensable tars and elutriated char fines were considered to be carbon losses; therefore, the utilization efficiency was calculated using the moles of carbon in the biomass feed ($n_{C,biomass}$), syngas ($n_{C,gas}$) and moles of CO_2 absorbed or desorbed by the sorbent (Δn_{CaCO_3}):

$$\eta_C = \frac{n_{C,gas} + \Delta n_{CaCO_3}}{n_{C,fuel}} \quad (4.10)$$

Over the course of a full gasification/ calcination cycle, equation 4.10 becomes:

$$\eta_C = \int_0^{t_{carb}} \frac{(X_{CO} + X_{CO_2} + X_{CH_4} + 2X_{C_2H_6} + 2X_{C_2H_4} + \dots) P \dot{V}_{Syngas} / (RT) + \Delta n_{CaCO_3} / t_{carb}}{\dot{m}_{bio} \times [C]_{bio} / 12} dt \quad (4.11)$$

where P is pressure in kPa, T is the temperature in K, V is the volumetric flow in LPM, m_{bio} is the fuel flow rate in g/min, and t_{carb} is the total carbonation time in minutes. A similar method is used to calculate the hydrogen utilization efficiency:

$$\eta_H = \frac{n_{H,gas}}{n_{H,bio} + n_{H,steam}} \quad (4.12)$$

where $n_{H,gas}$ is the moles of hydrogen in the syngas accounting for all produced gases except steam, $n_{H,bio}$ is the moles of hydrogen in the biomass feed (both moisture and elemental hydrogen) and $n_{H,steam}$ is the moles of hydrogen in the steam feed. The steam produced was not factored into the hydrogen utilization equation as it was too difficult to measure in the current reactor setup. Single cycle utilizations were used to compare different bed materials and were calculated based on the molar flow rates only during periods of biomass feeding. For cycle utilizations, the molar flows of feed and gases during both gasification and

calcination stages, were used. The higher heating value of the product syngas was calculated based on the heating values of the individual components [142].

A simple equilibrium model based on Gibbs free energy minimization was constructed in ASPEN Plus for comparison with the experimental results.

4.3 Results and Discussion

4.3.1 Effect of Bed Material

Gasification runs were performed with silica sand and limestone as bed materials to provide a base line for comparison with the L.E.G. These gasification runs typically lasted between 100 and 150 min, the duration of continuous biomass feeding. The bed mass was similar between experimental runs, see Table 4.6. The pre-calcined mass for all calcined limestone runs was 1750 ± 10 g, giving a calculated, calcined bed mass of 1 ± 0.01 kg. The mass of the bed material for the two CaO cycling runs was higher than this when injected into the bed, indicating that the limestone was not completely calcined. Complete calcination in the external furnace was difficult, despite calcining for 24 h, as mass transfer through the large crucible (140 x 140 mm) of deep solids (72 mm) is low.

Two gasification runs without cycling were conducted for each of the three bed materials: sand, limestone and lime. Then two runs were completed wherein the lime sorbent was cycled between gasification and calcination, one involving two gasification-carbonation cycles and the other eight cycles. During these cycling runs gasification proceeded for 70 - 100 min and a calcination stage prior to each gasification stage of approximately 90 min. In total, 8 runs were successfully completed using the three bed materials, see Table 4.6.

The bed pressure was intended to be similar for all runs, see Table 4.6, but varied between and during runs, as a result of condenser plugging. The condenser design led to periodic plugging of the inner tube by char and fines mixed with condensed water and tar. This led to a periodic rise in bed pressure, requiring cleaning of the condenser. For this reason, a new condenser system was designed and built and will be used in future experiments, see Appendix 20 for the full design. The bed pressure was limited by the feed hopper, which could not be safely operated above 50 kPa.

The pressure drop across the bed remained relatively constant for gasification in the sand and limestone beds, with a slight drop in the first limestone bed as a result of partial calcination of the bed material, see Table 4.6. The pressure drop across the bed increased for all runs where CaO was the initial bed material, confirming carbonation of the particles during gasification. The bed mass increases as CO₂ is absorbed, equation 1.2, and particle density increases, causing an increase in bed pressure drop according to:

$$\Delta P_{bed} = \rho_p (1 - \varepsilon) gh \quad (4.13)$$

where ΔP_{bed} is the bed pressure drop, ρ_p the particle density, ε the fluidized bed voidage, g is gravity and h the bed depth.

Table 4.6: Bed inventory and pressures of different gasification runs; bed pressure drop is the differential between the transducers at 5 and 40 cm above the distributor.

Run	Cycle	Bed Material	Initial Bed Mass (g)	Bed Pressure (kPa _g)	Bed Pressure Drop (kPa)			
					Carbonation Initial	Carbonation Final	Calcination Initial	Calcination Final
SB-04-12	-	Quartz Sand	1501	8.0 ± 0.9	1.09	0.99	-	-
SB-08-12	-	Quartz Sand	1768	21.7 ± 1.7	3.01	3.14	-	-
LB-04-12	-	Limestone	1504	14.3 ± 1.5	2.47	2.30	-	-
LB-06-12	-	Limestone	1503	15.1 ± 4.5	1.62	1.66	-	-
CB-06-12	-	Calcined Limestone	1754*	23.1 ± 4.1	2.18	2.46	3.67	1.56
CB-07-12	-	Calcined Limestone	1750*	33.9 ± 6.4	1.81	2.34	-	-
CCL-07-12	1	Calcined Limestone	1360	24.5 ± 2.3	2.26	2.39	1.79	1.81
	2	Calcined Limestone	809**	24.8 ± 2.3	1.79	2.27	-	-
CCL-10-12	1	Calcined Limestone	1462	24.8 ± 3.8	1.97	2.20	1.93	1.59
	2	Calcined Limestone	949**	21.9 ± 5.2	2.03	2.58	2.28	1.86
	3	Calcined Limestone	972**	24.8 ± 3.4	2.06	2.57	2.48	1.86
	4	Calcined Limestone	966**	22.5 ± 6.0	2.06	2.61	1.96	1.98
	5	Calcined Limestone	922**	28.7 ± 6.1	2.04	2.26	2.13	1.83
	6	Calcined Limestone	856**	24.2 ± 1.4	1.77	2.32	2.24	1.76
	7	Calcined Limestone	738**	23.4 ± 2.5	1.79	2.08	1.87	1.45
	8	Calcined Limestone	624**	24.5 ± 3.3	1.41	1.67	-	-

* mass of limestone prior to calcination

** calculated based on pressure drop

Results from the runs conducted using a sand bed (no limestone) showed that the bed took approximately 50 min after the initiation of biomass flow to reach steady-state, identified from a levelling off of the syngas concentrations and a sharp drop in the temperature of the bed directly above the biomass feed port, see Figure 4.5a. During this start-up period, char particles produced through pyrolysis were accumulating, primarily on the bed material. When the bed became fully saturated with char, the endothermic char gasification reactions dominated. Coupled with the continuous introduction of cold fuel particles, a localized decrease in bed temperature, down to 440°C, occurred directly above the biomass feed port. Only the thermocouple at 150 mm height, 50 mm above the feed point, recorded this zone of low temperature from the feed; a thermocouple at 200 mm did not experience the same degree of temperature drop. The higher heating value of the produced gases was greater during this start-up period than at steady-state, primarily due to the elevated CO concentration, see Figure 4.5b. The carbon utilization efficiency somewhat mirrored the bed temperature directly above the feed port. The cooler zone around the feed port reduced the heating rate of the fuel particles, reducing the carbon conversion efficiency. Full results from all runs are presented in Appendix 18.

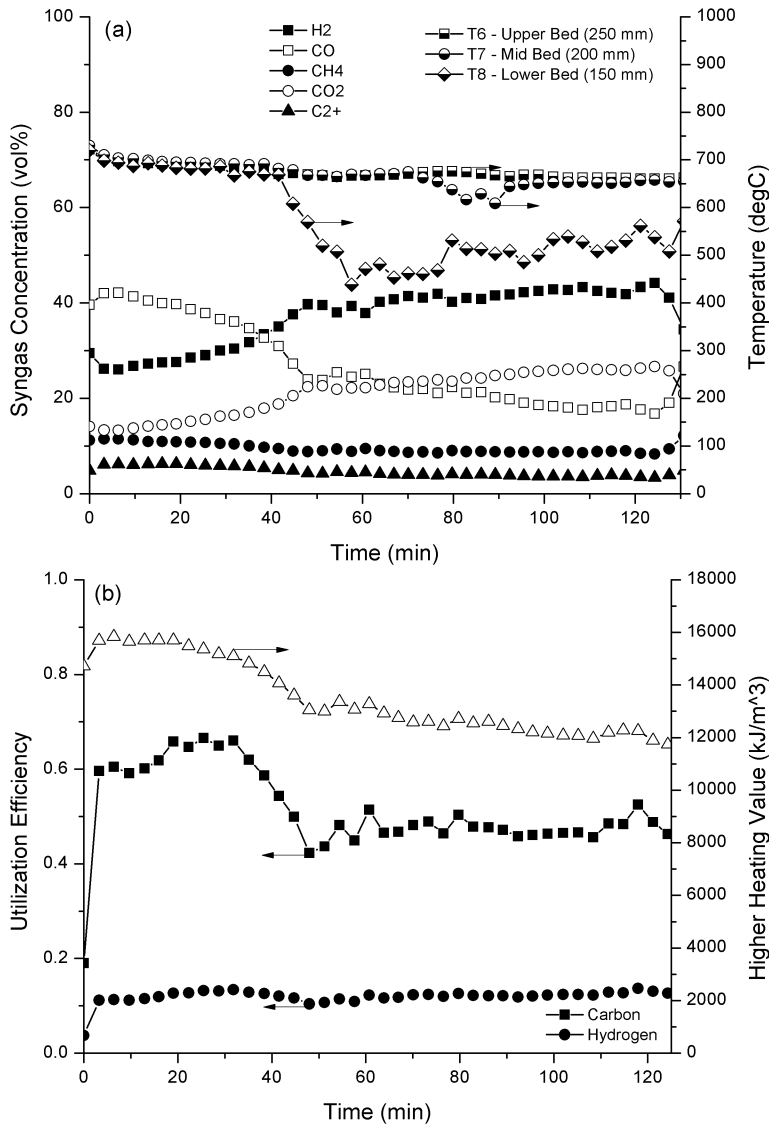


Figure 4.5: Gasification results for a sand bed (SB-08-12); a) water and nitrogen-free syngas composition and local temperatures, b) higher heating value and utilization efficiencies. Heights of the temperature probes above distributor are given in the legend.

The presence of un-calcined limestone particles in the fluidized bed caused a decrease in syngas quality and an increase in CO₂ concentration. It is suspected that this was due to partial calcination of CaCO₃ during gasification, as the difference between the equilibrium and CO₂ partial pressures was small, and it is likely that regions of the bed were in the calcination regime. Due to slightly elevated bed temperatures, some calcination occurred when the CO₂ partial pressure dropped below the equilibrium partial pressure, as can be seen in the first 25 min in Figure 4.6a. In order to maintain the bed temperature near 700°C during steam endothermic gasification, the reactor wall was heated to near 800°C. As a result, the temperature in the freeboard was higher than in the bed, and some limestone likely calcined at and above the bed surface. The high CO₂ concentration decreased the concentrations of the other gaseous species.

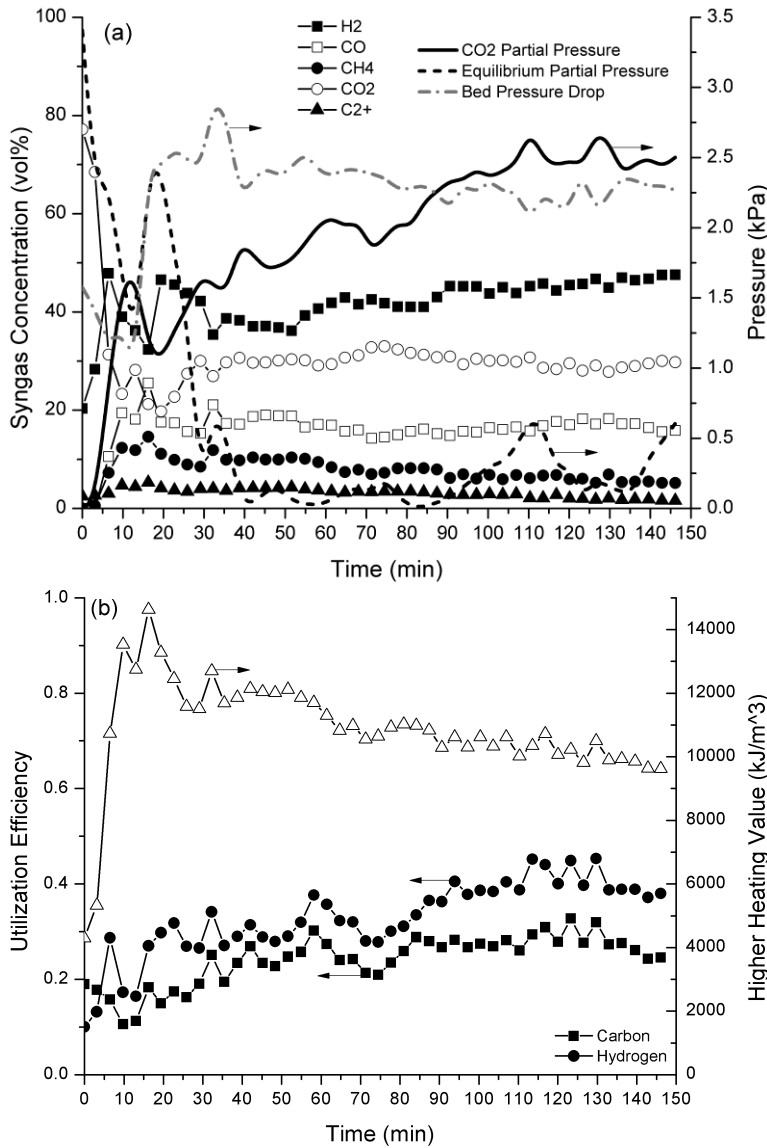


Figure 4.6: Gasification results for limestone bed (LB-04-12); a) water and nitrogen-free syngas composition and local temperatures, b) higher heating value and utilization efficiencies.

Runs conducted with CaO as the starting bed material showed the best syngas quality and utilization efficiencies. Decreasing carbonation of the CaO bed can be seen in Figure 4.7a, where a period of high H₂ production existed near the start of the run, during which a large fraction of sorbent particles were active in absorbing CO₂. Individual CaO particles gradually reached their carbonation limit, and the H₂ production gradually decreased. Mixing in the bed ensured that there was no sharp drop in H₂ concentration at the end of the breakthrough period, as particles moved through regions in the bed of different CO₂ partial pressures and hence carbonation driving force, $P_{CO_2} - P_{CO_2,eq}$.

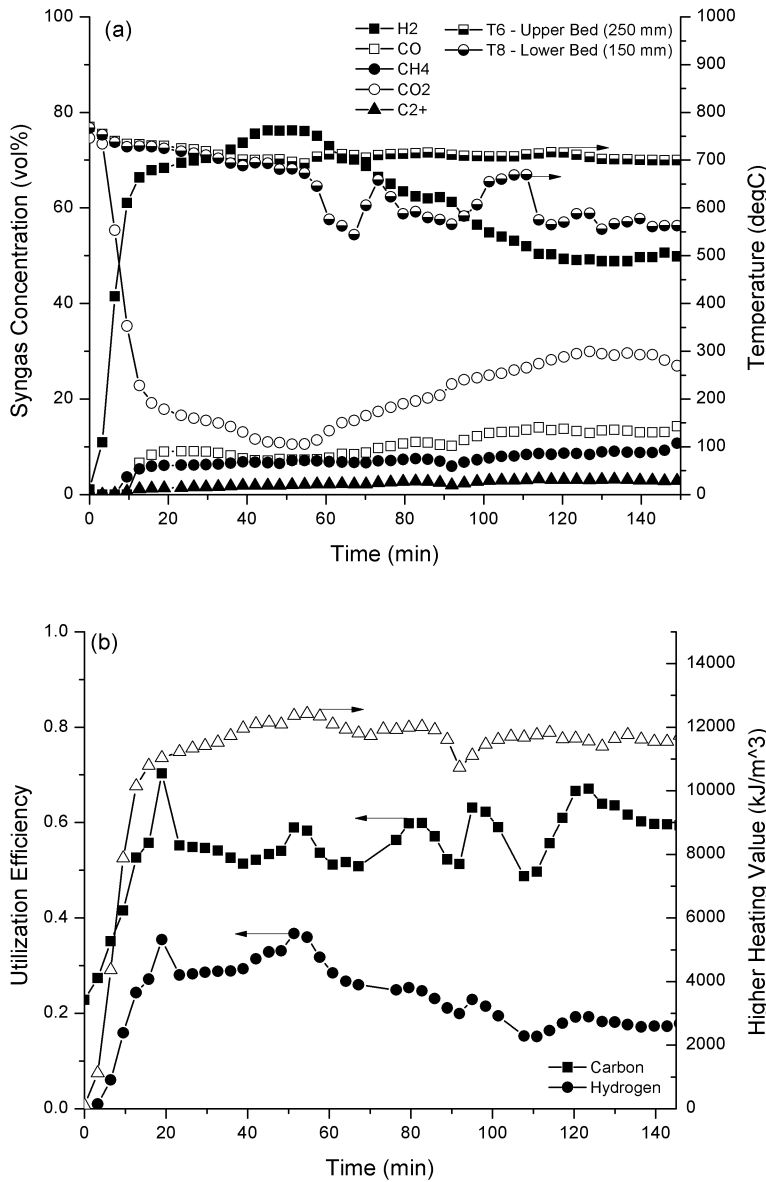


Figure 4.7: Gasification results for CaO bed (CB-06-12); a) water and nitrogen-free syngas composition and local temperatures, b) higher heating value and utilization efficiencies.

The hydrogen production reached a peak at around 50 min, with the opposite trend observed in the CO₂ concentration vs. time response, see Figure 4.7a. This resulted from the slightly elevated bed temperature at the beginning of gasification which favoured calcination in the upper, low-pressure region of the column. As the temperature dropped, more of the bed was activated towards carbonation. The bed temperature above the feed point showed a similar decrease following saturation of the bed with char as in the sand bed. As the run progressed, less CaO was available for carbonation, and the syngas composition gradually approached that of the sand bed. The hydrogen utilization efficiency decreased as the bed deactivated, resulting from the backward shift of the reversible reactions given by equations 4.3 and 4.5 in Table 4.1, lowering the conversion of H₂O. The carbon utilization remained elevated and increased slightly as the run progressed due to the increase in the CO₂ and CO concentrations. As there

was no way to measure the instantaneous uptake of CO₂ on CaO, it was averaged over the entire cycle. If a constant rate of uptake over the entire gasification stage is assumed, then carbon utilization would be under-estimated initially and over-estimated near the end. In reality, the rate of CO₂ uptake would be greater during the peak production phase and decrease as the gasification progresses. As well, CO₂ helps in the gasification of char, and a higher CO₂ concentration would promote the Boudouard reaction, equation 4.5 in Table 4.1.

The syngas compositions reported in Table 4.7 and Figure 4.8 are averaged from three consecutive GC samples during peak hydrogen production; the GC sampling rate was approximately one sample every 3 minutes. The higher heating value was calculated based on these peak gas compositions. Temperatures and pressures are averaged over the gasification stage; errors given in the table represent ± one standard deviation during gasification. Calcium utilization, produced gases and utilization efficiencies were calculated based on gasification stage totals.

Gasification was significantly enhanced through the use of a CO₂-sorbent as the bed material. Peak hydrogen concentration increased by 29 – 81%, while CO and CO₂ concentrations were reduced by 41 – 69% and 17 – 73%, respectively, compared to a sand bed. The carbon and hydrogen utilization efficiencies were increased significantly by the presence of CaO as well, as seen in Figure 4.8. The hydrogen utilization efficiency was low, due to the large excess of steam.

Table 4.7: Results from all runs; thermocouples distance above the distributor is indicated in brackets; pressures given are from 50 mm above distributor; the last digit of CCL runs refers to the cycle number.

Run	Temperatures (degC)			Peak Syngas (vol%)					HHV (kJ/m ³)	Calcium Utilization (%)	Produced Gases (m ³ /kg)	Utilization Efficiency	
	Freeboard (400 mm)	Upper Bed (250 mm)	Lower Bed (150 mm)	H2	CO	CH4	CO2	C2+				ηC	ηH
SB-04-12	801 ± 55	772 ± 44	660 ± 53	50.5	22.7	7.8	18.2	0.7	11002	-	0.45	34	13
SB-08-12	708 ± 4	675 ± 14	573 ± 88	42.8	17.9	8.7	26.1	3.7	12081	-	0.62	48	12
LB-04-12	828 ± 21	742 ± 26	585 ± 56	47.3	16.0	5.3	29.8	1.7	9711	-	0.93	24	24
LB-06-12	722 ± 12	695 ± 13	654 ± 53	39.2	17.0	3.1	39.1	1.0	7704	-	0.49	42	4
CB-06-12	741 ± 6	710 ± 16	631 ± 65	76.2	7.3	6.7	10.8	2.0	12205	45	0.98	62	25
CB-07-12	667 ± 2	662 ± 7	584 ± 56	76.5	5.8	8.6	7.2	2.0	12733	-	0.63	36	17
CCL-07-12-1	712 ± 4	668 ± 20	537 ± 102	69.4	8.3	8.0	11.9	3.0	13007	59	0.61	53	16
CCL-07-12-2	708 ± 10	678 ± 12	549 ± 104	74.3	7.3	6.9	9.2	2.6	12806	48	0.64	47	17
CCL-10-12-1	716 ± 3	703 ± 9	692 ± 15	75.2	4.0	6.8	12.8	1.8	11721	50	0.76	41	18
CCL-10-12-2	718 ± 6	712 ± 8	702 ± 13	70.0	8.0	5.2	15.0	1.3	10787	60	0.95	62	22
CCL-10-12-3	718 ± 5	709 ± 6	700 ± 8	71.4	7.6	5.9	13.6	1.5	11247	65	0.96	55	22
CCL-10-12-4	718 ± 5	709 ± 15	700 ± 19	73.1	6.9	5.9	12.8	1.6	11394	63	1.02	57	24
CCL-10-12-5	719 ± 6	707 ± 10	697 ± 10	71.9	7.2	6.0	13.8	1.8	11469	51	0.72	50	24
CCL-10-12-6	718 ± 10	699 ± 17	689 ± 41	65.5	10.6	6.6	15.1	2.1	11681	54	0.85	56	20
CCL-10-12-7	717 ± 6	701 ± 13	691 ± 17	69.5	9.2	6.9	12.2	2.2	12042	48	0.87	59	20
CCL-10-12-8	716 ± 9	699 ± 13	690 ± 12	68.7	8.6	7.1	12.8	2.6	12328	35	0.95	59	21

SB = sand bed; LB = limestone bed; CB = calcined bed; CCL = CaO-CaCO₃ looping.

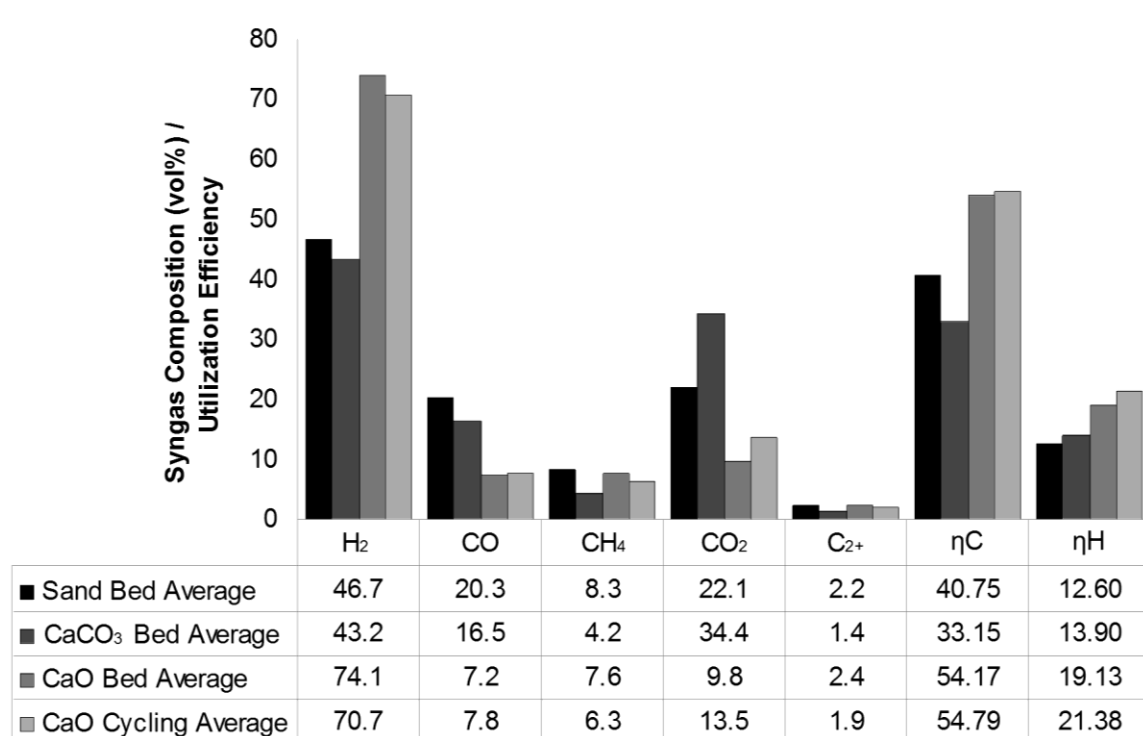


Figure 4.8: Syngas production with different bed materials.

The higher heating value of the produced gases showed only a modest increase due to lime-enhancement, with an average HHV of 11,508 kJ/m³ for a sand bed and 12,066 kJ/m³ for gasification with CaO. The gain in heating value from the increased H₂ and reduced CO₂ concentrations was partially offset by the loss in heating potential from reduced CO and CH₄ concentrations. As well, the small fraction of heavy gases (C₂₊) had a large effect on the heating value of the product gas due to their much larger heating values. For instance, ethylene (C₂H₄), which makes up the bulk of the heavier gases, see Figure 4.9, has a heating value of 57,069 kJ/m³, compared to 10,258 kJ/m³ for hydrogen. Figure 4.9 also shows how the presence of CaO helped to crack the heavier gaseous components. This cracking was greatest early in the gasification, when the highest concentration of CaO was available. The catalytic activity of CaO is much greater than that of CaCO₃ due to its basic and metallic sites [143]. As carbonation proceeds, these basic sites are eliminated.

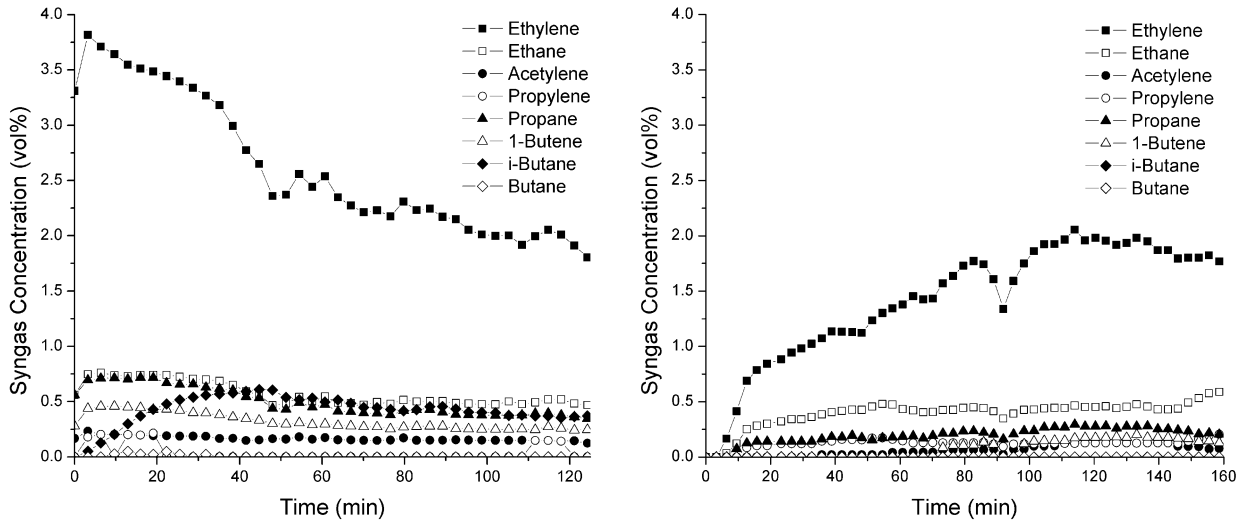


Figure 4.9: Concentration of heavier components in the produced gases for (a) sand bed (SB-08-12) and (b) CaO bed (CB-06-12), nitrogen and moisture-free.

4.3.2 Effect of Temperature

Even in the narrow range of bed temperatures covered during the gasification runs, there was a notable effect of temperature on the product gas composition, as expected [116]. During the two sand bed experimental runs, the bed temperature (measured mid-bed, 200 mm above the distributor) varied between 610°C and 790°C, see Figure 4.10a. Higher temperatures caused the H₂ and CO concentrations to increase from approximately 40 to 47% and from 18 to 24%, respectively, whereas concentrations of CO₂, and C₂₊ decreased from 27 to 18%, and 4 to <1%, respectively. The concentration of CH₄ remained relatively unchanged, increasing by only 0.7%. These effects are believed to have resulted from the higher temperature enhancing the kinetics of the endothermic gasification reactions, specifically the cracking of heavier gases and the Boudouard reaction. In addition, there are likely to have been significant chemical kinetic resistances in the system at lower temperatures, and raising the temperature pushed the system closer to chemical equilibrium.

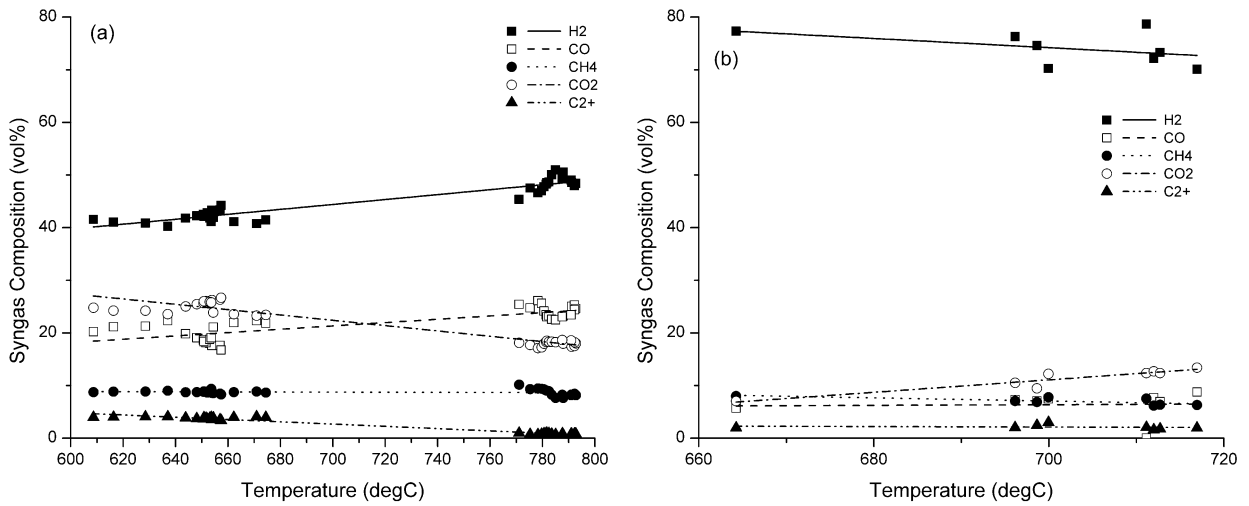


Figure 4.10: Effect of temperature on biomass gasification; points are experimental data, lines represent linear best fits; (a) data from two sand bed runs, (b) CaO bed.

The CaO bed shows the opposite trend in gas composition, with H₂ decreasing and CO₂ increasing as temperature increased from 665 to 717°C. This resulted from a loss in effectiveness of CO₂ absorption on CaO as the increased temperature caused an increase in the equilibrium partial pressure of CO₂ ($P_{CO_2,eq}$), requiring a higher partial pressure of CO₂ (P_{CO_2}) within the reactor for absorption to occur.

4.3.3 Tar and Char

Gravimetric analysis of the tar (see section 4.2) showed that the use of CaCO₃/CaO bed material decreased the quantity of tar generated, although the tar yield was still quite high due to low gasification temperatures [104]. CaO is known to catalytically crack tars produced by gasification through metal catalyzed de-hydrogenation [133]. Here the use of CaO reduced the tar yield by 54% to $38 \pm 9 \text{ g/m}^3$.

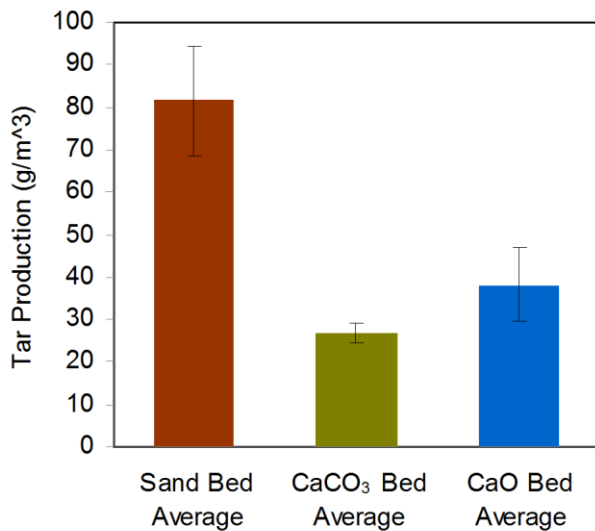


Figure 4.11: Tar yield for different bed materials.

The bed of un-calcined limestone (CaCO_3) gave the lowest tar yield. It is suspected this is a result of calcination of a portion of the limestone particles, giving the limestone bed a higher proportion of available CaO. During the gasification at 700°C , lower portions of the bed where CO_2 concentration is lower, could be favourable to calcination. CaO is much better at cracking tars than CaCO_3 , so any un-carbonated CaO in the bed would be beneficial for tar cracking [143].

During gasification, char accumulated in the bed and on the bed material. The bed material was classified, and each fraction was then analyzed using the TGA. Both sand and CaO bed gasification produced large agglomerates ($d_p > 10 \text{ mm}$) composed primarily of char ($\sim 90 \text{ wt\%}$). Figure 4.12 is a photograph of large char agglomerates produced during limestone bed gasification.



Figure 4.12: Large bed char from limestone bed gasification (LB-04-12)

In the sand bed these agglomerates contained the bulk of the char present in the bed, see Figure 4.13a. In the CaO bed, a large portion of the char produced ($\sim 50 \text{ wt\%}$ of total char) remained attached to the CaO bed material, see Figure 4.13b. This may have been caused by the larger specific surface area of the CaO particles, giving the char fines more surface to which to adhere. Surface carbon is also an intermediate in the tar cracking mechanism [143]. The catalytic effect of CaO on tar cracking leads to the accumulation of char on the particle surface. This adhering char would be of benefit to a dual-bed CO_2 capture system, as more char would be transported with the bed material to the combustion reactor.

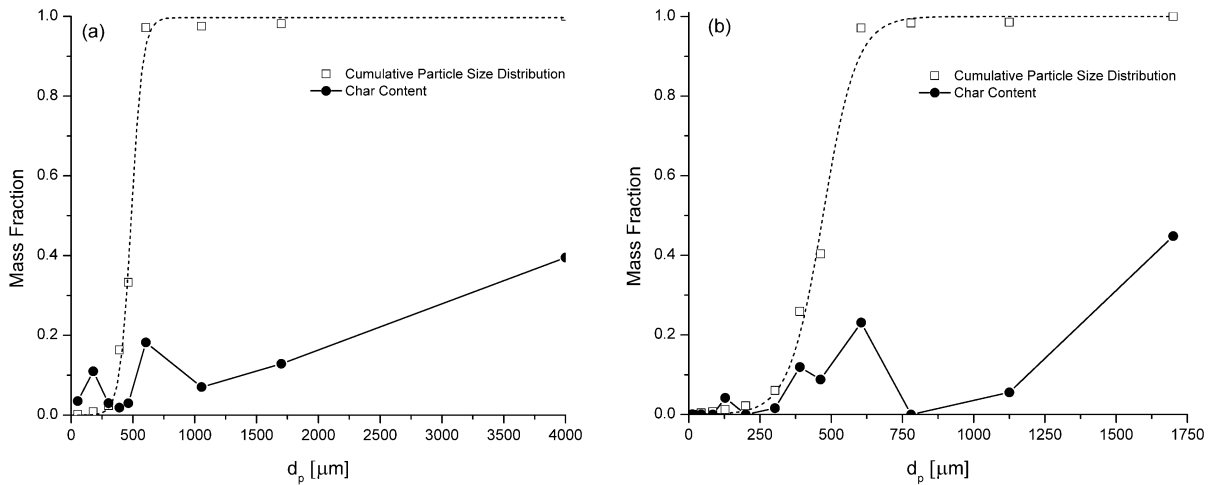


Figure 4.13: Particle size distribution and char content of bed after gasification: (a) sand bed (SB-08-12), (b) CaO bed (CB-06-12), dashed lines are fitted Boltzman functions of the cumulative distribution data.

The fines from both beds contained a high fraction of char, due to the increase in surface-area-to-volume ratio, allowing more char particles to adhere to the surface. In addition, some of these fines would undoubtedly be free char particles that neither agglomerated nor adhered to bed particles.

4.3.4 Sorbent Gasification Cycling

Gasification cycling was accomplished by feeding the biomass until the end of the breakthrough period, when the syngas composition reached that of the sand bed, as discussed in section 4.3.1, see Figure 4.14a. Calcination was accomplished using air and N₂. For most of the calcination intervals, gasification continued, as the O₂ supplied was insufficient for complete combustion of the residual char. When the char content was reduced enough to favour combustion, the temperature of the bed increased rapidly, causing the equilibrium CO₂ partial pressure to rise above the actual CO₂ partial pressure, so that calcination occurred, see Figure 4.14b. For complete results from the cycles, see Appendix 18. Although the temperature setting of the electrical heaters was maintained constant during the calcination stages, the bed temperature increased from 646 to 805°C due to heat supplied due to char combustion. Calcination was allowed to proceed until the CO₂ concentration in the product gas was less than 1%.

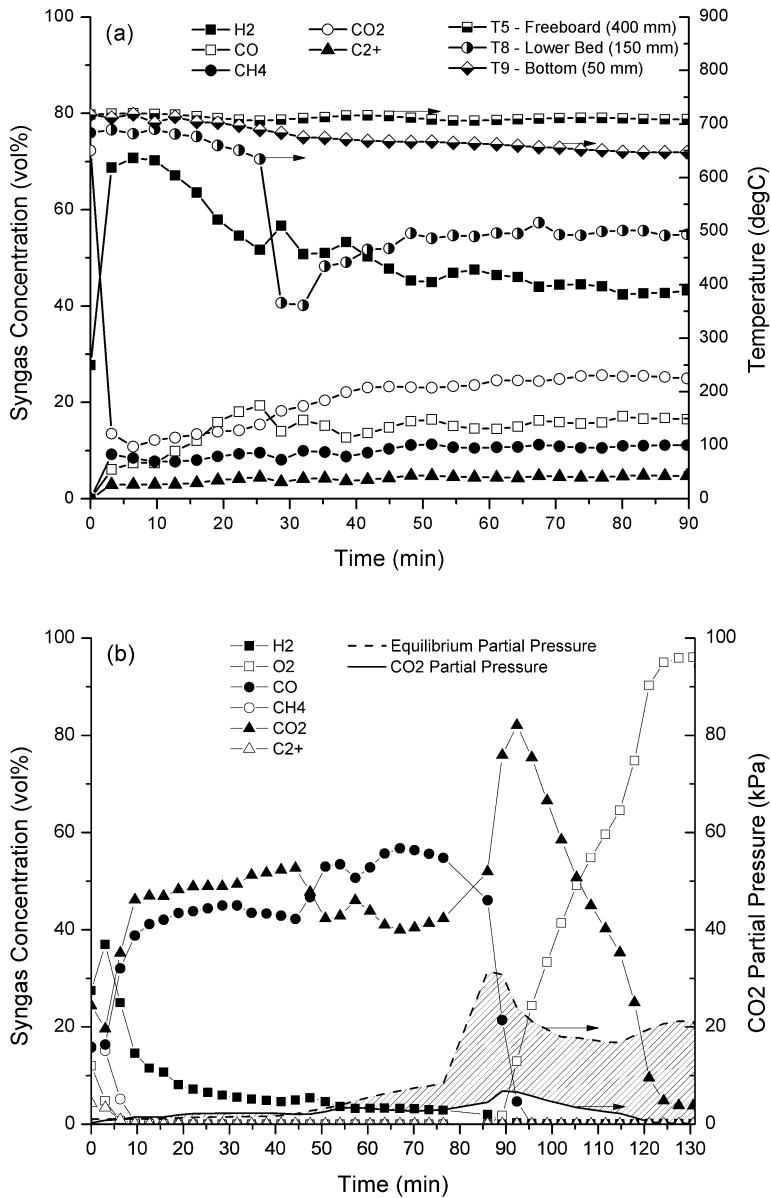


Figure 4.14: Concentrations, temperature and pressures during gasification cycling in a CaO bed (CCL-07-12): (a) cycle 1 gasification; (b) calcination, with shaded area representing difference between CO₂ equilibrium pressure and CO₂ partial pressure, ($P_{CO_2} - P_{CO_2,eq}$).

One experimental run was conducted with eight gasification/calcination cycles. Experimental results from gasification stages 1 and 8 are plotted in Figure 4.15. Results from all runs showed similar trends of syngas concentration, with an initial period of high H₂ production, followed by a gradual decrease due to carbonation of the CaO bed.

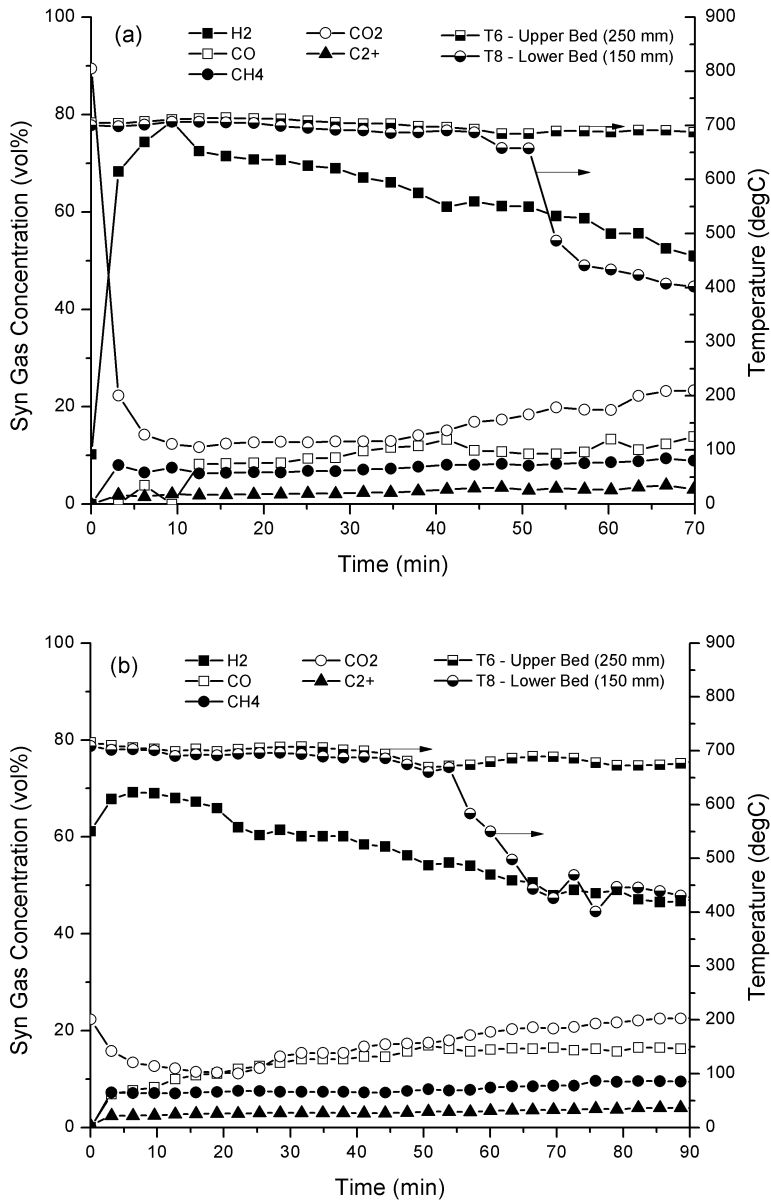


Figure 4.15: Concentrations and temperature during gasification cycling in a CaO bed (CCL-10-12): (a) cycle 1 gasification; (b) cycle 8 gasification.

The peak syngas concentration was similar for each of the eight cycles, decreasing by a few percentage points between the 1st and 8th cycles, see Table 4.7. This slight decrease, see Figure 4.16a, can be attributed to the reduction in CO₂ capture effectiveness of the bed as the calcium utilization decreased over the course of cycling due to sorbent sintering. The lower calcium utilization in cycles 1 and 5 resulted from slightly decreased gasification duration in those cycles of 73 and 66 min respectively, compared to the other five gasification cycles, which ranged from 95-115 min of carbonation / gasification.

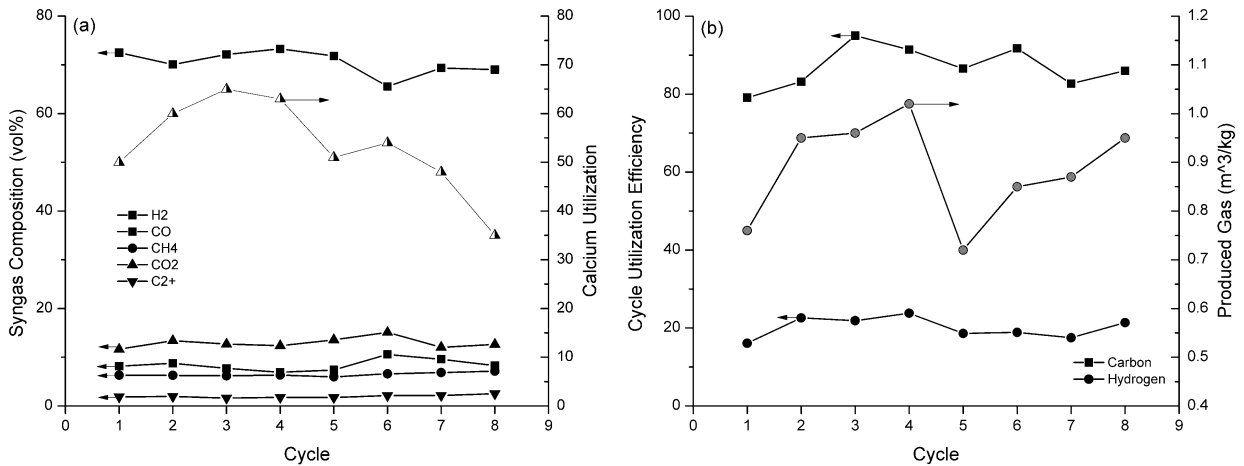


Figure 4.16: Effect of sorbent cycling on biomass gasification (CCL-10-12): (a) change in peak syngas composition and calcium utilization, (b) carbon and hydrogen utilization efficiency and syngas production rate (volume of syngas divided by mass of biomass).

The carbon and hydrogen utilization efficiencies were calculated on the basis of a complete gasification/calcination cycle, accounting for the gases produced during both stages and the relative degrees of carbonation of the bed solids, see Figure 4.16b. The carbon utilization efficiency varied between 79 and 95%, showing no clear trend with cycle number. The carbon utilization never reached 100% over the entire cycle because char fines and tar which escaped the reactor were considered losses. Hydrogen utilization efficiency varied between 19 and 29%, again with no clear trend with respect to cycle number. Syngas production was a function of many different parameters, including calcium utilization, bed temperature and the extent of the previous calcination. Over the eight cycles, the average syngas production was $0.88 \pm 0.10 \text{ m}^3[\text{syngas}] / \text{kg}[\text{biomass}]$.

Bed samples were taken following each stage of cycling. Char loading on the bed material was evident, as shown in Figure 4.17. The extent of calcination could also be approximately judged visually from the appearance of the bed samples.



Figure 4.17: Photograph of bed samples: (i) initial calcined bed; (1a to 7a) bed after corresponding gasification cycle; (1b to 7b) bed after re-calcination cycles 1 to 7; (8) final bed.

A bed sample was taken after each calcination stage, and a portion of this sample was then calcined to completion in an external oven at 800°C for 3 h in a flow of dry nitrogen. These samples are labelled "raw calcine" and "additional calcination," respectively, in Figure 4.18. Surface areas for these samples were determined using single point N₂ absorption BET. Results showed a general decrease in sorbent

surface area during cycling as expected [95]. It is this loss of surface area that leads to deactivation of the CaO sorbent and a reduction in calcium utilization.

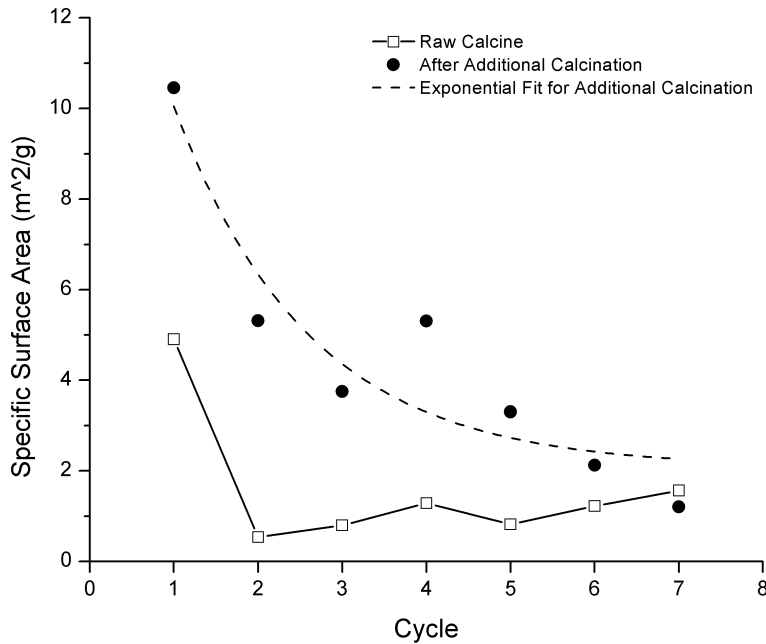


Figure 4.18: Change in sorbent specific surface area during gasification / calcination cycling obtained by single point N₂ absorption BET.

The duration of calcination was limited to between 90 and 120 min, to limit the overall gasification / calcination cycle time. As a result, calcination did not always go to completion. The difference between the two curves in Figure 4.18 is a measure of the residual carbonation of the calcine. Complete calcination of the sample increased the residual surface area. The 7th calcination stage was allowed to proceed to completion, taking 172 min, so that for this case the surface areas for the raw and calcined samples were very similar.

The bed material was collected after completing all CaO gasification experiments, with different degrees of cycling. From the particle size distributions, a shift toward a smaller average particle size can be seen in Figure 4.19. These cumulative distributions only include material in the bed at the end of the run, and do not include elutriated fines. The large initial shift can be attributed to attrition of the freshly calcined bed material, through abrasion of the CaO particles [144]. Following this initial attrition, the bed particles were gradually abraded, shifting the size distribution to even smaller particles. After 8 cycles, the size distribution broadened, with increases in the fraction of both large particles (> 500 μm) and fines (< 100 μm). The increase in fines can be attributed to further attrition of bed particles. These fines also contained a large proportion of char, due to the higher surface-area-to-volume ratio, which would increase their mass fraction. The increase in larger particles is the result of particle agglomeration within the bed. Over eight cycles, biomass ash accumulated on the CaO bed material, possibly leading to formation of compounds with melting points lower than that of the original CaO [145].

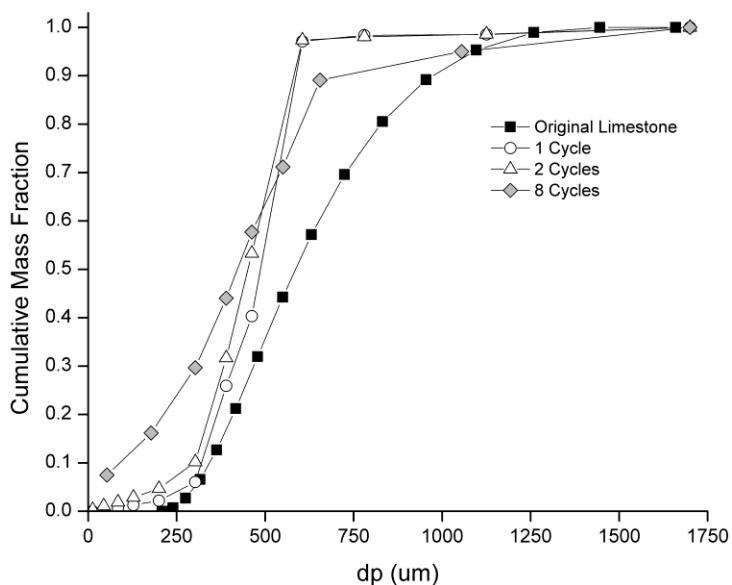


Figure 4.19: Cumulative particle size distributions after different degrees of cycling: "original limestone" sorbent pre-cursor, 1 cycle (CaO-06-12), 2 cycles (CCL-07-12) and 8 cycles (CCL-10-12).

4.3.5 Equilibrium Model

An ASPEN-based equilibrium model utilizing Gibbs free energy minimization was constructed. The ASPEN flowsheet is shown in Figure 4.20. The predictions from the equilibrium model shown in Figure 4.21 were obtained by modeling steam gasification of biomass with and without CaO sorbent. For a sample of the output from a typical run of the ASPEN simulation, see Appendix 19. In the temperature region of active CO₂ capture, H₂ production is predicted to increase and CO, CH₄ and CO₂ generation to decrease. At 750°C, the CO₂ equilibrium pressure was higher than the CO₂ partial pressure, so that no carbonation occurred, causing model predictions for both with and without sorbent to converge. CH₄ concentrations were zero above 650°C for both cases. Many equilibrium models, including this one, model the biomass as a simplified mixture of elements (C, H, O and N) based on its ultimate analysis. As a result of this simplistic representation of the fuel, the model did not predict the formation of higher molecular weight (C₂+) compounds, tar or char, while also significantly under-predicting the formation of CH₄.

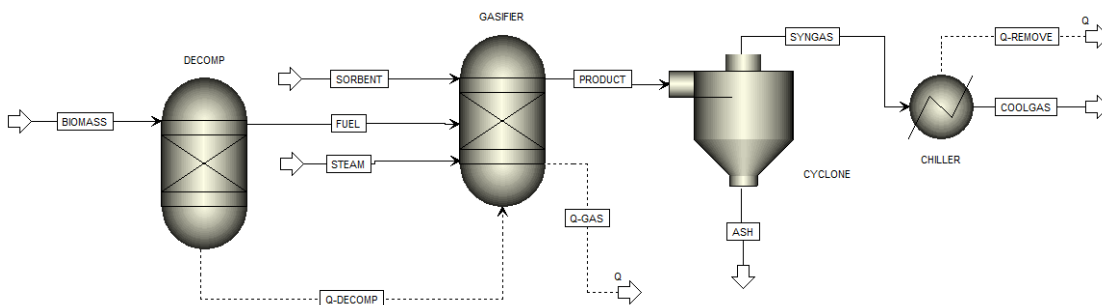


Figure 4.20: ASPEN flowsheet of enhanced biomass gasification model

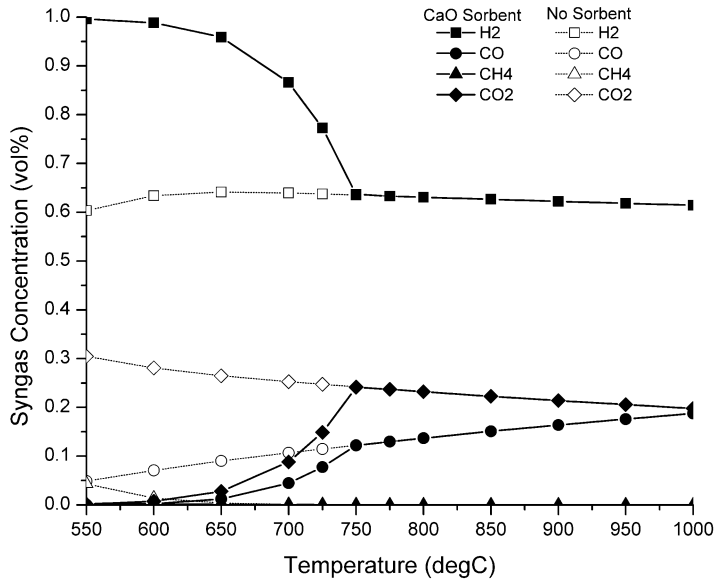


Figure 4.21: Results from equilibrium model of biomass gasification. Dark symbols indicate gasification with a CaO sorbent; light symbols indicate gasification without any sorbent.

Compared to the experimental results for sand bed gasification, the sorbent-free model over-predicts H₂ and CO₂ production and under-predicts CO and CH₄ concentrations, see Figure 4.22a. The bed temperatures used in the modeling was that as measured 250 mm above the distributor, The sorbent-free equilibrium model is not greatly affected by reactor temperature; however, experimentally as the reactor temperatures increased over the course of gasification runs, the hydrogen concentration approached that of the equilibrium model, see Figure 4.22b. The CH₄ concentration in the experiments varied between 10 and 15%, whereas the equilibrium model predicted no methane.

The equilibrium model was better at predicting the results from CaO-enhanced gasification. The model predicts the experimental results most accurately during the period of active CO₂ absorption. H₂ is over-predicted, but to a lesser extent than for sorbent-free gasification. CO₂ and CO concentrations are reasonably accurately predicted during this active CO₂ absorption stage, and the model prediction variation with temperature follows a similar trend to that seen in the data.

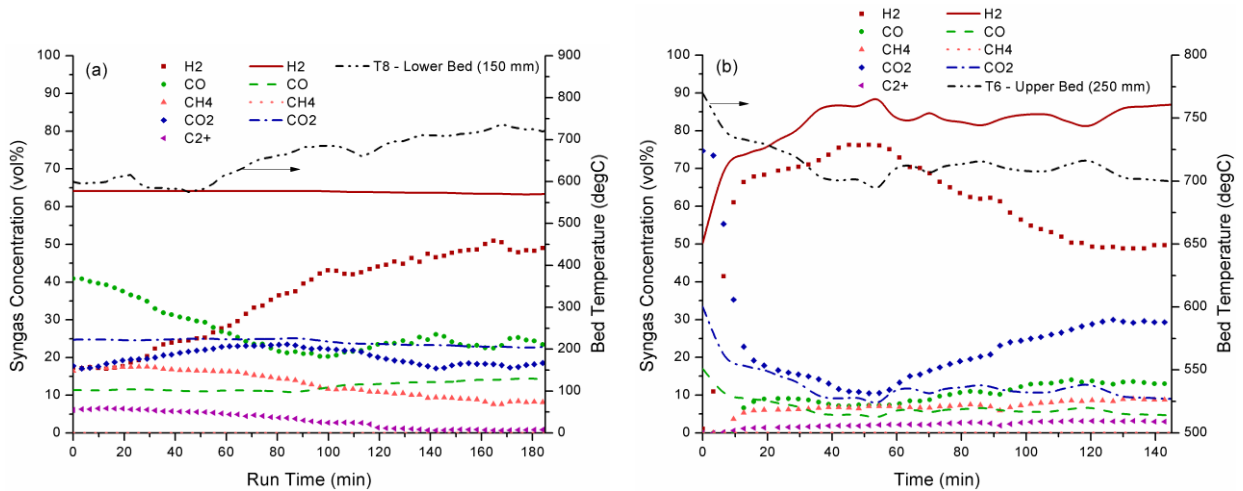


Figure 4.22: Comparison of equilibrium model predictions and experimental results for: (a) sand bed gasification (SB-04-12), and (b) CaO bed gasification (CB-06-12); points - experimental, lines - model.

The deviations of the model predictions from the experimental results and the closer fit of the sorbent-enhanced model are both likely related to the chemical kinetic limitations within the gasifier. The model assumes that all reactions proceed to equilibrium, in which case the methane reforming reaction, equation 4.2, would convert most methane to H_2 and CO at elevated temperatures and excess H_2O . In the case of sorbent-enhanced gasification, the reaction kinetics are enhanced by the catalytic action of the sorbent, which, coupled with removal of CO_2 by the carbonation reaction, pushes the reactions closer to equilibrium. The CH_4 concentration is; however, still poorly modeled, as methane is relatively stable and the methanation reaction, equation 4.6, is not directly influenced by the CO_2 concentration within the reactor.

The effect of temperature on the syngas composition can be seen in Figure 4.23. The data for the sand bed gasification was obtained from the two sand bed experiments after completing the start-up period of gasification. The CaO data points represent the syngas compositions during the phase of maximum CO_2 capture. Results are similar to those in Figure 4.22. The H_2 concentrations for both the sand and CaO beds move closer to the equilibrium values as the temperature increases, as a result of decreasing kinetic limitations. The trends in syngas composition with increasing temperature are similar for the model predictions and experimental data. Again the model predicts the CO_2 and CO concentrations in the CaO bed with fair accuracy.

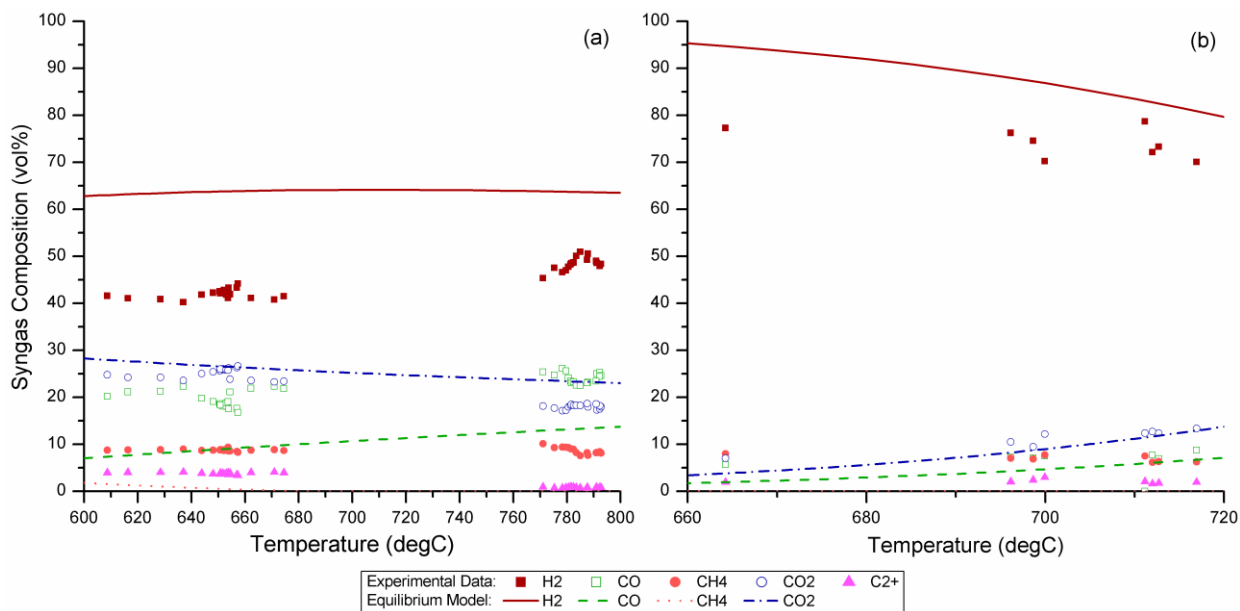


Figure 4.23: Comparison of equilibrium model predictions and experimental data for effect of temperature on syngas composition: (a) sand bed, and (b) CaO bed.

Although the equilibrium model fits poorly for gasification in the sand bed, it provides a reasonably close fit for the CaO bed, justifying the use of such a simplistic model in the design of CaO-based enhanced-gasification systems. With the addition of forced production of CH₄ and C₂₊, in particular ethylene, a better fit could be obtained, as suggested by Li et al. (2004), who introduced a bypass for a portion of the fuel C and H to form CH₄ in their equilibrium model [102]. This loss of carbon would cause a reduction in CO₂ and CO concentrations, indicating that the model is also over-predicting the capture of CO₂ by the CaO, so a capture efficiency term also needs to be incorporated into the model.

Empirical modifications to the model could be made to account for the deviation from experimental results. Such modifications could include the diversion of a portion of the incoming elemental hydrogen and carbon from the fuel feed, to the production of methane and tars. Li et al. (2004) showed that this method of empirical adjustment gave a good fit for biomass gasification in a fluidized bed. This would, however, introduce a system specific parameter into the model and make it less suitable for predictive in the design of different systems.

4.4 Conclusions

Removal of carbon dioxide during biomass steam gasification through the use of a high-temperature sorbent increases the yield of valuable product gases (H₂, CO and CH₄) by removing CO₂ and shifting the equilibrium of the gasification reactions towards the desired products. The CO₂ produced during gasification reacts with the CaO to form CaCO₃ in an exothermic reaction that provides most of the heat required for the endothermic steam gasification reactions. This chapter examined the use of a calcium oxide sorbent as the bed material in an experimental bubbling fluidized bed biomass gasifier. CaO-

enhanced steam gasification of biomass was conducted in a semi-batch fashion at temperatures of $\sim 700^\circ\text{C}$ and atmospheric pressure.

Three bed materials were tested: silica sand, limestone (CaCO_3) and calcined lime (CaO). The bed of pre-calcined (CaO) particles gave the best results in terms of syngas quality, producing $>70\%$ H_2 during the breakthrough period compared to gasification in a sand bed. CO was reduced by 71% and CO_2 by 42%. Carbon utilization efficiency increased from an average of 41% for sand bed gasification to 55% for a CaO bed. Hydrogen utilization increased from an average of 13% for the sand bed to 20% for CaO bed gasification. The average higher heating value of the gases produced by CaO -enhanced gasification was $11.9 \pm 0.5 \text{ MJ/m}^3$. Sand bed gasification produced similar heating values, $11.6 \pm 0.8 \text{ MJ/m}^3$, due to increased CO and CH_4 , making up for loss in heating value of H_2 . The CaCO_3 bed gave the worst results in terms of syngas quality and carbon conversion efficiency as it was likely that CaCO_3 particles were partially calcined during the gasification runs, releasing CO_2 , and thereby lowering the gas quality. The use of CaO in the bed catalytically reduced tar yield to $38 \pm 9 \text{ g/m}^3$.

Cycling of the CaO between gasification and calcination in the reactor was also conducted up to 8 cycles. Results indicate that char combustion could supply the heat required for the endothermic CaO calcination (re-generation) reaction. Cycling only slightly affected the syngas composition, with a reduction in the H_2 concentration of $< 5\%$. The calcium utilization of the sorbent bed decreased somewhat with cycling, but was affected more by the extent of carbonation and calcination. Calcination only went to completion prior to final gasification, but incomplete calcination did not have a substantial adverse effect on syngas production. The specific surface area of the CaO bed material decreased as cycling proceeded, indicating cycle-induced sintering.

A simple equilibrium model was developed to predict the syngas composition from gasification. In common with most equilibrium models, the model was limited in that it did not predict any higher molecular weight gases (C_2+) or condensable tars, due to the simplified representation of the biomass by its constituent elements. It also under-predicted CH_4 concentrations in all cases due to the kinetic limitations of the 'real' gasifier. For sorbent-free gasification, the model over-predicted H_2 and CO_2 concentrations while under-predicting CO . The model predicted the composition of CaO -enhanced gasification with greater accuracy, accurately predicting CO_2 and CO concentrations, but under-predicting the CH_4 concentration, while over-predicting H_2 concentrations. Its reasonable accuracy with enhanced gasification justifies the use of such a simplistic model to provide a best-case scenario in the design of a sorbent-enhanced gasification system. Empirical modifications to the model could be made to account for the deviation from experimental results.

5 Conclusions and Recommendations

Global greenhouse gas emissions continue to increase despite the knowledge that the resulting rise in CO₂ atmospheric concentration will have devastating effects on the climate. For existing fossil energy facilities that have many years of operation remaining, CO₂ capture and storage should be added to prevent future emissions. CaO-based CO₂ capture is one technology ready for immediate implementation. Limestone is a relatively low cost, readily available sorbent and, as a result, the CaO-CO₂ reaction has received considerable research attention in recent years. A thorough understanding of this reaction and its reversibility over multiple cycles is required to aid in the design of industrial capture processes, improve efficiency and reduce costs. It is in this context, research into CaO cycling in this thesis was conducted. A novel method of cycling involving pressure swing was demonstrated.

Biomass along with hydro, solar and wind are sustainable, low-carbon energy sources that can replace fossil fuels. Biomass is considered a carbon-neutral form of energy as the CO₂ released during its use is equal to the CO₂ absorbed from the atmosphere during its growth. Biomass can be converted into a number of different energy carriers, including electricity, gaseous and liquid fuels. The high temperatures of gasification allow for the conversion of more difficult forms of biomass, such as wood and wood by-products, into usable forms of energy. In-situ CaO-based CO₂ capture is ideal for biomass gasification as the optimal temperatures and CO₂ partial pressures for biomass gasification are similar to the conditions required for CaO-based CO₂ capture. Limestone-enhanced gasification (L.E.G.) of biomass could be a negative CO₂ emissions process if coupled with CO₂ storage. In addition to reduced CO₂ emissions, the quality of the gasification product gas can be improved as CO₂ removal shifts the gasification reactions towards desired products (H₂, CO and CH₄); the research in this thesis confirms and quantifies this effect. In addition, cycling of CaO between gasification and regeneration is examined to determine the effect of sorbent cycling for gasification.

5.1 Pressure Swing of CaO for CO₂ capture

The first portion of the research in this thesis involves detailed examination of cycling CaO for CO₂ capture by pressure swing. Most previous studies involved CaO cycling through temperature or partial pressure swing, and this was the first investigation of pressure swing cycling. Pressure swing could offer a lower energy input to the capture system. Cycling was conducted using three magnitudes of pressure swing (5, 10 and 20 bar_g). Cycling of CaO between carbonation and calcination was accomplished isothermally at 1000°C, by increasing the pressure for carbonation and decreasing it for subsequent re-calcination. Experiments were carried out in a pressurized thermo-gravimetric analyzer (PTGA) under a flow of pure CO₂ to minimize internal and external particle mass transfer effects.

Initial studies found that pressure swing cycling improved the residual calcium utilization over a high number of cycles (> 250), following an initial rapid decrease. The final asymptotic utilization was highest for 10 bar_g pressure swing and lowest for 5 bar_g, in the range of 12.5 to 27.7%. Sintering was found to be responsible for the rapid decrease in calcium utilization, as reported by many other authors. The elevated-pressure-induced sintering at 20 bar_g resulted in a decrease in residual utilization, compared to 10 bar_g cycling, suggesting that an optimum carbonation pressure exists for pressure swing calcination/carbonation.

In the initial studies, it was found larger samples displayed an increase in calcium utilization after ~30 cycles due to poor heat transfer within the sample, causing increased sintering in the sample interior during the exothermic carbonation reaction. Continued cycling gradually decreased this effect. An increased rate of de-pressurization prior to calcination caused an increase in residual calcium utilization from 11.9 to 16.1%. Rapid de-pressurization led to fracturing of the particle surfaces as CO₂ escaped. This explains a portion of the increase in residual utilization with increased pressure.

Cycling at carbonation pressures of 10 and 20 bar_g showed an increase in utilization after the initial rapid decrease. This effect has been seen by other researchers [63,90,91], but the mechanism had not been thoroughly investigated. To gain further understanding of the sintering mechanisms, a detailed analysis of the carbonation kinetics was performed. Pressure cycling was conducted under isothermal conditions at three temperatures, 975, 1000 and 1025°C. Changing kinetics during cycling of reaction-controlled and diffusion-controlled carbonation facilitated identification of a possible mechanism for the unique cycling behaviour of pressure swing cycling as follows. Cycling-induced sintering rapidly reduces particle surface area through pore coarsening in the first 10 cycles. Continued cycling-induced sintering causes grains to grow and reduces the number of grain boundaries. Carbonation and calcination of the particle surface nucleates at sites where lattice free energy is highest, such as vacancies, dislocations and grain boundaries. With fewer grain boundaries present, calcination nucleates at dispersed sites on the grain surface. The reduction in the molar volume accompanying calcination causes particle shrinkage around these dispersed sites, creating a highly textured surface and increasing the particle surface area. This increases the subsequent initial reaction rate and calcium utilization.

Sintering reduced the rate in diffusion-controlled carbonation as diffusion paths such as grain boundaries and lattice defects were blocked. It was also found that the reaction-controlled rate was a function of carbonation pressure, with increased pressure increasing the rate of reaction-controlled carbonation. The bulk diffusion rate was independent of pressure.

5.1.1 Research Significance

Pressure swing cycling could be applied to existing large scale facilities as a post-conversion method of CO₂ capture. It would reduce energy usage relative to temperature swing cycling, where a large fraction of the inert sorbent (85 - 95%) would need to be heated and cooled during each absorption/desorption cycle. If CO₂ partial pressure swing requires the use of large amount of steam imposing large heat duties on the system. An industrial CaO-CO₂ pressure swing system could be modeled after existing pressure swing absorption (PSA) which uses zeolites to remove impurities from produced hydrogen. These systems operate a minimum of two vessels in parallel, with one adsorbing and one desorbing impurities at any given time. The detailed kinetic analysis presented in this thesis would be crucial in the design and operation of such a pressure swing system for CaO-based CO₂ capture.

The kinetic work in this thesis adds to the limited body of data on the kinetics of CaO-CO₂ cycling. The proposed mechanism for sintering induced morphological changes within the sorbent particle could be used to gain insight into factors affecting the decay in utilization and potential help in the production of engineered CaO sorbents. The proposed sintering mechanism for could be a starting point for further research into utilization decay based on the crystal structure of the sorbent particle.

5.1.2 Future Research

It is likely in industrial systems employing a dual fluidized bed CaO-based capture system, some pressure differential will exist between the carbonation and calcination reactors. Further studies on pressure swing cycling should be conducted for conditions similar to those likely in these dual-bed systems – temperatures of 700 - 900°C, pressures close to atmospheric with 0.5 - 2 bar differential, and CO₂ concentrations in the gas less than 100%. A detailed parametric study of pressure swing cycling should be conducted, including reactor conditions, multiple limestone varieties and synthetic sorbents. Future investigations into the crystal structure of natural limestone sorbent and how it changes with cycling should also be conducted. Different limestone varieties behave differently when exposed to extreme conditions, for example in thermal pre-treatment [63,90,91]. This suggested impurities within the CaO affect particle sintering, but this requires further exploration with a focus on the crystal structure of the sorbent.

5.2 Lime-Enhanced Gasification of Biomass

In the second portion of this thesis work, the CaO-based CO₂ sorbent studied in pressure swing cycling was applied to a lime-enhanced gasification (L.E.G.) process. Calcined limestone was used as the bed material in steam gasification of ground wood pellets, in a bubbling fluidized bed reactor of internal diameter 76 mm. L.E.G. was performed in semi-batch fashion at temperatures of ~700°C and

atmospheric pressure. A biomass flow rate of 0.45 kg/h was used with a steam-to-biomass mass ratio of 2.5. Three different bed materials were used; inert silica sand, limestone and calcined limestone, CaO. In one case the CaO sorbent was cycled for eight gasification/calcination cycles, to examine the effect of sorbent cycling on enhanced gasification.

The removal of CO₂ in-situ during biomass steam gasification increased the yield of hydrogen as a result of the primary gasification reactions being shifted to the product through the removal of product CO₂. Hydrogen concentration in the outlet gas increased from 40-50% for gasification in an inert bed to > 70% in a bed of CaO, whereas CO was reduced by 71% and CO₂ by 42%. Carbon utilization efficiency increased from an average of 41% for sand bed gasification to 55% for a CaO bed. Hydrogen utilization increased from an average of 13% for a sand bed to 20% for gasification in a CaO bed. The heating value of the product gas was only modestly affected as the elevated levels of CO and CH₄ in the product gas made up for the heating value loss of reduced H₂. The average higher heating values from the sorbent-free sand bed and CaO bed were 11.6 ± 0.8 and 11.9 ± 0.5 MJ/m³, respectively. CaO also catalytically cracked the produced tar, and the tar yields from the limestone and CaO beds were half that for sand bed gasification. The tar yield for the CaO bed was 38 ± 9 g/m³.

During cycling experiments, the char accumulated in the bed from gasification was combusted to supply the heat for re-calcination of the bed material. Results indicated that char combustion could supply enough heat to drive the endothermic calcination reaction and raise the bed temperature. Repeated cycling of the sorbent had a small effect on the syngas composition, reducing hydrogen concentration in the product gas by ~ 5%.

The calcium utilization of the sorbent bed decreased by only a small amount with cycling, as expected. Examination of bed samples showed that the sorbent was fully calcined only during one extended period of calcination. The residual carbonation of the sorbent prior to gasification likely had more effect on the calcium utilization of the subsequent cycle than cycling. This incomplete calcination did not, however, have a significant effect on syngas production. The specific surface area of the CaO bed material decreased as cycling proceeded, indicating cycle-induced sintering. The first cycle saw a large decrease in surface area, followed by a levelling off.

A simple Gibbs reactor equilibrium model was constructed to predict the syngas composition from gasification with and without sorbent. The model did not predict any higher molecular weight gases (C₂+) or condensable tars, a common deficiency for equilibrium-based models. The model also under-predicted CH₄ concentrations, since it ignores kinetic resistances in the gasifier. The model fared poorly for sorbent-free gasification, but predicted the syngas composition of CaO-enhanced gasification with reasonable accuracy. In the latter case, CO₂ and CO concentrations were predicted to within a few

percentage points; however, H₂ concentration was 5-20% points higher in the model than in the experiments, becoming more accurate with increasing temperature, as kinetic resistances were reduced.

5.2.1 Research Significance

The results presented could be used in the design of larger scale L.E.G. systems and offer further experimental evidence for the benefits of L.E.G. of biomass. The amount of char in the bed material is an important factor in the thermal design of an industrial L.E.G. system. Most designs of dual-bed capture systems use char carried over from the gasifier to provide heat to the calciner and drive the endothermic calcination reaction; therefore, it is important to have some idea of the quantity of char in the system and where it resides. Moreover, the syngas concentration, yield and heating value data could provide a starting point for the design of an industrial scale system. The results also strengthen the case for implementation of L.E.G. of biomass for the production of hydrogen and other energy carriers, particularly transportation fuels. L.E.G. of biomass can be used to produce a number of these alternative fuels including, electricity for battery powered vehicles, H₂ for fuel cells, dimethyl ether (DME) for diesel engines and methanol for spark ignition engines, with net negative CO₂ emissions.

The data presented could also be used in the future to help improve computer based models. Despite the over-simplifications of the equilibrium model, the equilibrium model developed in this thesis proved to be relatively accurate for enhanced gasification. Such a simple model can provide a best-case scenario in the design of sorbent-enhanced gasification systems.

5.2.2 Future Research

Experimental studies in CaO-cycling for enhanced gasification have only become prevalent in recent years. The research covered in this thesis work could be expanded by increasing the number of gasification/calcination cycles. TGA studies show that calcium utilization decreases rapidly in the first 20 carbonation/calcination cycles; therefore experiments involving >20 cycles would offer further insight into how cycling affects the gasification products. In addition, a detailed parametric study of L.E.G. is required to determine the optimal operating conditions. Temperature, pressure and steam ratio all affect the gasification products and should be studied in detail. Different biomass feedstock will likely give slightly different results in terms of syngas production and agglomeration. Studies into the agglomeration characteristics of biomass ash and CaO are needed. In this project, combustion/re-calcination was accomplished using air. In a system with CO₂ capture and sequestration, pure oxygen would be used for combustion to avoid diluting the CO₂ and experiments utilizing pure oxygen combustion are needed.

The dual-fluidized bed design is the most likely design for an industrial scale L.E.G. process, as it can be operated continuously; its lack of moving parts makes it more reliable. Experimentation on such units is the next step towards industrial implementation from the lab scale unit investigated in this thesis.

References

- [1] Hansen J, Sato M, Kharecha P, Beerling D, Berner R, Masson-Delmotte V, Pagani M, Raymo M, Royer DL, Zachos JC. Target Atmospheric CO₂: Where Should Humanity Aim? *The Open Atmospheric Science Journal* 2008;2:217–31.
- [2] Lackner KS. A Guide to CO₂ Sequestration. *Science* 2003;300:1677–8.
- [3] Pacala S, Socolow R. Stabilization Wedges: Solving the Climate Problem for the Next 50 Years with Current Technologies. *Science* 2004;305:968–72.
- [4] Godec ML, Kuuskraa VA, Dipietro P. Opportunities for Using Anthropogenic CO₂ for Enhanced Oil Recovery and CO₂ Storage. *Energy & Fuels* 2013;27:4183–9.
- [5] National Energy Technology Laboratory (NETL). Carbon Dioxide Enhanced Oil Recovery - Untapped Domestic Energy Supply and Long Term Carbon Storage Solution (Report). Albany, New York: 2013.
- [6] Preston C, Monea M, Jazrawi W, Brown K, Whittaker S, White D, Law D, Chalaturnyk R, Rostron B. IEA GHG Weyburn CO₂ Monitoring and Storage Project. *Fuel Processing Technology* 2005;86:1547–68.
- [7] Perry RH, Green DW. *Chemistry Engineering Handbook*. 8th ed. McGraw-Hill Professional; 2008.
- [8] Kolbitsch P, Bolhàr-Nordenkampf J, Pröll T, Hofbauer H. Operating Experience with Chemical Looping Combustion in a 120kW Dual Circulating Fluidized Bed (DCFB) Unit. *International Journal of Greenhouse Gas Control* 2010;4:180–5.
- [9] Lyngfelt A. Oxygen Carriers for Chemical Looping Combustion - 4000 h of Operational Experience. *Oil & Gas Science and Technology – Revue d'IFP Energies Nouvelles* 2011;66:161–72.
- [10] Florin NH, Harris AT. Enhanced Hydrogen Production from Biomass with in Situ Carbon Dioxide Capture Using Calcium Oxide Sorbents. *Chemical Engineering Science*, 2008;63:287–316.

- [11] Hongjun Y, Shuanshi F, Xuemei L, Yanhong W, Jianghua N. Economic Comparison of Three Gas Separation Technologies for CO₂ Capture from Power Plant Flue Gas. *Separation Science and Technology* 2011;19:615–20.
- [12] Metz B, Davidson O, De Coninck H, Loos M, Meyer L. IPCC Special Report on Carbon Dioxide Capture and Storage. New York, NY: Cambridge University Press; 2005.
- [13] Abanades JC, Oakey JE, Alvarez D, Hämäläinen J. Novel Combustion Cycles Incorporating Capture of CO₂ with CaO. In: Gale J, Kaya Y, editors. *Greenhouse Gas Control Technologies - 6th International Conference*, Oxford: Pergamon; 2003, p. 181–6.
- [14] Abanades JC, Rubin ES, Anthony EJ. Sorbent Cost and Performance in CO₂ Capture Systems. *Industrial & Engineering Chemistry Research* 2004;43:3462–6.
- [15] Dumée L, Scholes C, Stevens G, Kentish S. Purification of Aqueous Amine Solvents Used in Post Combustion CO₂ Capture: A Review. *International Journal of Greenhouse Gas Control* 2012;10:443–55.
- [16] Yong Z, Mata V, Rodrigues AE. Adsorption of Carbon Dioxide at High Temperature—a Review. *Separation and Purification Technology* 2002;26:195–205.
- [17] Rodríguez N, Alonso M, Grasa G, Abanades JC. Heat Requirements in a Calciner of CaCO₃ Integrated in a CO₂ Capture System Using CaO. *Chemical Engineering Journal* 2008;138:148–54.
- [18] Dobner S, Sterns L, Graff RA, Squires AM. Cyclic Calcination and Recarbonation of Calcined Dolomite. *Industrial & Engineering Chemistry Process Design and Development* 1977;16:479–86.
- [19] Sun P, Grace JR, Lim CJ, Anthony EJ. Removal of CO₂ by Calcium-based Sorbents in the Presence of SO₂. *Energy Fuels* 2007;21:163–70.
- [20] Baker EH. The Calcium Oxide-carbon Dioxide System in the Pressure Range 1–300 Atmospheres. *Journal of the Chemical Society* 1962;70:464–70.
- [21] Hills AWD. Equilibrium Decomposition Pressure of Calcium Carbonate Between 700 and 900°C. *Transactions and Institute of Mining and Metallurgy* 1967:C241–C245.

- [22] Hu N, Scaroni AW. Calcination of Pulverized Limestone Particles Under Furnace Injection Conditions. *Fuel* 1996;75:177–86.
- [23] Weimer T, Berger R, Hawthorne C, Abanades JC. Lime Enhanced Gasification of Solid Fuels: Examination of a Process for Simultaneous Hydrogen Production and CO₂ Capture. *Fuel* 2008;87:1678–86.
- [24] Sun P, Grace JR, Lim CJ, Anthony EJ. Determination of Intrinsic Rate Constants of the CaO–CO₂ Reaction. *Chemical Engineering Science* 2008;63:47–56.
- [25] Squires AM. Cyclic Use of Calcined Dolomite to Desulfurize Fuels Undergoing Gasification. *Fuel Gasification: A Symposium* 1967.
- [26] Bhatia SK, Perlmutter DD. Effect of the Product Layer on the Kinetics of the CO₂-lime Reaction. *AIChE Journal* 1983;29:79–86.
- [27] Manovic V, Anthony EJ. Carbonation of CaO-Based Sorbents Enhanced by Steam Addition. *Industrial & Engineering Chemistry Research* 2010;49:9105–10.
- [28] Sun P, Grace JR, Lim CJ, Anthony EJ. A Discrete-pore-size-distribution-based Gas–solid Model and Its Application to the CaO-CO₂ Reaction. *Chemical Engineering Science* 2008;63:57–70.
- [29] Haul RAW, Stein LH, De Villiers JWL. Exchange of Carbon-13 Dioxide Between Calcite Crystals and Gaseous Carbon Dioxide. *Nature* 1953;171:619–20.
- [30] Szekely J, Evans JW, Sohn HY. *Gas-solid Reactions*. New York: Academic Press; 1976.
- [31] Alvarez D, Abanades JC. Determination of the Critical Product Layer Thickness in the Reaction of CaO with CO₂. *Industrial & Engineering Chemistry Research* 2005;44:5608–15.
- [32] Mess D, Sarofim AF, Longwell JP. Product Layer Diffusion During the Reaction of Calcium Oxide with Carbon Dioxide. *Energy & Fuels* 1999;13:999–1005.
- [33] Abanades JC, Alvarez D. Conversion Limits in the Reaction of CO₂ with Lime. *Energy & Fuels* 2003;17:308–15.
- [34] Sun P, Lim CJ, Grace JR. Cyclic CO₂ Capture by Limestone-derived Sorbent During Prolonged Calcination/carbonation Cycling. *AIChE Journal* 2008;54:1668–77.

- [35] Curran GP, Fink CE, Gorin E. Carbon Dioxide-acceptor (coal) Gasification Process. Studies of Acceptor Properties. Advances in Chemistry Series 1967;69:141–65.
- [36] Sun P, Grace JR, Lim CJ, Anthony EJ. The Effect of CaO Sintering on Cyclic CO₂ Capture in Energy Systems. AIChE Journal 2007;53:2432–42.
- [37] Nitsch W. Über Die Druckabhängigkeit Der CaCO₃ - Bildung Aus Dem Oxyd. Zeitschrift Für Elektrochemie, Berichte Der Bunsengesellschaft Für Physikalische Chemie 1962;66:703–8.
- [38] Symonds R, Lu D. CO₂ Capture from Simulated Syngas via Cyclic Carbonation/calcination for a Naturally Occurring Limestone: Pilot-plant Testing. Industrial & Engineering Chemistry Research 2009;48:8431–40.
- [39] Symonds RT, Lu DY, Macchi A, Hughes RW, Anthony EJ. CO₂ Capture from Syngas via Cyclic Carbonation/calcination for a Naturally Occurring Limestone: Modelling and Bench-scale Testing. Chemical Engineering Science 2009;64:3536–43.
- [40] Grasa G, Abanades JC. CO₂ Capture Capacity of CaO in Long Series of Carbonation/Calcination Cycles. Industrial & Engineering Chemistry Research 2006;45:8846–51.
- [41] Yang S, Xiao Y. Steam Catalysis in CaO Carbonation Under Low Steam Partial Pressure. Industrial & Engineering Chemistry Research 2008;47:4043–8.
- [42] Arias B, Grasa G, Abanades JC, Manovic V, Anthony EJ. The Effect of Steam on the Fast Carbonation Reaction Rates of CaO. Industrial & Engineering Chemistry Research 2012;51:2478–82.
- [43] Dedman AJ, Owen AJ. Calcium Cyanamide Synthesis. Part 4. The Reaction $\text{CaO} + \text{CO}_2 = \text{CaCO}_3$. Transactions of the Faraday Society 1962;58:2027.
- [44] Shewmon PG. Diffusion in Solids. New York, NY: McGraw-Hill; 1963.
- [45] German RM. Sintering Theory and Practice. John Wiley and Sons; 1996.
- [46] Beruto D, Barco L, Searcy AW. CO₂-Catalyzed Surface Area and Porosity Changes in High-Surface-Area CaO Aggregates. Journal of the American Ceramic Society 1984;67:512–6.

- [47] Philipp R, Fujimoto K. FTIR Spectroscopic Study of CO₂ Adsorption / Desorption on CaO / MgO Catalysts. *Journal of Physical Chemistry* 1992;96:9035–8.
- [48] Sakadjian BB, Iyer M V, Gupta H, Fan L-S. Kinetics and Structural Characterization of Calcium-based Sorbents Calcined Under Subatmospheric Conditions for the High-temperature CO₂ Capture Process. *Industrial & Engineering Chemistry Research* 2007;46:35–42.
- [49] Rodriguez-Navarro C, Ruiz-Agudo E, Luque A, Rodriguez-Navarro AB, Ortega-Huertas M. Thermal Decomposition of Calcite: Mechanisms of Formation and Textural Evolution of CaO Nanocrystals. *American Mineralogist* 2009;94:578–93.
- [50] Chen C, Zhao C, Liang C, Pang K. Calcination and Sintering Characteristics of Limestone Under O₂/CO₂ Combustion Atmosphere. *Fuel Processing Technology* 2007;88:171–8.
- [51] Borgwardt RH. Calcination Kinetics and Surface Area of Dispersed Limestone Particles. *AIChE Journal* 1985;31:103–11.
- [52] Ingraham TR, Marier P. Kinetic Studies on the Thermal Decomposition of Calcium Carbonate. *Canadian Journal of Chemical Engineering* 1963;41:170–3.
- [53] Rao TR, Gunn DJ, Bowen JH. Kinetics of Calcium Carbonate Decomposition. *Chemical Engineering Research and Design* 1989;67:38–47.
- [54] Rajeswara Rao T. Kinetic Parameters for Decomposition of Calcium Carbonate. *Canadian Journal of Chemical Engineering* 1993;71:481–4.
- [55] Samtani M, Dollimore D, Alexander KS. Comparison of Dolomite Decomposition Kinetics with Related Carbonates and the Effect of Procedural Variables on Its Kinetic Parameters. *Thermochimica Acta* 2002;392-393:135–45.
- [56] Koga N, Criado JM. The Influence of Mass Transfer Phenomena on the Kinetic Analysis for the Thermal Decomposition of Calcium Carbonate by Constant Rate Thermal Analysis (CRTA) Under Vacuum. *International Journal of Chemical Kinetics* 1998;30:737–44.
- [57] Florin NH, Harris AT. Hydrogen Production from Biomass Coupled with Carbon Dioxide Capture: The Implications of Thermodynamic Equilibrium. *Fuel Cells* 2007;32:4119–34.

- [58] Alvarez D, Abanades JC. Pore-size and Shape Effects on the Recarbonation Performance of Calcium Oxide Submitted to Repeated Calcination/recarbonation Cycles. *Energy & Fuels* 2005;19:270–8.
- [59] Galwey AK, Brown ME. *Thermal Decomposition of Ionic Solids: Chemical Properties and Reactivities of Ionic Crystalline Phases*. 86th ed. Elsevier Science; 1999.
- [60] Lin S, Wang Y, Suzuki Y. High-Temperature CaO hydration/Ca(OH)₂ Decomposition over a Multitude of Cycles. *Energy & Fuels* 2009;23:2855–61.
- [61] Lysikov AI, Salanov AN, Okunev AG. Change of CO₂ Carrying Capacity of CaO in Isothermal Recarbonation-decomposition Cycles. *Industrial & Engineering Chemistry Research* 2007;46:4633–8.
- [62] Abanades JC. The Maximum Capture Efficiency of CO₂ Using a Carbonation / Calcination Cycle of CaO / CaCO₃. *Chemical Engineering Journal* 2002;90:303–6.
- [63] Chen Z, Song HS, Portillo M, Lim CJ, Grace JR, Anthony EJ. Long-term Calcination/carbonation Cycling and Thermal Pretreatment for CO₂ Capture by Limestone and Dolomite. *Energy & Fuels* 2009;23:1437–44.
- [64] Manovic V, Anthony EJ. Parametric Study on the CO₂ Capture Capacity of CaO-Based Sorbents in Looping Cycles. *Energy & Fuels* 2008;22:1851–7.
- [65] Wang J, Anthony EJ. On the Decay Behavior of the CO₂ Absorption Capacity of CaO-based Sorbents. *Industrial & Engineering Chemistry Research* 2005;44:627–9.
- [66] Salvador C, Lu D, Anthony EJ, Abanades JC. Enhancement of CaO for CO₂ Capture in an FBC Environment. *Chemical Engineering Journal* 2003;96:187–95.
- [67] Borgwardt RH. Calcium Oxide Sintering in Atmospheres Containing Water and Carbon Dioxide. *Industrial & Engineering Chemistry Research* 1989;28:493–500.
- [68] Anthony EJ, Granatstein DL. Sulfation Phenomena in Fluidized Bed Combustion Systems. *Progress in Energy and Combustion Science* 2001;27:215–36.
- [69] Laursen K, Duo W, Grace JR, Lim CJ. Sulfation and Reactivation Characteristics of Nine Limestones. *Fuel* 2000;79:153–63.

- [70] Lu H, Reddy EP, Smirniotis PG. Calcium Oxide Based Sorbents for Capture of Carbon Dioxide at High Temperatures. *Industrial and Engineering Chemistry Research* 2006;45:3944–9.
- [71] Cheng J, Zhou J, Liu J, Zhou Z, Huang Z, Cao X, Zhao X, Cen K. Sulfur Removal at High Temperature During Coal Combustion in Furnaces: a Review. *Progress in Energy and Combustion Science* 2003;29:381–405.
- [72] Xie Y, Xie W, Pan W-P, Riga A, Anderson K. A Study of Ash Deposits on the Heat Exchange Tubes Using SDT/MS and XRD Techniques. *Thermochimica Acta* 1998;324:123–33.
- [73] Borgwardt RH. Sintering of Nascent Calcium Oxide. *Chemical Engineering Science* 1989;44:53–60.
- [74] Hanson C, Tullin C. Sintering of Calcium Carbonate and Lime Mud in a Carbon Dioxide Atmosphere. *Journal of Pulp and Paper Science* 1996;22:J327–J331.
- [75] Milne CR, Silcox GD, Pershing DW, Kirchgessner DA. High-temperature, Short-time Sulfation of Calcium-based Sorbents. 1. Theoretical Sulfation Model. *Industrial & Engineering Chemistry Research* 1990;29:2192–201.
- [76] Feng B, Liu W, Li X, An H. Overcoming the Problem of Loss-in-capacity of Calcium Oxide in CO₂ Capture. *Energy & Fuels* 2006;20:2417–20.
- [77] Silcox GD, Kramlich JC, Pershing DW. A Mathematical Model for the Flash Calcination of Dispersed CaCO₃ and Ca(OH)₂ Particles. *Industrial & Engineering Chemistry Research* 1989;28:155–60.
- [78] Mahuli SK, Agnihotr R, Jadhav R, Chauk S, Fan L-S. Combined Calcination, Sintering and Sulfation Model for CaCO₃-SO₂ Reaction. *AIChE Journal* 1999;45:367–82.
- [79] German RM, Munir ZA. Surface Area Reduction During Isothermal Sintering. *Journal of the American Ceramic Society* 1976;59:379–83.
- [80] Beruto D, Botter R, Searcy AW. Thermodynamics and Kinetics of Carbon Dioxide Chemisorption on Calcium Oxide. *The Journal of Physical Chemistry* 1984;88:4052–5.
- [81] Kuramoto K, Fujimoto S, Morita A, Shibano S, Suzuki Y, Hatano H, Shi-ying L, Harada M. Repetitive Carbonation-Calcination Reactions of Ca-Based Sorbents for Efficient CO₂ Sorption

- at Elevated Temperatures and Pressures. *Industrial & Engineering Chemistry Research* 2003;42:975–81.
- [82] Fuertes AB, Alvarez D, Rubiera F, Pis JJ, Marbán G, Palacos JM. Surface Area and Pore Size Changes During Sintering of Calcium Oxide Particles. *Chemical Engineering Communications* 1991;109:73–88.
- [83] Glasson DR. Reactivity of Lime and Related Oxides. I. Production of Calcium Oxide. *Journal of Applied Chemistry* 2007;8:793–7.
- [84] Borgwardt RH, Roache NF, Bruce KR. Surface Area of Calcium Oxide and Kinetics of Calcium Sulfide Formation. *Environmental Progress* 1984;3:129–35.
- [85] Ewing J, Beruto D, Searcy AW. The Nature of CaO Produced by Calcite Powder Decomposition in Vacuum and in CO₂. *Journal of the American Ceramic Society* 1979;62:580–4.
- [86] Zeman F. Effect of Steam Hydration on Performance of Lime Sorbent for CO₂ Capture. *International Journal of Greenhouse Gas Control*, 2008;2:203–9.
- [87] Hughes RW, Lu D, Anthony EJ, Wu Y. Improved Long-term Conversion of Limestone-derived Sorbents for In-situ Capture of CO₂ in a Fluidized Bed Combustor. *Industrial & Engineering Chemistry Research* 2004;43:5529–39.
- [88] Manovic V, Anthony EJ. Steam Reactivation of Spent CaO-based Sorbent for Multiple CO₂ Capture Cycles. *Environmental Science & Technology* 2007;41:1420–5.
- [89] Manovic V, Anthony EJ, Grasa G, Abanades JC. CO₂ Looping Cycle Performance of a High-purity Limestone After Thermal Activation/doping. *Energy Fuels* 2008;22:3258–64.
- [90] Manovic V, Anthony EJ, Loncarevic D. CO₂ Looping Cycles with CaO-based Sorbent Pretreated in CO₂ at High Temperature. *Chemical Engineering Science* 2009;64:3236–45.
- [91] Manovic V, Anthony EJ. Thermal Activation of CaO-based Sorbent and Self-reactivation During CO₂ Capture Looping Cycles. *Environmental Science & Technology* 2008;42:4170–4.
- [92] Silaban A, Harrison DP. High Temperature Capture of Carbon Dioxide: Characteristics of the Reversible Reaction Between CaO(s) and CO₂(g). *Chemical Engineering Communications* 1995;137:177–90.

- [93] Aihara M, Nagai T, Matsushita J, Negishi Y, Ohya H. Development of Porous Solid Reactant for Thermal-energy Storage and Temperature Upgrade Using Carbonation/decarbonation Reaction. *Applied Energy* 2001;69:225–38.
- [94] Iyer M V, Gupta H, Sakadjian BB, Fan L-S. Multicyclic Study on the Simultaneous Carbonation and Sulfation of High-reactivity CaO. *Industrial and Engineering Chemistry Research* 2004;43:3939–47.
- [95] Barker R. Reversibility of the Reaction $\text{CaCO}_3 \leftrightarrow \text{CaO} + \text{CO}_2$. *Journal of Applied Chemistry and Biotechnology* 1973;23:733–42.
- [96] Ridha FN, Manovic V, Anthony EJ, Macchi A. The Morphology of Limestone-based Pellets Prepared with Kaolin-based Binders. *Materials Chemistry and Physics* 2013;138:78–85.
- [97] Li ZS, Cai NS, Huang YY, Han HJ. Synthesis, Experimental Studies and Analysis of a New Calcium-based Carbon Dioxide Absorbent. *Energy & Fuels* 2005;19:1447–52.
- [98] Akiti, TT, Constant KP, Doraiswamy LK, Wheelock TD, Akiti TT. A Regenerable Calcium-based Core-in-shell Sorbent for Desulfurizing Hot Coal Gas. *Industrial & Engineering Chemistry Research* 2002;41:587–97.
- [99] Wu Y, Manovic V, He I, Anthony EJ. Modified Lime-based Pellet Sorbents for High-temperature CO₂ Capture: Reactivity and Attrition Behavior. *Fuel* 2012;96:454–61.
- [100] Satrio JA, Shanks BH, Wheelock TD. Development of a Novel Combined Catalyst and Sorbent for Hydrocarbon Reforming. *Industrial & Engineering Chemistry Research* 2005;44:3901–11.
- [101] Demirbaş A. Biomass Co-Firing for Boilers Associated with Environmental Impacts. *Energy Sources* 2005;27:1385–96.
- [102] Li XT, Grace JR, Lim CJ, Watkinson AP, Chen HP, Kim JR. Biomass Gasification in a Circulating Fluidized Bed. *Biomass and Bioenergy* 2004;26:171–93.
- [103] Pfeifer C, Puchner B, Hofbauer H. In-situ CO₂-absorption in a Dual Fluidized Bed Biomass Steam Gasifier to Produce a Hydrogen Rich Syngas. *International Journal of Chemical Reactor Engineering* 2007;5.

- [104] Narváez I, Orío A, Aznar MP, Corella J. Biomass Gasification with Air in an Atmospheric Bubbling Fluidized Bed. Effect of Six Operational Variables on the Quality of the Produced Raw Gas. *Industrial & Engineering Chemistry Research* 1996;35:2110–20.
- [105] Beenackers AAC. Biomass Gasification in Moving Beds, a Review of European Technologies. *Renewable Energy* 1999;16:1180–6.
- [106] Babu S. Thermal Gasification of Biomass Technology Developments: End of Task Report for 1992 to 1994. *Biomass and Bioenergy* 1995;9:271–85.
- [107] Blasi C Di. Heat, Momentum and Mass Transport Through a Shrinking Biomass Particle Exposed to Thermal Radiation. *Chemical Engineering Science* 1996;51.
- [108] Lv PM, Xiong ZH, Chang J, Wu CZ, Chen Y, Zhu JX. An Experimental Study on Biomass Air-steam Gasification in a Fluidized Bed. *Bioresource Technology* 2004;95:95–101.
- [109] Pan YG, Roca X, Velo E, Puigjaner L. Removal of Tar by Secondary Air in Fluidised Bed Gasification of Residual Biomass and Coal. *Fuel* 1999;78:1703–9.
- [110] Turn SQ, Kinoshita C, Zhang Z, Ishimura DM, Zhou J. An Experimental Investigation of Hydrogen Production from Biomass Gasification. *International Journal of Hydrogen Energy* 1998;23:641–8.
- [111] Gil J, Corella J, Aznar MP, Caballero MA. Biomass Gasification in Atmospheric and Bubbling Fluidized Bed: Effect of the Type of Gasifying Agent on the Product Distribution. *Biomass and Bioenergy* 1999;17:389–403.
- [112] Lv P, Yuan Z, Wu C, Ma L, Chen Y, Tsubaki N. Bio-syngas Production from Biomass Catalytic Gasification. *Energy Conversion and Management* 2007;48:1132–9.
- [113] Motay CT du, Maréchal C. Industrial Preparation of Hydrogen. *Bull Mensuel De La Société Chimique De Paris* 1868;9:334–334.
- [114] Mahishi MR, Goswami DY. Thermodynamic Optimization of Biomass Gasifier for Hydrogen Production. *TMS06: Symposium on Materials in Clean Power Systems* 2007;32:3831–40.
- [115] Lin S-Y, Suzuki Y, Hatano H, Harada M. Developing an Innovative Method, HyPr-RING, to Produce Hydrogen from Hydrocarbons. *Energy Conversion and Management* 2002;43:1283–90.

- [116] Florin NH, Harris AT. Mechanistic Study of Enhanced H₂ Synthesis in Biomass Gasifiers with In-situ CO₂ Capture Using CaO. *AIChE Journal* 2008;54:1096–109.
- [117] Hanaoka T, Inoue S, Uno S, Ogi T, Minowa T. Effect of Woody Biomass Components on Air-steam Gasification. *Biomass and Bioenergy* 2005;28:69–76.
- [118] Mahishi MR, Goswami DY. An Experimental Study of Hydrogen Production by Gasification of Biomass in the Presence of a CO₂ Sorbent. *International Conference on Materials for Hydrogen Energy: Solar Hydrogen (ICMHE 2004)* 2007;32:2803–8.
- [119] Lee DK. An Apparent Kinetic Model for the Carbonation of Calcium Oxide by Carbon Dioxide. *Chemical Engineering Journal* 2004;100:71–7.
- [120] Mahishi MR, Sadrameli MS, Vijayaraghavan S, Goswami DY. A Novel Approach to Enhance the Hydrogen Yield of Biomass Gasification Using CO₂ Sorbent. *Journal of Engineering for Gas Turbines and Power* 2008;130:1–8.
- [121] Bretado E, Vigil MDD, Martinez VHC, Ortiz AL. Thermodynamic Analysis for the Production of Hydrogen Through Sorption Enhanced Water Gas Shift (SEWGS). *International Journal of Chemical Reactor Engineering* 2008;6:51.
- [122] Blamey J, Anthony EJ, Wang J, Fennell PS. The Calcium Looping Cycle for Large-scale CO₂ Capture. *Progress in Energy and Combustion Science* 2010;36:260–79.
- [123] Manovic V, Charland J-P, Blamey J, Fennell PS, Lu DY, Anthony EJ. Influence of Calcination Conditions on Carrying Capacity of CaO-based Sorbent in CO₂ Looping Cycles. *Fuel* 2009;88:1893–900.
- [124] Alvarez D, Pena M, Borrego AG. Behavior of Different Calcium-based Sorbents in a Calcination/carbonation Cycle for CO₂ Capture. *Energy & Fuels* 2007;21:1534–42.
- [125] Li Y-J, Zhao CS. Carbonation Characteristics in Calcium-sorbents Cyclic Calcination/carbonation Reaction Process. *Proceedings of Chinese Society of Electrical Engineering* 2008;28:55–60.
- [126] German RM. Pressure-assisted Sintering. In: German RM, editor. *Sintering theory and practice*, New York: John Wiley and Sons; 1996, p. 313–72.

- [127] Kaviany M. Conduction Heat Transfer. In: Kaviany M, editor. Principles of heat transfer in porous media, vol. 2nd, New York: Springer; 1995, p. 119–53.
- [128] Sun P, Grace JR, Lim CJ, Anthony EJ. Simultaneous CO₂ and SO₂ Capture at Fluidized Bed Combustion Temperatures. 18th International Conference on Fluidized Bed Combustion, Toronto, Canada: American Society of Mechanical Engineers, New York, NY 10016-5990, United States; 2005, p. 917–33.
- [129] Stanmore BR, Gilot P. Review—calcination and Carbonation of Limestone During Thermal Cycling for CO₂ Sequestration. *Fuel Processing Technology* 2005;86:1707–43.
- [130] Cazorla-Amorós D, Joly JP, Linares-Solano A, Marcilla-Gomis A, Salinas-Martinez de Lecea C. CO₂-CaO Surface and Bulk Reactions: Thermodynamic and Kinetic Approach. *Journal of Physical Chemistry* 1991;95:6611–7.
- [131] Arias B, Abanades JC, Grasa G. An Analysis of the Effect of Carbonation Conditions on CaO Deactivation Curves. *Chemical Engineering Journal* 2011;167:255–61.
- [132] Warnecke R. Gasification of Biomass: Comparison of Fixed Bed and Fluidized Bed Gasifier. *Biomass and Bioenergy* 2000;18:489–97.
- [133] Abu El-Rub Z, Bramer EA, Brem G. Review of Catalysts for Tar Elimination in Biomass Gasification Processes. *Industrial & Engineering Chemistry Research* 2004;43:6911–9.
- [134] Walawender WP, Ganesan S, Fan LT. Steam Gasification of Manure in a Fluid Bed. Influence of Limestone as a Bed Additive. *Symposium Papers. Energy from biomass and wastes V*. Lake Buena Vista, Florida, January 26-30, 1981, Institute of Gas Technology; 1981, p. 517–27.
- [135] Simell PA, Leppälahti JK, Bredenberg JB. Catalytic Purification of Tarry Fuel Gas with Carbonate Rocks and Ferrous Materials. *Fuel* 1992;71:211–8.
- [136] Simell PA, Hirvensalo EK, Smolander VT. Steam Reforming of Gasification Gas Tar over Dolomite with Benzene as a Model Compound. *Industrial & Engineering Chemistry Research* 1999;38:1250–7.
- [137] Van der Drift A, Van Doorn J. Effect of Fuel Size and Process Temperature on Fuel Gas Quality from CFB Gasification of Biomass. In: Bridgwater A, editor. *Progress in Thermochemical Biomass Conversion*, John Wiley & Sons; 2008, p. 265–75.

- [138] Herguido J, Corella J, Gonzalez-Saiz J. Steam Gasification of Lignocellulosic Residues in a Fluidized Bed at a Small Pilot Scale. Effect of the Type of Feedstock. *Industrial & Engineering Chemistry Research* 1992;31:1274–82.
- [139] Sakaguchi M, Watkinson AP, Ellis N. Steam Gasification of Bio-Oil and Bio-Oil/Char Slurry in a Fluidized Bed Reactor. *Energy & Fuels* 2010;24:5181–9.
- [140] Sakaguchi M. Gasification of Bio-oil and Bio-oil/char Slurry. University of British Columbia, 2010.
- [141] CEN/TS 15439. Tar and Particles in Product Gases-Sampling and Analysis. 2006.
- [142] Channiwala S, Parikh P. A Unified Correlation for Estimating HHV of Solid, Liquid and Gaseous Fuels. *Fuel* 2002;81:1051–63.
- [143] Simell P, Hakala N. Catalytic Decomposition of Gasification Gas Tar with Benzene as the Model Compound. *Industrial & Engineering Chemistry Research* 1997;36:42–51.
- [144] Knight A. Sorbent Attrition in Fluidized Carbon Dioxide Capture Systems. M.A.Sc. Thesis, University of British Columbia, 2013.
- [145] Mettanant V, Basu P, Butler J. Agglomeration of Biomass Fired Fluidized Bed Gasifier and Combustor. *Canadian Journal of Chemical Engineering* 2009;87:656–84.
- [146] Sun P. CO₂ Removal in Power Based Systems Using Calcium-Based Sorbents. Ph.D. Thesis, The University of British Columbia, 2007.
- [147] Sun P, Grace JR, Lim CJ, Anthony EJ. Sequential Capture of CO₂ and SO₂ in a Pressurized TGA Simulating FBC Conditions. *Environmental Science & Technology* 2007;41:2943–9.
- [148] Sbirrazzuoli N, Vincent L, Mija A, Guigo N. Integral, Differential and Advanced Isoconversional Methods. *Chemometrics and Intelligent Laboratory Systems* 2009;96:219–26.
- [149] Constantineau JP. Fluidized Bed Roasting of Zinc Sulfide Concentrate Factors Affecting the Particle Size Distribution. The University of British Columbia (Canada), 2004.

- [150] Johnsen K, Ryu HJ, Grace JR, Lim CJ. Sorption-enhanced Steam Reforming of Methane in a Fluidized Bed Reactor with Dolomite as CO₂-acceptor. *Chemical Engineering Science* 2006;61:1195–202.

Appendix 1: Dual-Environment Thermogravimetric Reactor

This appendix outlines the work conducted on the dual-environment thermogravimetric reactor (DE-TGR). This involved the dismantling, re-construction and re-commissioning of the specialized thermogravimetric apparatus. The design incorporated two tube furnaces that could be maintained at different temperatures by means of two PLCs, stacked on one another and placed on a pneumatic lift. A quartz tube was suspended through both furnaces. The sample was suspended in the midpoint of the quartz tube, from a load cell (Transducer Techniques GSO series), by means of a Ni-Cd hang-down wire. Raising and lowering the lift allowed for a very rapid heating and cooling of the sample. This rapid cooling and heating allows for relatively short CaO-CO₂ cycle durations and allowed for prolonged cycling in previous experimental studies [19,24,34,36,128,146,147]. Figure A1.1 shows a CAD drawing of the reconstructed DE-TGR. The piping and instrumentation diagram for the re-commissioned DE-TGR is seen in Figure A1.2.

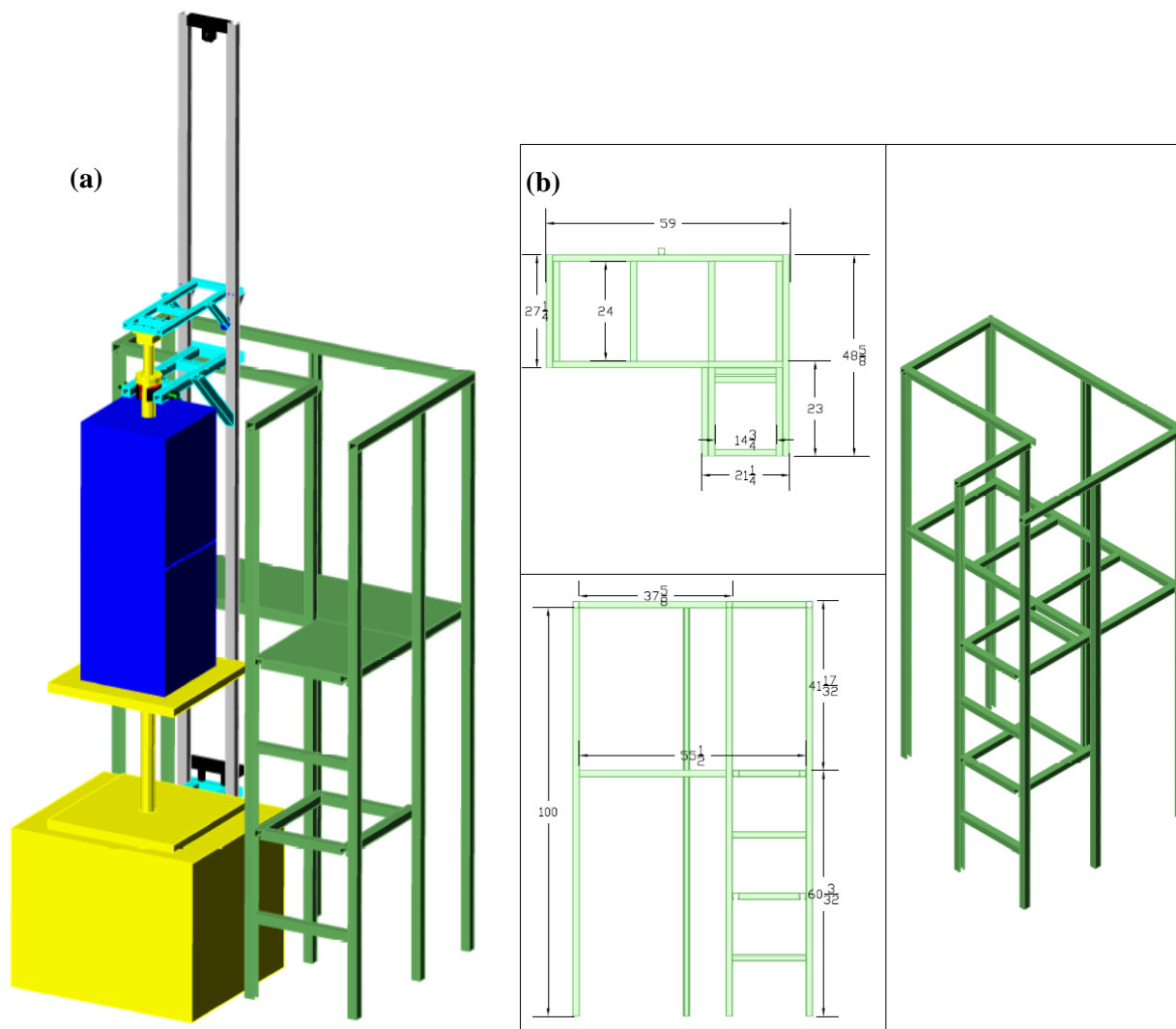


Figure A1.1: CAD drawing of the DE-TGR experimental apparatus; (a) entire system, (b) structural design.

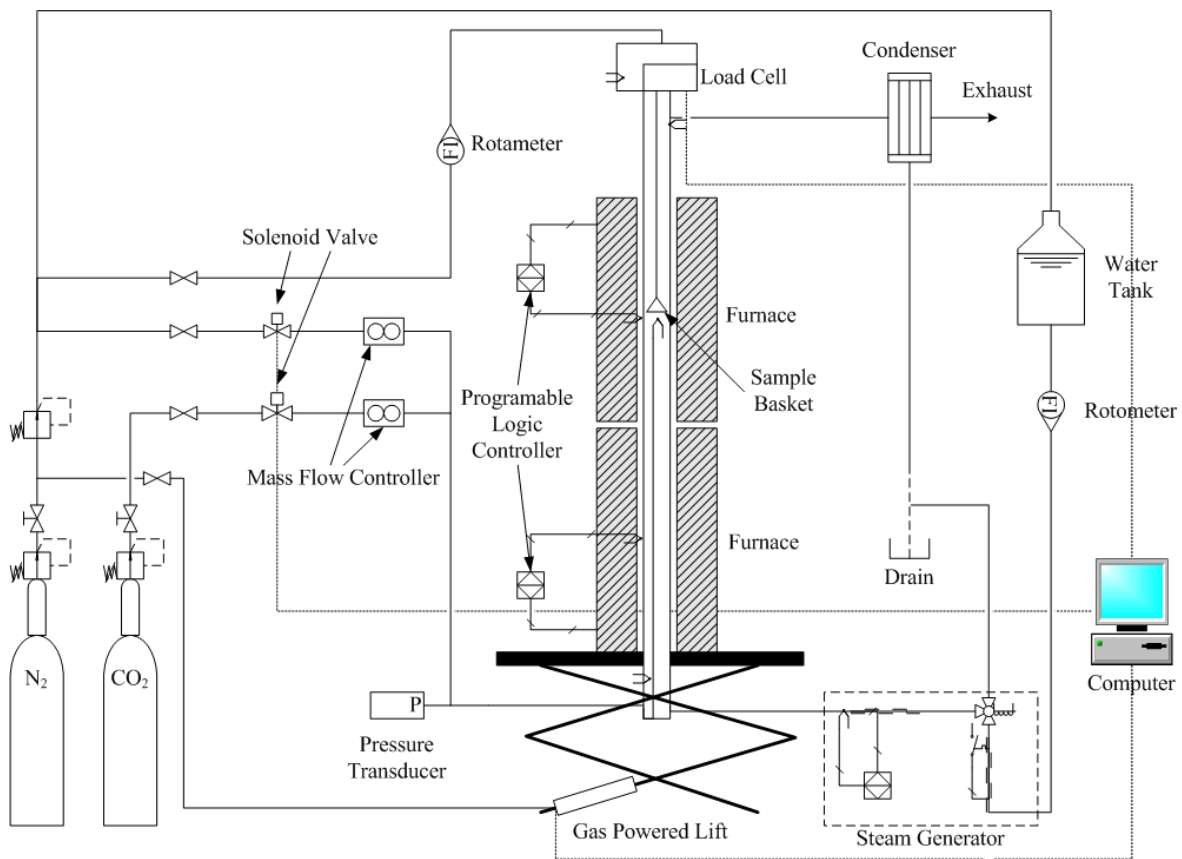


Figure A1.2: DE-TGR piping and instrumentation diagram.

Construction and commissioning of the DE-TGR was completed while experiments on the PTGA were underway. The experimental plan included testing for the effect of H₂O on calcium utilization over a large number of cycles, as H₂O is known to have a catalytic effect on carbonation and sintering of CaO. Table A1.1 lists the experiments conducted on the DE-TGR and experimental conditions. Re-commissioning of the DE-TGR was successful and the system was upgraded to include steam addition to the reaction tube. Initial runs cycling by means of temperature swing, Figure A1.3, and gas switching, Figures A1.4 and A1.5, were successful and demonstrated the stability of the system.

Table A1.1: DE-TGR Experimental conditions

Run	Description	Data File(s)	Cycle Time (min)	t (min)	T (°C)	Gas Flow	t (min)	T (°C)	Gas Flow	Number of Cycles	Sample Mass (mg)
T1	No Steam, 650-850 temperature swing	A (03-31)	22.08	10.00	650	100% CO ₂	10.00	850	--	15	708
T2	Steam in both stages	850-900 steam (04-21)	22.72	12.03	850	1:1 (H ₂ O:CO ₂)	10.69	850	1:1 (H ₂ O:N ₂)	20	590
T3	Steam and CO ₂ in calcination	850_N2 (04-24) & (04-25)	20.63	10.92	850	100% CO ₂	9.71	850	1:1 (H ₂ O:CO ₂)	36	434
T4	Steam in calcination	850 steam_N2	20	10.59	850	100% CO ₂	9.41	850	1:1 (H ₂ O:N ₂)	21	485
T5	Steam in both stages, 2x H ₂ O	850 steam_N2 (05-04)	18.41	9.75	850	1:1 (H ₂ O:CO ₂)	8.66	850	2:1 (H ₂ O:N ₂)	21	448
T6	Steam in both, 2x H ₂ O, 2x CO ₂	850 steam_N2 (05-05 & 06)	18.41	9.75	850	1:2 (H ₂ O:CO ₂)	8.66	850	2:1 (H ₂ O:N ₂)	48	468
T7	No Steam	850_N2 (05-19)	21.55	11.41	850	100% CO ₂	10.14	850	100% N ₂	75	440

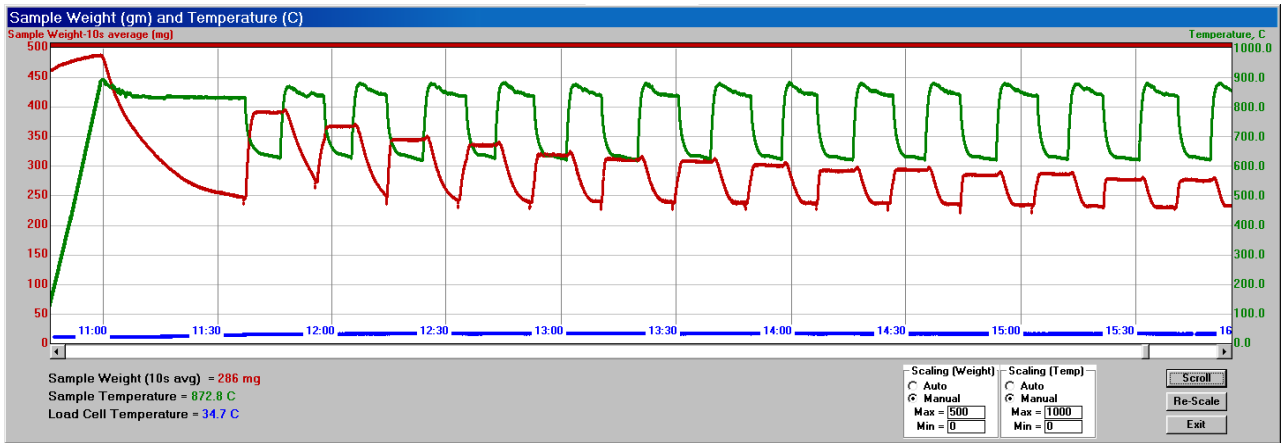


Figure A1.3: Typical weight data output.

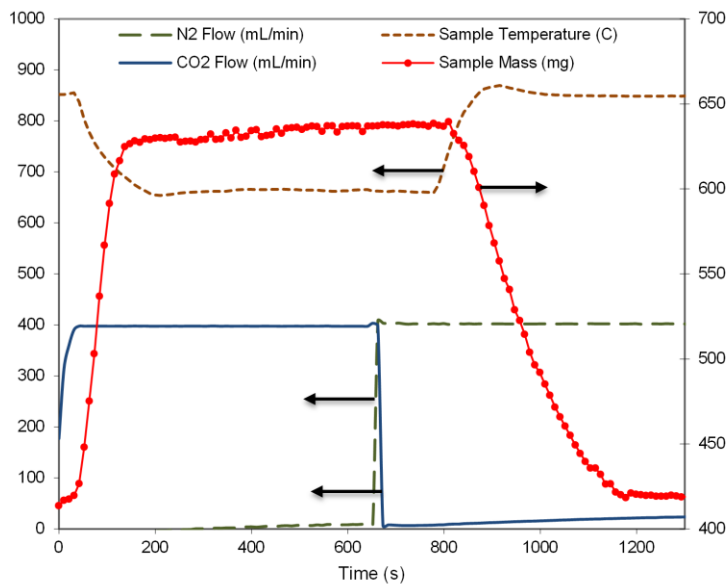


Figure A1.4: Preliminary N₂ - CO₂ cycling (650-850°C) run, first cycle (T1).

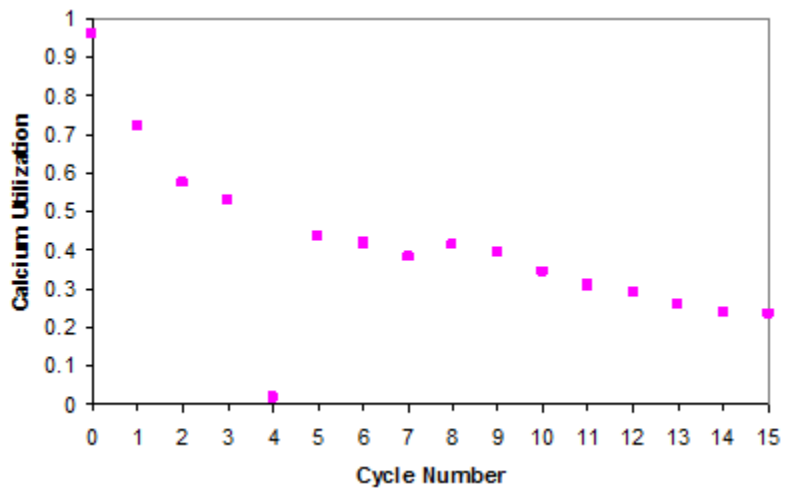


Figure A1.5: Preliminary N₂ - CO₂ cycling (650-850°C) run (T1).

The system was automated using a computer based DAQ system running a Visual Basic program that recorded temperature and weight data and allowed the user to automate the lift operating and turn the flow of gases on and off according to the desired cycle timing. The temperatures of the two furnaces, the steam generator and the preheater were set by the operator. This automation allowed for long term cycling to be carried out without the need for an operator present.

The steam was generated through the use of a flow of nitrogen or CO₂ bubbled through a heated, enclosed water bath. Assuming the gas left the bath saturated at the recorded temperature, the mass flow of water in the saturated gas could be calculated. Water was added to the water bath at the same rate as the vapour was drawn off from a pressurized water tank, metered using a rotometer. The reason for generating steam in this fashion was to reduce the problem of condensation when using a flow of pure steam. The assumption of a fully saturated gas was a rather large one and would have required a number of calibration tests to determine its accuracy. As well it is difficult to maintain equal flows of water into an out of the water bath. The system could also be used to generate steam in a more conventional manner if the water bath were kept at a temperature above 100°C and the rotometer utilized to control the flow of steam.

Following its generation, the steam flowed through a high temperature, 3-way solenoid valve, with one exit flowing to the reactor and the other to the drain. The valve was computer controlled and would allow for steam addition to the reactor to be switched on and off rapidly while maintaining the consistent generation of steam. After the solenoid valve the steam flowed into the pre-heater section, which consisted simply of a heated tube, where it was mixed with other reactant gases. From the pre-heater it flowed into the bottom of the quartz reaction tube. The bottom section of the reaction tube was filled with high temperature ceramic cylinders, in order to maintain a high temperature in the bottom half of the tube during cycling of the furnaces. During cycling the furnaces are moved up and down by a pneumatic lift. At an given time during the cycle, half of the quartz tube is exposed and un-heated. This posed a major problem when using steam as it quickly condensed on the exposed section. To avoid condensation when using steam the furnaces required cycling to alternately heat the exposed sections of tube. Despite these efforts, condensation in the system was in-evitable and although runs were conducted designed to use steam in the calcination gas only, see Figure A1.6, it was impossible to know the concentration of steam in the sweep gas and it was likely that there was steam present during carbonation as well.

Results were scattered and did not show any noticeable trend in calcium utilization decay over 20 to 40 cycles, see Figure A1.6. There may be a slight benefit to using steam during calcination, but further experiments are required. The use of both steam and CO₂ during calcination gave the most rapid decay in utilization. This is expected as the tertiary system of CaO-CaCO₃-Ca(OH)₂ has a eutetic point below the

temperatures used for cycling. This would have increased the rate of particle sintering and deactivation. Results from these series of experiments showed residual calcium utilizations after 40 cycles, higher than was expected, ~20% at 75 cycles for steam-free CaO cycling. This could be the result of extended carbonation (10 mins) or possibly experimental error, but requires further experimental investigation.

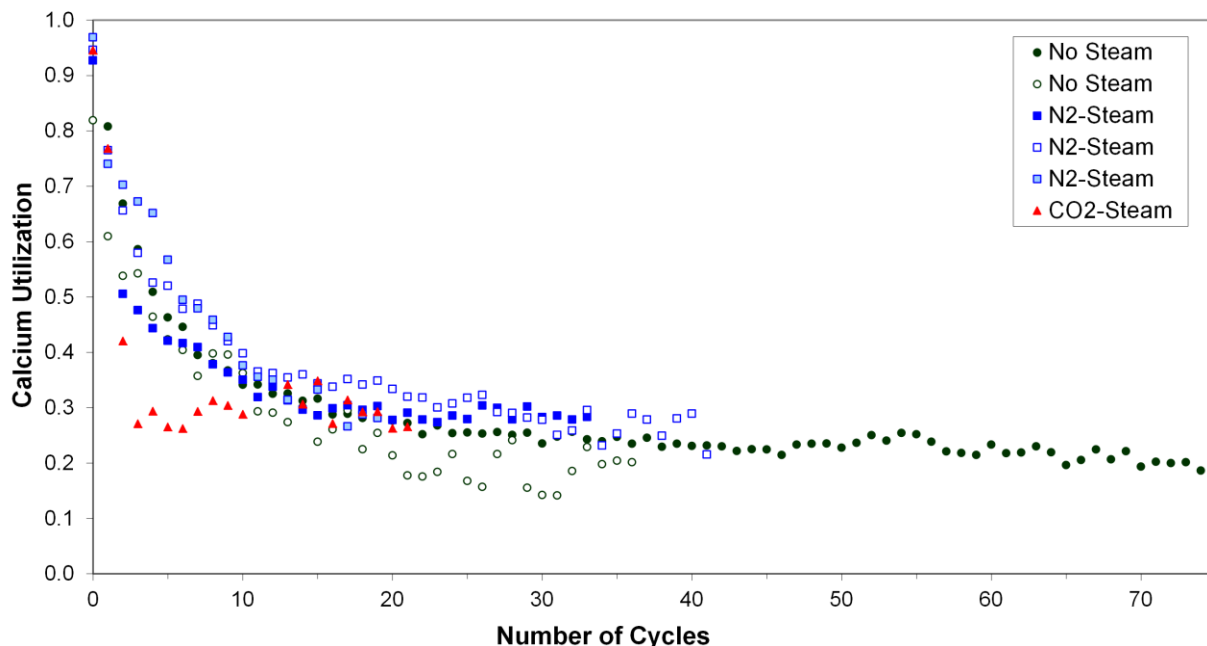


Figure A1.6: Preliminary isothermal cycling (850°C) runs comparing calcination in the presence of steam; carbonation in pure CO₂ for 10 min, 11 min calcination.

There were a number of reasons why these experimental investigations were halted. The primary reason was the difficulty in using steam in addition to other instabilities in the system including:

- Regular replacement of the load cell required,
- Static electricity build-up on the quartz tube affecting weight of sample,
- Periodic cracking of the quartz tube from cycling,
- Poor functionality / reliability of the lift system.

The system is adequate for steam-free usage, but would require some modifications for the possible use of steam. A smaller system where the reaction tube could be completely heated would be a better design for an experimental investigation requiring the use of steam; the exposed surfaces or the quartz tube presented a major obstacle to preventing condensation. If cycling of CaO through the use of temperature swing with the use of steam is desired, then there are some improvements that could be made to the DE-TGR system that might possibly facilitate this, including:

- Re-direct the flow of gases from the top to the bottom. Their current flow from the bottom to the top was designed to avoid dilution of the reaction gases by the nitrogen load cell sweep gas.

This would allow any condensation formed below the heated sections to simply be drained off the bottom.

- Switch the steam generating from a bubbler system to a more simple system where a metered flow of water enters a high temperature evaporative tube.
- Install a high temperature 'curtain' to trap heat in the tube when the upper portion is exposed.

Other general improvements that could be made include:

- Replacement / refurbishment of the aging mass flow controllers;
- Replacement / refurbishment of the faulty pneumatic lift system; and
- Refurbishment of the gas analyzer to measure CO₂ concentration in the exhaust gases.

The following pages include the DE-TGR operating procedures and calibration curves for the various flow meters.

Start-Up Procedure

1. Obtain sample
 - a. Obtain vial from dririte storage or drying furnace
 - b. Weight sample vial
 - c. Add sample to vial and weigh

2. Clean sample basket (if not already done)
 - a. Remove top clamshell clamp
 - b. Remove purge air line
 - c. Raise sample basket using hand crank to line on upright
 - d. Lift basket out of reactor using tweezers
 - e. Remove sample from basket and place in vial using funnel
 - f. Clean sample basket using compressed air to remove particles
 - i. If particles remain place sample basket in weak acid solution
 - ii. Place solution in ultrasonic bath for 15mins if available
 - iii. Dry sample basket for 30mins in drying oven
 - g. Replace basket on hangdown wire
 - i. **Do not pull down on hangdown wire as this *will* damage load cell**

3. Tare empty basket
 - a. Lower basket into reaction tube if furnace is cool
 - b. Tare load cell controller
 - c. Tare weight in DAQ program
 - i. start DAQ program
 - ii. select "calibration" from menu
 - iii. change "b" value to equal current voltage

4. Load sample
 - a. Raise basket and remove from reactor
 - b. Load sample evenly in the sample basket
 - c. Replace basket on hangdown wire *carefully*
 - d. Lower sample
 - e. Replace clamshell clamp
 - f. Reattach purge air line

5. Start flow of gases
 - a. Open gas cylinders
 - b. Adjust regulators to 15 psig
 - c. Open manual gas valves on panel
 - d. Start flow of purge gas
 - i. Turn on purge gas flow solenoid (S1)
 - ii. Adjust flow using rotometer according to: reaction gas + 50ml/min
 - e. Start flow of reaction gases
 - i. Turn on MFC box
 - ii. Turn on reaction gas solenoids
 - iii. Adjust MFCs to desired flow level using controller box

6. Set start-up conditions
 - a. Close reaction gas solenoids for gases not used in carbonation
 - b. Using DAQ program, move furnaces in to upper position

7. Set cycling condition

- a. Using “automation” window set desired cycling conditions
 - b. Start cycling with carbonation
 - c. Use upper furnace for calcination
8. Start furnaces
 - a. Set upper furnace to desired calcination temperature +50°C
 - b. Set lower furnace to desired carbonation temperature +50°C
9. Start heaters if using steam
 - a. Start flow of water
 - i. Pressurize tank by briefly opening three way valve
 - ii. Ensure steam solenoid is off (S5)
 - iii. Set flow of water to desired value using rotometer
 - b. Turn on steam generator
 - c. Turn on steam superheater
 - d. Turn on reactor pre-heater
10. Allow reactor to heat to operating conditions
11. Begin initial calcination
 - a. Switch to initial calcination gas flow
 - b. Move furnaces to lower position using DAQ program
 - c. Reset program timer
12. Start saving data
13. Calcine sample for desired amount of time
14. Start cycling
 - a. Once calcination is complete
 - b. Start automation of DAQ program

Shut-Down Procedure

1. Stop DAQ program automation
2. Stop data collection
3. Turn-off steam solenoid valve
4. Set to calcination conditions (if calcinaed sample is desired)
 - a. Lower furnaces
 - b. Switch gas flows to calcination
5. Allow sample to calcine
6. Turn off furnaces
7. Turn off heating tapes
8. Allow furnace to cool
 - a. Down to <200°C
9. Remove Sample
 - a. Open top clamshell clamp
 - b. Remove purge air line
 - c. Lift sample basket using hand crank
 - d. Lift basket out using tweezers
 - e. Put sample into vial
 - i. To prevent hydration do as quickly as possible
10. Dry reactor
 - a. Flow N₂ through reactor for ~2hrs or until no moisture is observed in reactor
 - b. Check for moisture in reactor using flash light

Calibrations

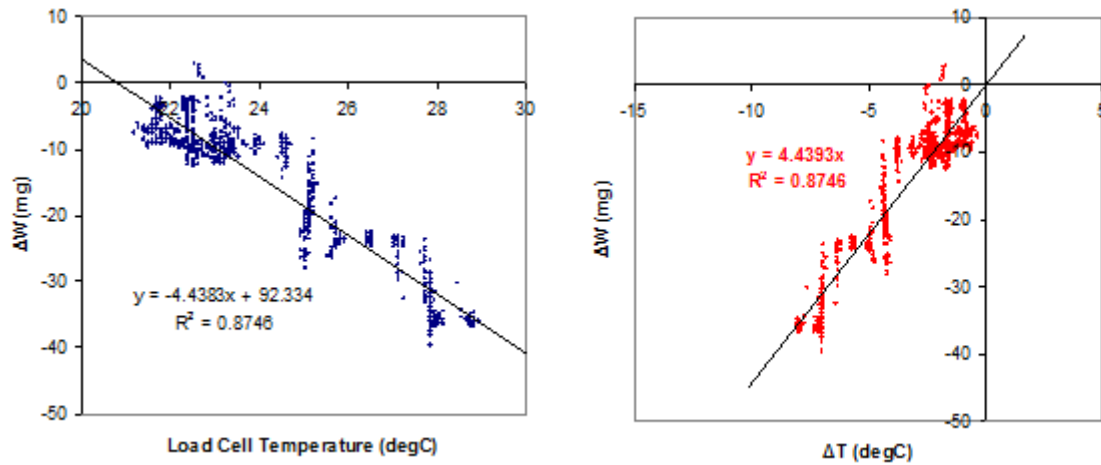


Figure A1.6: Temperature effect of load cell

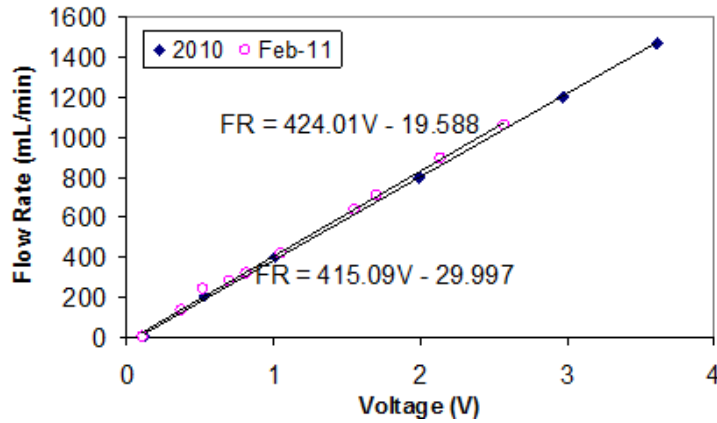


Figure A1.7: Aalborg gas flow meter 1 calibration for N₂.

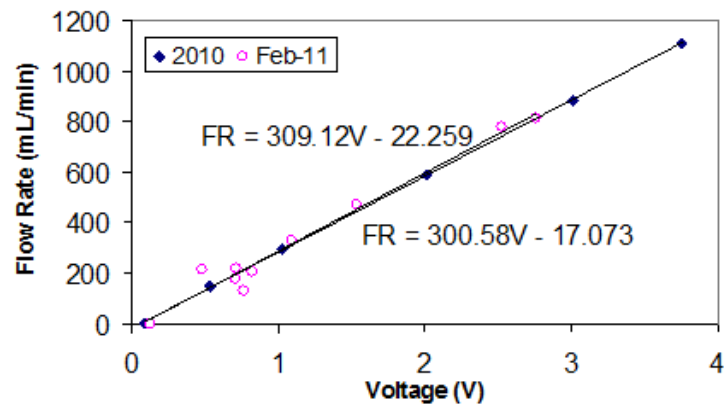


Figure A1.8: Aalborg gas flow meter 2 calibration for CO₂.

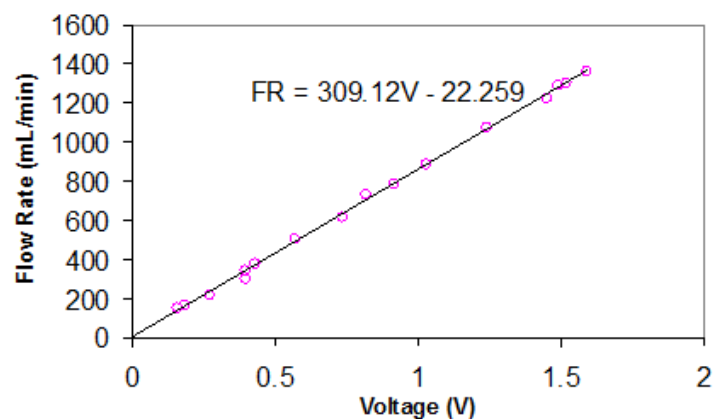


Figure A1.9: Brooks gas flow meter calibration for air.

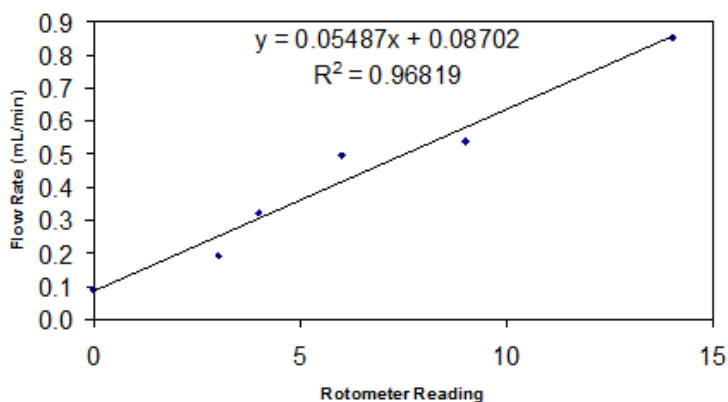


Figure A1.10: Rotometer calibration for water.

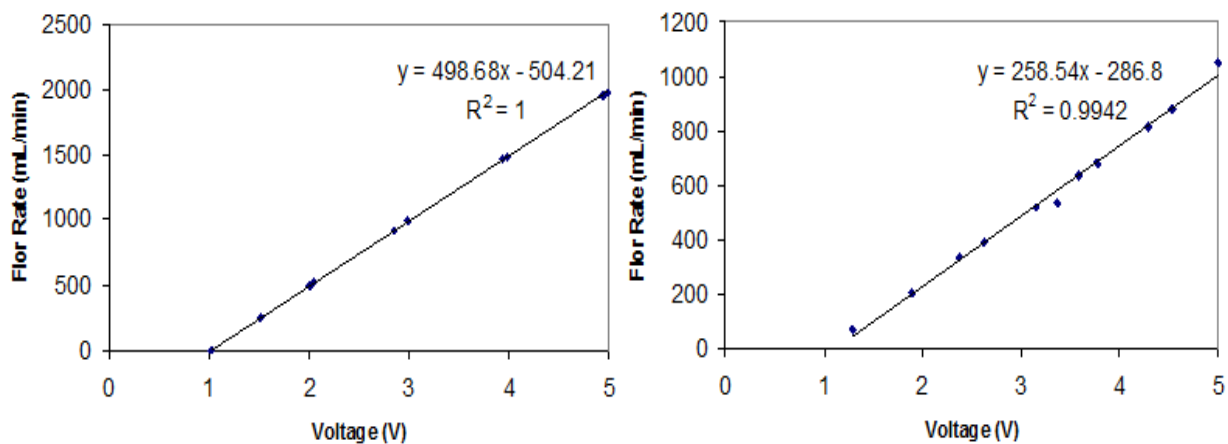


Figure A1.11: Omega gas flow meter 1 calibration for N₂ (left), and CO₂ (right).

Appendix 2: PTGA Start-Up Sequence

1. **Open pressure regulator program and start profile**
 - Start timer for initial high pressure state
2. **Close pressure program**
 - Make sure pressure release valve is open
3. **Open ThermalAnalyst DAQ program**
4. **Run calibration if necessary**
 - Run calibration if changing hardware (baskets, wire...)
 - Wait 2-5mins for balance to stabilize (time depends on desired accuracy)
5. **Tare balance with sample holder in zero flow**
6. **Load sample and record weight**
7. **Seal reactor**
8. **Start flow of gases**
 - Reaction gas (2) = N₂
 - Reaction gas (3) = CO₂
 - Purge gas (1) = Reaction gas flow + 2%
 - Furnace gas (4) = Reaction gas flow
9. **Record weight during flow**
10. **Close “Manual Pressure Release” valve**
11. **Input method**
 - Record file name
12. **Allow system to reach operating pressure**
13. **Start ThermalAnalyst method**


```

last=round(x2);
data(last:length,:)=[]; % cuts end of data
close

%% Correction for Pressure
data(:,6)=data(:,2) - data(:,4)/P_correction; % pressure correction
data(:,5)=data(:,4); % pressure
data(:,4)=data(:,3); % temperature
data(:,3)=data(:,2); % weight

[length,width]=size(data); % new matrix dimensions

%% Allows user to select initial carbonation weight
fig = figure('Name', 'Please Select the initial weight of the sample');
plotyy(1:1000,data(1:1000,3),1:1000,data(1:1000,5))
[x3,y3] = ginput(1);
close
x3 = round(x3);
mass_CaCO3 = (data(x3-2,3)+data(x3,3)+data(x3+2,3))/3;

%% Allows user to set select first carbonation peak
fig = figure('Name', 'Please Select the First Carbonation Peak');
plotyy(x3:x3+1500,data(x3:x3+1500,3),x3:x3+1500,data(x3:x3+1500,5))
[x4,y4] = ginput(1);
close
offset = round(x4);

%% Allows user to set select first calcination valley
    % Determines weight of CaO for fixed calculation &
    % Determines interval between carboantion and calcination for variable
fig = figure('Name', 'Please Select the Calcined Weight Immediately Prior to
the First Carbonation');
plotyy(x3:x3+1500,data(x3:x3+1500,3),x3:x3+1500,data(x3:x3+1500,5))
[x5,y5] = ginput(1);
close

if x5>0
    x5=round(x5);
elseif x5<0
    x5=3;
end

calcine = round(offset-x5); % Interval

% Averaged weight of CaO
mass_CaO = (data(x5-2,3)+data(x5,3)+data(x5+2,3))/3;

% Initial Carbonation
Initial = (mass_CaCO3-mass_CaO)/mass_CaO*56/44;

%% Determines the averaged value of each column
j=1;
starttime = data(1,1);

while (j<=width)
    i=offset;
    peak = offset;

```

```

count = 1;
avg = 0;

while (i<=length)
    if j==1                                % first column = run time
        x(count,j)=data(i,j)-starttime;
    elseif j==2
        x(count,j)=count;                  % second column = cycle number
    elseif j==6
        avgCaCO3 = data(i,j);
        avgCaO = data(i-calcine,j);

        for dev=1:pm
            avgCaCO3 = avgCaCO3 + data(i+dev,j) + data(i-dev,j);
            avgCaO = avgCaO + data(i+dev-calcine,j) + data(i-dev-
calcine,j);
        end
        avgCaCO3 = avgCaCO3/(2*dev+1);
        avgCaO = avgCaO/(2*dev+1);

        % 6th column = Average CaCO3 weight
        x(count,j) = avgCaCO3;

        % 7th column = Average Moving CaO weight
        x(count,7) = avgCaO;

        % 8th Column = CaO Utilization using a Fixed CaO Weight
        x(:,8) = (x(:,6)-mass_CaO)/mass_CaO/purity*56/44;

        % 9th column = CaO Utilization using a Moving CaO Weight
        x(count,9) = (x(count,6)-x(count,7))/x(count,7)/purity*56/44;

    else                                    % other columns, averaged values
        avg = data(i,j);
        for dev=1:pm
            avg = avg + data(i+dev,j) + data(i-dev,j);
        end
        avg = avg/(2*dev+1);
        x(count,j) = avg;
    end

    count = count + 1;
    peak = peak + interval;
    i = round(peak);
end

j=j+1;

end

%% Plots the Utilization Data
[n,m]=size(x);

plot(1:n,x(:,8),'ro','MarkerSize',2,'MarkerFaceColor','r')

hold on

```

```

[AX,H1,H2] = plotyy(1:n,x(:,9),1:n,x(:,5),'plot');
set(H1,'linestyle','none','marker','.');
set(H2,'linestyle','none','marker','.');

legend('Fixed Utilization','Variable Utilization','Pressure')
hold off

%% List of Variables
variable{1,1} = 'Variable';           variable{1,2} = 'Value';           variable{1,3}
= 'Unit';
variable{2,1} = 'Sample Rate';        variable{2,2} = rate;             variable{2,3}
= 's';
variable{3,1} = 'Offset';             variable{3,2} = offset;          variable{3,3}
= 'data points';
variable{4,1} = 'Cycle Interval';     variable{4,2} = interval;        variable{4,3}
= 'data points';
variable{5,1} = 'Number of Cycles';   variable{5,2} = count-1;
variable{6,1} = 'Calcine Offset';     variable{6,2} = calcine;         variable{6,3}
= 'data points';
variable{7,1} = 'Initial Weight';     variable{7,2} = mass_CaCO3;      variable{7,3}
= 'mg';
variable{8,1} = 'CaO Weight';         variable{8,2} = mass_CaO;        variable{8,3}
= 'mg';
variable{9,1} = 'Initial Carbonation'; variable{9,2} = Initial;
variable{10,1} = 'Pressure Correction Factor'; variable{10,2} =
P_correction;
variable{11,1} = 'CaCO3 purity';     variable{9,2} = purity;
v = variable;

```

Appendix 4: Pressure Swing Cycling – Supplemental Material

The following section presents the data from the initial studies into pressure swing cycling not included in Chapter 2. The data was excluded to ensure brevity as Chapter 2 was written as an article for publication and the presentation of excessive experimental results was undesirable. The experiments below help to strengthen the arguments made in Chapter 2, demonstrate the degree of repeatability, and confirm some findings found previously by other researchers investigating CaO based CO₂ capture. Table A4.1 lists the successful pressure swing and high pressure gas switching experiments and the experiments referred in Chapter 2. Table A4.2 gives the experimental details for the experiments.

Table A4.1: List of experiments

Run	Reference	Data File(s)	Sample Index
A	Chapter 2 (run1)	150-250 micron 5 bar long3	PC-5-1130
B	Chapter 2 (run2)	150-250 micron 10 bar 2 & 3	PC-10-268
C	Chapter 2 (run3)	150-250 micron 20 bar 1 & 2	PC-20-227
D	Chapter 2 (run8)	150-25- micron 5 bar fast3	PCF-5-173
E	Chapter 2 (run4)	150-250 micron 20 bar small1	PC-20-280
F		150-250 micron 20 bar long1	PC-20-320
G	Chapter 2 (run9)	150-25- micron 5 bar fast5	PCF-5-500
H	Chapter 2 (run10)	150-250 micron 5 bar faster2	PCF-5-345
I		150-250 um 5bar cycling medium1	PCF-5-69
J	Chapter 2 (run11)	150-250 um 5bar cycling medium9	PCF-5-378
K		150-250 20 bar mixture2	PCM-20-269
L	Chapter 2 (run5)	150-250 20 bar large1	PC-20-268
M	Chapter 2 (run7)	150-250 20 bar medium7	PC-20-254 (x3)
N		150-250 20 bar medium10	PC-20-282 (x3)
O		150-250 10 bar mixture	PCM-10-275
P		20 bar gas switching (3,4,5)	GS-20-100
Q		20 bar gas switching B(1-10)	GS-20-252
R	Chapter 2 (run12)	5 bar gas switching B(1-6)	GS-5-258
S		5 bar gas switching 850(1-7)	--
T	Chapter 2 (run6)	150 - 250 micro 20 bar mono2	PC-20-272
U		5 bar cycling 850C7	PC-5-850-267
V		5 bar pressure swing 850(1-10)	P+GS-5-280
W		5 bar switching round	GS-5-237
X		150-250 micron 5 faster	PCF-5-295
Y		150-250 un 5bar cycling medium2	PCF-5-69
Z		150-250 10 bar mixture2	PCM-10-42
AA		90-106 micron 5 bar	PC-5-50
AB		45-63 micron 5 bar	PC-5-30

Table A4.2: Cycling experiments conducted in the initial study

Run	Description	Particle Size (µm)	Cycle Time (min)	Carbonation				Calcination				Depressurization		Sample Mass (mg)	Number of Cycles	Final Utilization
				P (bar)	t (min)	T (°C)	Gas Flow	P (bar)	t (min)	T (°C)	Gas Flow	(s)	(bar/min)			
A	5 bar cycling baseline	150-200	35.16	5	23	1000	100% CO2	0	10	1000	100% CO2	150	2	347.3	1138	0.084
B	10 bar cycling baseline	150-200	35.16	10	24.5	1000	100% CO2	0	~14	1000	100% CO2	150	4	424.4	275	0.259
C	20 bar large sample size (320 mg calcined)	150-200	35.16	20	25.75	1000	100% CO2	0	~10	1000	100% CO2	150	8	566.9	228	0.189
D	5 bar fast de-pressurization (30s)	150-200	19.5	5	10	1000	100% CO2	0	9.5	1000	100% CO2	30	10	104.6	158	0.176
E	20 bar small sample size (61 mg calcined)	150-200	35.16	20	25.75	1000	100% CO2	0	~10	1000	100% CO2	150	8	108.3	241	0.186
F	20 bar medium sample (200 mg calcined)	150-200	35.16	20	~26.5	1000	100% CO2	0	~10	1000	100% CO2	150	8	356.3	319	0.173
G	5 bar fast de-pressurization (30s)	150-200	19.5	5	~10	1000	100% CO2	0	~10	1000	100% CO2	30	10	133.2	514	0.139
H	5 bar faster de-pressurization (22s)	150-200	19.5	5	~10	1000	100% CO2	0	~10	1000	100% CO2	22	13.6	131.1	345	0.162
I	5 bar medium de-pressurization (90s)	150-200	19	5	~10	1000	100% CO2	0	~10	1000	100% CO2	90	3.3	134.9	53	0.185
J	5 bar medium de-pressurization (120s)	150-200	19.5	5	~10	1000	100% CO2	0	~10	1000	100% CO2	120	2.5	137.8	378	0.115
K	20 bar CaCO3 - AlO2 mixture	150-200	35.16	20	~26.5	1000	100% CO2	0	~10	1000	100% CO2	150	8	355.8	269	0.125
L	20 bar large sample (475 mg calcined)	150-200	35.16	20	~26.5	1000	100% CO2	0	~10	1000	100% CO2	150	8	838.0	268	0.165
M	20 bar medium (202 mg calcined)	150-200	35.16	20	~26.5	1000	100% CO2	0	~10	1000	100% CO2	150	8	356.6	254	0.179
N	20 bar medium (203 mg calcined) packed	150-200	35.16	20	~26.5	1000	100% CO2	0	~10	1000	100% CO2	150	8	356.8	282	0.167
O	10 bar CaCO3 - AlO2 mixture	150-200	35.16	10	~21.7	1000	100% CO2	0	~10	1000	100% CO2	150	4	364.8	275	0.047
P	20 bar Gas switching	150-200	35.16	20	19.5	1000	100% CO2	20	15.5	1000	100% N2	N/A	N/A	121.0	57	0.124
Q	20 bar gas switching, fast cycle	150-200	17	20	9	1000	100% CO2	20	8	1000	100% N2	N/A	N/A	120.7	255	0.146
R	5 bar gas switching, fast cycle	150-200	17	5	7	1000	100% CO2	5	10	1000	100% N2	N/A	N/A	142.4	237	0.109
S	5 bar gas switching, fast cycle	150-200	17	5	9.75	850	100% CO2	5	7.25	850	100% N2	N/A	N/A	130.4	190	0.143
T	20 bar very small	150-200	35.16	20	23	1000	100% CO2	0	10	1000	100% CO2	150	8	51.9	272	0.132
U	5 bar pressure swing, 850C	150-200	19.5	5	10	850	20% CO2 / N2	0	9.5	850	20% CO2 / N2	120	2.5	102.7	234	0.000
V	5 bar 850 gas & pressure swing	150-200	17	5	9	850	100% CO2	0	8	850	100% N2	150	2	121.5	280	0.146
W	5 bar gas switching, attrited particles	300-355	17	5	9	1000	100% CO2	0	8	1000	100% N2	150	2	105.2	237	0.098
X	5 bar faster de-pressurization (22s)	150-200	19.5	5	~10	1000	100% CO2	0	~10	1000	100% CO2	22	13.6	132.7	295	0.126
Y	5 bar medium de-pressurization (90s)	150-200	19	5	~10	1000	100% CO2	0	~10	1000	100% CO2	90	3.3	131.7	235	0.128
Z	10 bar CaCO3 - AlO2 mixture	150-200	35.16	10	~21.7	1000	100% CO2	0	~10	1000	100% CO2	150	4	330.3	42	0.075
AA	5 bar small particles	90-160	35.16	5	23	1000	100% CO2	0	10	1000	100% CO2	150	2	265.0	50	0.160
AB	5 bar fine particles	45-63	35.16	5	23	1000	100% CO2	0	10	1000	100% CO2	150	2	409.8	52	0.163

As described in Chapter 2, experiments were conducted in the PTGA using a small sample of limestone particles in a platinum mesh basket of 1 cm² cross-sectional area. When the system is at high pressure, during the high pressure carbonation stage of the cycle, the pressure regulator opens and closes to maintain the pressure under a constant flow of CO₂. This leads to a fluctuation in the weight reading due a change in the flow over the sample as pressure regulator opens and closes, see Figure A4.1.

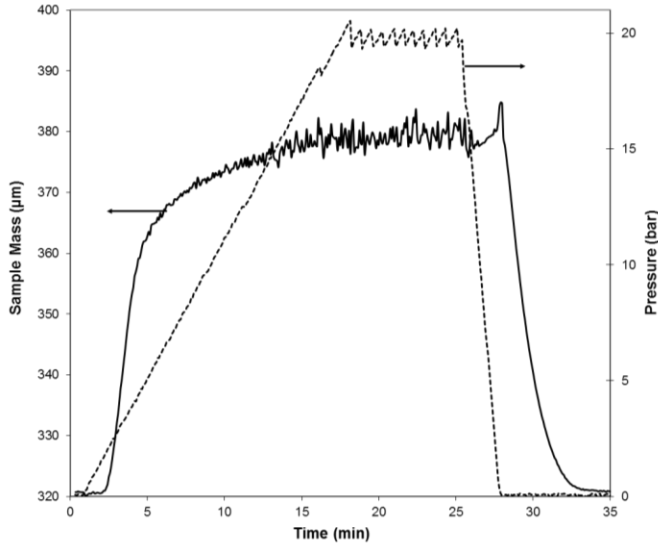


Figure A4.1: A typical 20 bar pressure cycle showing the fluctuations in weight at high pressure

In order to minimize the effect of the fluctuations on the weight measurement and subsequently the calcium utilization, a sufficiently large sample size had to be used. Results comparing the effect of sample size on the decay in calcium utilization for cycling conducted using 20 bar_g pressure swing cycles, can be found in Figure 2.7. Figure A4.2 below shows the effect of sample size on the utilization decay during 10 bar_g cycling.

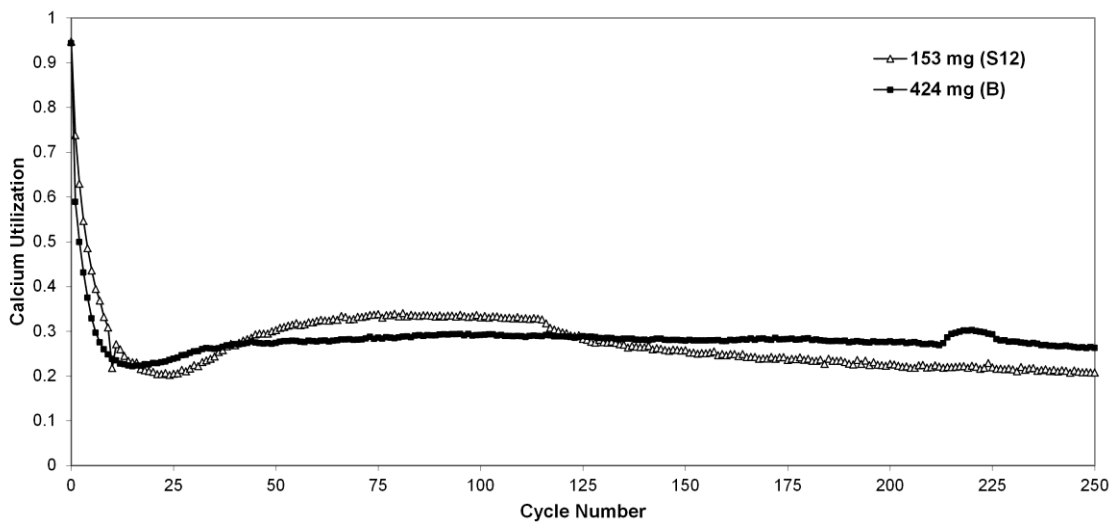


Figure A4.2: Effect of sample size on 10 bar cycling, S12 is a run from the 10 bar snapshot experiments.

The sample size had on a minor effect on the decay in calcium utilization, during 10 bar_g cycling, with a larger sample size showing a lower rise in calcium utilization following the initial rapid decrease. The utilization after 100 cycles is very similar, within 0.4. After cycle 112 the rate of utilization decay of the smaller sample (S12) increased abruptly and the residual utilization of the larger sample is higher as a result. It is not certain what brought about this abrupt change, but it could have resulted from a change in the CO₂ cylinder to one that had a high level of impurities, or a shifting of the particle bed, causing the particles to pack more closely together.

The packing of the particles in the 1 cm² platinum basket had a small but noticeable effect on the decay in calcium utilization, see Figure A4.3. When the particles were packed in a tight bed, obtained by tapping the sample basket. The rise in calcium utilization seen in the 20 bar_g runs was delayed when the particles were more closely packed. When the solids were placed in the basket in a pile, the peak utilization occurred at the 47th cycle. When the particles were placed in a level bed and a tapped, packed bed the peak utilization occurred at the 60th and 74th cycles respectively, with a decreased amplitude. This could be the result of a decreased temperature in the particle bed during the rapid, endothermic calcination reaction, decreasing the sintering, and causing a reduced effect from the "dispersed contraction." After 250 cycles, the utilization from all packings converged to very similar asymptotic values.

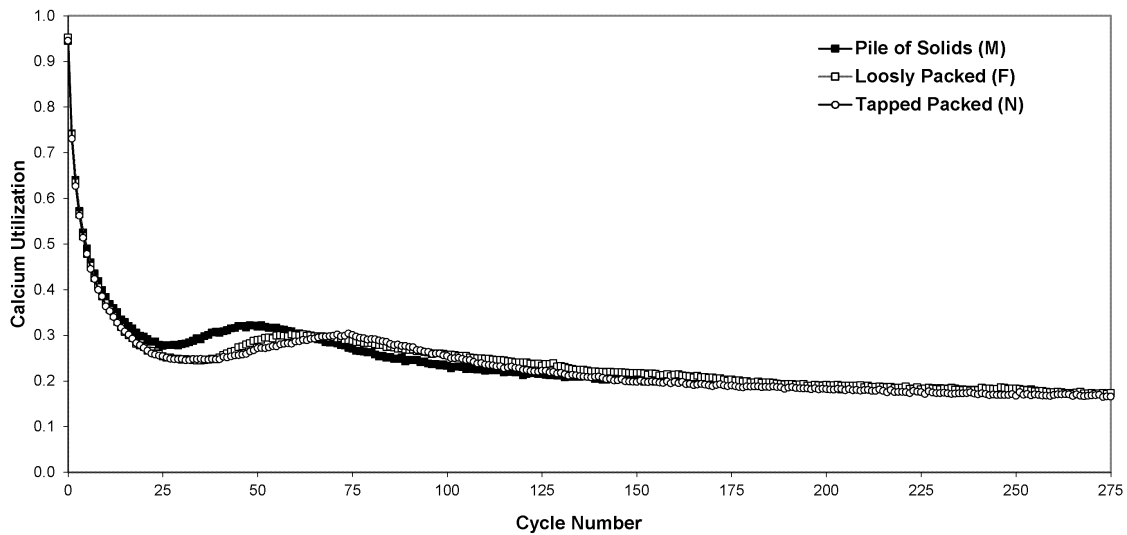


Figure A4.3: Effect of bed packing on 20 bar cycling.

The effect of particle shape on the utilization decay was also tested. A sample of Thames limestone was put into an ASTM jet attrition unit and run for a 36 h attrition test. The resulting rounded bed particles, see Appendix 5 for micrographs of the particles, were tested in a 5 bar pressure swing cycle. The rounded particles displayed a very similar decay in utilization, as compared to the un-attrited particles, reaching the same asymptotic utilization value after 100 cycles, see Figure A4.4. There was a slight

difference with the two types of particles, with the rounded particles reaching the asymptote sooner, after only 40 cycles. This is likely the result of the many surface features on the 'raw' particles taking slightly more time to be eliminated through sintering. This result is important for fluidized bed capture systems where particles are likely to undergo a great deal of attrition.

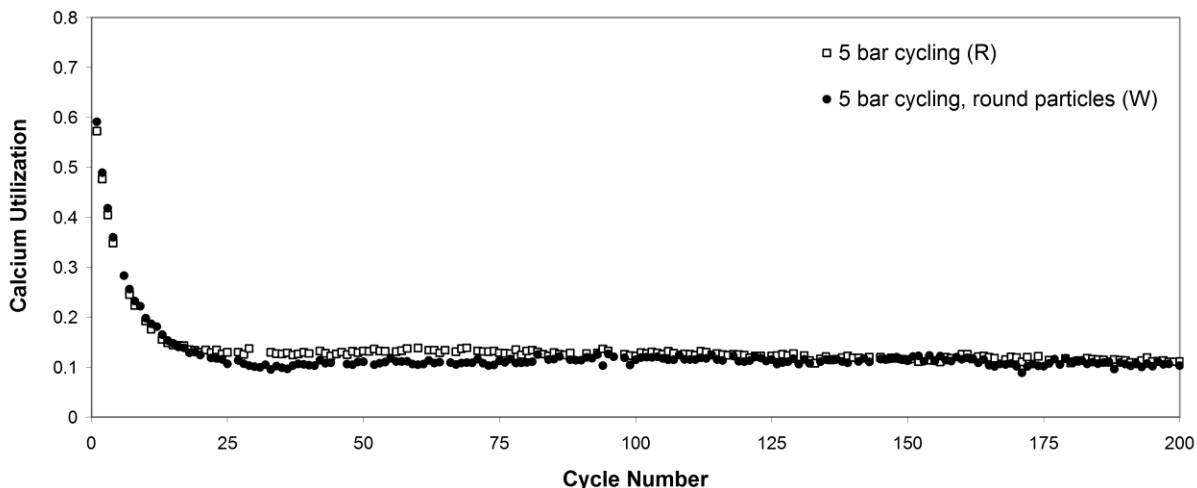


Figure A4.4: Effect of particle shape on 10 bar cycling.

The effect of depressurization time was described in Chapter 2, but a number of the runs presented in the body text was limited in order to highlight the main findings and prevent the results from being too cluttered. Figure A4.5 is a graph of all the runs conducted at 5 bar_g with different de-pressurization times to determine the effect of reactor de-pressurization and demonstrating experimental repeatability. In Figure A4.5, results presented for 22, 30 and 90 s de-pressurization time, represent the average value over two runs for each cycle, with error bars representing the standard deviation between the two. The Results between identical runs agree well, with the largest variation between 20-50 cycles. This is the region where the "dispersed contraction mechanism" described in Chapter 3 causes an increase in the calcium utilization due to elevated sintering. As seen in Figure A4.3, the onset and amplitude of the increase in utilization is affected by parameters such as particle packing and it is expected that the slight variability between runs, in terms of packing, is the cause of the larger variability in the 20-50 cycle range. The two runs with 30 s depressurization time (D & G) had the highest variability in this range.

The results in Figure A4.5 show only a small dependence on the residual utilization and rate of de-pressurization, with a more rapid de-pressurization leading to a slightly higher residual utilization. The more rapid de-pressurization could be opening up more micro pores on the sorbent particle surface, leading to an increased surface area for carbonation.

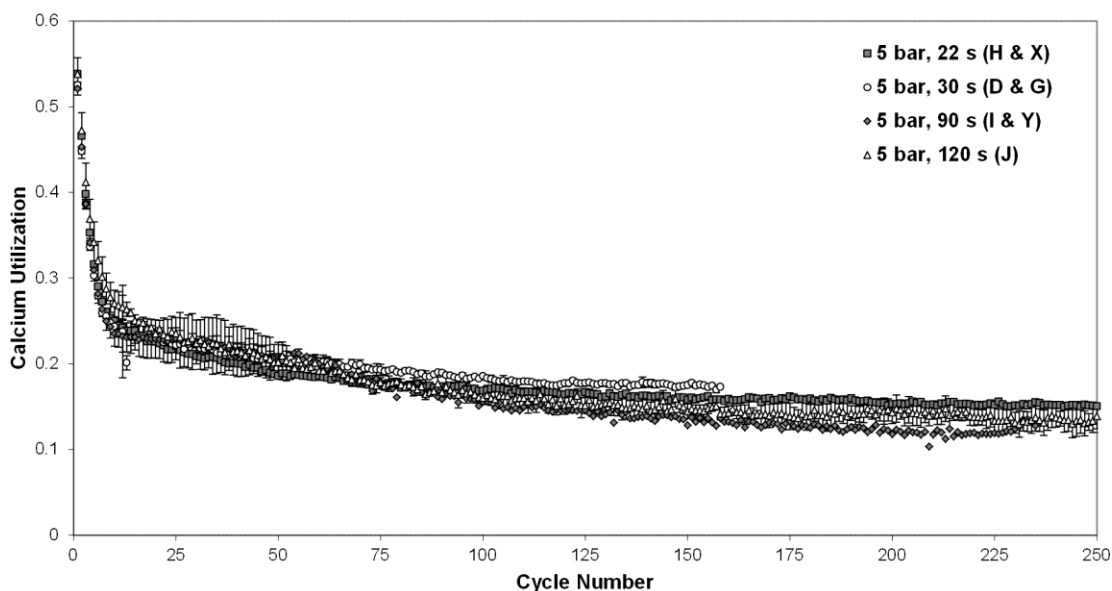


Figure A4.5: Effect of de-pressurization time / rate on 5 bar_g cycling, error bars represent the standard deviation between cycle values for two duplicate runs where available.

To determine if the increased carbonation was the result of the elevated pressure or the act of de-pressurization, a number of carbonation / calcination cycles were conducted by altering the partial pressure of CO₂ within the reactor at constant pressure. The CO₂ partial pressure was altered by stopping the flow of CO₂ and starting the flow of N₂, for calcination. The results for 20 bar_g carbonation pressure show that partial pressure swing (gas switching) at elevated pressure had a much lower utilization after 50 cycles and did not produce the rise in utilization seen in pressure swing cycling, run P in Figure A4.6. This is likely due in part to the de-pressurization of the sorbent particle, in which the rapid escape of CO₂ from the particle could open up micro pores, and generate a greater surface area.

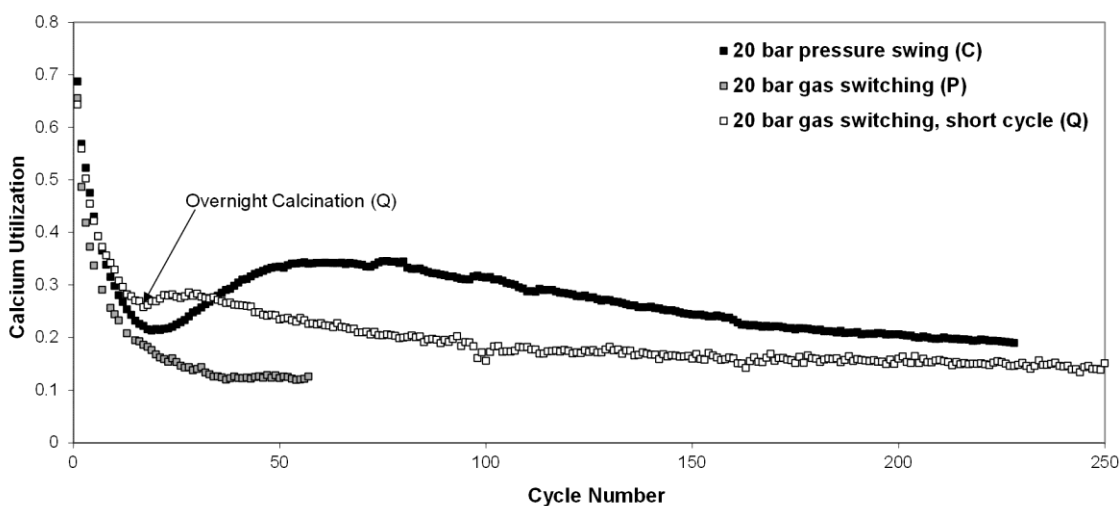


Figure A4.6: Comparison of pressure versus partial pressure swing cycling.

One partial pressure swing run Q, conducted using a shorter cycle time (17 mins), did show a slight increase in utilization following an extended period of calcination. This demonstrates that the rise in utilization is as a result of particle sintering, and the rise was likely the result of the dispersed contraction mechanism, outlined in Chapter 3. The absence of CO₂ during calcination would greatly reduce sintering, and minimize the effect of dispersed contraction in the partial pressure swing runs.

Partial pressure cycling at a constant 5 bar_g pressure also showed poorer utilization than pressure cycling between 0 and 5 bar_g, see Figure A4.7. Again, the absence of CO₂ during calcination appears to reduce / eliminate the beneficial effects of sintering during the calcination stage. The partial pressure cycling (gas switching) at 850°C (run S) showed the highest utilization in the first 50 cycles as the reduced temperature, reduced the detrimental effects of early sintering such as pore coarsening. The residual utilization is also high when partial pressure swing is conducted at a lower temperature. The fact that the residual utilization values for runs J and S are the same is likely coincidence.

The combination of partial pressure swing and pressure swing (run V) showed the same trend as partial pressure swing alone (run S), indicating that the modest rates of de-pressurization in 5 bar_g cycling had no effect on utilization.

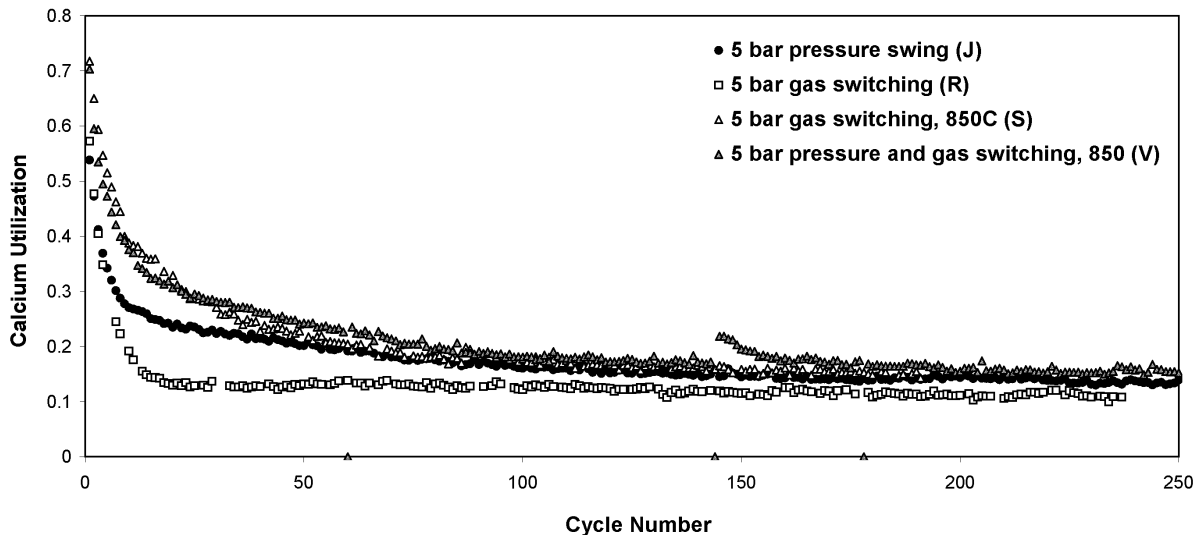


Figure A4.7: Effect of sample size on 10 bar cycling, S12 is a run from the 10 bar snapshot experiments.

The effect of partial pressure swing at different temperatures was also examined. In order to allow for full calcination to occur at lower temperatures, the CO₂ concentration during calcination had to be reduced. Two different CO₂ concentrations during calcination were examined, 20 vol% and 0 vol%, runs U and V respectively, with the balance nitrogen. For run U the gas concentration was held constant during both carbonation and calcination. For run V the gas flow was altered between pure CO₂ for carbonation and pure N₂ for calcination. All runs in Figure A4.6 involved a pressure swing of 5 bar.

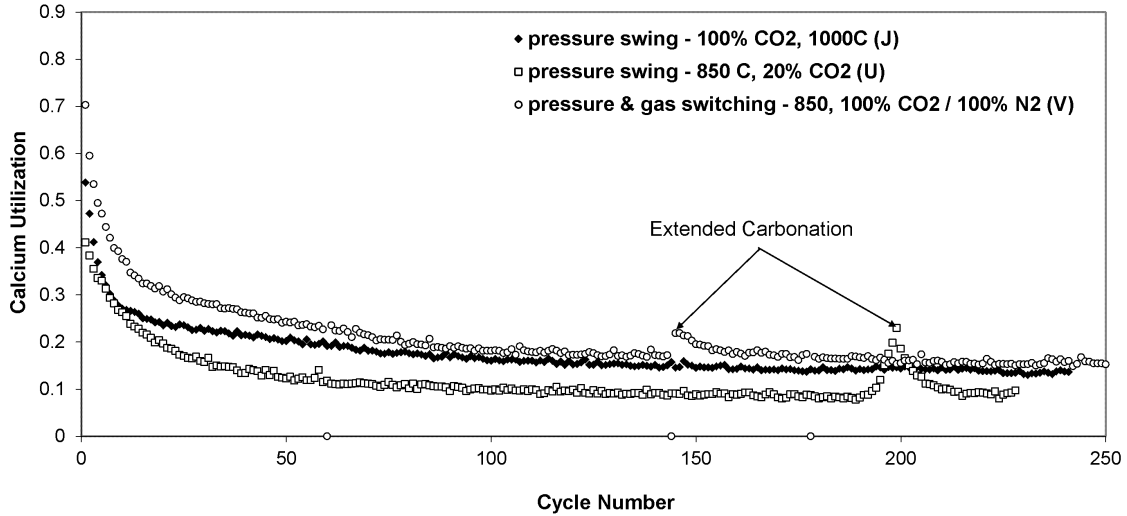


Figure A4.6: Comparison of pressure and partial pressure swing for 5 bar_g cycling.

In runs U and V there were periods of extended carbonation due to a loss of N₂ flow to the reactor, leaving a CO₂ concentration too high for calcination. In the case of run V the carbonation was extended to ~12 h for a single carbonation stage. For run U the duration of calcination decreased to zero over the course of a few cycles, eventually resulting in a 24 h long carbonation. In both cases, the extended carbonation resulted in an increase in calcium utilization, which lasted 10-20 cycles after the extended carbonation.

In an attempt to isolate the particles and reduce or eliminate the effect of bed packing on the utilization results, three runs were conducted using a 1:1 mixture of CaCO₃ and aluminum oxide (Al₂O₃), on a mass basis. The idea was to use the Al₂O₃ particles as inert 'spacers', separating the sorbent particles and reducing the temperature gradient in the bed during carbonation and calcination. The result was a much reduced residual utilization, without the characteristic increase in calcium utilization seen in other high pressure cycling runs, see Figure A4.7.

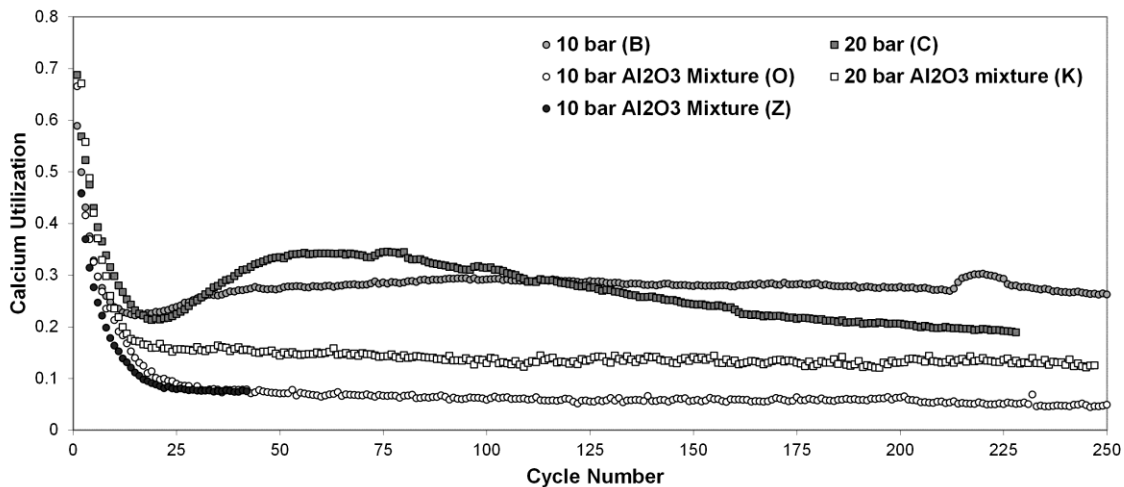


Figure A4.7: Mixing of CaCO₃ sorbent with Al₂O₃ particles.

Examining the SEM micrographs of the sorbent particles, it was found that the sorbent and Al₂O₃ sintered together and formed agglomerates, see Figure A4.8. It has been found that inert compounds Ca₁₂Al₁₄O₃₃ and/or Ca₃Al₂O₆ can be formed when CaO and Al₂O₃ are treated at high temperatures (> 800°C). It is likely that these compounds formed on the surface, reducing the calcium available for CO₂ capture, and giving a lower utilization. The asymptotic utilization was higher for 20 bar_g cycling compared to 10 bar_g, indicating a beneficial effect of pressure; however, this value was similar to that of the 5 bar_g cycling (run A) after 250 cycles. It is also likely that the Al₂O₃ reduced the temperature within the packed bed. This would explain the absence of the rise in utilization experienced by the other high pressure runs, as sintering would be reduced and the mechanism of dispersed contraction eliminated.

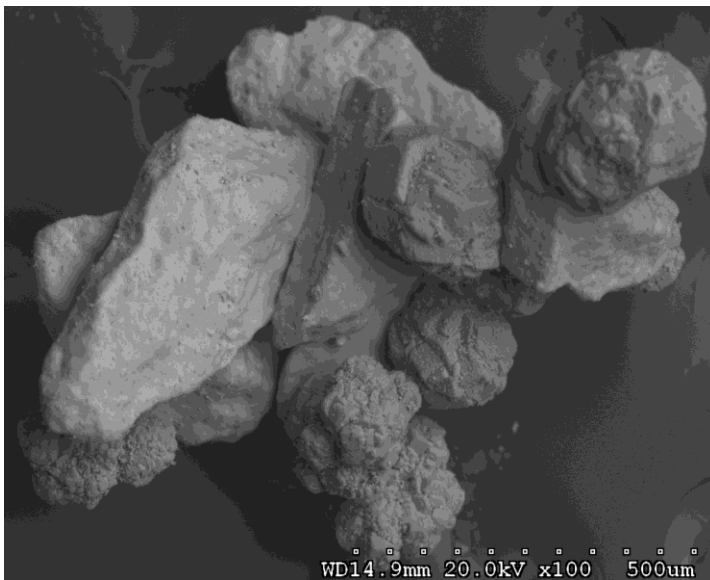


Figure A4.8: SEM micrograph of CaO and Al₂O₃ particle agglomerate.

The effect of particle size was also examined in a series of low cycle number experiments, see Figure A4.9. The effect of particle size on calcium utilization was minimal, with the utilization of all particle sizes converging before 50 cycles. Initially, <5 cycles the largest particle size gives the highest utilization. When examined using SEM, the 'fresh' CaCO₃ particles have a large number of fines on the particle surface, likely attached by electrostatic forces. These fines would provide an increase in the surface area in the first few cycles before sintering rapidly eliminates them, due to their high surface energy. The larger particles may have larger electrostatic forces, holding more fines per mass of sorbent. This would explain the initial higher utilization in first five cycles.

Between 5 and 40 cycles there is a slight benefit to using smaller particles. This is like the result of the plugging of micro pores on the sorbent particle surface, blocking access to the CaO in the particle interior, due to the formation of the larger molecular volume CaCO₃. The smaller particles would have a higher specific, exterior surface area and would be less affected by pore closure. This effect is short lasting, and after 50 cycles the surface pores have likely become coarse enough to eliminate the initial blocking effect.

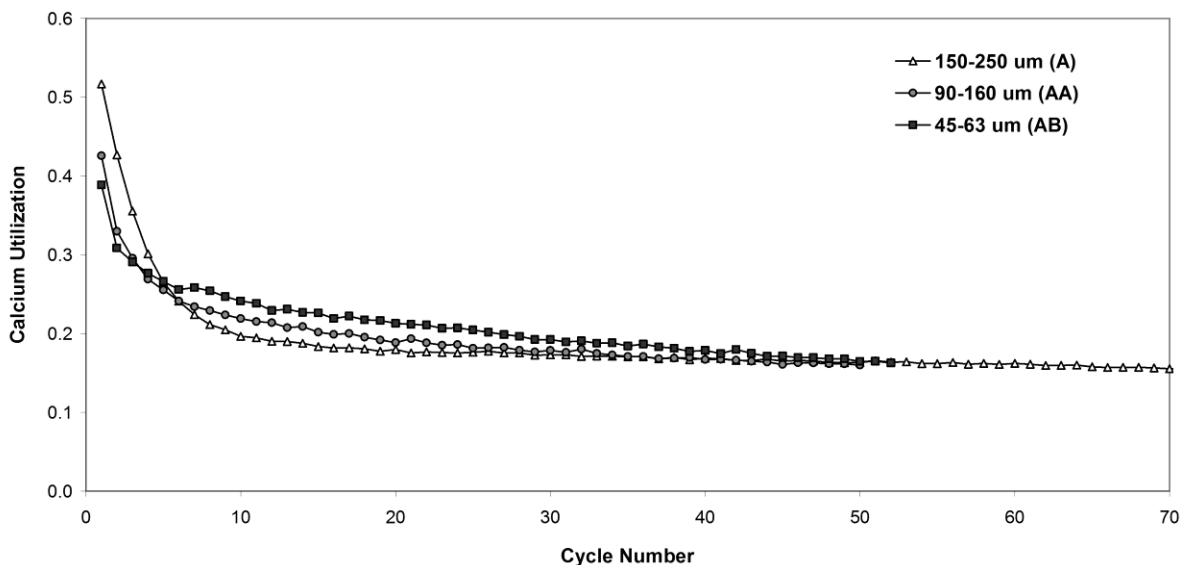


Figure A4.9: Effect of particle size on 5 bar_g cycling.

The effect of carbonation time on calcium utilization can also be examined by comparing runs A and J, with similar de-pressurization rates of 2 bar/min and 2.5 bar/min, respectively. It can be seen in Figure A4.10 that a shorter carbonation time had the effect of increasing the utilization within the first 100 cycles, after which time the utilization becomes the same for both runs. This is the result of decreased initial stage sintering, pore coarsening and rapid surface area loss, that occurs during the high temperature carbonation stage. It has been found in past studies and demonstrated above in Figure A4.6

that an extended carbonation can increase the utilization and even re-activate the sorbent somewhat; however, the incremental increase of carbonation time by 13 minutes was not enough to offset the impact of initial stage sintering. After 150 cycles, the utilization for each run is nearly the same as the initial sintering is nearly finished for both runs.

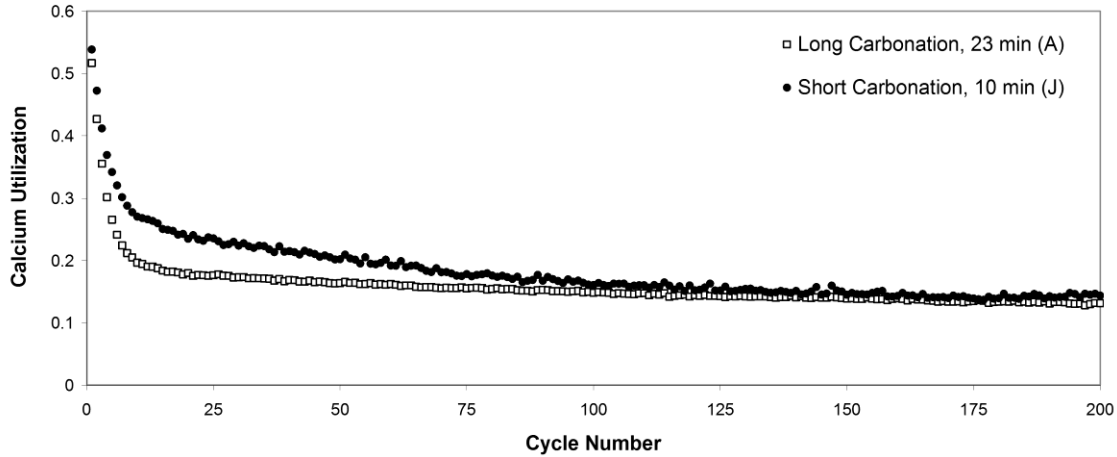


Figure A4.10: Effect of carbonation duration on 5 bar_g cycling, .

Due to the increase in carbonation duration, the sorbent was in the reactor at for a longer period of time. To determine if this was the reason behind the decrease in utilization, the utilization was plotted against residence time in the reactor, see Figure A4.11. It can be seen that the lower utilization seen in run A in the early cycles is a result of more that simply additional time at elevated temperature, but is the result of additional carbonation time. This suggests that the sintering occurring during carbonation is important in pore coarsening and loss of surface area in the initial stages of sintering. After 40 h (2400 min) in the reactor, the effect of longer carbonation was diminished and cycles with similar de-pressurization time showed similar utilizations.

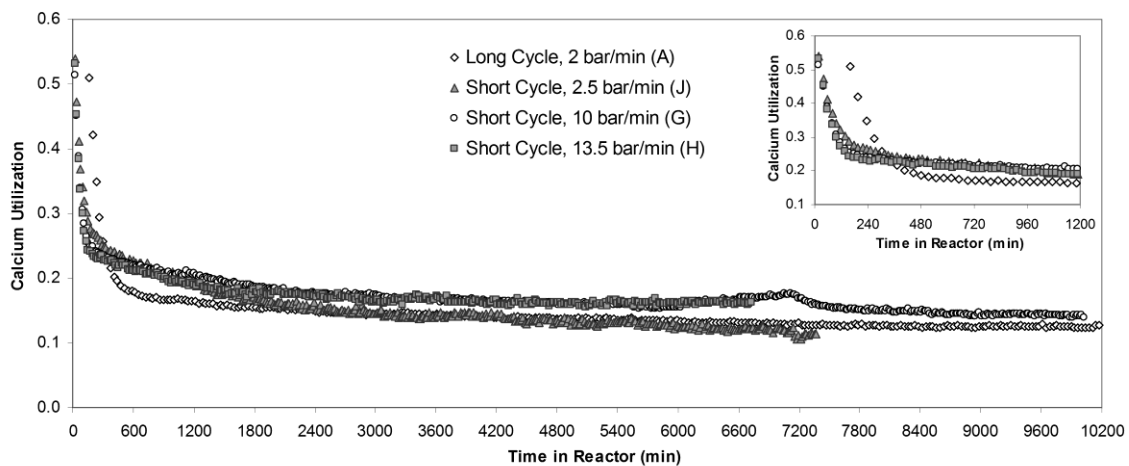
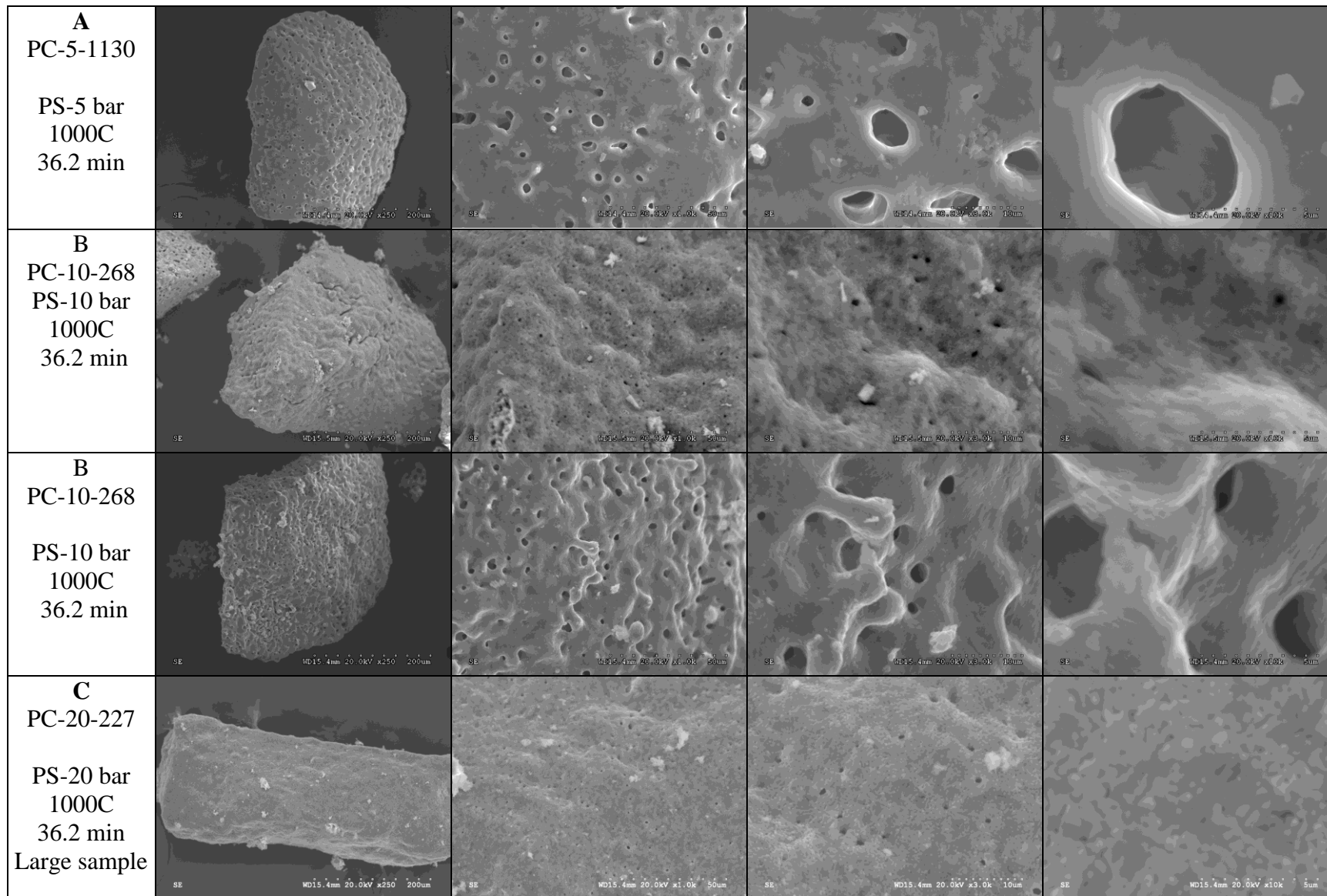


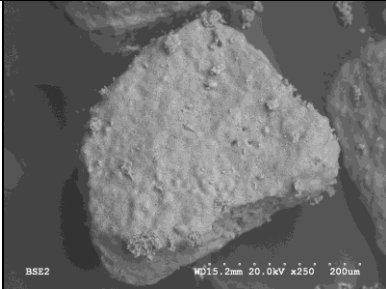
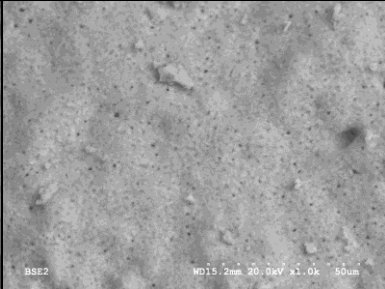
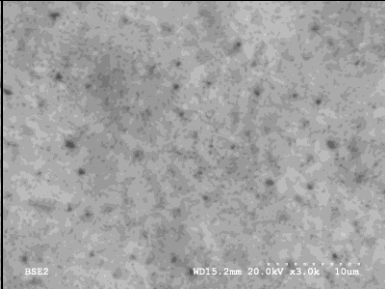
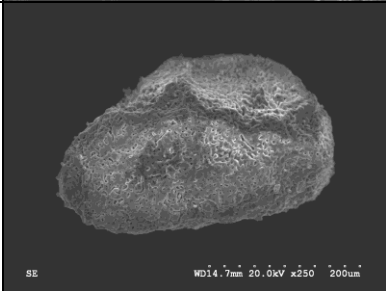
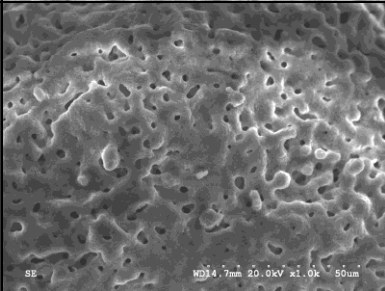
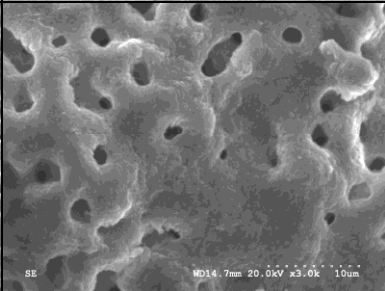
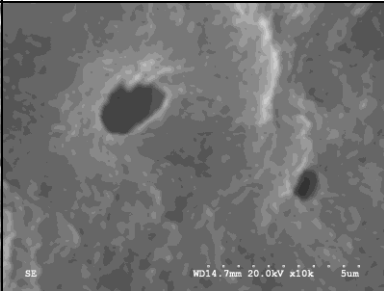
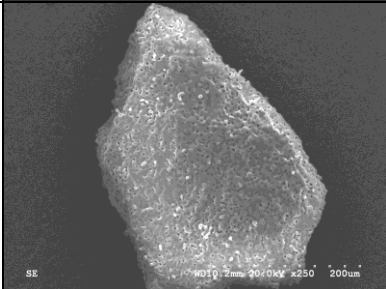
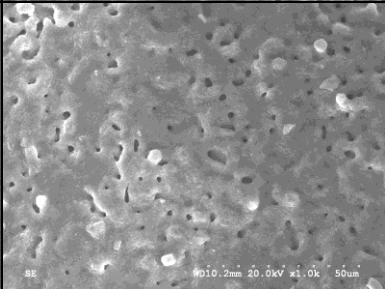
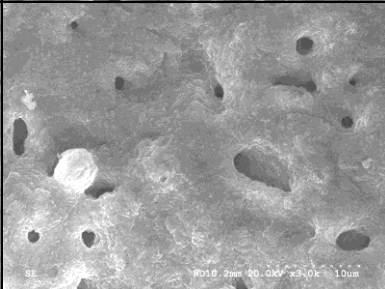
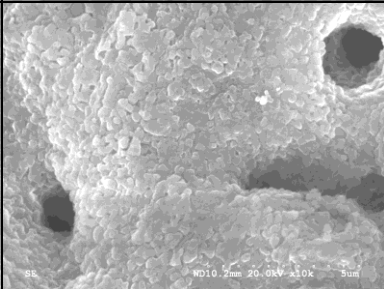
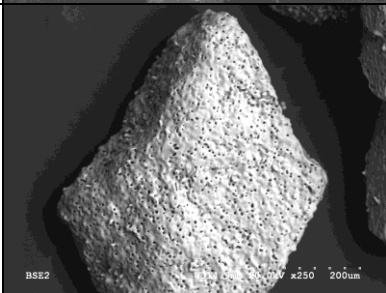
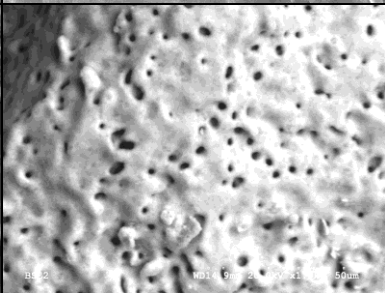
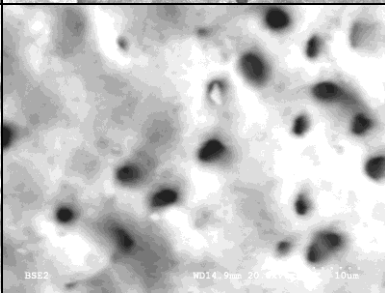
Figure A4.11: Decay in utilization with time in reactor, 5 bar_g pressure swing cycling.

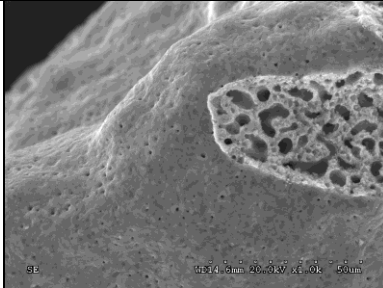
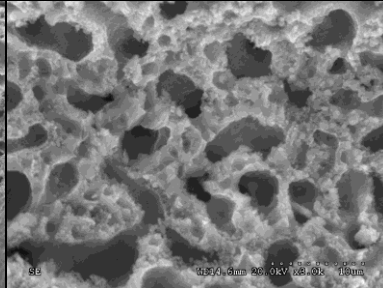
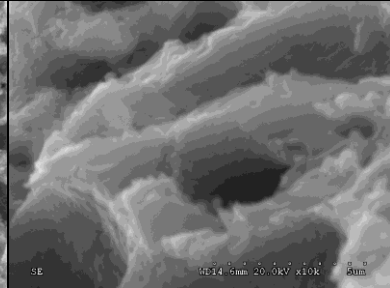
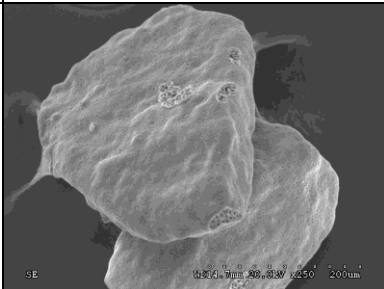
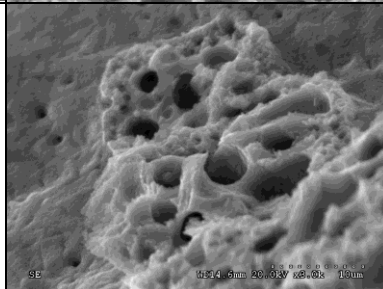
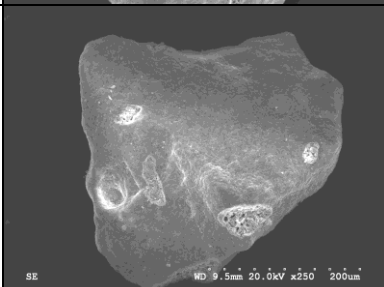
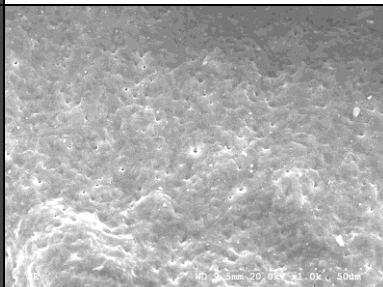
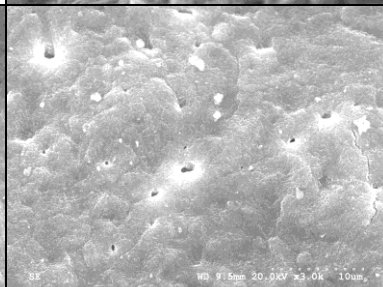
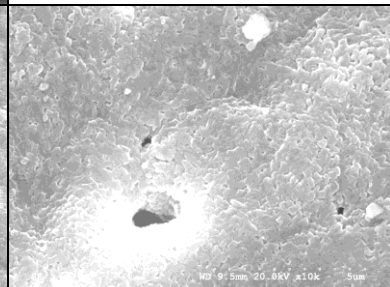
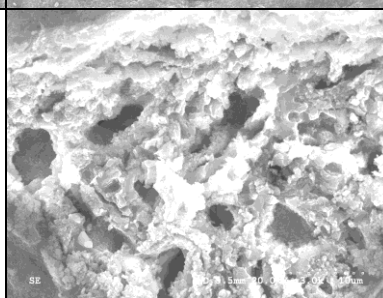
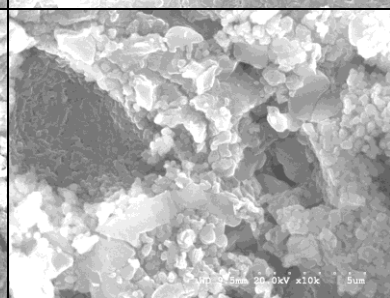
Appendix 5: SEM Micrographs of PTGA Runs

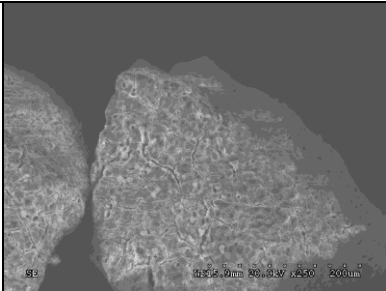
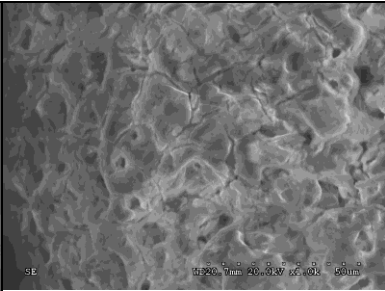
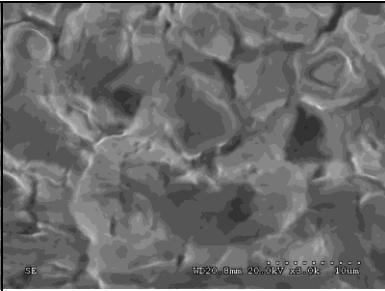
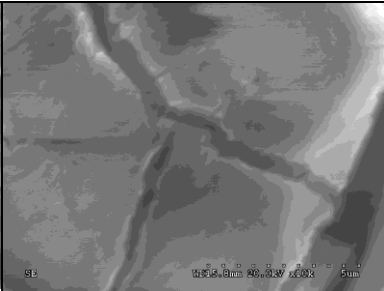
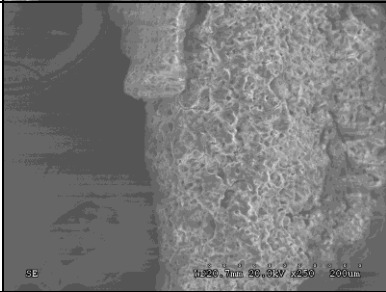
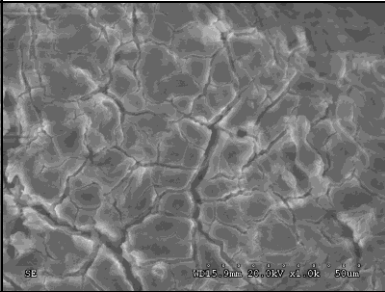
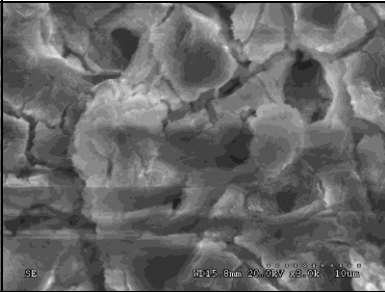
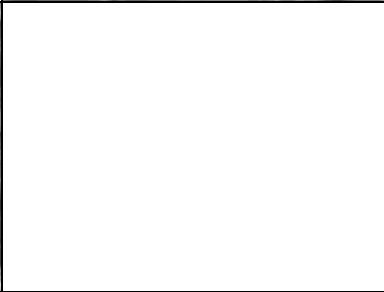
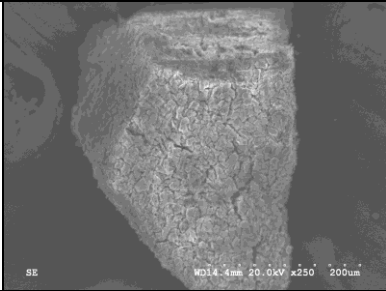
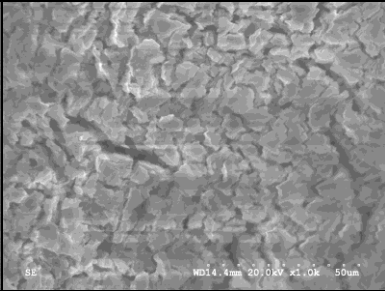
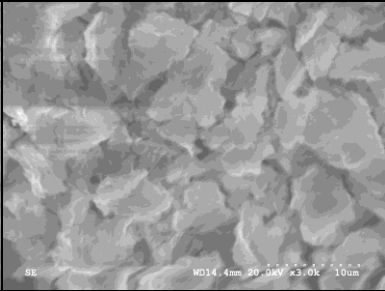
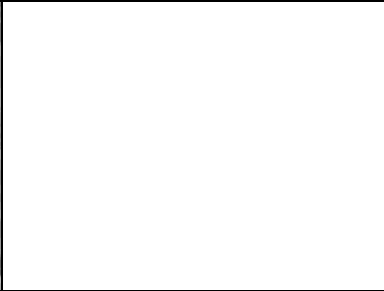
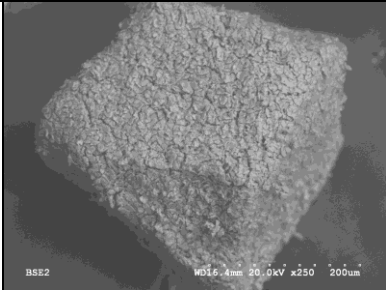
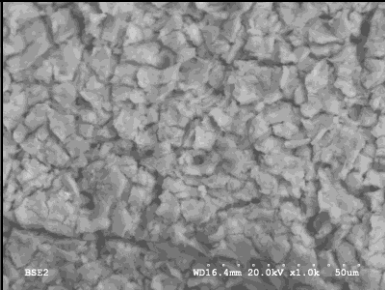
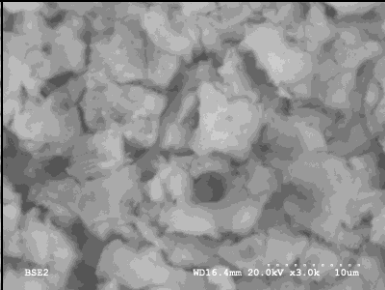
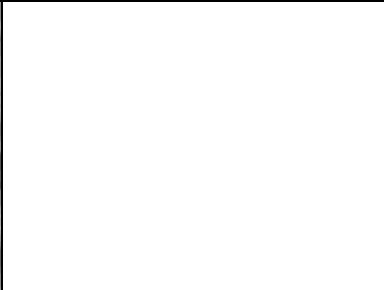
Table A5.1: SEM micrographs of exterior of sorbent particles from cycling at different conditions, sorted by sample index. Samples are indexed as follows: Cycling Type – Pressure or Temperature of Cycling – Number of Cycles, PC = pressure swing cycling, PCF = fast pressure swing cycling, GS = gas switching cycling. The total cycle time is given in minutes.

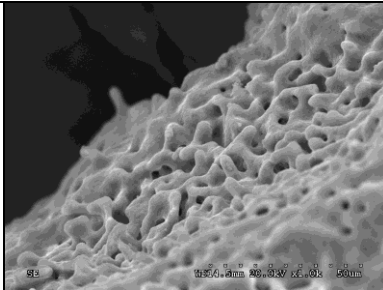
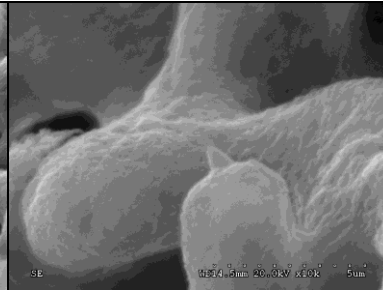
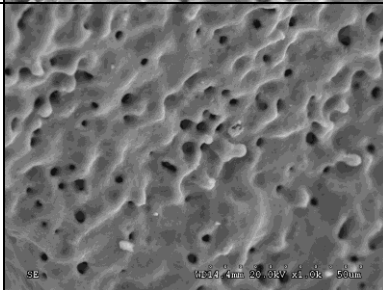
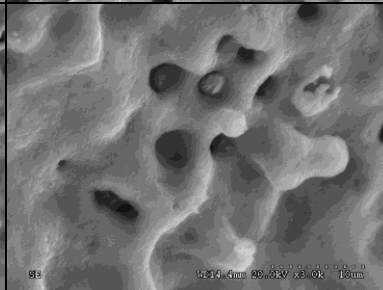
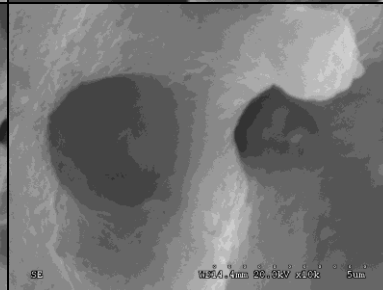
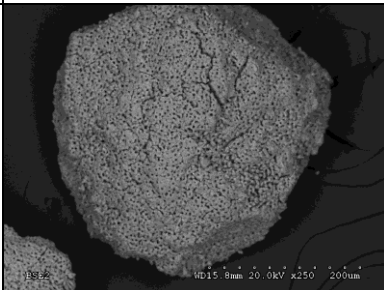
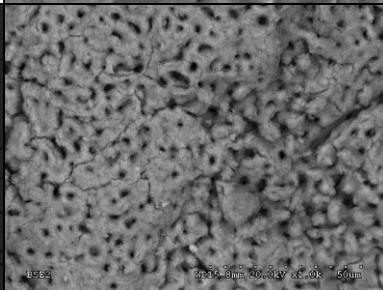
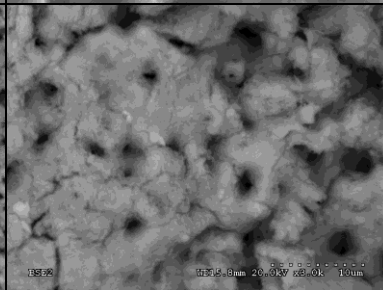
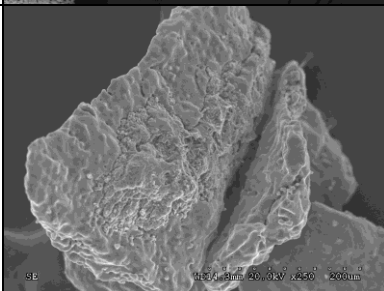
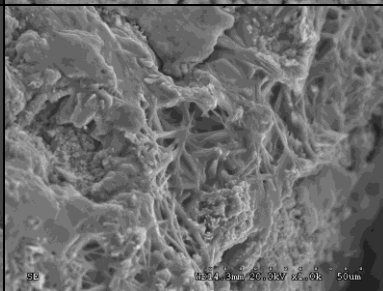
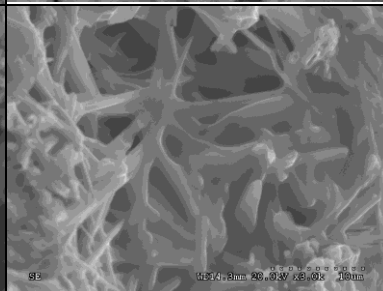
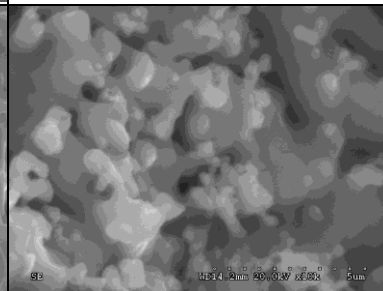
	250x	1000x	3000x	10,000x
Raw Limestone				
Calcined Limestone				
Calcined Limestone				

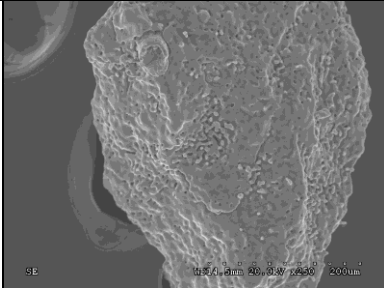
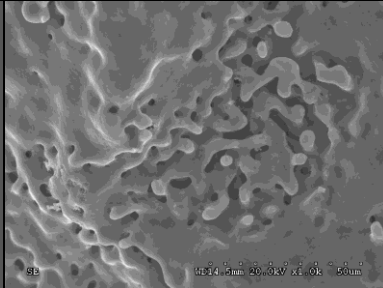
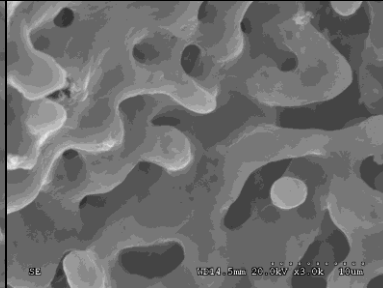
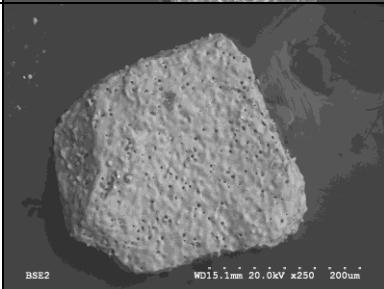
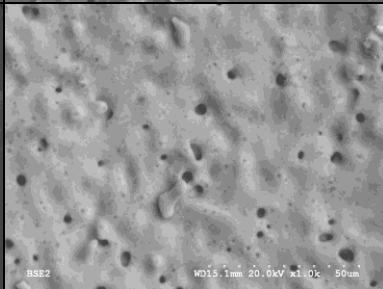
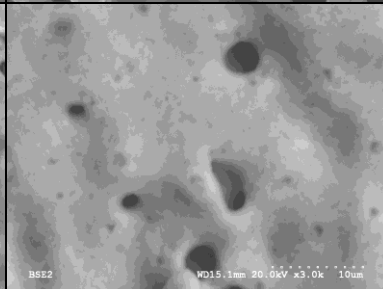
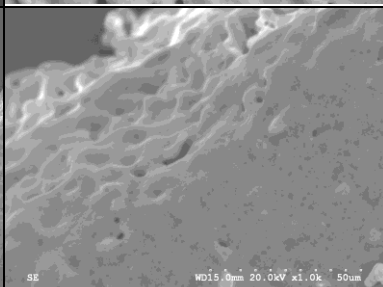
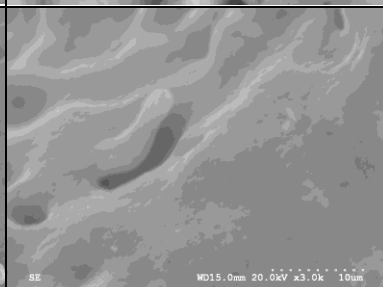
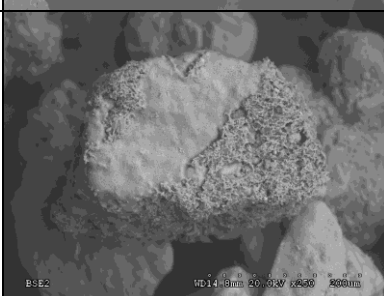
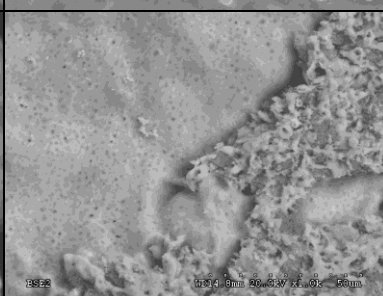
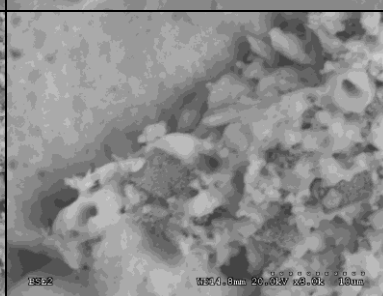


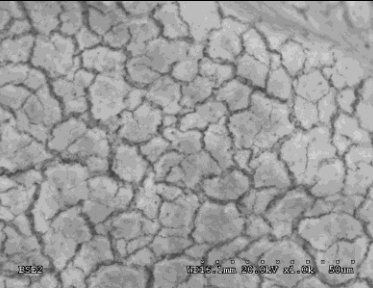
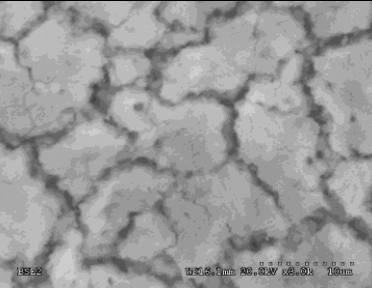
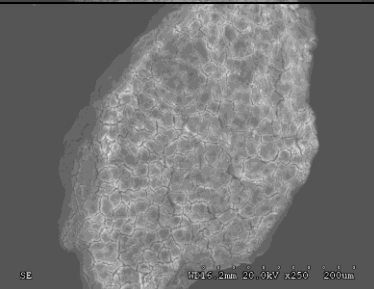
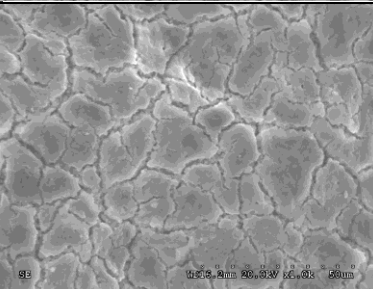
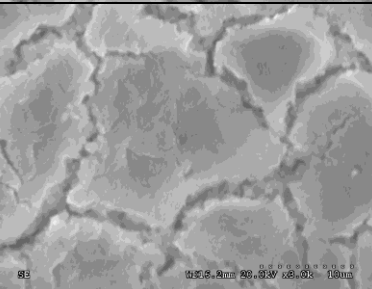
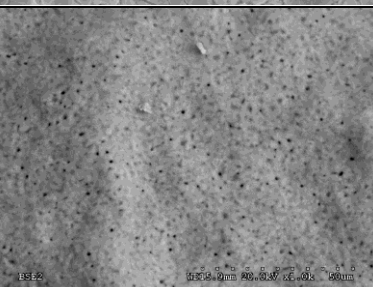
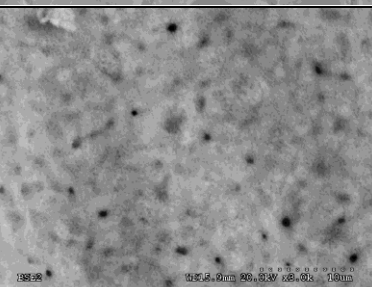
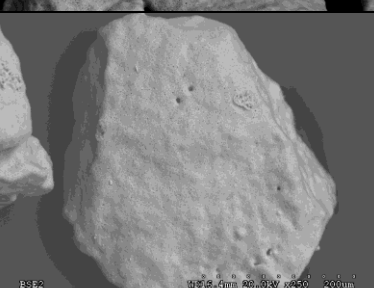
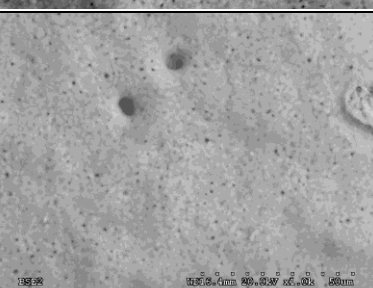
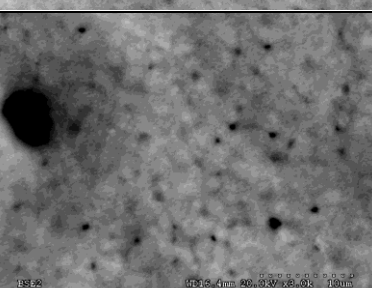
<p>C PC-20-227</p> <p>PS-20 bar 1000C 36.2 min Large</p>	 <p>BSE2 MD15.2mm 20.0kV x250 200um</p>	 <p>BSE2 MD15.2mm 20.0kV x1.0k 50um</p>	 <p>BSE2 MD15.2mm 20.0kV x3.0k 10um</p>	
<p>D PCF-5-173</p> <p>PS-5 bar 1000C 19 min 10 bar/min</p>	 <p>SE MD14.7mm 20.0kV x250 200um</p>	 <p>SE MD14.7mm 20.0kV x1.0k 50um</p>	 <p>SE MD14.7mm 20.0kV x3.0k 10um</p>	 <p>SE MD14.7mm 20.0kV x10k 5um</p>
<p>D PCF-5-173</p> <p>PS-5 bar 1000C 19 min 10 bar/min</p>	 <p>SE MD10.2mm 20.0kV x250 200um</p>	 <p>SE MD10.2mm 20.0kV x1.0k 50um</p>	 <p>SE MD10.2mm 20.0kV x3.0k 10um</p>	 <p>SE MD10.2mm 20.0kV x10k 5um</p>
<p>D PCF-5-173</p> <p>PS-5 bar 1000C 19 min 10 bar/min</p>	 <p>BSE2 MD14.9mm 20.0kV x250 200um</p>	 <p>BSE2 MD14.9mm 20.0kV x1.0k 50um</p>	 <p>BSE2 MD14.9mm 20.0kV x3.0k 10um</p>	

<p>E PC-20-280</p> <p>PS-20 bar 1000C 36.2 min Small</p>				
<p>E PC-20-280</p> <p>PS-20 bar 1000C 36.2 min Small</p>				
<p>F PC-20-320</p> <p>PS-20 bar 1000C 36.2 min Medium</p>				
<p>F PC-20-320</p> <p>PS-20 bar 1000C 36.2 min Medium</p>				

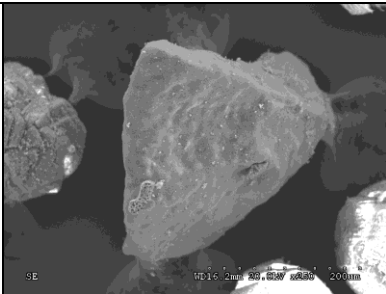
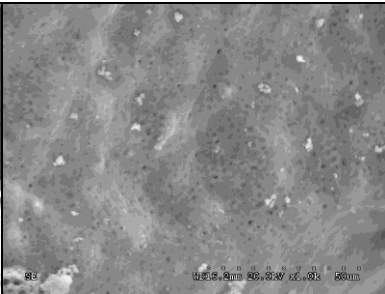
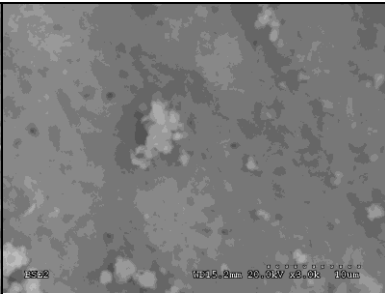
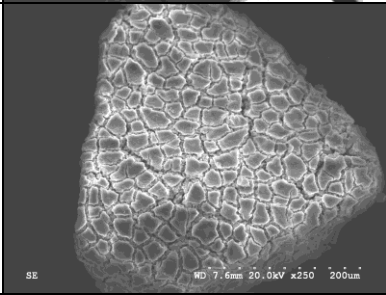
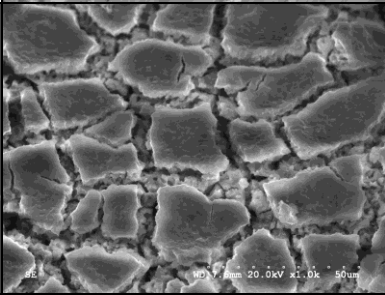
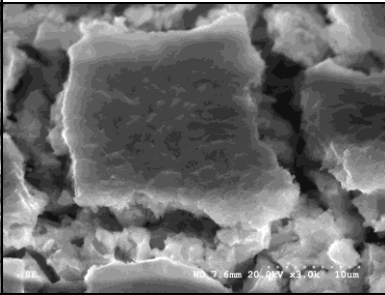
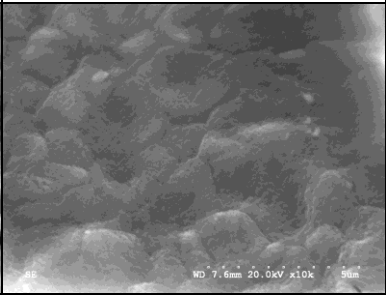
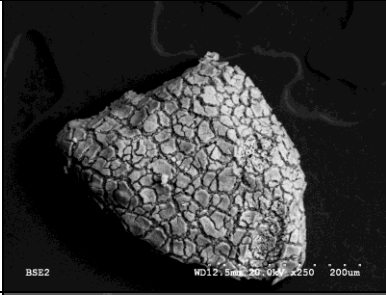
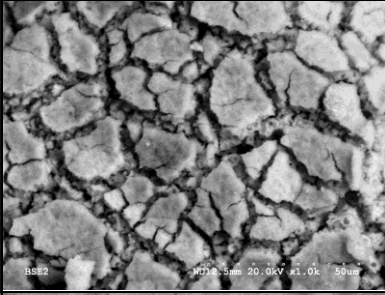
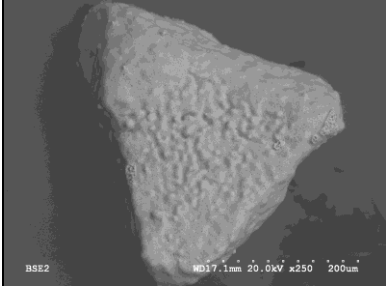
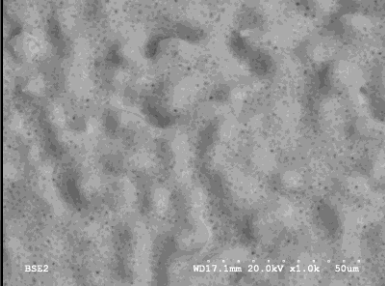
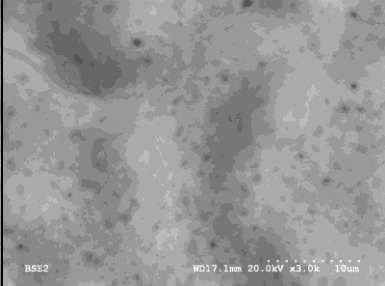
<p>G PCF-5-500</p> <p>PS-5 bar 1000C 19.5 min 10 bar/min</p>				
<p>G PCF-5-500</p> <p>PS-5 bar 1000C 19.5 min 10 bar/min</p>				
<p>G PCF-5-500</p> <p>PS-5 bar 1000C 19.5 min 10 bar/min</p>				
<p>G PCF-5-500</p> <p>PS-5 bar 1000C 19.5 min 10 bar/min</p>				

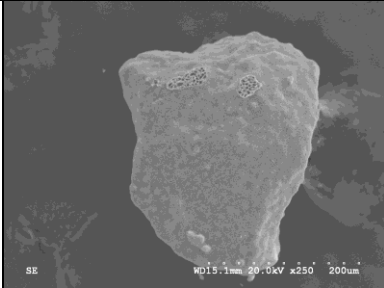
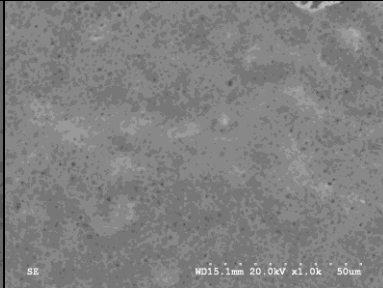
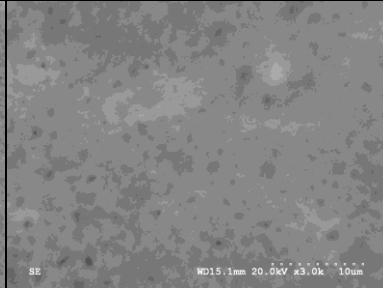
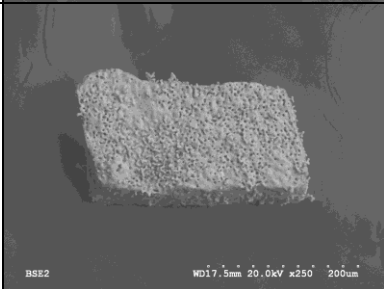
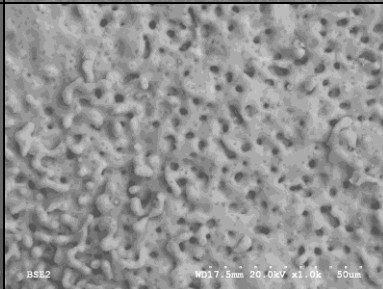
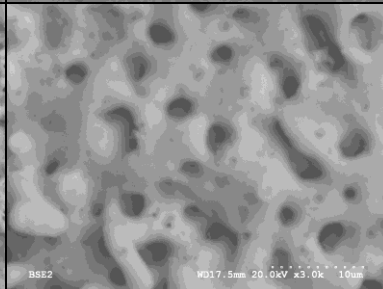
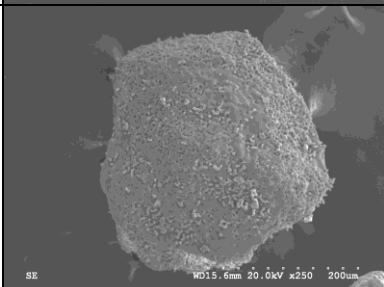
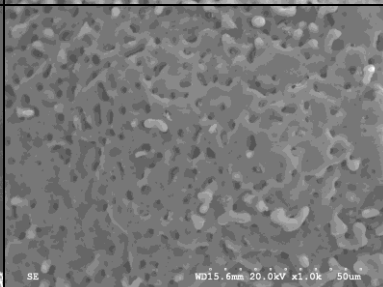
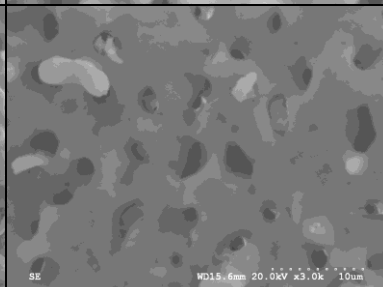
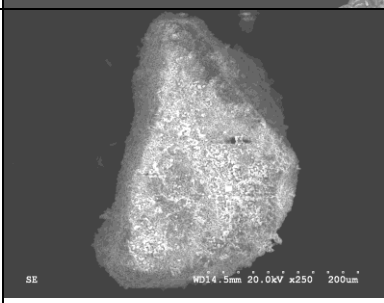
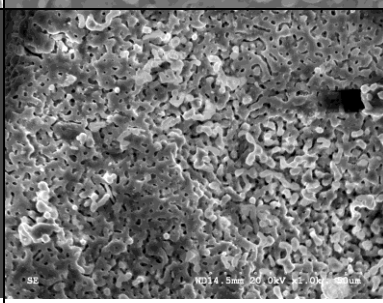
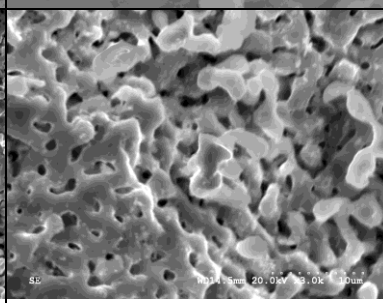
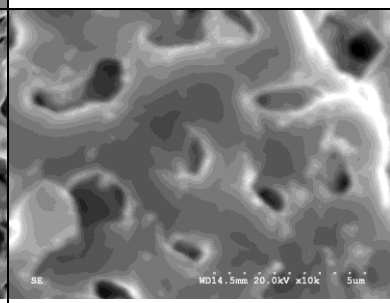
<p>H PCF-5-345</p> <p>PS-5 bar 1000C 19.5 min 13.6 bar/min</p>				
<p>H PCF-5-345</p> <p>PS-5 bar 1000C 19.5 min 13.6 bar/min</p>				
<p>I PCF-5-69</p> <p>PS-5 bar 1000C 19 min 3.3 bar/min</p>				
<p>J PCF-5-378</p> <p>PS-5 bar 1000C 19.5 min 2.5 bar/min</p>				

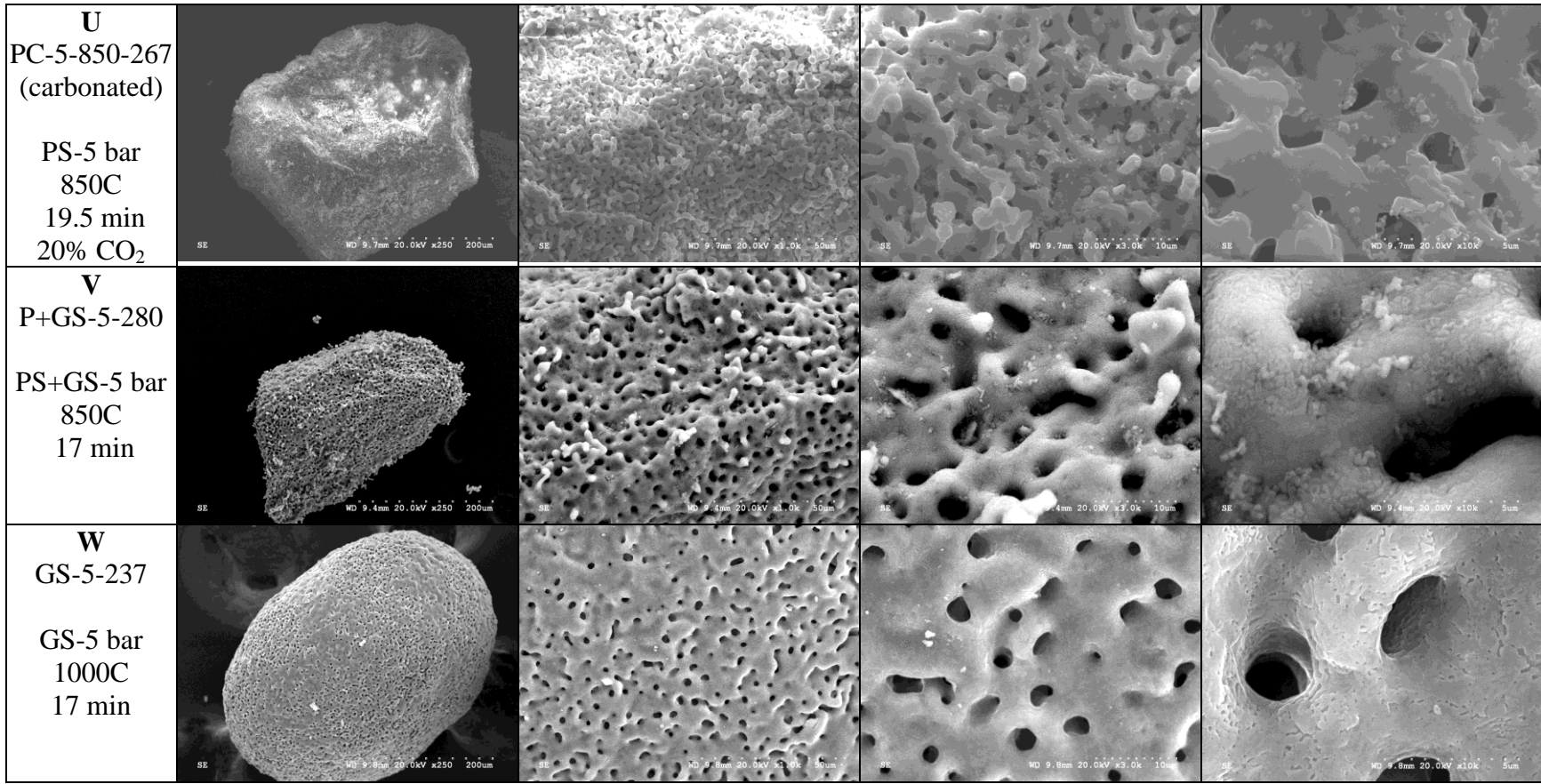
<p>J PCF-5-378</p> <p>PS-5 bar 1000C 19.5 min 2.5 bar/min</p>				
<p>J PCF-5-C-378 (calcined)</p> <p>PS-5 bar 1000C 19.5 min 2.5 bar/min</p>				
<p>J PCF-5-C-378 (calcined)</p> <p>PS-5 bar 1000C 19.5 min 2.5 bar/min</p>				
<p>K PCM-20-269</p> <p>PS-20 bar 1000C 35.2 min CaO-Al₂O₃</p>				

<p>M PC-20-254 Interior</p> <p>PS-20 bar 1000C 35.2 min</p>				
<p>M PC-20-254 Interior</p> <p>PS-20 bar 1000C 35.2 min</p>				
<p>M PC-20-254 Bulk</p> <p>PS-20 bar 1000C 35.2 min</p>				
<p>M PC-20-254 Exterior</p> <p>PS-20 bar 1000C 35.2 min</p>				

<p>N PC-20-282o Exterior</p> <p>PS-20 bar 1000C 35.2 min</p>				
<p>N PC-20-282o Exterior</p> <p>PS-20 bar 1000C 35.2 min</p>				
<p>N PC-20-282i Interior</p> <p>PS-20 bar 1000C 35.2 min</p>				
<p>N PC-20-282i Interior</p> <p>PS-20 bar 1000C 35.2 min</p>				

<p>O PCM-10-275</p> <p>PS-20 bar 1000C 36.2 min CaO-Al₂O₃</p>				
<p>P GS-20-100 (hydrated?)</p> <p>GS-20 bar 1000C 35.2 min</p>				
<p>P GS-20-100 (hydrated?)</p> <p>GS-20 bar 1000C 35.2 min</p>				
<p>Q GS-20-252</p> <p>GS-20 bar 1000C 17 min</p>				

<p>Q GS-20-252</p> <p>GS-20 bar 1000C 17 min</p>	 <p>SE WD15.1mm 20.0kV x250 200um</p>	 <p>SE WD15.1mm 20.0kV x1.0k 50um</p>	 <p>SE WD15.1mm 20.0kV x3.0k 10um</p>	
<p>R GS-5-258</p> <p>GS-5 bar 1000C 17 min</p>	 <p>BSE2 WD17.5mm 20.0kV x250 200um</p>	 <p>BSE2 WD17.5mm 20.0kV x1.0k 50um</p>	 <p>BSE2 WD17.5mm 20.0kV x3.0k 10um</p>	
<p>R GS-5-258</p> <p>GS-5 bar 1000C 17 min</p>	 <p>SE WD15.6mm 20.0kV x250 200um</p>	 <p>SE WD15.6mm 20.0kV x1.0k 50um</p>	 <p>SE WD15.6mm 20.0kV x3.0k 10um</p>	
<p>U PC-5-850-267 (carbonated)</p> <p>PS-5 bar 850C 19.5 min 20% CO₂</p>	 <p>SE WD14.5mm 20.0kV x250 200um</p>	 <p>SE WD14.5mm 20.0kV x1.0k 50um</p>	 <p>SE WD14.5mm 20.0kV x3.0k 10um</p>	 <p>SE WD14.5mm 20.0kV x10k 5um</p>



Appendix 6: Cycling Snapshot Data

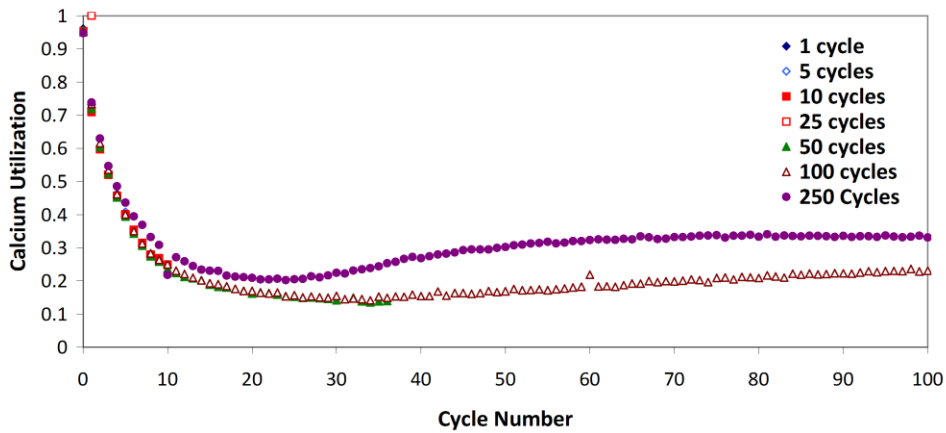


Figure A6.1: 10 bar cycling snapshots, calcium utilization

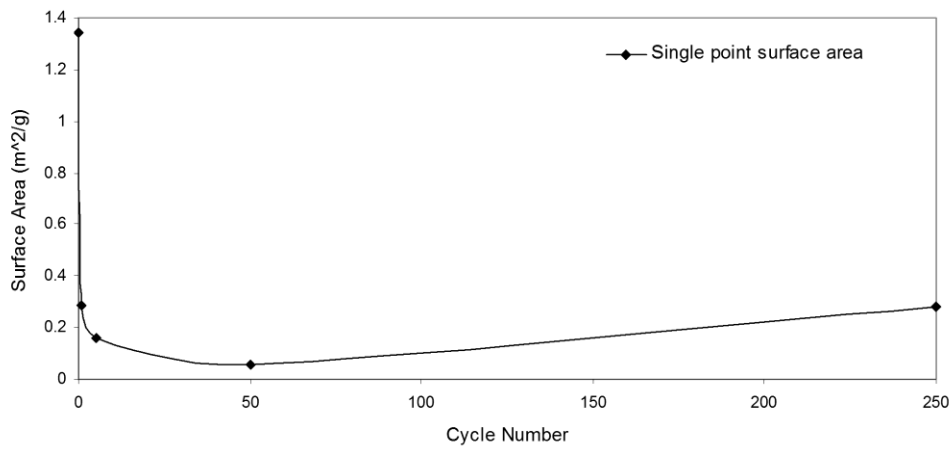


Figure A6.2: 10 bar cycling snapshots, surface area

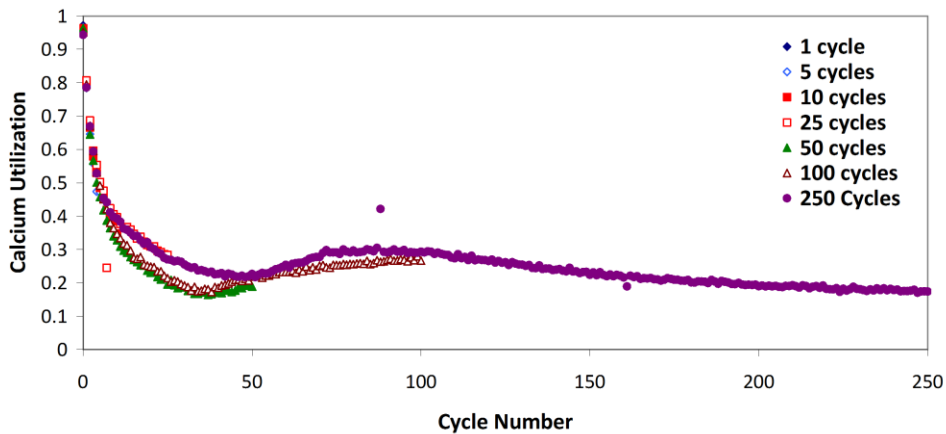


Figure A6.3: 20 bar cycling snapshots, calcium utilization

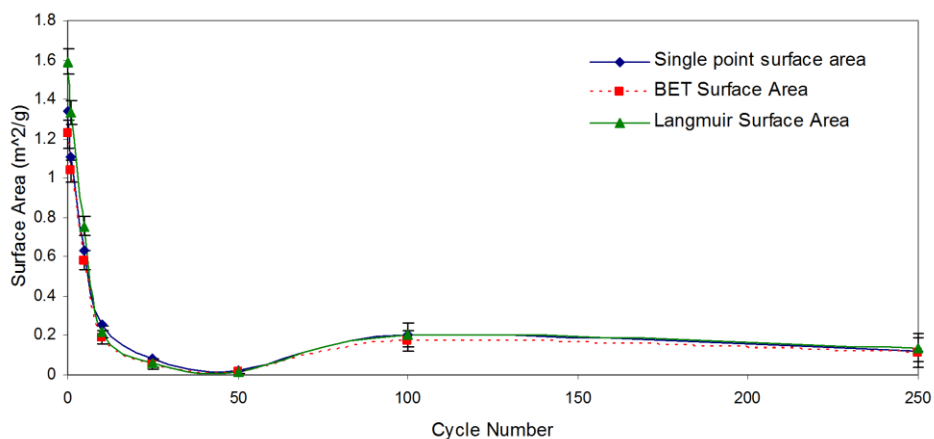


Figure A6.4: 20 bar cycling snapshots, surface area

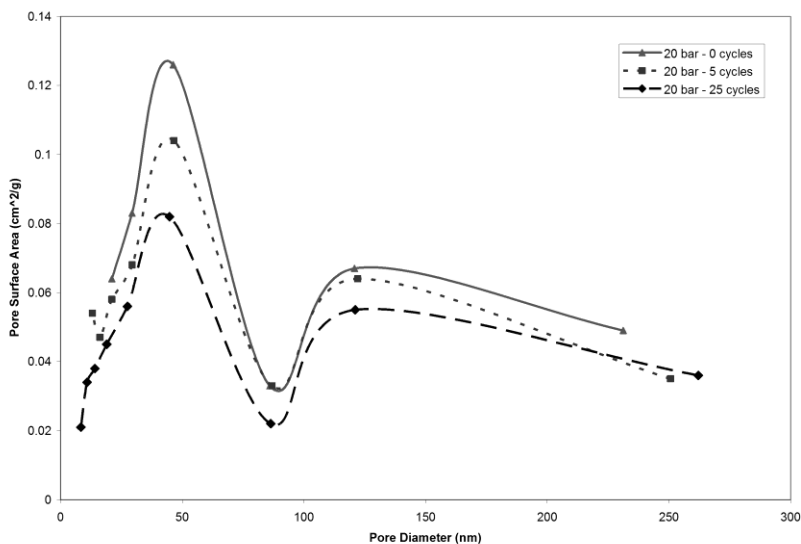


Figure A6.5: 20 bar cycling, BJH pore surface area

Table A6.1: Pressure cycling ‘snapshot’ experimental conditions

Run	Description	Particle Size (µm)	Cycle Time (min)	Carbonation				Calcination				Depressurization		Number of Cycles	Sample Mass (mg)
				P (bar)	t (min)	T (°C)	Gas Flow	P (bar)	t (min)	T (°C)	Gas Flow	Time (s)	Rate (bar/min)		
S1	20 bar snapshot, 25 cycles	180-250	35.16	20	25.75	1000	100% CO2	0	~10	1000	100% CO2	150	8	25	151.6
S2	20 bar snapshot, 1 cycle	180-250	35.16	20	25.75	1000	100% CO2	0	~10	1000	100% CO2	150	8	1	150.0
S3	20 bar snapshot, 5 cycles	180-250	35.16	20	25.75	1000	100% CO2	0	~10	1000	100% CO2	150	8	5	151.1
S4	20 bar snapshot, 50 cycles	180-250	35.16	20	25.75	1000	100% CO2	0	~10	1000	100% CO2	150	8	50	153.6
S5	20 bar snapshot, 10 cycles	180-250	35.16	20	25.75	1000	100% CO2	0	~10	1000	100% CO2	150	8	10	151.8
S6	20 bar snapshot, 100 cycles	180-250	35.16	20	25.75	1000	100% CO2	0	~10	1000	100% CO2	150	8	100	154.5
S7	20 bar snapshot, 5 cycles	180-250	35.16	20	25.75	1000	100% CO2	0	~10	1000	100% CO2	150	8	5	159.6
S8	20 bar snapshot, 25 cycles	180-250	35.16	20	25.75	1000	100% CO2	0	~10	1000	100% CO2	150	8	25	151.9
S9	20 bar snapshot, 25 cycles	180-250	35.16	20	25.75	1000	100% CO2	0	~10	1000	100% CO2	150	8	25	150.0
S10	20 bar snapshot, 250 cycles	180-250	35.16	20	25.75	1000	100% CO2	0	~10	1000	100% CO2	150	8	250	162.9
S11	20 bar snapshot, 0 cycles	180-250	35.16	20	25.75	1000	100% CO2	0	~10	1000	100% CO2	150	8	0	150.4
S12	10 bar snapshot, 250 cycles	180-250	35.16	10	24.5	1000	100% CO2	0	~10	1000	100% CO2	150	4	250	153.2
S13	10 bar snapshot, 25 cycles	180-250	35.16	10	24.5	1000	100% CO2	0	~10	1000	100% CO2	150	4	25	151.7
S14	10 bar snapshot, 5 cycles	180-250	35.16	10	24.5	1000	100% CO2	0	~10	1000	100% CO2	150	4	5	150.1
S15	10 bar snapshot, 10 cycles	180-250	35.16	10	24.5	1000	100% CO2	0	~10	1000	100% CO2	150	4	10	152.5
S16	10 bar snapshot, 1 cycle	180-250	35.16	10	24.5	1000	100% CO2	0	~10	1000	100% CO2	150	4	1	160.3
S17	10 bar snapshot, 50 cycles	180-250	35.16	10	24.5	1000	100% CO2	0	~10	1000	100% CO2	150	4	50	150.5
S18	10 bar snapshot, 83 cycles	180-250	35.16	10	24.5	1000	100% CO2	0	~10	1000	100% CO2	150	4	83	150.3
S19	10 bar snapshot, 100 cycles	180-250	35.16	10	24.5	1000	100% CO2	0	~10	1000	100% CO2	150	4	100	149.0
S20	10 bar snapshot, 0 cycles	180-250	35.16	10	24.5	1000	100% CO2	0	~10	1000	100% CO2	150	4	0	147.7

Appendix 7: SEM Micrographs of 10 bar Snapshot

Table A7.1: SEM micrographs of exterior of sorbent particles after different cycle numbers. See appendix 5 for description of sample index.

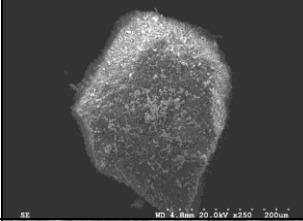
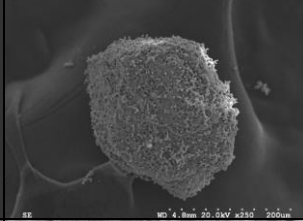
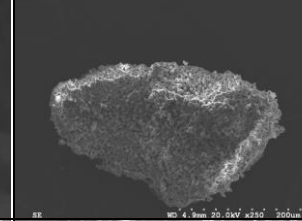
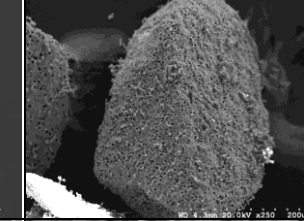
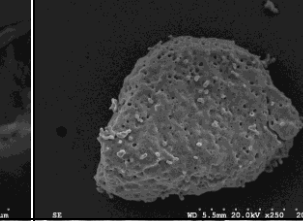
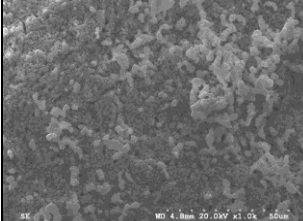
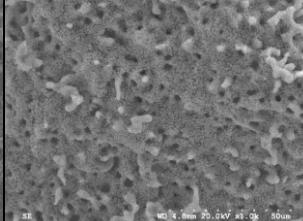
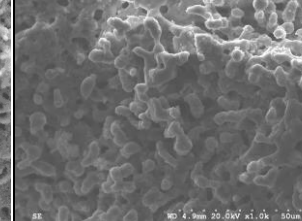
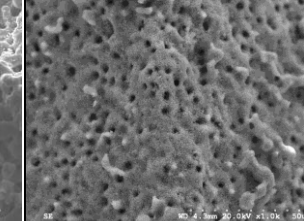
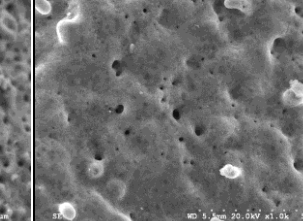
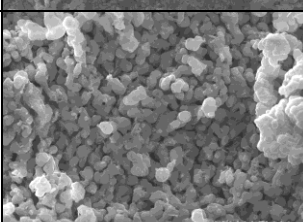
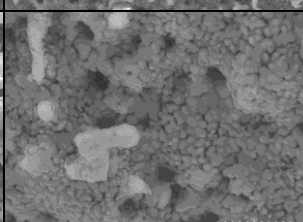
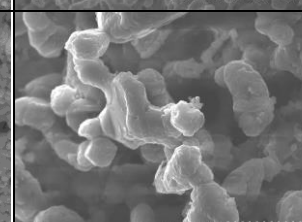
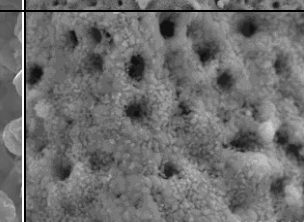
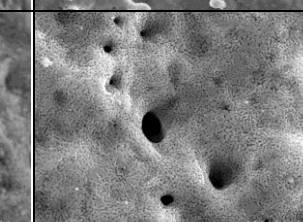
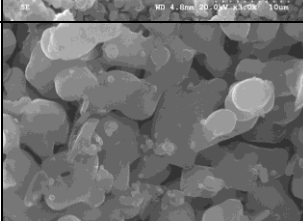
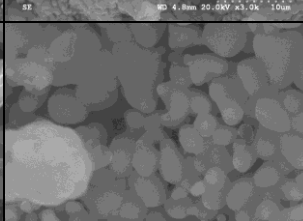
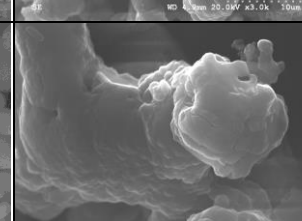
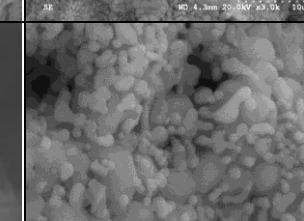
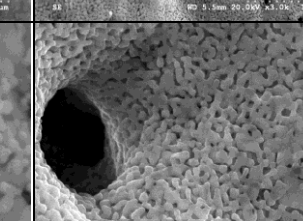
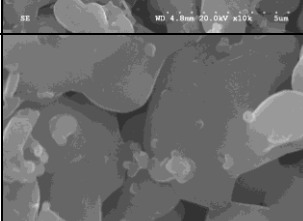
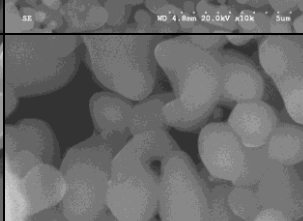
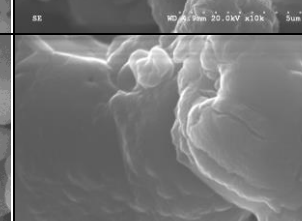
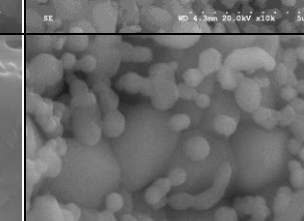
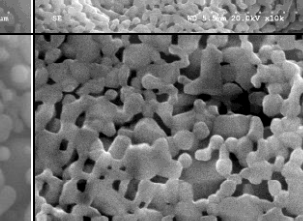
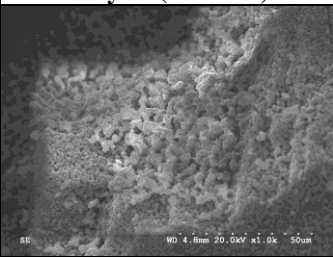
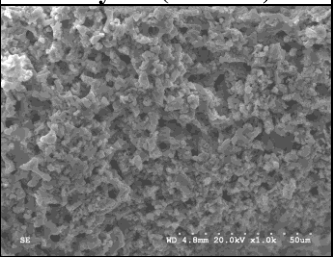
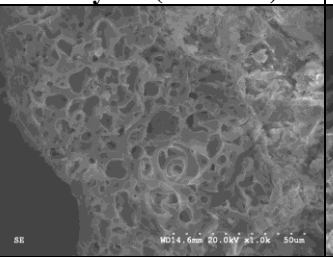
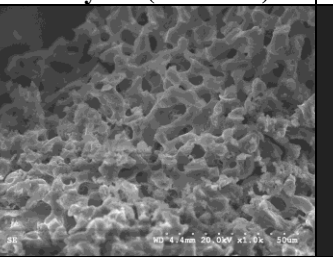
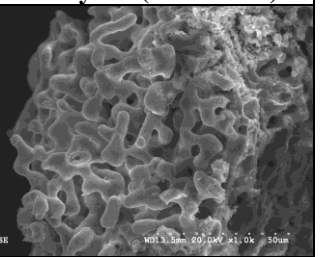
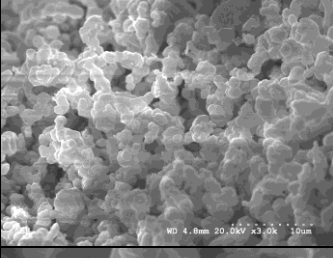
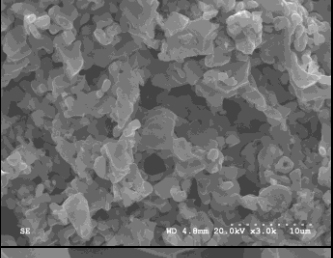
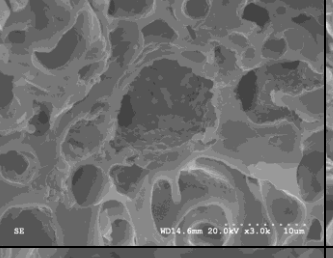
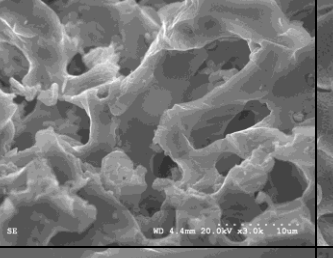
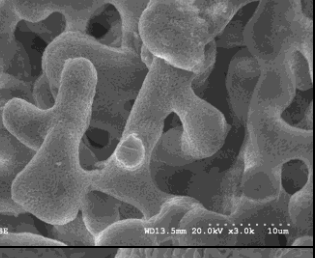
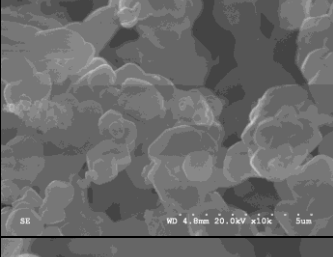
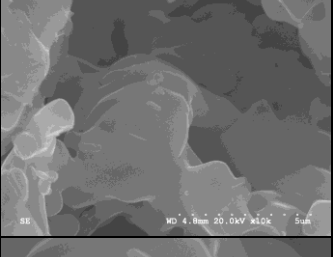
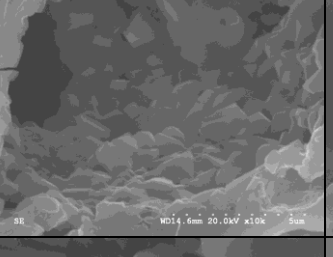
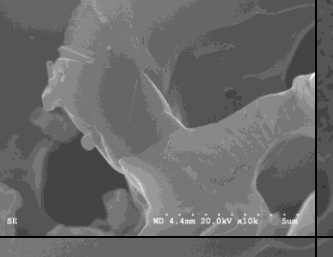
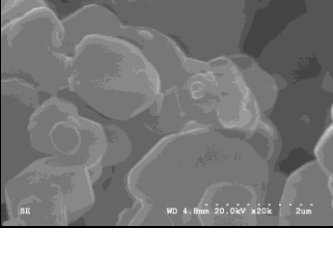
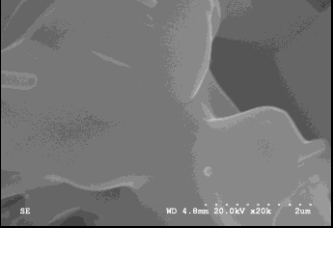
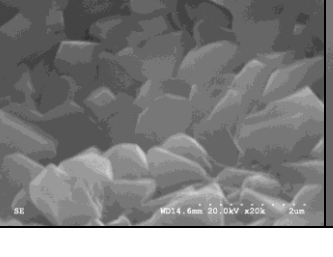
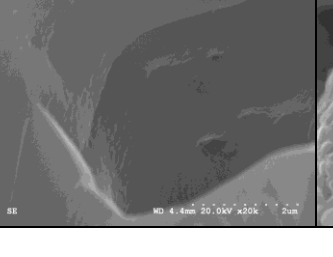
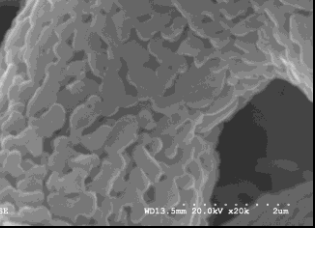
Magnification	1 Cycle (PC-10-1)	5 Cycles (PC-10-5)	10 Cycles (PC-10-10)	25 Cycles (PC-10-25)	250 Cycles (PC-10-250)
250					
1000					
3000					
10,000					
20,000					

Table A7.2: SEM micrographs of interior of sorbent particles after different cycle numbers

Mag.	1 Cycle (PC-10-1)	5 Cycles (PC-10-5)	10 Cycles (PC-10-10)	25 Cycles (PC-10-25)	250 Cycles (PC-10-250)
1000					
3000					
10,000					
20,000					

Appendix 8: SEM Micrographs of 20 bar Snapshots

Table A8.1: SEM micrographs of exterior of sorbent particles after different cycle numbers

Magnification	1 Cycle (PC-20-1)	5 Cycles (PC-20-5b)	10 Cycles (PC-20-10)	25 Cycles (PC-20-25)	50 Cycles (PC-20-50)
250					
1000					
3000					
10,000					
20,000					

Table A8.2: SEM micrographs of exterior of sorbent particles after different cycle numbers

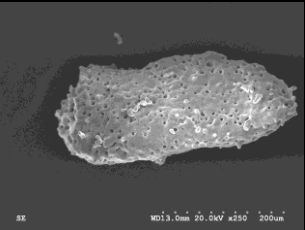
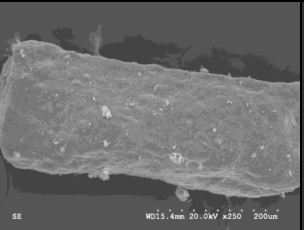
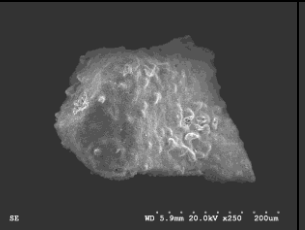
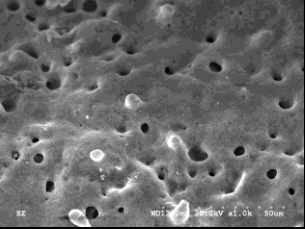
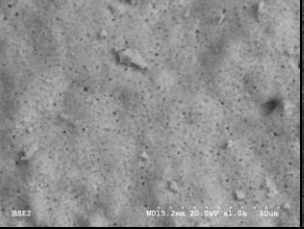
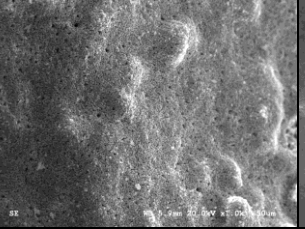
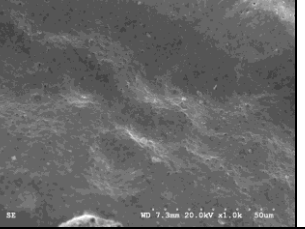
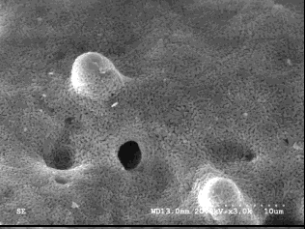
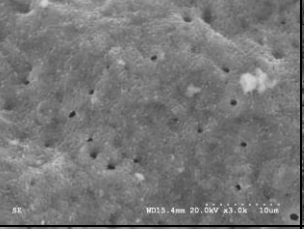
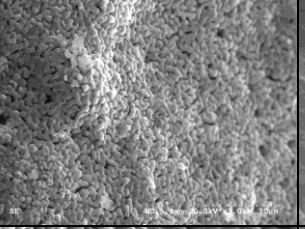
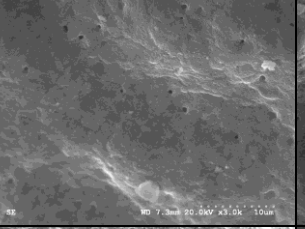
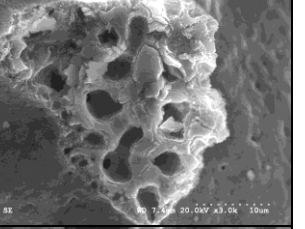
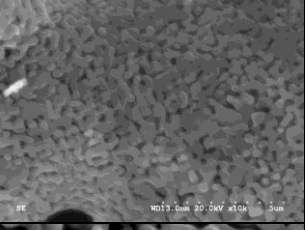
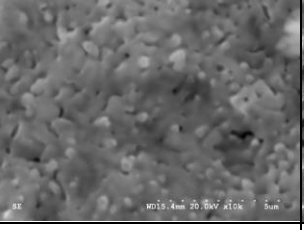
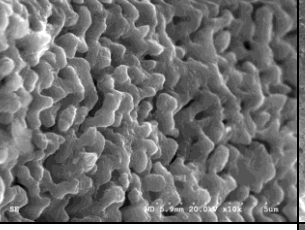
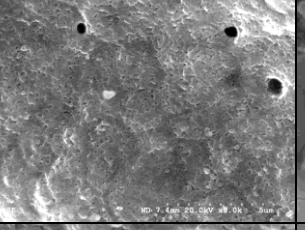
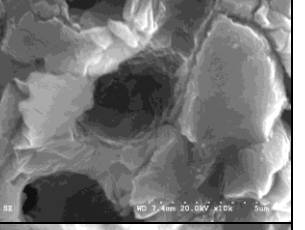
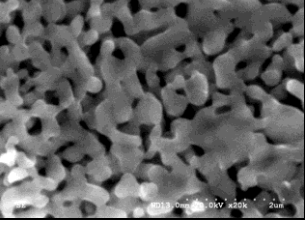
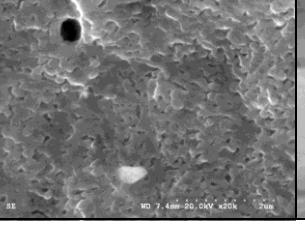
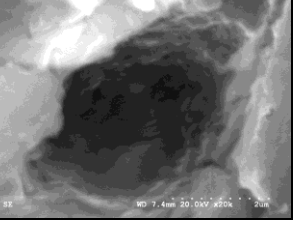
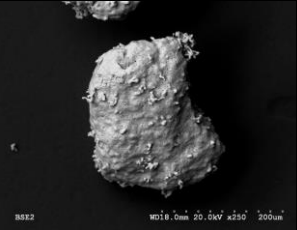
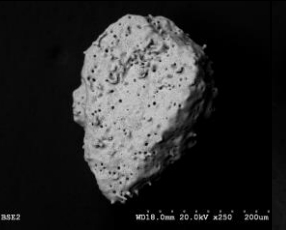
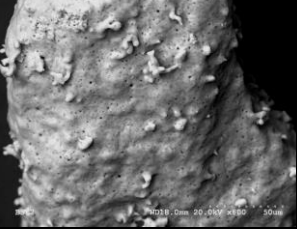
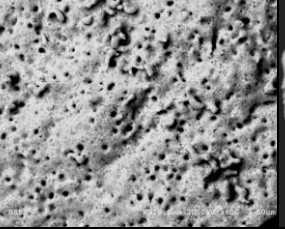
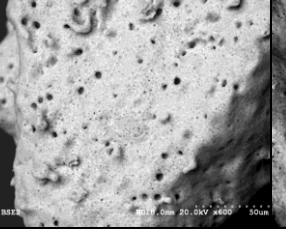
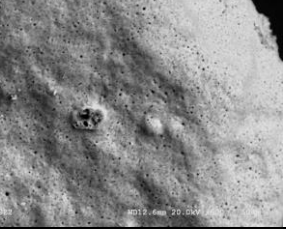
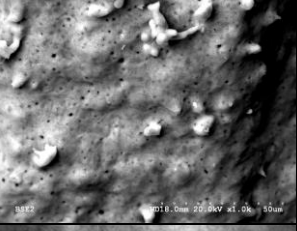
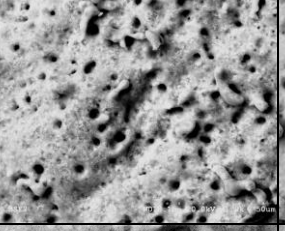
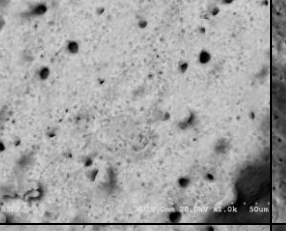
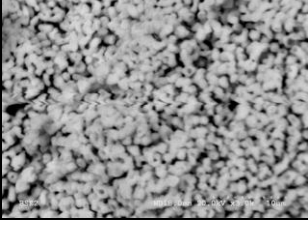
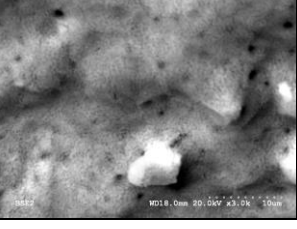
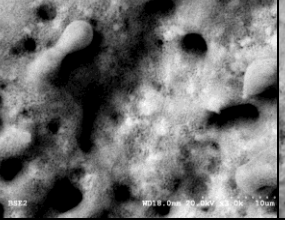
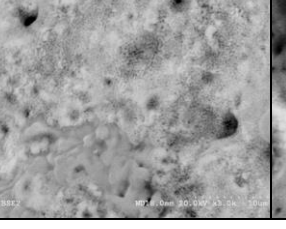
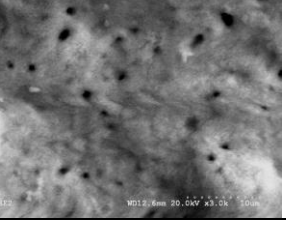
Magnification	100 Cycles (PC-20-100)	227 Cycles (PC-20-227)	250 Cycles (PC-20-250)	272 Cycles (PC-20-272)	272 Cycles (PC-20-272-interior)
250					
1000					
3000					
10,000					
20,000					

Table A8.3: SEM micrographs of exterior of sorbent particles after different cycle numbers

Magnification	1 Cycle PC-20-1	25 Cycles PC-20-25	50 Cycles PC-20-50	100 Cycles PC-20-100	282 Cycles PC-20-282o
250					
600					
1,000					
3,000					

Appendix 9: Utilization and Weight Change Curves During Individual Cycles

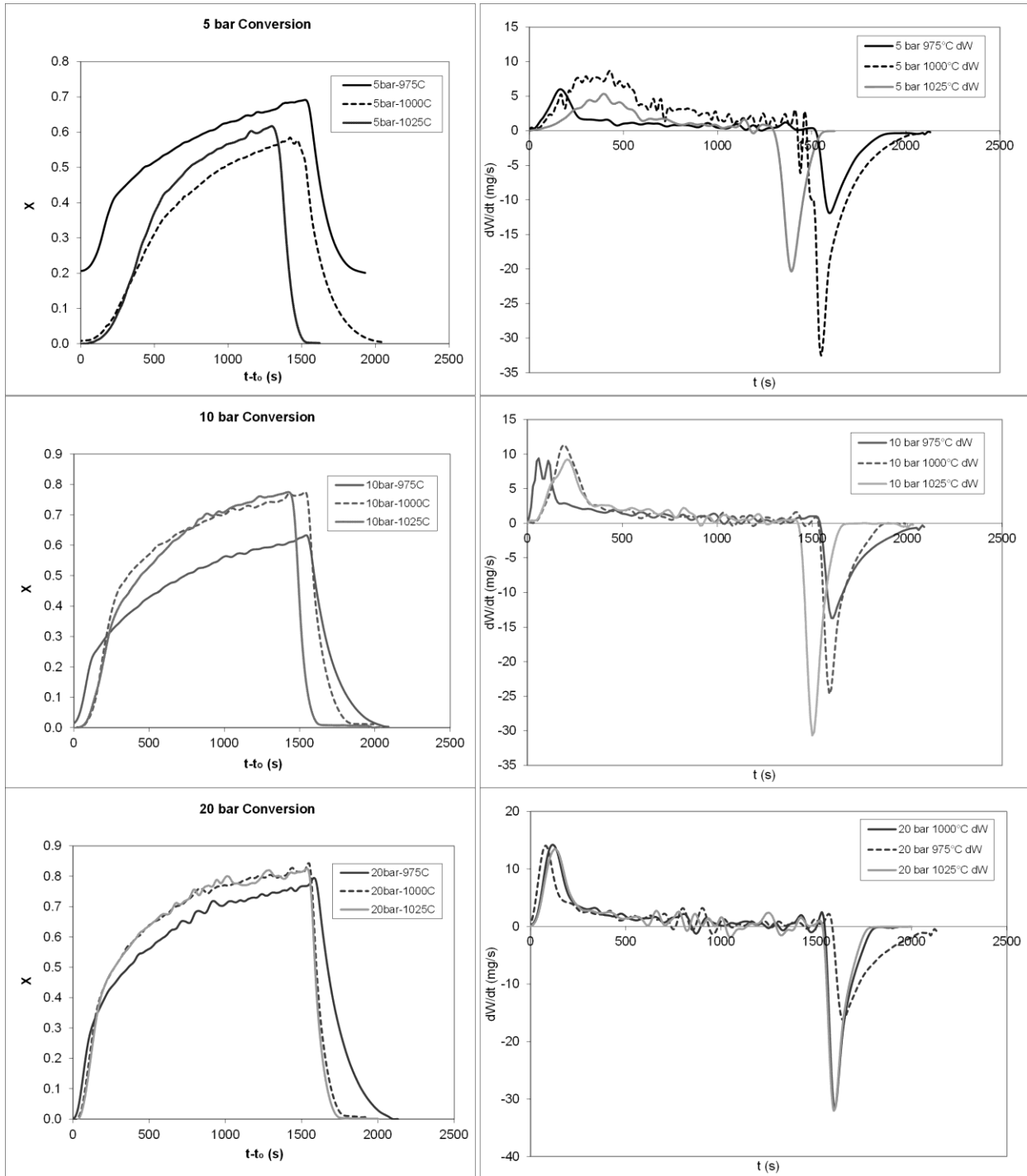


Figure A9.1: Utilization and weight change curves from cycle 1, X is calcium utilization.

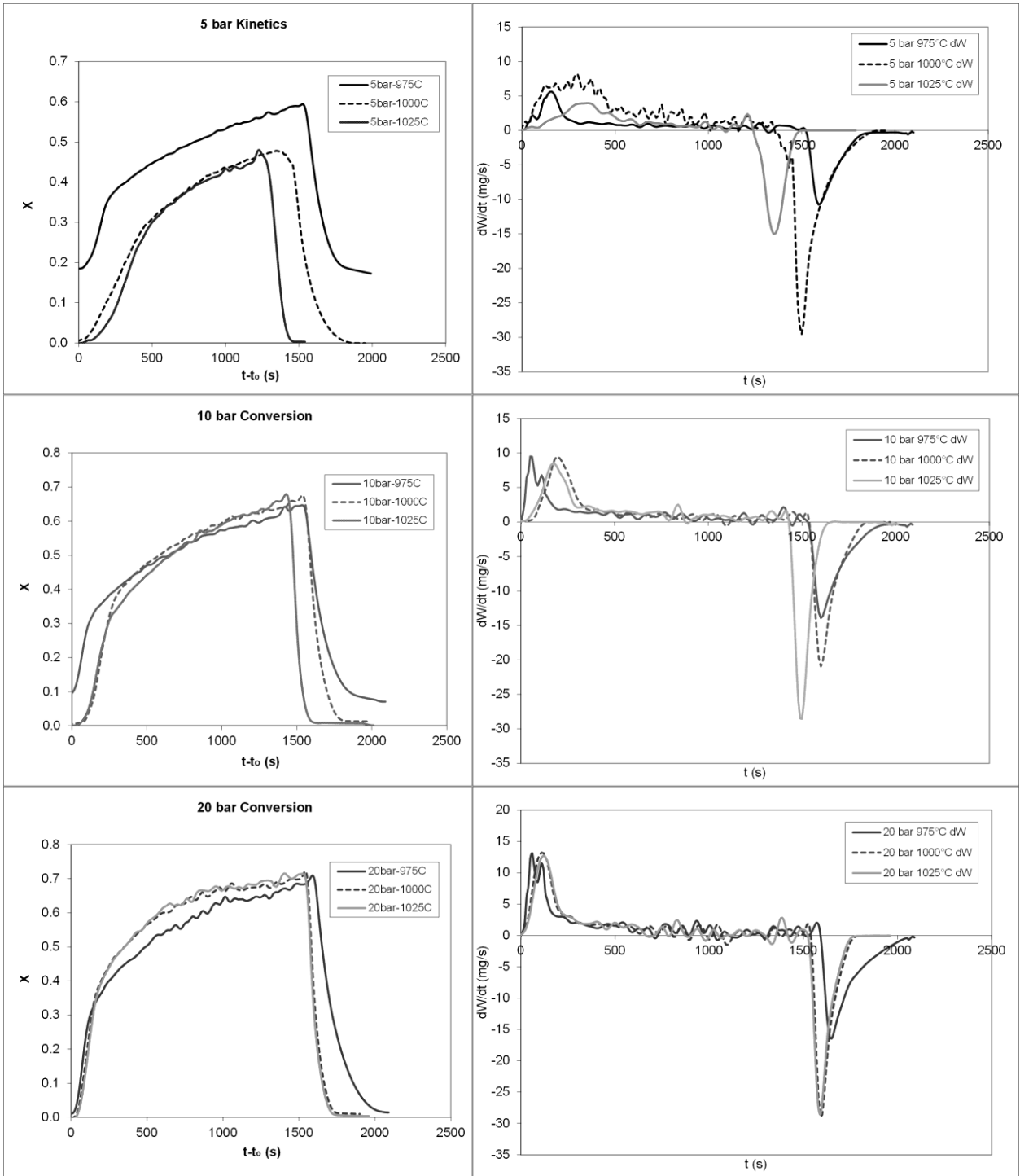


Figure A9.2: Utilization and weight change curves from cycle 2, X is calcium utilization.

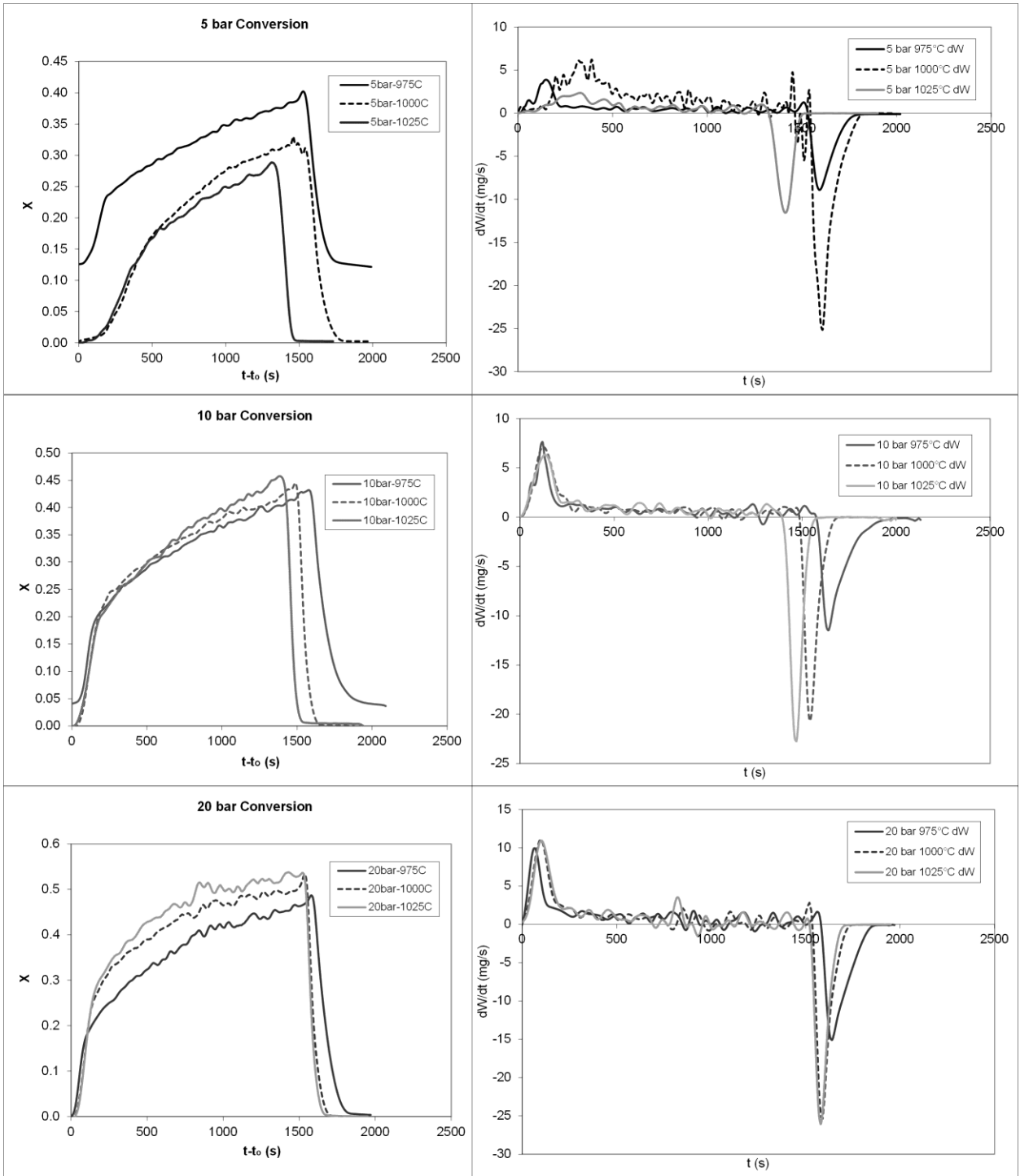


Figure A9.3: Utilization and weight change curves from cycle 5, X is calcium utilization.

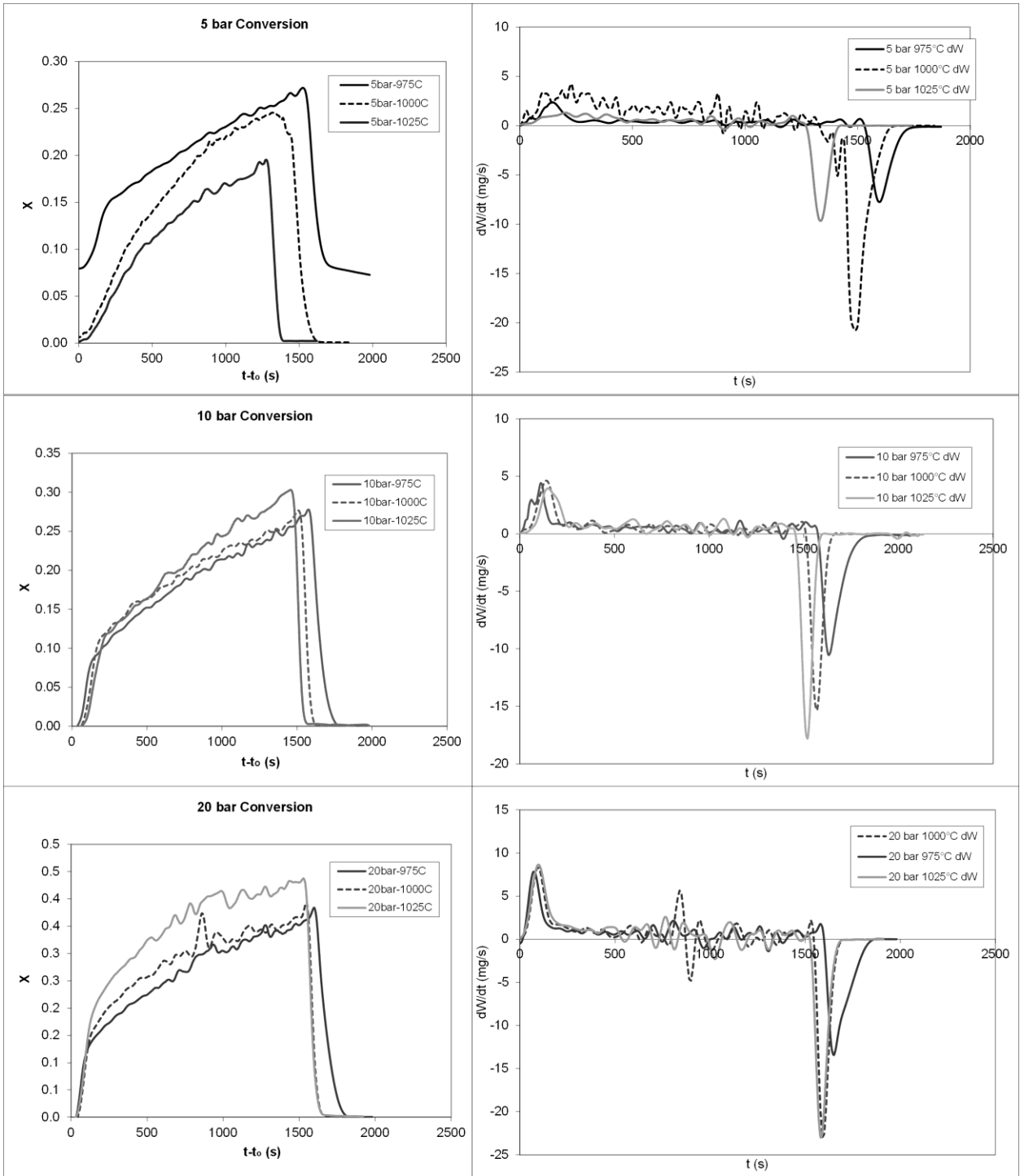


Figure A9.4: Utilization and weight change curves from cycle 10, X is calcium utilization.

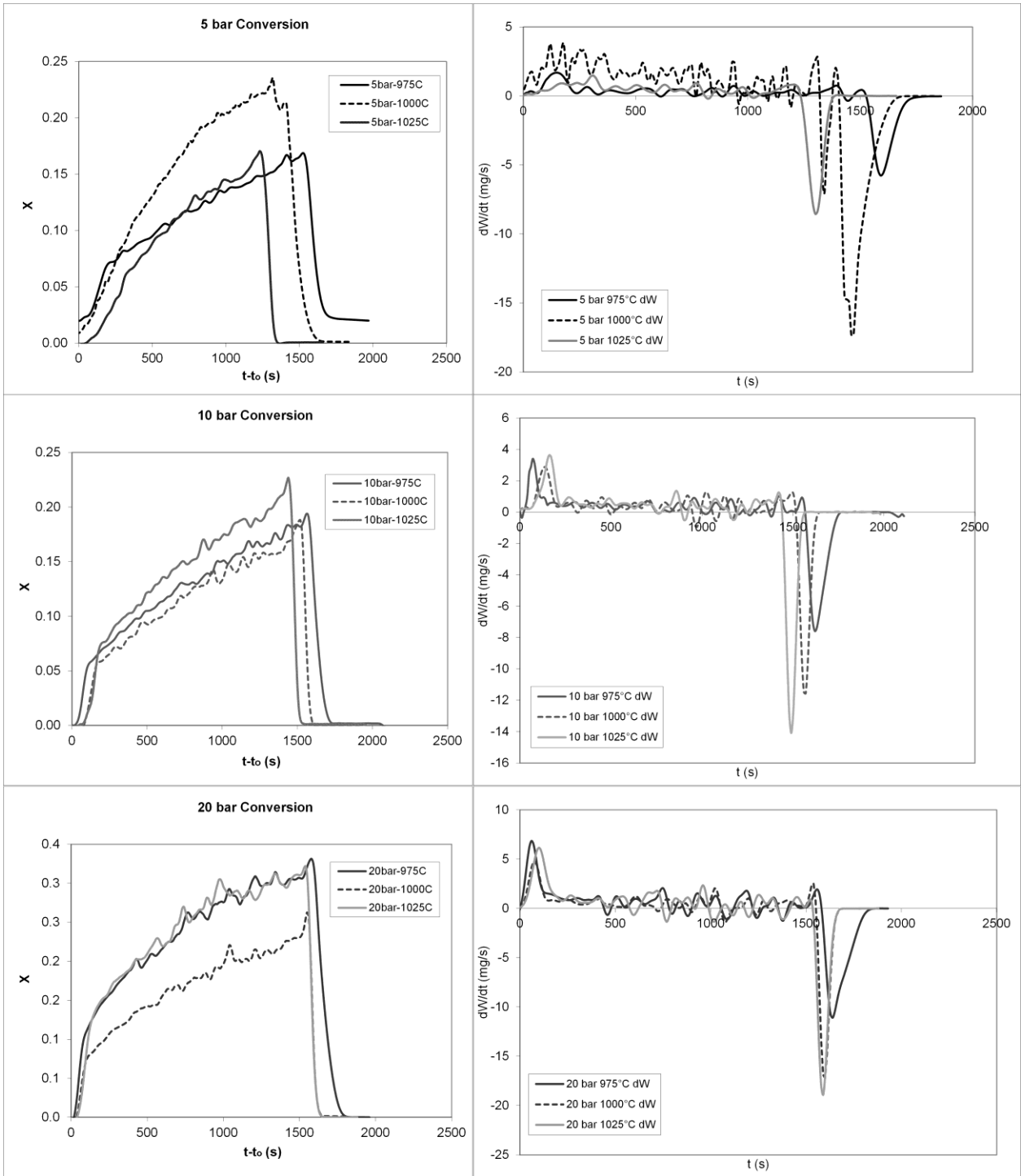


Figure A9.5: Utilization and weight change curves from cycle 25, X is calcium utilization.

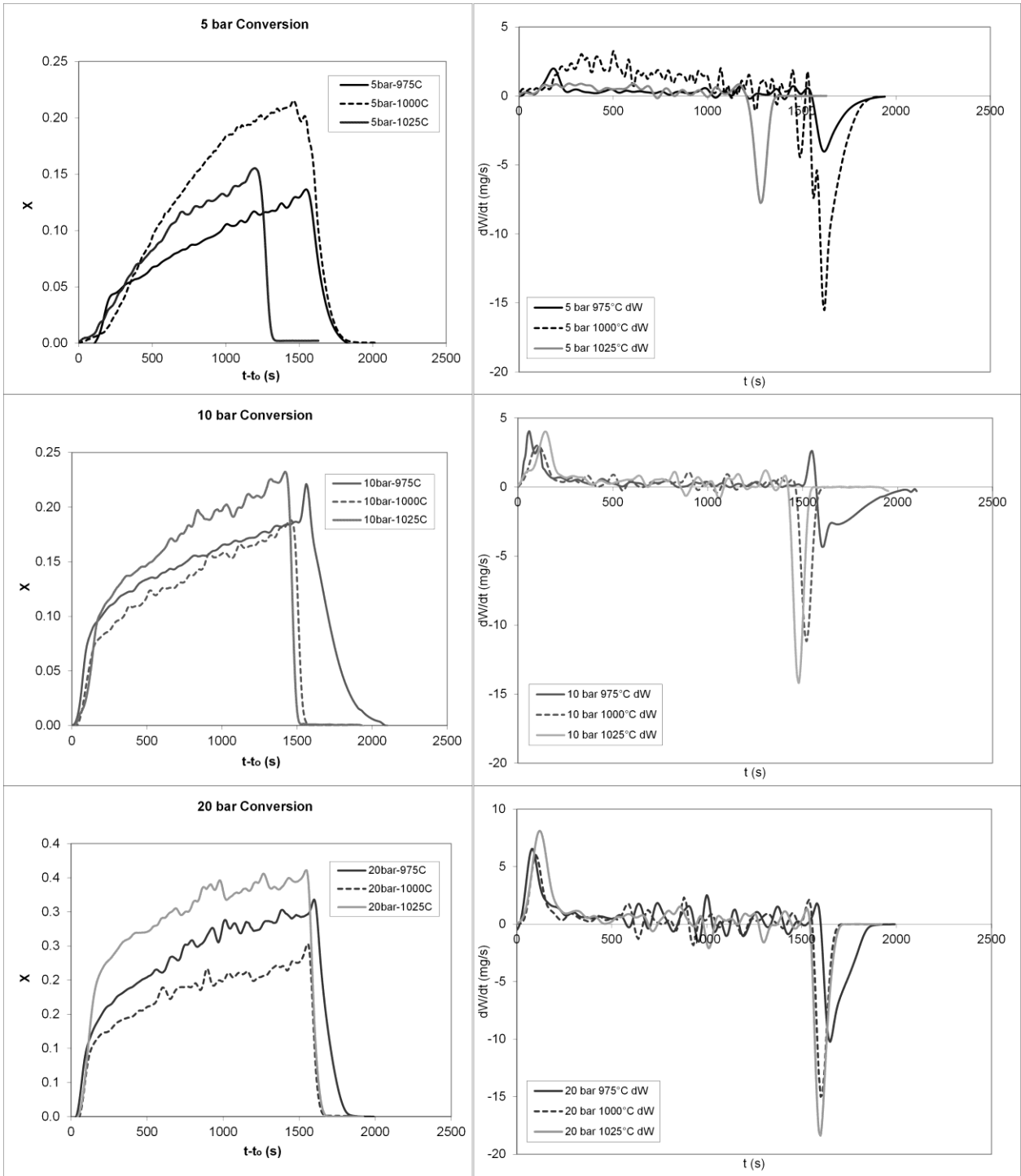


Figure A9.6: Utilization and weight change curves from cycle 50, X is calcium utilization.

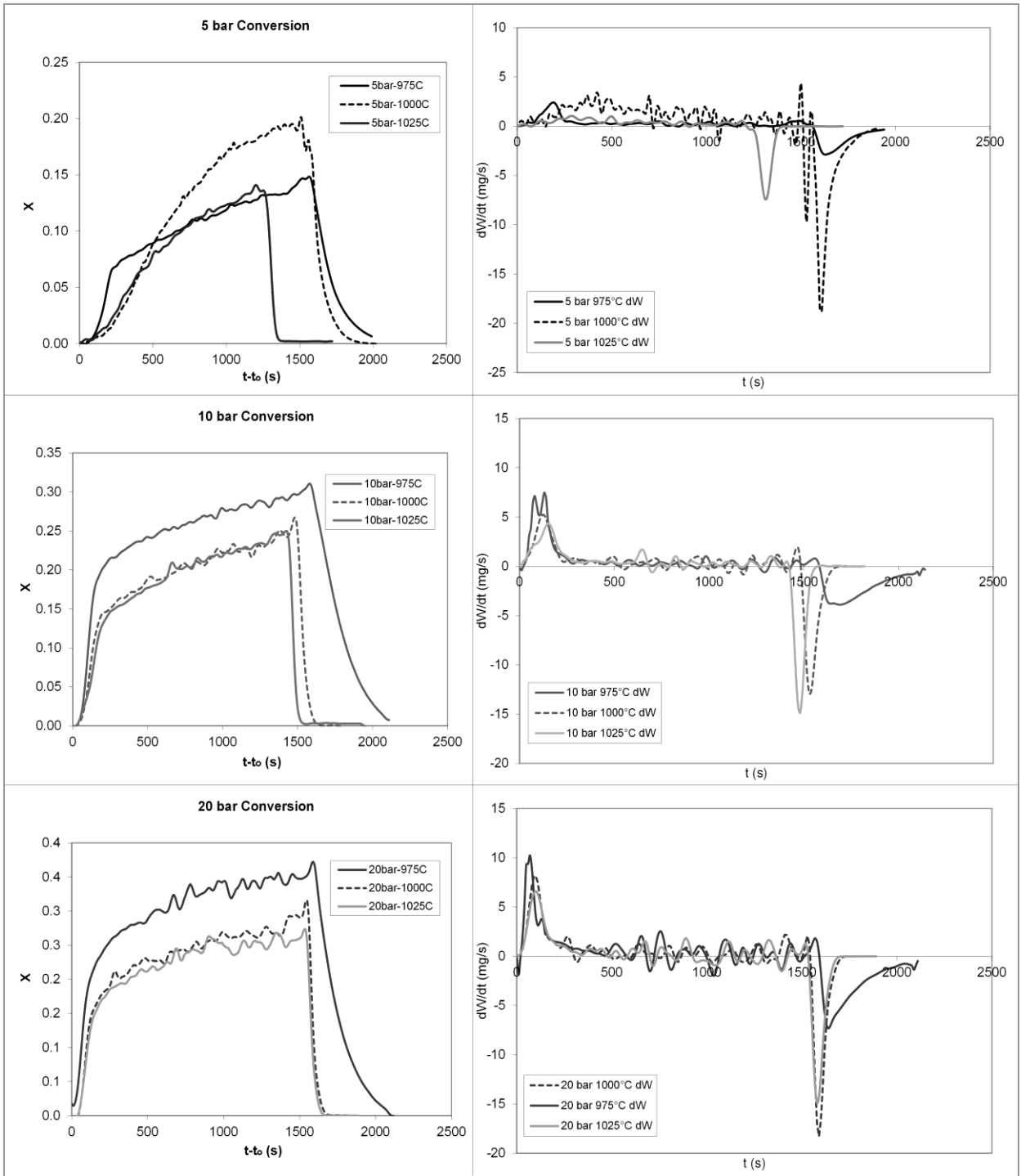


Figure A9.7: Utilization and weight change curves from cycle 100, X is calcium utilization.

Appendix 10: Grain Model Kinetic Plots for Determination of Reaction Rates

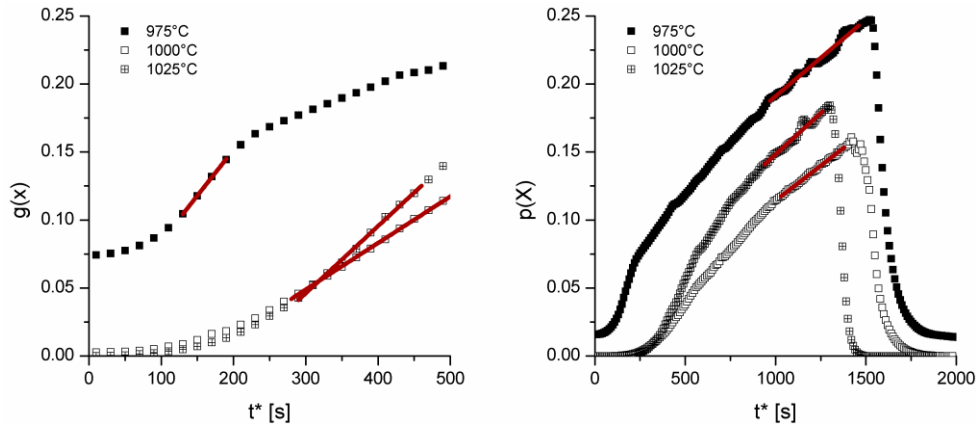


Figure A10.1: 1st cycle kinetics modeled using Szekely's grain model for cycling at 5 bar carbonation pressure, solid lines used to find rate of reaction, (right) grain model utilization for the reaction-controlled regime, $g(x)$, equation 4; (left) grain model utilization for the diffusion-controlled regime, $p(x)$, equation 5.

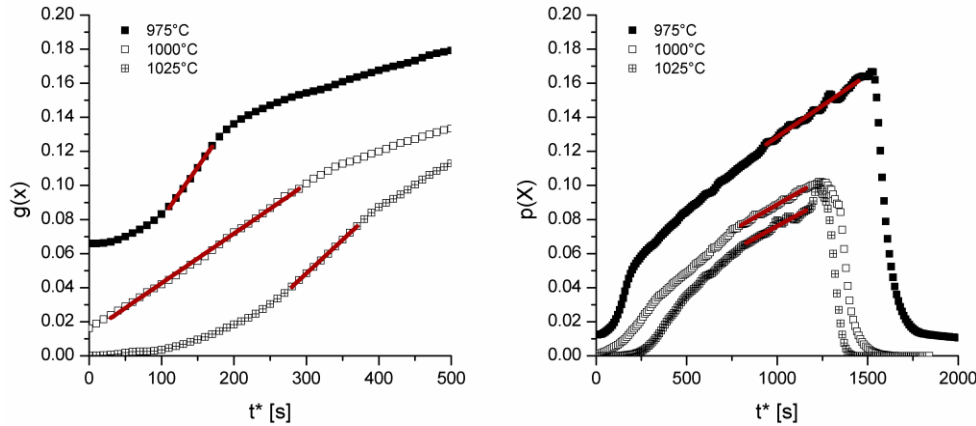


Figure A10.2: 2nd cycle kinetics modeled using Szekely's grain model for cycling at 5 bar carbonation pressure, solid lines used to find rate of reaction, (right) grain model utilization for the reaction-controlled regime, $g(x)$, equation 4; (left) grain model utilization for the diffusion-controlled regime, $p(x)$, equation 5.

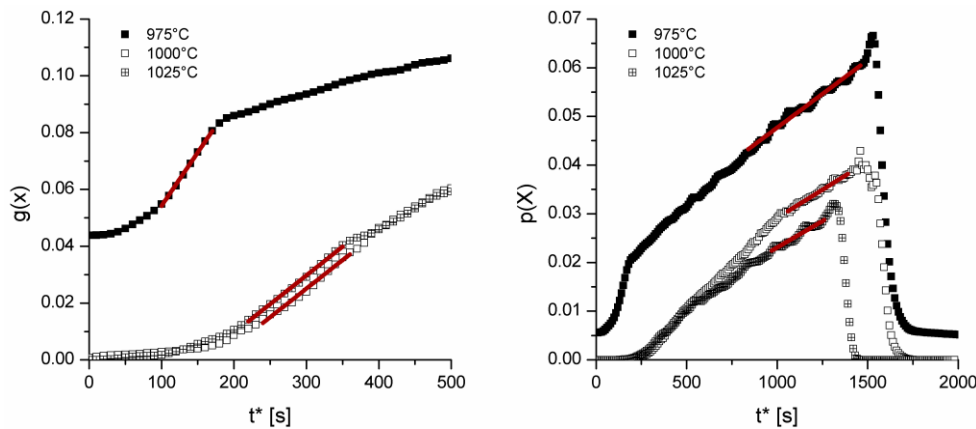


Figure A10.3: 5th cycle kinetics modeled using Szekely's grain model for cycling at 5 bar carbonation pressure, solid lines used to find rate of reaction, (right) grain model utilization for the reaction-controlled regime, $g(x)$, equation 4; (left) grain model utilization for the diffusion-controlled regime, $p(x)$, equation 5.

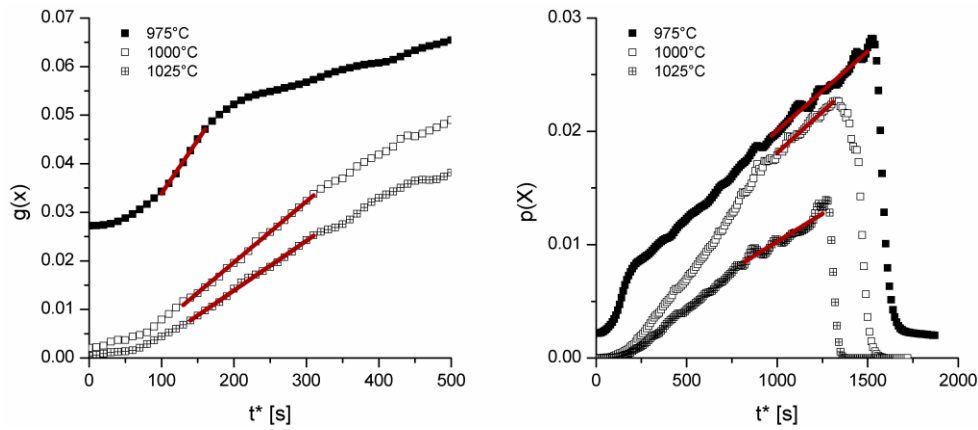


Figure A10.4: 10th cycle kinetics modeled using Szekely's grain model for cycling at 5 bar carbonation pressure, solid lines used to find rate of reaction, (right) grain model utilization for the reaction-controlled regime, $g(x)$, equation 4; (left) grain model utilization for the diffusion-controlled regime, $p(x)$, equation 5.

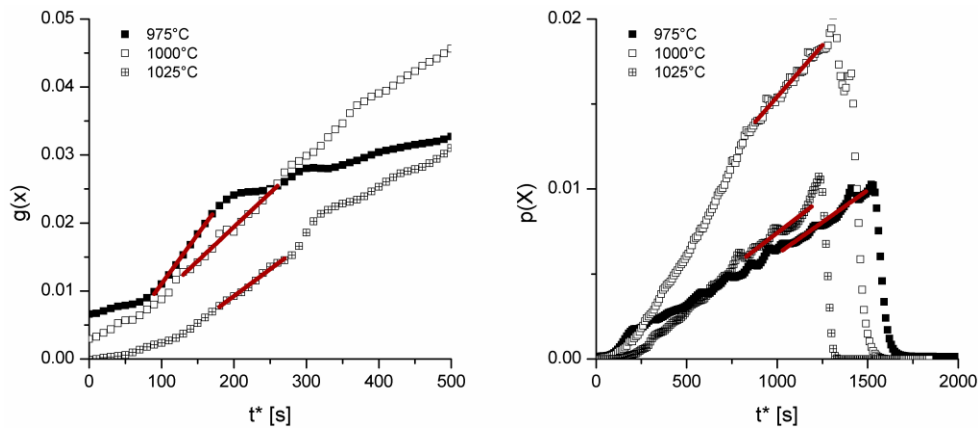


Figure A10.5: 25th cycle kinetics modeled using Szekely's grain model for cycling at 5 bar carbonation pressure, solid lines used to find rate of reaction, (right) grain model utilization for the reaction-controlled regime, $g(x)$, equation 4; (left) grain model utilization for the diffusion-controlled regime, $p(x)$, equation 5.

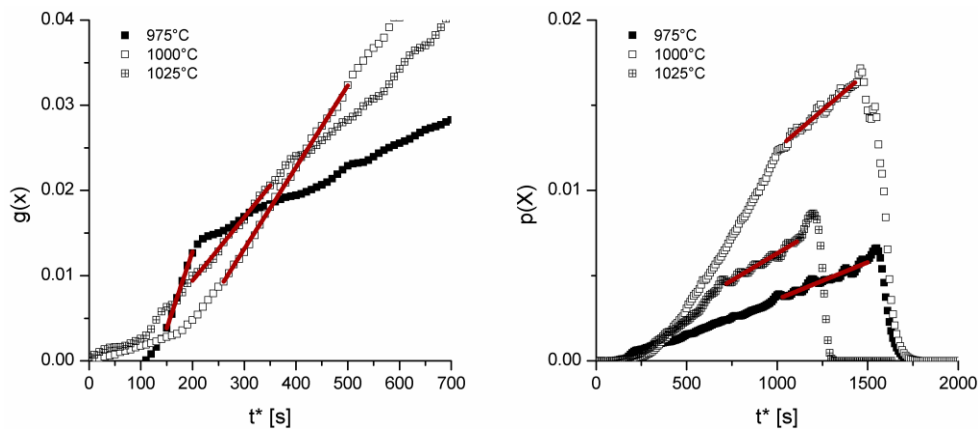


Figure A10.6: 50th cycle kinetics modeled using Szekely's grain model for cycling at 5 bar carbonation pressure, solid lines used to find rate of reaction, (right) grain model utilization for the reaction-controlled regime, $g(x)$, equation 4; (left) grain model utilization for the diffusion-controlled regime, $p(x)$, equation 5.

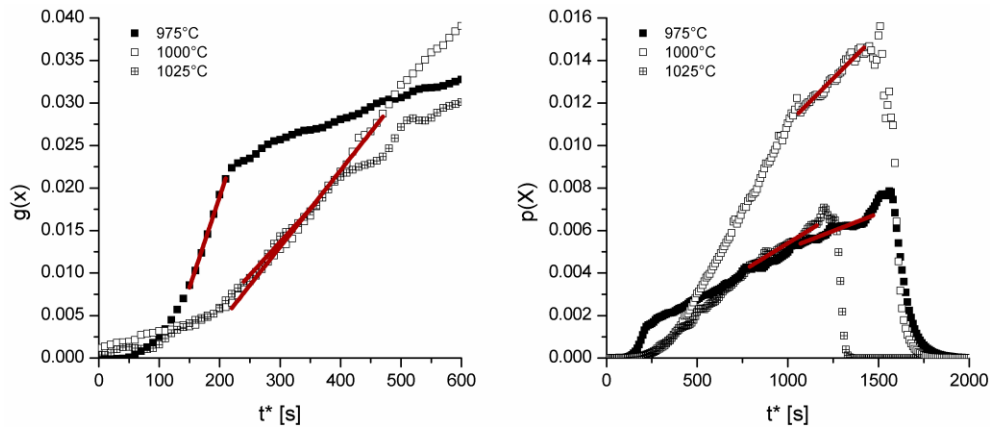


Figure A10.7: 100th cycle kinetics modeled using Szekely's grain model for cycling at 5 bar carbonation pressure, solid lines used to find rate of reaction, (right) grain model utilization for the reaction-controlled regime, $g(x)$, equation 4; (left) grain model utilization for the diffusion-controlled regime, $p(x)$, equation 5.

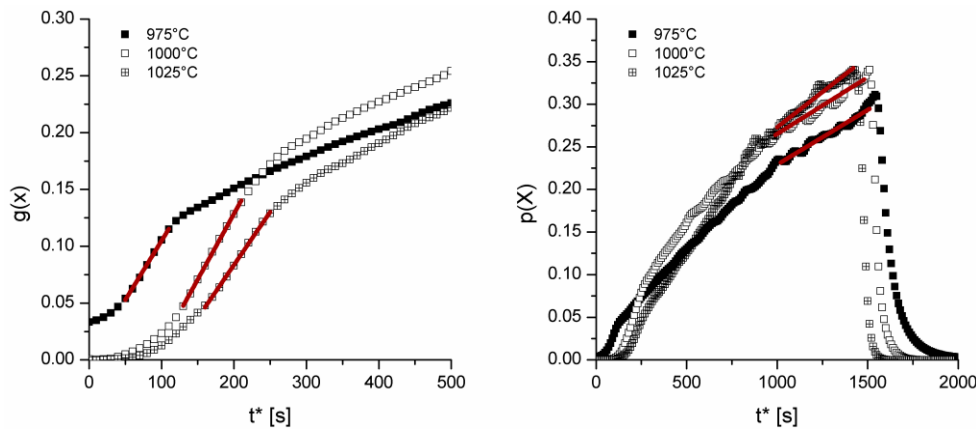


Figure A10.8: 1st cycle kinetics modeled using Szekely's grain model for cycling at 10 bar carbonation pressure, solid lines used to find rate of reaction, (right) grain model utilization for the reaction-controlled regime, $g(x)$, equation 4; (left) grain model utilization for the diffusion-controlled regime, $p(x)$, equation 5.

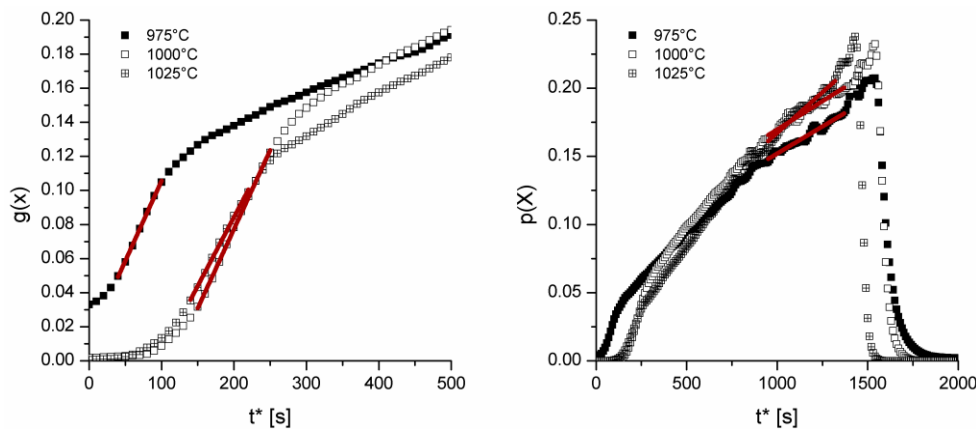


Figure A10.9: 2nd cycle kinetics modeled using Szekely's grain model for cycling at 10 bar carbonation pressure, solid lines used to find rate of reaction, (right) grain model utilization for the reaction-controlled regime, $g(x)$, equation 4; (left) grain model utilization for the diffusion-controlled regime, $p(x)$, equation 5.

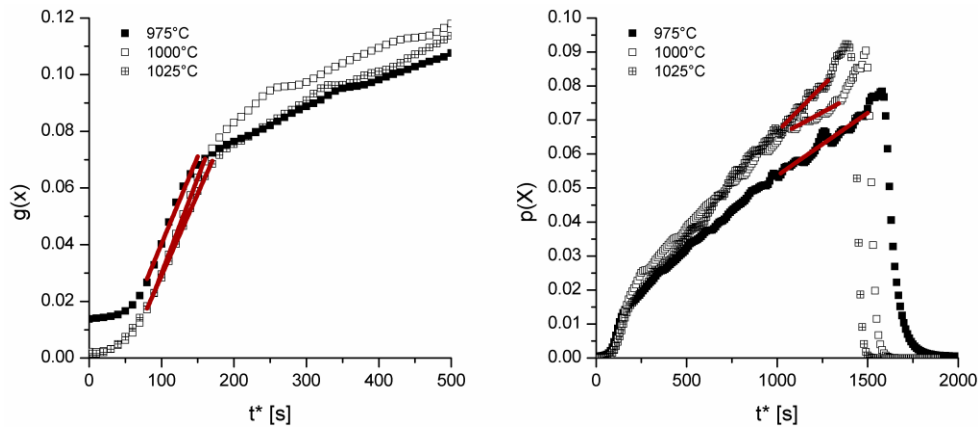


Figure A10.10: 5th cycle kinetics modeled using Szekely's grain model for cycling at 10 bar carbonation pressure, solid lines used to find rate of reaction, (right) grain model utilization for the reaction-controlled regime, $g(x)$, equation 4; (left) grain model utilization for the diffusion-controlled regime, $p(x)$, equation 5.

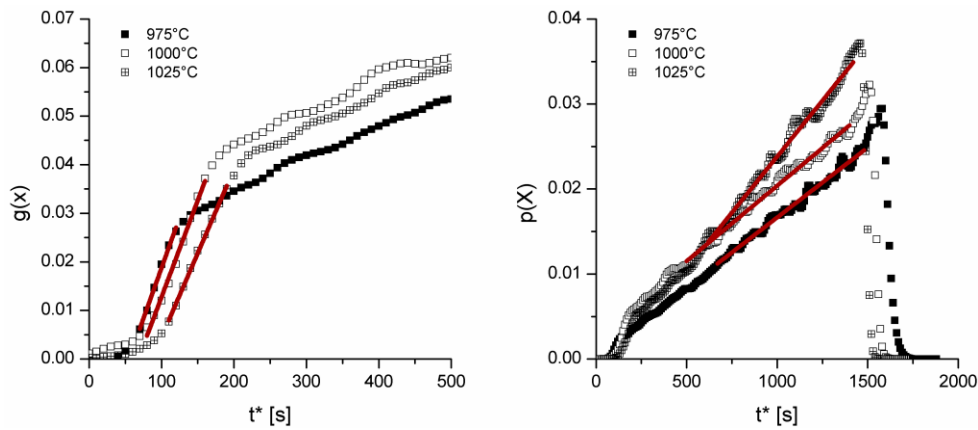


Figure A10.11: 10th cycle kinetics modeled using Szekely's grain model for cycling at 10 bar carbonation pressure, solid lines used to find rate of reaction, (right) grain model utilization for the reaction-controlled regime, $g(x)$, equation 4; (left) grain model utilization for the diffusion-controlled regime, $p(x)$, equation 5.

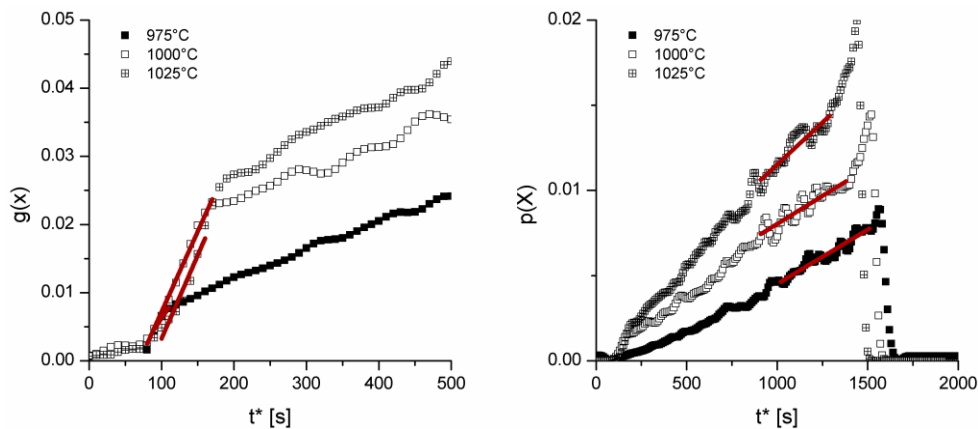


Figure A10.12: 25th cycle kinetics modeled using Szekely's grain model for cycling at 10 bar carbonation pressure, solid lines used to find rate of reaction, (right) grain model utilization for the reaction-controlled regime, $g(x)$, equation 4; (left) grain model utilization for the diffusion-controlled regime, $p(x)$, equation 5.

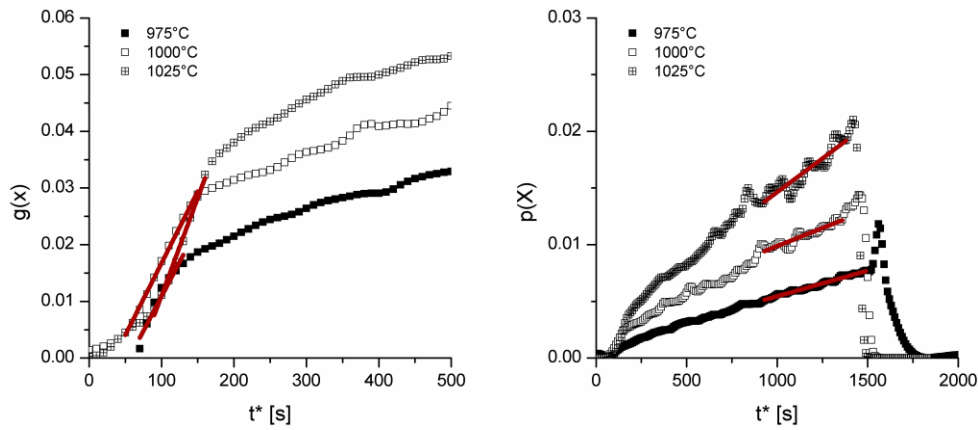


Figure A10.13: 50th cycle kinetics modeled using Szekely's grain model for cycling at 10 bar carbonation pressure, solid lines used to find rate of reaction, (right) grain model utilization for the reaction-controlled regime, $g(x)$, equation 4; (left) grain model utilization for the diffusion-controlled regime, $p(x)$, equation 5.

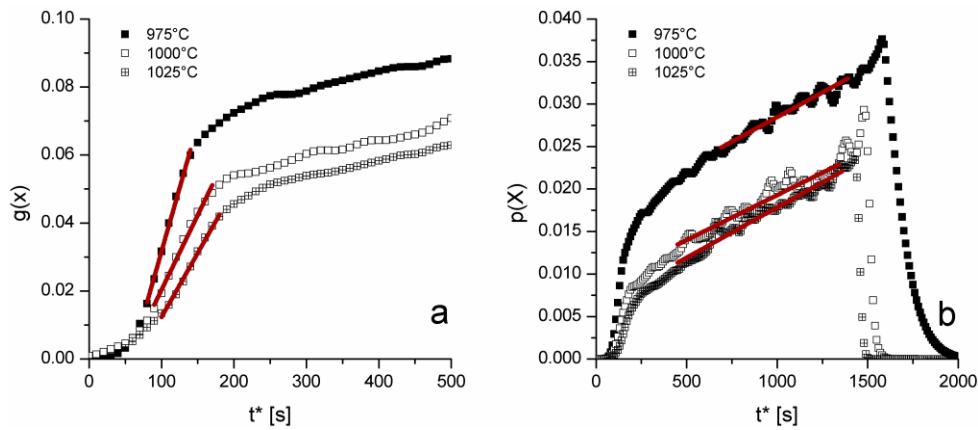


Figure A10.14: 100th cycle kinetics modeled using Szekely's grain model for cycling at 10 bar carbonation pressure, solid lines used to find rate of reaction, (right) grain model utilization for the reaction-controlled regime, $g(x)$, equation 4; (left) grain model utilization for the diffusion-controlled regime, $p(x)$, equation 5.

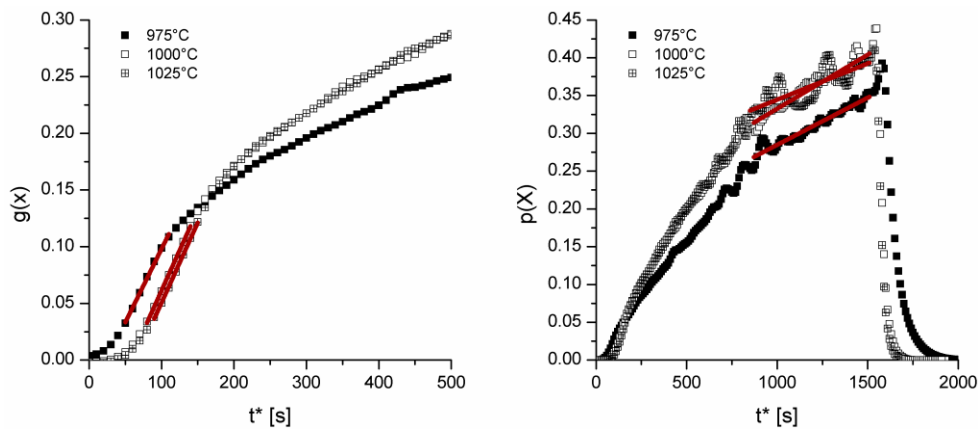


Figure A10.15: 1st cycle kinetics modeled using Szekely's grain model for cycling at 20 bar carbonation pressure, solid lines used to find rate of reaction, (right) grain model utilization for the reaction-controlled regime, $g(x)$, equation 4; (left) grain model utilization for the diffusion-controlled regime, $p(x)$, equation 5.

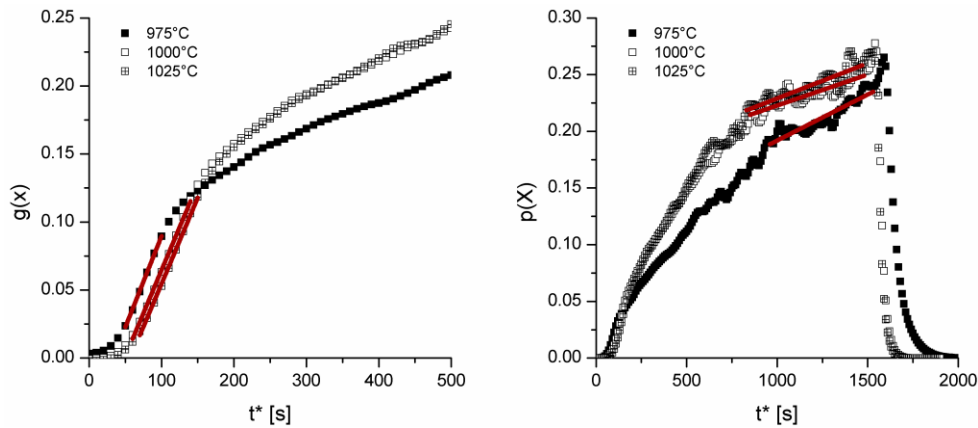


Figure A10.16: 2nd cycle kinetics modeled using Szekely's grain model for cycling at 20 bar carbonation pressure, solid lines used to find rate of reaction, (right) grain model utilization for the reaction-controlled regime, $g(x)$, equation 4; (left) grain model utilization for the diffusion-controlled regime, $p(x)$, equation 5.

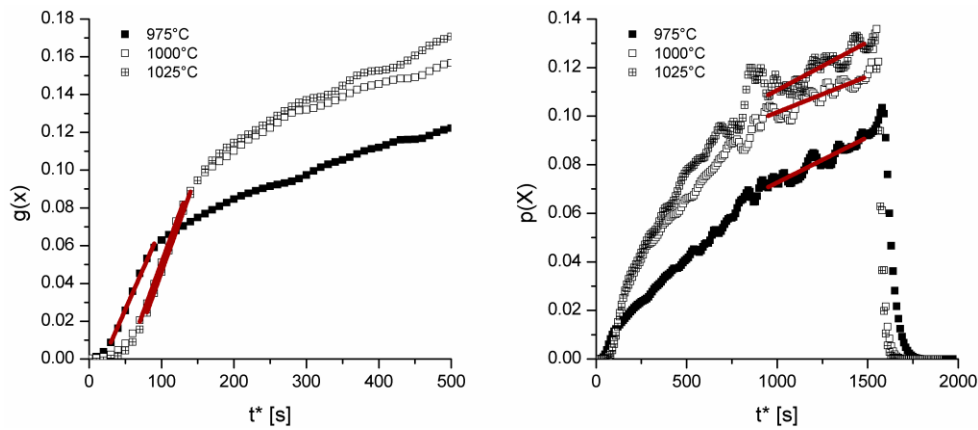


Figure A10.17: 5th cycle kinetics modeled using Szekely's grain model for cycling at 20 bar carbonation pressure, solid lines used to find rate of reaction, (right) grain model utilization for the reaction-controlled regime, $g(x)$, equation 4; (left) grain model utilization for the diffusion-controlled regime, $p(x)$, equation 5.

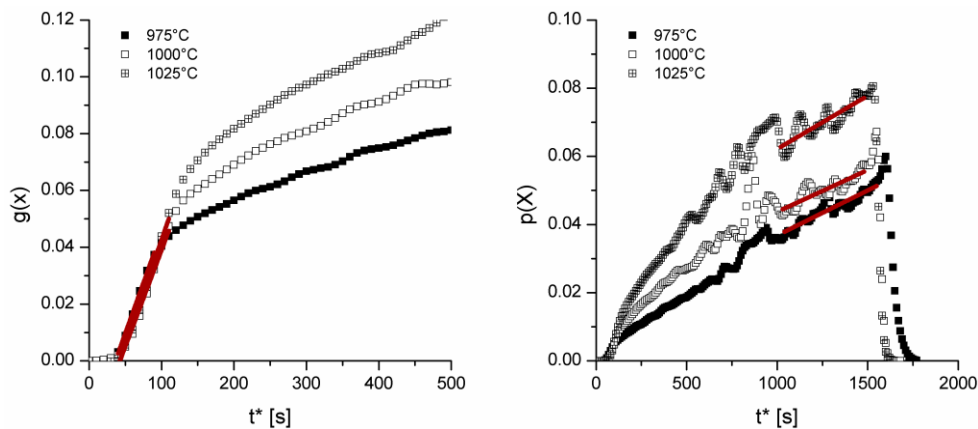


Figure A10.18: 10th cycle kinetics modeled using Szekely's grain model for cycling at 20 bar carbonation pressure, solid lines used to find rate of reaction, (right) grain model utilization for the reaction-controlled regime, $g(x)$, equation 4; (left) grain model utilization for the diffusion-controlled regime, $p(x)$, equation 5.

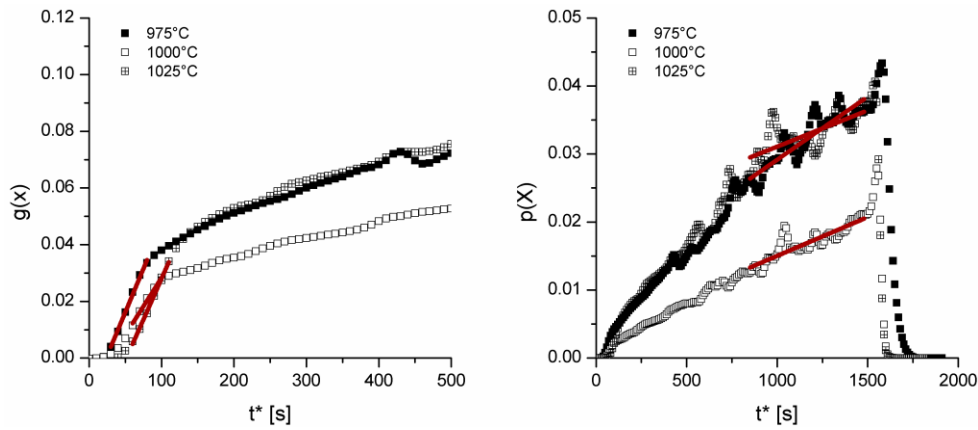


Figure A10.19: 25th cycle kinetics modeled using Szekely's grain model for cycling at 20 bar carbonation pressure, solid lines used to find rate of reaction, (right) grain model utilization for the reaction-controlled regime, $g(x)$, equation 4; (left) grain model utilization for the diffusion-controlled regime, $p(x)$, equation 5.

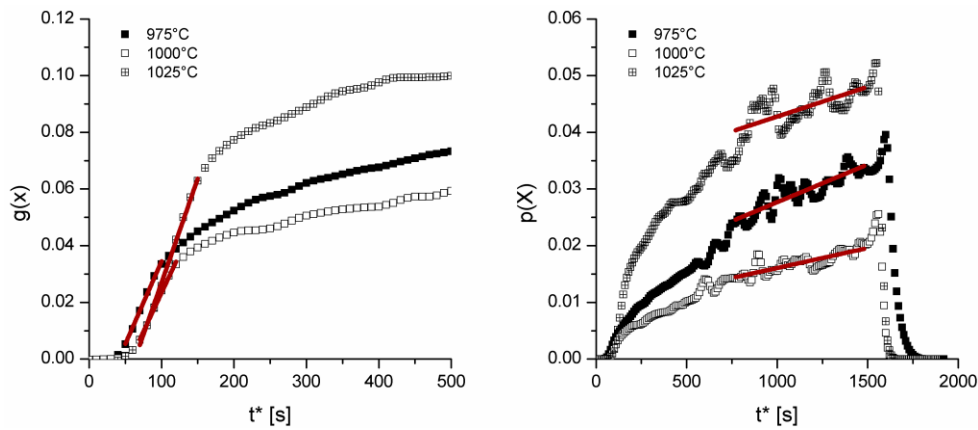


Figure A10.20: 50th cycle kinetics modeled using Szekely's grain model for cycling at 20 bar carbonation pressure, solid lines used to find rate of reaction, (right) grain model utilization for the reaction-controlled regime, $g(x)$, equation 4; (left) grain model utilization for the diffusion-controlled regime, $p(x)$, equation 5.

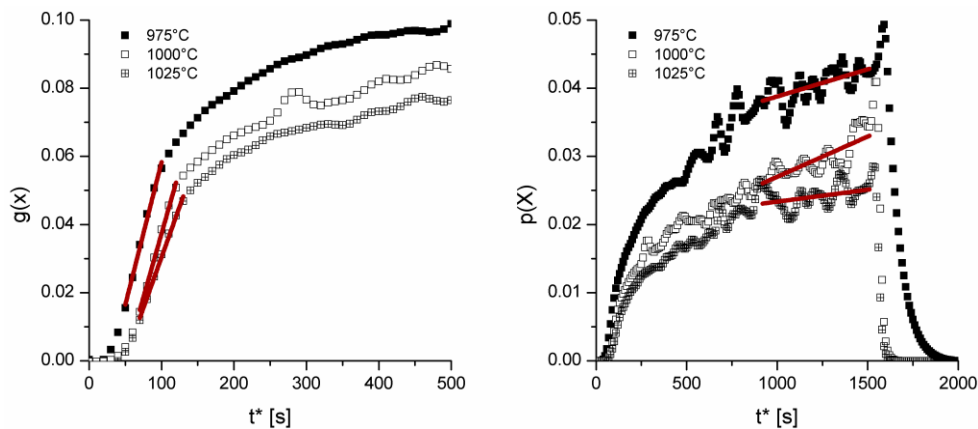


Figure A10.21: 100th cycle kinetics modeled using Szekely's grain model for cycling at 20 bar carbonation pressure, solid lines used to find rate of reaction, (right) grain model utilization for the reaction-controlled regime, $g(x)$, equation 4; (left) grain model utilization for the diffusion-controlled regime, $p(x)$, equation 5.

Appendix 11: Pressure Swing Kinetics - Supplemental Figures

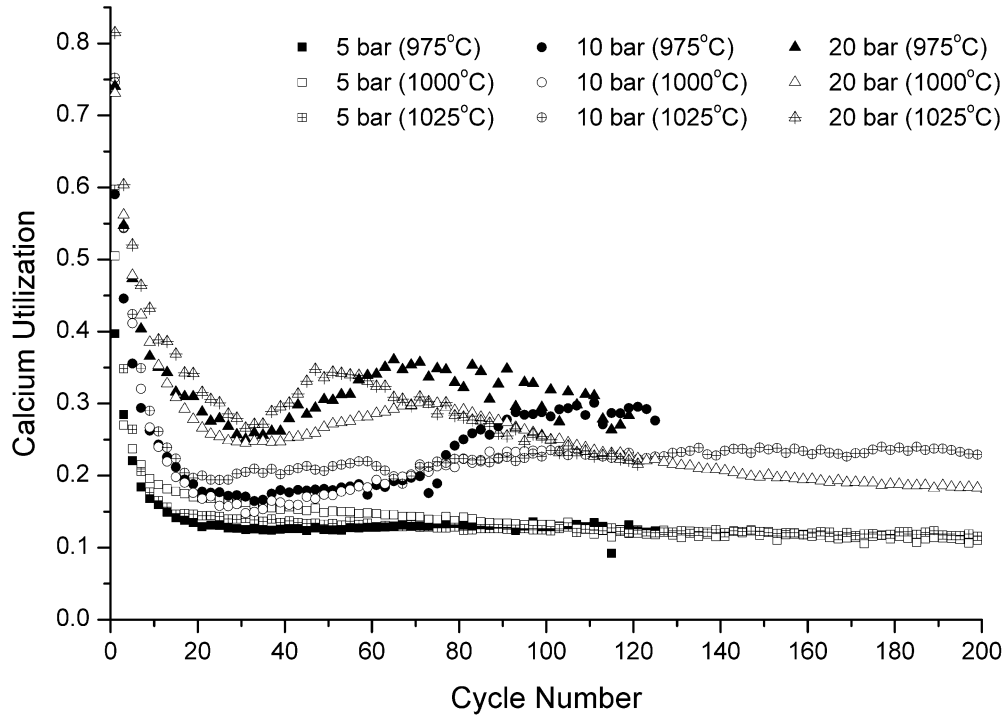


Figure A11.1: Cycling at different temperatures and pressures.

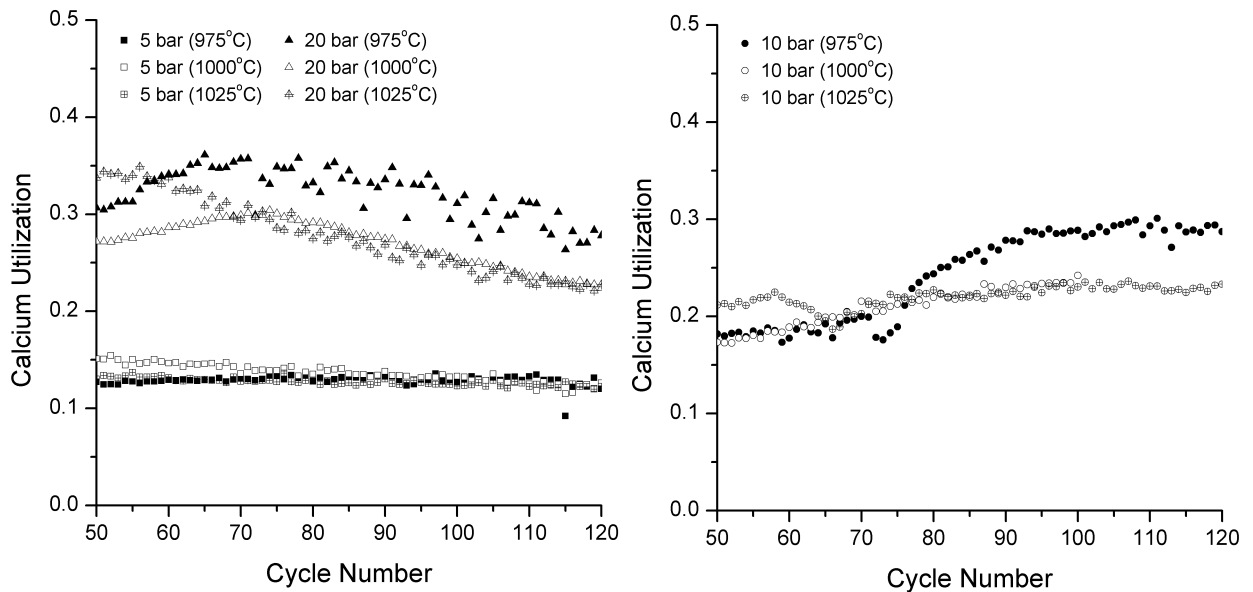


Figure A11.2: Cycling at different temperatures and pressures; cycles 50 to 120.

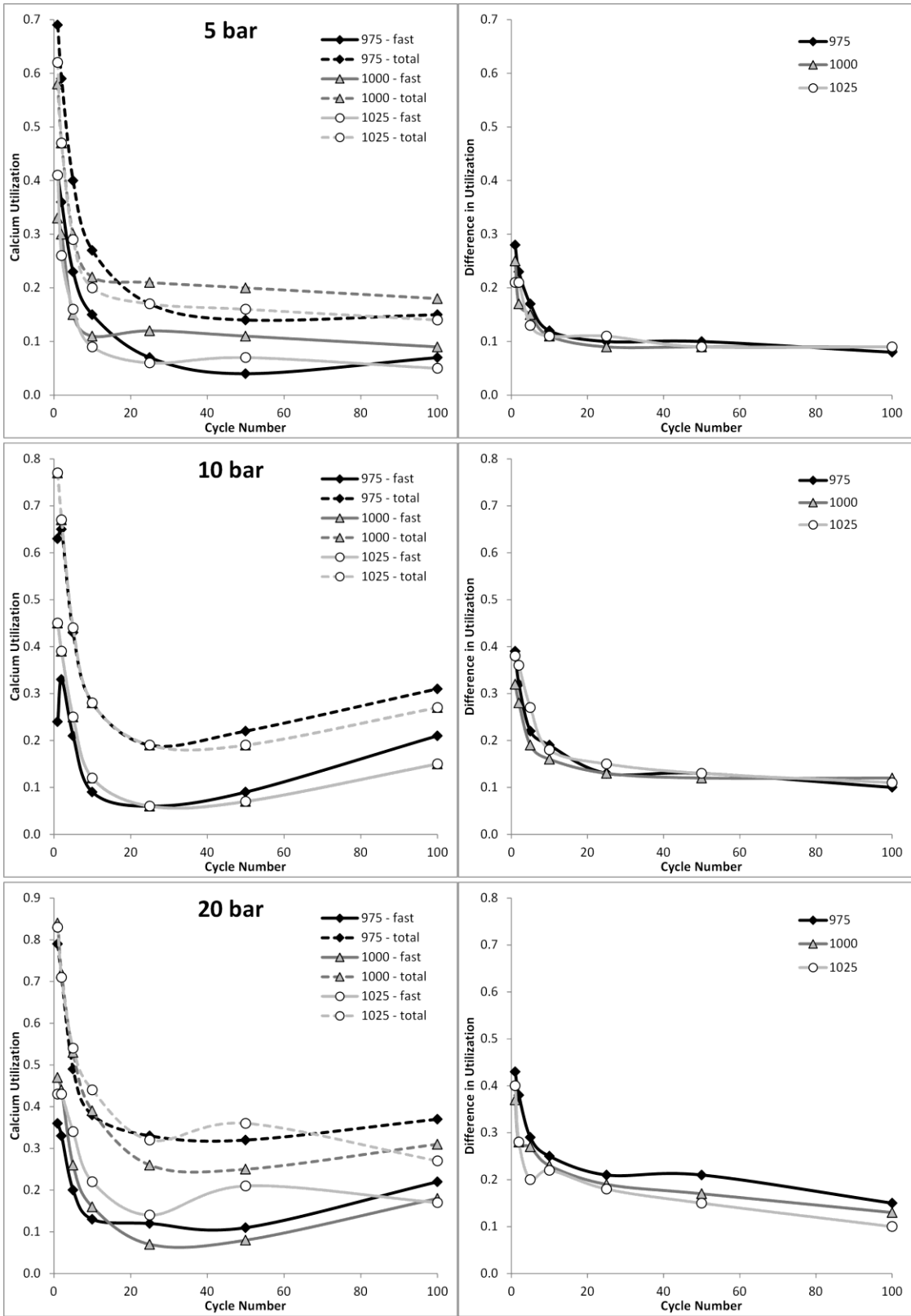


Figure A11.3: Calcium utilization change with time; (left) comparing the fast stage utilization to total cycle utilization, (right) difference between the two.

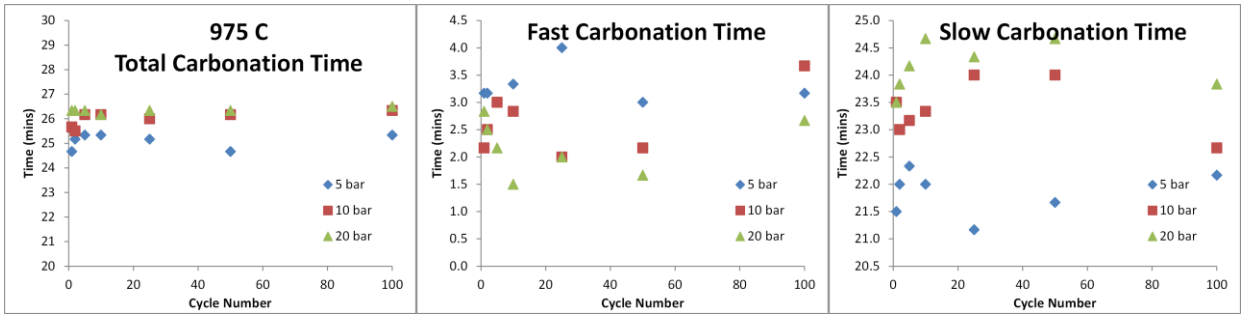


Figure A11.4: Change in duration of carbonation for different pressures at 975°C; (left) total carbonation time, (middle) fast stage duration, (right) slow stage duration.

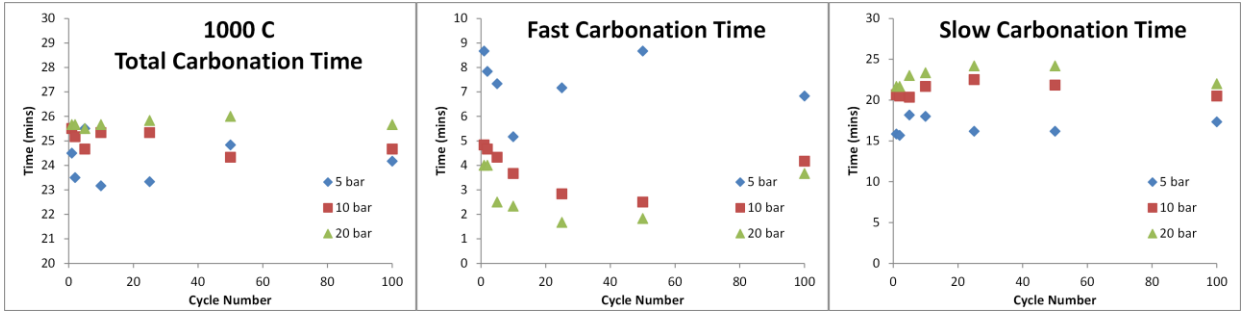


Figure A11.5: Change in duration of carbonation for different pressures at 1000°C; (left) total carbonation time, (middle) fast stage duration, (right) slow stage duration.

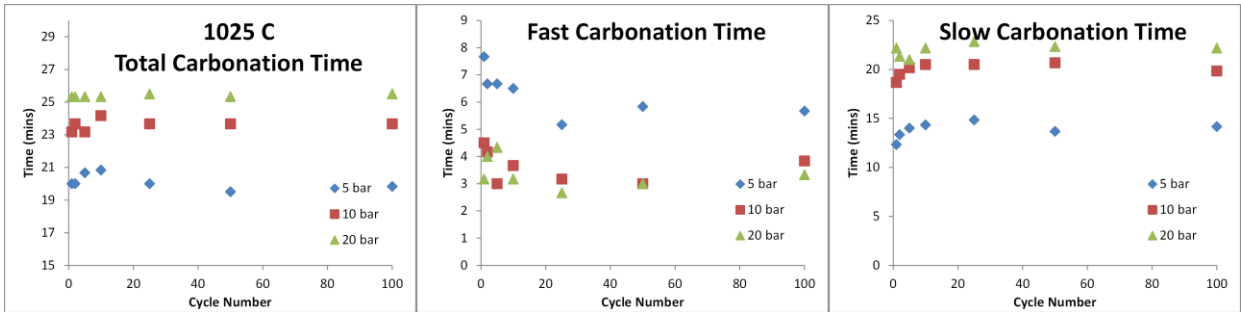


Figure A11.6: Change in duration of carbonation for different pressures at 1025°C; (left) total carbonation time, (middle) fast stage duration, (right) slow stage duration.

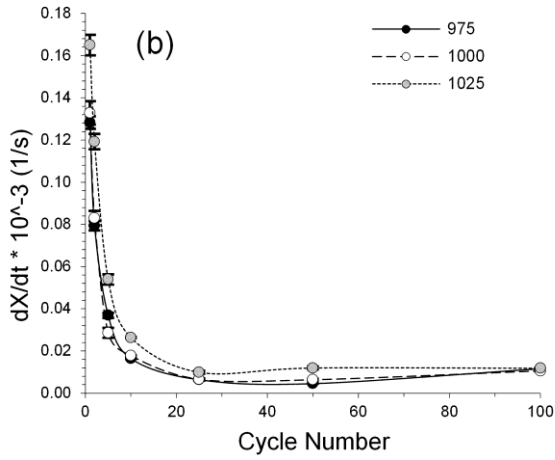


Figure A11.7: Kinetics of diffusion-controlled carbonation over 100 cycles at 10 bar_g; error bars represent standard errors in rates derived from grain model.

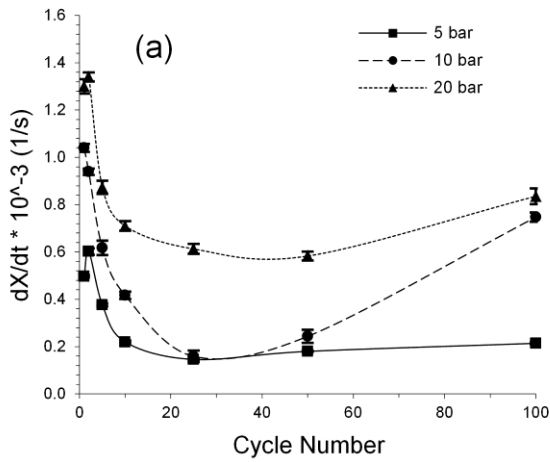


Figure A11.8: Kinetics of reaction-controlled carbonation over 100 cycles at 975°C; error bars represent standard errors in rates derived from grain model.

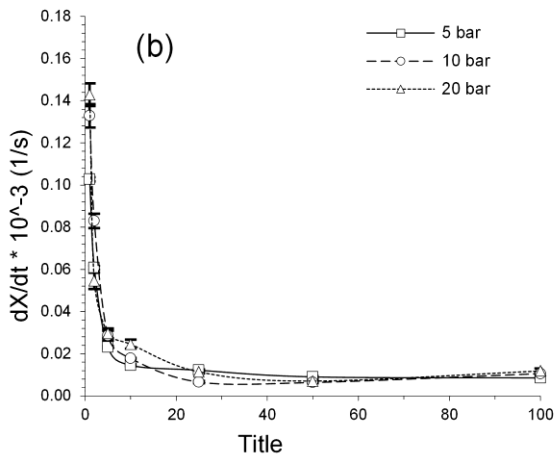


Figure A11.9: Kinetics of diffusion-controlled carbonation over 100 cycles at 1000°C; error bars represent standard errors in rates derived from grain model.

Appendix 12: Activation Energy of Pressure Swing Kinetics

Model-free isoconversional methods are amongst the most reliable in determining activation energies or thermally stimulated complex processes [148].

Friedman method:

$$\frac{dX}{dt} = k(T)f(X) \quad (\text{A12.1})$$

$$k(T) = A \exp\left(-\frac{E}{RT}\right) \quad (\text{A12.2})$$

$$\ln\left(\frac{dX}{dt}\right)_{X,i} = \ln(A_X f(X)) - \frac{E_X}{RT_{X,i}} \quad (\text{A12.3})$$

Plot left side vs. $1/T_{X,i}$ at constant conversion degree and find activation energy from slope.

Activation Energy

Reaction-Controlled Kinetics

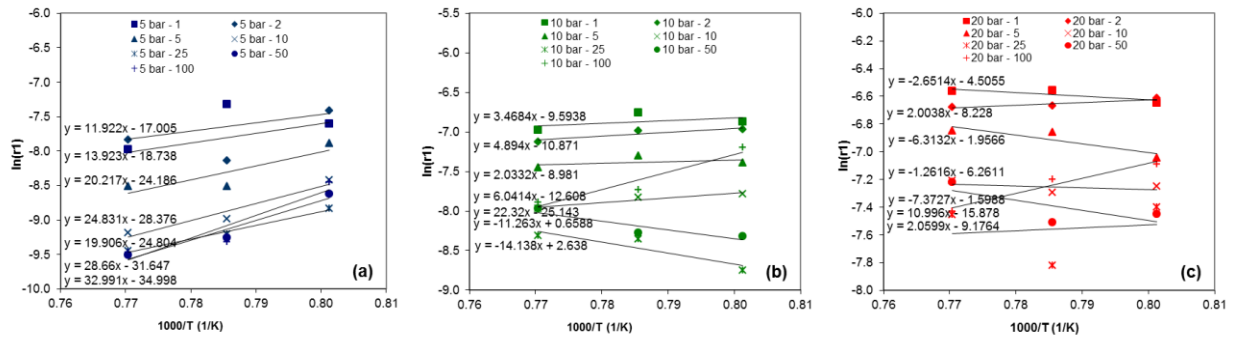


Figure A12.1: Arrhenius plot of reaction rate versus temperature in the reaction-controlled carbonation; a) 5 bar, b) 10 bar, c) 20 bar.

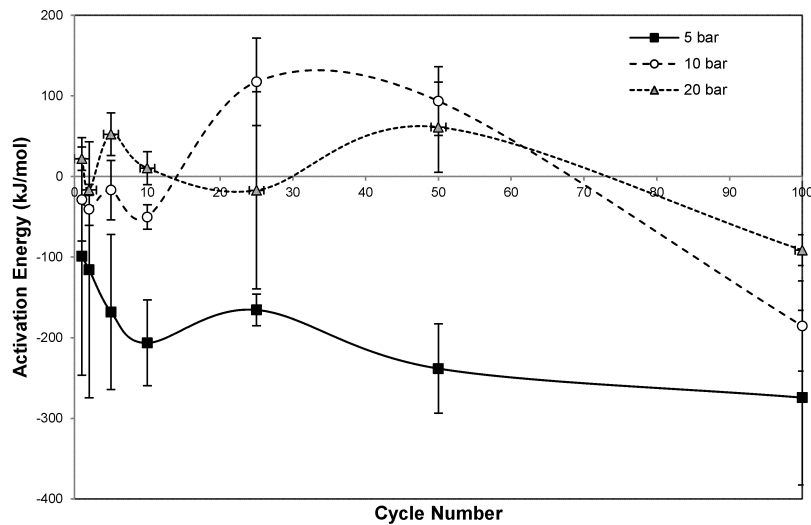


Figure A12.2: Activation energy of reaction-controlled carbonation during cycling; error bars are the standard error of the coefficient from linear regression.

Table A12.1: Regression values from Figure A10.1

Pressure	Cycle	Slope (-E/RT)	R-Squared	E (kJ/mol)	Std. Error
5	1	11.92	0.312	-99.1	147.3
	2	13.92	0.347	-115.8	159.0
	5	20.22	0.753	-168.1	96.2
	10	24.83	0.938	-206.4	53.1
	25	19.91	0.986	-165.5	19.7
	50	28.66	0.949	-238.3	55.4
10	100	32.99	0.865	-274.3	108.4
	1	3.47	0.240	-28.8	51.3
	2	4.89	0.807	-40.7	19.9
	5	2.03	0.172	-16.9	37.1
	10	6.04	0.917	-50.2	15.1
	25	-14.14	0.824	117.5	54.3
20	50	-11.26	0.828	93.6	42.6
	100	22.32	0.917	-185.6	55.9
	1	-2.65	0.696	22.0	14.6
	2	2.00	0.853	-16.7	6.9
	5	-6.31	0.796	52.5	26.6
	10	-1.26	0.208	10.5	20.5
20	25	2.06	0.019	-17.1	122.2
	50	-7.37	0.544	61.3	56.1
	50	-7.37	0.544	61.3	56.1
	100	11.00	0.958	-91.4	19.2

Diffusion-Controlled Kinetics

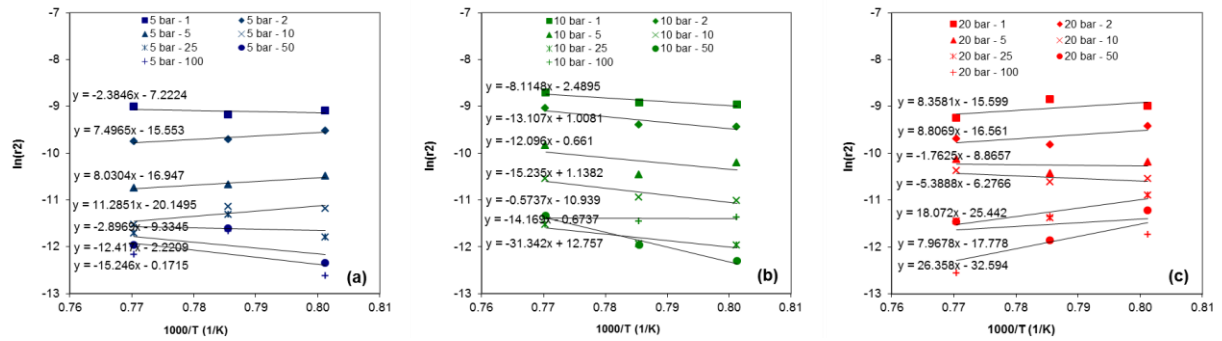


Figure A12.3: Arrhenius plot of reaction rate versus temperature in the diffusion-controlled carbonation; a) 5 bar, b) 10 bar, c) 20 bar.

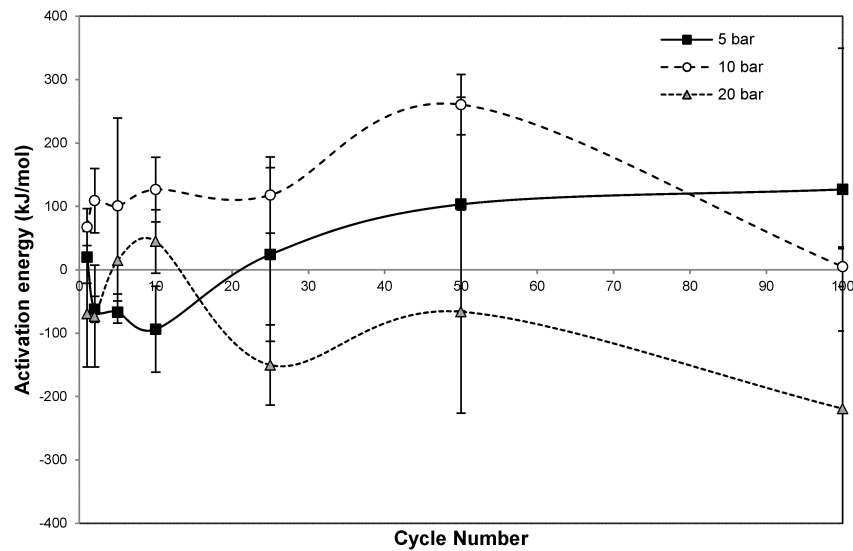


Figure A12.4: Activation energy of diffusion-controlled carbonation during cycling.

Table A12.2: Regression values from Figure A9.3

Pressure	Cycle	Slope (-E/RT)	R-Squared	E (kJ/mol)	Std. Error
5	1	-2.38	0.189	20	41
	2	7.50	0.902	-62	21
	5	8.03	0.936	-67	17
	10	11.29	0.657	-94	68
	25	-2.90	0.030	24	137
	50	-12.42	0.273	103	169
100	-15.25	0.244	127	223	
10	1	-8.11	0.844	67	29
	2	-13.11	0.822	109	51
	5	-12.10	0.345	101	139
	10	-15.23	0.860	127	51
	25	-14.17	0.793	118	60
	50	-31.34	0.968	261	48
100	-0.57	0.023	5	31	
20	1	8.36	0.407	-69	84
	2	8.81	0.454	-73	80
	5	-1.76	0.032	15	81
	10	-5.39	0.445	45	50
	25	18.07	0.849	-150	63
	50	7.97	0.146	-66	160
100	26.36	0.429	-219	253	

Reaction Order

Reaction-Controlled Order

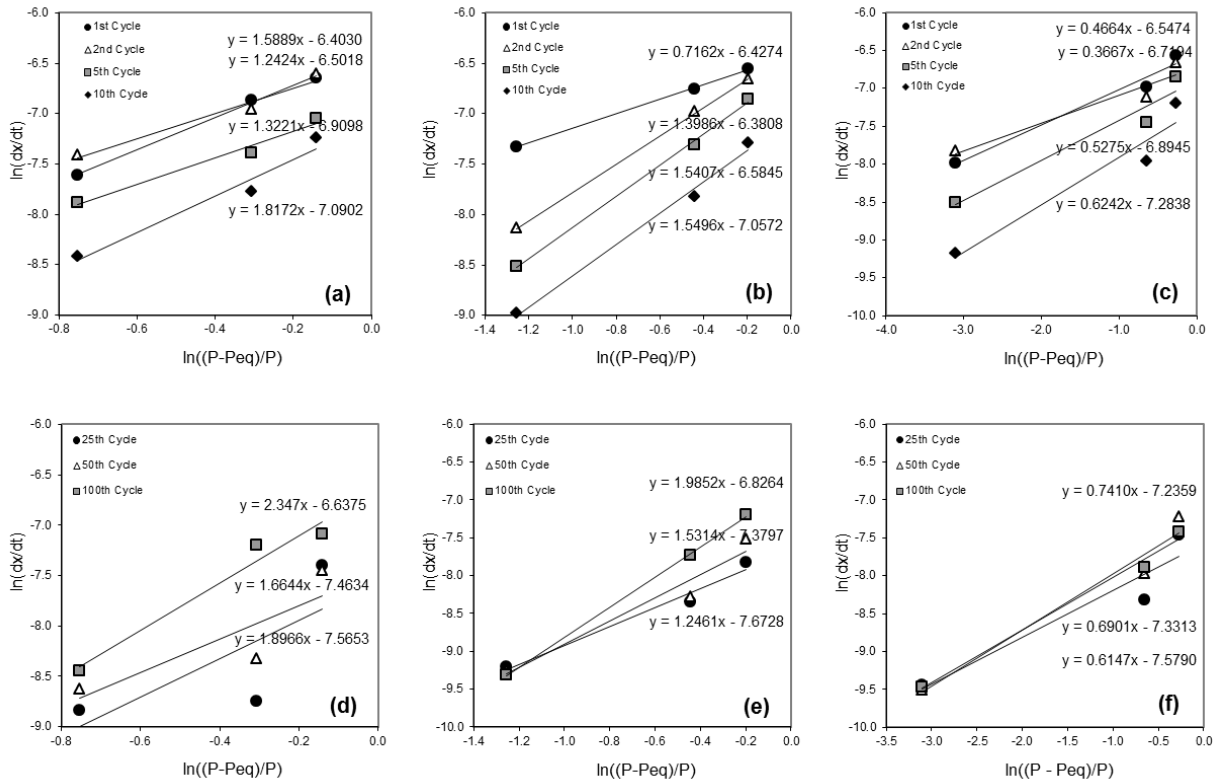


Figure A12.5: Determination of the reaction order reaction-controlled carbonation, (a) 5 bar, 1-10 cycles, (b) 10 bar, 1-10 cycles, (c) 20 bar, 1-10 cycles, (d) 5 bar, 25-100 cycles, (e) 10 bar, 25-100 cycles, (f) 20 bar, 25-100 cycles.

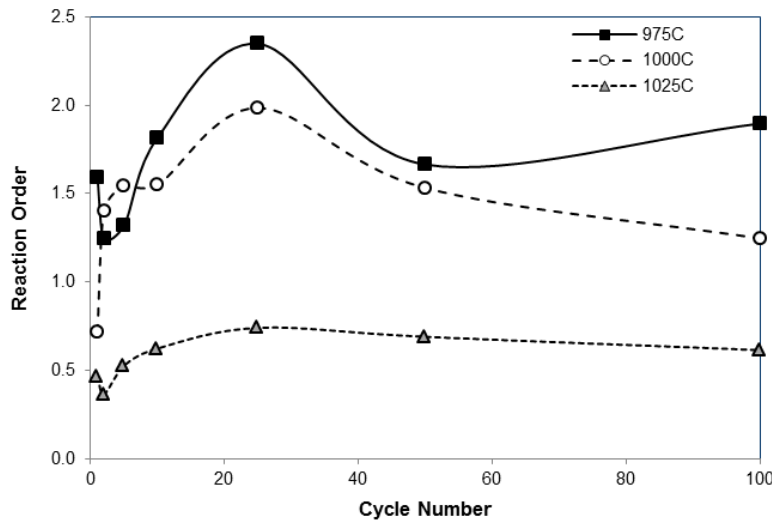


Figure A12.6: Change in reaction order of reaction-controlled carbonation with cycling.

Diffusion-Controlled Order

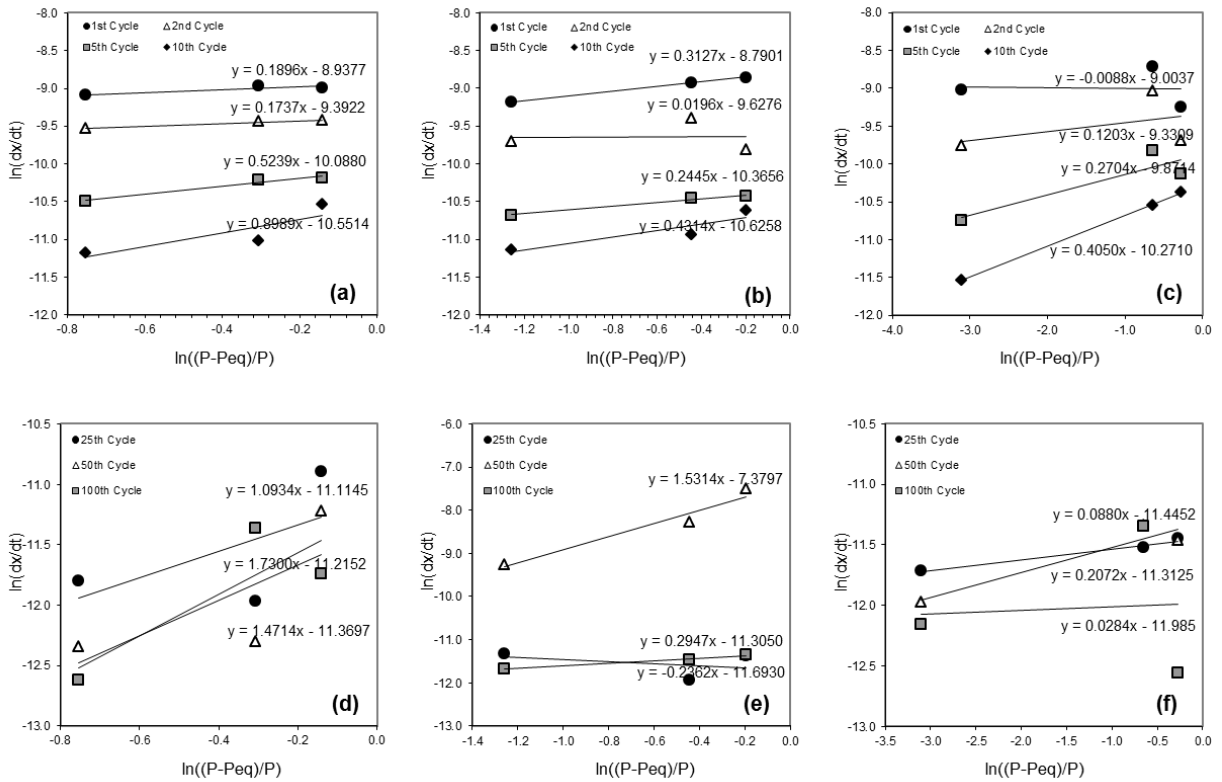


Figure A12.7: Determination of the reaction order for diffusion-controlled carbonation, (a) 5 bar, 1-10 cycles, (b) 10 bar, 1-10 cycles, (c) 20 bar, 1-10 cycles, (d) 5 bar, 25-100 cycles, (e) 10 bar, 25-100 cycles, (f) 20 bar, 25-100 cycles.

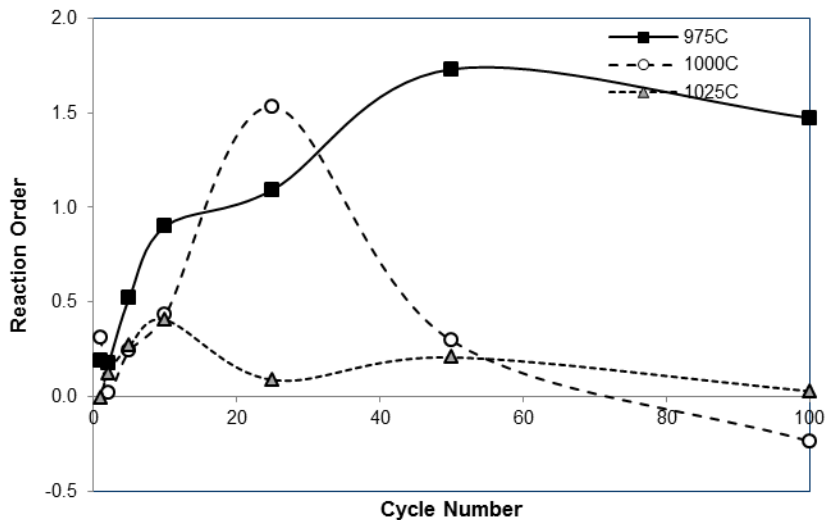


Figure A12.8: Change in reaction order of diffusion-controlled carbonation with cycling.

Appendix 13: AMPEL BFB

Originally experimental studies into limestone-enhanced gasification of biomass were to be conducted in a slightly larger lab scale (102 mm ID, 660 mm in height) bubbling fluidized bed, named the "AMPEL BFB" for its location in the AMPEL building. This apparatus was constructed by J.P. Constantineau and was used previously in studies on zinc roasting [149], and sorbent-enhanced steam methane reforming [150]. Figure A5.1 shows the original configuration of the BFB.

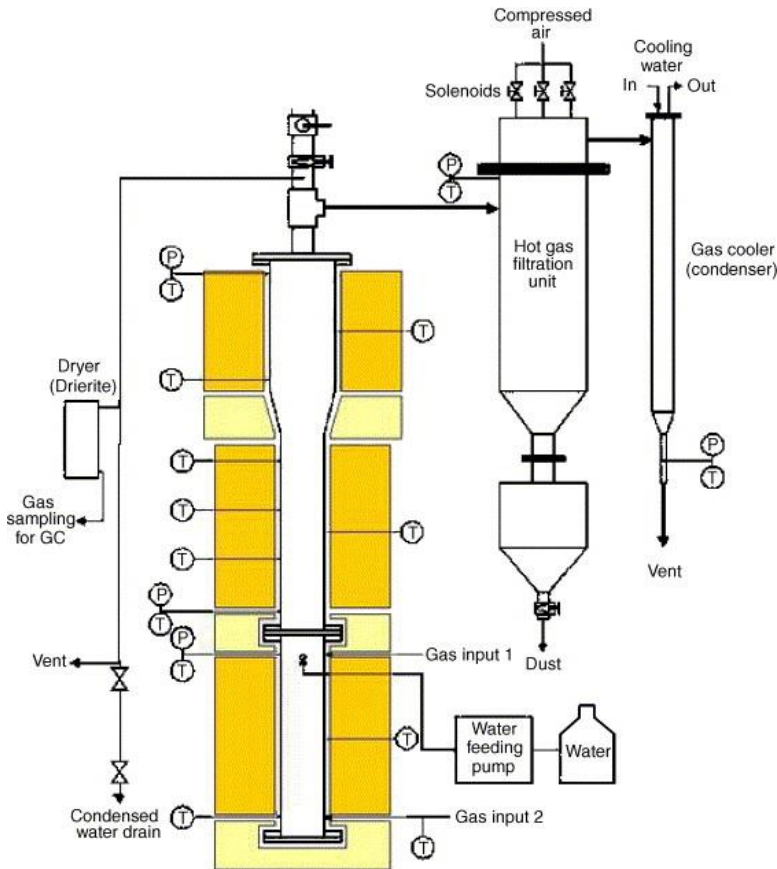
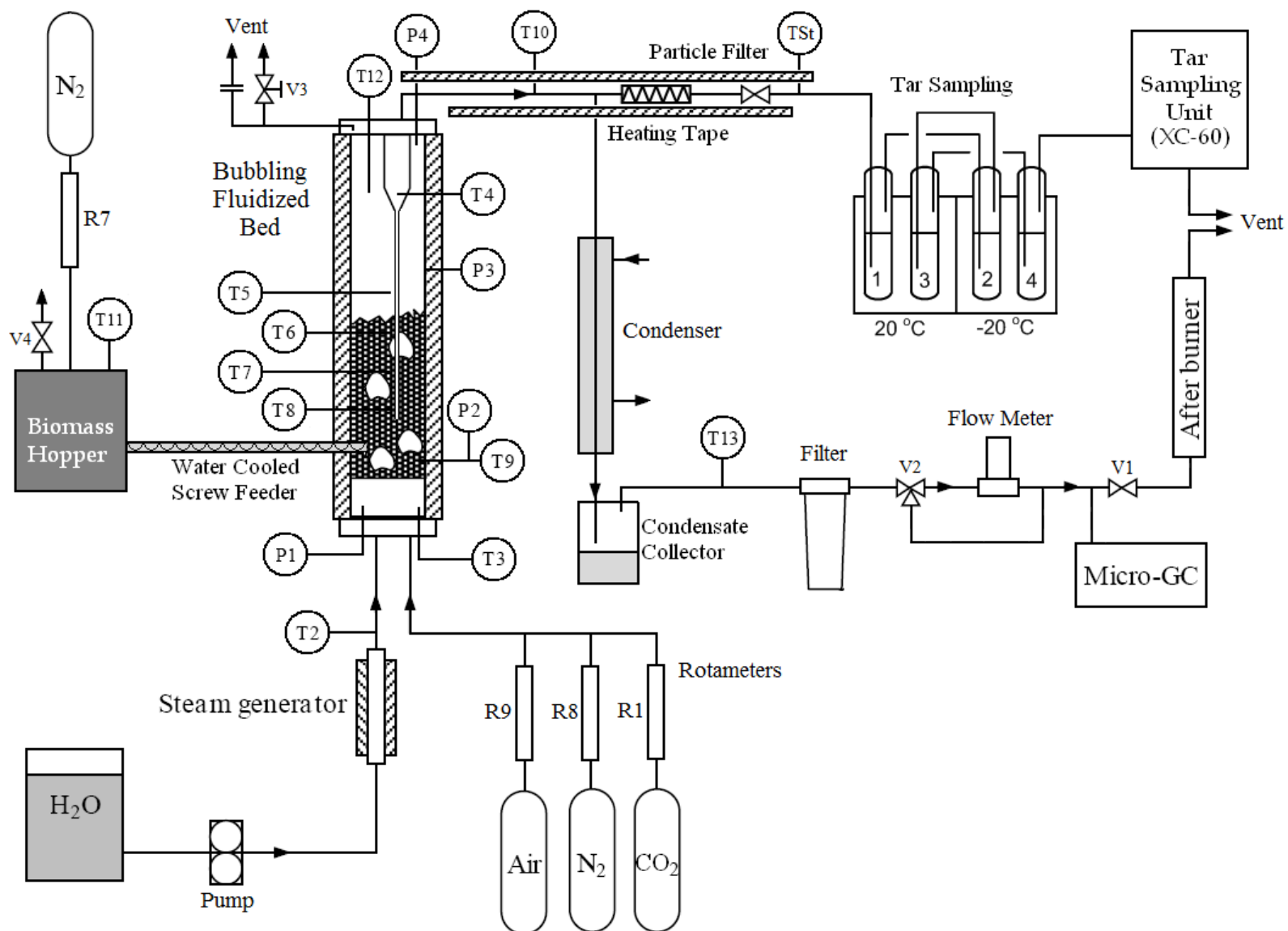


Figure A13.1: AMPEL BFB schematic

Major modifications were made to improve the operation of the system as well as allow for the use of a solid fuel feed and addition of steam. Approximately 6 months of works was undertaken for modification and re-commissioning. It was during the re-commissioning experiments that major flaws were found in the reactor system; specifically the walls of the reactor had eroded, creating holes around the thermocouple ports. Upon further inspection it was found that the reactor was made of inferior 316 grade stainless steel. This grade of steel is inadequate for continuous operation at temperatures above 500°C and a high grade such as 310 should have been used in the original construction. Use of the BFB would have required complete replacement of the reactor and pre-heater sections. For this reason the unit was abandoned and work on L.E.G. continued on the bubbling fluidized bed described in Section 4.

Appendix 14: BFB Gasifier Design and Operation

Piping and Instrumentation Diagram



BFB Gasifier Standard Operating Procedures **Diagrams**

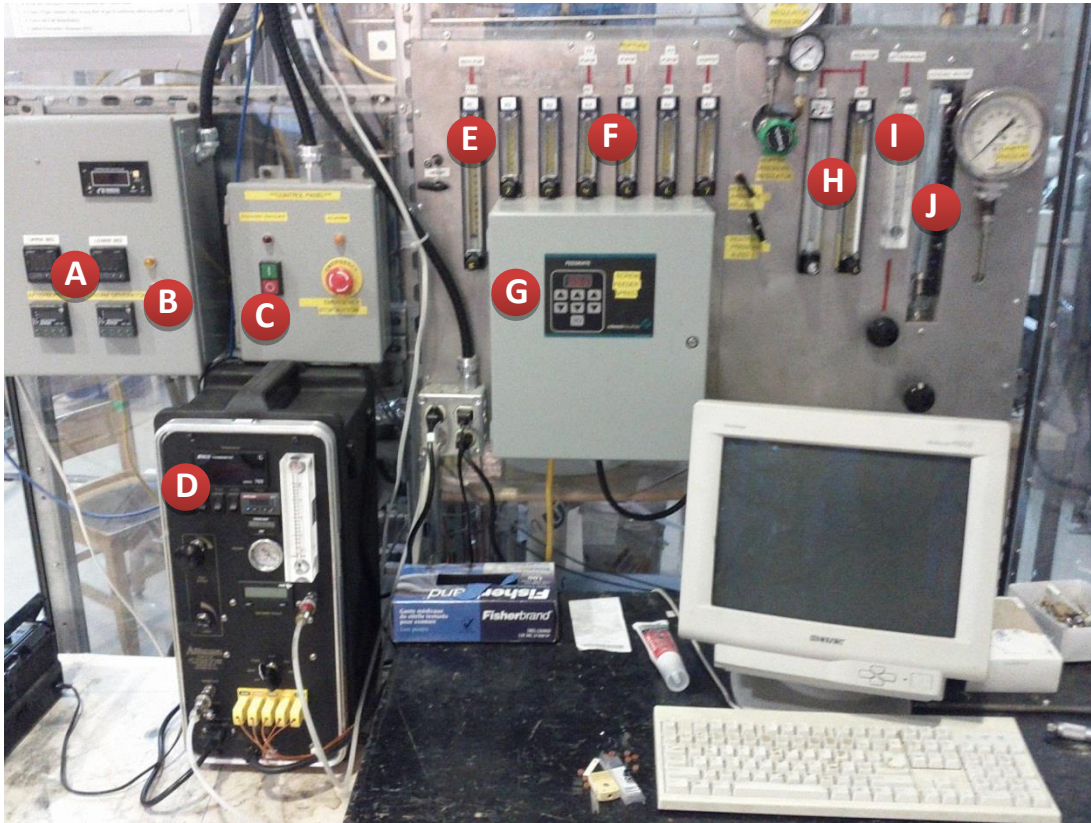


Figure A14.1: Front panel (A – temperature controllers, B – instrument power switch, C – heater power switch, D – tar sampling pump, E – CO₂ rotometer, F – purge rotometers, G – biomass screw feeder control, H – N₂ and air rotometers, I – afterburner air rotometer, J – cooling water rotometer) .



Figure A14.2: Rear of gasifier (A – water pump, B – DI water tank valve, C – reactor flow control valve, D – GC moisture trap, E – Flow meter diversion valve, F – screw feeder cooling water control valve, G – tar sampling impingers, H – condenser, I – condenser access port).

Adding Solids to Reactor

1. Detach screw feeder from reactor and pull screw out
2. Weigh desired amount of bed solids
3. Attach solid loader (see figures below) to screw feeder port on rear of reactor
4. Attach spare building air to solid loading device
5. Using a funnel, pour ~ 50mL of solids through the top valve into the loader
6. **Close the solids valve**
7. Ensure that V1 and “reactor pressure bleed” valves are open
8. Inject ~10 pulses of air into the loader
9. When you can hear air flowing freely into the reactor stop pulsing
 - a. When bed height goes above height of injection port loading becomes more difficult
 - b. If you can no longer hear the air flow through the injection tube it may be plugged
 - i. Try increasing the air pressure and leaving valve open longer to push plug through
10. Wait for reactor pressure to reach zero
 - a. Watch pressure gauge on tar sampling probe
11. Open solid valve and repeat steps 4 – 9 until all solids are injected into furnace
12. Reattach hopper
 - a. put screw back in feed port and secure
 - b. ensure hopper is sealed
 - c. start flow of N2 to hopper (rotometer max)

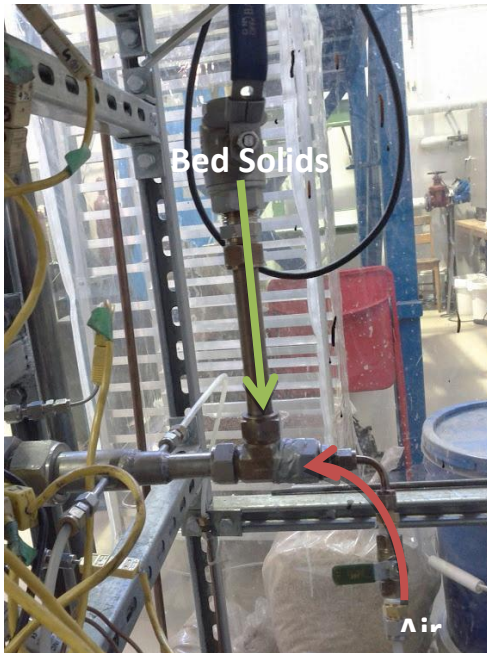


Figure A14.3: Method of adding bed solids

Removing Solids from Reactor

There are two ways to remove solids from the reactor. One, vacuuming the solids out of the reactor through the biomass feed port, and two, removing the bottom flanges. For biomass gasification runs, it is likely that large fuel agglomerates will have formed in the reactor, necessitating solid removal through the reactor bottom.

Solid Collection via Vacuuming

1. Allow reactor to cool down
2. Disconnect screw feeder from reactor at smaller Swagelok fitting
3. Empty small orange vacuum cleaner
4. Remove vacuum hose
5. Weigh empty vacuum bucket
6. Attach vacuum collection tube (funnel attached to ½" plastic hose) to vacuum inlet
7. Turn on vacuum
8. Feed collection tube into the biomass feed port to remove solids
 - a. The feed port is a couple inches above the bottom of the bed, so for the final solids, push the collection tube all the way to the reactor wall then push further to bend the end of the tube towards the distributor plate.
 - b. With the collection tube on the distributor plate, turn on the fluidizing air to the rotometer maximum (160); this will fluidize the remainder of the solids to allow collection.
9. Use the borescope camera to ensure that all solids are removed from the bed

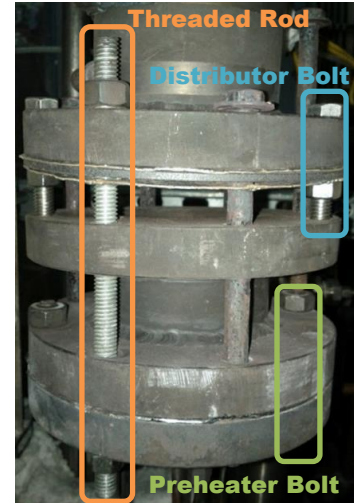
Solid Collection via Bottom Flanges

1. Allow reactor to cool down
2. Remove ring clamps from reactor shell
3. Remove insulation between clamshells
4. Separate clamshell heaters
5. Remove two bolts from the bottom flanges
6. Insert the long threaded rod into one of the empty holes and hand tighten
7. Insert a shorter bolt into the other empty hole through the bottom flange assembly only and hand tighten
8. Remove all bolts from reactor bottom (the two rear bolts will not come out, just leave them with no nuts attached)
9. Secure bottom flange with more shorter bolts
10. Use the long threaded rod to lower preheater
 - a. Slowly loosen threaded rod
11. Gently brush solids into a collection bag or alternatively use the small orange vacuum cleaner to collect solids
12. Firmly tap the reactor walls to remove any agglomerates
 - a. Biomass char agglomerates can become stuck between reactor wall and cyclone downcomer; pry the downcomer away from the wall to remove these.
13. When all solids are removed, take threaded rod out and place pre-heater section on stand
14. Re-attach the bottom preheater section



Distributor / Preheater Reassembly

1. Place a gasket between the bottom flange and the pre-heater section
2. Secure the bottom flange with two smaller bolts (preheater bolts)
3. Using two smaller bolts secure the distributor and gasket assembly (distributor bolts)
 - a. Aligned to the same holes as the preheater bolts
 - b. Put bolts in from above
4. Fill the preheater section with ceramic spacers for steam air distribution
5. With the preheater section supported from below, place the threaded rod into one of the remaining holes and secure with nut on bottom
6. Apply nickel anti-seize to threads of long bolts
7. Place long bolts in remaining holes
8. Use threaded rod to raise preheater section until nuts can be secured on long bolts
9. Remove threaded rod
10. Remove distributor and preheater short bolts
11. Place long bolts in empty holes
12. Tighten bolts in alternating fashion with ratcheting wrench
 - a. Tighten as much as possible



Reactor Pressure Test

1. Attach air cleaning line to biomass feed port
2. Close "reactor pressure bleed" valve V3
3. Close flow control valve V1
4. Open air cleaning line and pressurize to 15 psi by observing the pressure gauge next to V1
5. Snoop all connections, including gasket connections
 - a. Tighten gaskets and repeat if necessary
6. Open V1 to depressurize



Insulation Reassembly

1. Pull clamshell heater sections together as close as they will go
2. Push in baffles to form a tight seal around the reactor
 - a. The baffles prevent heat from rising away from the bottom of the reactor
3. Separate the clamshells slightly
4. Insert thick strips of fiber insulation suspended between the clamshell heaters
 - a. Don't push insulation up against reactor
5. Attach the three ring clamps around the clamshells
6. Tighten the ring clamps
 - a. The insulation between the clam shells should compress and form a tight seal
7. Layer additional strips of insulation in the gaps as needed
8. Pack small pieces of insulation into the bottom of the furnaces
9. Fill any insulation gaps on the top of the reactor



Cleaning Shell-in-Tube Condenser

The condenser should be cleaned prior to each gasification run as it becomes plugged easily

1. Remove the Swagelok plug from the condenser access port
 - a. The use of an extra pry bar will be necessary
2. Using a chair or step ladder, place the available short length of 3/8" stainless steel tube through the hole in the top of the gasifier enclosure
3. Thread the SS tube into the open condenser access port
4. When a blockage is reached, use a hammer to hit the end of the tube to clear the blockage while holding the tube tightly
 - a. The blockage may clear suddenly, avoid losing the tube down the condenser
5. Once the length of the short tube has been reached, switch to using the long length of tube
6. The blockage is cleared once the tube can be moved freely up and down the condenser
7. Remove the tube from the condenser
8. Apply Ni based thread lubricant to the condenser access tee junction
9. Tighten Swagelok plug on tee fitting using pry bar



Un-Plugging Screw Feeder

If the screw feeder stops turning it is likely plugged at the entrance to the fluidized bed. To un-plug, follow the procedure below.

1. Turn off screw feeder
2. Turn off all gas flows to the reactor
 - a. Including afterburner air
 - b. Leave the flow to the hopper on
3. Fully open valves V1 and "reactor pressure bleed"
4. Allow pressure in the reactor to reach atmospheric
5. Detach the feeder from the feed port at the Swagelok fitting
6. Place the length of plastic board under the feed port connection to collect solids in the screw feeder
7. Slide the screw out of the feed port
 - a. **CAUTION - if gases are escaping the feed port when the screw feeder is removed, leave the reactor enclosure and wait for gases to dissipate**
 - b. It is likely that the screw won't come out of the port through pulling
 - c. To extricate a jammed screw, turn the feeder on for short intervals until it can be easily pulled out
 - i. The turning screw will push the hopper backwards and the screw out
 - ii. If the screw will not turn on its own you may need to turn the screw manually by turning the rear gear using a screw driver
 - iii. **CAUTION - ensure the screw feeder is off when accessing the back gearing**
8. With the screw removed insert the available 1/4" tubing into the feed port
9. Using a hammer, tap the end of the tube to push the blocked fuel into the reactor
10. Once the tube can be moved freely into and out of the bed, remove the tube

11. Attach the spare air line to the feed port and inject a few burst of air to push any solids into the reactor
12. Re-insert the screw feeder and tighten Swagelok fittings

System Preparation

1. Ensure all circuit breakers are engaged
2. Ensure sufficient DI water in the tank
3. Loosen DI tank cap
4. Open compressed air line valve, N₂ cylinder, CO₂ cylinder
 - a. Set pressures to 20 psi
5. Ensure 3 way valve (V2) after the filter is open towards the flowmeter
6. Ensure needle valve (V1) before afterburner is open
7. Ensure hopper pressure relief valve is closed
8. Ensure reactor pressure relief valve is closed
9. Close the drain valve on the condensate collector
10. Turn on DAQ software and begin recording
 - a. The password for the computer login is 'cfx'
11. Open Hopper N₂ valve and set flow to a minimum of 100mL/min (60) to protect from back flow of hot gases into the hopper
12. Open cooling water valve and set flow to 5 mm
13. Open after burner air valve and set to 1 SLP
14. Purge pressure sampling ports
 - a. One at a time, fully open pressure purge rotometers for 10 seconds each
15. Purge reactor pressure relief line
 - a. Fully open purge rotometer for 10 seconds
16. Install the screw feeder
 - a. Ensure the screw enclosure tube is exposed to the correct amount
 - i. The marked line on the tube should align with the end of the rubber hopper
 - ii. If the tube is too far out the screw will not penetrate far enough into the reactor and will become plugged
 - b. Slide the screw into the feed port
 - i. If the screw does not go all the way in, there are solids blocking the feed port
 - ii. To unblock, attach the spare air line to the feed port and inject a few burst of air
 - c. Tighten the Swagelok fitting using two wrenches
17. Ensure that the CO detectors are powered and on



Gasification Run

Preheating

Preheating will take approximately 3 hours to reach a reactor temperature of 800 °C. The temperature controllers will rapidly increase to within 100 °C of their set point, but will then slow dramatically. To hasten bed heating increase controllers 100 °C beyond desired set point initially, until desired set point is reached.

1. Open Fluidization N₂ valve and set flow to ~8 LPM
2. Ensure afterburner air and cooling water flows are set according to 'system preparation'
3. Continuously monitor the hopper pressure to ensure that the hopper is at a slightly higher pressure than the reactor and that N₂ flow to the hopper does not stop
4. Ensure the hopper pressure is paralleling the pressure in the reactor
 - a. If the hopper pressure is consistently higher than the reactor pressure and is not changing with changes in reactor pressure there is likely a block in the biomass feed tube

5.2.2.1.1 Fluidized Bed Heaters

1. Set temperatures for the upper and lower reactor heaters
 - a. Set the upper heater controller to the desired bed temperature
 - b. Set the lower bed heater to 50-100°C above the desired bed temperature

Steam Generator

1. Set steam generator temperature to 350 °C

Afterburner

1. Set temperature to 600 °C
 - a. The auto ignition temperature of H₂ is approximately 500 °C
2. Open air valve to after burner and set flow to 1 SCFM

Steam Gasification

1. Ensure the reactor is preheated to the desired temperature
2. Ensure that the two "pressure bleed" valves are closed
3. Ensure that afterburner air and cooling water flows are correct
4. Start the GC acquisition sequence
5. Turn on the water feed pump to the desired stroke rate
6. Adjust the Fluidization N₂ to the desired flow rate
7. Adjust the Fluidization CO₂ to the desired flow rate
8. When steam has started entering the reactor the temperature in the preheater will drop significantly, wait for this temperature to stabilize
9. Turn on the biomass feeder to the desired feed rate
10. Monitor the pressure gauge at the GC sample port to ensure the back pressure is between 1 and 3 psi
 - a. Adjust valve V1 to increase back pressure
 - b. If the backpressure is too low then the produced gases will not make it to the GC
 - i. A significant He peak on the molesieve column is an indication of this
11. Monitor the afterburner exit temperature (T14) and adjust the afterburner air flow to maintain 600 °C at this point
 - a. If temperature is too high, increase air flow and vice versa
12. Monitor the screw feeder to ensure it is turning
 - a. If it is not, stop run and unplug

13. Monitor the bed pressure
 - a. Maximum hopper pressure is 30 kPa
 - b. If the pressure is increasing and back pressure is stable or falling, then there is likely a plug in the condenser or just upstream of the particle filter
 - c. Shut down run and un-plug
14. Monitor the gas temperature prior to the flow meter
 - a. If this increases beyond 30 °C, increase the cooling water flow rate
15. Monitor the water flow through the screw feeder cooling jacket
 - a. If flow stops, the flow is too low and steam is being generated in the cooling jacket
 - i. Increase flow by opening needle valve
 - ii. If flow refuses to go through the cooling jacket, temporarily increase the total cooling water flow significantly to push water through the jacket

Shutdown Procedure

1. Turn off the biomass feed
2. Stop water feed pump
3. Close valve on water feed tank to ensure no water flows into the reactor through gravity
4. If desired turn on fluidization Air flow to burn off residual carbon inside the reactor
 - a. The reactor temperature must not exceed 900 °C during this step, if the temperature is rising rapidly, decrease air flow and increase N₂ flow
 - b. Once all the carbon is burned off the temperature will fall rapidly
5. Set fluidization N₂ flow to 8 LPM
6. Wait until the GC reads 100% N₂
 - a. To ensure no syngas remains in the unit
7. Stop the GC
8. Stop DAQ on computer
9. Turn off reactor heaters and steam generator heaters
10. Set the fluidization N₂ to 2 LPM until reactor is completely cooled down
11. Wait until the reactor has cooled down below 300 °C
 - a. Turn off fluidization N₂ flow
12. Wait until the reactor has cooled down below 100 °C (may take overnight)
 - a. Turn off hopper N₂
 - b. Turn off cooling water
 - c. Turn off afterburner air flow

Micro GC Setup

1. Connect sample gas line (1/16") from moisture trap to inlet on GC stand
2. Connect carrier gas lines (AR and He)
 - a. Open gas cylinders
 - b. Regulate pressure to 80psi
 - c. Open flow valves on GC stand
3. Check the desiccant in the GC moisture trap (figure 3)
 - a. Be sure to use gloves when handling the desiccant
 - b. Remove the desiccant housing from the reactor exit line (Figure 1 - b)
 - c. Remove the elbow fitting from the housing top
 - d. If the desiccant is saturated replace with new desiccant (blue = dry, pink =saturated)
 - e. To regenerated desiccant cook in a furnace at 105 °C for several hours until material is blue.
4. Check the carrier gas O₂ and moisture traps on the GC cart
 - a. Check indicators and order new traps if spent
5. Turn on GC and laptop
 - a. These should be left on when not in use
 - b. If laptop does not connect with GC
 - i. Try re-starting laptop or
 - ii. Turn off both GC and laptop, turn on laptop, log into windows and turn on GC
6. Log into the GC software
7. If the GC has been idle for a long period of time a Bakeout cycle is necessary
 - a. Moisture builds up in the Molesieve column and causes the peaks to shift closer together
 - b. Run a Bakeout method
 - i. Maximum temperature (180°C) on the molesieve column overnight



Micro GC

Tar Sampling

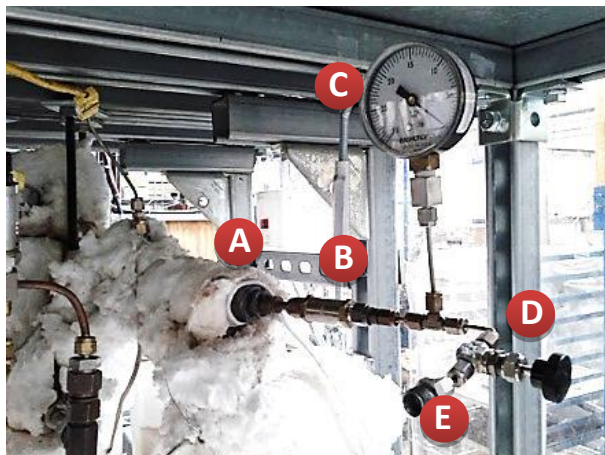
For full gasification tar sampling procedure please see standard: **CEN/TS 15439 from the European Committee for Standardization.**

This procedure describes the setup of the impinger sampling train for the CERC BFB gasifier. The sampling train is a slight modification of the CEN standard. The important differences are the lack of isokinetic sampling and the use of 4 impingers instead of 6.

Probe and Impinger Setup

1. Before assembly, ensure the filter and probe lines are clean of tar and obstructions.
2. Assemble the tar sampling probe and attach to the reactor sample port located on the exit line of the reactor above the external cyclone.
3. You may pressure test the probe now by pressurizing the system with the impinger flow control valve closed
4. Fill the four impingers with 150mL of iso-propanol each
5. Seal the implingers using a thin film of silicone vacuum grease
6. Attach the sampling probe to the impinger train.
7. Attach a thermocouple to the particle filter with a ring clamp
8. Attach a second thermocouple as close to the exit of the probe as possible to read the temperature of the exit gas
9. Wrap the heating tape around the sampling probe so that a portion of it is on the first impinger.
 - a. Preventing tar condensation in the probe
10. Attach the exit line from the impinger train to the inlet line to the APEX sampling unit
11. Attach the thermocouples and heating tap to the sampling unit
12. When ready to start the gasification run, fill the left impinger bath with a 4:1 mixture of ice and salt
13. Place a bucket below the ice bath drain spout
14. Place a thermocouple attached to the sampling unit into the ice bath
15. Cover the ice bath with Styrofoam
16. Ensure the impinger flow control valve is closed

Sampling Probe



A - Coupling to reactor

B - Particle filter

C - Vacuum pressure gauge

D - Impinger flow control valve

E - Coupling to impinger train



Impinger train



Tar Collection

1. Turn on the APEX sampling unit
2. Turn on the "Probe" to power the heating tape
3. Set a temperature of 300C at the probe outlet
 - a. Ensure the "probe" thermocouple is the one at the outlet
4. When temperature has been reached, reset the flow totalizer and turn on the pump
5. Adjust the 'impinger flow control valve' and the two flow control valves on the APEX unit to maintain a vacuum at the probe and a significant amount of flow
 - a. If a positive pressure exists at the impingers, gas may escape
6. Turn on and reset the timer to time the sampling
7. When sampling is complete, turn off the pump
8. Close the flow adjust valves on the APEX unit
9. Record the total flow value and time
10. Turn off the 'probe'
11. Turn off the APEX unit

Sample Collection

1. Remove the impinger train to a fume hood
2. Using the vacuum pump and filter assembly, draw the impinger solution through a 0.02um filter into the Erlenmeyer flask
3. Rinse the impingers and lines thoroughly with iso-propanol, filtering the rinse and collecting in the Erlenmeyer flask
4. Perform a final filter of the impingers with methyl chloride, again filtering the rinse into the Erlenmeyer flasks
5. Collect the fines from the particle filter
 - a. Weight a weigh boat
 - b. Put the loose fines into the weight boat
 - c. Rinse the particle filter with iso-propanol
 - d. Allow to dry and weigh the fines
 - e. If there appears to be tar in the fines, rinse with methyl chloride, vacuum filter the rinse and combine with the bulk tar / solvent
6. If there are concern that the tar sampling probe was not at 300C or above during sampling, you may want to rinse it with the solvents, filter the rinse and collect it.

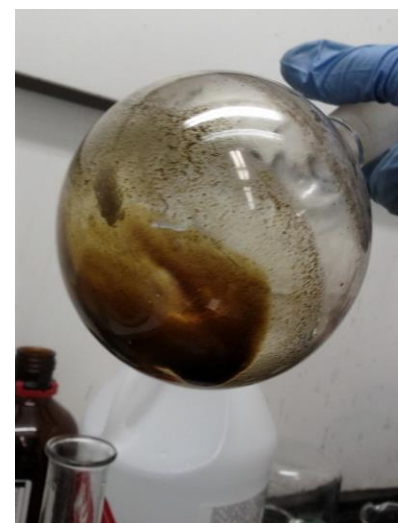
APEX Sampling Unit



Gravimetric Tar Measurements

1. Weight the evaporator flask
2. Pour a portion of the solvent/tar sample into the evaporator flask, half filling the flask
3. Attach the flask to the rotary evaporator in the fume hood in rm5.06
4. Fill the rotovap water bath
5. Turn on the rotovap
6. Set the temperature to 65C
 - a. The temp setting is ~3C higher than actual, set to 62C and monitor the thermometer
7. Ensure the condenser collection flask is empty
8. Turn on the cooling water, only a very low flow is required
9. Attach the vacuum pump inlet to condenser top outlet
10. Turn on the vacuum pump and adjust to maximum vacuum
 - a. vacuum should be maintained at -20inHg
11. When the majority of the solvent has evaporated off, add additional solvent/tar sample
12. Repeat until all the sample is in the rotovap
13. Rinse the solvent/tar Erlenmeyer flask with iso-propanol and ad to the evaporator flask
14. When all the solvent has evaporated off remove the sample and weight the evaporator flask
15. To remove the residual water in the sample, return it to the rotovap
16. Using the building line, add a small amount of air to the rotovap condenser section
 - a. be careful not to pressurize the condensor above -10inHg pressure
17. Alternate between vacuum and air addition until no visible droplets are present in the tar
18. Place the vacuum flask in a desiccator for 2hrs
19. Weight the flask

Rotary Evaporator Vacuum Setup

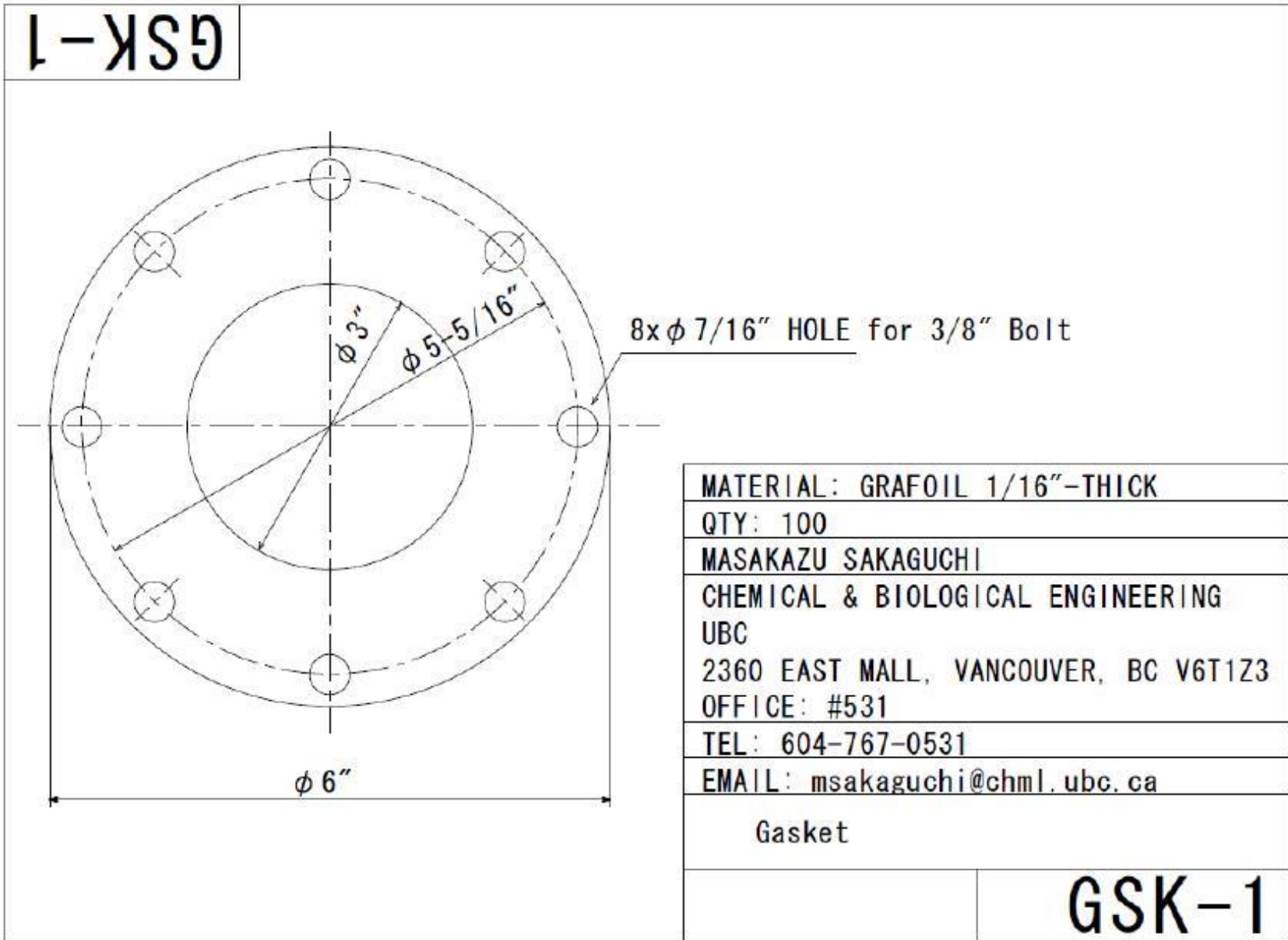


Water Free Tar

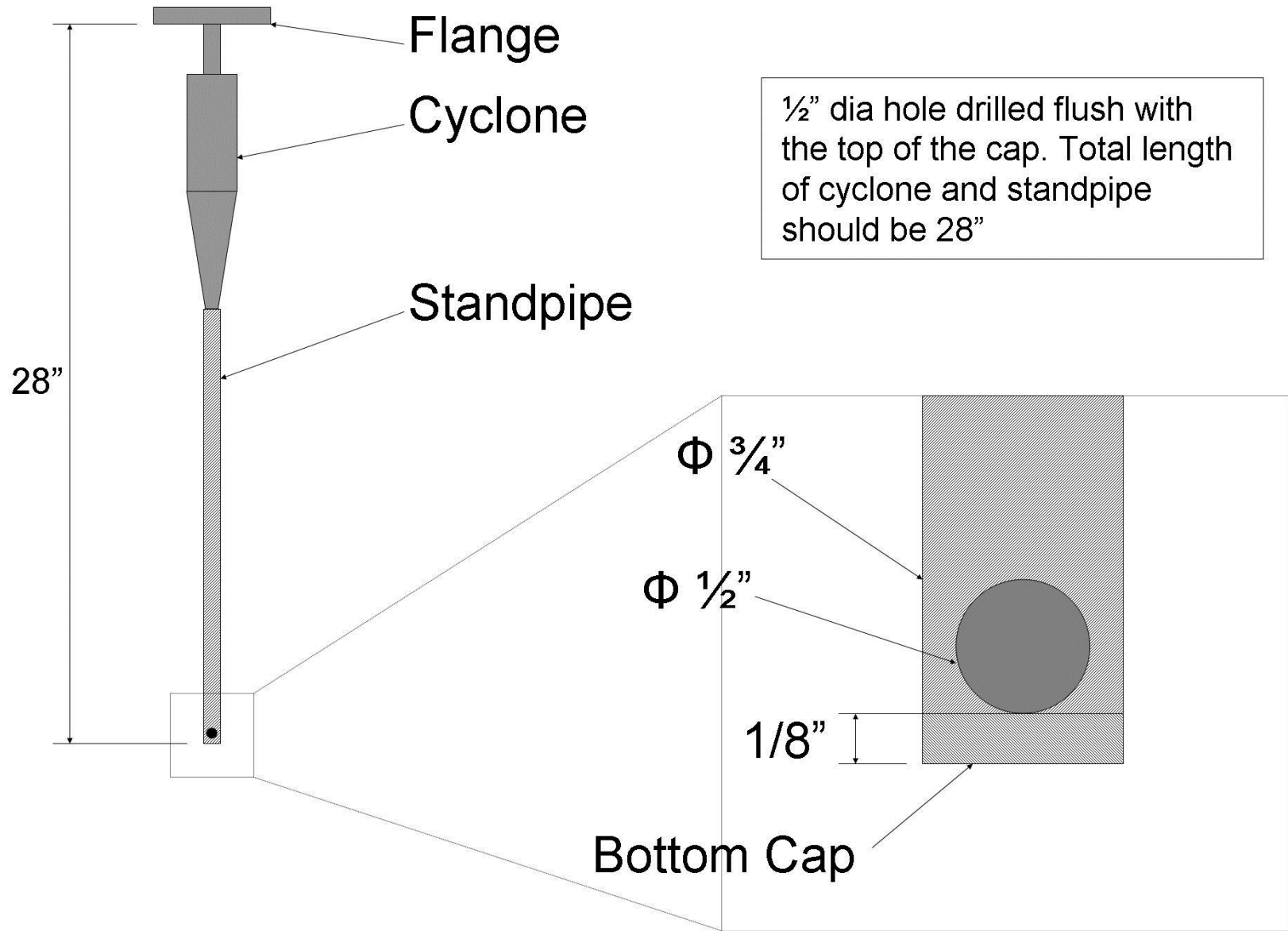
Tar Free Condensate



BFB Reactor Gasket Dimensions



Internal Cycle Standpipe and Trickle Valve Design



Appendix 15: BFB Gasifier Operational Issues

Feed System

The bottom section of the hopper is constructed of a flexible plastic, allowing it to be massaged by mechanized paddles connected to the screw feeder drive motor, that prevent bridging in the lower half of the hopper. This lower section and associated seals cannot handle elevated pressures and will begin to leak. In one instance a hole opened in the flexible section as a result of the repetitive massaging and over-pressurization, allowing flue gases from the bed to escape up the screw feeder and out the hole.

In addition to limiting the pressure of the system, the feed system had the additional operational issue of screw feeder plugging. Plugging occurred when gases from the bed flowed into the screw feeder, causing condensation of steam / biomass moisture in the screw feeder, forming plugs of wet biomass. Additionally, it was found that too fine a biomass particle size caused plugging. It is suspected that this is the result of fast pyrolysis occurring at the feed port on the reactor, causing a plug of biomass char and tar to form at this point.

Nitrogen flow into the hopper was essential to minimize plugging of the screw feeder and had to be maintained during the entire operation of the BFB gasifier. If system pressure became too high, the feed hopper was likely to leak, allowing the flow of steam and flue gases back up the screw feeder, leading to plugging. Despite efforts to prevent plugging, it occurred periodically, more commonly in early runs. Un-plugging the feed port involved removing the screw feeder and either using a hammer and rod to push the plug through into the reactor or drilling through the plug to dislodge it, using a drill and long drill bit.

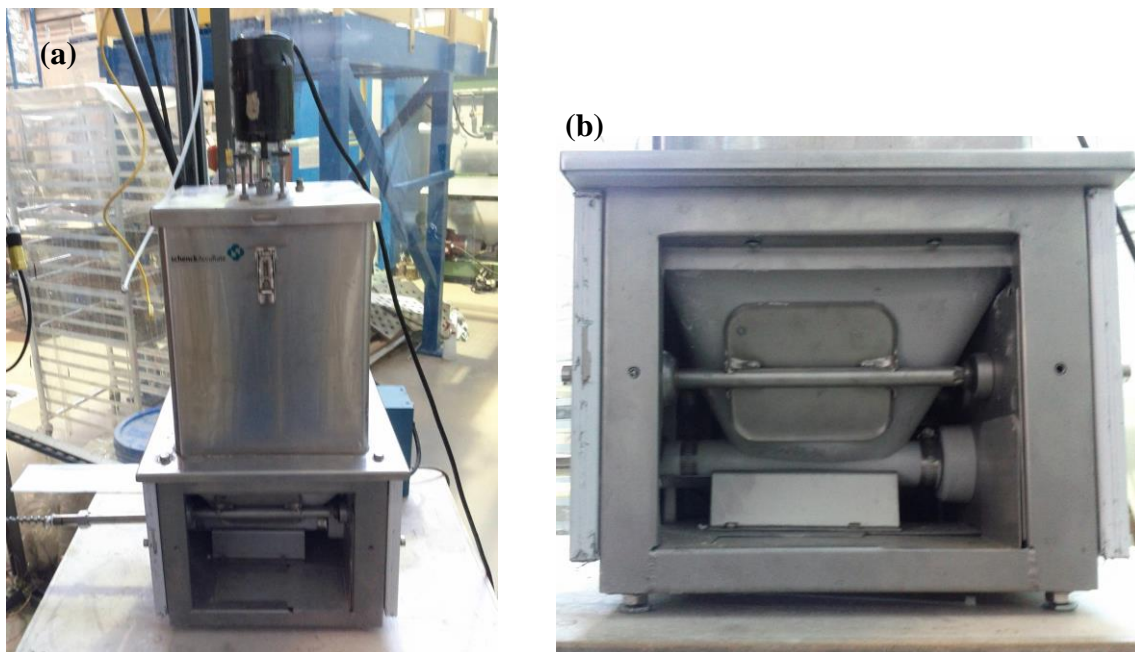


Figure A15.1: (a) feed hopper; (b) close-up of the flexible hopper bottom with paddles.

Condenser Plugging

Pressures above the operational range of the feed hopper typically resulted from plugging of the system downstream of the reactor. Plugs regularly formed in the flue gas condenser, where the gas was rapidly cooled and less volatile compounds condensed. These plugs were made up of condensed tar and water, and elutriated char and beds fines. The condenser was a simple shell in tube design that effectively cooled the gas from approximately 500°C to room temperature; however, the inner tube was too narrow (15mm ID) and plugged on a regular basis. As well plugs would form in the tubing leading from the condensate collection tank to the low temperature filter; however, formation of these plugs was much less frequent.

On average the condenser would plug after approximately 2-3 hours of gasification operation. Once the plug was formed, the system pressure would increase rapidly and the system operation would need to be halted to prevent damage to the feed hopper. Un-plugging the condenser involved opening an access port above the condenser and hammering a steel tube down in the condenser until the plug was freed. Occasionally the plugs were too severe for physical removal and a solvent had to be poured down the condenser to help break up the condenser tars and chars and make physical removal possible. The frequency of the condenser plugging prompted the design and construction of a new condenser system, as detailed in Appendix 19. The new condenser system features a much larger shell in tube design (51 mm ID), as well as an external cyclone for collection of fines.



Figure A15.2: Photo of condenser tube being un-plugged.

Fine Elutriation

The BFB gasifier was designed with an internal cyclone; however, the cyclone had no standpipe in the original design, rendering it in-effective. A standpipe with trickle valve was designed, as shown in Appendix 12 and the figures below. Testing of the effectiveness of the trickle valve was difficult and the design was simply based off of an empirical relation: $d_{opening} = 10*d_{particle}$. Testing did show that bed solids flowed freely out of the opening when un-obstructed; however it is not known if gas by-passing occurred or if standpipe became plugged during operation.

It was suspected that the separation efficiency of the internal cyclone was low due to the regular plugging of the condenser than suggested a high elutriation rate. It was very difficult to measure the fines production rate during experiments as iso-kinetic sampling of the product gas was impossible. Iso-kinetic sample was attempted, but the sample probe required for such a low flow system was very small (1/8") and plugged almost immediately.

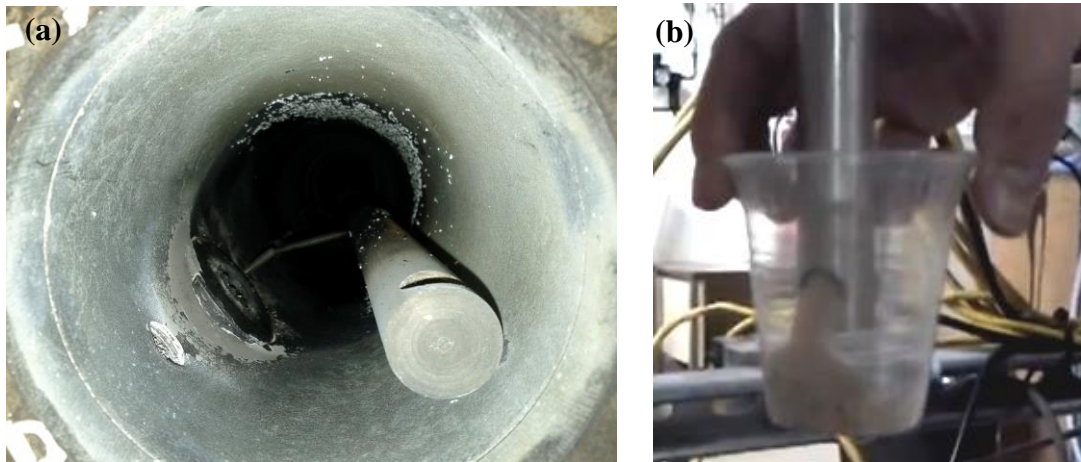


Figure A15.3: (a) photo from bottom of bed showing trickle valve; (b) trickle valve in un-obstructed testing.

Bed Agglomeration

During biomass gasification, the lighter biomass char rose to the surface of the bed and formed large agglomerates. These agglomerates grew very large over the short duration of gasification and if long gasification tests were performed, agglomerates could block large cross-sections of the reactor. Large agglomerates would form and become stuck between the cyclone standpipe and the wall as well on the bed thermocouples. To prevent these from forming in the future, a high gas velocity should be used to make a more vigorously bubbling bed to break-up the agglomerates.



Figure A15.4: Photo of sand bed material after gasification showing large agglomerates.

Reactor Leaking

The gaskets at the bottom and top of the reactor were exposed to very harsh conditions and frequently failed. To maintain gasification temperature inside the reaction, temperatures of the reactor walls were typically in the range of (750-850°C). Originally graphite gaskets were used as they are in-expensive and readily available. The interior of the gaskets were un-affected by the high temperatures as the reactor was typically a reducing environment; however, externally the graphite gaskets were oxidized at the high temperatures and needed regular replacement. The life of the graphite gaskets could be extended by applying a high temperature sealant over the gaskets prior to operation, but this was only a stop gap solution.

In later tests a high temperature ceramic gasket material was used (Garlock series 4122). This material was unaffected by the high temperature oxidizing and reducing conditions, but was affected by the

thermal cycling the system underwent between gasification runs. The gasket material became brittle at high temperature and upon subsequent cooling the thermal contraction of the stainless steel reactor system caused the gasket to form micro-fractures. These fractures allowed gas to leak from the reactor, especially when pressures became elevated. It is recommended that a metal reinforced ceramic gasket be used in the future.

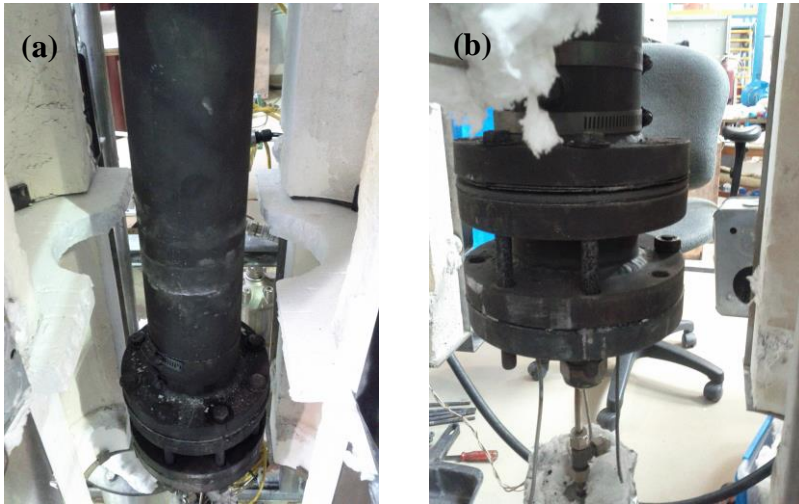


Figure A15.5: Photo of reactor bottom: (a) showing furnace sections and baffle, (b) showing gaskets.

Afterburner Failure

The original afterburner consisted of an electrically heated stainless tube packed with ceramic packing rods. Air and syngas were mixed prior to entering the afterburner. This original design failed, because the thermocouple used by the PLC to control the electric heaters was on the inside of the afterburner tube. During low flow conditions heat transfer through the tube to this thermocouple would be low and heating would be continuous and the temperature on the outside of the tube would be much higher than the set temperature, typically 600°C. This caused the afterburner stainless steel tube to melt and eventually the failure of the electric heaters, at a suspected temperature of >1100°C. A new electrically heated afterburner was constructed, with the control thermocouple on the exterior of the tube. The auto-ignition temperature of H₂ at the concentrations typical of gasification was found to be approximately 550°C; therefore, the after burner wall temperature is held at around 600°C.

Appendix 16: BFB Gasifier Parametric Design

Instructions Worksheet

User Instructions

This is the experimental design spreadsheet for operation of the Bubbling Fluidized Bed Gasifier in the CERC high head lab.

Before operation of the BFB all the desired operating parameters must be calculated.

The two main sheets are "Hydrodynamics" and "Stoichiometry".

Cells are colour coded according to the legend below to assist the user in using the worksheet.

Calibrations should be performed routinely on rotometers, pressure transducers and flow meters. It is required that a new calibration be done on the screw feeder if a different fuel is used.

Worksheets

"Hydrodynamics" will give an idea of the theoretical hydrodynamics expected, ie. $U(mf)$, bed pressure drop, size of particles elutriated,...

"Stoichiometry" will compute the set points for the control equipment of the BFB, ie. N₂ rotometer setting, air rotometer setting, screw feeder setting, etc...

"Flue Gas" gives the user a rough estimate of the syn gas generated based on a set of basic equations.

"Tabulated Values" contains constants used in the worksheet calculations.

"Heat Transfer" is underconstruction.

"Heat Balance" is underconstruction.

Legend

Green values indicate a user input value

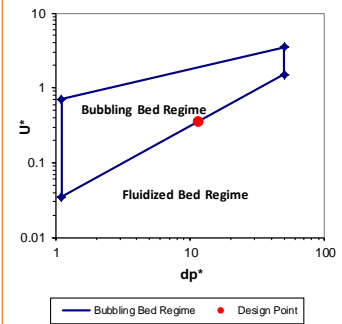
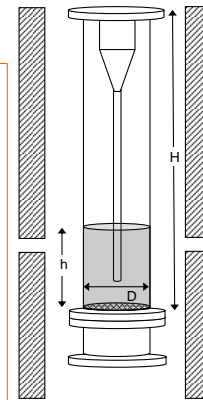
Red values indicate a setpoint for equipment operation based on in lab calibrations

Orange values indicate a critical design parameter dependent on a critical user input

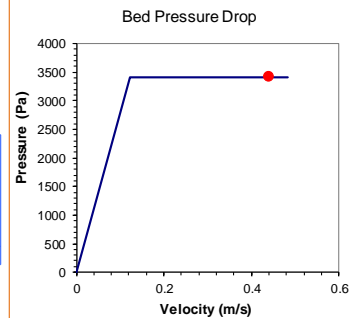
Blue values indicate a required "Goal Seek" iteration, typically by setting an error value to zero

Hydrodynamics Worksheet

Parameter	Symbol	Units	Value	Equation	Remarks
BED DIMENSIONS					
Reactor Diameter (ID)	D_r	in	3		
		m	0.0762		
Bed Height	h	in	14.00		
		m	0.356		
		cm	35.6		
Bed Area		m^2	0.0046		
PARTICLE PROPERTIES					
Mean Diameter	d_p	μm	623		
		m	6.23E-04		
Particle Density	ρ_p	kg/m^3	1955.5	$\rho_{CaCO_3} \cdot X + \rho_{CaO} \cdot (1-X)$	CaO / CaCO3 mixture
Voidage	ϵ_b		0.5		
Bulk Density	ρ_b	kg/m^3	977.75	$\rho_p \cdot \epsilon_b$	
Non-Dimensional Particle Dia.	d_p^*		11.492	$d_p^* = (d_p \cdot (\rho_p - \rho_g) / \mu_g^2)^{1/3}$	
Bed Solids Mass	m_{bed}	kg	1.586		
FLUIDIZING GAS					
At Ambient Temperature					
Gas Kinematic Viscosity	ν_g		0.000016		
Gas Density	ρ_g	kg/m^3	1.4363		
Gas Dynamic Viscosity	μ_g	m^2/s	1.85E-05		
Archimedes Number	Ar		19537		
At Furnace Temperature					
Gas Kinematic Viscosity	ν_g		1.42E-04		at furnace temp
Gas Density	ρ_g	kg/m^3	0.6599		at furnace temp
Gas Dynamic Viscosity	μ_g	m^2/s	4.49E-05		at furnace temp
Archimedes Number	Ar		1.52E+03	$\rho_g \cdot (\rho_p - \rho_g) \cdot g \cdot d_p^3 / \mu_g^2$	at furnace temp
Minimum Fluidizing Velocity	U_{mf}	m/s	0.122	$\mu_g / (d_p \cdot \rho_g) \cdot ((27.2 \cdot Ar^2 + 0.0408 \cdot Ar)^{0.5} - 27.2)$	at furnace temp
Minimum Fluidizing Flow Rate	Q_{mf}	m^3/s	0.001		at furnace temp
		L/min	33.336		at furnace temp
		L/min	15.315		at ambient
Minimum Bubbling Velocity	U_{mb}	m/s	0.049	$U_{mf} \cdot 4.1250 \cdot \mu_g^{0.9} \cdot \rho_g^{0.1} / ((\rho_p - \rho_g) \cdot g \cdot d_p)$	at furnace temp
Minimum Bubbling Flow Rate	Q_{mb}	L/min	0.225		at furnace temp
Non-Dimensional Velocity	U^*		0.350		
Fluidizing Gas Velocity	U_g	m/s	0.44	$U^* \cdot (\rho_p \cdot g / (\mu_g \cdot (\rho_p - \rho_g)))^{1/3}$	
Excess Gas Velocity	$U - U_{mf}$	m/s	0.32		
Design Gas Flow Rate	Q_g	m^3/s	0.0020		at furnace temp
		L/min	55.2		at ambient
		cfm	1.95		at ambient
		GPM	14.59		at ambient
		LPM	120.2		at furnace temp
PARTICLE ENTRAINMENT					
Gas Velocity	U_g	m/s	0.44		design velocity
Bed Particle					
Particle Density		kg/m^3	1956		
Particle Diameter		m	6.23E-04		
Terminal Diameter Initial	d_{p1}^*	μm	144		at design velocity
		m	1.44E-04		
Reynolds Number	Re_p		0.93	$U_g \cdot d_p \cdot \rho_g / \mu_g$	at furnace temp
$\log_{10}(Re_p)$	w		-0.03		
Drag Coefficient	C_D		28.96	$C_D = \frac{24}{(Re)_p} [1 + 0.1315(Re)_p^{0.82-0.95}]$	
Terminal Velocity	U_t	m/s	0.913		
Terminal Diameter	d_{p1}	μm	144	$U_t = \sqrt{\frac{4 \cdot d_p \cdot (\rho_p - \rho_r) \cdot g}{\rho_r \cdot C_D}}$	$U_t = U_g$
Iteration Error	i	μm	0.0%		goal seek to zero
Biomass Particle					
Particle Density	ρ_{bio}	kg/m^3	670		
Particle Diameter		m	4.69E-04		
Terminal Diameter Initial	d_{p1}^*	μm	254		at design velocity
		m	2.54E-04		
Reynolds Number	Re_p		1.64	$U_g \cdot d_p \cdot \rho_g / \mu_g$	at furnace temp
$\log_{10}(Re_p)$	w		0.22		
Drag Coefficient	C_D		17.49	$C_D = \frac{24}{(Re)_p} [1 + 0.1315(Re)_p^{0.82-0.95}]$	
Terminal Velocity	U_t	m/s	0.597		
Terminal Diameter	d_{p1}	μm	254	$U_t = \sqrt{\frac{4 \cdot d_p \cdot (\rho_p - \rho_r) \cdot g}{\rho_r \cdot C_D}}$	$U_t = U_g$
Iteration Error	i	μm	0.0%		goal seek to zero
PRESSURE DROP					
Bed Pressure Drop	ΔP_{bed}	Pa	3411		
		in H2O	13.72		
		psi	0.49		
Bed Pressure Drop (P4-P2)		kPa	2931		
Distributor Pressure Drop	ΔP_{dis}	Pa	1023.25		
Total Pressure Drop	ΔP_{total}	Pa	7379.51		
		in H2O	29.68		
		psi	1.07		



1.1	0.7
50	3.5



Stoichiometry Worksheet

Property	Symbol	Unit	Value	Equation	Remarks
Fuel Flow Rate	G_{fuel}	g/min kg/s g/hr	7.5 1.25E-04 450		
		Screw Feeder	223	$SF = (G_{fuel} + 2.1065) / 0.431$	Calibration
DESIGN CRITERIA					
Ambient Temperature	T_{amb}	°C	20		
Furnace Temperature	T_{fur}	°C	700		
		K	973		
Furnace Pressure	P_{fur}	kPa	20	gauge	
		kPa	121.33	absolute	
Fraction Fly Ash by Weight	X_{fa}	%	20%		
Unburnt Carbon	X_{uC}	%	2.00%	1- Combustion Efficiency	
Biomass N2 Purge Flow	Q_{purge}	mL/min	1000		at ambient
		m ³ /s	3.24E-05		at furnace temperature
	G_{purge}	kg/s	2.32E-05		
FLUIDIZING GAS					
Equivalence Ratio	ER	%	0%		
Steam to Biomass Ratio	R_{H2O}	kg/kg _{fuel}	2.50		
N2 Fraction	R_{N2}	kg/kg _{fuel}	1.23		
CO2 Fraction	R_{CO2}	kg/kg _{fuel}	0.00		
Stoichiometric Dry Air	M_{da}	kg/kg _{fuel}	5.631	$11.53 * C + 34.34 * (H - O/8) + 4.34S$	
Actual Dry Air To Gasifier	T_{da}	kg/kg _{fuel}	0.000	$M_{da} * EAC$	
Stoichiometric Wet Air	M_{wa}	kg/kg _{fuel}	0.000	$M_{da} * (1 + M_w)$	
Actual Wet Air To Gasifier	T_{wa}	kg/kg _{fuel}	0.00	$M_{wa} * EAC$	
Steam	G_{steam}	kg/s	3.03E-04	$G_{fuel} * R_{H2O} - G_{fuel} * [H_2O]$	
		g/min	18.20		
	Q_{steam}	m ³ /s	1.12E-03		at furnace temperature
	Q_{water}	mL/min	18.2	G_{steam} / ρ_{water}	
		strokes/min	40.6	$SR = (F - 0.7676) / 0.4291$	Calibration at 50% stroke length
Fluidizing Air	G_{air}	kg/s	0.00E+00		
	Q_{air}	m ³ /s	0.00E+00		at furnace temperature
		L/min	0.000		
		Rotometer	0.0	$R = (F + 0.0757) / 0.0602$	Calibration at 20 psi inlet
Fluidizing N2	G_{N2}	kg/s	1.53E-04	$G_{fuel} * R_{N2}$	
	Q_{N2}	m ³ /s	3.66E-04		at furnace temperature
		L/min	6.604		at ambient
		Rotometer	11.6	$R = (F - 1.6736) / 0.4251$	Calibration at 20 psi inlet
Fluidizing CO2	G_{CO2}	kg/s	0.00E+00	$G_{fuel} * R_{CO2}$	
	Q_{CO2}	m ³ /s	0.00E+00		at furnace temperature
		L/min	0.000		at ambient
		Rotometer	0.0	$R = (F + 0.194) / 0.03$	Calibration at 20 psi inlet
Total Fluidizing Gas	G_{FG}	kg/s	4.80E-04		
	Q_{FG}	m ³ /s	1.52E-03		at furnace temperature
Syn Gas Flow	$Q_{syn\ gas}$	m ³ /s	3.56E-05		See Flue Gas Spreadsheet
Total Gas Flow	$Q_{total\ gas}$	m ³ /s	1.56E-03		See Flue Gas Spreadsheet
Calculated Gas Velocity	U_{FG}	m/s	0.341		
Design Gas Velocity	U_d	m/s	0.341		from Hydrodynamics
Excess Velocity		m/s	0.000	$U_{FG} - U_d$	goal seek to zero
BIOMASS					
Density	ρ_p	µm	400		
Particle Diameter		m	0.0004		
	ρ_{bio}	kg/m ³	1100		
Carbon	[C]	%	46.60%	User Defined	
Hydrogen	[H]	%	5.71%	User Defined	
Oxygen	[O]	%	39.78%	User Defined	
Nitrogen	[N]	%	0.03%	User Defined	
Sulphur	[S]	%	0.07%	User Defined	
Ash	[ASH]	%	0.41%	User Defined	
Moisture	[H ₂ O]	%	7.40%	User Defined	
Specific Heat	cp	kJ/kg*K	0.975	Tables	
Higher Heating Value	HHV	kJ/kg	16832		Calculated as received
		kcal/kg	3647		Measured as received
		kJ/kg	15269		Measured as received
LIMESTONE					
Calcium Carbonate	[CaCO ₃]	%	92.99%		
Magnesium Carbonate	[MgCO ₃]	%	0.80%		
Inert Fraction	X_{inert}	%	5.21%		
Moisture	X_{mL}	%	1.20%		
Limestone Density	ρ_{CaCO3}	kg/m ³	2711		
Lime Density	ρ_{CaO}	kg/m ³	1200		
Limestone Molar Volume	V_{CaCO3}	m ³ /kmol	0.036918923	$MM_{CaCO3} / \rho_{CaCO3}$	
Limestone Quantity	M_{CaCO3}	kg	2.426	$\rho_{CaCO3} * (1 - \epsilon) * (A_{bed} * h_{bed})$	based on bed height
	mol_{CaCO3}	kmol	0.024	M_{CaCO3} / MM_{CaCO3}	
Lime Quantity	M_{CaO}	kg	1.3593	$mol_{CaCO3} * MM_{CaO}$	
Change in Bed Pressure	ΔP_{CaO}	Pa	2295	$(M_{CaCO3} - M_{CaO}) * g / A_{bed}$	
Lime Bed Pressure Drop	ΔP_{bed}	Pa	1470		
Lime Utilization	X		0.50		
CO2 Capture Efficiency	ϵ_{CO2}		0.90		
CO2 Produced	[CO ₂]	kg/kg _{fuel}	1.709	$[C] * (MM_{CO2} / MM_C)$	
	G_{CO2}	kg/s	2.14E-04	$G_{fuel} * [CO_2]$	
	F_{CO2}	kmol/s	4.85E-06		
Carbonation Rate	r_{carb}	kmol/s	4.37E-06	$F_{CO2} * \epsilon_{CO2}$	
Lime breakthrough time	t_{carb}	min	46.23	$mol_{CaO} * X / (F_{CO2} * \epsilon_{CO2}) / 60$	Duration of carbonation
		hr	0.7705		

Flue Gas Work Sheet

Would you like to use assumed values for flue gas composition or use system of equations?
 Enter "a" for assumed or "e" for system of equations: **a**

Assumed Flue Gas Composition

[H ₂]	0.83	Forin and Harris (2007)	
[CO ₂]	0	Forin and Harris (2007)	assuming 90% capture
[CO]	0.005	Forin and Harris (2007)	
[CH ₄]	0.165	Forin and Harris (2007)	

F	0.2850 m³/kg
Q _{syn gas}	3.5625E-05 m ³ /s
Q _{steam}	6.4765E-04 m ³ /s ??
Q _{total gas}	1.0488E-03 m ³ /s
V _{CO}	0.02%
V _{CO₂}	0.00%
V _{CH₄}	0.56%
V _{H₂}	2.82%
V _{H₂O}	61.75%
V _{N₂}	34.85%
V _{O₂}	0.00%

Flue Gas Composition Solved Using System of Equations

P	121325 Pa	
S	2.5000 kg _{steam} /kg _{dry fuel}	
A	0.0000 kg _{air} /kg _{dry fuel}	
O _a	0.231	
N _a	0.769	30%
X _C	0.503 kg/kg _{dry fuel}	
X _H	0.062 kg/kg _{dry fuel}	
X _O	0.430 kg/kg _{dry fuel}	
X _N	0.000 kg/kg _{dry fuel}	
X _S	0.001 kg/kg _{dry fuel}	
X _{ash}	0.004 kg/kg _{dry fuel}	
W	0.080 kg/kg _{dry fuel}	

Preliminary Estimates:

V _{CO₂}	0.1368
V _{H₂}	0.0793

Solution Matrix:

V _{CO}	V _{CH₄}	V _{H₂O}	V _{N₂}	F	C	
1	1	0	0	-0.9391	-0.1368	(1)
0	2	1	0	-3.8902	-0.0793	(2)
0.5	0	0.5	0	-1.9084	-0.1368	(3)
0	0	0	1	-0.0003	0.0000	(4)
1	1	1	1	0	0.7832	(5)

Inverse:

0.618	-0.382	0.474	-0.145	0.145
0.306	0.306	-0.775	-0.081	0.081
-0.925	0.075	0.301	-0.774	0.774
0.000	0.000	0.000	1.000	0.000
-0.080	-0.080	-0.321	-0.241	0.241

Solution (S⁻¹·c):

V _{CO}	-0.0056
V _{CH₄}	0.1034
V _{H₂O}	0.6853
V _{N₂}	0.0001
F	0.2497 kg/m ³
	4.0043 m ³ /kg

Therefore:

	Error	
V _{CO₂}	0.0069	-1888.6%
V _{H₂}	-0.2122	137.4%

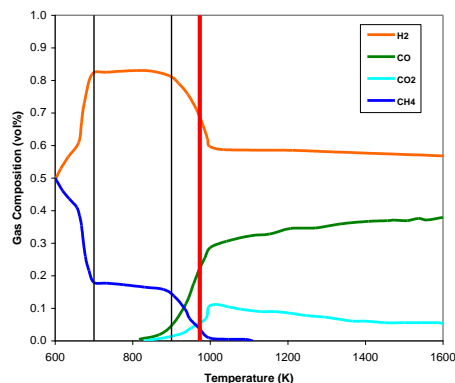
Governing Equations:

(1)	$V_{CO} + V_{CO_2} + V_{CH_4} = 1.866FX_C$
(2)	$V_{H_2} + V_{H_2O} + 2V_{CH_4} = 1.24FS + 11.21FX_H + 1.24FW$
(3)	$0.5V_{CO} + V_{CO_2} + 0.5V_{H_2O} = 0.623(FS + FW) + 0.701(FX_O + FAO_a)$
(4)	$V_{N_2} = 0.8FX_N + 0.8FAN_a$
(5)	$V_{CO} + V_{CO_2} + V_{CH_4} + V_{H_2} + V_{H_2O} + V_{N_2} = 1$
(6)	$K_{pb} = \frac{V_{CO}^2 P}{V_{CO_2}}$
(7)	$K_{pw} = V_{H_2} V_{CO} \frac{P}{V_{H_2O}}$

Iterate composition estimates to reduce error close to zero. Use "Goal Seek" and set error cell to 0 by changing estimate cell. May need to iterate a number of times

Equilibrium Data from Florin and Harris (2007)

H2	CO	CO2	CH4
Temp (K) mol %			
602 0.50	816 0.01	828 0.00	600 0.50
615 0.53	869 0.02	882 0.01	619 0.46
634 0.57	903 0.05	925 0.02	636 0.44
661 0.61	937 0.11	950 0.04	656 0.41
668 0.67	957 0.18	988 0.07	663 0.38
675 0.73	971 0.22	996 0.10	668 0.35
695 0.82	986 0.26	1017 0.11	678 0.26
733 0.83	1000 0.29	1047 0.10	687 0.22
809 0.83	1042 0.31	1078 0.10	700 0.18
852 0.83	1105 0.32	1129 0.09	733 0.18
896 0.81	1153 0.33	1168 0.09	777 0.17
918 0.79	1207 0.35	1204 0.08	831 0.17
942 0.76	1272 0.35	1248 0.08	879 0.16
964 0.71	1335 0.36	1294 0.07	906 0.14
981 0.66	1408 0.37	1367 0.06	935 0.10
993 0.62	1457 0.37	1399 0.06	947 0.07
998 0.60	1474 0.37	1450 0.06	971 0.04
1034 0.59	1508 0.37	1500 0.06	996 0.01
1212 0.58	1537 0.38	1544 0.06	1047 0.00
1316 0.58	1559 0.37	1585 0.06	1090 0.00
1602 0.57	1600 0.38	1600 0.05	1110 0.00



Tabulated Values Worksheet

Specific Heats of Biomass Combustion

Gas	(%) flue gas	a	b	c	d	M (kg/kmol)
N ₂	34.9%	28.9	-1.571E-03	8.081E-06	-2.873E-09	28
H ₂ O	61.8%	32.24	1.923E-03	1.055E-05	-3.595E-09	18
CO ₂	0.0%	22.26	5.981E-02	-3.501E-05	7.469E-09	44
SO ₂	0.1%	25.78	5.795E-02	-3.812E-05	8.612E-09	46
O ₂	0.0%	25.48	1.520E-02	-7.155E-06	1.312E-09	32
CO	0.0%	28.16	1.675E-03	5.372E-06	-3.595E-09	28
H ₂	2.8%	29.11	-1.967E-03	4.003E-06	-8.704E-10	2
CH ₄	0.6%	19.89	5.024E-02	1.269E-05	-1.101E-08	16
Syn Gas		28.11	0.001967	0.000004802	-1.966E-09	28.97

	Ambient	Syn Gas	°C
C _p (kJ/kg*K)	20	700	
C _p (N ₂)	1.0379	1.1563	kJ/kg*K
C _p (H ₂ O)	1.8677	2.2660	kJ/kg*K
C _p (CO ₂)	0.8402	1.2316	kJ/kg*K
C _p (SO ₂)	0.8631	1.1741	kJ/kg*K
C _p (O ₂)	0.9173	1.0845	kJ/kg*K
C _p (CO)	1.0365	1.1273	kJ/kg*K
C _p (H ₂)	14.4277	15.0920	kJ/kg*K
C _p (CH ₄)	2.2139	4.4153	kJ/kg*K
C _p (syn gas)	1.5157	1.8030	kJ/kg*K
C _p (air)	1.0027	1.1308	kJ/kg*K
I _{air} ^o (kW)	358	14116	kW

Equilibrium Constants

Temperature (K)	K _{p,w}	K _{p,b}	K _{p,m}	
400	7.71E-11	5.23E-14	2.99E+05	
600	5.06E-05	1.87E-06	9.24E+01	
800	4.41E-02	1.09E-02	1.34E+00	
1000	2.62E+00	1.90E+00	9.63E-02	
1500	6.08E+02	1.62E+03	2.51E-03	
973	2.27E+00	1.64E+00	2.64E-01	(Intrepolation)

Heat of Combustion Gases

Gas	HHV (MJ/kg mol)	LHV (MJ/kg mol)
CO	282.99	282.99
H ₂	285.84	241.83
CH ₄	890.36	802.34
H ₂ S	562.59	518.59

Density

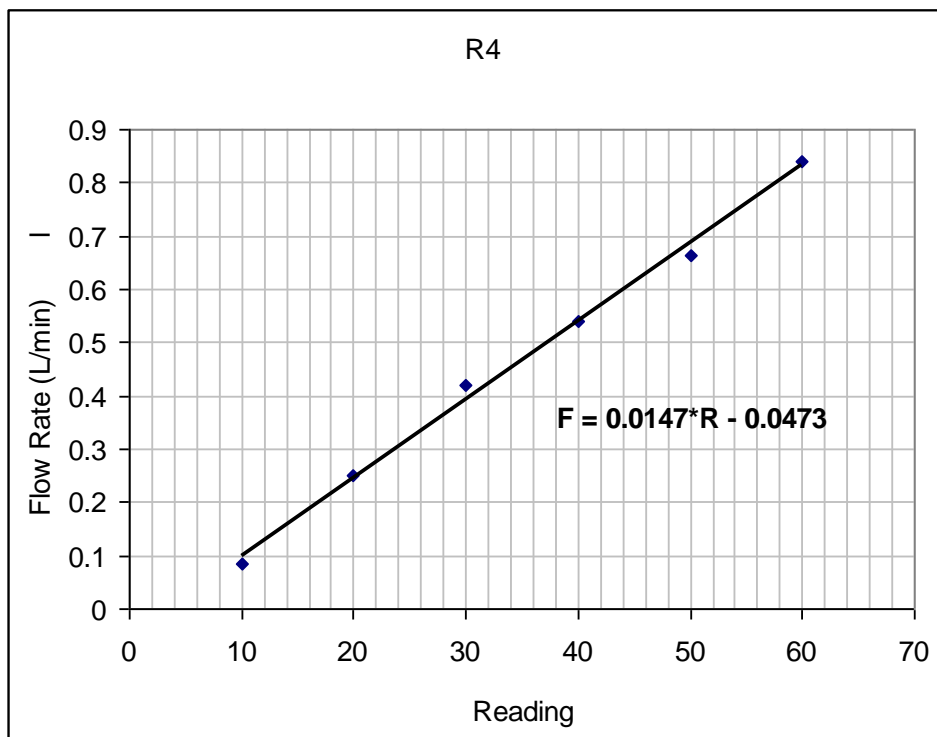
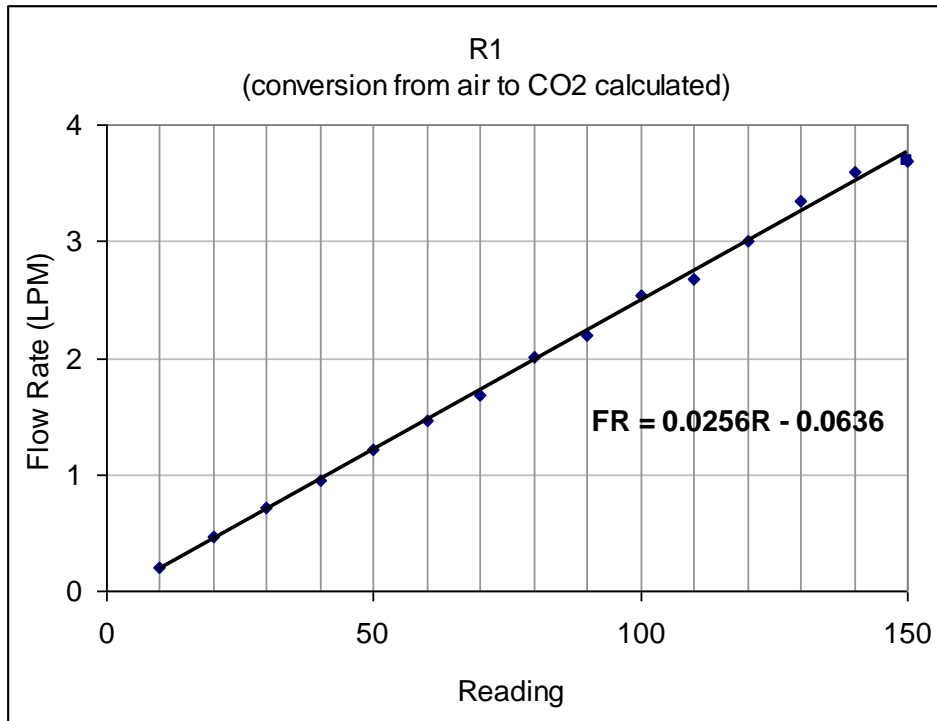
ρ (kg/m ³)	Temperature (°C)	
	Ambient	Furnace Exit
	20	700
ρ(N ₂)	1.394488767	0.419923133
ρ(H ₂ O)	0.896457064	0.269950586
ρ(CO ₂)	2.19133949	0.659879209
ρ(SO ₂)	2.290945831	0.689873719
ρ(O ₂)	1.593701448	0.479912152
ρ(CO)	1.394488767	0.419923133
ρ(H ₂)	0.09960634	0.02999451
ρ(CH ₄)	0.796850724	0.239956076
ρ(product gas)	1.0412	0.3135
ρ(air)	1.4363	0.6599

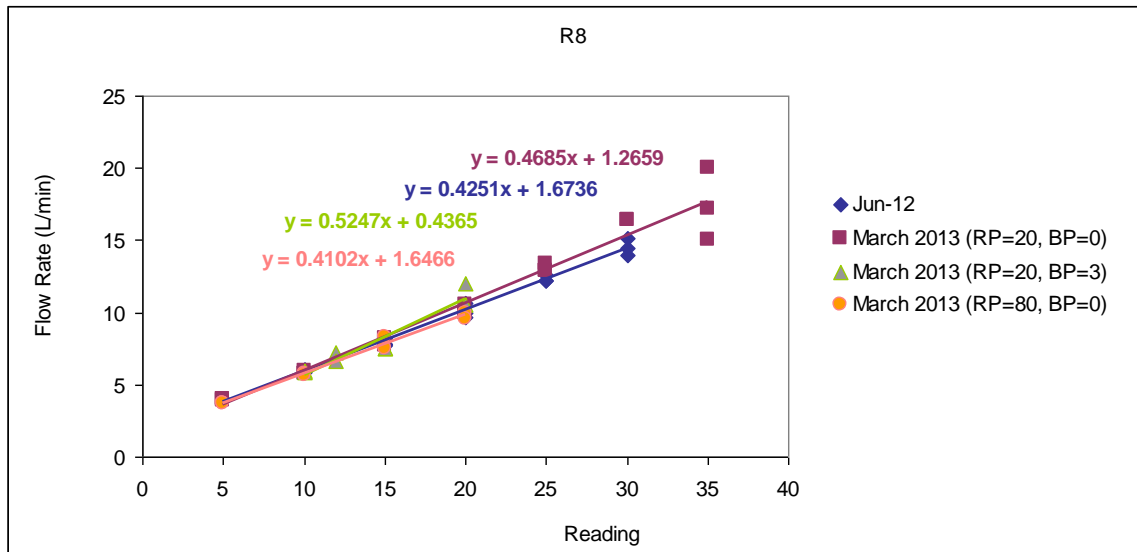
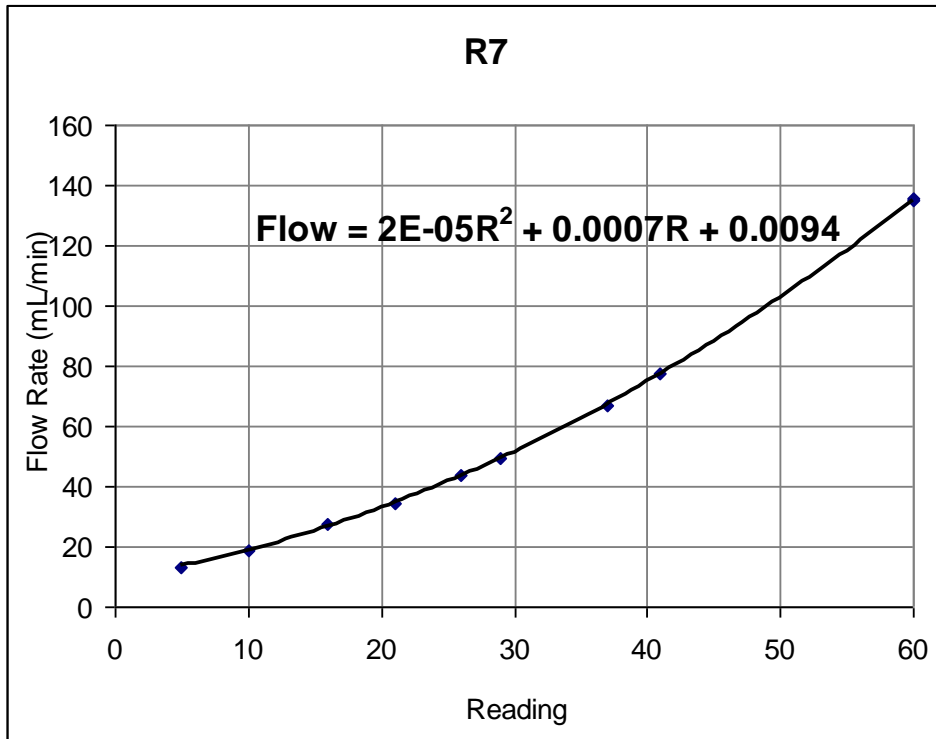
Viscosity (air)

Temperature (K)	μ (Ns/m ²)	ν (m ² /s)
300	1.85E-05	1.59E-05
400	2.30E-05	2.64E-05
500	2.70E-05	3.88E-05
600	3.06E-05	5.27E-05
700	3.39E-05	6.81E-05
800	3.70E-05	8.49E-05
900	3.98E-05	1.03E-04
1000	4.24E-05	1.42E-04
1100	4.49E-05	1.42E-04
1200	4.73E-05	1.63E-04
1300	4.96E-05	1.85E-04

Appendix 17: BFB Gasifier Equipment Calibrations

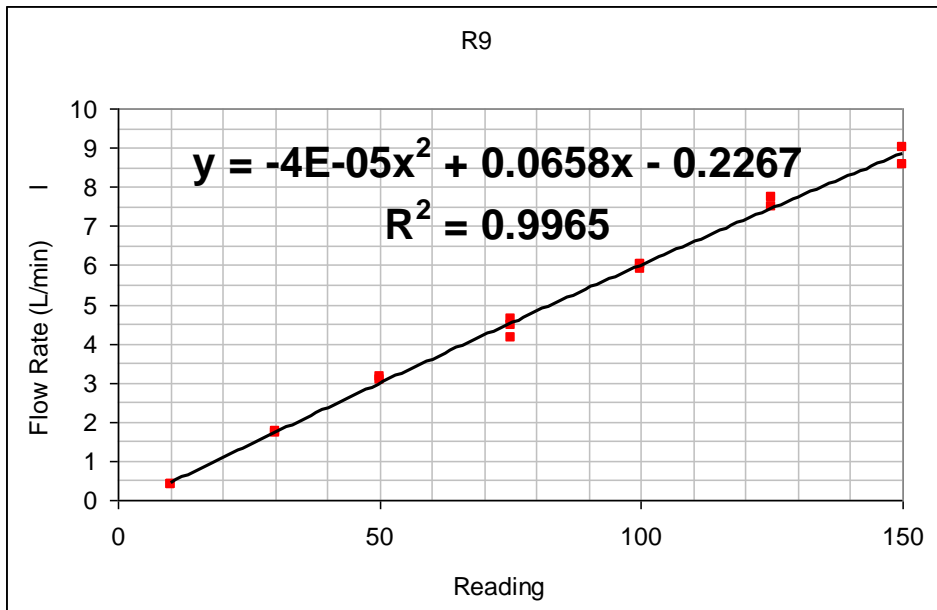
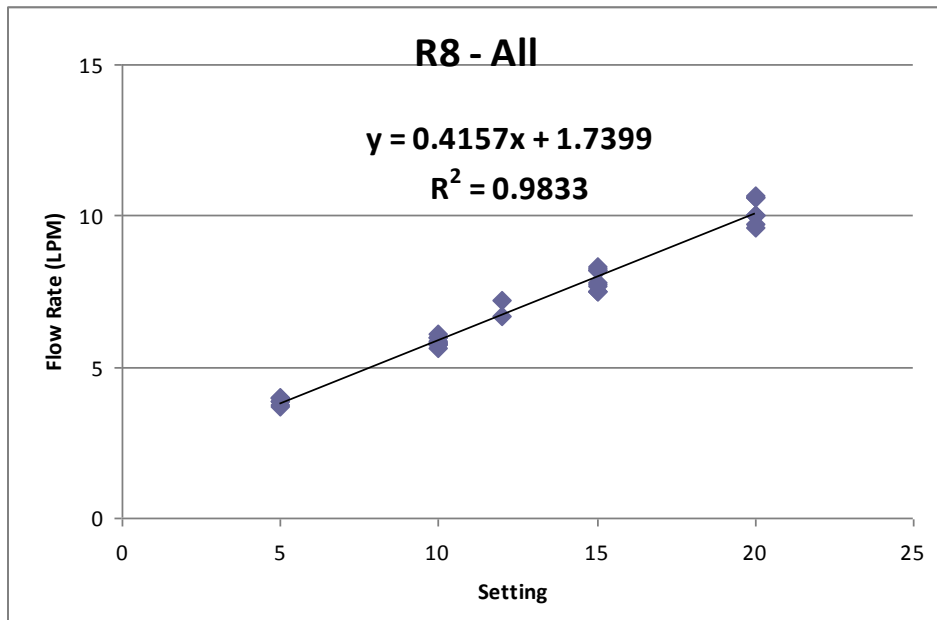
Rotometers



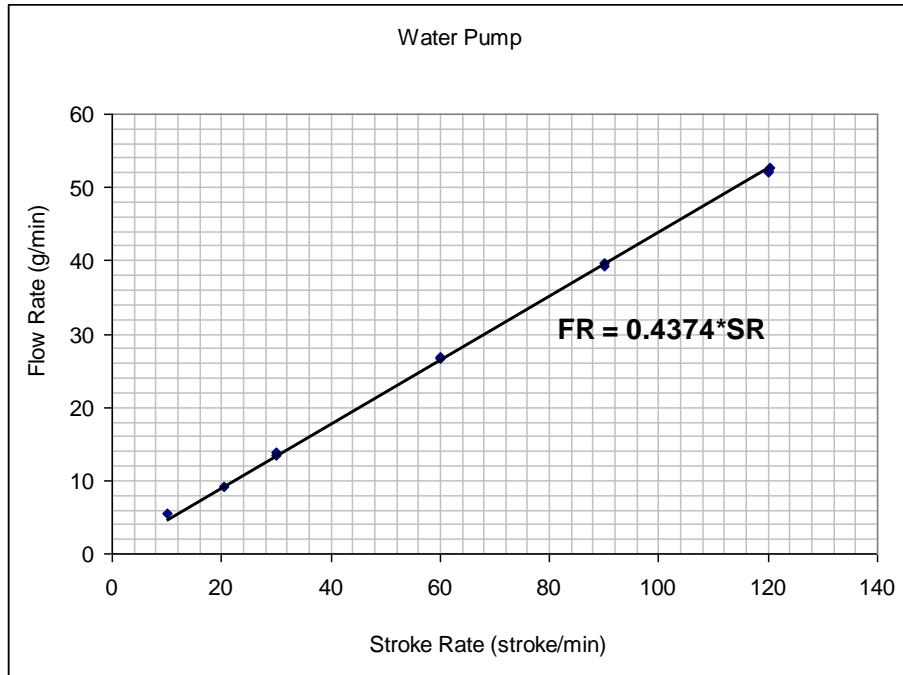


RP = regulator pressure (psi)

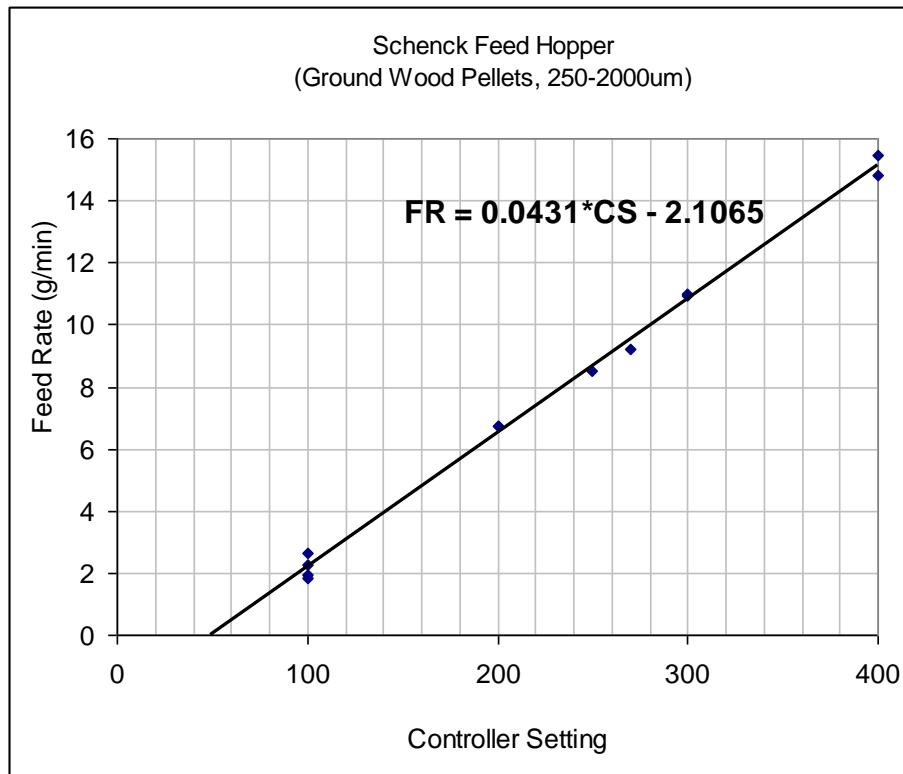
BP = back pressure (psi)



Water Pump

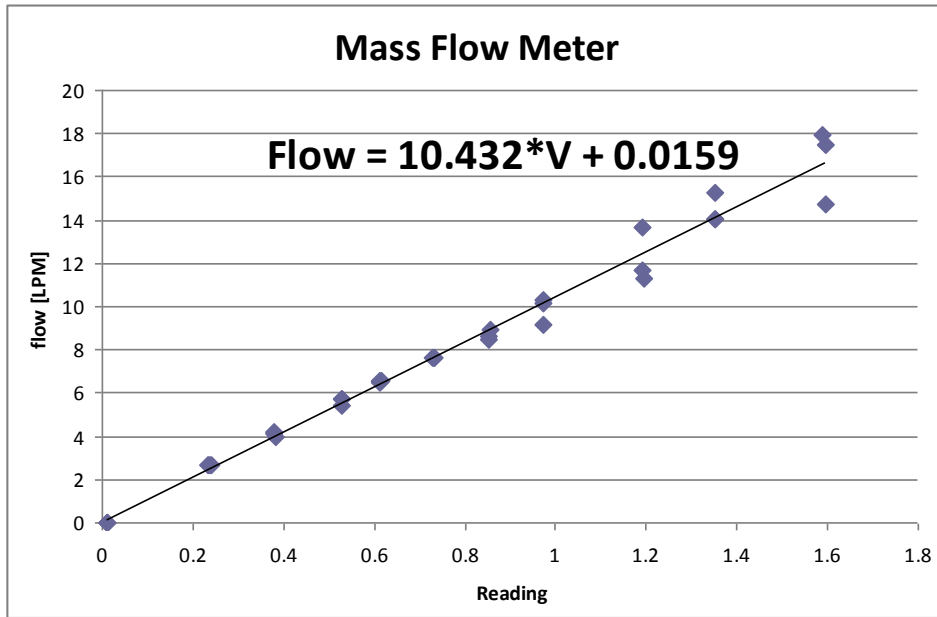


Screw Feeder

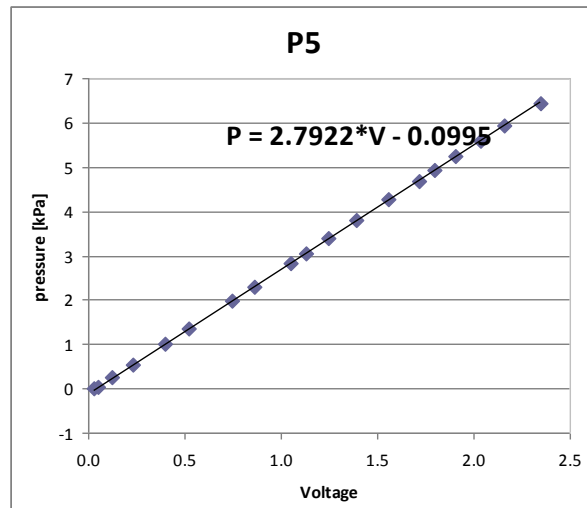
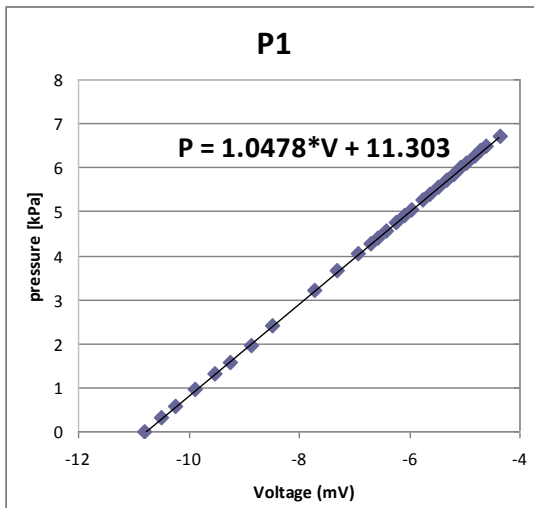


*Specific to ground pine wood pellets. Different fuels require new calibrations.

Electronic Mass Flow Meter



Pressure Transducers



Appendix 18: Enhanced Gasification Supplementary Material

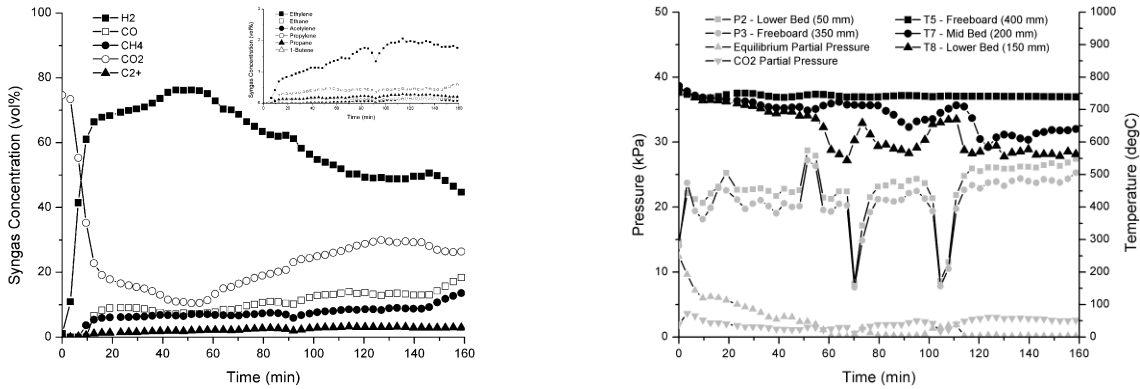


Figure A18.1: Gasification cycle using a CaO bed (CB-06-12)

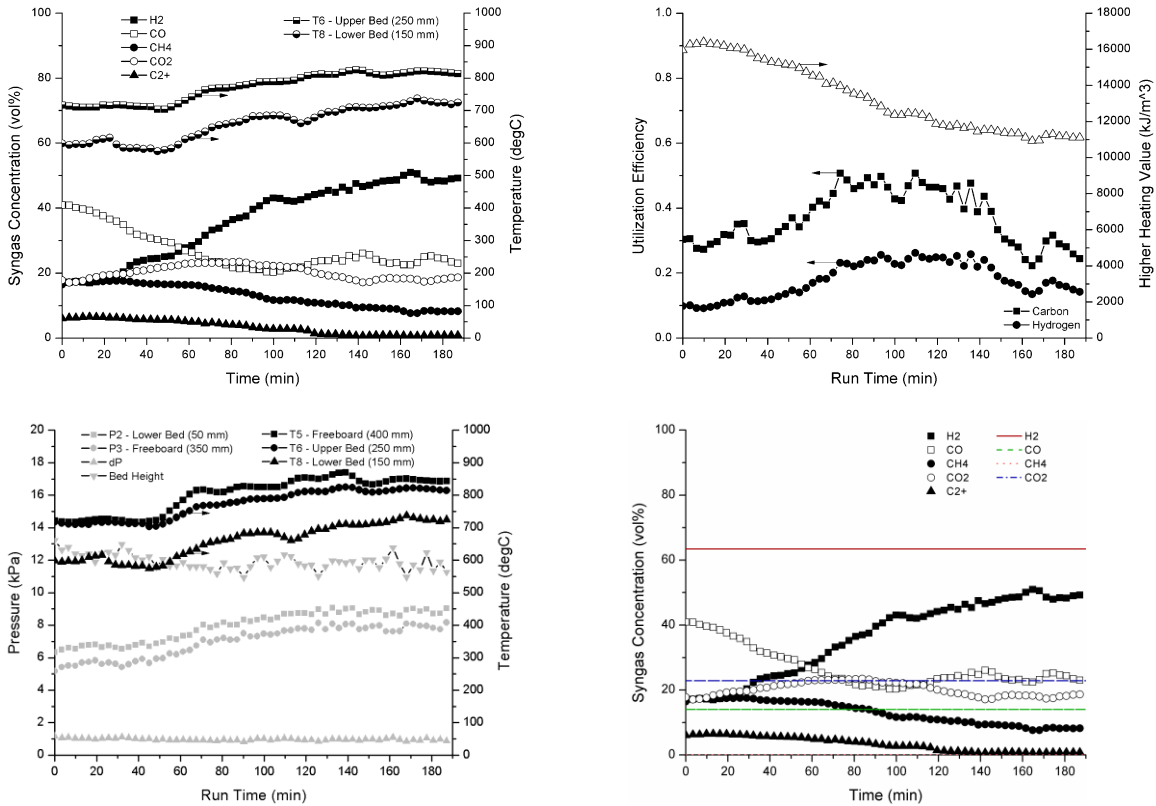


Figure A18.2: Gasification cycle using a sand bed (SB-04-12)

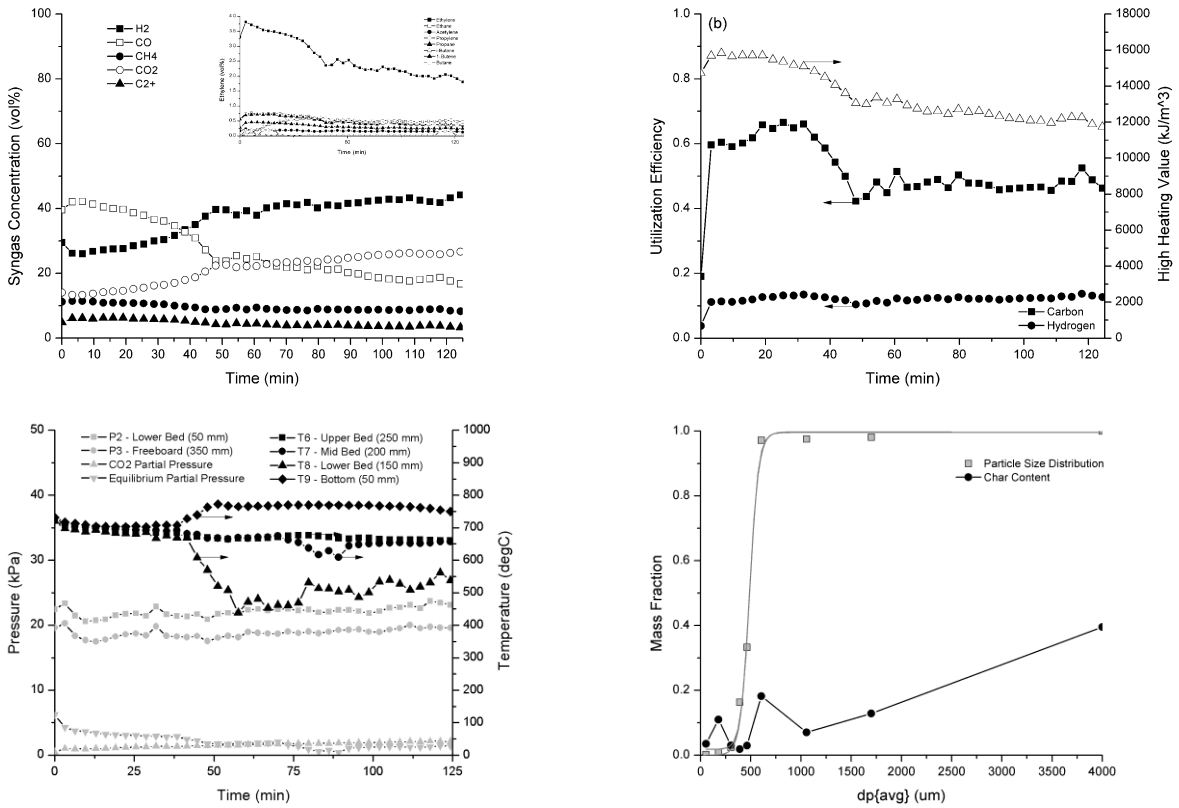


Figure A18.3: Gasification using a sand bed (SB-08-12).

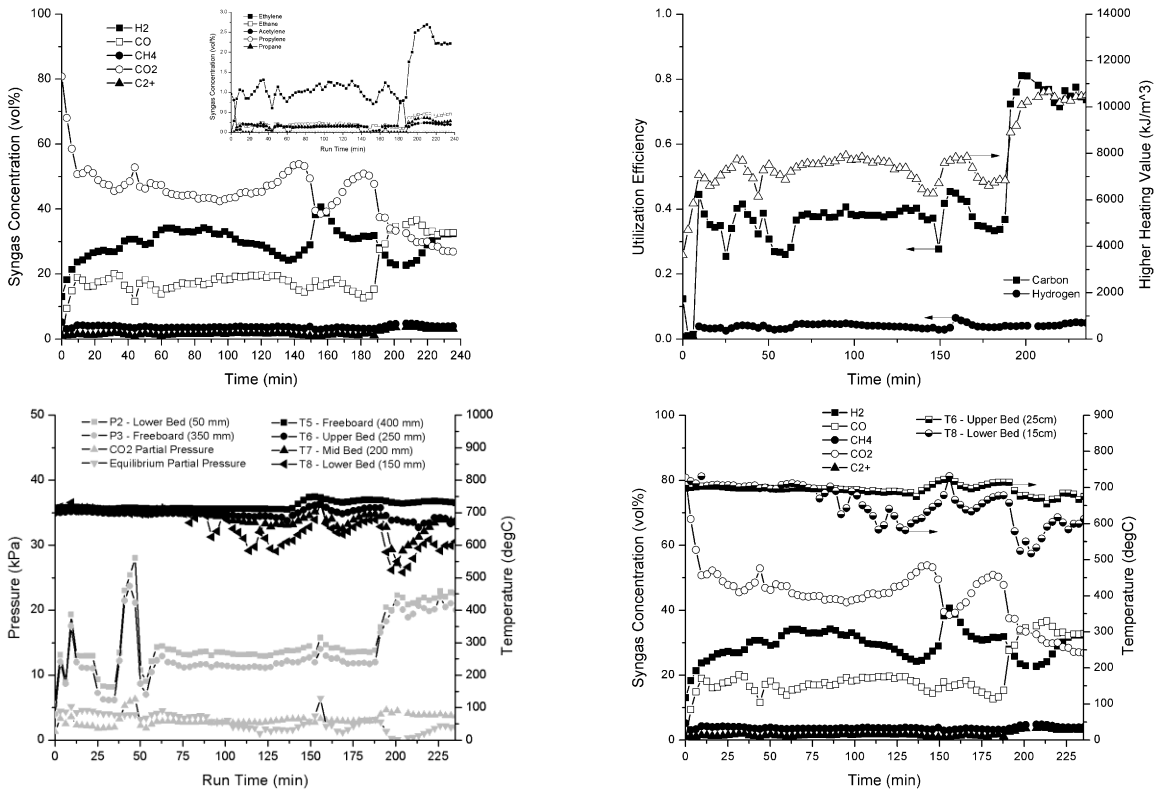


Figure A18.4: Gasification cycle using a limestone bed (LB-06-12)

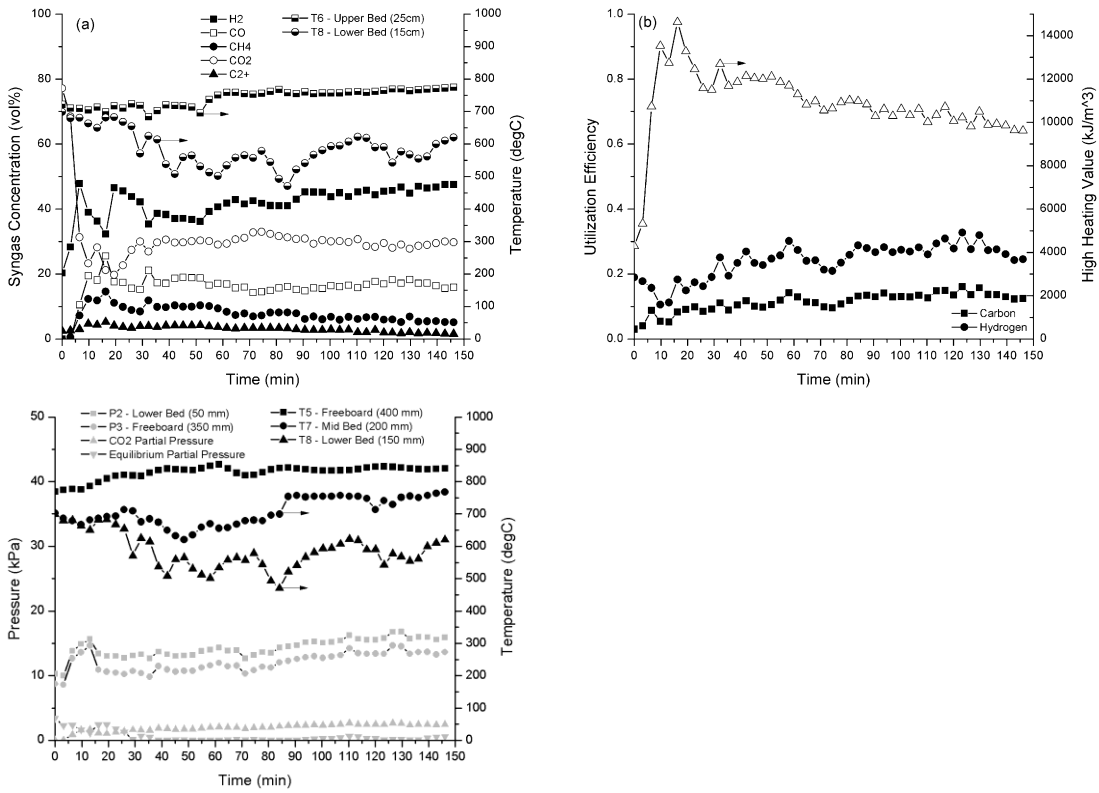


Figure A18.5: Gasification cycle using a limestone bed (LB-04-12)

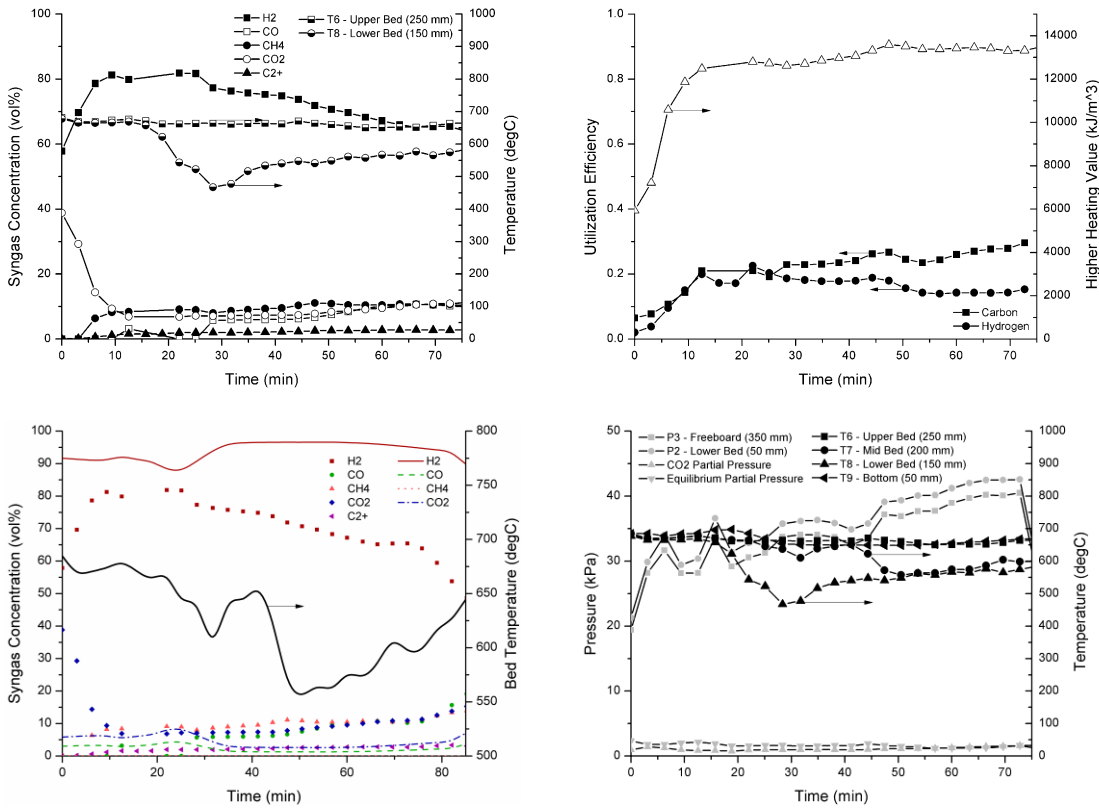


Figure A18.6: Gasification cycle using a CaO bed (CB-07-12)

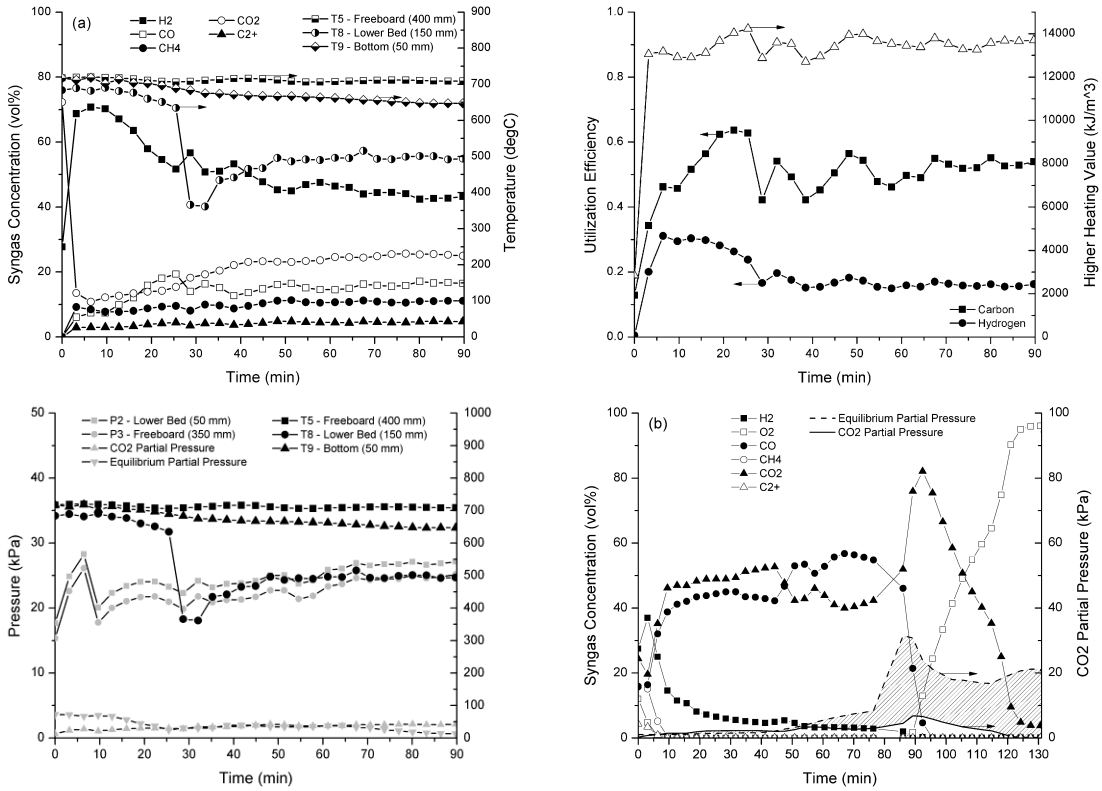


Figure A18.7: Gasification using a CaO bed cycle 1 (CCL-07-12-1).

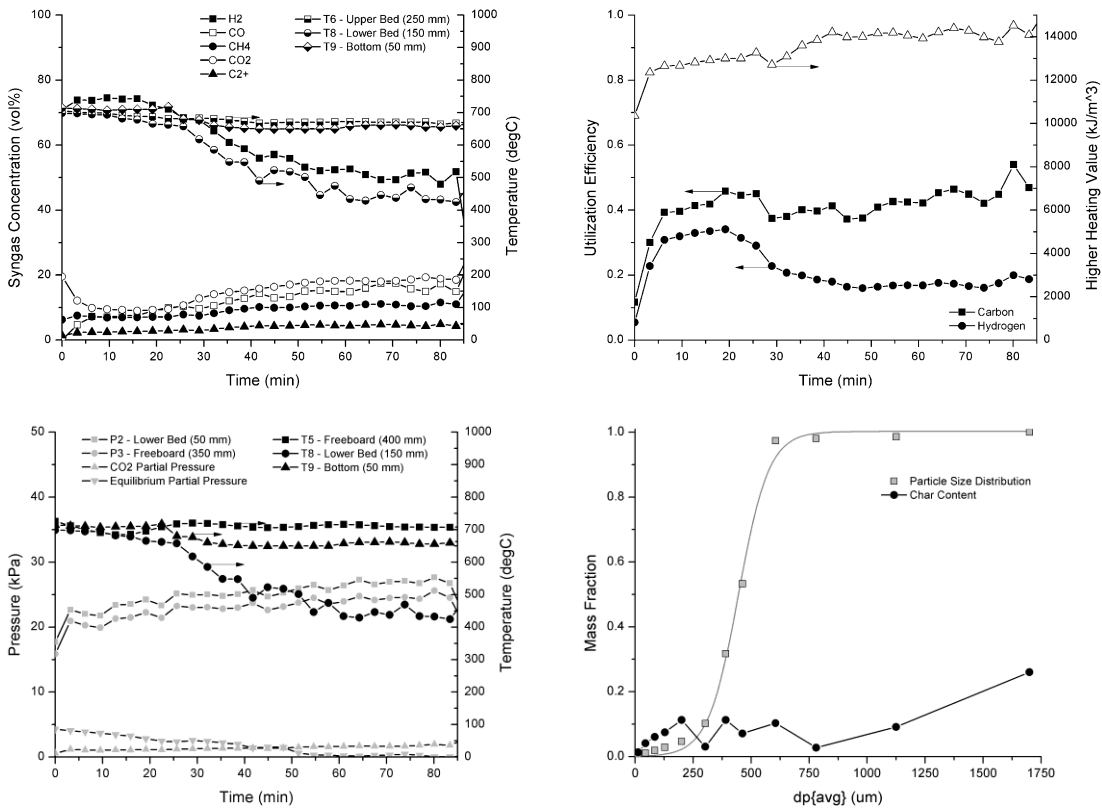


Figure A18.8: Gasification using a CaO bed cycle 2 (CCL-07-12-2).

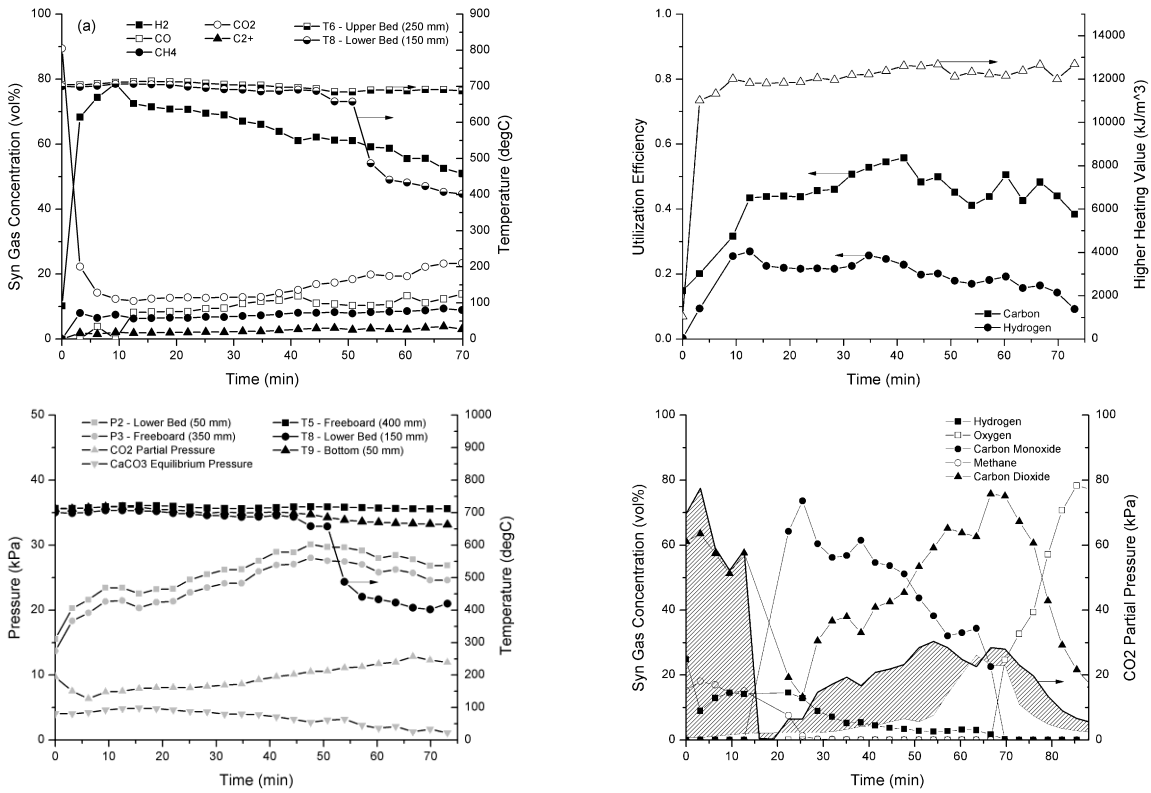


Figure A18.9: Gasification cycle 1 using a CaO bed (CCL-10-12-1)

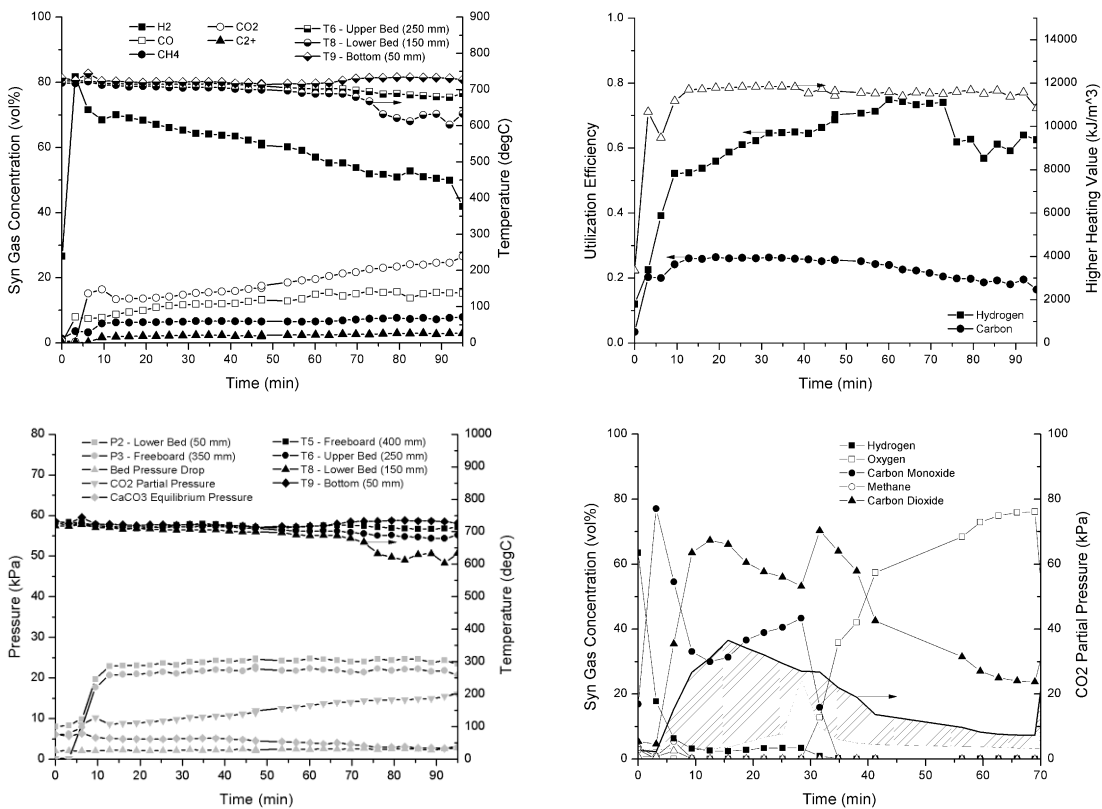


Figure A18.10: Gasification cycle 2 using a CaO bed (CCL-10-12-2)

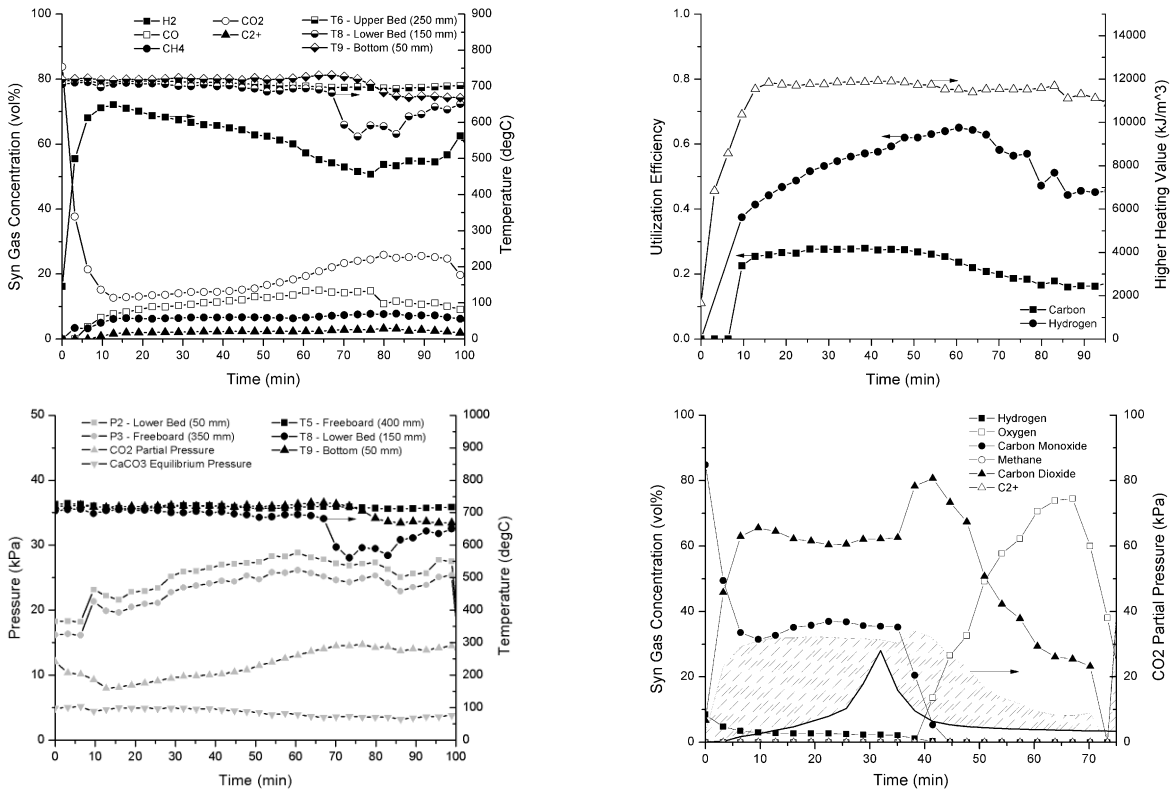


Figure A18.11: Gasification cycle 3 using a CaO bed (CCL-10-12-3)

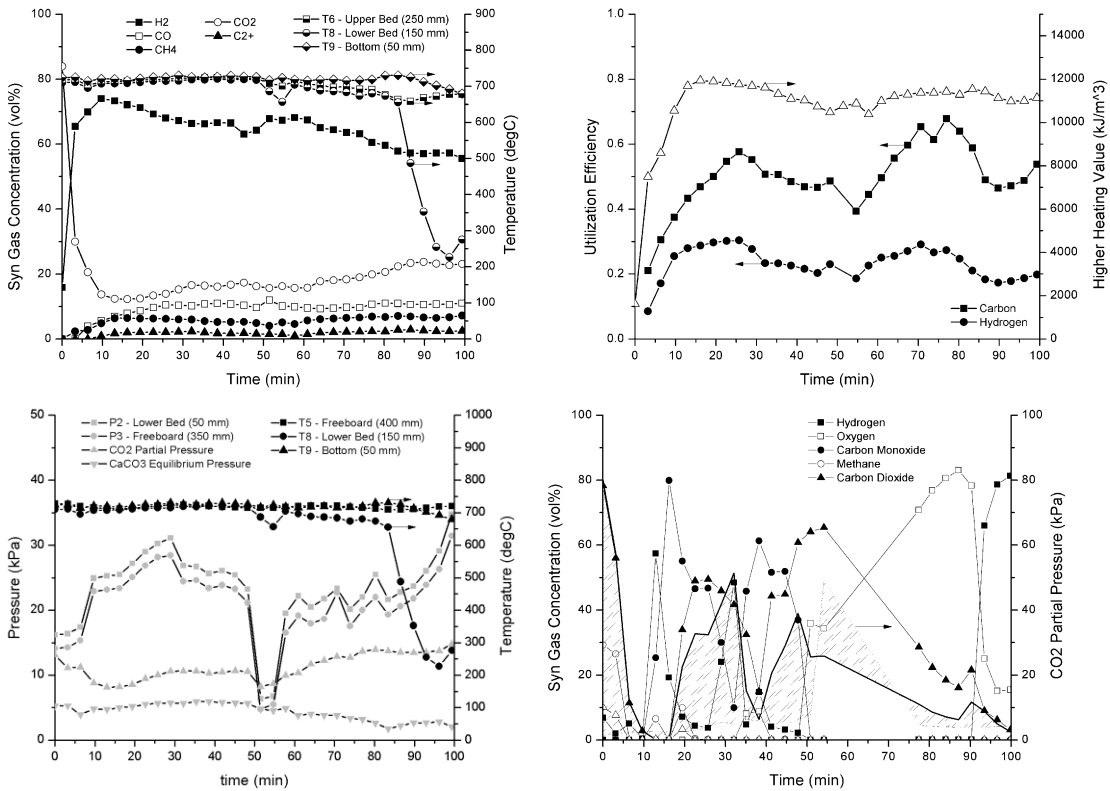


Figure A18.12: Gasification cycle 4 using a CaO bed (CCL-10-12-4)

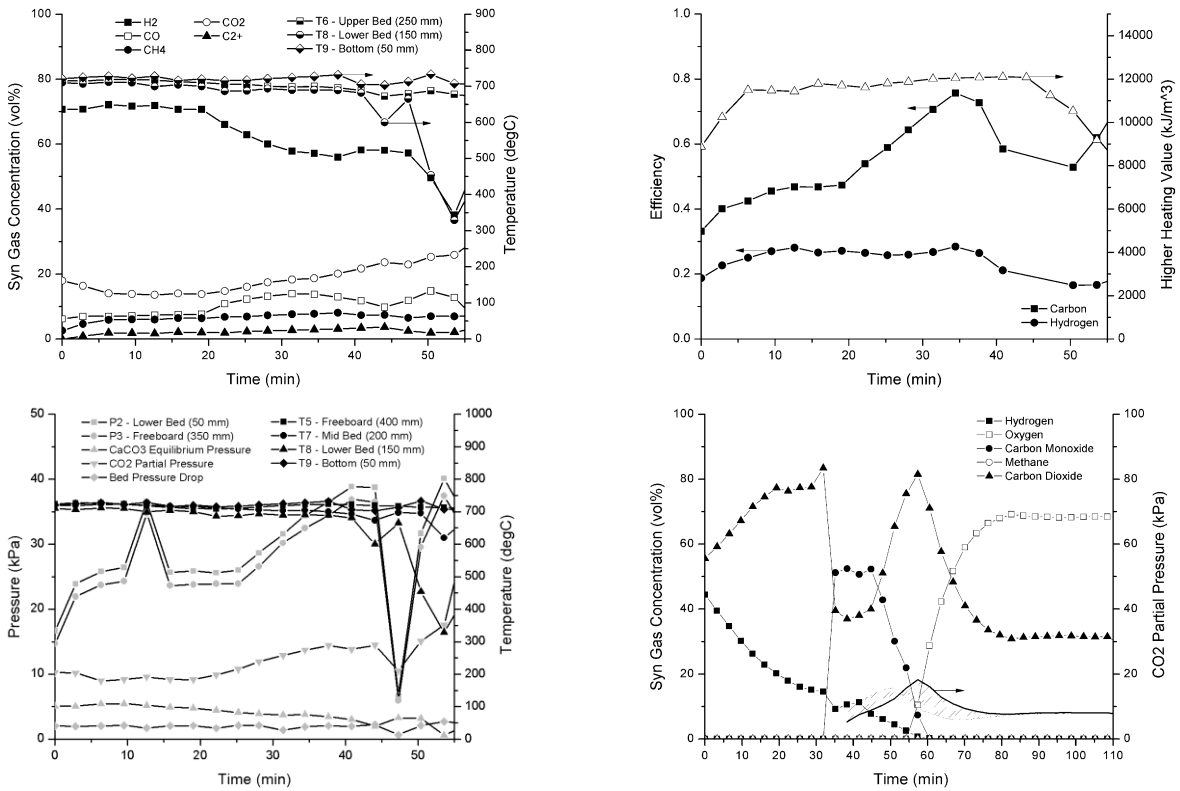


Figure A18.13: Gasification cycle 5 using a CaO bed (CCL-10-12-5)

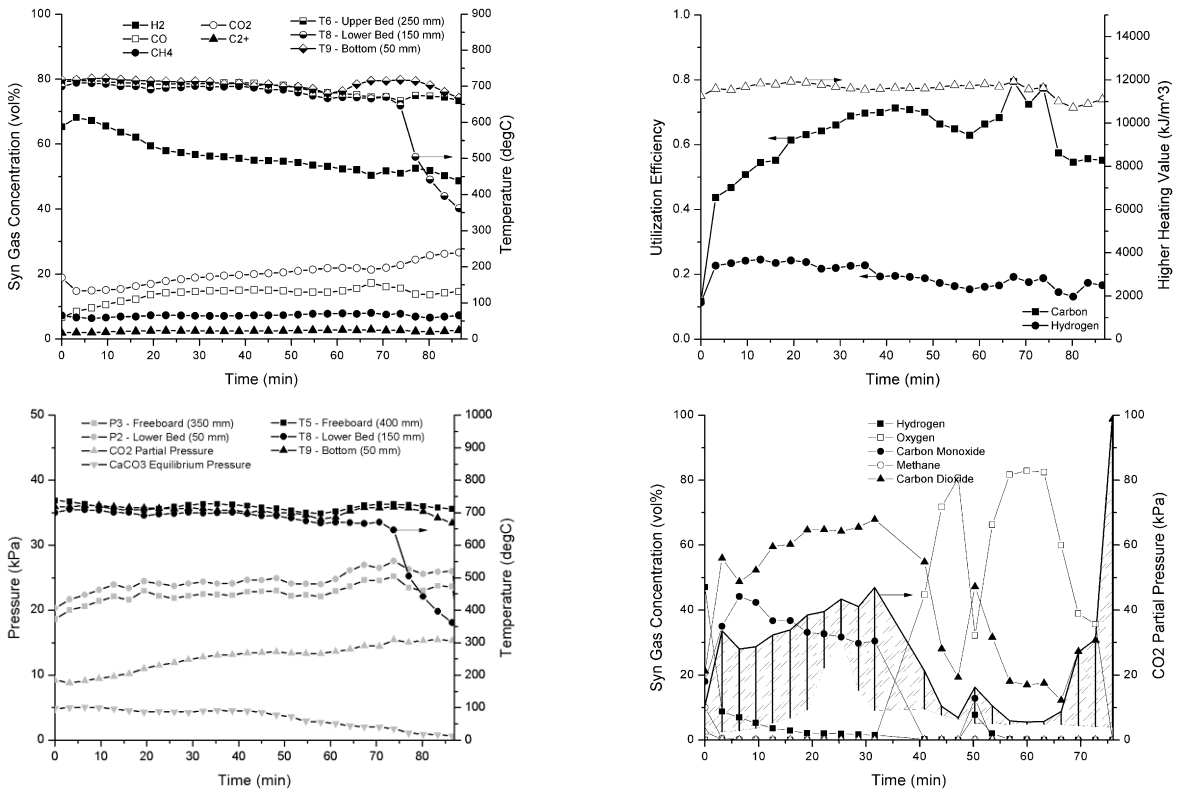


Figure A18.14: Gasification cycle 6 using a CaO bed (CCL-10-12-6)

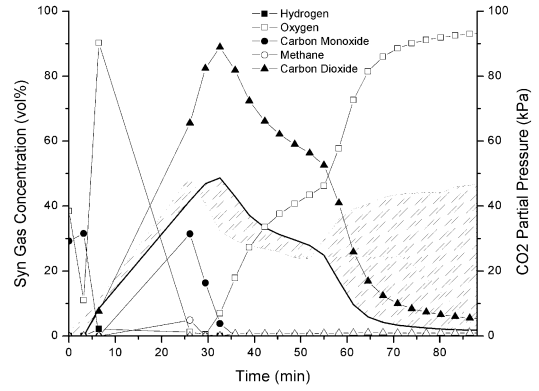
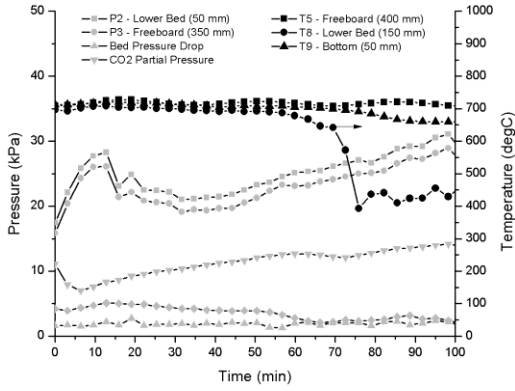
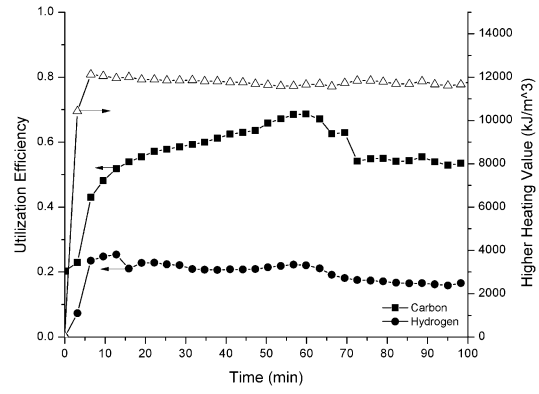
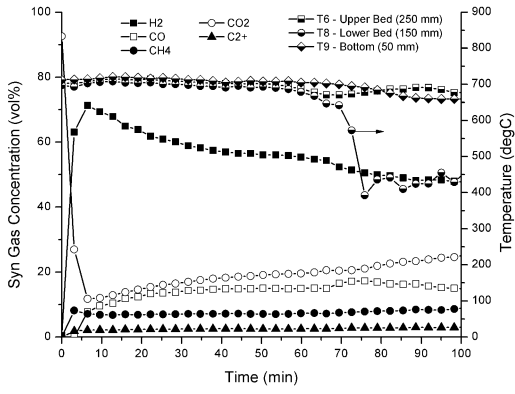


Figure A18.15: Gasification cycle 7 using a CaO bed (CCL-10-12-7)

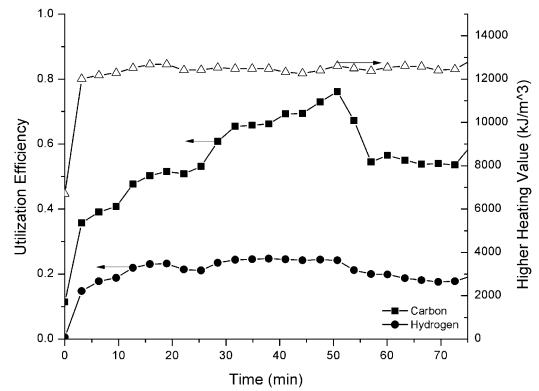
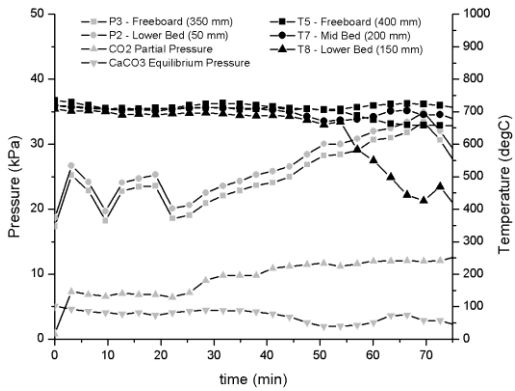


Figure A18.16: Gasification cycle 8 using a CaO bed (CCL-10-12-8)

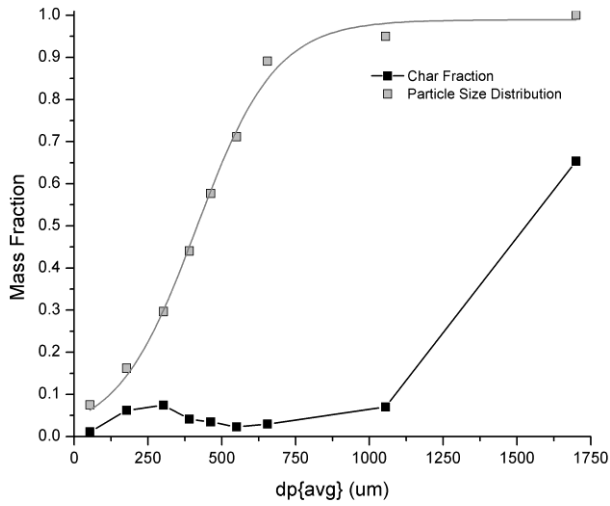


Figure A18.17: Particle size distribution and char content of bed long cycling (CCL-07-12)

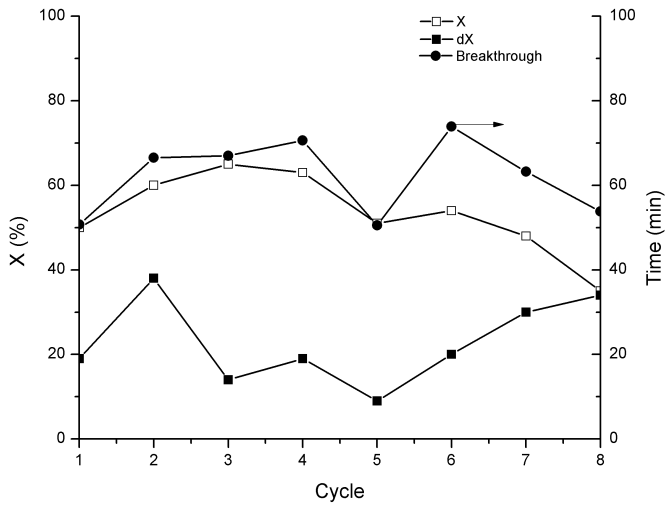


Figure A18.18: Calcium utilization over 8 gasification / calcination cycles (CCL-10-12)

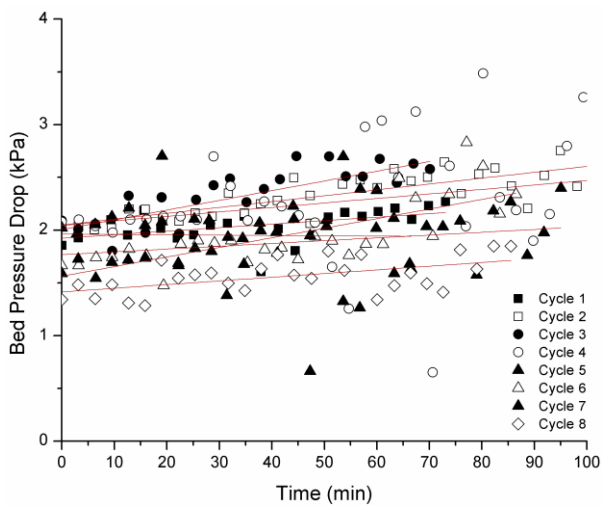


Figure A18.19: Bed pressure drop during gasification (CCL-10-12)



Figure A18.20: Bed samples from difference stages of 2 cycle gasification / calcination (CCL-07-12)

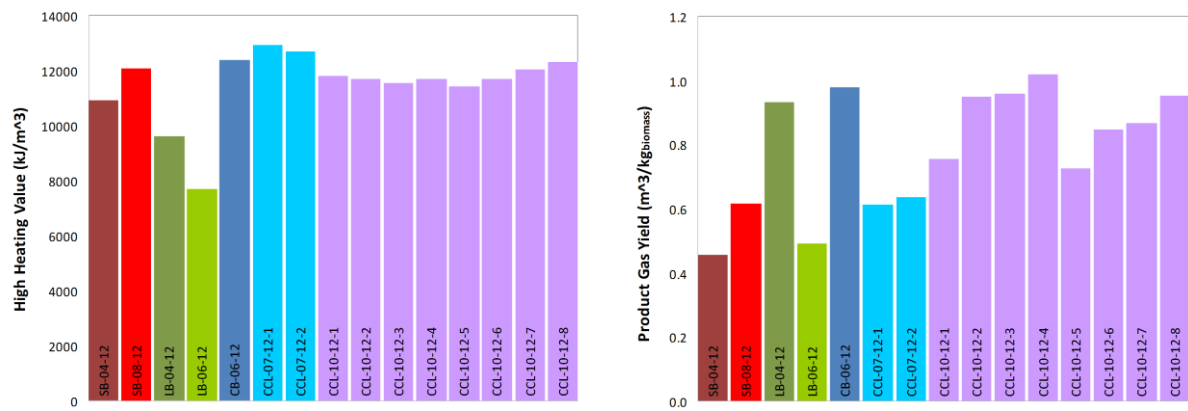


Figure A18.21: HHV (left) and product gas yield (right) during maximum product gas yield of different gasification runs; see Table A11.1 for conditions.

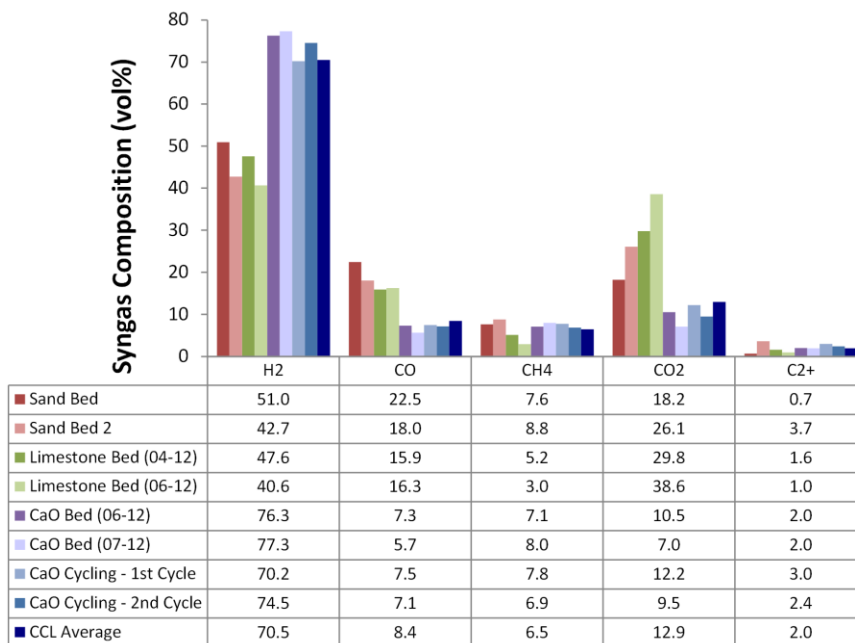


Figure A18.22: Maximum syngas production

Table A18.1: Cycle average and cumulative values

Run	Tar Production (g/m ³)		Fines		Temperature (degC)				Pressure (kPa)		d Pressure Drop (kPa)		Bed Mass (g)		Final Mass (g)						
	All Synes	N2 Free	% of Firductio	T5 (avg)	T6 (avg)	T7 (avg)	T8 (avg)	T9 (avg)	P2 (avg)	P3 (avg)	Initial	Final	Initial	Final	Hydroxide	Char	Carbonat	CaO	Ash		
Sand Bed	SB-04-12	41.65	72.23	0.23	9.15	801 ± 55	772 ± 44	728 ± 48	660 ± 53	778 ± 56	8.0 ± 0.9	7.0 ± 1	1.16	0.97	-	1100.0	-	-	-	-	
Sand Bed 2	SB-08-12	12.13	31.87	0.13	1.78	708 ± 4	675 ± 14	688 ± 25	573 ± 88	746 ± 26	21.7 ± 1.7	18.5 ± 1.4	2.85	2.49	1767.5	1870.0	0.0	446.9	0.0	0.0	1404.3
Limestone Bed (04-12)	LB-04-12	16.58	29.24	0.47	13.3	828 ± 21	742 ± 26	706 ± 42	585 ± 56	829 ± 28	14.3 ± 1.5	12.0 ± 1.5	1.58	2.27	1504.3	1088.2	-	-	-	-	-
Limestone Bed (06-12)	LB-06-12	17.78	36.9	0.62	22	722 ± 12	695 ± 13	681 ± 34	654 ± 53	719 ± 14	15.1 ± 4.5	13.4 ± 4.4	1.60	1.98	1502.9	1305.4	-	-	-	-	-
CaO Bed (06-12)	CB-06-12	16.74	23.3	0.19	4.32	741 ± 6	710 ± 15	684 ± 44	631 ± 65	741 ± 4	23.1 ± 4.1	21.0 ± 3.9	1.83	2.98	1753.8	1410.7	3.11	164.54	305.9	912	0
CaO Bed (07-12)	CB-07-12	4.38	8.87	-	-	667 ± 2	662 ± 7	626 ± 39	584 ± 56	670 ± 19	33.9 ± 6.4	31.8 ± 6.1	1.92	1.63	1750.4	1211.3	-	-	-	-	-
CaO Cycling - 1st Cycle	CCL-07-12-1	33.44	67.72	-	-	712 ± 4	668 ± 20	639 ± 53	537 ± 102	676 ± 23	24.5 ± 2.3	22.2 ± 2.2	2.34	2.05	1086.6	951.9	0.0	19.5	287.4	643.3	0.0
CaO Cycling - 2nd Cycle	CCL-07-12-2	33.44	67.72	-	-	708 ± 10	678 ± 12	638 ± 60	549 ± 104	673 ± 26	24.8 ± 2.3	22.7 ± 2	1.74	2.39	808.9	1110.7	0.0	55.1	276.0	770.5	0.0
CCL (29-10-12) - 1st cycle	CCL-10-12-1	22.59	45.76	-	-	716 ± 3	703 ± 9	707 ± 8	692 ± 15	705 ± 9	24.8 ± 3.8	22.8 ± 3.8	1.86	2.27	862.5	1055.2	0.0	37.6	277.8	739.8	0.0
CCL (29-10-12) - 2nd cycle	CCL-10-12-2	22.59	45.76	-	-	718 ± 6	712 ± 8	716 ± 8	702 ± 13	722 ± 7	21.9 ± 5.2	19.6 ± 5.1	2.04	2.52	949.0	1170.5	0.0	31.4	354.6	784.5	0.0
CCL (29-10-12) - 3rd cycle	CCL-10-12-3			-	-	718 ± 5	709 ± 6	713 ± 6	700 ± 8	722 ± 4	24.8 ± 3.4	22.4 ± 3.2	2.09	2.20	971.7	1024.2	0.0	35.1	324.6	664.5	0.0
CCL (29-10-12) - 4th cycle	CCL-10-12-4	13.08	25.71	-	-	718 ± 5	709 ± 15	713 ± 14	700 ± 19	723 ± 5	22.5 ± 6.0	20.2 ± 5.8	2.08	2.15	965.8	1000.5	0.0	7.9	321.0	671.6	0.0
CCL (29-10-12) - 5th cycle	CCL-10-12-5	13.08	25.71	-	-	719 ± 6	707 ± 10	712 ± 9	697 ± 10	722 ± 7	28.7 ± 6.1	26.8 ± 6.1	1.98	2.23	922.1	1035.9	0.0	33.7	277.7	724.6	0.0
CCL (29-10-12) - 6th cycle	CCL-10-12-6	16.98	34.72	-	-	718 ± 10	699 ± 17	703 ± 20	689 ± 41	709 ± 11	24.2 ± 1.4	22.4 ± 1.2	1.84	2.34	856.0	1087.4	7.7	26.6	303.3	749.8	0.0
CCL (29-10-12) - 7th cycle	CCL-10-12-7	16.98	34.72	-	-	717 ± 6	701 ± 13	705 ± 13	691 ± 17	711 ± 6	23.4 ± 2.5	21.6 ± 2.4	1.59	2.17	738.5	1008.2	2.5	11.5	264.0	730.2	0.0
CCL (29-10-12) - 8th cycle	CCL-10-12-8			-	-	716 ± 9	699 ± 13	704 ± 13	690 ± 12	710 ± 4	24.5 ± 3.3	23.0 ± 3.2	1.34	1.85	624.3	859.3	0.0	39.4	169.5	650.4	0.0
Sand Bed Average		26.89	52.05	0.18	5.47	755	724	708	617	762	14.8	12.8	2.01	1.73	1767.5	1485.0	0	446.88	0	0	1404.3
CaCO3 Bed Average		17.18	33.07	0.55	17.7	775	719	694	620	774	14.7	12.7	1.59	2.13	1503.6	1196.8	-	-	-	-	-
CaO Bed Average		22.00	41.90	0.19	4.32	707	680	647	575	690	26.6	24.4	1.96	2.26	1349.9	1171.2	1.036667	79.7	289.8	775.3	0
CaO Cycling Average		17.55	35.40			718	705	709	695	716	24.3	22.3	1.8525	2.21625	861.2275	1030	1.265	27.9	286.6	714.4	0
Change with CaO bed vs Sand Bed		-26%	-26%	6%	-21%																

Calcium Utilization (%)		Breakthrough Time (min)	Gas Flow (l) Produced	Measured Flows		Gases (m ³ /kg)	Utilization Efficiency (%)		Cycle Utilization Efficiency (%)		Average HHV (kJ/m ³)	Syngas Energy/mass Frier		Cold Gas Efficiency	
X	dX			Biomass (g)	Water (g)		ηC	ηH	Carbon	Hydrogen		kW	kW		
-	-	-	719.0	1585	2235	0.454	33.6	12.8	-	-	13348	0.53	1.273	29.7%	
-	-	-	606.0	981	2306	0.618	47.9	12.4	-	-	13250	0.92	1.273	40.2%	
-	-	-	1017.1	1088	1713	0.934	24.1	24	-	-	10867	1.35	1.273	49.9%	
-	-	-	587.0	1199	3399	0.490	42.2	3.8	-	-	7717	0.40	0.849	18.6%	
	45	104.5	1377.0	1407	3362	0.979	62	24.5	-	-	11311	1.85	1.273	54.4%	
		66	305.0	486	1339	0.628	36	17.4	-	-	12478	0.89	1.105	38.5%	
	59	64.3	413.0	673	1609	0.613	53.3	15.5	-	-	13069	1.40	1.273	39.4%	
	48	67.5	404.0	634	1514	0.638	47.2	17.4	-	-	13545	1.45	1.273	42.4%	
	50	19	50.7	429.0	568	1398	0.756	41.4	18.2	79.1	16.1	12127	1.44	1.273	45.0%
	60	38	66.5	743.7	783	1871	0.950	61.7	21.9	83.2	22.6	11630	1.33	1.273	54.2%
	65	14	67	688.4	718	1850	0.958	54.7	22.2	95	21.9	11587	1.34	1.273	54.5%
	63	19	70.6	792.2	778	1934	1.018	56.6	23.8	91.4	23.8	11277	1.42	1.273	56.4%
	51	9	50.5	332.7	459	867	0.725	49.9	24	86.5	18.6	11667	1.37	1.273	41.5%
	54	20	73.9	644.4	760	1591	0.848	56	19.6	91.7	18.9	11677	1.37	1.273	48.6%
	48	30	63.2	635.4	732	1803	0.868	59	19.9	82.7	17.5	11734	1.32	1.273	50.0%
	35	34	53.8	663.9	697	1666	0.952	59	21.4	86	21.4	12110	1.07	1.273	56.6%
	-	-	662.5	1283	2271	0.536	40.75	12.60	-	-	13299	0.72	1.273	35.0%	
	-	-	802.0	1143	2556	0.712	33.15	13.90	-	-	9292	0.83	1.061	32.5%	
	50.67	-	75.575	624.8	800	1956	0.714	54.17	19.13	-	-	12642	1.40	1.252	44.4%
	53.25	22.875	62.025	616	687.0	1622.5	0.88	54.79	21.38	86.95	20.10	11726	1.33	1.273	50.9%
							49%	34%	61%			-8%	89%	-1%	36%

Table A18.2: Cycle values from peak production

Run	Syn Gas Concentration (vol%)						Produced Gases							Gas Yield			HHV (kJ/m ³)		
	H ₂	CO	CH ₄	CO ₂	C2+	total	P2	T5	T6	T7	T8	T9	Gas Flow (LPM)	Fuel Flow (g/min)	(m ³ [gas]/kg[fuel])	ηC		ηH	
Sand Bed	SB-04-12	50.5	22.7	7.8	18.2	0.7	100.00	8.6	850	819	785	729	832	2.90	7.50	0.386	0.2229	0.1349	11002
Sand Bed 2	SB-08-12	42.8	17.9	8.7	26.1	3.7	99.26	22.7	706	663	653	539	767	4.59	7.50	0.611	0.4661	0.1240	12081
Limestone Bed (04-12)	LB-04-12	47.3	16.0	5.3	29.8	1.7	100.00	15.9	840	775	768	620	850	8.31	7.50	1.108	0.2457	0.3799	9711
Limestone Bed (06-12)	LB-06-12	39.2	17.0	3.1	39.1	1.0	99.36	15.8	747	725	732	731	737	3.08	5.01	0.616	0.4164	0.0289	7704
CaO Bed (06-12)	CB-06-12	76.2	7.3	6.7	10.8	2.0	102.98	28.7	745	696	697	682	743	9.09	7.50	1.211	0.5393	0.3285	12205
CaO Bed (07-12)	CB-07-12	76.5	5.8	8.6	7.2	2.0	100.00	35.8	670	664	637	467	654	4.18	6.51	0.641	0.3473	0.1863	12733
CaO Cycling - 1st Cycle	CCL-07-12-1	69.4	8.3	8.0	11.9	3.0	100.53	20.1	719	700	705	690	702	6.44	7.50	0.858	0.4572	0.2947	13007
CaO Cycling - 2nd Cycle	CCL-07-12-2	74.3	7.3	6.9	9.2	2.6	100.44	21.8	690	699	703	694	707	6.80	7.50	0.906	0.3960	0.3194	12806
CCL (29-10-12) - 1st cycle	CCL-10-12-1	75.2	4.0	6.8	12.8	1.8	100.52	23.4	720	713	716	707	717	7.38	7.50	0.983	0.4342	0.2695	11721
CCL (29-10-12) - 2nd cycle	CCL-10-12-2	70.0	8.0	5.2	15.0	1.3	99.53	22.9	714	717	720	712	723	7.38	7.50	0.983	0.5236	0.2604	10787
CCL (29-10-12) - 3rd cycle	CCL-10-12-3	71.4	7.6	5.9	13.6	1.5	99.98	22.2	715	712	715	706	717	7.17	7.50	0.956	0.4137	0.2547	11247
CCL (29-10-12) - 4th cycle	CCL-10-12-4	73.1	6.9	5.9	12.8	1.6	100.25	25.3	713	713	716	708	720	7.45	7.50	0.993	0.4329	0.2794	11394
CCL (29-10-12) - 5th cycle	CCL-10-12-5	71.9	7.2	6.0	13.8	1.8	100.65	36.5	718	718	720	699	728	7.19	7.50	0.958	0.4684	0.2810	11469
CCL (29-10-12) - 6th cycle	CCL-10-12-6	65.5	10.6	6.6	15.1	2.1	100.00	23.1	719	713	718	707	722	7.04	7.50	0.938	0.5077	0.2420	11681
CCL (29-10-12) - 7th cycle	CCL-10-12-7	69.5	9.2	6.9	12.2	2.2	100.00	27.7	719	712	715	706	717	6.56	7.50	0.874	0.4810	0.2475	12042
CCL (29-10-12) - 8th cycle	CCL-10-12-8	68.7	8.6	7.1	12.8	2.6	99.79	19.7	710	703	708	701	709	5.22	7.50	0.695	0.4082	0.1884	12328
Sand Bed Average		46.7	20.3	8.3	22.1	2.2	99.63	15.62	778	741	719	634	799	3.74	7.505	0.499	0.3445	0.1295	11542
CaCO ₃ Bed Average		43.2	16.5	4.2	34.4	1.4	99.68	15.84	794	750	750	676	794	5.70	6.255	0.862	0.3311	0.2044	8708
CaO Bed Average		74.1	7.2	7.6	9.8	2.4	100.99	26.58	706	690	686	633	701	6.63	7.257	0.904	0.4350	0.2822	11952
CaO Cycling Average		70.7	7.8	6.3	13.5	1.9	100.09	25.10	716	713	716	706	719	6.92	7.505	0.923	0.4587	0.2529	11584
Change with CaO bed vs Sand Bed		55%	-63%	-16%	-47%	-4%										83%	30%	107%	2%

Appendix 19: Typical Equilibrium Model Output

Table A19.1: Typical stream table from ASPEN equilibrium model

Sorbent Enhanced Gasification									
Stream ID		SYNGAS	BIOMASS	COOLGAS	FUEL	PRODUCT	SORBENT	STEAM	ASH
Temperature	C	650.0		20.0	25.0	650.0		400.0	
Pressure	bar	1.200	1.000	1.200	1.200	1.200	1.200	1.200	
Vapor Frac		1.000		0.486	0.921	1.000		1.000	
Mass Flow	kg/hr	0.850	0.000	0.850	0.242	0.850	0.000	1.092	0.000
Volume Flow	cum/hr	4.906	0.000	0.758	0.386	4.906	0.000	2.822	0.000
Enthalpy	Gcal/hr	-0.002		-0.003	> -0.001	-0.002		-0.003	
Density	kg/cum	0.173		1.120	0.627	0.173		0.387	
Mass Flow	kg/hr								
H2		0.071		0.071	0.025	0.071			
CO		0.012		0.012		0.012			
CH4		0.001		0.001		0.001			
CO2		0.045		0.045		0.045			
O2		trace		trace	0.180	trace			
N2		< 0.001		< 0.001	< 0.001	< 0.001			
C									
CAO									
CACO3									
H2O		0.721		0.721	0.036	0.721		1.092	
S					< 0.001				
SO2		trace		trace		trace			
H2S		< 0.001		< 0.001		< 0.001			
Mole Flow	kmol/hr								
H2		0.035		0.035	0.013	0.035			
CO		< 0.001		< 0.001		< 0.001			
CH4		< 0.001		< 0.001		< 0.001			
CO2		0.001		0.001		0.001			
O2		trace		trace	0.006	trace			
N2		trace		trace	trace	trace			
C									
CAO									
CACO3									
H2O		0.040		0.040	0.002	0.040		0.061	
S					trace				
SO2		trace		trace		trace			
H2S		trace		trace		trace			
Temperature	C	650.0	25.0	20.0	25.0	650.0	20.0	400.0	650.0
Pressure	bar	1.200	1.000	1.200	1.200	1.200	1.200	1.200	1.200
Mass VFrac		1.000	0.000	0.165	0.473	0.310	0.000	1.000	0.000
Mass Flow	kg/hr	0.850	0.450	0.850	0.450	2.742	1.200	1.092	1.892
Volume Flow TOTAL	cum/hr	4.906	< 0.001	0.758	0.386	4.906	< 0.001	2.822	0.001
Enthalpy	Gcal/hr	-0.002	-0.001	-0.003	> -0.001	-0.007	-0.003	-0.003	-0.005
Density TOTAL	kg/cum	0.173	1261.242	1.120	1.166	0.559	3297.631	0.387	2765.569
Mass Flow TOTAL	kg/hr								
H2		0.071		0.071	0.025	0.071			
CO		0.012		0.012		0.012			
CH4		0.001		0.001		0.001			
CO2		0.045		0.045		0.045			
O2		trace			0.180	trace			
N2		< 0.001		< 0.001	< 0.001	< 0.001			
C					0.207				
CAO						0.320	1.200		0.320
CACO3						1.571			1.571
H2O		0.721		0.721	0.036	0.721		1.092	
S					< 0.001				
SO2		trace		trace		trace			
H2S		< 0.001		< 0.001		< 0.001			
BIOMASS			0.450						
ASH					0.001	0.001			0.001

Table A19.: Typical stream table from ASPEN equilibrium model, continued.

MOLECONC	mol/l								
H2		0.007	0.000	0.046	0.033	0.007	0.000	0.000	0.000
CO		< 0.001	0.000	0.001	0.000	< 0.001	0.000	0.000	0.000
CH4		< 0.001	0.000	< 0.001	0.000	< 0.001	0.000	0.000	0.000
CO2		< 0.001	0.000	0.001	0.000	< 0.001	0.000	0.000	0.000
O2		< 0.001	0.000	0.000	0.015	< 0.001	0.000	0.000	0.000
N2		< 0.001	0.000	< 0.001	< 0.001	< 0.001	0.000	0.000	0.000
C		0.000	0.000	0.000	0.045	0.000	0.000	0.000	0.000
CAO		0.000	0.000	0.000	0.000	0.001	58.805	0.000	8.334
CACO3		0.000	0.000	0.000	0.000	0.003	0.000	0.000	22.941
H2O		0.008	0.000	0.053	0.005	0.008	0.000	0.021	0.000
S		0.000	0.000	0.000	< 0.001	0.000	0.000	0.000	0.000
SO2		< 0.001	0.000	< 0.001	0.000	< 0.001	0.000	0.000	0.000
H2S		< 0.001	0.000	< 0.001	0.000	< 0.001	0.000	0.000	0.000
BIOMASS		0.000		0.000	0.000	0.000	0.000	0.000	0.000
ASH		0.000	0.000	0.000			0.000	0.000	
MASSSFRA		0.000	1.000	0.000	0.462	0.690	1.000	0.000	1.000
Temperature	C				25.0	650.0	20.0		650.0
Pressure	bar		1.000	1.200	1.200	1.200	1.200	1.200	1.200
Vapor Frac					0.000	0.000	0.000		0.000
Mass Flow	kg/hr	0.000	0.000	0.000	0.207	1.891	1.200	0.000	1.891
Volume Flow	cum/hr	0.000	0.000	0.000	< 0.001	0.001	< 0.001	0.000	0.001
Enthalpy	Gcal/hr				< 0.001	-0.005	-0.003		-0.005
Density	kg/cum				2250.021	2765.118	3297.631		2765.118
Mass Flow	kg/hr								
H2									
CO									
CH4									
CO2									
O2									
N2									
C					0.207				
CAO						0.320	1.200		0.320
CACO3						1.571			1.571
H2O									
S									
SO2									
H2S									
Mole Flow	kmol/hr								
H2									
CO									
CH4									
CO2									
O2									
N2									
C					0.017				
CAO						0.006	0.021		0.006
CACO3						0.016			0.016
H2O									
S									
SO2									
H2S									
Temperature	C		25.0		25.0	650.0			650.0
Pressure	bar		1.000	1.200	1.200	1.200	1.200	1.200	1.200
Vapor Frac			0.000		0.000	0.000			0.000
Mass Flow	kg/hr	0.000	0.450	0.000	0.001	0.001	0.000	0.000	0.001
Enthalpy	Gcal/hr		-0.001		> -0.001	> -0.001			> -0.001
Density	kg/cum		1261.242		3486.884	3486.884			3486.884
Mass Flow	kg/hr								
BIOMASS			0.450						
ASH					0.001	0.001			0.001

Output data file

BLOCK: CHILLER MODEL: HEATER

INLET STREAM: SYNGAS
OUTLET STREAM: COOLGAS
OUTLET HEAT STREAM: Q-REMOVE
PROPERTY OPTION SET: PENG-ROB STANDARD PR EQUATION OF STATE

*** MASS AND ENERGY BALANCE ***

	IN	OUT	RELATIVE DIFF.
CONV. COMP.(KMOL/HR)	0.766912E-01	0.766912E-01	0.00000
(KG/HR)	0.849696	0.849696	0.00000
NONCONV. COMP(KG/HR)	0.00000	0.00000	0.00000
TOTAL BALANCE			
MASS(KG/HR)	0.849696	0.849696	0.00000
ENTHALPY(GCAL/HR)	-0.203627E-02	-0.203627E-02	-0.212978E-15

*** INPUT DATA ***

TWO PHASE TP FLASH
SPECIFIED TEMPERATURE C 20.0000
SPECIFIED PRESSURE BAR 1.20000
MAXIMUM NO. ITERATIONS 30
CONVERGENCE TOLERANCE 0.000100000

*** RESULTS ***

OUTLET TEMPERATURE C 20.000
OUTLET PRESSURE BAR 1.2000
HEAT DUTY GCAL/HR -0.81953E-03
OUTLET VAPOR FRACTION 0.48618
PRESSURE-DROP CORRELATION PARAMETER 0.0000

V-L PHASE EQUILIBRIUM :

COMP	F(I)	X(I)	Y(I)	K(I)
H2	0.45879	0.14980E-06	0.94366	0.62996E+07
CO	0.57264E-02	0.88017E-09	0.11779E-01	0.13382E+08
CH4	0.54500E-03	0.10111E-08	0.11210E-02	0.11087E+07
CO2	0.13342E-01	0.37412E-06	0.27443E-01	73353.
N2	0.38528E-04	0.73454E-11	0.79247E-04	0.10789E+08
H2O	0.52150	1.0000	0.15780E-01	0.15780E-01
SO2	0.11035E-11	0.46208E-14	0.22648E-11	490.12
H2S	0.67318E-04	0.71170E-07	0.13839E-03	1944.5

BLOCK: CYCLONE MODEL: SSPLIT

INLET STREAM: PRODUCT
OUTLET STREAMS: ASH SYNGAS
PROPERTY OPTION SET: PENG-ROB STANDARD PR EQUATION OF STATE

*** MASS AND ENERGY BALANCE ***

	IN	OUT	RELATIVE DIFF.
--	----	-----	----------------

CONV. COMP.(KMOL/HR)	0.980902E-01	0.980902E-01	0.00000
(KG/HR)	2.74051	2.74051	0.00000
NONCONV. COMP(KG/HR)	0.148991E-02	0.148991E-02	0.00000
TOTAL BALANCE			
MASS(KG/HR)	2.74200	2.74200	0.00000
ENTHALPY(GCAL/HR)	-0.714058E-02	-0.714058E-02	0.00000

*** INPUT DATA ***

FRACTION OF FLOW

SUBSTRM=	STRM=	FRAC=
MIXED	SYNGAS	1.00000
CIPSD	ASH	1.00000
NCPSD	ASH	1.00000

*** RESULTS ***

STRM= ASH	SUBSTRM= MIXED	SPLIT FRACT=	0.0
	CIPSD		1.00000
	NCPSD		1.00000

STRM= SYNGAS	SUBSTRM= MIXED	SPLIT FRACT=	1.00000
	CIPSD		0.0
	NCPSD		0.0

BLOCK: DECOMP MODEL: RYIELD

 INLET STREAM: BIOMASS
 OUTLET STREAM: FUEL
 OUTLET HEAT STREAM: Q-DECOMP
 PROPERTY OPTION SET: PENG-ROB STANDARD PR EQUATION OF STATE

*** MASS AND ENERGY BALANCE ***

	IN	OUT	GENERATION	RELATIVE DIFF.
CONV. COMP.(KMOL/HR)	0.00000	0.374877E-01	0.374877E-01	0.00000
(KG/HR)	0.00000	0.448510	-1.00000	
NONCONV COMP(KG/HR)	0.450000	0.148991E-02		0.996689
TOTAL BALANCE				
MASS(KG/HR)	0.450000	0.450000		0.246716E-15
ENTHALPY(GCAL/HR)	-0.695364E-03	-0.695364E-03		0.00000

*** INPUT DATA ***

TWO PHASE TP FLASH
 SPECIFIED TEMPERATURE C 25.0000
 SPECIFIED PRESSURE BAR 1.20000
 MAXIMUM NO. ITERATIONS 30
 CONVERGENCE TOLERANCE 0.000100000

MASS-YIELD

SUBSTREAM MIXED :
 H2 0.567E-01 O2 0.400 N2 0.184E-03
 H2O 0.803E-01 S 0.368E-03
 SUBSTREAM CISOLID :

C 0.459
SUBSTREAM NC :
ASH 0.331E-02

*** RESULTS ***

OUTLET TEMPERATURE C 25.000
OUTLET PRESSURE BAR 1.2000
HEAT DUTY GCAL/HR 0.56188E-03
VAPOR FRACTION 0.92080

V-L PHASE EQUILIBRIUM :

COMP	F(I)	X(I)	Y(I)	K(I)
H2	0.62339	0.12819E-06	0.67702	0.52812E+07
O2	0.27733	0.92173E-06	0.30119	0.32676E+06
N2	0.14565E-03	0.17997E-10	0.15818E-03	0.87889E+07
H2O	0.98872E-01	0.99679	0.21636E-01	0.21706E-01
S	0.25448E-03	0.32130E-02	0.12406E-11	0.38613E-09

BLOCK: GASIFIER MODEL: RGIBBS

INLET STREAMS: STEAM FUEL SORBENT
INLET HEAT STREAM: Q-DECOMP
OUTLET STREAM: PRODUCT
OUTLET HEAT STREAM: Q-GAS
PROPERTY OPTION SET: PENG-ROB STANDARD PR EQUATION OF STATE

*** MASS AND ENERGY BALANCE ***

	IN	OUT	GENERATION	RELATIVE DIFF.
CONV. COMP.(KMOL/HR)	0.119502	0.980902E-01	-0.214118E-01	-0.232260E-15
(KG/HR)	2.74051	2.74051	0.113432E-14	
NONCONV COMP(KG/HR)	0.148991E-02	0.148991E-02		0.00000
TOTAL BALANCE				
MASS(KG/HR)	2.74200	2.74200	0.113371E-14	
ENTHALPY(GCAL/HR)	-0.725306E-02	-0.725306E-02	0.119586E-15	

*** INPUT DATA ***

EQUILIBRIUM SPECIFICATIONS:
ONLY CHEMICAL EQUILIBRIUM IS CONSIDERED, THE FLUID PHASE IS VAPOR
SYSTEM TEMPERATURE C 650.00
TEMPERATURE FOR FREE ENERGY EVALUATION C 650.00
SYSTEM PRESSURE BAR 1.2000

FLUID PHASE SPECIES IN PRODUCT LIST:

H2 CO CH4 CO2 O2 N2 H2O SO2 H2S

SOLIDS IN PRODUCT LIST:

C CAO CACO3

ATOM MATRIX:

ELEMENT	H	C	N	O	S	CA
H2	2.00	0.00	0.00	0.00	0.00	0.00

CO	0.00	1.00	0.00	1.00	0.00	0.00
CH4	4.00	1.00	0.00	0.00	0.00	0.00
CO2	0.00	1.00	0.00	2.00	0.00	0.00
O2	0.00	0.00	0.00	2.00	0.00	0.00
N2	0.00	0.00	2.00	0.00	0.00	0.00
C	0.00	1.00	0.00	0.00	0.00	0.00
CAO	0.00	0.00	0.00	1.00	0.00	1.00
CACO3	0.00	1.00	0.00	3.00	0.00	1.00
H2O	2.00	0.00	0.00	1.00	0.00	0.00
S	0.00	0.00	0.00	0.00	1.00	0.00
SO2	0.00	0.00	0.00	2.00	1.00	0.00
H2S	2.00	0.00	0.00	0.00	1.00	0.00

*** RESULTS ***

TEMPERATURE	C	650.00
PRESSURE	BAR	1.2000
HEAT DUTY	GCAL/HR	-0.44940E-03
NET DUTY	GCAL/HR	0.11248E-03
VAPOR FRACTION		1.0000
NUMBER OF FLUID PHASES		1

FLUID PHASE MOLE FRACTIONS:

PHASE	VAPOR
OF TYPE	VAPOR
PHASE FRACTION	1.000000
PLACED IN STREAM	PRODUCT
H2	0.4587850
CO	0.5726433E-02
CH4	0.5450026E-03
CO2	0.1334208E-01
O2	0.5730241E-22
N2	0.3852798E-04
H2O	0.5214956
SO2	0.1103452E-11
H2S	0.6731758E-04

KMOL/HR 0.7669118E-01

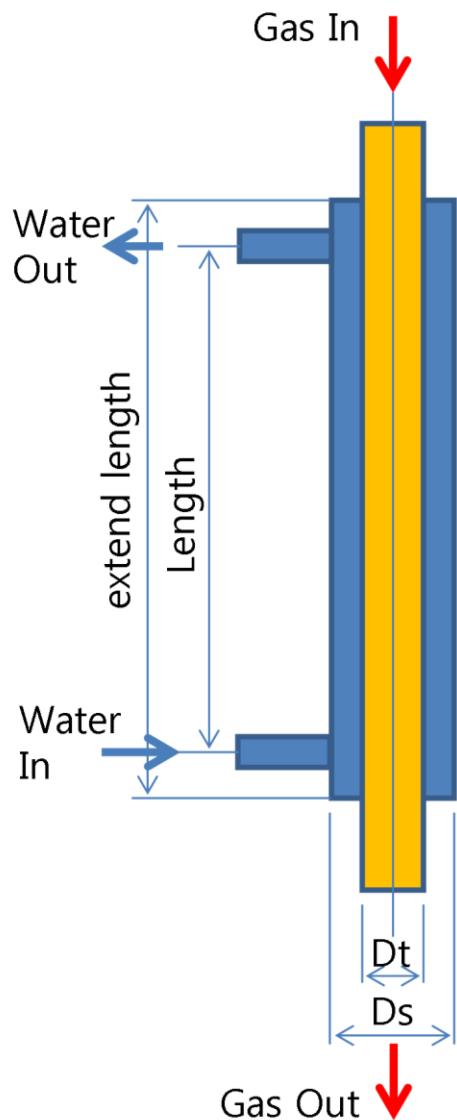
SOLIDS PRESENT AT EQUILIBRIUM, PLACED IN STREAM PRODUCT

SOLID FLOW RATES (KMOL/HR) :

CAO	0.5702162E-02
CACO3	0.1569683E-01

Appendix 20: Condenser System Design Upgrade

Condenser Design



Design Condition

- Counter-flow double pipe
- Gas : assumed N₂
- Cooling Liquid : Water
- Material : Stainless Steel

Gas Condition

- Flow rate : 1.20 kg/h
- Inlet temp. : 400 °C
- Dew temp. : 45 °C
- Pressure : 0.2 kg/cm²G

Cooling Water

- Inlet temp. : 22 °C
- Outlet temp. : 28.5°C
- Flow rate : 16.0 kg/h

Design Result

Heat duty : 104 kcal/kg
 Δt_m : 125 °C

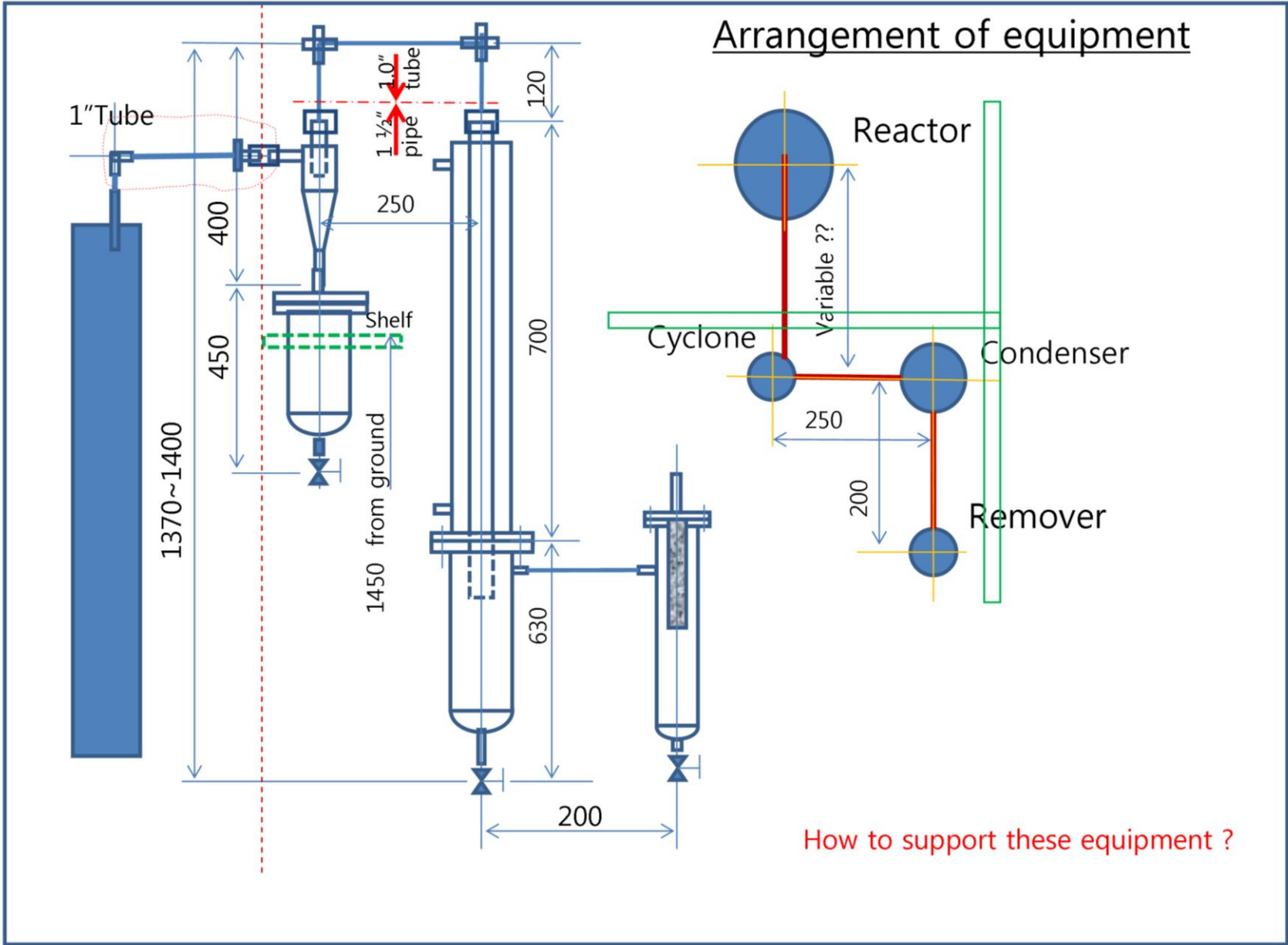
Calculated cooling area : 0.035m²

Gas flow tube (Dt)

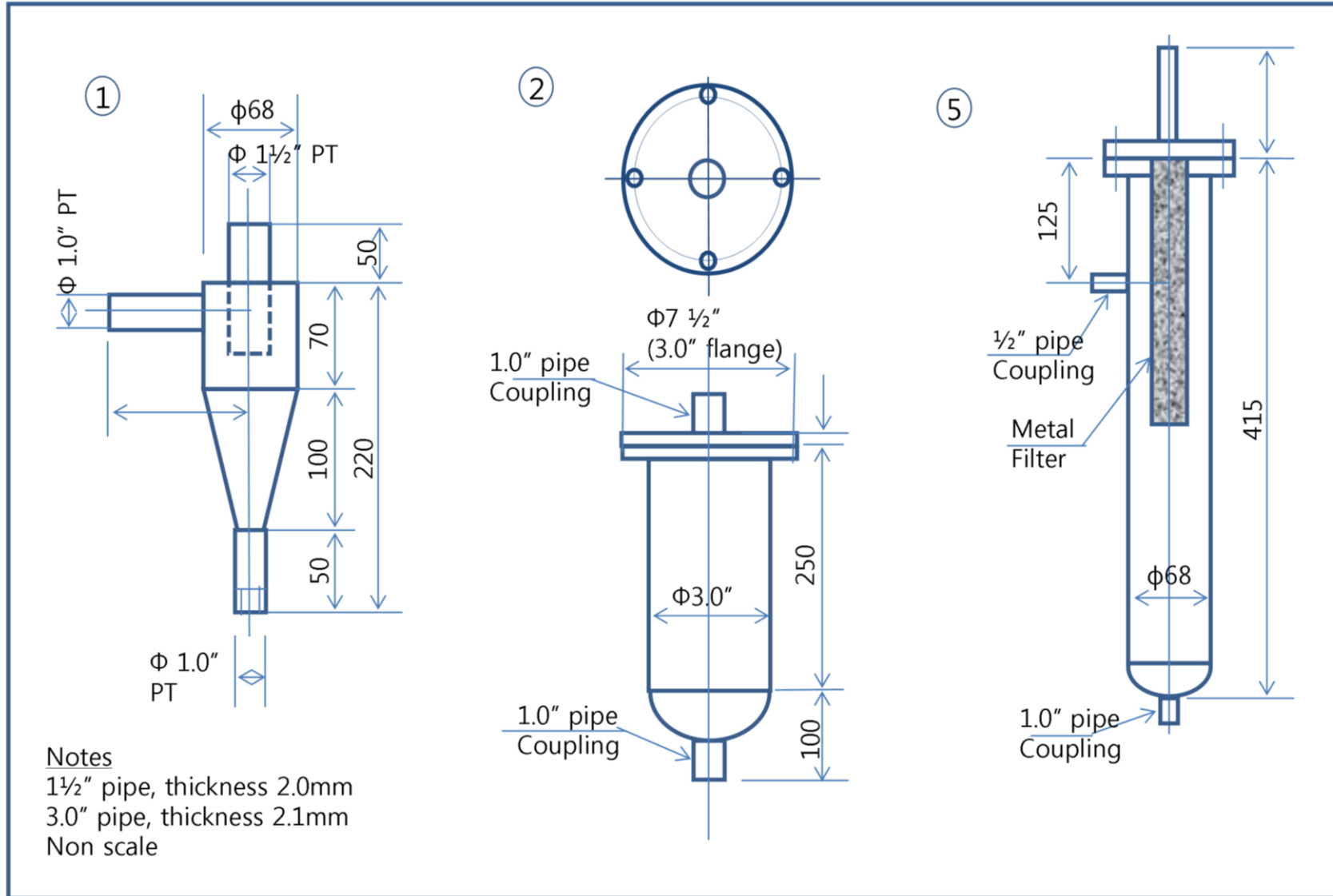
- Di : Φ 44.6mm
- De : Φ 48.6mm(40A)
- thickness : 2.0 mm

Cooling water flow tube

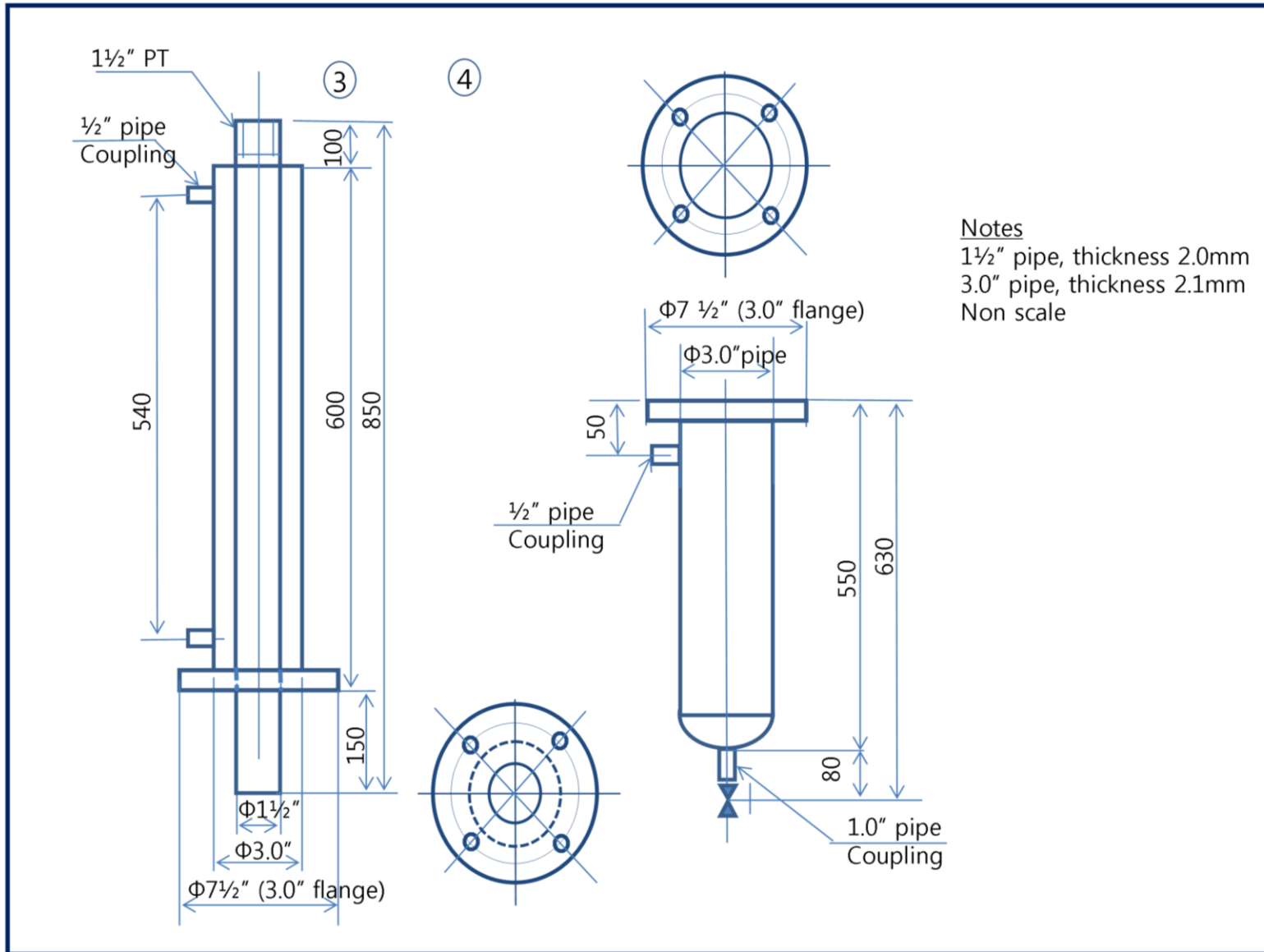
- Ds : Φ 76.3mm(65A)
- length : 540mm
- extend length : 600mm



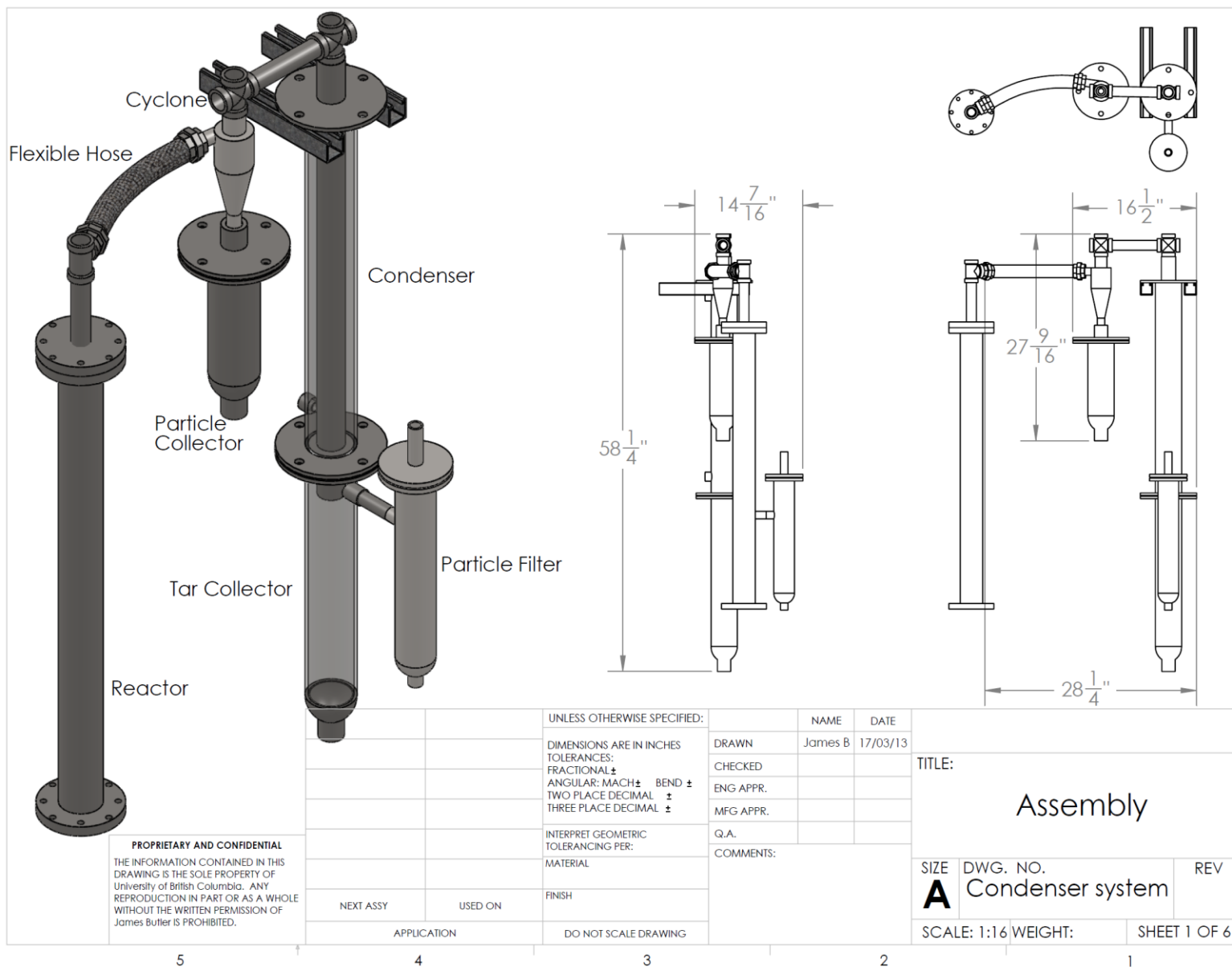
Cyclone, Char Receiver & Tar Remover



Condenser & bio-oil Receiver



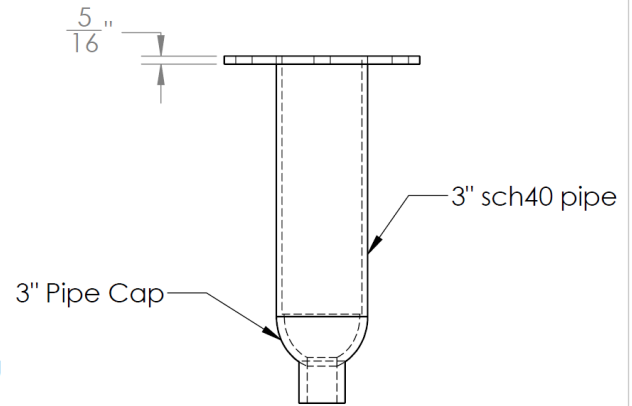
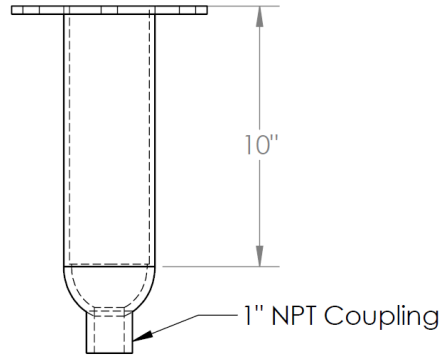
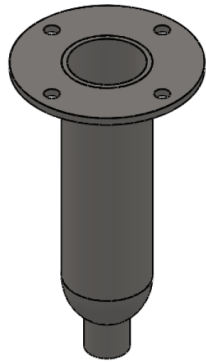
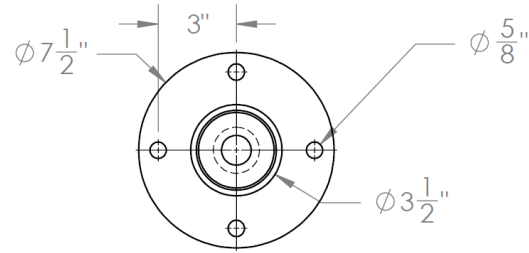
Condenser System Drawings



PROPRIETARY AND CONFIDENTIAL
 THE INFORMATION CONTAINED IN THIS DRAWING IS THE SOLE PROPERTY OF University of British Columbia. ANY REPRODUCTION IN PART OR AS A WHOLE WITHOUT THE WRITTEN PERMISSION OF James Butler IS PROHIBITED.

UNLESS OTHERWISE SPECIFIED:		NAME	DATE
DIMENSIONS ARE IN INCHES		DRAWN	James B 17/03/13
TOLERANCES:		CHECKED	
FRACTIONAL ±		ENG APPR.	
ANGULAR: MACH ± BEND ±		MFG APPR.	
TWO PLACE DECIMAL ±		Q.A.	
THREE PLACE DECIMAL ±		COMMENTS:	
INTERPRET GEOMETRIC TOLERANCING PER:			
MATERIAL			
FINISH			
NEXT ASSY	USED ON		
APPLICATION			
DO NOT SCALE DRAWING			

TITLE:		
Assembly		
SIZE	DWG. NO.	REV
A	Condenser system	
SCALE: 1:16	WEIGHT:	SHEET 1 OF 6



PROPRIETARY AND CONFIDENTIAL
 THE INFORMATION CONTAINED IN THIS DRAWING IS THE SOLE PROPERTY OF University of British Columbia. ANY REPRODUCTION IN PART OR AS A WHOLE WITHOUT THE WRITTEN PERMISSION OF James Butler IS PROHIBITED.

		UNLESS OTHERWISE SPECIFIED:		NAME	DATE	
		DIMENSIONS ARE IN INCHES		DRAWN	James B	17/03/13
		TOLERANCES:		CHECKED		
		FRACTIONAL ±		ENG APPR.		
		ANGULAR: MACH ± BEND ±		MFG APPR.		
		TWO PLACE DECIMAL ±		Q.A.		
		THREE PLACE DECIMAL ±		COMMENTS:		
		INTERPRET GEOMETRIC TOLERANCING PER:				
		MATERIAL				
		FINISH				
NEXT ASSY	USED ON					
APPLICATION		DO NOT SCALE DRAWING				
			TITLE:		Particle Collector	
			SIZE	DWG. NO.	REV	
			A	Condenser system		
			SCALE: 1:6	WEIGHT:	SHEET 2 OF 6	

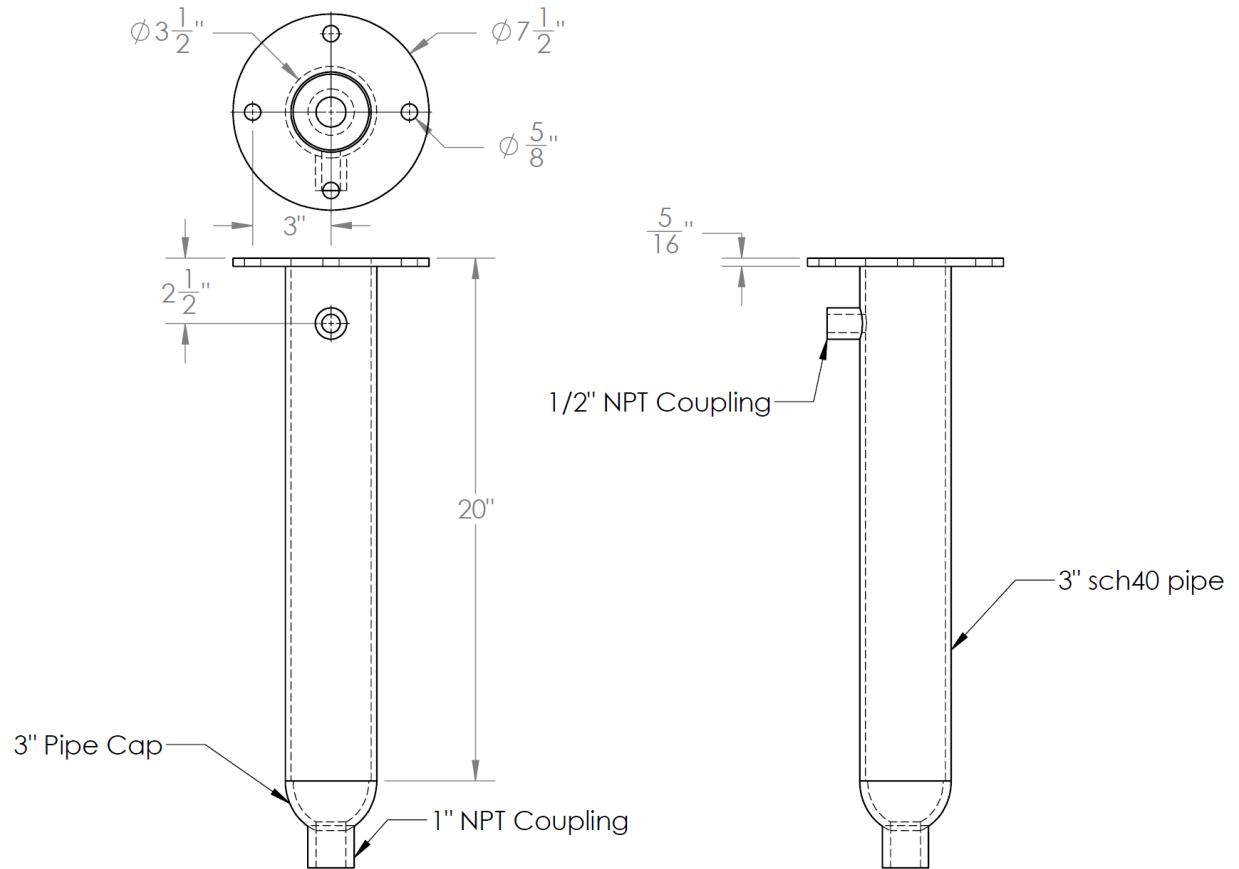
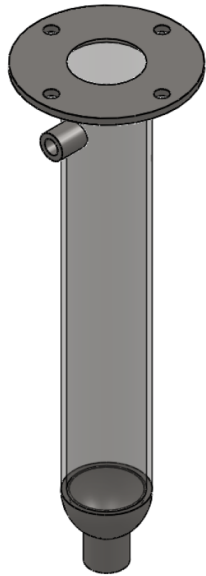
5

4

3

2

1



PROPRIETARY AND CONFIDENTIAL
 THE INFORMATION CONTAINED IN THIS DRAWING IS THE SOLE PROPERTY OF University of British Columbia. ANY REPRODUCTION IN PART OR AS A WHOLE WITHOUT THE WRITTEN PERMISSION OF James Butler IS PROHIBITED.

		UNLESS OTHERWISE SPECIFIED:		NAME	DATE			
		DIMENSIONS ARE IN INCHES	DRAWN	James B	17/03/13	TITLE:		
		TOLERANCES:	CHECKED			Tar Collector		
		FRACTIONAL \pm	ENG APPR.					
		ANGULAR: MACH \pm BEND \pm	MFG APPR.					
		TWO PLACE DECIMAL \pm	Q.A.					
		THREE PLACE DECIMAL \pm	COMMENTS:			SIZE	DWG. NO.	REV
		INTERPRET GEOMETRIC TOLERANCING PER:				A	Condenser system	
		MATERIAL				SCALE: 1:6	WEIGHT:	SHEET 3 OF 6
		FINISH						
NEXT ASSY	USED ON							
APPLICATION		DO NOT SCALE DRAWING						

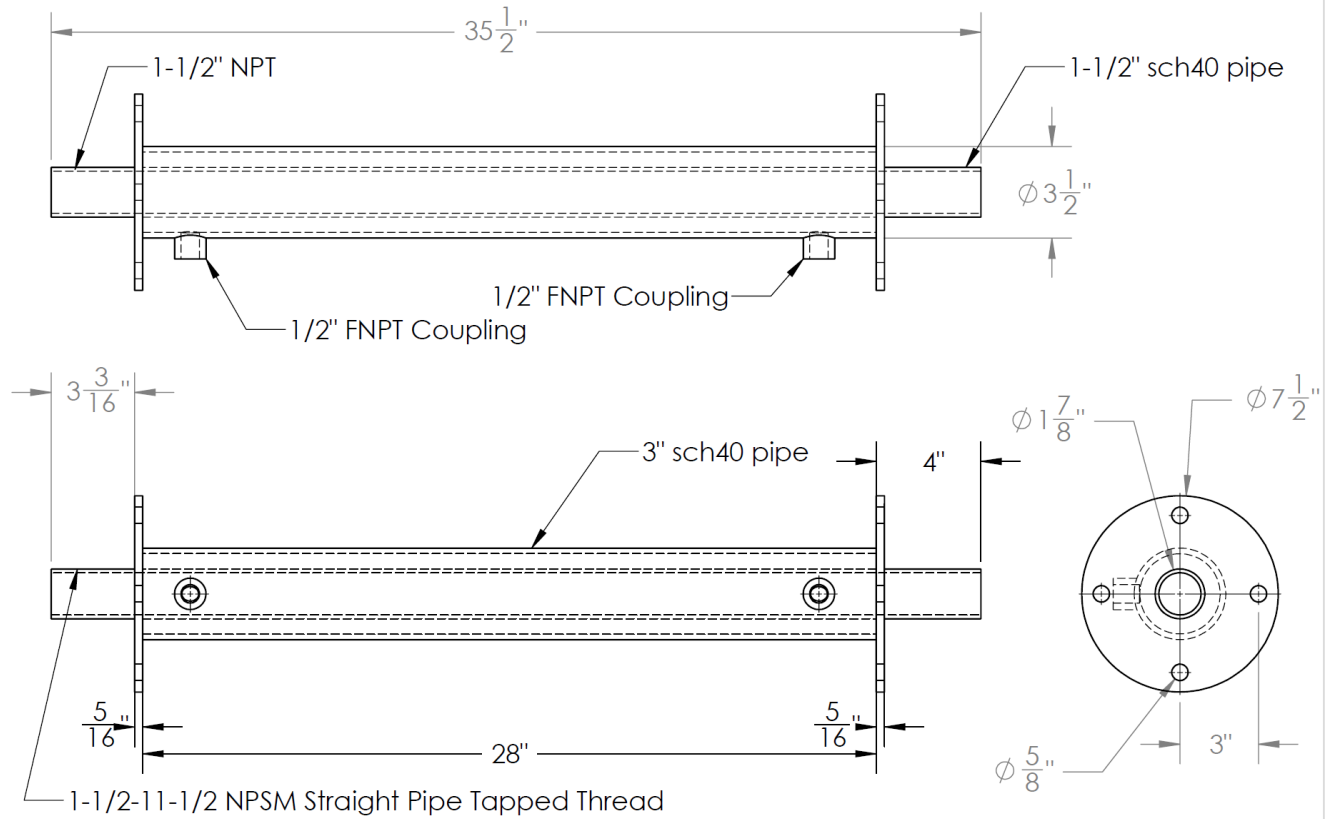
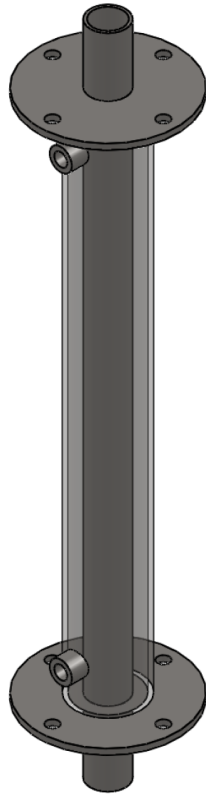
5

4

3

2

1



PROPRIETARY AND CONFIDENTIAL
 THE INFORMATION CONTAINED IN THIS DRAWING IS THE SOLE PROPERTY OF University of British Columbia. ANY REPRODUCTION IN PART OR AS A WHOLE WITHOUT THE WRITTEN PERMISSION OF James Butler IS PROHIBITED.

		UNLESS OTHERWISE SPECIFIED:		NAME	DATE	
		DIMENSIONS ARE IN INCHES	DRAWN	James B	17/02/13	
		TOLERANCES:	CHECKED			TITLE:
		FRACTIONAL ±	ENG APPR.			Condenser
		ANGULAR: MACH ± BEND ±	MFG APPR.			
		TWO PLACE DECIMAL ±	Q.A.			SIZE DWG. NO. REV
		THREE PLACE DECIMAL ±	COMMENTS:			A Condenser system
		INTERPRET GEOMETRIC TOLERANCING PER:				SCALE: 1:6 WEIGHT: SHEET 4 OF 6
		MATERIAL				
		FINISH				
NEXT ASSY	USED ON					
APPLICATION		DO NOT SCALE DRAWING				

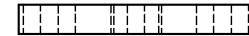
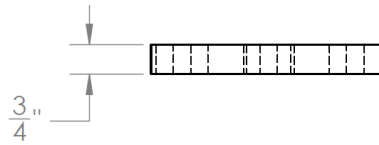
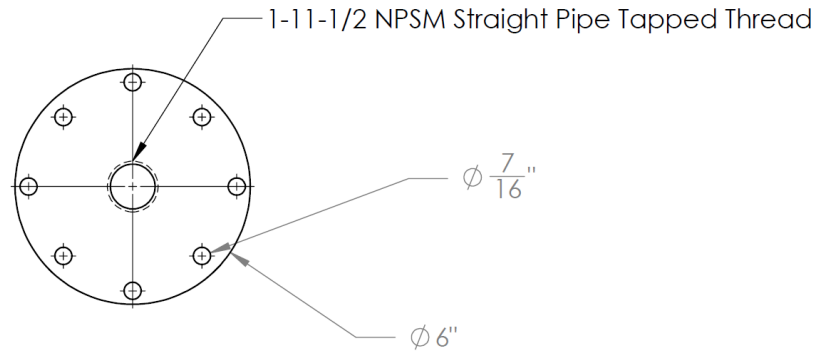
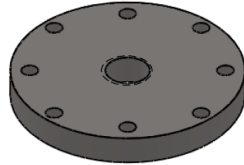
5

4

3

2

1



PROPRIETARY AND CONFIDENTIAL
 THE INFORMATION CONTAINED IN THIS DRAWING IS THE SOLE PROPERTY OF <INSERT COMPANY NAME HERE>. ANY REPRODUCTION IN PART OR AS A WHOLE WITHOUT THE WRITTEN PERMISSION OF <INSERT COMPANY NAME HERE> IS PROHIBITED.

		UNLESS OTHERWISE SPECIFIED:		NAME	DATE	
		DIMENSIONS ARE IN INCHES	DRAWN			TITLE:
		TOLERANCES:	CHECKED			
		FRACTIONAL <MOD-PM>	BEND <MOD-PM>			
		ANGULAR: MACH <MOD-PM>	ENG APPR.			
		TWO PLACE DECIMAL <MOD-PM>	MFG APPR.			SIZE DWG. NO.
		THREE PLACE DECIMAL <MOD-PM>	Q.A.			REV
		INTERPRET GEOMETRIC TOLERANCING PER:	COMMENTS:			Condenser system
		MATERIAL				SCALE: 1:4 WEIGHT:
		FINISH				SHEET 6 OF 6
NEXT ASSY	USED ON	APPLICATION	DO NOT SCALE DRAWING			

5

4

3

2

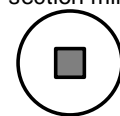
1

Appendix 21: Heat Generation in the Sample Bed

Assumptions:

- no gas flow through bed
- bed treated as single phase (averaged thermal properties)
- lumped capacitance method for heat transfer (isothermal bed)

Parameter	Symbol	Equation	Value	Units	Notes
CaCO ₃ Density	ρ_{CaCO_3}		2021		
Molecular Weight of CaO	MM_{CaO}		50	kg/kmol	
Packed Bed Voidage	ϵ		0.38		
Bed Mass	m_b		150	mg	
Reactor Temperature	T_R		0.00015	kg	
			1000	°C	
Packed Bed Dimensions					
Width of Basket	W_b		0.8	cm	
			0.008	m	
Area of the Basket	A_b	W_b^2	0.000064	m ²	
Bed Volume	V	$\epsilon C_{p(CO_2)} / ((1-\epsilon) \rho_{CaCO_3})$	1.20E-07	m ³	
Bed Height	h		0.0019	m	
			1.87	mm	
Thermal Properties					
Heat Capacity of Air	$C_{p(CO_2)}$		1.278	kJ/kg*K	(@ 900C & 20 bar)
Heat Capacity of CaCO ₃	$C_{p(CaCO_3)}$		0.908	kJ/kg*K	
Heat Capacity of Bed	C_p	$\epsilon C_{p(CO_2)} + (1-\epsilon) C_{p(CaCO_3)}$	1.0486		
Kinematic Viscosity	ν_{CO_2}		5.12E-06	m ² /s	(@ 900C & 20 bar)
Thermal Diffusivity	α_{CO_2}		7.13E-06	m ² /s	(@ 900C & 20 bar)
Thermal Conductivity	k_{CO_2}		8.18E-02	W/m*K	(@ 900C & 20 bar)
Prandtl Number	Pr	$\nu_{CO_2} / \alpha_{CO_2}$	7.19E-01		
Heat of Reaction	Q_R''		178	kJ/mol	
	Q_R'	$Q_R'' * MM_{CaO}$	3560	kJ/kg	
Heat Generated	Q_R	$Q_R' * X * m_b$	0.267	kJ	
Conversion	X		0.5		
Carbonation Rate	r_{carb}		12	mg/s	from experimental data
Calcination Rate	r_{calc}		-30	mg/s	from experimental data
Carbonation Energy	E_R	$r_{carb} * Q_R'$	0.04272	kW	
Carbonation Energy	E_R	$r_{calc} * Q_R'$	-0.1068	kW	
Temperature wo Heat Transfer	T_{wo}	$T_R + Q_R / (m_b * C_{p(CO_2)})$	2698	°C	
Reactor Hydrodynamics					
Gas flow in Reactor	q_R		0.93125	LPM	at ambient
		$T_R / T_{amb} * q_R \{T_{amb}\}$	4.044	LPM	at reactor temperature
			6.74E-05	m ³ /s	
Ractor Diameter	d_R		1.25	in	
			0.03175	m	
Area of Reactor	A_R'	$\pi/4 * d_R^2$	0.000792	m ²	total cross section
	A_R	$A_R' - A_b$	0.000728	m ²	cors section minus basket
Gas Velocity in Reactor	V_R	q_R / A_R	0.0926	m/s	
Reynolds Number	Re_D	$V_R * W_b / \nu_{CO_2}$	144.62		



Parameter	Symbol	Equation	Value	Units	Notes
-----------	--------	----------	-------	-------	-------

Convective Heat Transfer (Lumped Capaciance Method)					
Constant	C		0.246		(Incropera & Dewitt, 2002)
Constant	m		0.588		(Incropera & Dewitt, 2002)

Nusselt Number	Nu_D	$C * Re_D^m * Pr^{1/3}$	4.11		
Heat Transfer Coefficient	h	$Nu_D / D * k_{CO2}$	42.00 W/m ² *K		
			0.042 kW/m ² *K		

$$E_{reaction} - E_{conv} = mc_p \frac{dT}{dt}$$

$$E_R - h(T - T_\infty) = mc_p \frac{dT}{dt}$$

$$\frac{dT}{dt} = \frac{E_R - h(T - T_\infty)}{mc_p}$$

$$\int_{T_\infty}^{T_w} \frac{1}{E_R - h(T - T_\infty)} dT = \int_0^t \frac{1}{mc_p} dt$$

$$\frac{\log[E_R - h(T_2 - T_\infty)]}{h} + \frac{\log[E_R - h(T_1 - T_\infty)]}{h} = \frac{t}{mc_p}$$

since $T_1 = T_\infty$

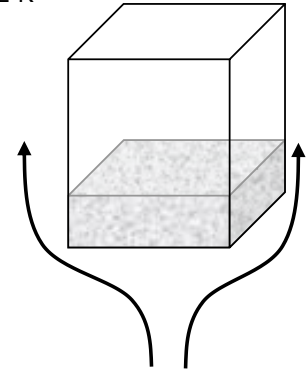
$$\log\left(\frac{E_R}{E_R - h(T_2 - T_\infty)}\right) = \frac{th}{mc_p}$$

$$\frac{E_R}{E_R - h(T_2 - T_\infty)} = 10^{\frac{th}{mc_p}}$$

$$T_2 = T_\infty + \frac{E_R}{h} - \frac{E_R}{h \times 10^{th/(mc_p)}}$$

since $10^{th/(mc_p)} = 10^{80107}$

$$T_2 = T_\infty + \frac{E_R}{h}$$



Particle Bed Temperature	T_2	$T_\infty + E_R / h$	1001.02 °C	Carbonation
Particle Bed Temperature	T_2	$T_\infty + E_R / h$	997.46 °C	Calcination